Large Eddy Simulations of Premixed Turbulent Flame Dynamics: Combustion Modeling, Validation and Analysis

by
Gaurav Kewlani

B. Tech., Mechanical Engineering (2007)
Indian Institute of Technology, Delhi

S. M., Mechanical Engineering (2009)
Massachusetts Institute of Technology, Cambridge

Submitted to the Department of Mechanical Engineering
in Partial Fulfillment of the Requirements for the Degree of
Doctor of Philosophy in Mechanical Engineering
at the
MASSACHUSETTS INSTITUTE OF TECHNOLOGY

September, 2014

Signature of Author ..... Signature redacted .....

Department of Mechanical Engineering
15 August, 2014

Certified By ..... Signature redacted

Professor Ahmed F. Ghoniem
Ronald C. Crane ('72) Professor
Department of Mechanical Engineering
Thesis Supervisor

Signature redacted

Accepted By .....

Professor David E. Hardt
Chairman, Department Committee on Graduate Students

Large Eddy Simulations of Premixed Turbulent Flame Dynamics: Combustion Modeling, Validation and Analysis

by
Gaurav Kewlani

Submitted to the Department of Mechanical Engineering
on 15 August, 2014
in partial fulfillment of the requirements for the degree of
Doctor of Philosophy in Mechanical Engineering

ABSTRACT

High efficiency, low emissions and stable operation over a wide range of conditions are some of the key requirements of modern-day combustors. To achieve these objectives, lean premixed flames are generally preferred as they achieve efficient and clean combustion. A drawback of lean premixed combustion, however, is that the flames are more prone to dynamics. The unsteady release of sensible heat and flow dilatation in combustion processes create pressure fluctuations which, particularly in premixed flames, can couple with the acoustics of the combustion system. This acoustic coupling creates a feedback loop with the heat release that can lead to severe thermo-acoustic instabilities that can damage the combustor. Understanding these dynamics, predicting their onset and proposing passive and active control strategies are critical to large-scale implementation.

For the numerical study of such systems, large eddy simulation (LES) techniques with appropriate combustion models and reaction mechanisms are highly appropriate. These approaches balance the computational complexity and predictive accuracy. This work, therefore, aims to explore the applicability of these methods to the study of premixed wake stabilized flames. Specifically, finite rate chemistry LES models that can effectively capture the interaction between different turbulent scales and the combustion fronts have been implemented, and applied for the analysis of premixed turbulent flame dynamics in laboratory-scale combustor configurations.

Firstly, the artificial flame thickening approach, along with an appropriate reduced chemistry mechanism, is utilized for modeling turbulence-combustion interactions at small scales. A novel dynamic formulation is proposed that explicitly incorporates the influence of strain on flame wrinkling by solving a transport equation for the latter rather than using local-equilibrium-based algebraic models. Additionally, a multiple-step combustion chemistry mechanism is used for the simulations.

Secondly, the presumed-PDF approach, coupled with the flamelet generated manifold (FGM) technique, is also implemented for modeling turbulence-combustion interactions. The proposed formulation explicitly incorporates the influence of strain via the scalar dissipation rate and can result in more accurate predictions especially for highly unsteady flame configurations. Specifically, the dissipation rate is incorporated as an additional coordinate to presume the PDF and strained flamelets are utilized to generate the chemistry databases.

These LES solvers have been developed and applied for the analysis of reacting flows in several combustor configurations, i.e. triangular bluff body in a rectangular channel, backward facing step configuration, axi-symmetric bluff body in cylindrical chamber, and cylindrical sudden expansion with swirl, and their performance has been be validated against experimental observations.

Subsequently, the impact of the equivalence ratio variation on flame-flow dynamics is studied for the swirl configuration using the experimental PIV data as well as the numerical LES code, following which dynamic mode decomposition of the flow field is performed. It is observed that increasing the equivalence ratio can appreciably influence the dominant flow features in the wake region, including the size and shape of the recirculation zone(s), as well as the flame dynamics. Specifically, varying the heat loading results in altering the dominant flame stabilization mechanism, thereby causing transitions across distinct flame configurations, while also modifying the inner recirculation zone topology significantly.

Additionally, the LES framework has also been applied to gain an insight into the combustion dynamics phenomena for the backward-facing step configuration. Apart from evaluating the influence of equivalence ratio on the combustion process for stable flames, the flame-flow interactions in acoustically forced scenarios are also analyzed using LES and dynamic mode decomposition (DMD). Specifically, numerical simulations are performed corresponding to a self-excited combustion instability configuration as observed in the experiments, and it is observed that LES is able to suitably capture the flame dynamics.

These insights highlight the effect of heat release variation on flame-flow interactions in wall-confined combustor configurations, which can significantly impact combustion stability in acoustically-coupled systems. The fidelity of the solvers in predicting the system response to variation in heat loading and to acoustic forcing suggests that the LES framework can be suitably applied for the analysis of flame dynamics as well as to understand the fundamental mechanisms responsible for combustion instability.

KEY WORDS – large eddy simulation, LES, wake stabilized flame, turbulent premixed combustion, combustion modeling, artificially thickened flame model, triangular bluff body, backward facing step combustor, presumed-PDF model, flamelet generated manifold, axi-symmetric bluff body, cylindrical swirl combustor, particle image velocimetry, dynamic mode decomposition, combustion instability, forced response

Thesis Supervisor: Professor Ahmed F. Ghoniem
Title: Ronald C. Crane ('72) Professor, Department of Mechanical Engineering

To *my* Teachers & Guides, Family & Friends, Collaborators & Colleagues

THIS PAGE INTENTIONALLY LEFT BLANK

TABLE OF CONTENTS

LIST OF FIGURES

Chapter 1

Chapter 2

Chapter 3

Chapter 4

Chapter 5

Chapter 6

Chapter 7

LIST OF TABLES

ABBREVIATIONS

ATF	Artificially Thickened Flame
CFD	Computational Fluid Dynamics
CRZ	Central Recirculation Zone
DMD	Dynamic Mode Decomposition
DNS	Direct Numerical Simulations
EBU	Eddy Break-Up
EDC	Eddy Dissipation Concept
FDF	Flame Describing Function
FFT	Fast Fourier Transform
FGM	Flamelet Generated Manifold
FTF	Flame Transfer Function
ILDM	Intrinsic Low Dimensional Manifold
IRZ	Inner Recirculation Zone
ISL	Inner Shear Layer
LDV	Laser Doppler Velocimetry
LES	Large Eddy Simulations
OASPL	Overall Sound Pressure Level
ORZ	Outer Recirculation Zone
OSL	Outer Shear Layer
PaSR	Partially Stirred Reactor
PDF	Probability Density Function
PEA	Partial Equilibrium Assumption
PIV	Particle Image Velocimetry
PLIF	Planar Laser Induced Fluorescence
POD	Proper Orthogonal Decomposition
PSD	Power Spectral Density
PVC	Precessing Vortex Core
QSSA	Quasi Steady State Assumption
RANS	Reynolds Averaged Navier Stokes
SGS	Sub-Grid Scale
TKE	Turbulent Kinetic Energy
VBB	Vortex Breakdown Bubble

Large Eddy Simulations of Premixed Turbulent Flame Dynamics: Combustion Modeling, Validation and Analysis

by
Gaurav Kewlani

Submitted to the Department of Mechanical Engineering
on 15 August, 2014
in partial fulfillment of the requirements for the degree of
Doctor of Philosophy in Mechanical Engineering

ABSTRACT

High efficiency, low emissions and stable operation over a wide range of conditions are some of the key requirements of modern-day combustors. To achieve these objectives, lean premixed flames are generally preferred as they achieve efficient and clean combustion. A drawback of lean premixed combustion, however, is that the flames are more prone to dynamics. The unsteady release of sensible heat and flow dilatation in combustion processes create pressure fluctuations which, particularly in premixed flames, can couple with the acoustics of the combustion system. This acoustic coupling creates a feedback loop with the heat release that can lead to severe thermo-acoustic instabilities that can damage the combustor. Understanding these dynamics, predicting their onset and proposing passive and active control strategies are critical to large-scale implementation.

For the numerical study of such systems, large eddy simulation (LES) techniques with appropriate combustion models and reaction mechanisms are highly appropriate. These approaches balance the computational complexity and predictive accuracy. This work, therefore, aims to explore the applicability of these methods to the study of premixed wake stabilized flames. Specifically, finite rate chemistry LES models that can effectively capture the interaction between different turbulent scales and the combustion fronts have been implemented, and applied for the analysis of premixed turbulent flame dynamics in laboratory-scale combustor configurations.

Firstly, the artificial flame thickening approach, along with an appropriate reduced chemistry mechanism, is utilized for modeling turbulence-combustion interactions at small scales. A novel dynamic formulation is proposed that explicitly incorporates the influence of strain on flame wrinkling by solving a transport equation for the latter rather than using local-equilibrium-based algebraic models. Additionally, a multiple-step combustion chemistry mechanism is used for the simulations.

Secondly, the presumed-PDF approach, coupled with the flamelet generated manifold (FGM) technique, is also implemented for modeling turbulence-combustion interactions. The proposed formulation explicitly incorporates the influence of strain via the scalar dissipation rate and can result in more accurate predictions especially for highly unsteady flame configurations. Specifically, the dissipation rate is incorporated as an additional coordinate to presume the PDF and strained flamelets are utilized to generate the chemistry databases.

These LES solvers have been developed and applied for the analysis of reacting flows in several combustor configurations, i.e. triangular bluff body in a rectangular channel, backward facing step configuration, axi-symmetric bluff body in cylindrical chamber, and cylindrical sudden expansion with swirl, and their performance has been be validated against experimental observations.

Subsequently, the impact of the equivalence ratio variation on flame-flow dynamics is studied for the swirl configuration using the experimental PIV data as well as the numerical LES code, following which dynamic mode decomposition of the flow field is performed. It is observed that increasing the equivalence ratio can appreciably influence the dominant flow features in the wake region, including the size and shape of the recirculation zone(s), as well as the flame dynamics. Specifically, varying the heat loading results in altering the dominant flame stabilization mechanism, thereby causing transitions across distinct flame configurations, while also modifying the inner recirculation zone topology significantly.

Additionally, the LES framework has also been applied to gain an insight into the combustion dynamics phenomena for the backward-facing step configuration. Apart from evaluating the influence of equivalence ratio on the combustion process for stable flames, the flame-flow interactions in acoustically forced scenarios are also analyzed using LES and dynamic mode decomposition (DMD). Specifically, numerical simulations are performed corresponding to a self-excited combustion instability configuration as observed in the experiments, and it is observed that LES is able to suitably capture the flame dynamics.

These insights highlight the effect of heat release variation on flame-flow interactions in wall-confined combustor configurations, which can significantly impact combustion stability in acoustically-coupled systems. The fidelity of the solvers in predicting the system response to variation in heat loading and to acoustic forcing suggests that the LES framework can be suitably applied for the analysis of flame dynamics as well as to understand the fundamental mechanisms responsible for combustion instability.

KEY WORDS – large eddy simulation, LES, wake stabilized flame, turbulent premixed combustion, combustion modeling, artificially thickened flame model, triangular bluff body, backward facing step combustor, presumed-PDF model, flamelet generated manifold, axi-symmetric bluff body, cylindrical swirl combustor, particle image velocimetry, dynamic mode decomposition, combustion instability, forced response

Thesis Supervisor: Professor Ahmed F. Ghoniem
Title: Ronald C. Crane ('72) Professor, Department of Mechanical Engineering

THIS PAGE INTENTIONALLY LEFT BLANK

THIS PAGE INTENTIONALLY LEFT BLANK

1 INTRODUCTION

1.1 Motivation

Lean premixed combustion is a promising approach for many industrial applications (such as large-scale gas turbine systems, automotive and aero-engines) primarily because of its benefits such as lower pollutant emissions and more efficient combustion when compared to non-premixed systems and configurations. A drawback of premixed combustion, however, is that the flame is more prone to thermo-acoustic instability and/or flashback. Combustion instability, therefore, has been one of the more critical phenomena encountered during the development of combustor systems. Specifically, flames at one limit, if not anchored properly, may blow off leading to what is referred to as lean flammability limit or 'static' instability. Recirculating flow in the wake of a bluff body, behind sudden expansion or downstream a swirler, is often used to expand the stability range. However, as the fuel concentration is raised, high amplitude pressure and flow oscillations, i.e. dynamic instability (thermo-acoustic or combustion instability), is often observed. This can cause flame extinction, flame flashback, structural vibration, significant noise or even structural damage (figure 1.1). As such, in order to develop high efficiency, low emission and compact combustors capable of stable operation over a wide range of operating conditions, fundamental mechanisms responsible for these instabilities must be elucidated.

Understanding turbulent combustion mechanisms in such configurations has been challenging and remains an active area of research in the combustion community [1.1]. Numerical modeling and simulations as well as experimental techniques are being increasingly used, therefore, to predict the performance of such systems, for the purpose of developing a fundamental understanding of combustion dynamics and flame stability, as well as assessing the performance in terms of power density, efficiency and emissions, which is critical to their large-scale implementation in practical applications. While detailed measurements of various gaseous species, temperature and velocity profiles inside the combustor can be performed using advanced laser diagnostics with relative ease, repeated measurement of all these variables is an expensive task especially when incorporating geometric changes to modify the combustor performance. Computational Fluid Dynamics (CFD) methods have great potential in predicting the performance of these combustors, and the approach is relatively easy to implement, flexible and cost effective as compared to a detailed experimental investigation.

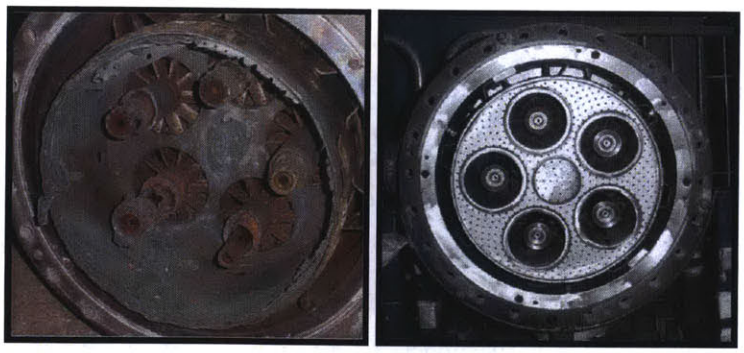

Figure 1.1: (a) Burner assembly damaged by combustion instability, (b) New burner assembly.

Large Eddy Simulations (LES) with appropriate turbulent combustion models and reaction mechanisms is considered as one of the more promising CFD approaches, balancing computational complexity and predictive accuracy. While Direct Numerical Simulation (DNS) resolves all the turbulent scales, it is computationally expensive and impractical for high Reynolds number large-scale applications. Solving the Reynolds Averaged Navier Stokes (RANS) equations, on the other hand, models the influence of turbulence on the mean flow and hence cannot capture the unsteady flow. In LES, rather than averaging the effect of turbulence, the equations are filtered. The larger turbulent eddies are explicitly resolved and computed (as with DNS), and the smallest ones are modeled (as with RANS modeling). This results in better predictions as compared to RANS technique, because the effect of turbulence is represented more accurately since the large eddies (often dependent on the geometry) are explicitly computed. The approach is computationally manageable, as the smaller scales (having more universal features) are modeled. Further, the approach is especially applicable for combustion instability studies, since such flows are highly unsteady and typically exhibit large coherent structures.

Over the past decade, therefore, 3D numerical simulations using the LES framework have been performed for both laboratory-scale research combustors as well as industry test rigs, to study the dynamic behavior of gas turbine combustion [1.1]. The effects of swirl and equivalence ratio on flame dynamics in a swirl combustor has been investigated by researchers [1.2], using a flamelet model (G-Equation) to capture the unsteady vortex-flame and acoustic-flame interactions, and it was observed that the fluctuating pressure amplitudes are attenuated significantly for large values of the swirl number. In another study [1.3], the role of large-scale vortices on the combustion oscillations in a coaxial combustor with and without swirl has been examined, and a passive method of using coaxial flows to decrease the influence of large-scale vortices on the flame has been proposed. Recent work in LES of flame dynamics has also involved the study of equivalence ratio fluctuations

at the combustion chamber inlet and its effect on self-excited combustion instabilities [1.4] for a swirl combustor. LES and experimental fields have been compared in terms of mean and rms fields of temperature, species, velocities and mixture fraction pdfs corresponding to stable and unstable regimes. In a related study [1.5], researchers considered a premixed swirl burner for both non-reacting and reacting cases, and noted a strong precessing vortex core in the non-reacting flows, which disappears when combustion occurs. In another study [1.6], the influences of inlet flow conditions on the combustion dynamics in a lean pre-mixed swirl stabilized combustor has been examined, and the flame bifurcation phenomena and stability boundary as a function of burner operating conditions is investigated. Studies have also been performed for a backward step combustor and the forced response of the combustor to acoustic wave excitations and to equivalence ratio modulations have been compared to experimental measurements [1.7]. Additionally, work has also been performed to evaluate the performance of finite-rate chemistry LES combustion models relative to the flamelet-based approaches, and it has been observed that the former approach resulted in more accurate predictions when compared with experimental measurements for a swirl-stabilized premixed flame in a laboratory gas turbine combustor [1.8]. A more comprehensive summary of the recent work in combustion instabilities can be found in [1.9].

Table 1.1: LES studies of premixed combustion dynamics

Configuration	**Focus of Study**
Swirl stabilized combustor with axi-symmetric chamber [1.2]	Control of combustion instabilities through swirl/equivalence ratio variation
Premixed axi-symmetric combustor with/without swirl [1.3]	Control of combustion oscillations using coaxial flows
Premixed swirl combustor [1.4]	Mean and fluctuating flow fields
Premixed swirl combustor [1.5]	Precessing vortex core
Swirl stabilized combustor with axi-symmetric chamber [1.6]	Flame bifurcation phenomenon and stability boundary
Backward step combustor [1.7]	Forced response to acoustic excitations

These studies have generated significant amount of information about combustion dynamics and flow evolution in specific geometries of concern under well-defined operating conditions. However, substantial work is still required to be able to extract phenomenological information contributing to a deeper understanding and subsequent modeling of the processes of concern. This work, therefore, focuses on the development of suitable combustion models for the analysis of the effects of operating conditions (especially the equivalence ratio) on flame-flow interactions, combustion dynamics, and flame stability.

1.2 Objectives

The primary goal of this research study is to explore the dependence of flame-vortex interaction driven combustion dynamics on the operating conditions (especially the equivalence ratio), using advanced combustion modeling approaches. Specific tasks that have been performed are based on the following objectives:

1.2.1 Implementation of LES Turbulent Combustion Models

The focus is on developing sub-grid scale combustion models for conducting large eddy simulation studies into turbulent premixed combustion. In this regard, LES solvers are implemented that adequately model the flow and turbulence-chemistry interactions, and appropriately account for the effects of strain, detailed combustion chemistry and the boundary conditions.

1.2.2 Validation of LES Solvers

The focus is on evaluating the performance of the high-fidelity LES solvers in simulating turbulent premixed combustion for wake stabilized flames. In this regard, the emphasis is on adequately predicting the unsteady turbulent combustion phenomena, for a variety of combustor geometries, under diverse operating conditions. Specifically, isothermal flow computations as well as stable reacting flow simulations are conducted for canonical combustor configurations, such as a triangular bluff body in a rectangular channel, a backward-facing step, and an axi-symmetric bluff body in a cylindrical duct. Subsequently, the numerical predictions are validated against experimental measurements for each case, to assess the performance of the computational framework in resolving the fundamental flow features and flame dynamics.

1.2.3 Analysis of Flame Dynamics in Laboratory-Scale Combustors

The focus is on utilizing the LES solvers to study combustion dynamics in case of two laboratory-scale combustor configurations: a cylindrical sudden-expansion swirl geometry, and a backward-facing step geometry. The preliminary emphasis is on evaluating the predictive accuracy of the combustion models by comparing the flame macrostructures as well as flow statistics, at different equivalence ratios, with those observed in the experiments. Subsequently, the focus is on analyzing the ability of the numerical framework to resolve the dynamic flow features, as observed in experiments, using the dynamic mode decomposition technique. The dynamic response of the flame for the backward-facing step combustor is also studied, by explicitly imposing velocity perturbations at the inlet. The response of the flame to changes in the operating conditions (equivalence ratio and perturbation amplitude) are analyzed and compared with experimental observations.

1.3 Contributions

1.3.1 Thickened Flame Combustion Model

A novel dynamic formulation to estimate the efficiency function is proposed that explicitly incorporates the influence of strain and time-history effects on flame wrinkling by solving a transport equation for the evolution of the flame surface area. Additionally, a multiple-step combustion chemistry mechanism is used, and reacting flow simulations are performed using the LES solver. Results show that the approach is effective in simulating turbulent premixed combustion and that solving a transport equation to estimate the flame wrinkling rather than using local-equilibrium-based algebraic models can result in more accurate predictions, especially for highly unsteady flame configurations.

1.3.2 Presumed-PDF Combustion Model

A novel presumed-PDF approach, coupled with the flamelet generated manifold (FGM) technique, is utilized for modeling turbulence-combustion interactions in lean premixed reacting flows. The proposed formulation explicitly incorporates the influence of strain via the scalar dissipation rate, which can result in more accurate predictions especially for highly unsteady flame configurations. Specifically, the dissipation rate is incorporated as an additional coordinate to presume the PDF and strained flamelets are utilized to generate the chemistry databases. Reacting flow simulations are performed using the LES solver, and results show that the framework is effective in simulating turbulent premixed combustion and is able to capture the fundamental flame-flow features.

1.3.3 Swirl Combustor Analysis

Turbulent premixed combustion is studied using numerical simulations and modal decomposition techniques in an acoustically-uncoupled cylindrical sudden expansion swirl combustor. The impact of the equivalence ratio on flame-flow dynamics is analyzed. It is observed that increasing the equivalence ratio can appreciably influence the dominant flow features in the wake region, including the size and shape of the recirculation zone(s), as well as the flame dynamics. Specifically, modifying the fuel concentration affects the dominant flame stabilization mechanism, thereby causing transitions across distinct flame configurations; the flow-field topology is also significantly impacted. The numerical framework is able to suitably resolve the effect of heat loading variation on the flow, as well as flame macro-structure, and results match closely with experimental observations. The LES computations are also able to capture the prominent dynamic flow features, estimated using the dynamic mode decomposition technique.

1.3.4 Step Combustor Analysis

Turbulent premixed combustion is studied using numerical simulations in an acoustically-uncoupled backward-facing step combustor. The impact of the equivalence ratio on flame-flow dynamics is analyzed for stable flame configurations. It is observed that increasing the equivalence ratio can appreciably influence the dominant flow features in the wake region, including the size of the recirculation zone(s), as well as the flame dynamics. The numerical framework is able to suitably resolve the effect of heat loading variation on the flow, as well as flame macro-structure, and results match closely with experimental observations. Subsequently, the response of the flame to explicitly imposed inlet velocity perturbations is evaluated for different equivalence ratios and perturbation amplitudes, and it is observed that both these factors result in significantly altering the dynamic response of the flame front. Dynamic mode decomposition of the heat release response and the flow field is also performed to understand the dynamics of flame-flow interactions.

1.4 Organisation of the Thesis

This thesis is organized as follows. In Chapter 2, an introduction to turbulent premixed combustion along with the numerical modeling strategies is presented. This is followed by a description of the artificially thickened flame model in Chapter 3, and the presumed-PDF approach in Chapter 4. Validation studies for each combustion model are also shown. In Chapter 5, the dynamic mode decomposition technique is described and examples to illustrate the applicability of the approach are included. Subsequently, the thickened flame approach is utilized to analyze premixed combustion in a cylindrical swirl geometry in Chapter 6, while results from the application of the model to analyze flame dynamics in a backward-facing step combustor are shown in Chapter 7. Finally, conclusions from the work are presented in Chapter 8, followed by the references.

2 MODELING TURBULENT PREMIXED COMBUSTION

High efficiency, low emissions and stable operation over a wide range of conditions are some of the key requirements of modern-day combustors. To achieve these objectives, lean premixed flames are generally preferred as they achieve efficient and clean combustion. However, since the flames are more sensitive to flame-flow interactions, developing a fundamental understanding of these dynamics is critical prior to large-scale implementation in practical systems. Numerical modeling affords a relatively easy, flexible, and cost-effective means to analyze combustion dynamics and predict the performance of such systems. This chapter provides an overview on premixed combustion, turbulence-flame interactions and the state-of-the-art modeling approaches that have been developed to analyze combustion phenomena.

2.1 Premixed Combustion Overview

The combustion of gaseous fuels involves chemical reactions between the fuel gas and the oxidizer (often air). In technical applications, flames are distinguished as: (i) premixed flame, where fuel and oxidizer are homogeneously mixed before combustion, (ii) non-premixed flame, where mixing and combustion occur simultaneously, and (iii) partially-premixed combustion, where both premixed and non-premixed regions appear. The distinction between premixed and diffusion flame configurations is typically imposed by the geometry of the burner [2.1]. If fuel and oxidizer are injected separately and burning takes place by mixing, a diffusion flame is formed. The process of mixing primarily controls the flame position, i.e. the spatial distribution of heat release, provided the fuel is supplied to the reaction zone at a rate sufficient to sustain the flame. On the contrary, if the fuel and oxidant are homogeneously mixed prior to ignition, a perfectly premixed flame is formed. In this scenario, the chemical aspect is dominant, in general.

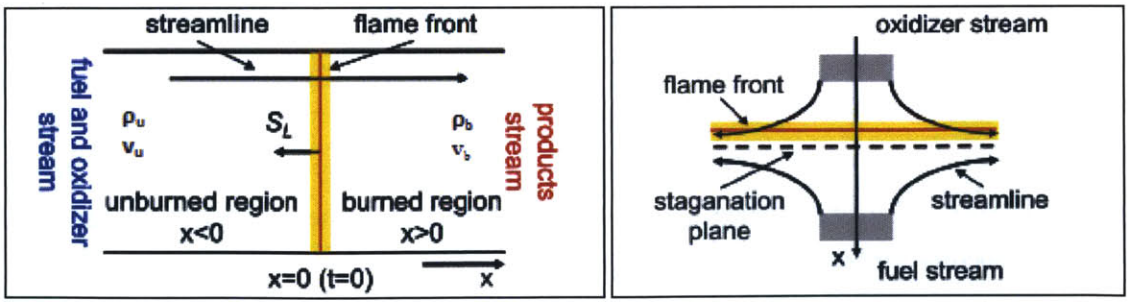

Figure 2.1: (a) Sketch of a planar flame propagating in a stright pipe, (b) Sketch of a counter-flow diffusion flame.

The diffusion flames have a distinct advantage over premixed flames, since they are safer to operate. The fuel is unable to burn before mixing with the oxidant, which prevents the flame from propagating upstream (flashback phenomenon) and damaging the system. Additionally, the system is also easier to design since there is no need to develop a section for premixing. However, a drawback of diffusion flames is that the burning efficiency is controlled and eventually reduced by the mixing of the species. The speed of chemical reactions can slow down when mixing processes do not bring fast enough the reactants into the reaction zone.

In contrast, combustion is typically more efficient in case of a premixed flame configuration. Additionally, the control of the flame speed is simpler with premixed flames than with diffusion flames. The flame velocity scales with the thermal diffusion and does not depend directly on mixing of species; it can therefore be altered by modifying the temperature of the incoming unburned mixture. Moreover, the flame temperature is directly controlled by the stoichiometry of the mixture (as opposed to diffusion flames, where the mixing-dependent flame temperature is not easily controlled). Thus, the production of NO_x can be regulated, since it largely depends on the flame temperature, allowing ease in development of burners with lower pollutant emissions. However, premixed flames are more prone to flashback and thermo-acoustic instability (in particular, for rich mixtures), and can have higher sensitivity to variations in inlet mixture stoichiometry and the flow (in particular, for lean mixtures).

2.2 Premixed Flame Fundamentals

When fuel and oxidizer are well mixed and the mixture ratio keeps within certain flammability limits, the mixture is able to form self-sustaining, propagating reactive waves after ignition. Thus, a premixed flame can be regarded as a wave phenomenon in that the flame propagates towards the combustible mixture while consuming it. Two modes of combustion wave propagation may be identified: (i) detonation, where the wave propagates at supersonic speed as a shock wave and the temperature rise across the shock exceeds the explosion limits of the mixture, and (ii) deflagration: where the wave is sustained by diffusion of species and energy from the reaction zone into the fresh gases ahead. Since diffusive processes are rather slow, the speed of the deflagration wave is in the order of 20-100cm/s for common fuel-air combinations.

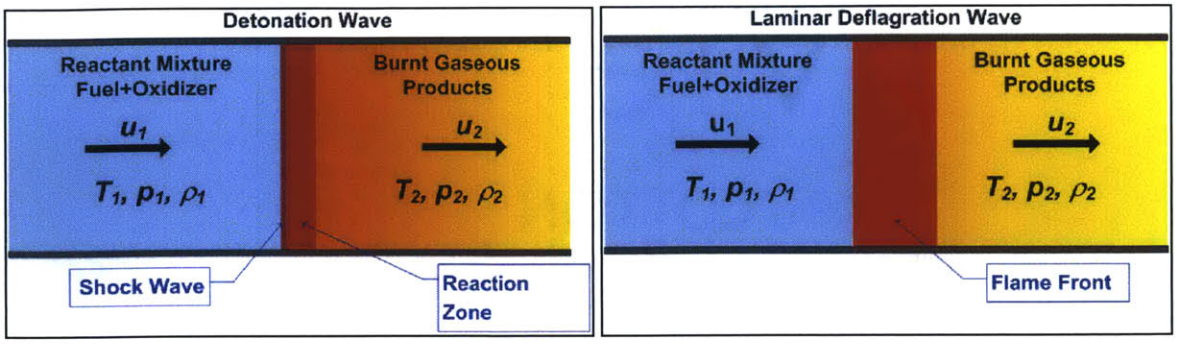

Figure 2.2: (a) Sketch of a detonation wave, (b) Sketch of a laminar deflagration wave.

Specifically, in detonation, combustion is initiated by the advancing of a shock wave, which compresses and heats up the reactant mixture rapidly. This shock wave is then sustained by the energy released from the combustion. Contrary to this, a deflagration wave is sustained by the chemical reaction, and its travelling speed is controlled by the heat conduction and radical diffusion. A prominent difference between the detonation and the deflagration is the pressure jump across the flame. Across the detonation flame, pressure increases greatly (the pressure in burnt side is generally 10-50 times higher than that in unburned side), while in deflagration, the pressure is almost constant across the flame (actually there is a very small decrease). The deflagration wave, which is of interest in case of modern-day combustor systems, can further be categorized as laminar and turbulent premixed flames.

2.2.1 Laminar Premixed Flame

The simplest form of a deflagration wave is the unstretched laminar flat flame, wherein the combustible mixture and combustion products are separated by a thin reacting interface (the flame front). The laminar flame propagates with a flame speed, s_L^o, which is defined as the propagation velocity of the flame front normal to itself and relative to the flow speed of the unburned mixture. The principal structure of a premixed laminar flame is sketched in figure 2.3. The flame front can be divided into three sub-regions: (i) preheat zone, (ii) inner layer, and (iii) oxidation layer.

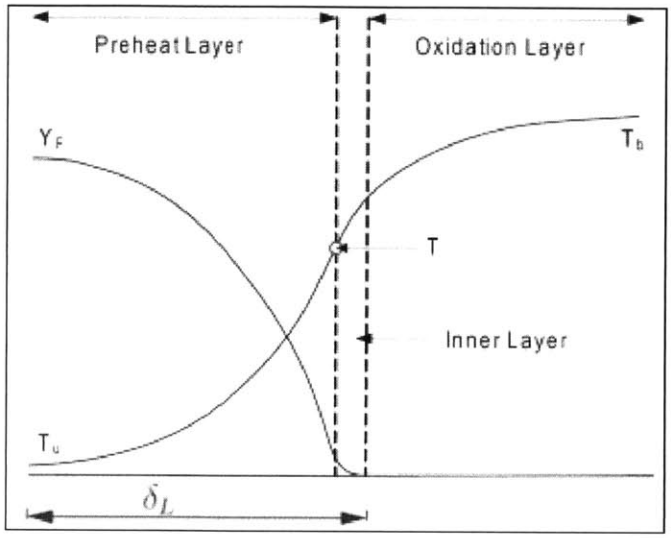

Figure 2.3: Principal structure of a laminar premixed flame.

In the narrow reaction zone, the fuel and oxidizer are rapidly consumed, resulting in significant heat release and a corresponding increase in the temperature. It is important to point out that most of the chemical reactions occur in this thin inner layer, and a peak of concentration of intermediate species such as CO and other radicals is observed as shown in figure 2.4. From this high-temperature zone, radicals and energy diffuse against the convective flow into the fresh gases and cause a temperature rise in the preheat zone. In the preheat zone, the temperature is below the cross-over temperature (1000K), and radical recombination reactions are dominant over radical branching reactions. Hence few chemical reactions occur in this region, which is governed by convection and diffusion processes.

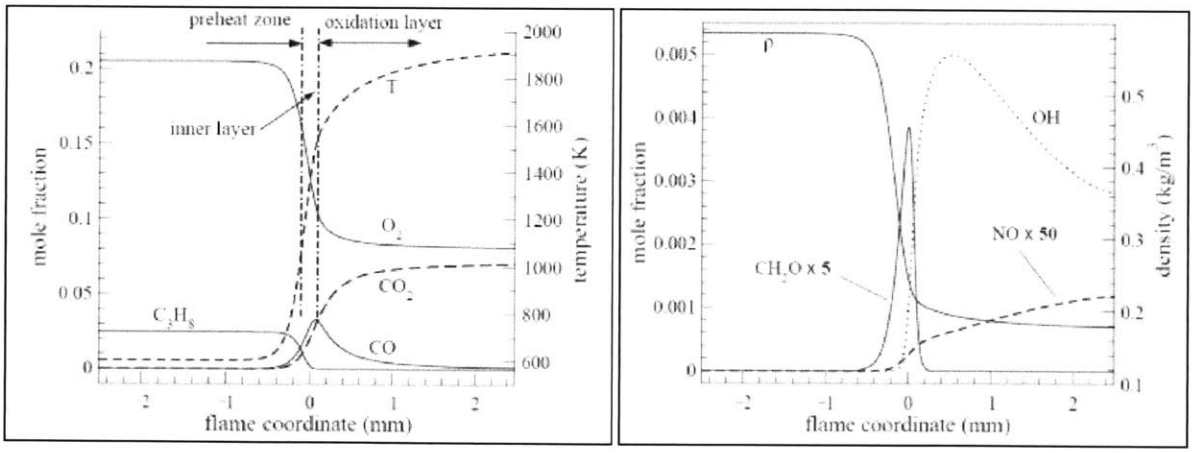

Figure 2.4: C_3H_8-air flame at 1atm, φ=0.6, and with unburned mixture preheated at 600K:
(a) composition and temperature, (b) composition of radicals, NO mole fraction and density.

In the post-flame zone, the radicals and other intermediate species are oxidized, with the product species approaching a steady state. Slow reactions occur in the oxidation layer with minor heat release, with most of the chemical reactions eventually reaching equilibrium. The temperature and the combustion products exhibit a rather flat profile; however, due to high temperature, a few reactions occur such as NO formation and OH radical oxidation (figure 2.4). A control over the oxidation-layer temperature (or residence time of the gas) is necessary in order to prevent formation of harmful pollutant such as NOx or the incomplete combustion of CO or unburned hydrocarbons [2.1].

In order to resolve the flame in numerical computations, the mesh cell size should be smaller than the thickness of the flame. In this regard, the term "flame thickness" generally refers to the thickness of the preheat zones and the reaction zone together, where temperature and species concentrations change as discussed above. Although different definitions of the laminar flame thickness exist, the most common ones include:

- **Diffusive Thickness**

From scaling laws, the flame thickness, δ_L, may be approximated as:

$$\delta_L = \frac{\lambda_u}{\rho_u c_p s_L^o} = \frac{\alpha_u}{s_L^o} \tag{2.1}$$

where λ_u is the conductivity, ρ_u is the density, c_p is the specific heat, s_L^o is the unstrained laminar flame speed, and α_u is the diffusivity. The equation, however, gives too small estimates for the flame thickness.

- **Thermal Thickness**

Based on the temperature profile, the thickness may be expressed as:

$$\delta_L = \frac{T_b - T_u}{\max\left(\frac{dT}{dx}\right)} \tag{2.2}$$

where T_u is the temperature of the unburned mixture, T_b is the temperature of burnt gas, x is the coordinate normal to the flame front, and $\max(dT/dx)$ is the maximum value of the gradient of temperature across the flame front. The equation is usually recommended, because the term with the temperature gradient provides a more precise information for the choice of the mesh refinement.

- **Global Thickness**

This is defined by the distance from $\Theta = 0.01$ to 0.99, where Θ is the reduced temperature based on the unburned T_u and the burnt T_b temperatures.

- **Reaction Thickness**

This considers the inner part of the flame front and may be defined as:

$$\delta_r = \frac{\delta_L}{Ze},\ Ze = \frac{E_a}{RT_b^2}(T_b - T_u) \qquad (2.3), (2.4)$$

where Ze is the Zeldovitch number. The thickness value yields crucial information when compared with the scales of turbulence.

From the laminar flame thickness estimated above, and the laminar flame speed, it is also possible to define a characteristic chemical time scale, t_c. This may be written as:

$$t_c = \frac{\delta_L}{s_L^o} \qquad (2.5)$$

where δ_L and s_L^o refer to the flame thickness and the unstrained laminar flame speed, respectively.

2.2.2 Turbulent Premixed Flame

In most combustion devices of technical importance, the flow is strongly turbulent. Flames in such devices are affected by the turbulent eddies, and the reaction zone is significantly influenced due to interaction with the flow. The flame front in such scenarios also has a significant impact on the flow field resulting in significant deviations, as against the corresponding isothermal scenario [2.2]. This is briefly discussed next.

- **Effect of flame on turbulence**

The presence of a reaction zone can influence the flow turbulence in different ways. Heat release can result in a reduction of the turbulence intensity compared to the cold flow configuration, due to an increase in temperature dependent kinematic viscosity, $\nu(T)$, and a corresponding lowering of the Reynolds number. Specifically, the increased molecular viscosity tends to homogenize the flow, reducing the local magnitude of the velocity gradient, and thus the energy transfer between the different turbulent scales. In contrast, the presence of a flame can also induce additional turbulence due to its fluctuating surface. At the flame interface, where the unburned and burnt gas mix, changes in the local density and baroclinic effects can influence flow dynamics, and the intermittency may result in production of turbulent kinetic energy and the flow may exhibit enhanced turbulence in the presence of combustion.

- **Effect of turbulence on flame**

The propagation of the flame front in a turbulent flow field typically results in a deformation of the reaction zone, which is influenced by the presence of the local flow structures. The turbulent eddies have a significant impact on the flame front: the small eddies ($r < \delta_L$) are likely to enter the flame front, up to the reaction zone and modify the intrinsic structure of the flame front, while the larger coherent vortex structures ($r > \delta_L$) generally augment the wrinkling of the flame. The effect of the turbulent eddies on the flame front, in terms of the stretching and wrinkling of the interface, also depends on the velocity ratio u_t / s_L^o, where u_t is the turbulent flow velocity (figure 2.5).

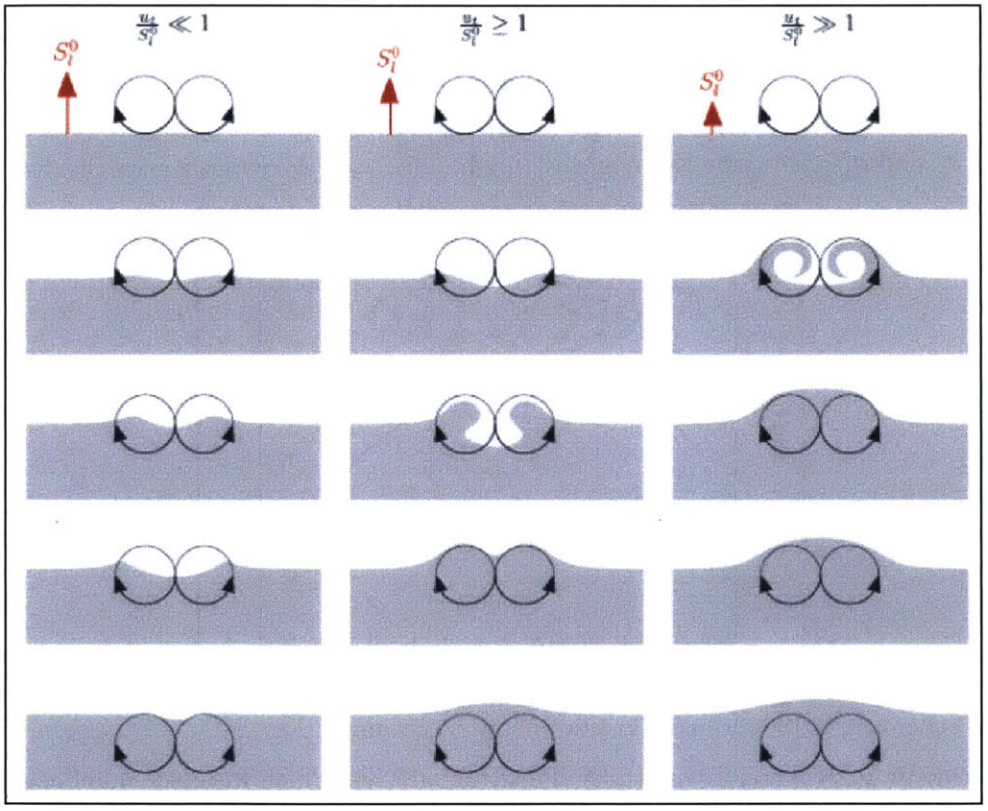

Figure 2.5: Influence of the eddy velocity on turbulence-flame interaction.

Since turbulence contains a large spectrum of eddy size and velocity, dimensionless numbers (comparing different time and length scales respectively) have been defined to represent and qualify the interaction between a premixed flame and the turbulent eddies, and to establish the different regimes of turbulent premixed combustion. This is discussed in the next section, wherein the length and time scales are presented, followed by the dimensionless numbers, and subsequently, the combustion diagram and the different regimes are explained.

2.3 Premixed Combustion Regimes

2.3.1 Length and Time Scales

In case of a turbulent flow field, eddies of varying sizes possess different amounts of kinetic energy. The turbulent kinetic energy contained in the large-scale eddies is continuously transferred to eddies of smaller and smaller sizes, until it is dissipated by viscous action. Kolmogorov postulated that for sufficiently high Reynolds numbers, the statistics of the small-scale turbulent motions are determined by the kinematic viscosity of the fluid, ν, and the rate of dissipation of the turbulent kinetic energy, ε. The Kolmogorov length, time, and velocity scales which represent the smallest scales in the turbulent flow are given by the following expressions:

$$\eta_k = \left(\frac{\nu^3}{\varepsilon}\right)^{1/4}, \tau_k = \sqrt{\frac{\nu}{\varepsilon}}, u'_k = (\nu\varepsilon)^{1/4} \qquad (2.6), (2.7), (2.8)$$

where η_k, τ_k and u'_k refer to the Kolmogorov length, time, and velocity scale respectively.

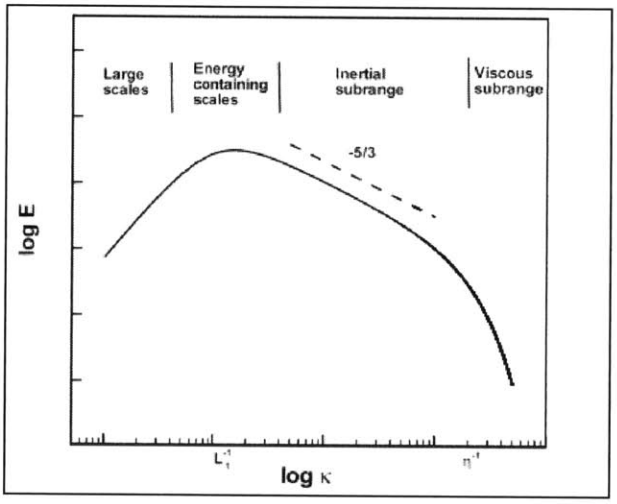

Figure 2.6: Schematic of the turbulent kinetic energy spectrum.

Furthermore, Kolmogorov postulated that for sufficiently high Reynolds numbers, there is a range of length scales through which the energy transfer rate is uniquely determined by ε. This range of length scales, defined for the region where $L_t \gg \ell \gg \eta_k$ (here L_t and η_k refer to the integral and Kolmogorov length scales respectively) is called the inertial sub-range. On dimensional grounds, the rate of energy transfer in this range is found to be:

$$\varepsilon \approx \frac{u'^3}{L_t} \approx \frac{k^{3/2}}{L_t} \qquad (2.9)$$

where u' and k refer to the rms velocity fluctuation and turbulent kinetic energy respectively.

Another length scale of interest, which is intermediate between L_t and η_k, is the Taylor micro-scale, λ_T. It can be understood as the distance that a large eddy convects an eddy of size η_k during the time τ_k, and is given by:

$$\lambda_T = \left(\frac{15\nu u'^2}{\varepsilon}\right)^{1/2} \qquad (2.10)$$

The fundamental time scales other than the Kolmogorov time scale include the time scale of premixed combustion, τ_c, and the turbulent mixing time scale, τ_t, given as:

$$\tau_c = \frac{\delta_L}{s_L^o}, \tau_t = \frac{L_t}{u'} = \frac{k}{\varepsilon} \qquad (2.11), (2.12)$$

$$where\ u' = \sqrt{k}, L_t = \frac{u'^3}{\varepsilon} \qquad (2.13), (2.14)$$

where L_t, u', δ_L, k, ε and s_L^o are the integral length scale, the root mean square (RMS) velocity fluctuation, the laminar flame thickness, the turbulent kinetic energy, the rate of dissipation of the turbulent kinetic energy, and the laminar flame speed respectively.

2.3.2 Dimensionless Numbers

The regimes of premixed flames have been developed to help the understanding of the possible interaction between the premixed flame front and the turbulent eddies [2.1-2.4]. These regimes, commonly visualized in the form of a combustion diagram, are usually discussed in terms of velocity and length scale ratios, are quite well delimited (figure 2.7), and are based on non-dimensional numbers defined below.

- **Turbulent Reynolds number**

The Reynolds number, Re, evaluates the convective force relative to the diffusion force. It is based on global scale and a sole value is relevant for a geometry (which gives the reference scale, L), and for a duty point (which gives the reference velocity, U). A turbulent Reynolds number, Re_t, is similarly defined locally, using the turbulent scales, and compares the kinematic diffusion due to turbulence to the molecular kinematic diffusion:

$$Re_t = \frac{u'L_t}{\nu} \qquad (2.15)$$

With the assumption $Sc = 1$, and using $\delta_L = \alpha_u / s_L^o = \nu / s_L^o$, the turbulent Reynolds number can be re-written as:

$$Re_t = \frac{u' L_t}{s_L^o \delta_L} \tag{2.16}$$

The turbulent Reynolds number is directly expressed with turbulent variables and provides a more precise evaluation of the actual and local turbulence property, since the integral length scale L_t and velocity fluctuations u' are likely to differ at different locations of the geometry considered. It also measures the ratio between the largest L_t and the smallest Kolmogorov turbulent scales:

$$\frac{L_t}{\eta_k} = Re_t^{3/4} \tag{2.17}$$

- **Turbulent Damköhler Number**

The (turbulent) Damköhler number, Da, is the ratio between the characteristic time scale of the flow, based on the integral length and velocity scales, and the characteristic chemical time scale, based on the laminar heat diffusion and the laminar flame speed:

$$Da = \frac{\tau_t}{\tau_c} = \frac{L_t s_L^o}{u' \delta_L} \tag{2.18}$$

A Damköhler number smaller than unity ($Da < 1$) corresponds to slow chemistry: the turbulent time scale is smaller than the chemical time scale, and therefore turbulence is faster than combustion. Reciprocally, a Damköhler number larger than unity ($Da > 1$) indicates a fast reaction process which is most common for industrial burners.

- **Turbulent Karlovitz Number**

The turbulent Karlovitz number, Ka_t, is the ratio between the characteristic chemical time scale to the characteristic time scale of the flow based on the Kolmogorov length scale:

$$Ka_t = \frac{\tau_c}{\tau_k} = \frac{\delta_L}{s_L^o}\sqrt{\frac{\varepsilon}{\nu}} = \begin{cases} \dfrac{\delta_L^2}{\nu}\sqrt{\dfrac{\varepsilon}{\nu}} = \dfrac{\delta_L^2}{\eta_k^2} \\ \dfrac{\nu}{s_L^{o2}}\sqrt{\dfrac{\varepsilon}{\nu}} = \dfrac{u_k'^2}{s_L^{o2}} \end{cases} \tag{2.19}$$

It indicates whether the smallest eddies have any influence on the flame front, and is related to the Karlovitz number, Ka, for which the flame stretch K is based on the strain rate produced by the smallest eddies:

$$Ka = K \cdot \frac{\delta_L}{s_L^o} = \frac{1}{\tau_\eta}\frac{\delta_L}{s_L^o} \tag{2.20}$$

A second turbulent Karlovitz number, Ka_δ, based on the inner layer characteristic thickness (reactive layer on the flame front), can also be defined to indicate whether the smallest eddies are small enough to enter the reactive layer, δ_r:

$$Ka_\delta = \frac{\delta_r^2}{\eta_k^2} = \delta^2 Ka_t \approx \frac{Ka}{100} \tag{2.21}$$

where $\delta = Ze^{-1}$ states for the relative thickness of the reactive layer δ_r in the flame front δ_L. It is thus used to quantify the level of interaction of turbulent eddies with the flamelet layers, and relates the reaction zone thickness, $\delta_r = \delta . \delta_L$, to the size of the Kolmogorov eddies, η^3.

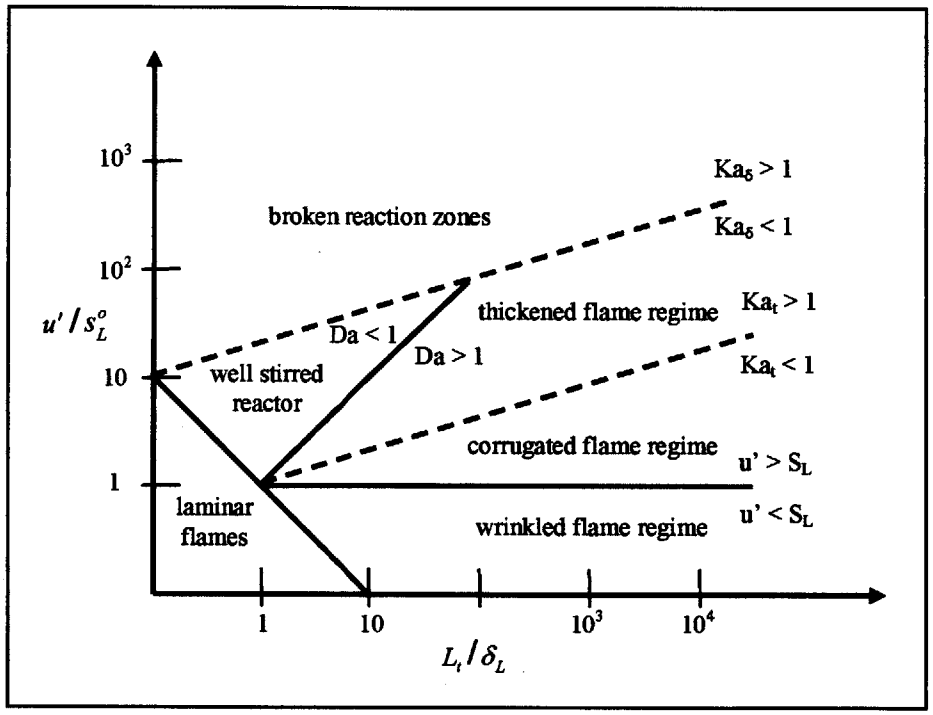

Figure 2.7: Combustion diagram depicting different premixed flame regimes.

2.3.3 Combustion Diagram and Regimes

In figure 2.7, the combustion diagram that highlights the different premixed combustion regimes is presented. The regions are separated by the lines of constant Reynolds, Damköhler, and Karlovitz numbers, which can be easily constructed based on the following relations between the characteristic scales:

$$\frac{u'}{s_L^o} = Ka^{2/3}\left(\frac{L_t}{\delta_L}\right)^{1/3} = Re_t\left(\frac{L_t}{\delta_L}\right)^{-1} = Da^{-1}\left(\frac{L_t}{\delta_L}\right) \tag{2.22}$$

It should be pointed out that the diagram is based on scaling laws applicable to homogeneous isotropic turbulence without heat release and without consideration of any non-adiabatic, non-unity Lewis number, or non-unity Schmidt number effects. Also note that a diffusive flame thickness is employed to construct the diagram. Nevertheless, the diagram provides an order-of-magnitude estimation of the regimes characterizing the flame-turbulence interaction, with the lines $Re_t = 1$, $Da = 1$, $Ka_t = 1$, $Ka_\delta = 1$, and $u'/s_L^o = 1$, setting the boundaries between the various combustion regimes [2.1-2.4]. The various regimes displayed in figure 2.7 consist of laminar flames, well-stirred reactor, corrugated and wrinkled flamelets, thickened flame regime, and broken reaction zones, and are discussed next.

- **Laminar Flames**

When $Re_t < 1$, the flow is essentially laminar and the combustion lies in the laminar flame regime. As Re_t increases, different turbulent flame regimes can be identified depending on the flame-flow interactions and the resultant reaction zone configuration.

- **Well-Stirred Reactor**

This regime is principally defined for scenarios with reduced Damköhler number ($Da < 1$) with moderate turbulence intensity ($Ka_\delta < 1$). While the turbulent time scale is smaller than the chemical time scale, the small-scale eddies are unable to disrupt the inner layer of the flame front. In this regime, turbulence effects homogenize the mixture as it undergoes combustion, with the chemical mechanism governing the reaction process; the notion of flame front is therefore irrelevant.

- **Flamelet Regime**

In the flamelet region, while the turbulent time scales are larger than the chemical time scales ($Da > 1$), the smallest scales (Kolmogorov eddies) in the flow are larger than the laminar flame thickness ($\delta_L < \eta_k$) such that the flame front is embedded in the smallest eddies and the turbulent eddies are unable to perturb the internal structure of the quasi-steady laminar flame. The flame front therefore remains thin, its local inner structure is essentially that of a laminar flame, and the interaction between flame and turbulence is purely kinematic. The flame front is considered as a continuous collection of laminar flamelets, which move and behave differently because of the local action of eddies, and the regime may be sub-divided into wrinkled flamelets and corrugated flamelets:

- **Wrinkled Flamelets**

The wrinkled flame regime corresponds to the configuration where the flame is placed in a weakly turbulent flow. If $u' / s_L^o < 1$, i.e. the turbulent fluctuations are rather small compared to the laminar flame propagation, and turbulence cannot compete with the advancement of the flame front, and only slight wrinkling of the flame front is observed.

- **Corrugated Flamelets**

As the turbulent fluctuations become larger than the laminar flame speed, flame topology changes begin to take place as a result of significant wrinkling of the flame front, and formation of pockets of fresh and burnt gas is also possible.

- **Thin Reaction Zones (Thickened Flame Regime)**

For this regime, $\delta_L > \eta_k > \delta$, therefore, the Kolmogorov eddies are smaller than the flame thickness and can influence the local structure of the laminar flame front layer. They are, however, still larger than the inner layer ($Ka_\delta < 1$), suggesting that the small eddies can only penetrate into the preheat zone and the oxidation layer, but not into the inner layer. They can therefore distort the laminar structure of the flame front, and also modify the flame speed, since turbulence may enhance or weaken the transport of species or energy in the preheat zone, but the chemical reactions are not influenced by turbulence. The flame front is substantially wrinkled, and the Kolmogorov eddies increase the diffusion within the flame front, so that the flame front thickness is increased leading to the formation of the thickened flamelets. In other words, for this regime, turbulence and combustion cannot be dissociated, and flame and turbulent characteristics become implicitly dependent.

The thickened flamelet regime and the corrugated flame regime are of significant importance for industrial applications, and can be associated with 'high-intensity, small-scale' turbulence and 'small-intensity, large-scale' turbulence, respectively (figure 2.8). For small-intensity turbulence, the Kolmogorov scale is larger than the flame thickness, and the interaction between the flame front and the turbulence field is purely kinematic, i.e. turbulence can wrinkle the flame but cannot disturb its local structure. For high-intensity turbulence, the Kolmogorov eddy-scale is smaller than the preheat zone; hence, the eddies can enter into the preheat zone, and enhance the transport of radicals and heat between the reaction zone and the unburned gas.

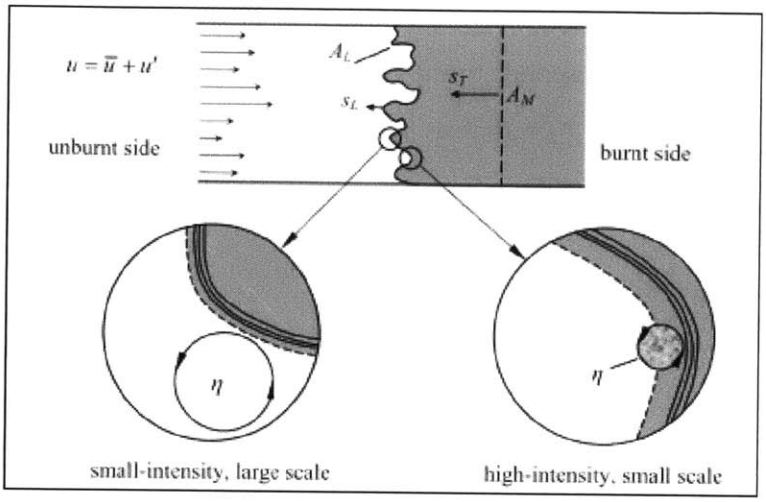

Figure 2.8: Schematic drawing of an idealized steady premixed flame in a duct with corrugated and thickened flame front locations highlighted.

- **Broken Reaction Zones**

This regime occurs when turbulence is more intensive than in the thickened flame regime, such that the Kolmogorov eddies in the flow are smaller than the inner layer thickness of the flame, $\delta > \eta_k$, and can enter the inner layer and influence the internal structure of the flame ($Ka_\delta > 1$). By increasing the heat and the radicals loss to the preheat zone, they can perturb or suppress the chemical reactions and lead to local extinction of the flame, resulting in the broken reaction zone regime.

The limit between the thickened flame regime and the broken zone regime is difficult to define. This is very much dependent on the instantaneous and local turbulent condition and also on the chemical properties of the mixture. In the thickened flame regime, the flamelet velocity is becoming larger than the laminar flame speed, because of the increased diffusion in the preheated zone. In the broken zone region, the effect of eddies penetrating the inner-layer zone may tend to reduce the flamelet velocity, and may lead to local extinction, which is classically described as quenching.

NOTE: This work is limited to configurations where the flames are considered as thin reaction zones or corrugated flamelets.

2.4 Combustion Modeling: Governing Equations

As suggested earlier, combustion process involves strong interaction between fluid mechanics, chemical reactions, and both heat and mass transfer. These phenomena are characteristically

represented in conservation equations. In the following sections, the mathematical formulation of the basic conservation laws is presented.

2.4.1 Mass Conservation Equation

The temporal change of mass in a closed space-fixed control volume is equal to the sum of mass that is transported over the boundaries of the domain and mass that is removed or added inside the control volume per unit time. The continuity equation, in its differential form, describes the local change of the density ρ because of density fluxes through the surfaces of the volume control:

$$\frac{\partial \rho}{\partial t}+\frac{\partial\left(\rho u_j\right)}{\partial x_j}=0 \tag{2.23}$$

where ρ is the bulk mixture density and u_j is the velocity vector component.

2.4.2 Momentum Conservation Equations

The temporal change of momentum in a closed, space-fixed control volume is equal to the sum of volume forces f_i (typically the gravity effect), surface forces T_i (typically pressure and viscosity effects), the flux of momentum through the boundaries of the control volume, and momentum that vanishes or is produced inside the control volume per unit time. The Navier-Stokes equation, in its differential form, can be written as:

$$\frac{\partial \rho u_i}{\partial t}+\frac{\partial\left(\rho u_j u_i\right)}{\partial x_j}=-\frac{\partial p}{\partial x_i}+\frac{\partial \sigma_{ji}}{\partial x_j}+\rho f_i \tag{2.24}$$

where p is the pressure field, σ is the stress tensor, f is the external force. The Stokes formulation of the stress tensor is used to close the stress tensor in the conservation equation:

$$\sigma_{ji}=\mu\left(\frac{\partial u_i}{\partial x_j}+\frac{\partial u_j}{\partial x_i}\right)-\frac{2}{3}\mu\frac{\partial u_k}{\partial x_k}\delta_{ij} \tag{2.25}$$

where μ is the viscosity of the mixture and δ_{ij} is the Kronecker delta tensor.

2.4.3 Species Transport Equations

The velocity of species transport across the control volume boundaries, v_k, can be different from the flow velocity, u. In other words, each species is drifting or diffusing relative to the flow with the diffusion velocity: $u_k = v_k - u$. A conservation equation for the mass of each species is valid using its own velocity components $v_{k,j}$ and defining a source term $\dot{\omega}_k$:

$$\frac{\partial \rho Y_k}{\partial t}+\frac{\partial\left(\rho Y_k v_{k,j}\right)}{\partial x_j}=\dot{\omega}_k \tag{2.26}$$

The source term $\dot{\omega}_k$ appears in the *r.h.s.* of the equation, since species mass can be destroyed or produced by chemical reactions. In order to write the species mass fraction conservation equation in a similar way to the previous balance equations, the *l.h.s.* is written with the flow velocity u:

$$\frac{\partial \rho Y_k}{\partial t} + \frac{\partial \left(\rho Y_k u_j\right)}{\partial x_j} = -\frac{\partial \left(\rho Y_k u_{k,j}\right)}{\partial x_j} + \dot{\omega}_k \tag{2.27}$$

The diffusion velocity depends on pressure, temperature and concentration gradients but usually only the concentration gradient is accounted (isotropy hypothesis). This leads to Fick's law:

$$\rho Y_k \boldsymbol{u}_k = -\rho D_k \nabla Y_k \tag{2.28}$$

where D_k is the diffusion coefficient of the species k into the mixture.

The species mass fraction conservation equations can eventually be written as:

$$\frac{\partial \rho Y_k}{\partial t} + \frac{\partial \left(\rho Y_k u_j\right)}{\partial x_j} = \frac{\partial}{\partial x_j}\left(\rho D_k \frac{\partial Y_k}{\partial x_j}\right) + \dot{\omega}_k \tag{2.29}$$

Note that if the mass of all species is summed up, the global mass conservation equation must be recovered. So, the sum of all species source terms and diffusion velocities should equate to zero.

2.4.4 Energy/Enthalpy Conservation Equation

The transport equation for the energy can be written as:

$$\frac{\partial \rho E}{\partial t} + \frac{\partial \left(\rho u_j E + u_j p\right)}{\partial x_j} = -\frac{\partial q_j}{\partial x_j} + \frac{\partial \sigma_{jk} u_k}{\partial x_j} \tag{2.30}$$

where q_j is the heat flux, given in terms of the thermal conductivity, κ_t, and the temperature, T, as:

$$q_j = -\kappa_t \frac{\partial T}{\partial x_j} \tag{2.31}$$

Alternative formulations for the energy balance equation may also be written, and include the enthalpy form, the temperature form, the pressure form, and the entropy form [2.5].

2.4.5 Equation of State

The connection between the different state variables is given by equations of state, which depend on the fluid under consideration. Often, all species and the mixture are assumed to be perfect gases, and ideal mixing is presumed as well. For a perfect gas, the ideal gas relation between pressure, temperature and density, is represented as:

$$p = \rho \frac{\Re}{M} T \tag{2.32}$$

where $\Re$ is the gas constant, and M is the molecular weight.

2.5 Combustion Modeling Approaches

Solving the conservation equations is challenging, particularly in case of turbulent reactive flows, which involve a wide spectrum of length and time scales. The multi-scale and multi-physics attributes of turbulent combustion necessitates the use of modeling approaches in order to simplify the mathematical description of the complex physical phenomena.

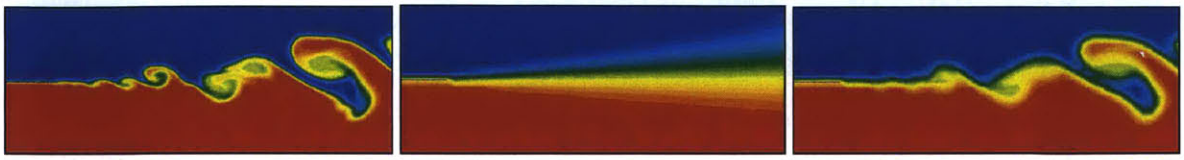

Figure 2.9: Comparative results from DNS, RANS, and LES.

Three different approaches may be identified: (i) Direct Numerical Simulation (DNS), (ii) Reynolds-Averaged Navier-Stokes (RANS), and (iii) Large-Eddy Simulation (LES). In comparison to one another, each of these methods possesses various advantages and drawbacks, and is discussed next.

2.5.1 Direct Numerical Simulations (DNS)

In the Direct Numerical Simulation (DNS) approach, the whole spectrum of turbulence is explicitly resolved, requiring the use of a fine mesh to enable the discretization of the smallest (Kolmogorov) eddies, and the use of small time steps to capture all the dynamic flow and chemical phenomena. While modeling is avoided, the accurate resolution requirement makes DNS computationally expensive and generally impractical for engineering problems. The number of grid points required to simulate the full range of turbulence scales, even for somewhat simple flow geometries, is estimated to be proportional to $Re_t^{9/4}$. For many practical applications, the turbulent Reynolds number is very large, making computational requirements for DNS enormous. DNS can be even more unfeasible for reacting flows and/or for flows having complex geometries. It should be pointed out, however, that DNS has its place in the numerical prediction of turbulent combustion. It has been applied with considerable success to low Reynolds number flows and effectively employed as a research tool for model development.

2.5.2 Reynolds-Averaged Navier-Stokes (RANS) Simulations

RANS approaches introduce the notion of averages of flow variables, and time-averaged governing equations, and involve predicting the macroscopic effect of turbulence, by considering the averaged flow equations. RANS methods do not resolve any part of the turbulent fluctuations, which introduces unclosed correlation terms from the time-averaging procedure, and must be modeled to include the effect of the turbulent fluctuations and the unclosed terms on the mean flow. In general,

the complexity of turbulence makes it impossible for a single RANS model to represent all turbulent flows and thus some adjustment of model parameters is often required. A primary attraction of RANS approaches is that it is the least expensive approach of the possible methods in terms of computational effort.

2.5.3 Large-Eddy Simulations (LES)

In case of Large Eddy Simulation (LES) technique, rather than averaging the effect of turbulence, the equations are filtered: while the larger turbulent eddies (which have a more significant influence on the flow and are more dependent on the geometry) are explicitly resolved and computed, the effect of smallest eddies (which tends to be somewhat isotropic) is modeled using sub-filter-scale models. Thus, in contrast to RANS, there is partial resolution of the turbulent fluctuations in LES, which decreases the importance of modeling and effects of modeling uncertainty, but increases the computational cost. In the next section, a more comprehensive description of the LES approach is presented.

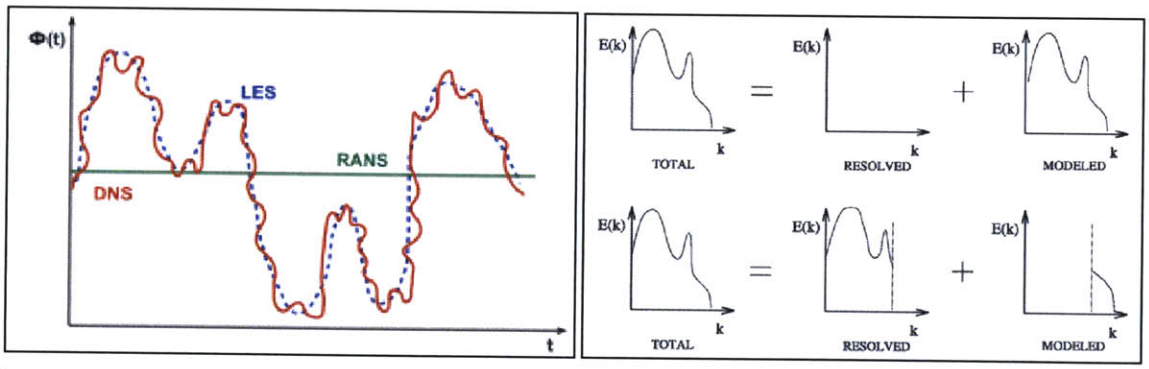

Figure 2.10: Symbolic representation of predictive accuracy and energy spectrum decomposition associated with RANS and LES

2.6 Large Eddy Simulation Methodology

In turbulent flows, eddies with various characteristic time and length scales overlap in space, from the largest length scale (determined by the geometry of the flow) down to the smallest scales (at which the kinetic energy is dissipated into heat). In figure 2.11, the energy content corresponding to the eddy length scales is depicted. Under the hypothesis of homogeneous and isotropic turbulence, and assuming that the rate of production and dissipation of the turbulent kinetic energy are in balance, it has been demonstrated that turbulence follows an energy cascade, wherein energy is continuously transferred from the large eddies to the small eddies where it is dissipated into heat. The various sub-ranges may be categorized as follows:

- **Energy Containing (Large-Scale) Range**

The large-scale spectrum contains the small wave number eddies which account for the transfer of energy from the mean flow to turbulence. This domain of the turbulence spectrum is dominated by the mean flow characteristics (e.g. mean strain rate), and therefore depends on the geometry.

- **Inertial Sub-Range**

The inertial range or equilibrium range is the most important domain of the turbulence spectrum, and is comprised of the transfer of turbulent kinetic energy from the largest integral length scales (L_t) to the smallest Kolmogorov length scales (η_k).

- **Viscous Sub-Range**

The dissipation range corresponds to the domain where the turbulent kinetic energy is transformed to heat due to viscous effects.

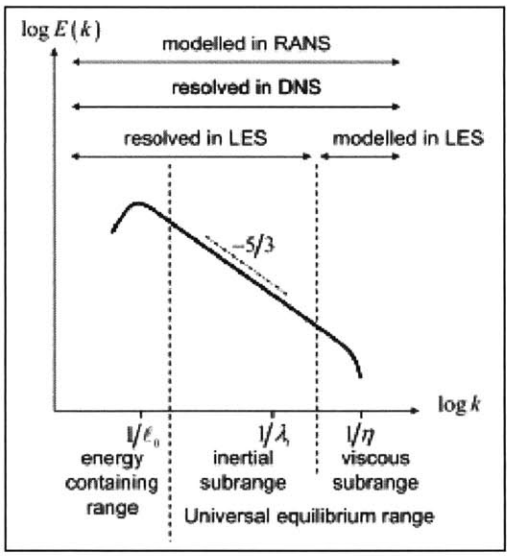

Figure 2.11: Energy spectrum $E(\kappa)$ as a function of wave number κ.

For small wave numbers, the energy per unit wave number, E, increases with a power-law between x^2 and x^4, and the spectrum peaks at a wave number that corresponds to the integral length scale. For larger wave numbers, in the inertial sub-range, E decreases following the $x^{-5/3}$ law. In this domain, the energy spectrum has the form:

$$E(\kappa) = C_k \varepsilon^{2/3} \kappa^{-5/3} \tag{2.33}$$

where C_k is the Kolmogorov constant. For wave numbers larger than the one corresponding to the Kolmogorov scale, E decreases exponentially due to viscous dissipation.

In the DNS approach, all scales down to the Kolmogorov scales are resolved, which requires fine grid resolution and renders the framework impractical for high Reynolds number flow conditions (considering the present-day available computational resources). However, in general, the large eddies are anisotropic (geometry dependant), while according to Kolmogorov's hypothesis, the inertial sub-range and the viscous sub-range are statistically similar or universal for high Reynolds number flows; hence they correspond to the universal equilibrium range, and local isotropic turbulence is a valid approximation at small-scales. The LES approach takes advantage of the above property i.e. existence of a universal range in turbulent flows. In LES, the large scale turbulent motions that are dependent on the flow configuration are resolved while the smaller scales, that are universal, are modeled.

The various flow quantities Φ are therefore filtered in the spectral space (components greater than a given cut-off length are suppressed) or in the physical space (weighted averaging in a given volume). The filtered quantity Φ is defined as:

$$\overline{\Phi}(x) = \int \Phi(x') g(x - x') dx' \tag{2.34}$$

where g is a filter function and can take different forms e.g. Gaussian, etc. For non-constant density flows, as considered in this work, Favre, or mass-weighted, filtered quantity Φ is defined as:

$$\overline{\rho}\ \widetilde{\Phi}(x) = \overline{\rho\ \Phi} \tag{2.35}$$

Often, the grid is used as the spatial filter. In figure 2.12, the LES regime diagram is depicted, which highlights the non-dimensional filter width as a function of the Karlovitz number.

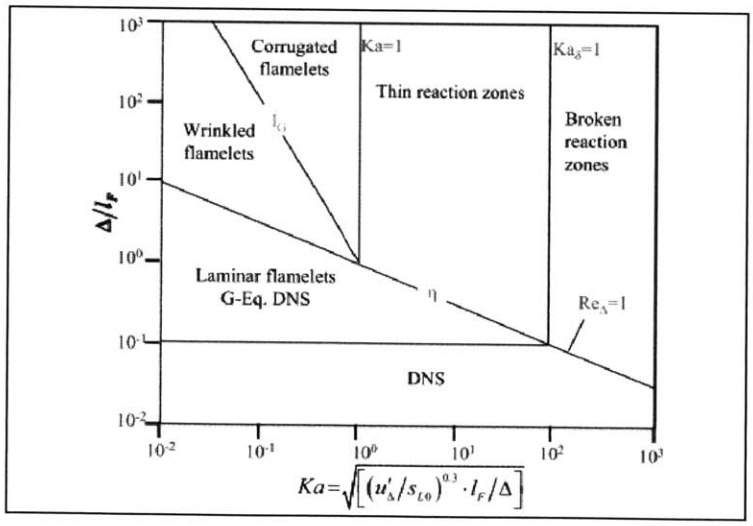

Figure 2.12: LES regime diagram showing the non-dimensional filter width as a function of the Karlovitz number.

2.7 Governing Equations for LES

The governing equations for LES, obtained by applying the Favre filtering operation to each term in the conservation equations of mass, momentum and energy, and the species transport equations are shown below.

2.7.1 Mass Conservation Equation

$$\frac{\partial \bar{\rho}}{\partial t}+\frac{\partial\left(\bar{\rho}\tilde{u}_j\right)}{\partial x_j}=0 \tag{2.36}$$

where $\tilde{u}$ is the filtered velocity vector.

2.7.2 Momentum Conservation Equations

$$\frac{\partial \bar{\rho}\tilde{u}_i}{\partial t}+\frac{\partial\left(\bar{\rho}\tilde{u}_j\tilde{u}_i\right)}{\partial x_j}=-\frac{\partial \bar{p}}{\partial x_i}+\frac{\partial \bar{\sigma}_{ji}}{\partial x_j}+\frac{\partial \tau_{u_j u_i}}{\partial x_j} \tag{2.37}$$

where σ and τ refer to the filtered viscous stress tensor and the corresponding sub-grid scale (SGS) term respectively. The unknown SGS correlations above can be modeled using different approaches, such as the dynamic Smagorinsky model for the SGS stress tensor term.

2.7.3 Species Transport Equations

$$\frac{\partial \bar{\rho}\tilde{Y}_k}{\partial t}+\frac{\partial\left(\bar{\rho}\tilde{Y}_k\tilde{u}_j\right)}{\partial x_j}=\frac{\partial}{\partial x_j}\left(\bar{\rho}D_k\frac{\partial \tilde{Y}_k}{\partial x_j}\right)-\frac{\partial}{\partial x_j}\left[\bar{\rho}\left(Y_k u_j-\tilde{Y}_k\tilde{u}_j\right)\right]+\bar{\dot{\omega}}_k \tag{2.38}$$

where D is the molecular diffusivity, and Y_k and $\bar{\dot{\omega}}_k$ refer to the specie mass fraction and filtered reaction rate respectively.

2.7.4. Energy/Enthalpy Conservation Equation

$$\frac{\partial \bar{\rho}\tilde{E}}{\partial t}+\frac{\partial\left(\bar{\rho}\tilde{u}_j\tilde{E}+\tilde{u}_j\bar{p}\right)}{\partial x_j}=-\frac{\partial \bar{q}_j}{\partial x_j}+\frac{\partial \overline{\sigma_{jk}u_k}}{\partial x_j}+\frac{\gamma R}{\gamma-1}\frac{\partial \tau_{u_j T}}{\partial x_j}+\frac{\partial \tau_{u_j u_k}u_k}{\partial x_j} \tag{2.39}$$

where $\tilde{E}$ refers to the filtered total specific energy, and $\bar{q}_j$ is the filtered heat flux. More details on modeling the unresolved terms can be found in [2.6].

2.8 LES Combustion Modeling Techniques

During turbulent combustion, chemical reactions are confined to thin reacting layers at small scales that cannot be resolved on typical LES grids. As a consequence, most of the turbulence-chemistry interactions need to be modeled. This modeling of the reaction rates presents a major challenge in turbulent premixed combustion because reaction rates are highly nonlinear functions of temperature and species mass fractions. An integral component of LES therefore is the turbulent combustion

sub-grid model, which is necessary to incorporate the effect of turbulence-chemistry interactions at the under resolved scales on the reaction rate. Various approaches have been adopted by researchers to model the filtered reaction rates [2.7], typically corresponding to specific flame regimes (figure 2.7), which may be characterized as follows:

2.8.1 Turbulence Mixing Based (Finite Reaction Zone) Methods

Models based on turbulence mixing are usually a direct extension of existing RANS models and based on the assumption that at high Damköhler number, turbulent mixing (rather than chemical reaction rates) controls the combustion process. In other words, the underlying concept is that the mean reaction rate is governed by the turbulent mixing processes, especially in scenarios where the chemistry is *fast*. Models falling into this group include the eddy break up (EBU) model and the eddy dissipation concept (EDC) model.

- **Eddy-Break-Up (EBU) Model**

In the EBU approach, the formulation of the reactive source term is essentially estimated based on turbulence, rather than on chemical considerations [2.2]. In the LES context, the reaction rate can be expressed as:

$$\dot{w} = C_{EBU}\bar{\rho}\frac{1}{\tau_t}\left(\overline{Y_p''^2}\right)^{1/2} = C_{EBU}\bar{\rho}\frac{\varepsilon}{k}\bar{c}\left(1-\bar{c}\right) \qquad (2.40)$$

where τ_t the sub-grid turbulent time-scale, C_{EBU} is a model constant, and $\overline{Y_p''^2}$ is the product mass fraction variance, modeled in terms of c, the reduced temperature (reaction progress variable):

$$c = \frac{T - T_u}{T_b - T_u} \qquad (2.41)$$

The drawbacks of the formulation include its dependence on the turbulent time, and thus on the sub-grid turbulent velocity, and the dependence of the model constant on the flow conditions and mesh size. Furthermore, it has been suggested that the reaction rate is often over-predicted in zones with high strain rates, using the EBU approach.

2.8.2 Flame Front Topology Approaches

The turbulent flame in the flamelet regime can be viewed as an ensemble of locally stretched, thin laminar flames (flamelets) embedded in an otherwise non-reacting turbulent flow field. Turbulence and chemistry influence each other in the following manner: the flamelet introduces heat expansion and flow acceleration across the flame front, which changes the turbulent flow field on either side of the reaction zone; on the other hand, the turbulent eddies convect and distort the flame front, but are not able to disturb the internal structure of the flamelets. Thus, the calculation of turbulence and

chemistry may be decoupled, for scenarios where the Kolmogorov length-scale is larger than the flame thickness ($Ka_\delta < 1$).

While this corresponds to the corrugated flamelets and wrinkled flamelets regimes, it has been shown that the applicable region for flamelet concept can be extend to $Ka < 100$, i.e. when the turbulent Karlovitz number is moderately larger than unity. For these configurations, the turbulent eddies can broaden the preheat zone and increase the heat and species diffusion; however, they are unable to penetrate the thin reaction zone because of the increased viscous dissipation by high temperature near the flame. In this range, the reaction zone remains thin, and the primary effect of increasing turbulence is to wrinkle the flame front and increase the reaction rate, without changing the thin layer structure. Thus, if the flame thickness is thin compared to the size of the turbulent vortices, the reactive layer is unaffected by turbulence and the interaction between turbulence and chemistry is purely kinematic, i.e. the flame is a thin surface that is wrinkled by the turbulent eddies but its structure across the thickness is the same as for the laminar flame sheet.

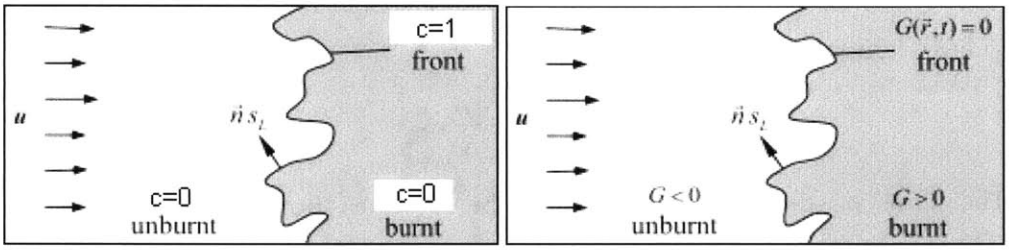

Figure 2.13: Schematic representing the progress-variable and level-set approaches.

In numerical simulations, the laminar flamelet structure is computed using flamelet equations that describe the reactive-diffusive structure in the vicinity of the flame front. The turbulent flame sheet is treated as an ensemble of quasi-laminar flames embedded in a turbulent flow, and the location of the flamelet in the turbulent flow field is typically denoted by a geometrical surface, which is in generally an iso-c (reaction progress variable) surface, or an iso-G (signed distance function) surface for premixed flames (figure 2.13). These models are based on the assumption that the flame sheet may be considered as propagating locally as a laminar flame, and the main effect of sub-grid turbulence is to wrinkle and stretch this flame sheet. The approach, for the most part, ignores the internal structure of the flame and detailed chemical kinetics.

- **Reaction Progress Variable**

The approach represents combustion occurring at the flame front in terms of a transport equation of a reaction progress variable, c, such that $c = 0$ in the reactants, and $c = 1$ in the combustion

products. The progress variable, a unique parameter, evolves monotonically from the unburned region to the burned region across the flame front. It thus quantifies the progress of reaction and may be defined as a reduced temperature or reduced fuel mass fraction (*Le=1*):

$$c = \frac{T - T_u}{T_b - T_u}, c = \frac{Y_F - Y_{F,u}}{Y_{F,b} - Y_{F,u}} \qquad (2.42), (2.43)$$

where T, T_u, and T_b are respectively the local, the unburned, and burned gas temperatures. Similarly, Y_F, $Y_{F,u}$, and $Y_{F,b}$ are the local, the unburned, and the burned fuel mass fractions.

The transport equation for the progress variable, in the filtered form is written as:

$$\frac{\partial \bar{\rho}\tilde{c}}{\partial t} + \frac{\partial \left(\bar{\rho}\tilde{c}_i\tilde{u}_j\right)}{\partial x_j} + \frac{\partial}{\partial x_j}\left(\bar{\rho}\widetilde{cu_j} - \bar{\rho}\tilde{c}_i\tilde{u}_j\right) = \frac{\partial}{\partial x_j}\left(\overline{\rho D \frac{\partial c}{\partial x_j}}\right) + \bar{\omega}_c \qquad (2.44)$$

where the three terms on the *l.h.s.* are unsteady effects, resolved convective flux and unclosed transport flux, respectively. The two terms on the *r.h.s.* denote the filtered molecular diffusion and the filtered reaction rate respectively. The unclosed sub-grid-scale transport flux is generally modeled with a gradient-diffusion assumption:

$$\bar{\rho}\left(\widetilde{cu_j} - \bar{\rho}\tilde{c}_i\tilde{u}_j\right) = -\frac{\mu_t}{Sc_t}\nabla\tilde{c} \qquad (2.45)$$

The terms on the right hand side can be re-written from the freely-propagating one-dimensional flame analysis as:

$$\frac{\partial}{\partial x_j}\left(\overline{\rho D \frac{\partial c}{\partial x_j}}\right) + \bar{\omega}_c = \overline{\rho S_d |\nabla c|} \qquad (2.46)$$

where S_d is the local displacement speed of the iso-surface c, and depends on the physical-chemical characteristics of the combustible mixture and the local turbulence at the sub-grid level. The closure for the flame front displacement term, $\rho S_d |\nabla c|$, may be achieved in terms of the flame surface density or the flame wrinkling factor, and is discussed next.

- **Flame Surface Density**

The flame surface density, Σ_Δ, is the flame surface area per unit volume, i.e. the relative quantity of flame surface within each cell, and increases with more intense wrinkling of the flame surface. The flame surface is relevant for combustion modeling, since the burning rate correlates with it, as the wrinkling of the flame increases the burning rate. In the FSD technique, the expression can be re-written as:

$$\overline{\rho S_d |\nabla c|} \approx \rho_u S_L \Sigma_\Delta \qquad (2.47)$$

where Σ_Δ is the flame surface density per unit volume at the sub-grid-level, ρ_u is the density of the unburned gas, S_L is the laminar flame speed.

For the evaluation of the flame surface density Σ_Δ, there are different strategies using algebraic relations, a similarity model or a transport equation. In its simplest form, the flame surface density (FSD) model provides an algebraic expression for the amount of flame surface area per unit volume Σ at each point within the premixed turbulent flame brush [2.8]. If the flamelet assumption holds, then the local flame structure remains quasi-laminar and the local propagation speed remains close to the unstrained planar laminar burning velocity, S_L. For example, an algebraic model for the LES modeling using a DNS analysis has been written as:

$$\tilde{\Sigma}_\Delta = 4\beta \frac{\overline{c}(1-\overline{c})}{\Delta} \qquad (2.48)$$

where the parameter β depends on the sub-grid-scale flame front wrinkling.

The estimation of the flame surface density using transport equation(s) offers a more accurate evaluation of the reaction rate in order to resolve the progress variable. For example, one-equation and two-equation approaches have previously been developed. More details can be found in [2.9-2.10].

- **Flame Wrinkling Factor**

An alternative to the flame surface density is the flame surface wrinkling factor Ξ_Δ. It can be interpreted as the ratio of the SGS turbulent flame surface to the flame surface projected in the propagation direction, and is expressed as:

$$\Sigma_\Delta = \Xi_\Delta |\nabla c| \qquad (2.49)$$

where Σ_Δ is the SGS flame surface density per unit volume, and Ξ_Δ is the sub-grid-scale wrinkling factor.

The same algebraic models as for the flame surface density can be used in this case. A model based on two transport equations, to resolve the regress variable ($b = 1 - c$) and the sub-grid scale flame front wrinkling, respectively, has been developed. More details can be found in [2.11].

- **G-Equation (Level-Set) Approach**

A method that is able to describe the temporal evolution of surfaces with arbitrary complexity in space is the level-set method [2.1-2.3]. The base of this method is a scalar field, and the surface

under consideration is defined as an iso-surface of this field. The well-known level set equation has a general form as:

$$\frac{\partial \phi}{\partial t} + F(x, \nabla\phi, k)|\nabla\phi| = 0 \qquad (2.50)$$

In the level set equation, the zero level set $\phi = 0$ corresponds to the moving front, k is the curvature of the level set surface. It describes the front propagating along its normal direction with a speed F, which is a function of multiple variables like $x, \nabla\phi$, k. If the propagating front is also passively advected by an underlying flow field $\boldsymbol{u}$, then the equation can be rewritten as:

$$\frac{\partial \phi}{\partial t} + F(x, \nabla\phi, k)|\nabla\phi| + \boldsymbol{u}\cdot\nabla\phi = 0 \qquad (2.51)$$

When the approach corresponds to a geometrical description of the flame front using an iso-level surface of a scalar field G (iso-contour in two dimensions), the iso-surface of G is typically fixed at $G=G_0$, and the level set of the scalar at this value represents the spatial location of the flame surface. Figure 2.12 depicts an instantaneous flame surface, which is represented by the zero level set of the quantity G, $G(\vec{r}, t) = 0$, where r denotes the spatial position, $\boldsymbol{n}$ is the unit normal vector to the front and points into the unburned zone, and is defined by $\vec{n} = -\nabla G/|\nabla G|$. This zero level set divides the flow field into two zones: $G > 0$, the burnt zone, and $G < 0$, the unburned zone. The level set equation may then be expressed as:

$$\frac{\partial G}{\partial t} + \nabla G \cdot \frac{d\vec{r}}{dt} = 0 \qquad (2.52)$$

where the propagation speed of the flame front, $d\vec{r}/dt$, results from two contributions: the flow velocity $\boldsymbol{u}$, and the (burning) velocity of the flame-front normal to itself:

$$\frac{d\vec{r}}{dt} = \boldsymbol{u} + \vec{n}S_L \qquad (2.53)$$

Thus, substituting the above, the basic propagation equation for the scalar G, the well-known G-equation, is obtained as:

$$\frac{\partial G}{\partial t} + \boldsymbol{u}\cdot\nabla G = S_L|\nabla G| \qquad (2.54)$$

where S_L stands for the laminar flame displacement speed. The equation describes a surface propagating in space with a velocity S_L (normal to itself) relative to the local unburned flow velocity, $\boldsymbol{u}$. A turbulent flame speed relation is also derived for the averaged representation to

describe the displacement of the iso-value G_0 [2.12]. Therefore, the adaptation of this model to different turbulent combustion regimes depends on the relevant evaluation of S_L. Further, for LES of turbulent combustion, the above equation needs to be filtered.

The laminar flame speed, S_L, is not always equivalent to the unstretched laminar flame speed, s_L^o, as the effect of the local curvature and strain should be considered. The combined effects are often referred to as the flame stretch, K, defined by the fractional rate of change of a flame surface element A [2.13]:

$$K = \frac{1}{A}\frac{dA}{dt} \tag{2.55}$$

A general expression of stretch, for a thin flame sheet can be found in [2.14]. If only the local curvature effects are considered in the level-set approach, the equation becomes [2.3]:

$$\frac{\partial G}{\partial t} + \boldsymbol{u}\cdot\nabla G = S_L\left(1 - L_o\kappa\right)\left|\nabla G\right| \tag{2.56}$$

where L_o is the Markstein length [2.3] and κ is the local curvature:

$$\kappa = \nabla\cdot\vec{n} = \nabla\cdot\left(-\frac{\nabla G}{\left|\nabla G\right|}\right) \tag{2.57}$$

Different from the c-equation, the G-equation has several special properties, in that it is a Hamilton–Jacobi type equation, and is only well-defined at the zero level set. Since the scalar G surrounding the flame front (zero level set) is not uniquely defined, it may be assigned arbitrarily without changing the physics of the problem, and at the same time keep the zero iso-surface of this assigned G field coincide with the original flame surface. By this way, the flame front becomes an iso-surface of a scalar, which is defined in the whole field, therefore the G-equation turns into a front capturing method. To guarantee uniqueness, it has been proposed to define the surrounding G field as a signed-distance function, which can be expressed in a first-order partial differential equation: $\left|\nabla G\right| = 1$. Typically, therefore, the flame position is associated with $G=G_0$; the values of G are typically chosen such that $G=0$ at the flame front, $G<0$ in the unburned mixture and $G>0$ in the burned gases.

The signed-distance is a well-defined physical quantity, and represents the shortest distance from a local point to the zero level set but with a sign: if this point lies in the $G>0$ side, it is positive, otherwise, it is negative. However, during the evolution of G within the whole computational

domain, G will not necessarily remain as the signed-distance, though the initial G-field maybe initialized to satisfy the signed-distance function. Therefore, it is necessary to reshape the level set G-field to the signed-distance function but without change its zero level set often. This reshaping is called signed-distance re-initialization.

Once the front evolves, the coupling with the one-dimensional flame structure requires spatial information (mapping). It is therefore convenient to let the scalar G be defined as a signed distance function. At each point, within a close region of the flame front, the scalar G corresponds to the closest distance to the front. Additionally by convention the unburned region is defined by negative values ($G<0$) and the burned region by positive values ($G>0$). Since the transport equation does not preserve the distance property, an additional equation is solved, $\nabla G = 1$ (re-initialization step). Fulfilling this requirement, the flame structure can be readily mapped onto the domain through the scalar G values. The density, temperature and viscosity are given by a flamelet library.

To summarize, combustion modeling with the level set method is not based on solving the species mass fraction equations. Instead, the flame is treated as a geometric entity, i.e. a surface which is convected by the flow and self-propagating normal to itself with its flame speed. For computing the flame speed, correlation equations are used. Thus, no closure of the chemical source term is required since its effect is included in the flame speed. Although the G-equation approach is an elegant description of the flame front geometry, the solution of the G-equation is numerically expensive and difficult to implement because the G field is discontinuous due to $|\nabla G| = 1$. Special discretization schemes are required and a frequent re-initialization of the scalar field. Another difficulty is the coupling of the artificial quantity G with the mass and energy equations such that their conservation properties are preserved.

2.8.3 Finite-Rate Chemistry Models

As explained earlier, incorporation of finite rate chemistry effects is critical for the prediction and analysis of combustion instability. In this regard, various methods have been developed to estimate the filtered reaction rates, which typically require a multiple step (reduced) reaction mechanism. Further, unlike in the RANS, where the mean turbulent flame is solved, and therefore the computed flame is very thick, in LES the filtered instantaneous flame is solved, and its flame thickness is generally smaller than the LES mesh size, especially for premixed flames. The finite-rate chemistry models to address these concerns are discussed next.

- **Artificially Thickened Flame Approach**

The thickened flame approach involves artificially thickening the flame-front so that it can be resolved on the LES grid, while maintaining the same laminar flame speed and turbulence-flame interaction. From fundamental theories (dimension analysis of a laminar premixed flame), it follows for a one step reaction:

$$s_L^0 \propto \sqrt{D\bar{\omega}},\ \delta_L^0 \propto D/s_L^0 = \sqrt{D/\bar{\omega}} \qquad (2.58), (2.59)$$

where s_L^0 is the laminar flame speed, δ_L^0 is the laminar flame thickness, D is the diffusion coefficient, and $\bar{\omega}$ is the average reaction rate. Increasing the flame thickness by a factor F, while maintaining a constant flame speed, can therefore be achieved by suitably modifying the diffusivity D and the mean reaction rate $\bar{\omega}$ (i.e. increasing D by a factor F, and reducing $\bar{\omega}$ by the same magnitude). Thus, the modified expressions become:

$$\overline{s_L^0} \propto \sqrt{FD\frac{\bar{\omega}}{F}} = s_L^0,\ \overline{\delta_L^0} \propto FD/\overline{s_L^0} = F\delta_L^0 \qquad (2.60), (2.61)$$

If F is sufficiently large, the thickened flame front can be resolved on the LES computational grid. Furthermore, in this method, the reaction rate is still calculated using the Arrhenius law; therefore various phenomena (quench, ignition etc.) may be accounted for without turning to sub-models. The thickening of the flame front, however, leads to a modified interaction between turbulence and chemistry since the Damköhler number is decreased by the factor F. The effect of turbulent vortices is to wrinkle the flame and enhance the laminar flame speed to a higher turbulent flame speed. This interaction is altered, when the flame thickness changes, since the flame becomes less sensitive to turbulence motions.

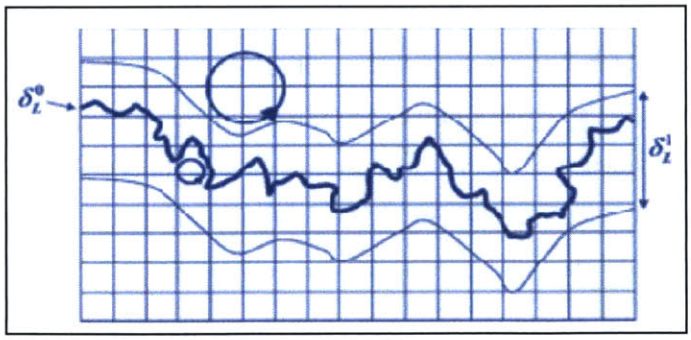

Figure 2.14: Thickening of the reaction zone to resolve the flame front on the LES mesh.

To account for the wrinkling effect of the unresolved features on the (thickened) flame front, an efficiency function, E, is introduced. The filtered transport equation for the chemical

species then takes the form:

$$\frac{\partial \bar{\rho}\tilde{Y}_i}{\partial t}+\frac{\partial\left(\bar{\rho}\tilde{Y}_i\tilde{u}_j\right)}{\partial x_j}=\frac{\partial}{\partial x_j}\left(\bar{\rho}EFD_i\frac{\partial \tilde{Y}}{\partial x_j}\right)+\frac{E\bar{\dot{\omega}}_i}{F} \qquad (2.62)$$

A key aspect of the thickened flame approach is the definition of the function E. Different models have been proposed to define E in terms of a dimensionless wrinkling factor Ξ, which can be treated as the ratio of flame surface to its projection in the direction of propagation. The model has specifically been adopted for the simulation of turbulent pre-mixed combustion and the analysis of unsteady flame dynamics. In this work, the models suggested by Colin [2.15] and Charlette [2.16-2.17] have been implemented, and a dynamic formulation has also been developed (chapter 3).

- **Partially Stirred Reactor (PaSR) Method**

As aforementioned, premixed flames in general are much thinner than the typical LES computational cell, and assuming the entire cell as a perfect reactor is an overestimation [2.18-2.19]. Thus, in the PaSR model, the computational cells are split into a reacting part, and a non-reacting part. The reacting part is treated like a perfectly stirred reactor, in which all present species are homogeneously mixed and reacted. After reactions have taken place, the species are assumed to be mixed due to turbulence for the mixing time, and the resulting concentration gives the final concentration in the entire, partially stirred, cell.

In other words, the PaSR model phenomenologically incorporates the sequential processes of micro-mixing and chemical reactions. The micro-scale processes responsible for the molecular mixing, as well as the dissipation of turbulent kinetic energy, concentrated in isolated regions, and occupy only a small fraction of the fluid volume. These fine flow structures in which most of the dissipation and mixing take place form topologically complex regions, whose characteristic dimensions are small compared to the LES filter width. Since most of the mixing occurs in the fine structures, the reactions also take place in these regions as the reactants are mixed at scales down to the molecular scales provided that the temperature is high enough. Therefore, each LES cell can be viewed as partially stirred reactor containing the reactive fine structures (ideally viewed as perfectly stirred reactors), exchanging mass and energy with its surroundings.

The fraction of the computational cell constituting the reactor, κ^*, is governed by the turbulent mixing time and the residence time and is explicitly computed. The reacting volume fraction may be estimated as the ratio between the chemical reaction time and the total conversion time in the reactor, i.e. the sum of the micro-mixing time and the chemical reaction time. The

chemical reaction time is estimated from the laminar flame speed at the laminar flame thickness whereas the mixing time, ranging from the sub-grid time, to the Kolmogorov time is modeled as the geometrical mean of the two. In this approach no a priori assumption is necessary on the combustion regime:

$$\kappa^* = \frac{\tau_c}{\tau_c + \tau_t} \tag{2.63}$$

$$\frac{c_1 - c_0}{\tau_c} = \frac{c - c_1}{\tau_t} \Rightarrow c_1 = \kappa^* c + \left(1 - \kappa^*\right) c_0 \tag{2.64}$$

$$RR_t = \kappa^* \times \omega_t \tag{2.65}$$

where RR_t is the chemical source term, ω_t is the reaction rate from solving the chemical system.

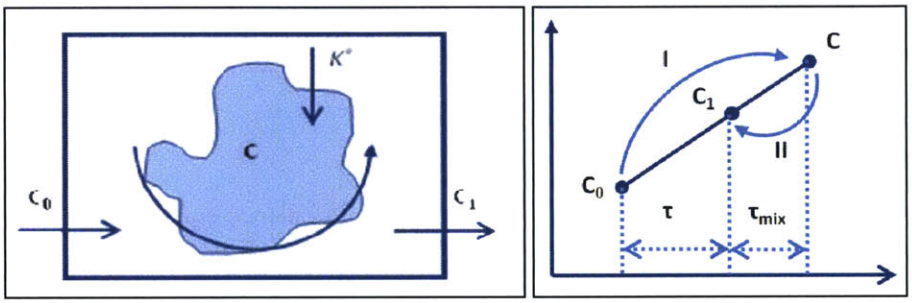

Figure 2.15: Schematic representation of the PaSR model fundamentals.

To summarize, the finite rate chemistry approaches (in contrast to some of the other LES sub-grid scale combustion modeling methods) allow the use of multiple-step (reduced) chemistry mechanisms [2.20], thereby enabling the reaction rates to be calculated much like a direct numerical simulation (DNS) calculation without the need of any ad-hoc sub-models (to take into account phenomena such as ignition and flame-wall interactions). Use of detailed chemistry can also be important, especially when studying non-conventional combustion (such as oxy-combustion) or when specific specie distributions (such as CO or OH) are required to be predicted. Another approach to account for detailed chemistry is through the use of statistical approach, and is discussed next.

2.8.4 Statistical Techniques (PDF Approaches)

The probability density function (PDF) models are based on one-point statistical analysis: if the probability of locating a variable at a location is known, then its mean value at this location can be estimated. This idea is easily extended to take into account multiple variables [2.21-2.22]. For example, the instantaneous reaction rate, a function of species mass fractions and temperature, can

be written as: $\omega = \omega(Y_1, Y_2, ..., T)$. If the joint probability $p(Y_1, Y_2, ..., T)$ for $Y_1, Y_2, ..., T$ in the range $Y_i \in \left(Y_i - \frac{1}{2}dY_i, Y_i + \frac{1}{2}dY_i\right), T \in \left(T - \frac{1}{2}dT, T + \frac{1}{2}dT\right)$ is known, then the mean reaction rate can be determined as: $\bar{\omega} = \int_{Y_1, Y_2, ...T} \omega(Y_1, Y_2, ..., T)\, p(Y_1, Y_2, ..., T)\, dY_1 dY_2 ... dT$.

The PDF-based statistical description of turbulent reactive flow has some theoretical advantages: the complex chemistry is treated exactly without applying assumptions such as 'flamelet' and 'fast reaction'. The PDF schemes provide a closed form representation of the chemical source terms and can be applied to different combustion regimes. They can be applied equally well to non-premixed, premixed, and partially premixed flames. In general, the sub-grid PDF, the joint probability density function of all concentrations and the temperature, can be determined either by the solution of a transport equation (transported PDF method), or modeled assuming its shape (presumed PDF method). These techniques are discussed next.

- **Transported PDF Approach**

In this method, the joint PDF is determined by the use of a balance equation. More details can be found in [2.23-2.24]. Since the chemical reaction term is closed and does not include any modeling, the framework can handle any complex chemical mechanism. In this respect, the transport PDF method can have a considerable advantage over other turbulent combustion models. However, the numerical solution of the transport equation is expensive because of the high dimensionality of the PDF. Thus, application of transported PDF methods in LES generally requires high computational costs and robust solution algorithms.

Current implementations therefore apply Monte-Carlo methods for the solution of the PDF equation, since the memory requirements in such a scenario only depends linearly on the dimensionality. In Monte-Carlo simulations a number of stochastic particles are tracked which may be regarded of as realizations of the PDF. The histogram of the particles properties in a cell then recovers the PDF. In order to enable proper statistics, the number of particles per cell has to be large, which may still be attractive for two-dimensional RANS calculations, but can render the technique expensive for large-scale three-dimensional applications using LES.

- **Presumed PDF Approach**

The expensive solution of the PDF balance equation can be avoided by assuming a specific shape for the PDF. Although a PDF function can take any shape and have multiple extrema, in many combustion cases, it is observed (through experimental data and DNS studies) that probability

distributions show some common features; therefore it is reasonable to represent them with a special shape but with different controlling parameters [2.21, 2.25]. One of the most popular approaches is to assume the PDF as a β-function, and its controlling parameters are the mean and variance of the variable. Thus, the structure of the PDF is given by some empirical function which still contains a small number of freely selectable parameters. These parameters are then determined from the moments of the stochastic variables for which transport equations have to be solved. Although the influence of chemical reactions on the PDF shape cannot be accounted for on a physical basis as it is the case with a PDF balance equation, the method is attractive because of its much lower computational effort.

The disadvantage of the presumed-PDF method is that while it is relatively simple to find shape functions for one-dimensional PDF's, it is very difficult to presume or measure multi-dimensional joint-PDFs. A common practice is to assume statistical independence between the parameters of the PDF and to apply one-dimensional functions for each of them. Thus, a joint PDF can be expressed as: $p(Y_1, Y_2, ..., T) = p_{Y_1}(Y_1)\, p_{Y_2}(Y_2) ... p_T(T)$. Unfortunately, this assumption may not hold in all practical combustion situations, since variables, such as temperature and species mass fraction, are closely related in flames. In other words, the influence of the PDF shape on the results may be small when the circumstances are favorable, i.e. the reaction rates are high. In contrast, the results can become strongly dependent on the PDF shape for other scenarios e.g. for nitric oxide formation which is very sensitive to the temperature.

2.9 Chemistry Reduction/Acceleration Techniques

Apart from implementation of the combustion models, reaction chemistry must also be appropriately represented. Chemical mechanisms usually contain a large number of species and reactions. To compute a reacting flow using such a mechanism, an equally large number of transport equations would have to be solved, often involving a large number of intermediate species. Furthermore, the involved radicals have a short lifetime and very high net productions rates which depend strongly nonlinearly on the concentrations of other species and temperature. This leads to very stiff equations and modeling problems that grow with the size of the mechanism. Therefore, both the mechanism's size and its associated stiffness are important factors to be addressed, and it is highly desirable to somehow reduce the dimensionality of the chemical reaction system. Different methods have been developed in order to address these issues and are discussed briefly below.

2.9.1 Reduced Chemistry Mechanisms

Traditional approaches to chemistry reduction are based on the quasi-steady state assumption (QSSA) for species and the partial equilibrium assumption (PEA) for elementary reactions [2.26]. Significant progress has been achieved in automating the chemistry reduction based on QSSA and PEA based on data from canonical combustion problems, such as 1-D premixed and non-premixed flames and simpler 0-D reactor models [2.26]. The final outcome of chemistry reduction is a skeletal mechanism or a reduced mechanism made up of global steps, with a significant reduction in the number of reaction steps and species.

- **One-Step Global Chemistry**

The most simplistic approach is to describe the entire reaction system by a single reaction, using a fitted rate constant based on experimental measurements. Only the major species are considered and the intermediate species are not included. Moreover, the reaction, in general, may be applicable only over a specific range of combustion operating conditions. Note that if a homogeneous combustion system is described by a one-step reaction, a single combustion progress variable is sufficient to describe the chemistry, and the flame front approaches are generally applicable.

- **Multi-Step Reduced Chemistry**

Chemistry reduction approaches, which result in a skeletal mechanism or a reduced mechanism made up of global steps, with a significant reduction in the number of reactions and species, are often adopted to account for the complexity of chemistry in turbulent flames, while ensuring that the schemes can be efficiently incorporated in numerical computations [2.27-2.30]. These multiple-step reduced combustion chemistry mechanisms are often considered to include the effects of reaction chemistry, and to get a better insight about the emissions while ensuring that the calculations are not computationally intensive.

2.9.2 Low-Dimensional Manifolds

While these simplified schemes are often used in LES and can provide adequate results if the main species concentrations are of interest, they cannot be expected to work as well under unconventional combustion. Further, predicting the flame shape, its stabilization process, and pollutant emissions in practical burners also requires the use of sufficiently detailed chemistry. Additionally, mechanism reduction does not guarantee the elimination of the shortest time scales. In a skeletal mechanism, the fastest reactions may still be retained. In global mechanisms, algebraic relations for quasi-steady state (QSS) species or resulting from the PEA may still preserve some of the stiffness in the original detailed mechanism [2.26]. Since the use of detailed chemistry directly within the LES simulations

can be computationally intensive, significant efforts have been made in order to integrate chemistry effects accurately and efficiently using alternative approaches, such as the low-dimensional manifold strategy. The technique involves a dynamical systems-based approach to identify the fast and slow time scales of chemical reacting flows. The method is based on the premise that the system in composition space, parameterized with a limited set of composition variables, lie on or around a low-dimensional manifold, which is characterized by the slow time scales of the system [2.26]. By constructing databases of relevant quantities using detailed simulations of simple flames, the approach can reduce the cost of performing reacting flow computations with extensive chemical kinetic mechanisms, while still retaining the accuracy of the detailed results. The intrinsic low-dimensional manifold (ILDM) and the flamelet generated manifold (FGM) are such examples.

- **Intrinsic Low-Dimensional Manifolds (ILDMs)**

The general idea behind ILDM is explained using figure 2.16a, which displays the reaction paths of a homogeneous methane-air system in the chemical state space [2.31-2.32]. This space is spanned by the mass fractions of all species, Y_i, the pressure, p, and the enthalpy, h. At a certain time, the state of the system is represented by a point in this multi-dimensional state space. Chemical reactions change the species composition of the system and during the reaction process, so the system state moves along a trajectory through the state space. The trajectory connects the initial state with the final state, i.e. the equilibrium state.

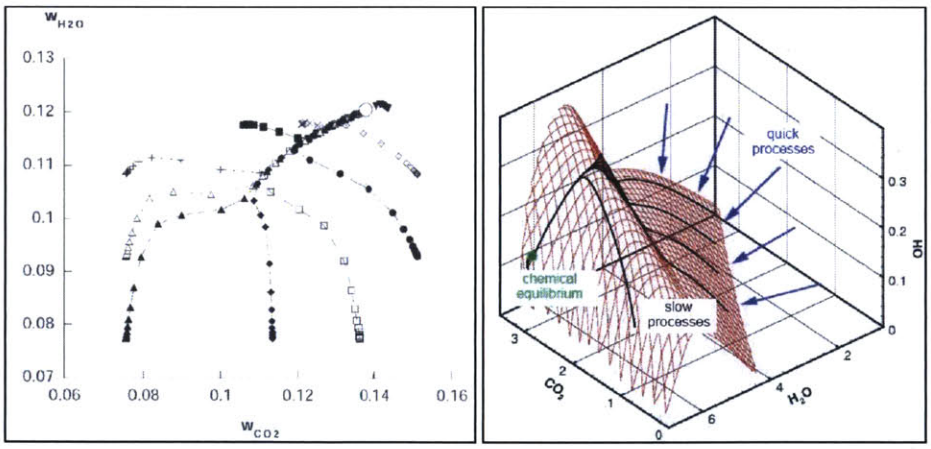

Figure 2.16: (a) Reactions paths of a homogeneous CH_4-air system, projected onto the Y_{CO2}-Y_{H2O} plane, (b) 3-D schematic of ILDM.

The projections of trajectories onto a certain plane in state space are displayed in figure 2.16a. Lines with different symbols denote paths from different initial compositions. Since all initial compositions were chosen to have the same elementary composition, they all end up in the same

equilibrium point (denoted with an empty circle). The remarkable feature of the system behavior is that all trajectories converge together towards an attracting manifold, long before the system state reaches the equilibrium. The velocity of the system along the trajectory is not apparent from 2.16a, but it may be noted here, that the movement along the common manifold is very slow, compared to movement towards this manifold. This is depicted in figure 2.16b, showing the multi-dimensional trajectories and the approach towards the attracting manifold.

The common manifold is referenced to as Intrinsic Low-Dimensional Manifold (ILDM) of the chemical system, and the observation leads to the following idea concerning the modeling: System states off the manifold quickly relax towards the manifold. This happens within time scales that cannot be resolved. The system state then moves slowly along the common manifold, which can be suitably resolved. It is therefore reasonably sufficient to presume that the system state is always on the manifold, due to the fast relaxation towards the manifold. Since the manifold has a lower dimension than the entire state space, a smaller number of parameters are sufficient to represent the system state, and instead of solving equations for each species mass, equations for the manifold parameters can be solved. These parameters are usually properly chosen mass fractions or linear combinations of mass fractions.

- **Flamelet Generated Manifolds (FGMs)**

The FGM approach involves performing detailed simulations of laminar one-dimensional flames to generate a look-up table prior to LES computations [2.33-2.35]. Specifically, the principal idea is that the thermo-chemical states in a laminar flamelet lie on a one-dimensional attracting manifold in state space. Thus, after computation of a laminar flamelet, a suitable parameterization has to be chosen (usually a linear combination of selected species mass fractions) and the states from the flamelet can be readily tabulated. When heat losses or a variable mixture fraction have to be considered, multiple flamelets with different initial temperatures or compositions have to be computed. The number of flamelets depends on the desired tabulation resolution. The advantage of this manifold computation method over the formerly introduced ones is that diffusion is included in a natural way and furthermore it is relatively easy to compute the chemistry table because reliable codes for flamelet computation exist and can be used.

For example, in case of premixed flames, the chemical flame structure can be reproduced by a collection of one dimensional laminar pre-mixed flames calculated at various equivalence ratios and for different enthalpy levels (to account for heat losses) using detailed chemistry. A lookup table can then be generated to store the chemical information, with coordinates that typically include the

progress of reaction (Y_c), the mixture fraction characterizing the local equivalence ratio (Y_z) and the enthalpy (h), thereby combining the advantages of mathematically reduced databases with a good estimation of the whole chemical flame structure. When coupled with the presumed-PDF based approach, the mean filtered values for any particular thermo-chemical property can then be obtained by performing integration over the corresponding PDF, thereby reducing the cost of reacting flow calculations, while retaining the accuracy of complex chemistry mechanisms.

3 ARTIFICIALLY THICKENED FLAME MODEL

3.1 Overview

As mentioned in Chapter 2, an important component of LES is the turbulent combustion sub-grid model, which is necessary to incorporate the effect of turbulence-chemistry interactions at the unresolved scales on the reaction rate. Various approaches have been developed [3.1], that can be broadly categorized into finite reaction zone approaches (eddy break-up type models, eddy dissipation concept etc), flame front topology methods (flame surface density and flame wrinkling descriptions, the level-set flame front tracking technique, or G-equation approach etc), statistical framework based approaches (presumed or transported PDF method), and finite-rate chemistry models (artificially thickened flame technique, partially stirred reactor concept etc). Evaluating the performance of these sub-models in simulating turbulence-chemistry interactions is crucial to developing higher fidelity CFD methods for predicting flame-flow dynamics and conducting combustion instability studies. In this chapter, the focus is on the thickened flame model, which has distinct advantages over some of the other approaches, since it allows the use of suitably detailed reaction chemistry and can be applied to different combustion regimes, in general.

LES validation studies have been conducted previously [3.2-3.6] for the thickened flame approaches to assess their predictive capabilities while simulating turbulent combustion. As briefly explained earlier in section 2.8.3, a critical aspect of the modeling technique is the determination of the efficiency function that accounts for the reduced wrinkling of the thickened flame front due to turbulence. Current models define the efficiency function using an algebraic formulation for the flame wrinkling, which is estimated based on the assumption of local-equilibrium between production and destruction of SGS flame surface density. It has been suggested that in case of highly unsteady systems or in configurations prone to thermo-acoustic instabilities, deviation from local-equilibrium and the lack of 'time-history effects' in the simpler algebraic models can result in prediction inaccuracies [3.5],[3.7-3.10]. Therefore, further development of the model is warranted so that the approach can be applied to the analysis of strongly unsteady systems.

This work addresses some of these concerns, by incorporating a dynamic formulation for the efficiency function that explicitly incorporates the influence of strain and 'time-history effects' on flame wrinkling by solving a transport equation for the flame surface area evolution. Multiple-step reaction chemistry that can be appropriately used with the thickened flame approach [3.11] is also included, and numerical simulations are performed using a compressible, finite-volume LES

code. The following canonical configurations that provide a reasonably comprehensive framework for the validation of the combustion model are considered: a triangular bluff-body in a rectangular duct, and a backward facing step, and the predictions are compared with experimental data.

The next section provides a description of the combustion model and the reaction mechanism employed in this study, following which the experimental configuration and the simulation setups for the validation cases are described. The LES predictions are compared against experimental measurements with the results indicating that the modified combustion model can result in more accurate predictions as opposed to the conventional approach.

3.2 Artificial Flame Thickening Approach

Modeling of the filtered reaction rates in the species transport equations presents a major challenge in simulating turbulent premixed combustion using LES. This is because reaction rates are highly nonlinear functions of temperature and species mass fractions, and because chemical reactions are confined to thin reacting layers at small scales that cannot be resolved on typical LES grids. In this regard, the artificial flame thickening technique, a finite-rate chemistry combustion modeling approach, essentially involves artificial thickening of the flame-front so that it can be resolved on the LES grid, while maintaining the same laminar flame speed and turbulence-flame interaction. From the theory of laminar premixed flames, it is known that the laminar flame speed, s_L^0, and the laminar flame thickness, δ_L^0, are related to the molecular diffusivity (D) and the mean reaction rate ($\bar{\omega}$) as follows:

$$s_L^0 \propto \sqrt{D\bar{\omega}},\ \delta_L^0 \propto D/s_L^0 = \sqrt{D/\bar{\omega}} \qquad (3.1), (3.2)$$

Increasing the flame thickness by a factor F while maintaining a constant flame speed can be achieved by suitably modifying the diffusivity and the mean reaction rate (by replacing D with FD, and $\bar{\omega}$ with $\bar{\omega}/F$). If F is sufficiently large, the thickened flame front can then be resolved on the LES computational grid. The filtered species transport equation can therefore be written as:

$$\frac{\partial \bar{\rho}\tilde{Y}_i}{\partial t} + \frac{\partial\left(\bar{\rho}\tilde{Y}_i\tilde{u}_j\right)}{\partial x_j} = \frac{\partial}{\partial x_j}\left(\bar{\rho}FD_i\frac{\partial \tilde{Y}_i}{\partial x_j}\right) + \frac{\bar{\omega}_i}{F} \qquad (3.3)$$

where $\bar{\rho}$ is the filtered density, $\tilde{Y}_i$ is the species mass fraction, $\tilde{\boldsymbol{u}}$ is the filtered velocity vector, and $\bar{\omega}_i$ is the filtered species reaction rate.

The thickening of the flame front, however, leads to a modified interaction between turbulence and chemistry since the Damköhler number is decreased by the factor F. The flame becomes less sensitive to turbulence, and wrinkling of the flame front is reduced. To account for this, an efficiency function, E, is introduced [3.3] that recovers the underestimation of the flame surface wrinkling due to the thickening approach. The balance equation for the chemical species then takes the form:

$$\frac{\partial \overline{\rho}\tilde{Y}_i}{\partial t}+\frac{\partial\left(\overline{\rho}\tilde{Y}_i\tilde{u}_j\right)}{\partial x_j}=\frac{\partial}{\partial x_j}\left(\overline{\rho}EFD_i\frac{\partial \tilde{Y}}{\partial x_j}\right)+\frac{E\bar{\dot{\omega}}_i}{F} \qquad (3.4)$$

It should be noted, however, that the above methodology modifies the diffusion term in the entire computational domain, which can lead to inaccuracies in the prediction of the species mass fractions. To overcome this, a dynamic formulation has been proposed [3.12], wherein the thickening factor and the diffusivity are represented locally as follows:

$$F_{loc}=1+(F-1)\Psi(c)\ ,\ D_{i,loc}=\frac{\mu}{Sc}EF_{loc}+(1-\Psi(c))\frac{\mu_t}{Sc_t} \qquad (3.5),\ (3.6)$$

$$\Psi(c)=16[c(1-c)]^2,\ c=1-\frac{Y_F}{Y_F^{in}} \qquad (3.7),\ (3.8)$$

where, $\Psi(c)$ is a locally defined sensor function based on the reaction progress variable, c, prescribed in terms of the ratio of the fuel mass fraction in the cell (Y_F) to that at the inlet (Y_F^{in}). The symbols μ and Sc refer to the dynamic viscosity and the Schmidt number respectively, while F_{loc} and D_{loc} refer to the local thickening factor and local diffusivity respectively. The filtered species transport equation can then be rewritten as:

$$\frac{\partial \overline{\rho}\tilde{Y}_i}{\partial t}+\frac{\partial\left(\overline{\rho}\tilde{Y}_i\tilde{u}_j\right)}{\partial x_j}=\frac{\partial}{\partial x_j}\left(\overline{\rho}EF_{loc}D_{i,loc}\frac{\partial \tilde{Y}}{\partial x_j}\right)+\frac{E\bar{\dot{\omega}}_i}{F_{loc}} \qquad (3.9)$$

As mentioned earlier, an important aspect of the thickened flame approach is the evaluation of the efficiency function E, in order to appropriately account for the reduced wrinkling of the thickened flame front due to turbulence. Based on DNS studies of flame-vortex interactions [3.3], different models have been proposed to define E in terms of the dimensionless wrinkling factor Ξ, which can be treated as the ratio of flame surface to its projection in the direction of propagation [3.3]-[3.6].

Previously, researchers have suggested modeling the efficiency function in terms of the local filter width, Δ_e, the unstrained laminar flame speed, s_L^0, the thickness of the laminar (δ_L^0) and thickened flames (δ_L^1), and the local SGS turbulent velocity, u'_{Δ_e} as follows [3.3]:

$$E = \frac{\Xi|_{\delta_L=\delta_L^0}}{\Xi|_{\delta_L=\delta_L^1}} \geq 1, \quad \Xi|_{\delta_L=\delta_L^0} = 1 + \alpha \left(\frac{2\ln 2}{3C_{ms}(\mathrm{Re}_t^{1/2} - 1)} \right) \frac{u'_{\Delta_e}}{s_L^0} \Gamma\left(\frac{\Delta_e}{\delta_L^0}, \frac{u'_{\Delta_e}}{s_L^0} \right) \quad (3.10), (3.11)$$

$$\Gamma\left(\frac{\Delta_e}{\delta_L^0}, \frac{u'_{\Delta_e}}{s_L^0} \right) = 0.75 \exp\left[-1.2 \left(\frac{u'_{\Delta_e}}{s_L^0} \right)^{-0.3} \right] \left(\frac{\Delta_e}{\delta_L^0} \right)^{2/3} \quad (3.12)$$

where Re_t is the turbulent Reynolds number, α is a model constant of order unity, and C_{ms} is a model constant, with a value of 0.28, to maintain consistency with DNS results.

A possible limitation of the approach above, as highlighted in [3.5], is that under highly unsteady conditions, the efficiency function model can result in inaccurate predictions, since it assumes local equilibrium between production and destruction of SGS flame surface density. In addition, the model assumes that the laminar flame speed is unaffected by strain and curvature and therefore employs the unstrained laminar flame speed while estimating the flame wrinkling. This has been shown to result in predictive inaccuracies [3.13], as in most cases, strain effects cannot be ignored. For example, for flames trapped in the shear layer behind a backward-facing step, the strain effects near the step are important in reducing the effective reaction rate and preserving the Kelvin-Helmholtz instability. In other words, if the laminar flame is assumed independent of strain rate, the heat release in the shear layer inhibits the growth of the instability, resulting in a near smooth flame [3.7]. Likewise, in case of confined swirling flames, significant strain effects combined with heat loss can provoke extinction of the flame that stabilizes in the outer shear layer of the annular jet, particularly under lean conditions [3.13]. Further, accurately including the 'time-history effects' of flame-vortex interaction on stretching and wrinkling of turbulent flames is of fundamental importance [3.8-3.10].

Figure 3.1: Reaction source term in a swirl-stabilized combustor: (a) Thickened flame model with unstrained laminar flame speed and no heat loss, (b) Thickened flame model with strained flame speed and no heat loss, (c) Thickened flame model with strained flame speed and heat loss effects.

In order to address these concerns, a transport equation for the sub-grid flame wrinkling can be used to dynamically evaluate the magnitude of the efficiency function, by appropriately determining the flame wrinkling and subsequently updating the model parameter α during the LES computations. The transport equation for the flame wrinkling factor can be written as [3.14-3.17]:

$$\frac{\partial \Xi}{\partial t}+\hat{U}\cdot\nabla\Xi=-\widehat{n\cdot(\nabla U_s)\cdot n}\Xi+\hat{n}\cdot\left(\nabla\widehat{U_t}\right)\cdot\hat{n}\Xi+\left(\widehat{U_t}-\widehat{U_s}\right)\cdot\frac{\nabla\left|\nabla\bar{b}\right|}{\left|\nabla\bar{b}\right|}\Xi \qquad (3.13)$$

where U_t is the surface-filtered effective velocity of the flame, U_s is the local instantaneous velocity of the flame surface, n is the normal to the flame surface, and b is the reaction regress variable. The terms on the *r.h.s.* in (3.13) represent the effects of strain, propagation and differential propagation respectively. A simplified formulation to (3.13) may be written, as in [3.7], as:

$$\frac{\partial \Xi}{\partial t}+\widehat{U_s}\cdot\nabla\Xi=G\Xi-R(\Xi-1)+(\sigma_s-\sigma_t)\Xi \qquad (3.14)$$

$$\widehat{U_s}=\tilde{U}+\left(\frac{\bar{\rho}_u}{\bar{\rho}}-1\right)s_u\Xi\tilde{n}-\frac{\nabla\cdot\left(\bar{\rho}D\nabla\tilde{b}\right)}{\bar{\rho}\left|\nabla\tilde{b}\right|}\tilde{n} \qquad (3.15)$$

$$G=R\frac{2c\left(\Xi_{eq}^{*}-1\right)}{1+2c\left(\Xi_{eq}^{*}-1\right)},\quad R=\frac{0.28}{\tau_\eta}\frac{\Xi_{eq}^{*}}{\Xi_{eq}^{*}-1},\quad \Xi_{eq}^{*}=1+0.62\sqrt{\frac{u'}{s_u}}R_\eta \quad (3.16), (3.17), (3.18)$$

where τ_η is the Kolmogorov timescale, u' is the sub-grid turbulence intensity, c is the reaction progress variable, and R_η is the Kolmogorov Reynolds number. The terms σ_s and σ_t refer to the resolved strain rate and the surface filtered resolved strain rate respectively, while s_u is the strained laminar burning velocity. The resolved strain rates can be obtained as follows:

$$\sigma_s=\frac{\nabla\cdot\tilde{U}-\tilde{n}\cdot\left(\nabla\tilde{U}\right)\cdot\tilde{n}}{\Xi}+\frac{(\Xi+1)\left\{\nabla\cdot\left(s_u\tilde{n}\right)-\hat{n}\cdot\left[\nabla\left(s_u\tilde{n}\right)\cdot\tilde{n}\right]\right\}}{2\Xi} \qquad (3.19)$$

$$\sigma_t=\nabla\cdot\left(\tilde{U}+s_u\Xi\tilde{n}\right)-\tilde{n}\cdot\left[\nabla\left(\tilde{U}+s_u\Xi\tilde{n}\right)\right]\cdot\tilde{n} \qquad (3.20)$$

The strained laminar burning velocity can be obtained as follows:

$$\frac{\partial s_u}{\partial t}+\widehat{U_s}\cdot\nabla s_u=-\sigma_s s_u+\sigma_s s_u^{\infty}\frac{\left(s_L^0-s_u\right)}{\left(s_u-s_u^{\infty}\right)},\quad s_u^{\infty}=s_L^0\max\left(1-\frac{\sigma_s}{\sigma_{ext}},0\right) \quad (3.21), (3.22)$$

where s_L^0 is the unstrained laminar flame speed and σ_{ext} is the strain rate at extinction [3.18]. Additional details on the modeling can be found in [3.7]. An alternative approach to estimate the

laminar burning velocity, which accounts for the influence of strain and heat losses, is to use empirical relations that can be derived based on strained laminar flamelet computations [3.13]. This has however not been considered in the present analysis.

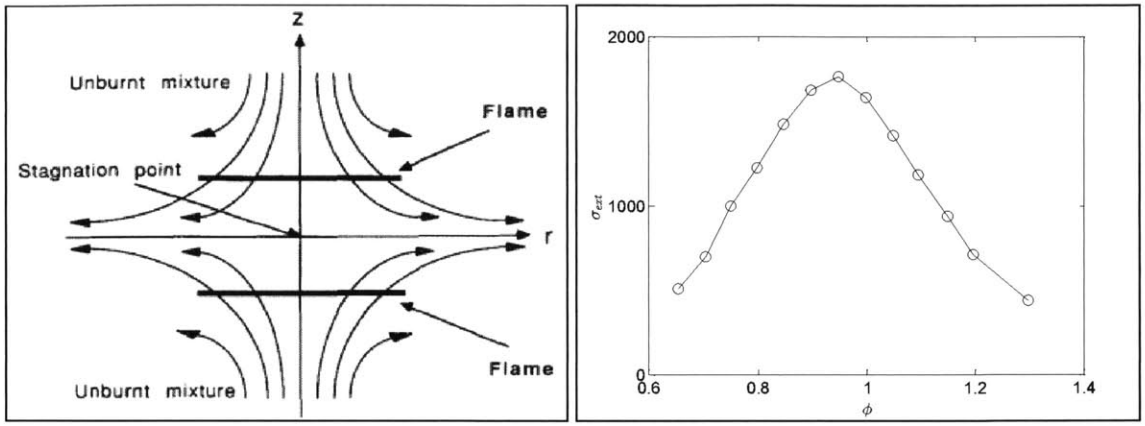

Figure 3.2: (a) Axi-symmetric twin flame configuration for strained flames, (b) Extinction limits of strained premixed methane-air flame as a function of equivalence ratio [3.18].

Once the flame surface wrinkling is estimated using the above formulation, the model parameter α can be updated in equation (3.11), and the efficiency function can therefore be dynamically evaluated during the computations. Additionally, the strained flame speed, as determined in equation (3.21), can be used to replace the unstrained value in equation (3.11).

A distinct advantage of the thickened flame approach is that the reaction rates can be calculated using Arrhenius rate laws (much like a DNS calculation, without the need of any *ad-hoc* sub-models), while allowing the explicit use of multi-step chemistry mechanisms as well. Moreover, phenomena such as ignition and flame-wall interactions are directly accounted for, without requiring additional sub-modeling. In addition, the proposed wrinkling based approach is an improvement over the existing algebraic models, since deviation from local-equilibrium, and the absence of time-history and strain effects in the equilibrium models can result in inaccurate predictions, especially in case of lean premixed flames under highly unsteady conditions.

As regards the chemical reaction schemes, an appropriate multiple-step chemistry mechanism for propane combustion in air (Jones-Lindstedt mechanism [3.19]), as indicated in table 3.1, has been utilized. While simplified global schemes can provide adequate results if the main species concentrations are of interest, they cannot be expected to work as well under unconventional combustion conditions (e.g. oxy-fuel combustion), and are likely to inaccurately estimate the temperature in the absence of an adequate set of reactions [3.20]. The role of reaction chemistry can

also be significant in combustion systems prone to thermo-acoustic instabilities [3.21], near extinction and re-ignition phenomena, as well as in influencing the flame speed [3.22]. However, the reaction schemes used within the thickened flame framework should typically include a limited number of intermediate species as it can lead to difficulties for wrinkled and/or stretched flame fronts [3.2], [3.11].

Table 3.1: Jones-Lindstedt reaction mechanism for propane-air combustion.

JONES-LINDSTEDT (CHEMKIN)	*A (pre-exponential factor)*	*β*	*E_a (activation energy)*
C3H8 + 1.5 O2 => 3CO+ 4H2	7.1E+13	0.00	3.0E+4
FORD /C3H8 0.5/ FORD /O2 1.25/			
C3H8 + 3H2O => 3CO + 7H2	3.0E+11	0.00	3.0E+4
H2 + 0.5 O2 => H2O	1.21E+18	-1.0	4.0E+4
FORD /H2 0.25/ FORD /O2 1.5/			
H2O + 0 O2 +0 H2 => H2 + 0.5 O2	7.06E+17	-0.877	9.8E+4
FORD /H2 -0.75/ FORD /O2 1/ FORD /H2O 1/			
CO + H2O = CO2+H2	2.75E+12	0.00	2.0E+4

3.3 Validation Study: Triangular Bluff-Body in a Rectangular Channel

A triangular bluff-body in a rectangular channel [3.23- 3.26] provides a reasonably comprehensive framework for validation since it is comprised of many aspects of practical combustors such as anchored flames, regions of recirculation and shear layers. A parallelized, unstructured, finite volume LES code for solving compressible 3D Navier Stokes equations with second order spatial and temporal accuracy is used, and the one-equation eddy viscosity model is employed to estimate the sub-grid scale (SGS) stress terms. The numerical predictions are compared against experimental data for non-reacting and reacting cases, and the relative performance of the conventional (algebraic model for Ξ) and modified (dynamic formulation for Ξ) efficiency function models is investigated.

3.3.1 Experimental Configuration

The bluff-body configuration [3.23] consists of a straight channel 700 mm long with a rectangular cross section of 120 mm × 240 mm (figure 3.3). The flame is anchored on a bluff-body that has a triangular cross section with each side of length (L) 40 mm, located 600 mm upstream of the exit. A mixture of air and propane is introduced at an equivalence ratio of 0.65, at a bulk inlet velocity (U_{BL}) of 17.0 m/s (Reynolds number, Re_{BL} = 48000, based on the bluff-body characteristic dimension L and the bulk fluid velocity U_{BL}). The inlet temperature (T_B) is 288 K and the nominal pressure is 101 kPa.

3.3.2 Simulation Setup

The choice of the numerical grid is based on estimates of the physical length scales associated with the flow configuration. For example, the bluff-body boundary layer plays a critical role in the shear layer formation. Its thickness is inversely proportional to the square root of the macroscopic Reynolds number, Re_{BL} and is thus estimated to be 4.5 mm. In comparison, the Kolmogorov length scale ($Re_{BL}^{-3/4}L$) is noted to be 12.5 μm. In addition to the boundary layer thickness, it has been suggested that in order to directly capture the bulk of the energy containing structures and resolve at least 80% of the turbulent kinetic energy, a filter-width (Δ) to integral length scale (L_I) ratio of approximately 0.083 should be maintained [3.27]. Using the bluff-body characteristic dimension (L) as the integral length scale, the filter-width can be estimated to be 3.3 mm. It should be noted however, that the above theory does not focus on resolving near-wall structures and may not be applicable for reacting flow. Therefore, appropriate grid clustering may be required to resolve the structures near the walls and in the shear layer region for reacting flow. Based on these arguments, the non-uniform mesh utilized in the present work is comprised of approximately 31,500 hexahedral cells in the x-y plane, and gets coarser along the stream-wise direction. Downstream of the bluff-body, the total number of cells in the x and y directions are 560 and 48 respectively; therefore, the average Δx and Δy values in the wake region are approximately 1.05 mm and 2.50 mm respectively, while the minimum Δx value, in the shear layer region, is approximately 0.75 mm.

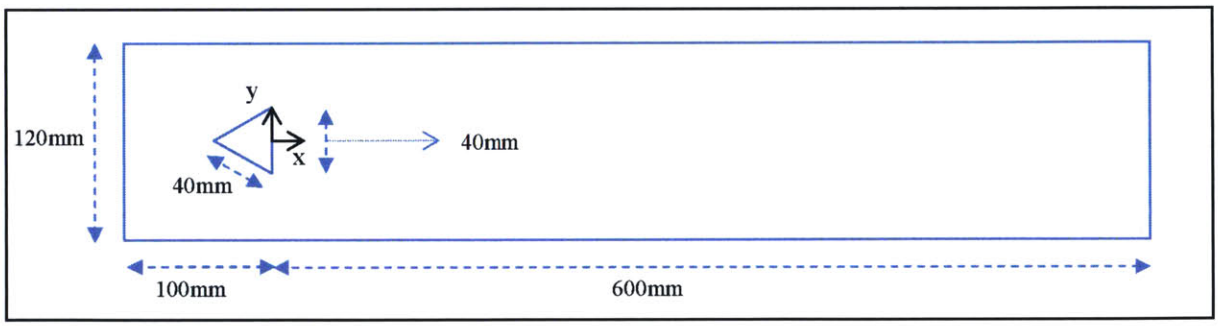

Figure 3.3: Bluff-body setup used for flame stabilization.

Temporal resolution is determined based on physical time scale estimates in order to prevent excessive numerical dissipation and numerical instability, as well as on chemical time scales. For the non-reacting flow, a vortex shedding frequency (f_{vs}) of 105 Hz is reported in the experiments [3.24]. Based on this observation, a vortex shedding based time scale of 9.5 ms can thus be estimated. The integral time scale can be obtained using the ratio of the length scale (L) and the measured turbulent velocity fluctuation at the shear layer (u') as 4 ms, while the Kolmogorov time scale (proportional to

the product of the integral time scale and the inverse square root of the macroscopic Reynolds number), in comparison, is estimated to be 18 μs. In addition, using the CFL criterion (C_{max} = $(U_{BL}+U_t)\Delta t/\Delta x$; C_{max} = 1, U_t = 340m/s, Δx = 0.8 mm), the time step for the simulations is estimated to be approximately 2.2 μs. Based on these considerations, a conservative value of 1 μs is used in the reacting flow simulations, to take into account local refinement and acceleration of the fluid above the bulk inlet velocity, and to adequately resolve the chemical time scales. Note that in order to better understand the effect of heat release on the flow, the range of the magnitudes for the contours of some of the flame-flow variables have been fixed corresponding to the non-reacting and reacting cases. The key quantities relevant to the configuration are summarized in table 3.2.

Table 3.2: Parameters for the bluff-body configuration.

PARAMETER	SYMBOL/EXPRESSION	VALUE
Duct Length	L_{BL}	700 mm
Duct Height	L_{BH}	120 mm
Duct Width	L_{BW}	240 mm
Bluff-Body Side (Characteristic Length)	L	40 mm
Integral Length Scale	L_I (=L)	40 mm
Equivalence Ratio	φ	0.65
Bulk Inlet Velocity (Characteristic Flow Velocity)	U_{BL}	17 m/s
Macroscopic Reynolds Number	Re_{BL}	48,000
Inlet Temperature	T_B	288 K
Nominal Pressure	P	101 kPa
Bluff-Body Boundary Layer	$Re_{BL}^{-1/2}$	4.5 mm
Kolmogorov Length Scale	$Re_{BL}^{-3/4}L$	12.5 μm
Cold Flow Filter Width (Pope's Criterion)	$\Delta=0.083L_I$	3.3 mm
Vortex Shedding Frequency	f_{vs}	105 Hz
Vortex Shedding Time Scale	$1/f_{vs}$	9.5 ms
Shear Layer Fluctuation (measured)	u'	~10 m/s
Integral Time Scale	$T_I=L/u'$	4 ms
Kolmogorov Time Scale	$Re_{BL}^{-1/2}T_I$	18 μs
CFL Criterion Time Scale	$C_{max}\,\Delta x/(U_{BL}+U_t)$	2.2 μs

Three dimensional simulations with periodic boundary conditions in the span-wise direction over 40mm of the channel width are performed. At the inlet, Dirichlet conditions are used for all variables except the pressure, for which zero Neumann conditions are specified. The inlet velocity has a flat profile to which fluctuations of 5% turbulence intensity are imposed. At the exit, zero Neumann conditions are specified for all variables except the pressure, for which wave-transmissive conditions are used. No-slip conditions are applied for the flow at the top and bottom walls of the duct as well as the bluff-body, while zero Neumann conditions are specified for the other variables. Heat transfer is also considered at the walls to account for any thermal losses. In order to maintain reasonable computational efficiency, appropriate wall functions are utilized to resolve the flow features in the wall boundary layer. Numerical computations start from quiescent conditions and the

unsteady flow characteristics evolve naturally. In order to initiate the flame, a high temperature pulse is applied at the inlet section which ignites the fuel; the reacting mixture convects downstream, and eventually stabilizes as a flame at the edge of the bluff-body. Averaging is performed over approximately 10 flow-through cycles once the flow is established in the computational domain.

3.3.3 Results and Discussions: Non-Reacting Flow

Isothermal flow is considered prior to simulating reacting flow, with the prominent flow features in the wake region of the bluff-body comprising of the shear layer and the shed vortices, the recirculation zone, and the stagnation region. The flow structures begin to form as the boundary layer along the bluff-body separates at its edge, developing into a thin shear layer. As the flow progresses downstream, unsteady behavior is observed due to vortices that are shed alternatively from the mixing layers at the trailing edges of the bluff-body, forming a von-Karman vortex street pattern downstream. The eddy structures entrain irrotational fluid from the non-turbulent region outside the shear layer, which causes the formation of a low velocity recirculating vortex structure in the wake region downstream of the bluff-body. Due to the favorable pressure gradient created by the fluid entrained, the shear layer curves towards the mid-plane (centerline) axis eventually resulting in a stagnation zone. Note that the location of this region fluctuates due to the inherently unsteady motion of the shear layer.

In figure 3.4, the instantaneous z-vorticity contour at a specific time-instant is shown, depicting the coherent vortices that develop due to the roll-up of vortex sheets formed at the bluff-body edges. These large-scale structures break down into smaller eddies as they convect downstream, eventually dissipating due to vortex stretching and viscosity effects.

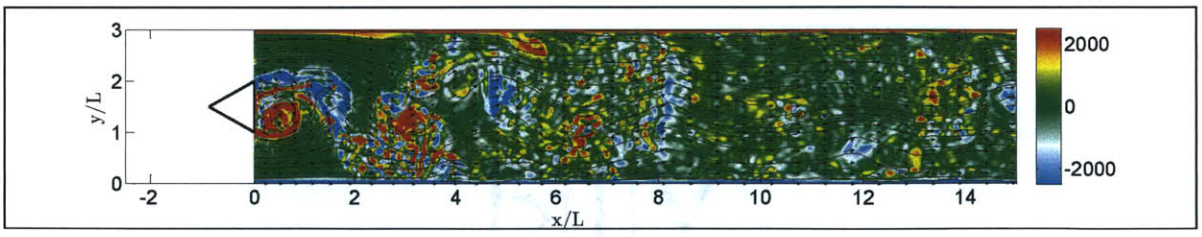

Figure 3.4: Instantaneous z-vorticity (1/s) at a specific time-instant, with the instantaneous 2D velocity vectors and streamlines.

The instantaneous z-vorticity contours at different time-instants (figure 3.5) clearly suggest that these (primary) vortices are shed asymmetrically from the shear layer. Additionally, vortices are also shed from the upper and lower walls of the duct, attributed to the regions of separation caused by the presence of an adverse pressure gradient. It has been suggested that the interaction of these

(secondary) vortices with the primary vortices contributes significantly to the three-dimensional breakdown and generation of smaller turbulent structures downstream [3.24].

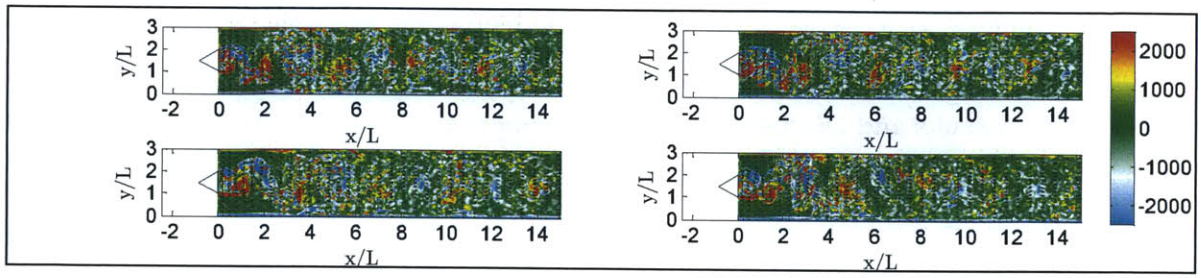

Figure 3.5: Instantaneous z-vorticity (1/s) at different time-instants, with the corresponding instantaneous 2D velocity vectors.

The average z-vorticity contour, shown in figure 3.6 on a reduced scale, also indicates the presence of these secondary vortical structures (near the walls at x/L=3), apart from highlighting the primary recirculation region.

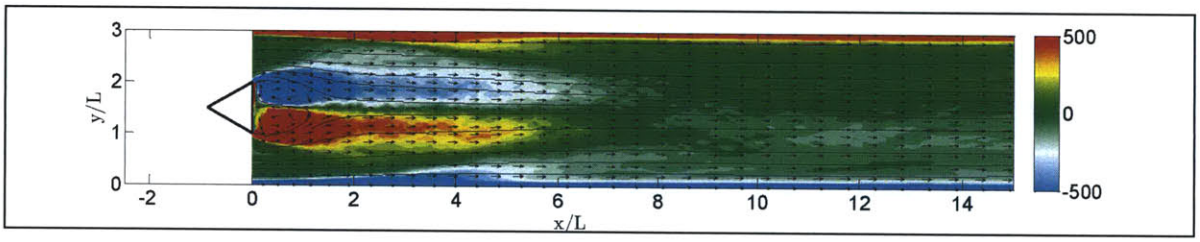

Figure 3.6: Average z-vorticity (1/s), with the mean 2D velocity vectors and streamlines.

The contours of the average axial velocity and the instantaneous axial velocity (at a specific time-instant) are presented along with the corresponding streamlines in figures 3.7 and 3.8, respectively. The cross-sections at which numerical and experimental data are compared are also marked. The flow is dominated by the presence of strong recirculation zone in the immediate wake region downstream of the bluff-body, with the zero velocity region (shown in white) running through its core.

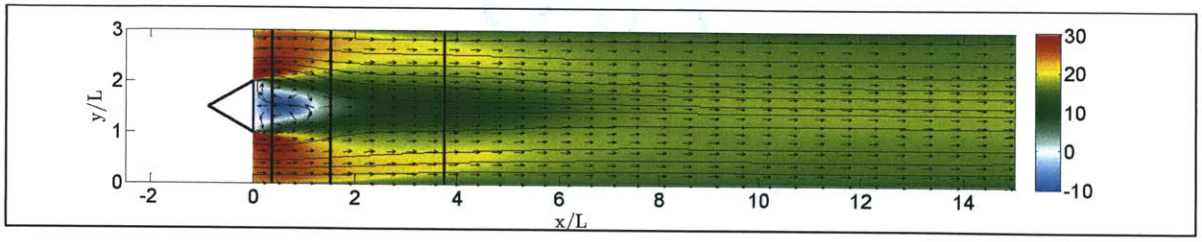

Figure 3.7: Average axial velocity (m/s), with the mean 2D velocity vectors and streamlines. The cross-sections at which data are compared are also shown.

As noted from the mean flow streamlines, the recirculation zone extends to an average length of approximately $1.25L$ downstream of the bluff-body. However, the instantaneous span of the recirculatory region varies significantly, due to the unsteady nature of the shear layer vortex shedding. This is also evident from the instantaneous axial velocity contours at different time-instants, as shown in figure 3.9.

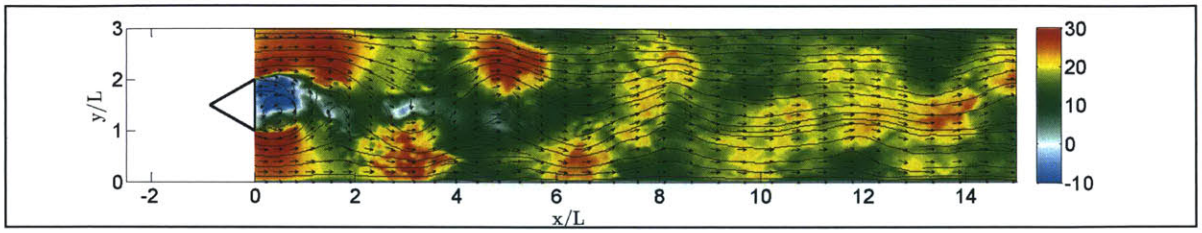

Figure 3.8: Instantaneous axial velocity (m/s) at a specific time-instant, with the instantaneous 2D velocity vectors and streamlines.

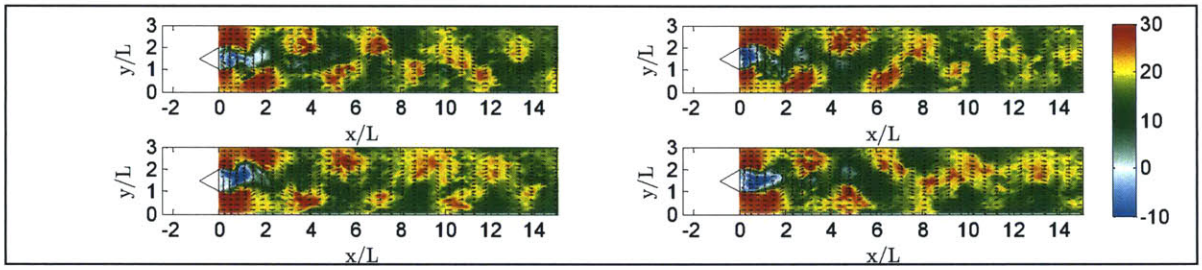

Figure 3.9: Instantaneous axial velocity (m/s) at different time-instants, with the corresponding instantaneous 2D velocity vectors.

The contour of the rms axial velocity is presented in figure 3.10, indicating high turbulence activity in the immediate wake of the bluff-body, primarily around the periphery of the recirculation zone, in the region corresponding to significant vortex shedding activity. The coherent structures generated in the mixing layer, and shed downstream sequentially due to Kelvin–Helmholtz instability, contribute significantly to the generation of turbulent kinetic energy in the shear layers, as indicated by the contour of the Reynolds stress tensor term (figure 3.11).

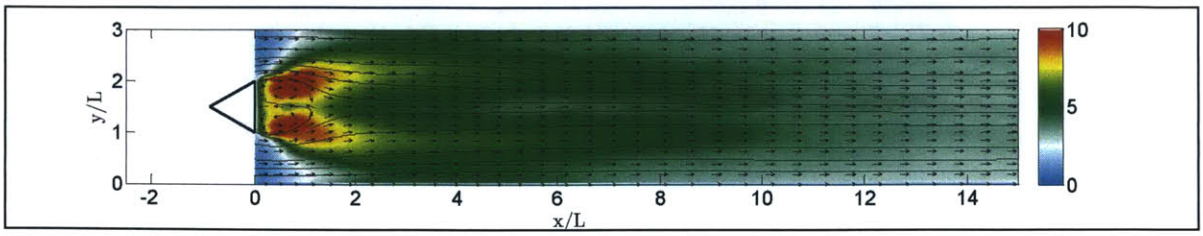

Figure 3.10: rms axial velocity (u_x', m/s), with the mean 2D velocity vectors and streamlines.

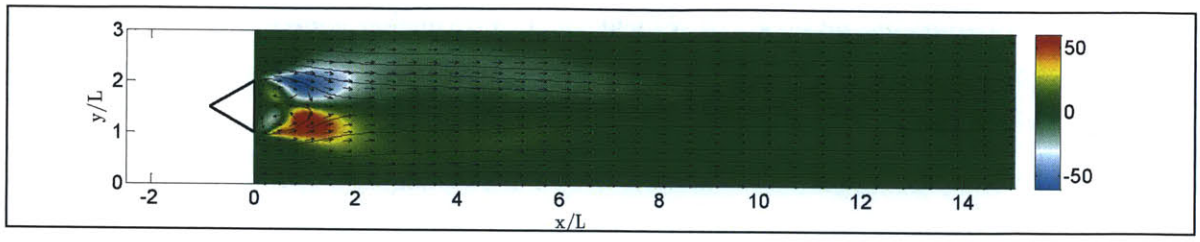

Figure 3.11: Reynolds stress tensor term ($u'_x u'_y$, m^2/s^2), with the mean 2D velocity vectors and streamlines.

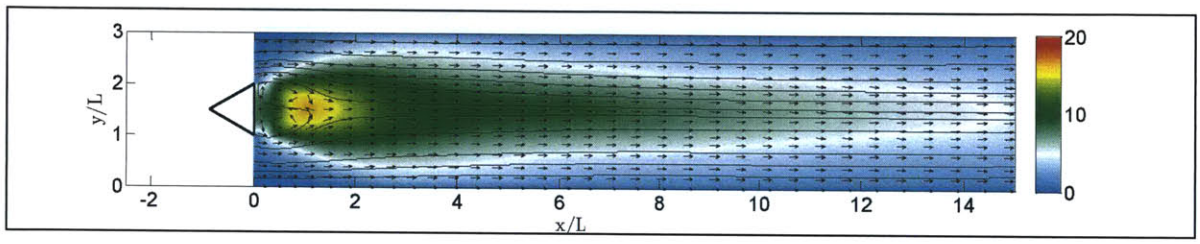

Figure 3.12: rms transverse velocity (u'_y, m/s), with the mean 2D velocity vectors and streamlines.

As depicted in the rms transverse velocity contour in figure 3.12, the flow field fluctuations are also generally high near the stagnation zone where entrainment and flow reversal takes place. As the flow proceeds downstream, the large coherent structures break down into smaller eddies, which subsequently dissipate due to viscous effects. In the downstream section, the relative influence of the large-scale vortical structures on turbulence reduces, and the turbulent flow field becomes significantly more isotropic. The viscous dissipation per unit volume, Θ, shown in figure 3.13, can be as estimated in Cartesian coordinates [3.28] as:

$$\Theta = 2\mu\left[\left(\frac{\partial u_x}{\partial x}\right)^2+\left(\frac{\partial u_y}{\partial y}\right)^2+\left(\frac{\partial u_z}{\partial z}\right)^2-\frac{1}{3}\left(\frac{\partial u_x}{\partial x}+\frac{\partial u_y}{\partial y}+\frac{\partial u_z}{\partial z}\right)^2\right] + \mu\left[\left(\frac{\partial u_x}{\partial y}+\frac{\partial u_y}{\partial x}\right)^2+\left(\frac{\partial u_y}{\partial z}+\frac{\partial u_z}{\partial y}\right)^2+\left(\frac{\partial u_z}{\partial x}+\frac{\partial u_x}{\partial z}\right)^2\right] \tag{3.23}$$

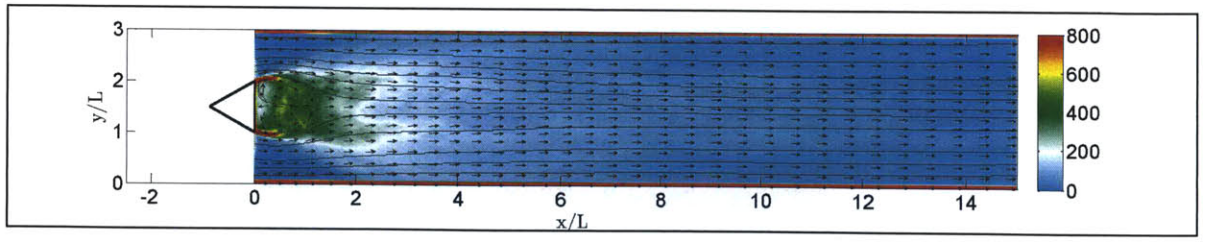

Figure 3.13: Average viscous dissipation per unit volume (kg/ms^3), with the mean 2D velocity vectors and streamlines.

The normalized profiles for the average axial velocity and rms axial velocity as well as the Reynolds stress tensor term, comparing LES predictions with experimental measurements at cross-sections in the region downstream of the bluff-body, are shown in figure 3.14. The simulated results agree well with experimental data and the underlying flow field is suitably resolved, as indicated by the velocity statistics in the wake region. The location of the shear layer is predicted with reasonable accuracy, as is the extent of the recirculation zone. As aforementioned, the fluctuations peak in the shear layers and increase sharply in the stream-wise direction before gradually reducing in magnitude as the flow proceeds downstream, and the large-scale turbulent eddies induced by the bluff-body break down and dissipate.

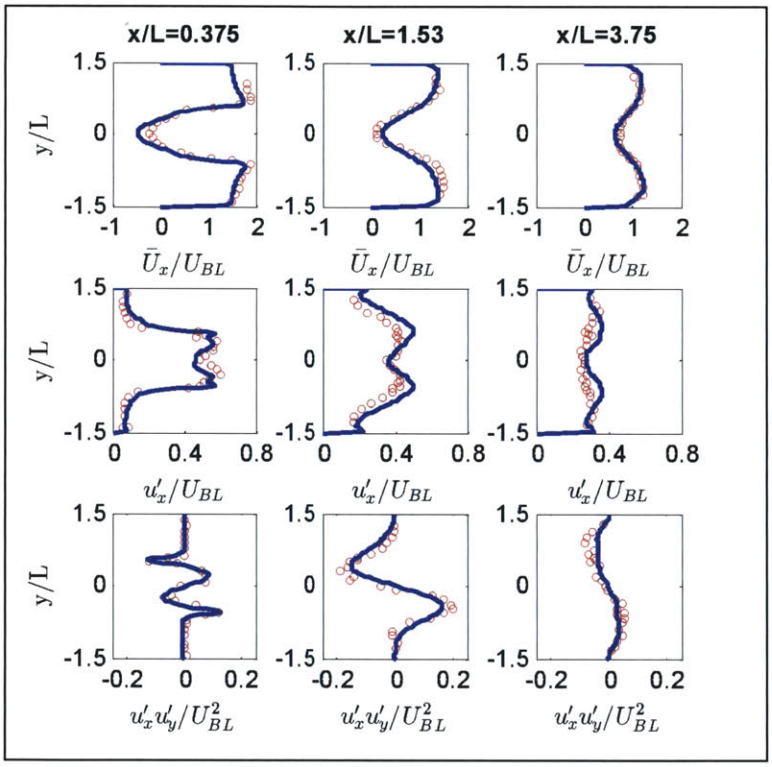

Figure 3.14: Normalized profiles for average axial velocity (top), rms axial velocity (middle) and Reynolds stress tensor term (bottom): ooo Experiment, --- LES

Figure 3.15 displays the normalized average axial velocity, anisotropy and fluctuation level along the centerline, where anisotropy, η, and fluctuation level, ζ, are defined as follows:

$$\eta = \frac{u'_{cy}}{u'_{cx}}, \quad \zeta = \frac{\sqrt{u'^{\,2}_{cx} + u'^{\,2}_{cy}}}{U_{BL}} \qquad (3.24), (3.25)$$

where u'_{cx} and u'_{cy} refer to the rms fluctuation level for the x and y centerline velocity components respectively.

Simulation results are in reasonable agreement with the experiments, and the velocity statistics in the recirculation zone, including the fluctuations in u_{cx} and u_{cy}, are predicted fairly well. It is observed that in the immediate wake of the bluff-body, the velocity is negative and the peak reverse velocity (attained at about 0.7L) is about 60% of the inflow velocity. The flow then gradually accelerates and the mean centerline velocity approaches the free stream velocity magnitude further downstream as seen in figure 3.15. As regards the fluctuations along the centerline, they tend to peak in the recirculation zone region due to the shedding vortices; turbulence anisotropy is also high in the stagnation zone region, where flow reversal takes place. Further downstream of the bluff-body, as aforementioned, the turbulence intensity is somewhat suppressed as the relative influence of the vortices on the turbulent flow field reduces.

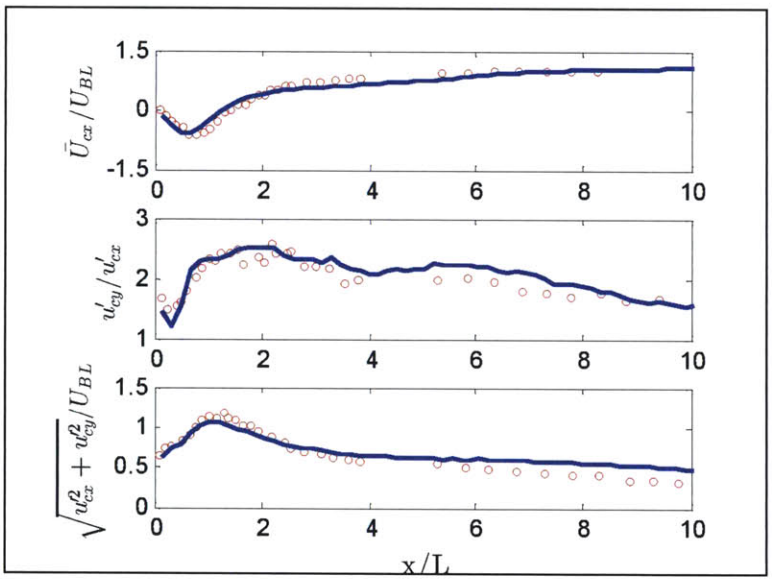

Figure 3.15: Normalized profiles for average velocity (top), anisotropy (middle) and fluctuation level (bottom) along the centerline: ooo Experiment, --- LES

3.3.4 Results and Discussions: Reacting Flow

Next, reacting flow for the configuration is considered and simulations are performed using the conventional and modified efficiency function models. The LES contours of the instantaneous temperature and CO mass fraction, as well as the normalized average heat release are shown in figures 3.16-3.19, indicating the presence of a somewhat symmetric, thin flame that anchors at the edge of the flame-holder. The flame stabilizes due to the recirculation of the combustion products in

the wake region, and is essentially confined to a surface originating in the shear layers downstream of the flame-holder edges. Large-scale mixing between cold reactants and hot products thus takes place in these shear layer regions, forming a composition in which combustion can occur, with the flame surrounding the recirculation region. The use of the detailed chemistry mechanism also allows the tracking of intermediate species such as CO, which can be critical from an emissions perspective in practical combustor systems, and can be used to predict the extent of reaction as well.

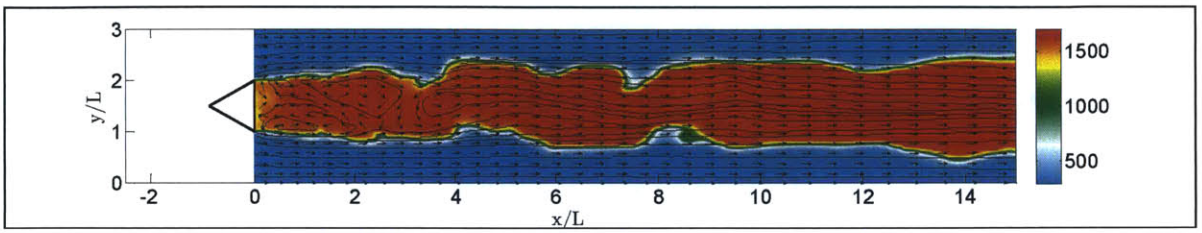

Figure 3.16: Instantaneous temperature (K), with the instantaneous 2D velocity vectors and streamlines.

It is well established that turbulent combustion and stabilization of the flame in the reacting shear layer is a sequential phenomenon that involves preheating of the incoming reactant mixture near the flame-holder base, followed by its ignition due to the heat flux transported radially outward from the recirculation zone. These processes result in a relatively thin reaction zone near the bluff-body periphery and combustion in this ignition/thin-flame region is typically characterized by reaction kinetics for low equivalence ratios, given the low flame propagation speed and heat release rates. In such scenarios, the flame stabilizes in the presence of an elongated recirculation zone, often larger than that for the cold flow [3.29].

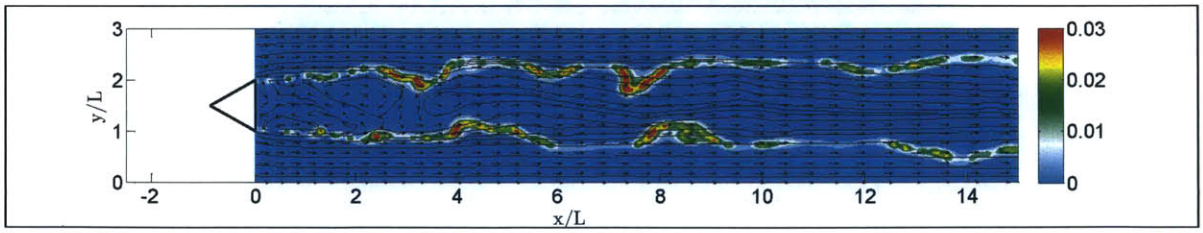

Figure 3.17: Instantaneous CO mass fraction at a specific time-instant, with the instantaneous 2D velocity vectors and streamlines.

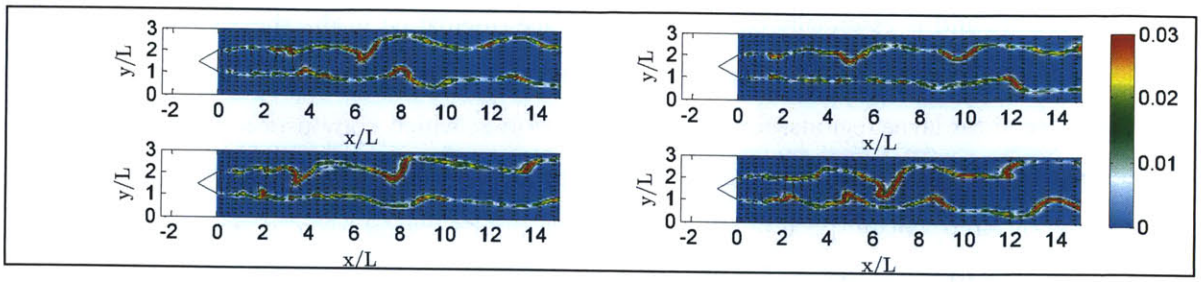

Figure 3.18: Instantaneous CO mass fraction at different time-instants, with the corresponding instantaneous 2D velocity vectors.

As the flow progresses downstream of the bluff-body edge, the shear layer expands and subsequently, due to Kelvin-Helmholtz instability, is transformed into a series of roll up eddies. As the eddy structures are carried downstream through the mixing layer, they begin to grow in size, forming as folds around the flame edge, resulting in a slightly convoluted reaction zone that consists of partially burned-unburned gases. The small-scale shear-generated turbulence in the region augments entrainment and results in appreciable velocity and scalar (temperature, density) fluctuations in the region. This also contributes to anchoring the flame, as well as increasing its intensity, since the penetration of the inner layers of the shear layer by small eddies can cause the reaction rate to be strongly affected by turbulence, while significantly enhancing heat diffusion from inner layers towards the preheat zone.

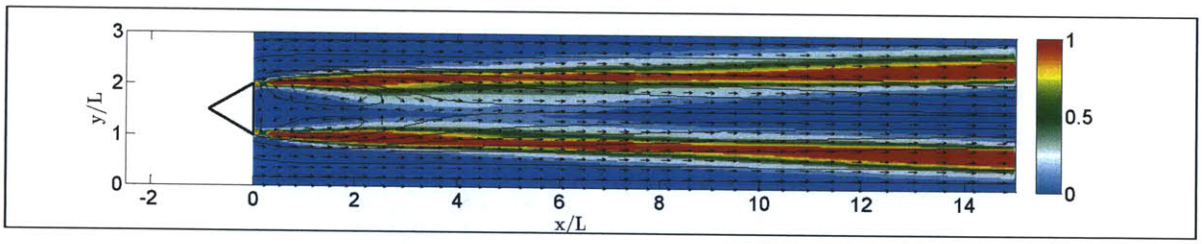

Figure 3.19: Normalized average heat release contour, with the mean 2D velocity vectors and streamlines.

The large-scale coherent structures, therefore, result in a thickened average flame that is characterized by the mixing and entrainment processes, and the flow field in the region is dominated by turbulent dilatation effects. Furthermore, the curving of the shear layer towards the mid-plane (centerline) results in a slight 'necking' of the flame. The region in the vicinity of the stagnation point is comprised of pockets of hot-product and cold-reactant gas, and significant flow and scalar oscillations are observed, resulting from flow reversal and mixing events. The high turbulence decreases mixing time and increases entrainment between the fresh mixture and the flame, ie the flame loading is increased and the reaction zone is thickened (figure 3.19).

In figure 3.20, the instantaneous z-vorticity contour at a specific time-instant is shown, suggesting the presence of a nearly symmetric flow field: the recirculation zone is characterized by periodic symmetric vortex shedding, as opposed to asymmetric vortex shedding in the non-reacting flow. This aligns with previous studies indicating that for premixed bluff-body stabilized flames, if the density ratio between the reactants and products is high enough, the heat release results in suppression of the asymmetric vortex shedding characteristic of non-reacting flow [3.24]. These transient eddies issued from the bluff-body edge are primarily responsible for the downstream convection of the hot products, stored inside the wake. The shed vortices also significantly enhance the mixing of the combustion products (within the recirculation zone) with the incoming fuel-air mixture, and play a dominant role in stabilizing the flame.

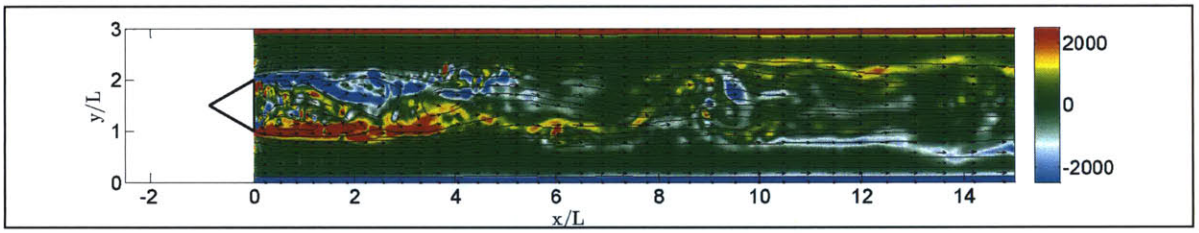

Figure 3.20: Instantaneous z-vorticity (1/s) at a specific time-instant, with the instantaneous 2D velocity vectors and streamlines.

It is also observed that as compared to the non-reacting case, the vorticity field is somewhat diffuse, and the large-scale vortices are broken up after they have been formed, due to heat release and thermal expansion in the vortex cores. It has been suggested that the combustion in the vortex cores results in a decrease in the density as a result of thermal expansion, and the conservation of angular momentum coupled with the increase in vortex area results in a decrease in the intensity [3.25]. The strong baroclinic torque, resulting from pressure and density gradients strongly weakens the Kelvin-Helmholtz instability responsible for the von-Karman street. The vortex shedding that occurs at the corners of the bluff body in the non-reactive case is now delayed, and a pair of stationary vortices forms at the two edges. Subsequently, flow instabilities in these vortices lead to symmetric vortex shedding. As the flow convects downstream, the vortices undergo pairing and during this process the flame is wrinkled and its surface area increases rapidly, enhancing both turbulent mixing and combustion. The reacting flow field, therefore, differs substantially from that in the isothermal scenario. This appreciable shift in the flow physics due to heat release is thus reproduced reasonably well with the combustion model (figure 3.21).

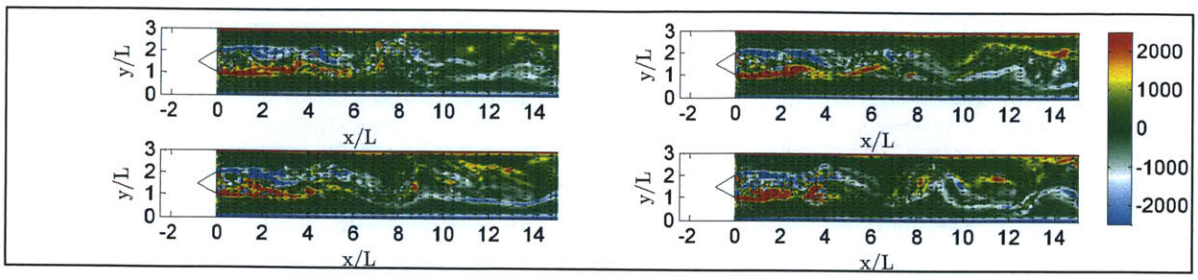

Figure 3.21: Instantaneous z-vorticity (1/s) at different time-instants, with the corresponding instantaneous 2D velocity vectors.

In figure 3.22, the contour of the average z-vorticity is depicted on a reduced scale. In the wake region, the velocity field is dominated by a pair of almost stationary counter rotating vortices, primarily responsible for flame stabilization through recirculation of hot combustion products. Fluctuations in velocity and density fields induce instability in this vortex pair, eventually leading to vortex shedding. Further downstream, the effects of dilatation and diffusion of vorticity become increasingly important resulting in the gradual suppression of the shed vortices.

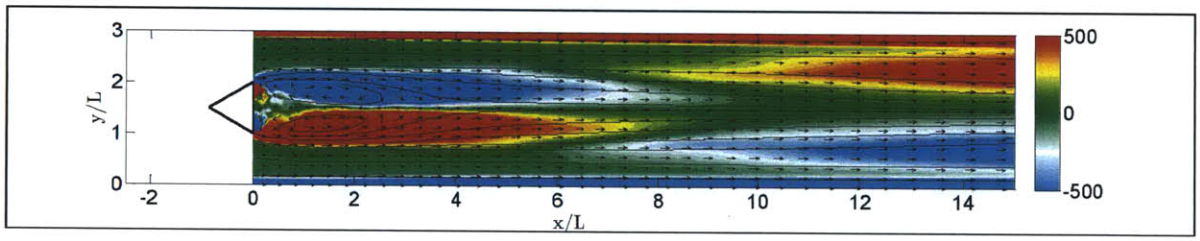

Figure 3.22: Average z-vorticity (1/s), with the mean 2D velocity vectors and streamlines.

It should also be noted, in contrast to the non-reacting case, that no vortices are shed from the upper and lower walls of the duct for the reacting case, and that the interaction of the wake with the walls is also significantly lower. Further, while the direction of vortex rotation is clockwise in the upper half of the combustor duct, it switches to an anti-clockwise direction further downstream, caused due to the generation of baroclinic vorticity by the flame [3.24]. Additionally, while the vortices appear to periodically shed off the upper and lower edges of the bluff-body, the shedding is actually initiated at a distance slightly downstream of the flame-holder, and not immediately at the edges, as in the non-reacting case (figure 3.23). This is due to the marginal increase in the stability of the shear layer near the bluff body edge, as a result of exothermicity and reduction in the Reynolds number.

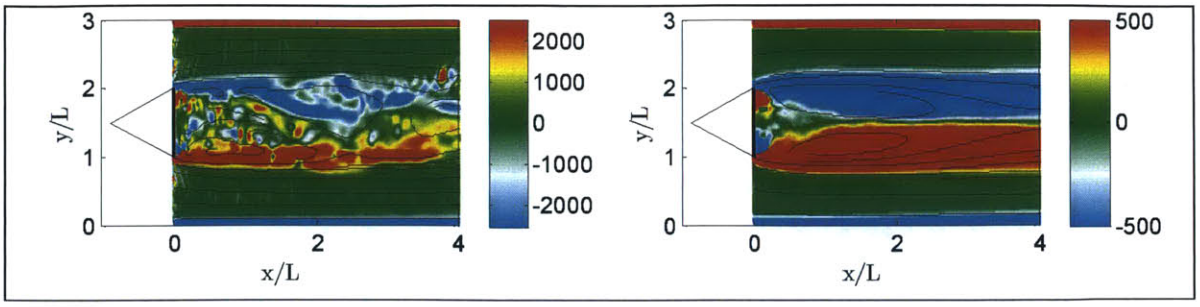

Figure 3.23: Instantaneous and average z-vorticity (1/s) in the recirculation region, with the corresponding streamlines.

In figures 3.24-3.26, the contours of the average and instantaneous axial velocity (at a specific time-instant) are depicted along with the corresponding streamlines. The cross-sections at which numerical and experimental data are compared are also shown. A strong recirculation zone in the immediate wake region downstream of flame-holder is observed that serves to stabilize the flame: hot products stored inside the wake convect downstream and periodically mix with the co-flowing fresh mixture due to the action of the shed vortices, while chemical reaction takes place in the shear layers between the wake and co-flowing fresh mixture. Moreover, in contrast to the isothermal flow, the reverse velocity is higher due to exothermicity, and peaks at a distance of $2L$ downstream of the flame holder, along the centerline.

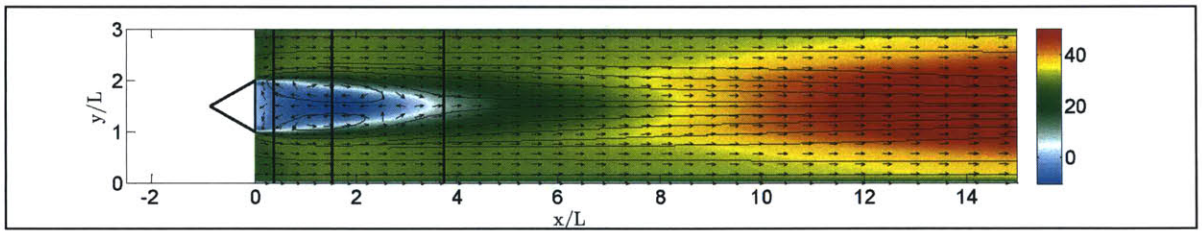

Figure 3.24: Average axial velocity (m/s), with the mean 2D velocity vectors and streamlines. The cross-sections at which data are compared are also shown.

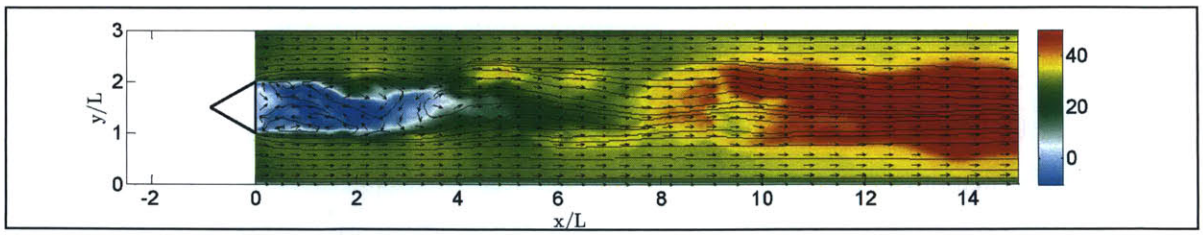

Figure 3.25: Instantaneous axial velocity (m/s) at a specific time-instant, with the instantaneous 2D velocity vectors and streamlines.

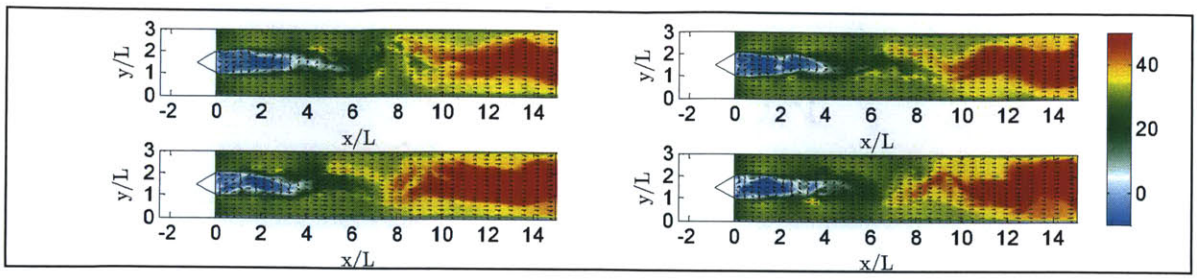

Figure 3.26: Instantaneous axial velocity (m/s) at different time-instants, with the corresponding instantaneous 2D velocity vectors.

Further investigation of the mean flow-field in the wake region suggests that the primary recirculation zone required to stabilize the flame extends to a length of about 4*L*. This elongation of the recirculatory flow field, in contrast to that observed for the isothermal case, has been observed in earlier studies of an axi-symmetric bluff-body geometry [3.29]. Typically, for low equivalence ratios, and low inlet turbulence intensity, the recirculation zone is marginally more elongated than in the isothermal flow. An underlying physical explanation is that coupled with momentum dissipation effects, the acceleration of the flow due to turbulent dilatation together with prevention of mean streamline curvature by the confining walls causes the flow to better overcome the adverse pressure gradients (figure 3.27).

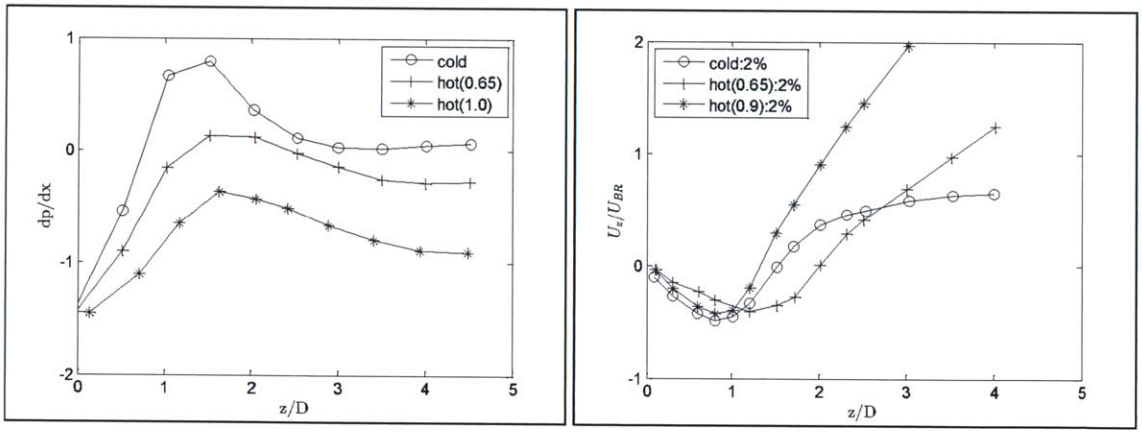

Figure 3.27: (a) Combustor wall pressure gradients for isothermal and reacting flows in a confined axi-symmetric bluff-body geometry, (b) Mean centerline velocity for different equivalence ratios (2% inlet velocity fluctuation).

The reduced shear layer growth rate (as a consequence of heat release and thermal expansion in the vortex cores), the reduction in the Reynolds number (due to the increase in viscosity with reaction), and the marginal suppression of entrainment in the mixing layer (due to the lower adverse pressure gradients), may also contribute to elongation of the recirculation zone (figure 3.28).

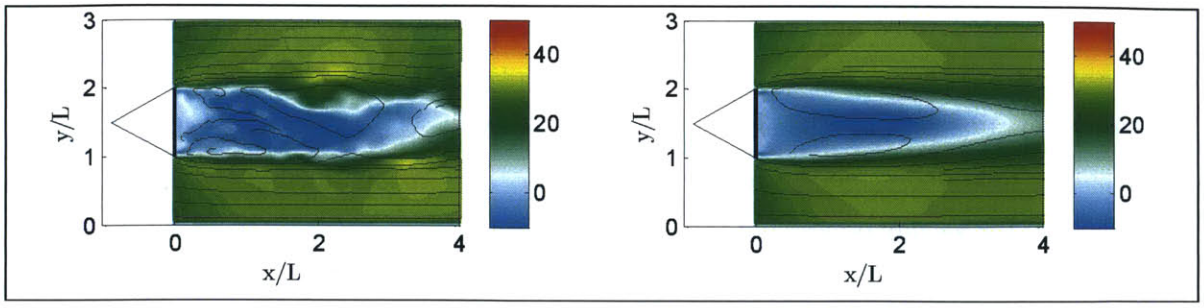

Figure 3.28: Instantaneous and average axial velocity (m/s) in the recirculation region, with the corresponding streamlines.

The contour of the rms axial velocity presented in figure 3.29 suggests a high fluctuation level in the wake of the bluff-body slightly downstream of the flame-holder, attributed to the shear-generated turbulence and intense vortex shedding activity in the region. These processes result in generation of significant turbulent kinetic energy in the mixing layer, as indicated by the contour of the Reynolds stress term (figure 3.30). High turbulence intensity is also observed near the stagnation zone because in the proximity of the region, flow direction quickly reverses: the fluid parcels are stretched and strong gradients of mean and turbulence quantities are present. Subsequently, the turbulent flow field is somewhat isotropic ($x/L \approx 6$) and the shear layer turbulence is suppressed due to the effect of dilatation and dissipation. As the flow convects downstream ($x/L > 10$), due to combustion induced turbulence, mixing is enhanced, and axial flow fluctuation intensity is significant in this section of the combustion chamber.

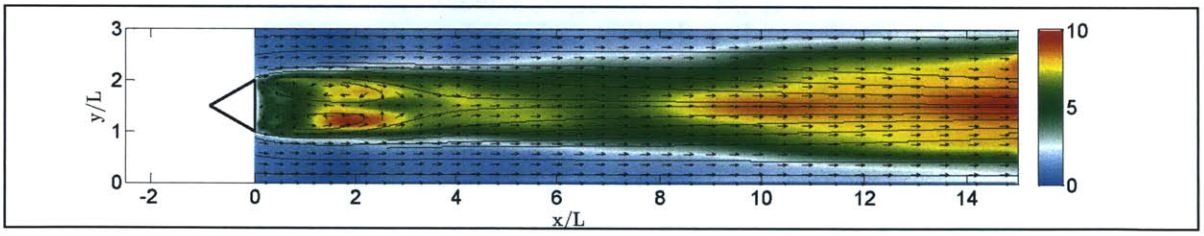

Figure 3.29: rms axial velocity (u'_x, m/s), with the mean 2D velocity vectors and streamlines.

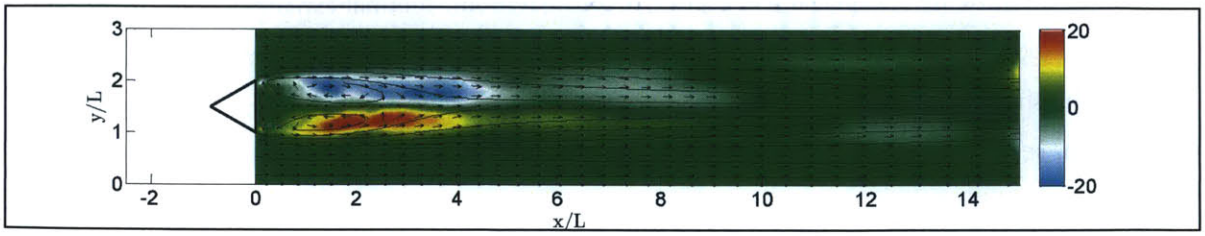

Figure 3.30: Reynolds stress term ($u'_x u'_y$, m^2/s^2), with the mean 2D velocity vectors and streamlines.

As depicted in the rms transverse velocity contour in figure 3.31, the flow field fluctuations are predominatly high near the stagnation zone, and marked anisotropy of turbulence prevails, with the transverse turbulence component fairly constant within the recirculation zone. Note that in this region, high flow and temperature fluctuations exist, because the curving of the outer flow streamlines in the vicinity brings cold reactants towards the hot products flowing through the mid-plane of the combustor. This results in high turbulence intensity in the region, as a consequence of entrainment, flow reversal and mixing events.

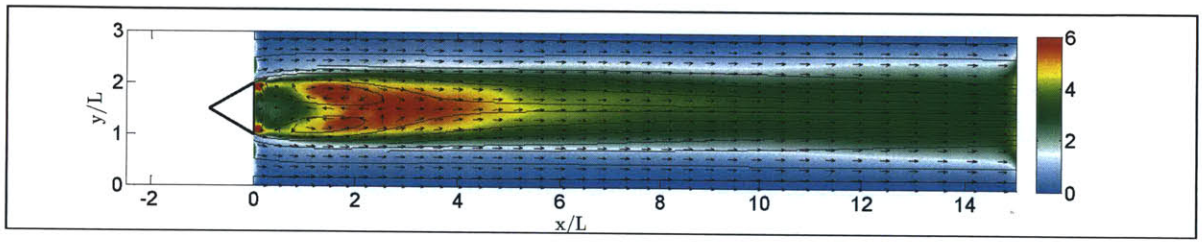

Figure 3.31: rms transverse velocity (u'_y, m/s), with the mean 2D velocity vectors and streamlines.

The viscous dissipation per unit volume is also shown in figure 3.32, and as opposed to the isothermal case, higher dissipation values are observed in the wake region, that suppress the vortex shedding, and reduce the level of turbulence intensity in the shear layers, thereby influencing the growth rate of the mixing layer and the size of the recirculation region as well.

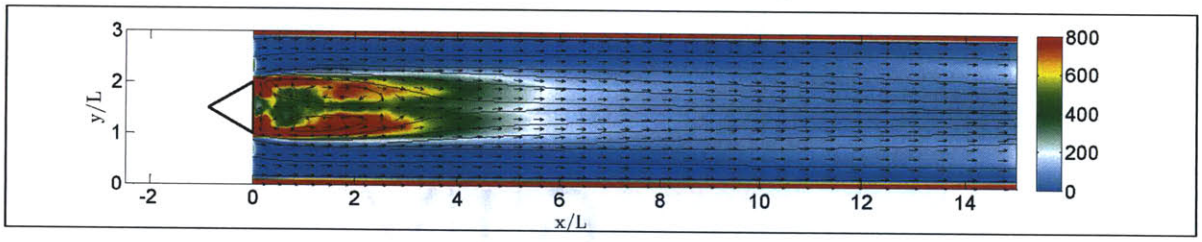

Figure 3.32: Average viscous dissipation per unit volume (kg/ms^3), with the mean 2D velocity vectors and streamlines.

The average turbulent dilatation, ψ, shown in figure 3.33, also plays a significant role in influencing the flow field, especially in confined configurations: thermal expansion and the resultant flow acceleration tends to reduce the vortex growth and development of the mixing layer, while also lowering the shear generated turbulence, and in general, suppressing the turbulence anisotropy in the downstream sections. The dilatation term can be as estimated in Cartesian coordinates [3.30] as:

$$\psi = \nabla . \boldsymbol{u} = \frac{\partial u_x}{\partial x} + \frac{\partial u_y}{\partial y} + \frac{\partial u_z}{\partial z} \qquad (3.26)$$

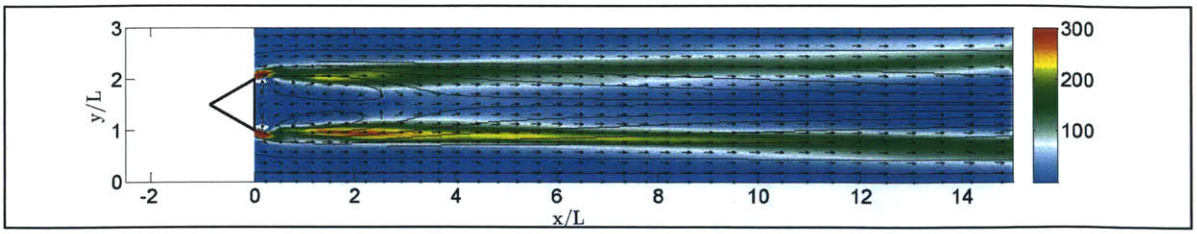

Figure 3.33: Average turbulent dilatation (1/s) with the mean 2D velocity vectors and streamlines.

The normalized profiles for the average axial velocity, rms axial velocity as well as the Reynolds stress tensor term, at different cross-sections across the length of the combustor, are shown in figure 3.34. Simulation results generally agree well with experimental measurements and the depth and height of the recirculation zone are reproduced fairly accurately by LES. The simulated stream-wise velocity profiles correlate well with the measured values; the location of the shear layer, indicated by the steep gradient in axial velocity, is well resolved numerically, though the predicted wake region is noted to be marginally narrower than that observed in the experiments. Careful examination of the plots also indicates a higher peak reverse velocity, as compared to the non-reactive case, due to exothermicity.

It is also seen that the unsteadiness in the flow field as indicated by the rms profiles is better predicted using the dynamic formulation for the efficiency function, especially within the recirculation zone and shear layer regions. It should however be noted that three-dimensional effects in the reacting case may be important since the chemical reaction rates can depend critically on the small-scale three dimensional flow structures. The use of periodic boundary conditions in the span-wise direction, therefore, might explain the slight discrepancy in the simulation results and the under-estimation in the axial flow fluctuation within the shear layer.

In figure 3.35, the average axial velocity, anisotropy and fluctuation level along the centerline are displayed indicating that the simulation results are in reasonable agreement with the experiments. Compared to the cold flow, volumetric expansion results in an increase in the recirculation zone and cross-flow area. The heat release and decrease in density due to thermal expansion also cause a reduction in the turbulence intensity within the mixing layer. The peak reverse velocity reaches about 75% of the inflow velocity, at about $2L$. Further downstream, the mean centerline velocity accelerates due to the addition of thermal energy from combustion, and reaches a magnitude approximately 2 times the inflow velocity.

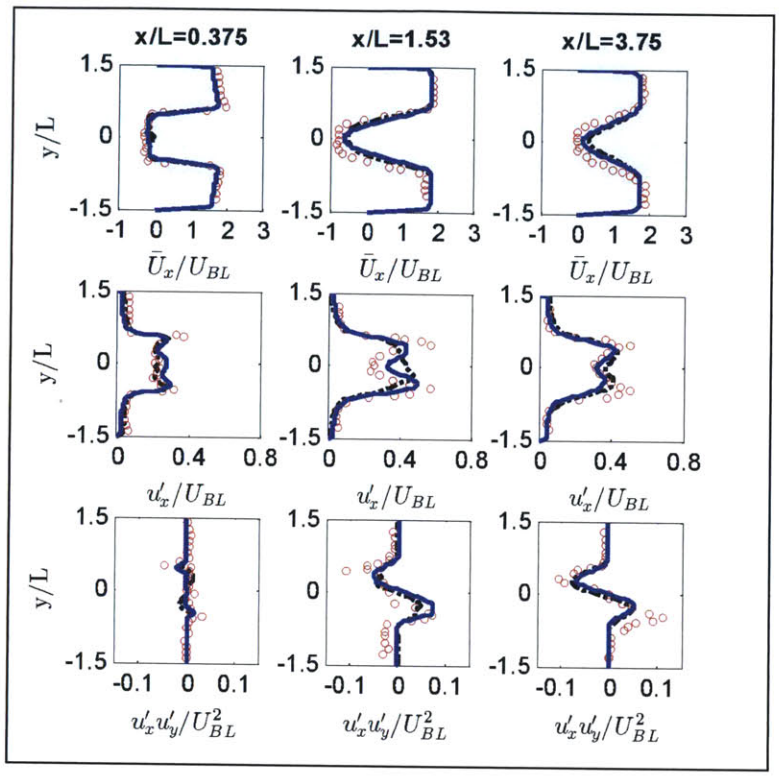

Figure 3.34: Normalized profiles for average axial velocity (top), rms axial velocity (middle) and Reynolds stress tensor term (bottom): ooo Experiment, –·–· LES (Algebraic Model), ––– LES (Dynamic Formulation).

As pointed out earlier, the recirculation zone plays an important facilitating role in anchoring the flame, as hot products are stored inside the wake, convected downstream and periodically mixed with the co-flowing fresh mixture by the shed vortices, while the chemical reaction takes place around the shear layers between the wake and co-flowing fresh mixture. It is critical therefore that the flow field and the turbulence-flame interactions in these regions, which are subject to high levels of strain, are accurately predicted using LES. Results indicate that the proposed dynamic approach performs better as compared to the conventional efficiency function model, and more accurately reproduces the recirculation region downstream of the bluff-body.

The slight discrepancy in the predictions, however, may result from uncertainties or fluctuations in the experimental conditions (equivalence ratio, reactant mixture velocity etc) or the use of periodic boundary conditions in the simulations. Precise knowledge of experimental inlet conditions coupled with fully 3D simulations that can effectively capture the effects of all four walls (for example, boundary layer thickening) and vortex stretching effects may result in more accurate predictions for the velocity statistics.

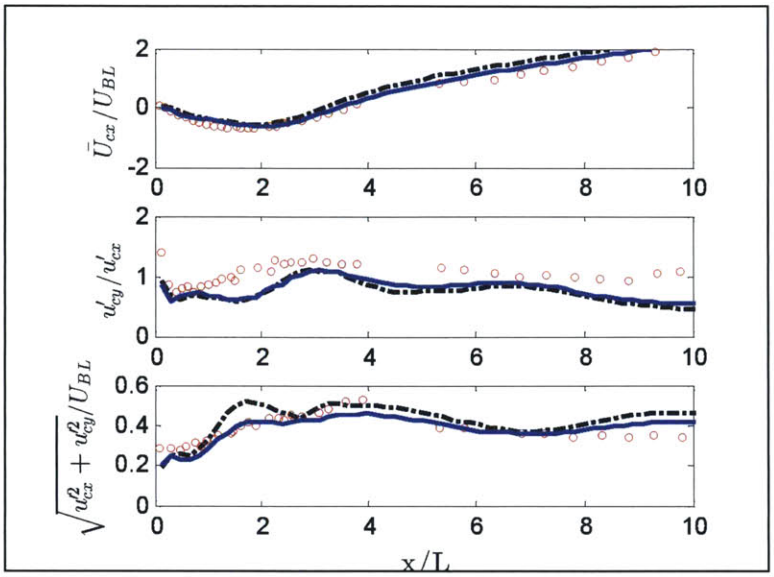

Figure 3.35: Normalized profiles for average velocity (top), anisotropy (middle) and fluctuation level (bottom) along the centerline: ooo Experiment, −·−· LES (Algebraic Model), −−− LES (Dynamic Formulation).

In figure 3.36, the normalized average temperature profiles estimated using LES are compared with the experimental data and it is observed that the combustion modeling approaches predict the spreading rate of the flame, and the peak temperature fairly accurately. The predictions from the dynamic formulation correspond with the experimental data more closely, as compared to results obtained using the algebraic model. Thus, the mean flow field topology and the flow fluctuations, as well as the flame-flow interactions are resolved more accurately using the modified approach, in both near-field and far-field regions. The flame predicted using the modified approach is more wrinkled and the accompanying spreading rate of the temperature is larger at downstream sections due to this effect (in conjunction with the experimental measurements), which highlights and establishes the validity of the dynamic formulation.

It is well known that the penetration of the inner layers of the shear layer by small eddies can cause the reaction rate to be strongly affected by turbulence. Furthermore, heat diffusion from the inner layers towards the preheat zone is significantly enhanced. Not appropriately accounting for the interactions between the chemical reaction and turbulent stirring processes can therefore result in smoother flames than experimentally observed. Preliminary results indicate that the modified approach is able to reproduce the effect of the eddy penetration of the inner layers in the regions of high turbulence intensity more accurately, resulting in convoluted flame fronts and reaction zones of

appropriate thickness. The accurate prediction of flame wrinkling and efficiency function, and hence the heat release, thereby results in more accurate estimation of the temperature field.

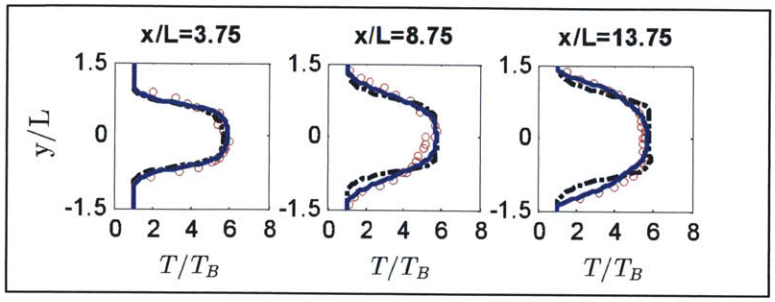

Figure 3.36: Normalized profiles for average temperature: ooo Experiment, −·−· LES (Algebraic Model), −−− LES (Dynamic Formulation).

In figure 3.37, the average temperature contour is shown, indicating the presence of a high temperature field in the wake region of the flame holder, that gradually spreads as the flow convects downstream. The cross-sections at which numerical and experimental data are compared in figure 3.36 are also shown. It can be seen that the temperature distribution is nearly uniform in the transverse direction at downstream locations within the recirculation zone, suggesting that combustion in the region is almost complete. The temperature then drops steeply to the ambient temperature, outward from the shear layer, into the incoming reactant mixture. These locations of high temperature gradients, where cold and hot gases mix, are predicted accurately, especially by the dynamic formulation.

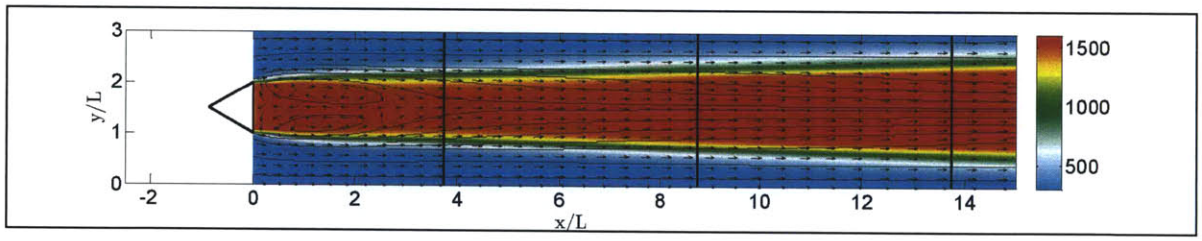

Figure 3.37: Mean temperature (K) with the mean 2D velocity vectors and streamlines. The cross-sections at which data are compared are also shown.

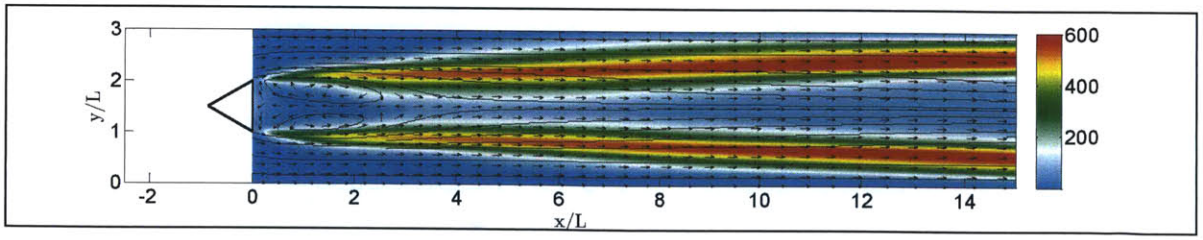

Figure 3.38: rms temperature (K) with the mean 2D velocity vectors and streamlines.

A high average temperature region is also observed downstream of the wake region (x/L≈7), as also previously noted in [3.23]. This may be attributed to the roll-up of vortices downstream, enhancing the turbulence and wrinkling of the flame, thereby resulting in an increase of the flame surface, and producing intermittent fast local heat release. This also results in slightly higher temperature fluctuations in the region as depicted by the rms temperature contour in figure 3.38. Correspondingly, the dynamic model predicts the temperature profile more accurately in this downstream region ($x/L>7$), highlighting the importance of effectively capturing flame wrinkling and turbulence-flame interactions, and its impact on predictive accuracy. Further downstream ($x/L>8$), due to turbulence enhanced mixing, flow fluctuation intensity is significant; the mean temperature is also high, suggesting that combustion is almost complete in this region. The thick flame in the region also spreads outwards towards the wall, while decreasing the mid-section scalar fluctuations by inhibiting heat transport between the hot products and the cold reactants, as evident in the temperature and heat release contours.

3.4 Validation Study: Backward Facing Step

A backward facing step [3.31, 3.32] provides a reasonably comprehensive framework for validation since it is comprised of many aspects of practical combustors such as anchored flames, regions of recirculation and shear layers. Therefore, the canonical configuration is studied using LES in this section. The numerical predictions are compared against experimental data for non-reacting and reacting cases, and the relative performance of the conventional (algebraic model for Ξ) and modified (dynamic formulation for Ξ) efficiency function models is investigated.

3.4.1 Experimental Configuration

The backward facing step configuration [3.31] consists of a step of height (H) 25.4 mm and a rectangular cross section of 50.8 mm x 38.1 mm downstream of the step (figure 3.39). A mixture of air and propane is introduced at an equivalence ratio of 0.57, at a bulk inlet velocity (U_{SH}) of 13.3 m/s (Reynolds number, Re_{SH} = 22100, based on the step height H and the bulk fluid velocity U_{SH}). The inlet temperature (T_S) is 293 K and the nominal pressure is 101 kPa.

3.4.2 Simulation Setup

The choice of the numerical grid is governed by estimates of the physical length scales associated with the flow configuration. Based on the Pope's criterion defined in [3.27], and using the step height (H) as the integral length scale, the filter-width is estimated to be 2 mm. It should be noted that the above theory does not focus on resolving near-wall structures and may not be applicable for reacting flow. Therefore, appropriate grid clustering may be required to resolve the structures near

the walls and in the shear layer region for reacting flow. Based on the above, the non-uniform mesh utilized in the current work is comprised of approximately 15,500 hexahedral cells in the x-y plane, and gets coarser along the stream-wise direction. Downstream of the step, within the rectangular section, the number of cells in the x and y directions are 206 and 60 respectively; therefore, the average Δx and Δy values in the wake region are approximately 1.00 mm and 0.85 mm respectively, while the minimum Δx and Δy values, in the shear layer region, are approximately 0.75 mm and 0.55 mm respectively.

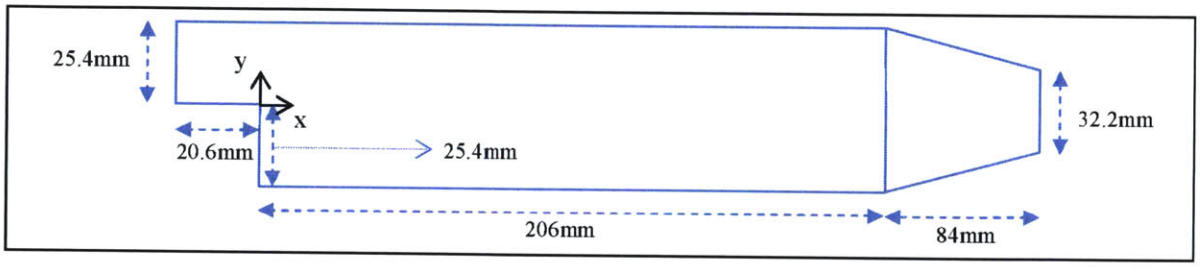

Figure 3.39: Backward facing step configuration used for flame stabilization.

Similar to the previous configuration, temporal resolution is determined based on physical time scale estimates, in order to prevent excessive numerical dissipation and numerical instability, as well as on chemical time scales. Based on the CFL criterion ($C_{max} = (U_{SH}+U_s)\Delta t/\Delta x$; $C_{max} = 1$, $U_s =$ 340m/s, $\Delta x = 0.8$ mm), the time step for the simulations is estimated at approximately 2.2 μs. A conservative value of 1 μs is used in the reacting flow simulations, to take into account local refinement and acceleration of the fluid above the bulk inlet velocity, and to adequately resolve the chemical time scales. The key quantities relevant to the configuration are summarized in table 3.3.

Table 3.3: Parameters for the backward facing step configuration.

PARAMETER	SYMBOL/EXPRESSION	VALUE
Duct Width	L_{SW}	38 mm
Step Height (Characteristic Length)	H	25.4 mm
Integral Length Scale	L_I (=L)	25.4 mm
Equivalence Ratio	γ	0.57
Bulk Inlet Velocity (Characteristic Flow Velocity)	U_{SH}	13.3 m/s
Macroscopic Reynolds Number	Re_{SH}	22,100
Inlet Temperature	T_S	293 K
Nominal Pressure	P	101 kPa
Kolmogorov Length Scale	$Re_{SH}^{-3/4}L$	14 μm
Cold Flow Filter Width (Pope's Criterion)	$\Delta=0.083L_I$	2 mm
Shear Layer Fluctuation (measured)	u'	~5 m/s
Integral Time Scale	$T_I=L/u'$	5 ms
Kolmogorov Time Scale	$Re_{SH}^{-1/2}T_I$	33.6 μs
CFL Criterion Time Scale	$C_{max}\Delta x/(U_{SH}+U_s)$	2.2 μs

Three-dimensional simulations with periodic boundary conditions in the span-wise direction over the entire channel width are performed. At the inlet, Dirichlet conditions are used for all variables except the pressure, for which zero Neumann conditions are specified. The inlet velocity has a flat profile on which fluctuations of 4% turbulence intensity are imposed. At the exit, zero Neumann conditions are specified for all variables except the pressure, for which wave-transmissive conditions are used. No-slip conditions are applied for the flow at the top and bottom walls of the duct, while zero Neumann conditions are specified for the other variables. Heat transfer is also considered at the walls to account for any thermal losses. In order to maintain reasonable computational efficiency, appropriate wall functions are utilized to resolve the flow features in the wall boundary layer. Numerical computations start from quiescent conditions and the unsteady flow characteristics evolve naturally. In order to initiate the flame, a high temperature pulse is applied at the inlet section which ignites the fuel; the reacting mixture convects downstream, and eventually stabilizes as a flame at the edge of the step. Averaging is performed over approximately 10 flow-through cycles once the flow is established in the computational domain. Note that in order to better understand the effect of heat release on the flow, the range of the magnitudes for the contours of some of the flame-flow variables have been fixed corresponding to the non-reacting and reacting cases.

3.4.3 Results and Discussions: Non-Reacting Flow

Non-reacting flow is simulated prior to considering reacting flow, with the fundamental flow features comprising of the mixing layer and the shed vortices, the primary and corner recirculation zones, and the reattachment zone. As indicated by the contour of the instantaneous z-vorticity (at a specific time-instant), depicted in figure 3.40 along with the corresponding streamlines, the flow structures begin to form as the upstream boundary layer separates at the edge of the step, subsequently developing into a thin shear layer. Vortices begin to develop slightly downstream of the step, as a consequence of Kelvin Helmholtz instability, and the shear layer grows in size as the turbulent eddies contained within begin to coalesce. Unsteady flow features in the shear layer, such as shedding, convection and pairing of the small vortices are thus suitably resolved using LES, and the roll-up of the mixing layer into a sequence of large-scale structures that convect downstream along with the turbulence generated eddies can be observed in figure 3.41.

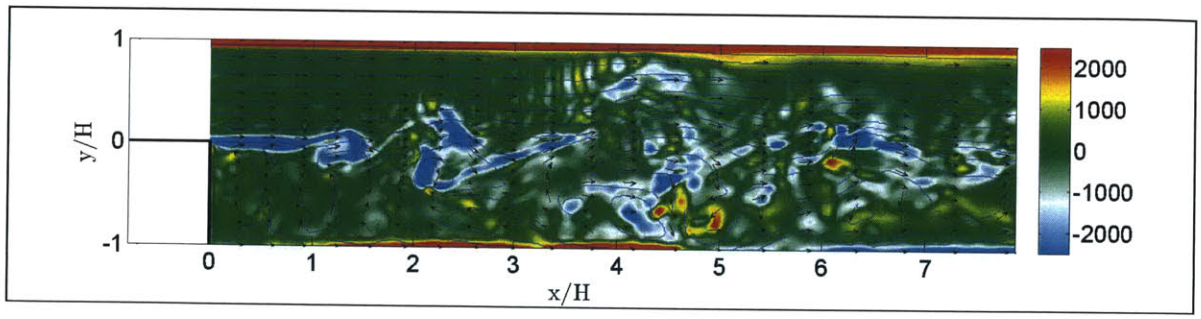

Figure 3.40: Instantaneous z-vorticity (1/s) at a specific time-instant, with the instantaneous 2D velocity vectors and streamlines.

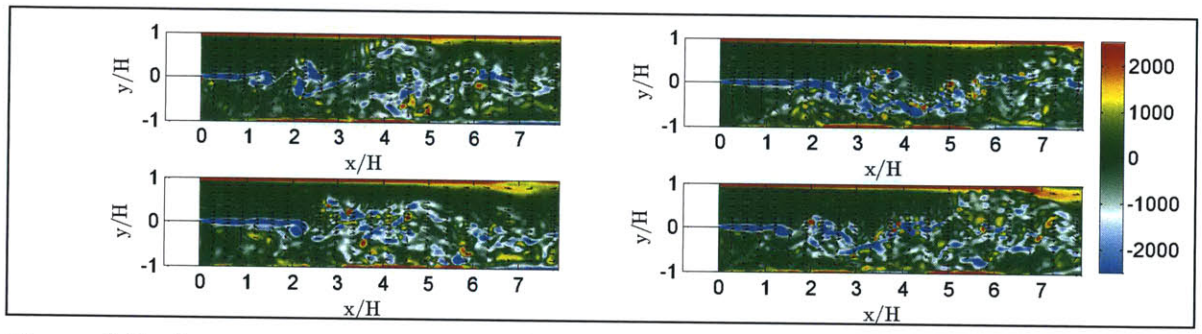

Figure 3.41: Instantaneous z-vorticity (1/s) at different time-instants, with the corresponding instantaneous 2D velocity vectors.

The eddy structures thus formed entrain irrotational fluid from the non-turbulent region outside the shear layer which causes the formation of a low velocity recirculation in the wake region. This recirculation zone is mainly comprised of a primary vortex (located between the shear layer and the bottom wall) that typically extends a few step-heights, and a secondary vortex adjacent to the corner of the step formed primarily due to geometric considerations (and rotates in the opposite direction to the primary eddy). Due to the favorable pressure gradient created by the fluid entrained, the shear layer eventually curves down and impinges the wall resulting in the formation of the reattachment zone; however, the reattachment location is observed to fluctuate significantly, due to the inherent unsteady motion of the shear layer. The strongest vorticity is observed near the edge of the step, while the intensity tends to decrease subsequently, as the vortices dissipate in the downstream section.

In figures 3.42-3.43, the contours of the average and instantaneous axial velocity along with the corresponding streamlines are depicted. The cross-sections at which numerical and experimental data are compared are also shown. A strong primary recirculation zone downstream of the step is observed, with the zero velocity region (shown in white) running through the core of the mean

vortex structure; the predicted reattachment length (x/H=6.5) matches closely with experimental observations, and the size of the separation bubble is reproduced with reasonable accuracy numerically, along with the shear layer growth rate. An almost stationary corner recirculation vortex cell is also observed in the simulations, and the unsteady nature of the shear layer and the reattachment location is clearly evident as well (figure 3.43). Additionally, flow separation from the upper wall is also evident, and the position at which separation occurs varies as well (figure 3.44), due to flow unsteadiness.

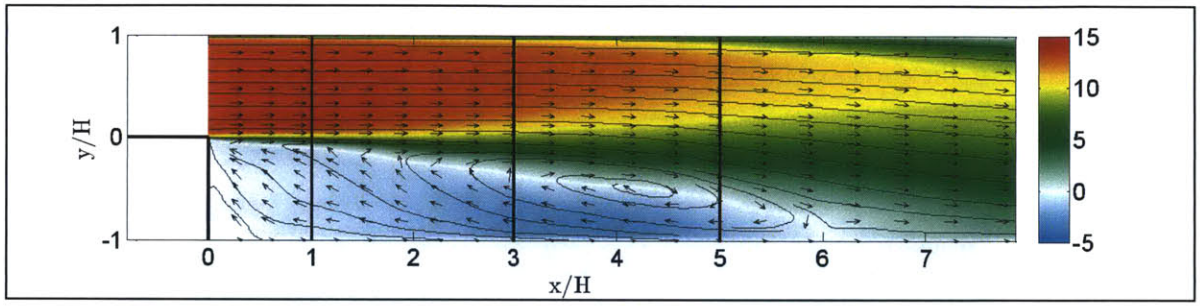

Figure 3.42: Average axial velocity (m/s) with the mean 2D velocity vectors and streamlines. The cross-sections at which data are compared are also shown.

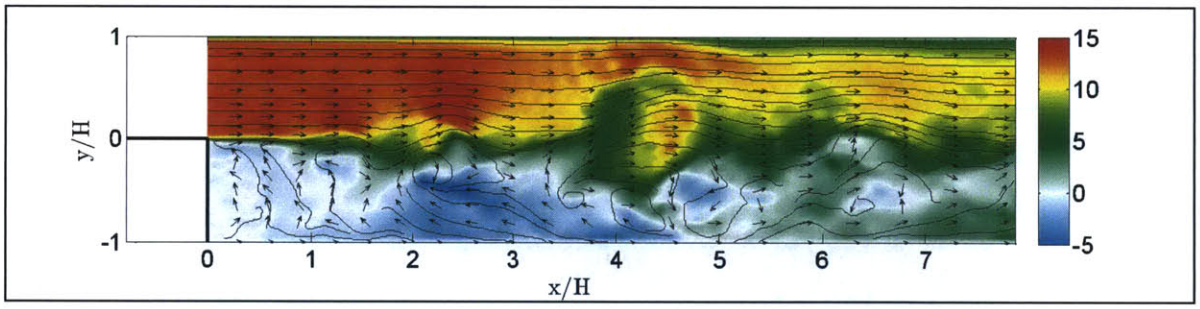

Figure 3.43: Instantaneous axial velocity (m/s) at a specific time-instant, with the instantaneous 2D velocity vectors and streamlines.

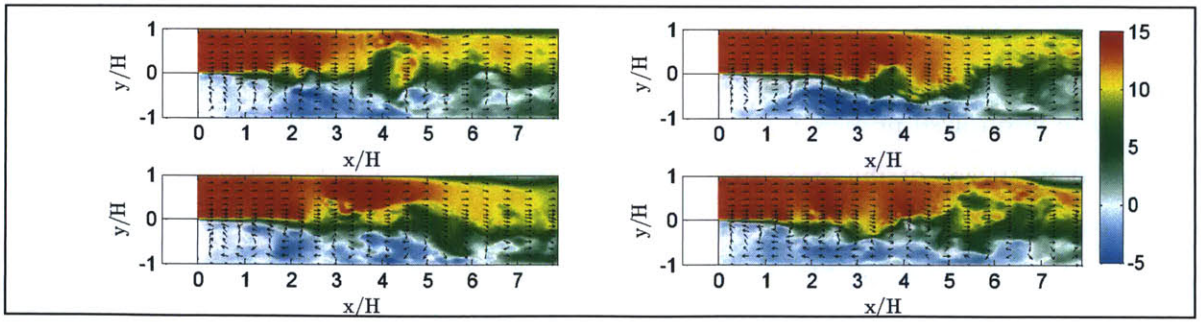

Figure 3.44: Instantaneous axial velocity (m/s) at different time-instants, with the corresponding instantaneous 2D velocity vectors.

Examination of the rms axial velocity contour in figure 3.45 shows a strong turbulence intensity region in the shear layer, slightly downstream of the step, corresponding to the gradual rolling up of the mixing layer into a sequence of large-scale structures. These coherent vortices grow and convect downstream along with turbulence-generated smaller eddies, resulting in the growth of the shear layer. The turbulent flow fluctuations are significant in this region, which is also characterized by high viscous dissipation (figure 3.46). Turbulent kinetic energy is also high near the reattachment zone, associated with the flapping of the shear layer, along with flow reversal in the region. In contrast, the corner recirculation zone is comprised of a nearly stationary vortex with very low level of turbulence intensity, primarily due to geometric constraints.

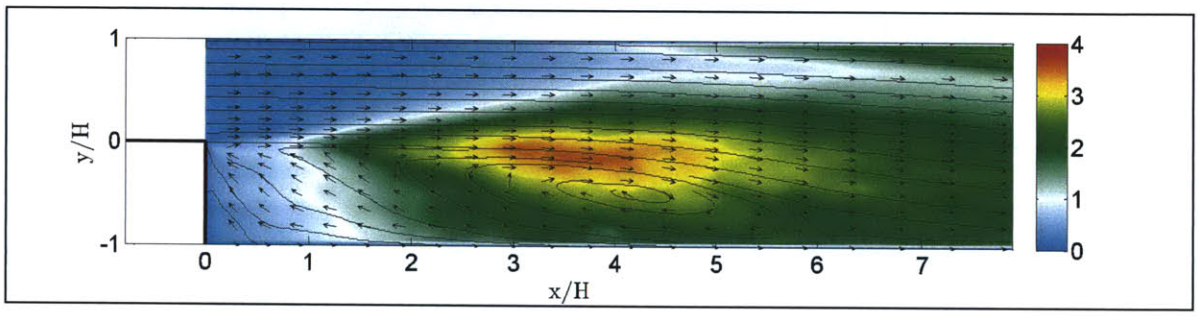

Figure 3.45: rms axial velocity (m/s) with the mean 2D velocity vectors and streamlines.

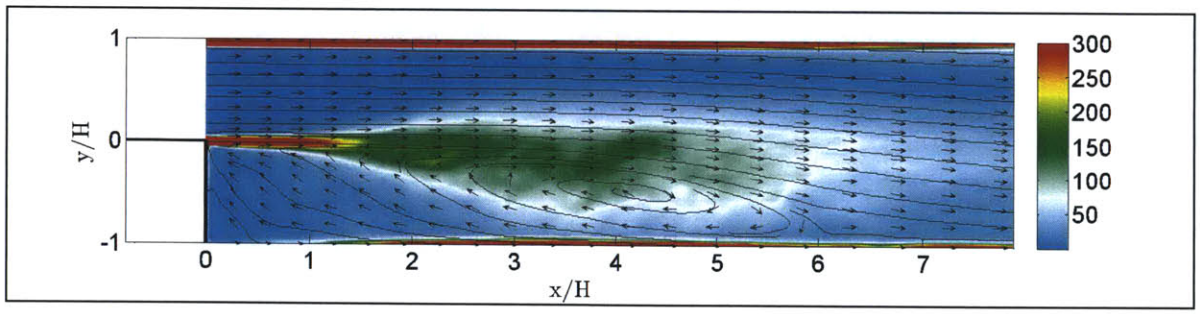

Figure 3.46: Average viscous dissipation per unit volume (kg/ms^3) with the mean 2D velocity vectors and streamlines.

The normalized profiles for the average axial velocity and the rms axial velocity, at cross-sections downstream of the step, are shown in figure 3.47. Predicted results show reasonable agreement with experimental measurements and the underlying flow field in the recirculation zone and shear layer region is suitably resolved, as indicated by the velocity statistics. The mixing layer growth rate as well as the extent of the primary recirculating vortex is predicted with reasonable accuracy. It is observed that the fluctuations peak in the shear layer in the vicinity of the step; as the flow convects further downstream, turbulence tends to become somewhat isotropic, as the relative

influence of the shear-generated turbulence begins to diminish, and large-scale eddy structures dominate the flow. Subsequently, the large coherent vortices dissipate into smaller eddies as the flow convects downstream into the exhaust section.

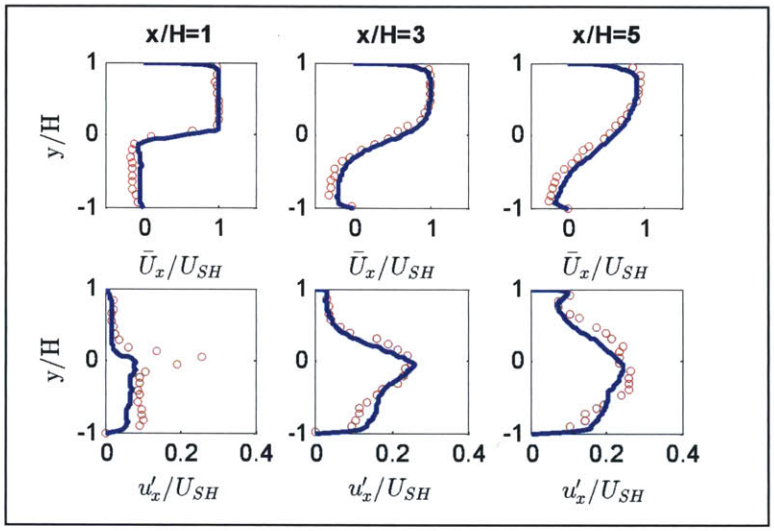

Figure 3.47: Normalized profiles for average axial velocity (top) and rms axial velocity (bottom): ooo Experiment, --- LES

3.4.4 Results and Discussions: Reacting Flow

Next, reacting flow for the configuration is considered and simulations are performed using the conventional and modified efficiency function models. The LES contours of the instantaneous temperature and CO mass fraction, as well as the normalized average heat release are shown in figures 3.48-3.51 respectively. The stabilization of the flame in the reacting shear layer downstream of the step is a sequential phenomenon that involves preheating of the incoming reactant mixture near the step, followed by its ignition due to the heat flux transported outward from the recirculation zone. These processes result in a thin flame, with the reaction zone taking the form of a sheet-like interface. In the vicinity of the step, the strain is high and the moderate flame propagation speed results in a combustion process that is typically characterized by reaction kinetics in this location. The penetration of the inner layers of the reacting shear layer by the convecting eddies causes the kinetics to be affected by turbulence, while enhancing the heat diffusion from the inner layers towards the preheat zone.

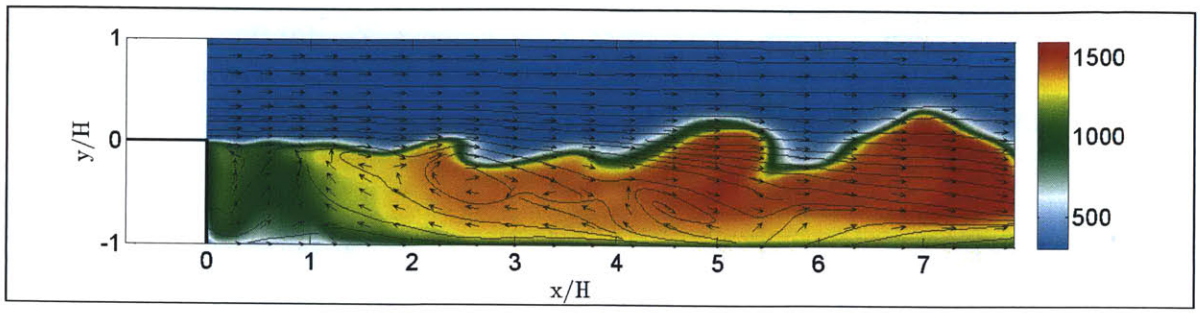

Figure 3.48: Instantaneous temperature (K) at a specific time-instant, with the instantaneous 2D velocity vectors and streamlines.

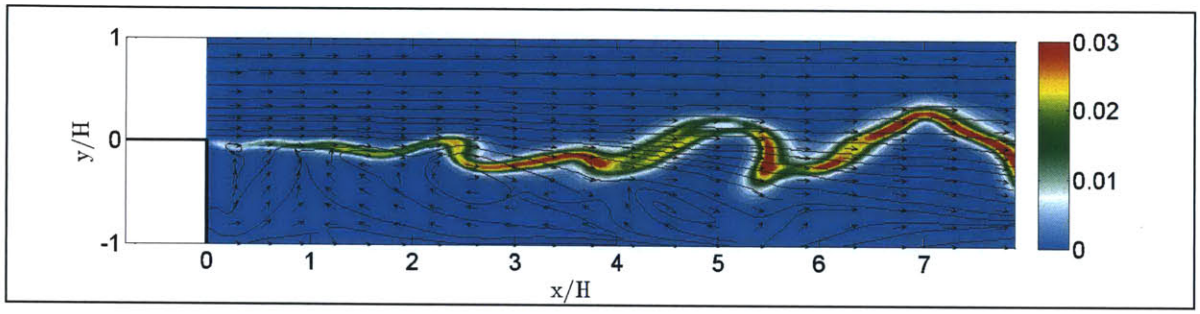

Figure 3.49: Instantaneous CO mass fraction at a specific time-instant, with the instantaneous 2D velocity vectors and streamlines.

The average reaction zone eventually thickens as the flow proceeds downstream, with entrainment as the dominant mechanism, and combustion is characterized by transport and mixing processes. The high turbulence in the region due to eddy breakdown and induced by combustion enhances mixing and entrainment, resulting in augmented heat release and a strongly burning flame. In the downstream section, the instantaneous flame surface is characterized by intense heat release and takes the form of a wrinkled sheet-like interface, while the flow field is dominated by dilatation and dissipation effects.

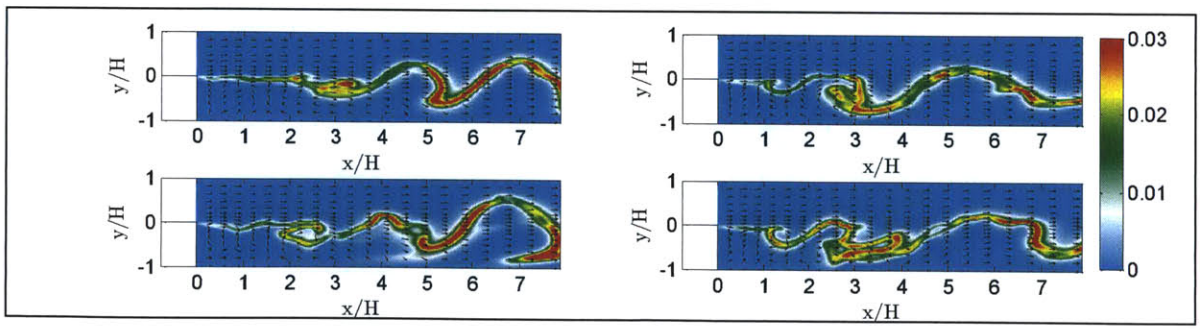

Figure 3.50: Instantaneous CO mass fraction at different time-instants, with the corresponding instantaneous 2D velocity vectors.

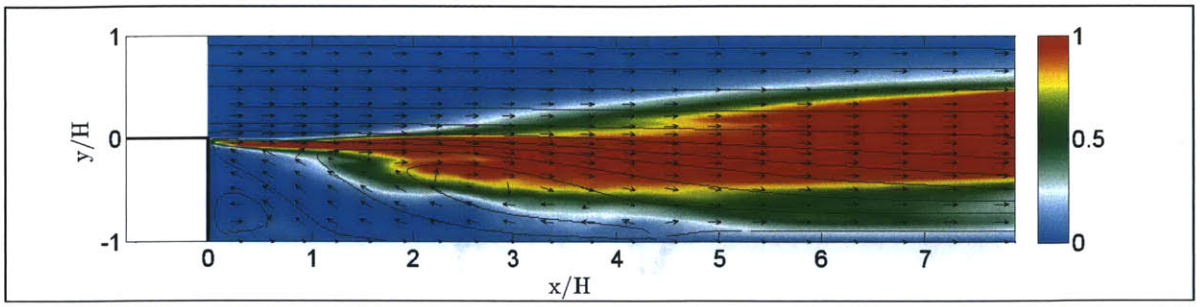

Figure 3.51: Normalized average heat release with the mean 2D velocity vectors and streamlines.

In figure 3.52, the contours of the instantaneous z-vorticity (at a specific time-instant) are depicted, along with the corresponding streamlines. Downstream of the step, eddies begin to form within the reacting shear layer as a result of Kelvin-Helmholtz instability, eventually increasing in size and spacing, and forming large-scale coherent structures as they convect downstream and coalesce. The vortical structures form as folds around the flame-edge and grow in size further downstream to produce a convoluted reaction zone. The large vortices contain the reaction zone of the flame and the roll-up of each eddy corresponds to engulfment of hot products from the recirculation zone into the layer of fresh reactants in which the reaction front propagates. This process also results in a thicker flame as the flow proceeds downstream, as evident in figure 3.51.

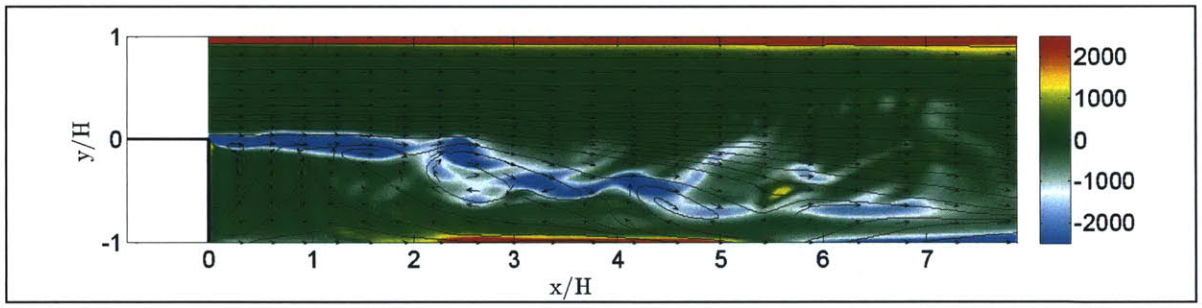

Figure 3.52: Instantaneous z-vorticity (1/s) at a specific time-instant, with the instantaneous 2D velocity vectors and streamlines.

For the reacting flow configuration, it is observed that vorticity is significant in the laminar shear layer immediately downstream of the step. Note, however, that exothermicity results in an increase in temperature dependent viscosity and consequently a reduction in the Reynolds number. While this factor alone may not appreciably affect the flame or flow structure, it can cause a marginal increase in the stability of the initial layer, a lengthening of the distance of the eddy formation position with respect to the step edge, thicker vortical structures, and a decrease in the small scale turbulence inside the large eddies. In the downstream section, heat release in vortex cores result in breakdown of eddies, and the fluid dynamic effects of heat release (increase in viscosity,

dilation effect of combustion, and flow acceleration in the shear layer) appear to exert a significant influence on the flow, resulting in reduction of overall vorticity (despite the combustion induced baroclinic effects).

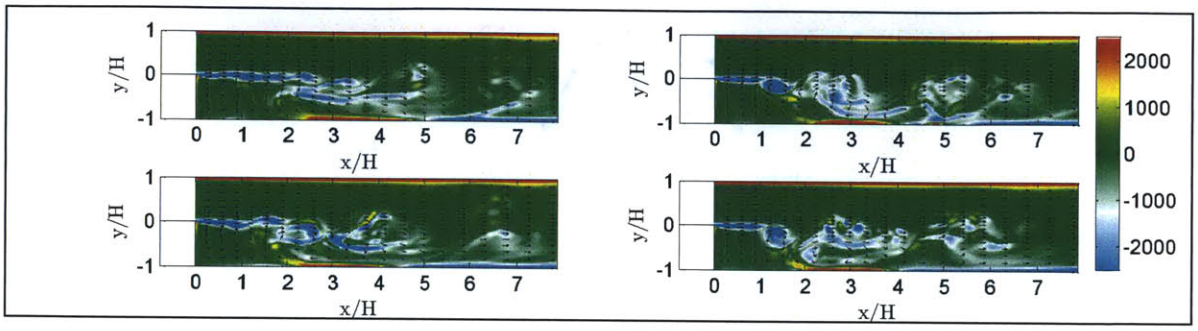

Figure 3.53: Instantaneous z-vorticity (1/s) at different time-instants, with the corresponding instantaneous 2D velocity vectors.

In figures 3.54-3.56, the contours of the average and instantaneous axial velocity, along with the corresponding streamlines, are depicted. The cross-sections at which numerical and experimental data are compared are also shown. A strong primary recirculation zone similar to the one present for the non-reacting case is noted for the reactive flow, which however is shorter in this case. The simulations predict a reattachment length (x/H=4.4) that corresponds closely with the experimental value. The magnitudes of the reverse axial velocity within the recirculation vortex and the axial velocity downstream of the reattachment point are also observed to be marginally higher due to exothermicity.

It is worth noting that for the backward-step configuration, the recirculation size shrinks for the reacting case, in contrast to the isothermal flow. In general, for low equivalence ratios, given the low flame propagation speed and moderate heat release rates, an elongated recirculation zone, often larger than that for the cold flow, is required to stabilize a flame, as observed in the bluff-body configuration. This is primarily due to the fluid dynamic effects of heat release (turbulent dilatation, increase in viscosity, and a gradual dissipation of momentum) on the recirculating vortex field. However, with an increase in the heat loading, a reduction in recirculation zone size as compared to isothermal flow is observed, which is typically associated with the influence of flame propagation and resultant temperature gradients on the flow field topology [3.29].

For this particular flow and geometric configuration, the equivalence ratio threshold (figure 3.27b) at which the recirculation zone begins to reduce in size compared to that for cold flow (ie flame propagation effects begin to dominate over the fluid dynamic effects of heat release) appears

to be much lower than that in the bluff-body case, thereby resulting in a contraction of the primary eddy, despite the lower equivalence ratio (0.57 vs 0.65). This change in the 'critical threshold limit' with the combustor configuration could presumably be due to the relative effect of the shed vortices on the flow, which appears to be low for the backward step geometry, with a somewhat diffuse vorticity field. For the bluff-body configuration on the other hand, the higher Reynolds number flow is significantly characterized by shear layer vortices; the vorticity field is observed to be quite strong, and exerts a dominant influence on the overall flow field, including the recirculation zone.

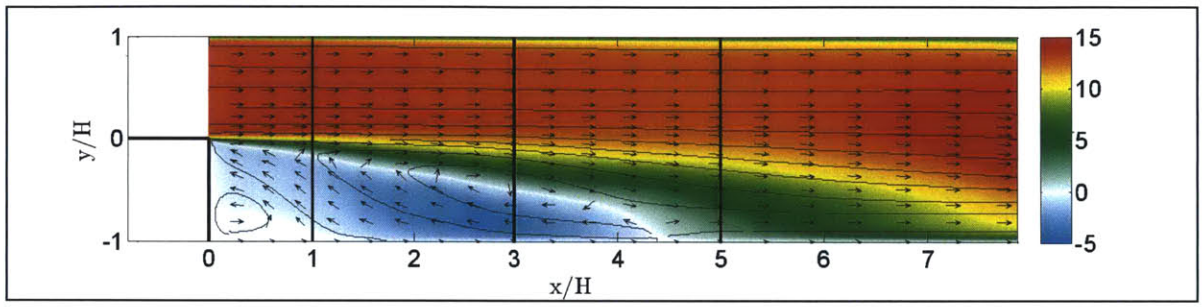

Figure 3.54: Average axial velocity (m/s) with the mean 2D velocity vectors and streamlines. The cross-sections at which data are compared are also shown.

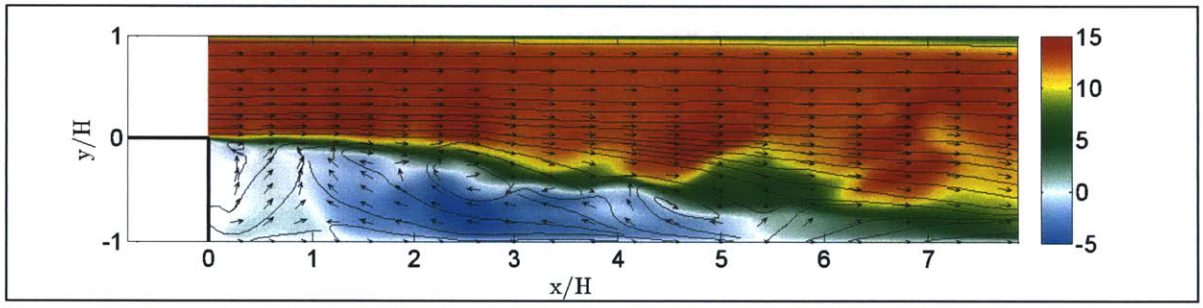

Figure 3.55: Instantaneous axial velocity (m/s) at a specific time-instant, with the instantaneous 2D velocity vectors and streamlines.

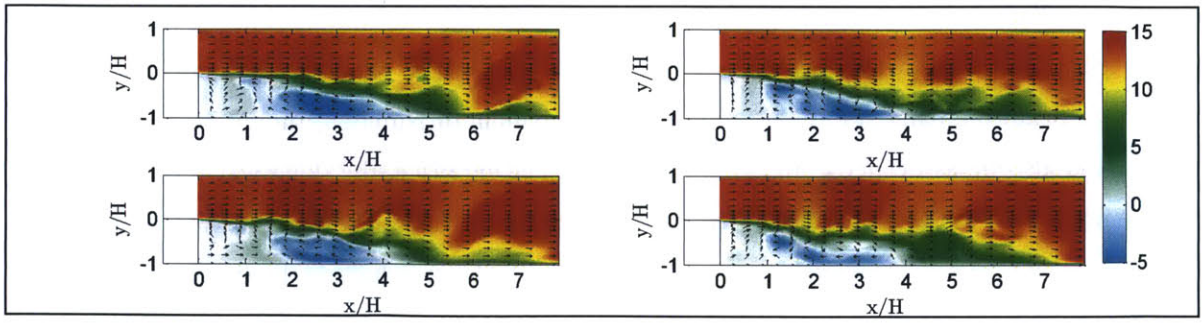

Figure 3.56: Instantaneous axial velocity (m/s) at different time-instants, with the corresponding instantaneous 2D velocity vectors.

Examination of the rms axial velocity contour in figure 3.57 shows high rms fluctuations within the shear layer caused due to the growth of a local instability mode along the layer and the roll-up of coherent vortex structures, although there is a marginal reduction in small scale turbulence in the mixing layer, immediately downstream of the step, due to heat release. It should be mentioned that in reacting flows, turbulent dilatation and viscous dissipation processes suppress flame turbulence, whereas turbulent advection and shear-generated turbulence augment flame turbulence. For low heat loadings, given the relatively low mean streamline curvature, the production of turbulence is primarily due to shear-stress/mean-strain interaction and is a fraction of the damping due to dilatation and dissipation, resulting in an overall suppression of turbulence intensity in the shear layer. With a further increase in equivalence ratio, however, the shear generated turbulence is significant, owing to the high streamline curvature, and turbulence intensity in the shear layer is similar to that observed in the cold flow scenario despite the effects of heat release in the shear layer (which typically result in somewhat lower Reynolds shear stresses, turbulence intensities and turbulent kinetic energy within the mixing layer)

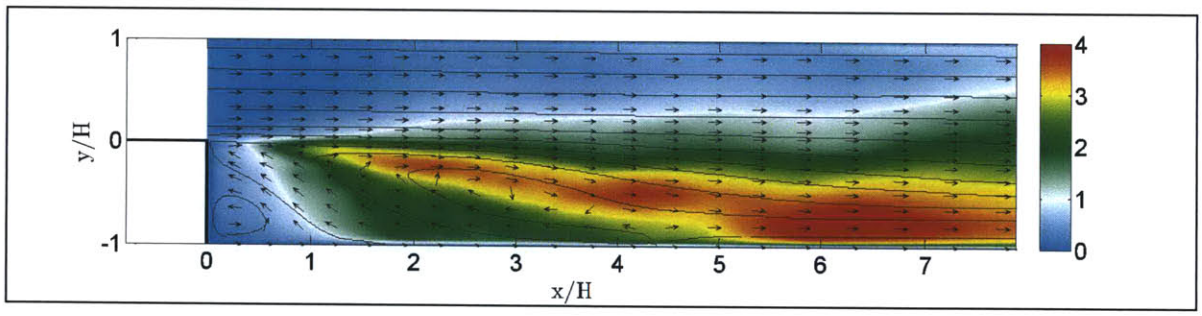

Figure 3.57: rms axial velocity (m/s) with the mean 2D velocity vectors and streamlines.

For the present configuration, the higher streamline curvature shifts the high turbulence region to within the recirculation zone, while the dilatation effects contribute to marginally reducing the flow oscillations in the mixing layer. Thus, the region of high turbulence shifts to the lower half of the channel, and the turbulence intensity is observed to be high within the primary recirculation zone underneath the flame. Flow fluctuations are also high in proximity to the reattachment region; these could also be associated with roll-up of vortices taking place, the (long-wave) oscillations of the longitudinal and transverse flow velocities, coupled with more vigorous flapping of the shear layer, and flow reversal respectively. Further, the mean turbulence is high in the downstream section of the combustion chamber, typically due to combustion induced turbulence. The flow here is primarily governed by turbulent dilatation effects, as the relative influence of the shear generated turbulence begins to diminish. The viscous dissipation per unit volume and dilatation are shown in

figures 3.58-3.59, and play a dominant role in influencing the flow field downstream of the step, particularly the growth rate of the mixing layer and the evolution of the shear layer eddies.

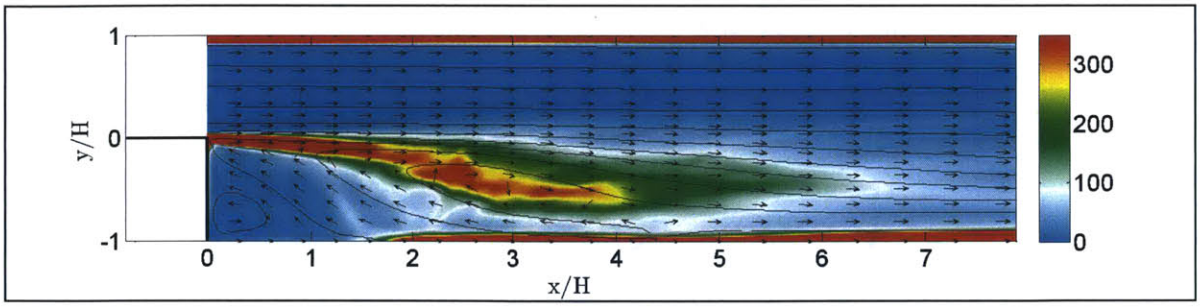

Figure 3.58: Average viscous dissipation per unit volume (kg/ms^3) with the mean 2D velocity vectors and streamlines.

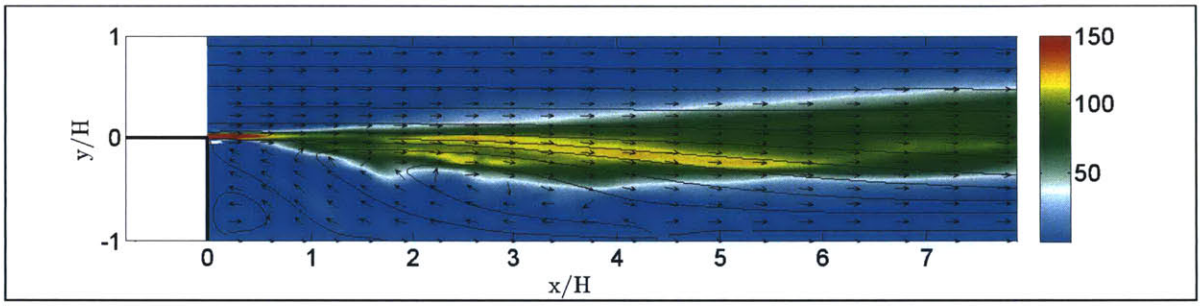

Figure 3.59: Average turbulent dilatation (1/s) with the mean 2D velocity vectors and streamlines.

In figure 3.60, the normalized profiles for the average axial velocity and rms axial velocity, at different cross-sections downstream of the step, corresponding to the LES combustion models, are shown. The results indicate reasonable agreement with experimental data for the average velocity profiles, and the peak reverse velocity is observed to be higher in this case, as compared to the non-reacting flow, resulting from exothermicity and gaseous expansion. The reduction in the mean curvature radius of the streamlines is also quite evident and is suitably reproduced in the simulations.

It is also noted that the dynamic efficiency function formulation results in more accurate predictions and resolves the shear layer growth rate more effectively, as compared to the conventional algebraic approach. However, a slight under-prediction of the negative velocity near the wall is observed, and could be improved by appropriate mesh resolution near the walls and/or the choice of suitable wall functions. The marginal under-estimation of the average reattachment location could also be corrected by performing fully 3D simulations instead of using periodic boundary conditions in the span-wise direction.

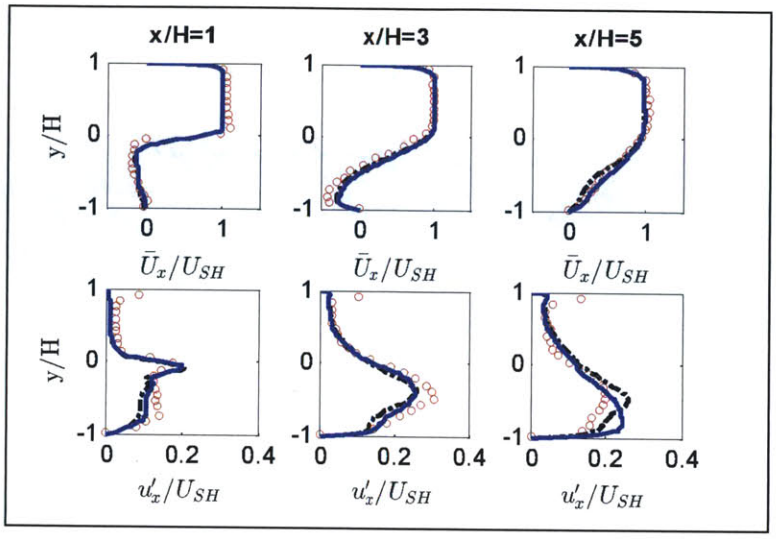

Figure 3.60: Normalized profiles for average axial velocity (top) and rms axial velocity (bottom): ooo Experiment, –·–· LES (Algebraic Model), – – – LES (Dynamic Formulation).

Further, examination of the rms velocity profiles shows that in contrast to the non-reacting case, the turbulence intensity is predominantly high in the recirculation region as opposed to the mixing layer, indicating the suppression of shear-generated turbulence due to heat release. The drastic shortening of the recirculation zone shifts regions with strong concentration of both shear stress and turbulent kinetic energy (TKE) from the outer periphery of the recirculation zone to inward locations; turbulence appears to be concentrated in the region around the maximum streamline curvature near the reattachment zone. This is due to the rapid curving of the outer flow streamlines in the vicinity of the reattachment point, and the flow fluctuations are significantly high in the region where the flapping shear layer impinges on the wall. The high turbulence region is therefore bounded by the shear layer and widens with downstream distance from the step. Further beyond the reattachment region (x>5.0H), the turbulent intensity continues to remain high due to combustion induced turbulence.

In figure 3.61, the normalized average temperature profiles estimated numerically are compared with the experimental data and it is observed that the models predict the spreading rate of the flame, and the peak temperature reasonably accurately. The mean temperature contour is also shown in figure 3.62, along with the cross-sections where data are compared. The steep gradient in the temperature profile (x/h < 1) corresponds to the laminar shear layer, which gradually rolls-up in a sequence of large-scale structures. As the mixing layer spreads due to the growth of the vortices

downstream (as a result of entrainment, exothermicity, convective mixing and coalescence), it results in broadening of the temperature profile (x/h>2) as well [3.32].

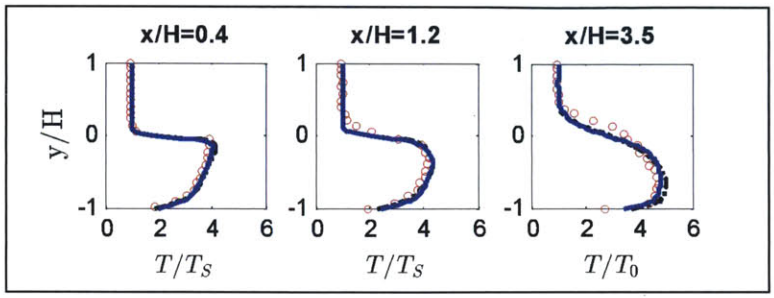

Figure 3.61: Normalized profiles for average temperature: ooo Experiment, −·−· LES (Algebraic Model), −−− LES (Dynamic Formulation).

Note that the reaction zone near the step takes the form of a sheet-like interface and is typically characterized by low scalar fluctuations. However, in the vicinity of the reattachment point, mass entrainment of fresh reactants is the dominant mechanism at work, resulting in a thick flame-front and high mean temperatures. In this region, large flow perturbations also exist. As the shear layer grows downstream, the high-turbulence region (and consequently the progress of reaction) bounded by the layer also spreads, as does the region with significant scalar fluctuations. Likewise, the high temperature region beneath the flame surface also spreads, as indicated by the average temperature contour. While these trends are reproduced by the combustion models adequately, the development of the high-turbulence region is more accurately predicted (figure 3.60) using the proposed dynamic technique, thereby highlighting the importance of estimating the flame wrinkling dynamically while explicitly incorporating strain-rate effects, and the corresponding impact on predictive accuracy.

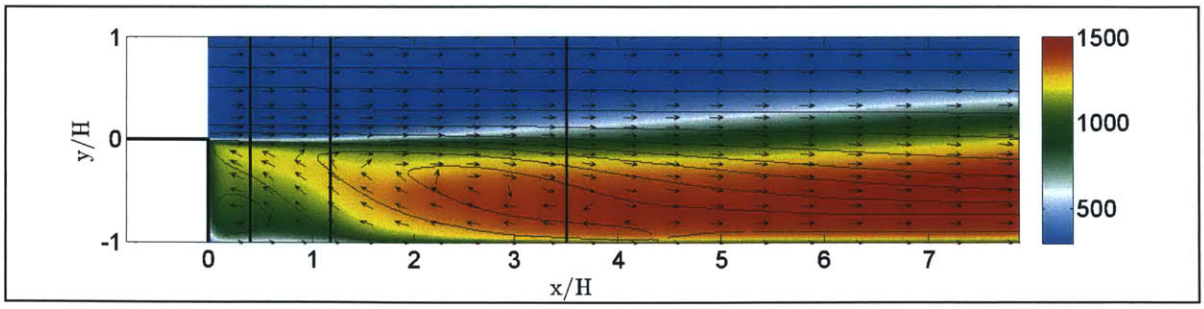

Figure 3.62: Average temperature (K) with the mean 2D velocity vectors and streamlines. The cross-sections at which data are compared are also shown.

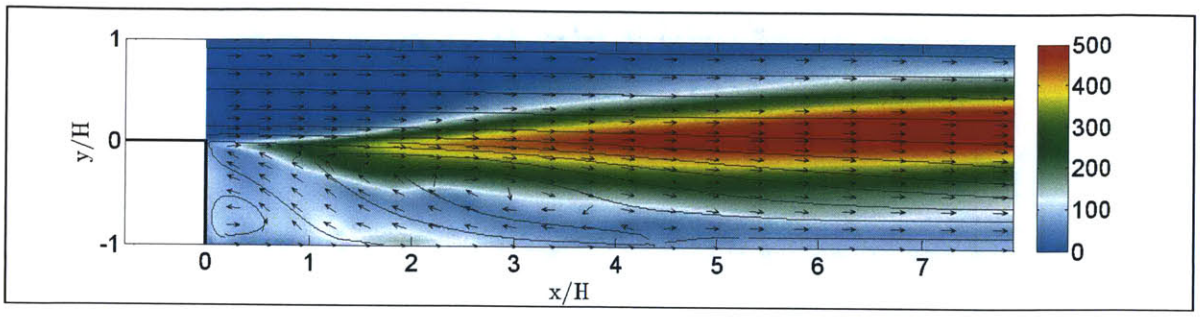

Figure 3.63: rms temperature (K) with the mean 2D velocity vectors and streamlines.

3.4 Conclusions

This chapter focuses on investigating the predictive capabilities of the thickened flame LES combustion model as applied to well-studied, canonical wake-stabilized flame configurations. A preliminary analysis is conducted to assess the performance of turbulence-chemistry interaction sub-models on LES predictions for different combustor configurations. The simulation results are compared with experimental measurements, and the turbulent flow features are resolved fairly well. More accurate predictions are obtained using a dynamic formulation for the efficiency function, along with a multiple-step reaction mechanism. Specifically, it is observed that the fluctuations in the shear layer are reproduced more accurately using the modified approach, both for the triangular bluff-body and the backward step combustor. This suggests that the proposed approach is an improvement over the existing models, since deviation from local equilibrium, and the absence of time history and strain effects in the equilibrium models can result in inaccurate predictions, especially in case of lean premixed flames under highly unsteady conditions. In addition, the model employs the strained laminar flame speed in its calculations to account for the effects of strain and curvature on the laminar flame speed, which can further enhance the accuracy of the numerical predictions.

4 PRESUMED-PDF MODEL

4.1 Overview

Another framework to account for detailed reaction mechanisms, aside from the finite-rate chemistry models such as the thickened flame and partially-stirred reactor techniques, involves statistical approaches, comprising of the transported-PDF and presumed-PDF combustion models. As mentioned in Chapter 2, the application of transported PDF methods in LES generally requires high computational costs and robust solution algorithms; the expensive solution of the PDF balance equation can be avoided by assuming a specific shape for the PDF, resulting in the presumed PDF models.

LES validation studies have been conducted in the past [4.1-4.5] using the presumed-PDF approaches to assess their predictive capabilities in turbulent combustion. In the context of premixed combustion, these have mostly focused upon using the reaction progress variable and the enthalpy as coordinates to presume the probability density function (PDF) to obtain the filtered thermo-chemical properties and reaction rates. However, it is well known that in case of highly unsteady systems or in configurations prone to thermo-acoustic instabilities, strain can play a significant role in altering the flame speed and thus the turbulence-chemistry interactions. As an example, for flames trapped in the shear layer behind a backward-facing step, the strain effects near the step are important in reducing the effective reaction rate and preserving the Kelvin-Helmholtz instability. Likewise, in case of confined swirling flames, significant strain effects can provoke extinction of the flame that stabilizes in the outer shear layer of the annular jet, particularly in lean conditions. Therefore, it is imperative to explicitly account for the strain, while simulating turbulent premixed combustion. More recently, this has been attempted in a RANS context [4.6-4.7], by incorporating strain (via the scalar dissipation rate) as an additional coordinate to presume the PDF, while utilizing strained laminar flamelets to obtain the chemical database. Additionally, to account for the detailed chemistry effects, the use of techniques such as the flamelet generated manifold (FGM), which generates mathematically reduced databases in order to estimate the chemical flame structure efficiently and effectively, can be employed [4.8-4.10].

In this work, a similar formulation is adopted, in an LES context, and the predictive accuracy of the numerical framework is assessed using a canonical wake flow stabilized flame configuration: an axi-symmetric bluff-body in a cylindrical duct. Simulations are performed using a compressible,

finite-volume LES code, and the predictions are compared with experimental data, for the validation of the proposed combustion model.

The next section provides a description of the modeling approach employed in this study, following which the experimental configuration and the simulation setups corresponding to the combustor geometry are described. The LES predictions are validated against experimental measurements and initial results indicate that the suggested combustion model is an improvement over the conventional approach and can accurately predict unsteady flow features and flame dynamics in premixed combustor systems.

4.2 PDF Modeling

As described in section 2.8.4, in the presumed-PDF framework, the reaction rate and the thermo-chemical properties are averaged over the joint probability density function (PDF) which is presumed, and does not require solving a transport equation (as in the transported-PDF approach) that can be computationally intensive. Further, reaction chemistry can be taken into account using the flamelet generated manifold (FGM) approach. This technique focuses on including detailed chemistry effects within the combustion model by reducing the chemical subspace using a set of reference laminar flamelet computations (based on detailed chemistry mechanisms) and storing the chemical flame structure inside a lookup table. Therefore, by constructing databases of relevant quantities using detailed simulations of simple flames, the approach can reduce the cost of performing reacting flow computations with extensive chemical kinetic mechanisms, while still retaining the accuracy of the detailed results. In the current work, the focus is on the presumed-PDF approach coupled with the FGM technique, and a description of the method, as implemented in this study, is presented in detail below.

4.2.1. Presumed-PDF Technique coupled with FGM Approach

In an attempt to model the filtered reaction rate while simulating premixed turbulent combustion, within the context of presumed-PDF method, previous researchers [4.11] have tabulated detailed chemistry using a collection of one-dimensional premixed laminar flamelets (flame prolongation of intrinsic low-dimensional manifolds), following which the mean flame structure can be estimated by averaging over the presumed probability density function of the progress variable. The assumption behind the approach is that the premixed turbulent flame can be considered as an ensemble of thin, locally one-dimensional laminar flamelets embedded in turbulent flow. Mathematically, a closure for the mean reaction rate is typically provided as:

$$\bar{\dot{\omega}} = \int_{Y_{ca}}^{Y_{cb}} \dot{\omega}(Y_c) P(Y_c) dY_c = \bar{\dot{\omega}}(Y_c) \qquad (4.1)$$

where Y_c is the sample space variable for c, $P(Y_c)$ is the marginal PDF of c, and $\dot{\omega}(Y_c)$ is the reaction rate in the unstrained planar laminar flame obtained from flamelet calculations. The basis of the approach therefore is the combustion progress variable that defines the local position on the low-dimensional manifold. The progress of reaction is determined such that it increases monotonically, and is typically chosen as one of the species mass fractions (eg Y_{CO2}) or a linear combination thereof (eg $Y_{CO_2} + Y_{CO}$). In this work, with the focus on lean, premixed methane-air flames, the mass fraction of CO_2 (Y_{CO_2}) is chosen to represent the progress of reaction [4.12].

The closure in (4.1), however, implicitly assumes that the local reaction rate and the flamelet structure in the turbulent flame correspond to a freely propagating planar laminar flame, which does not include the effect of fluid-dynamic stretch rate on the laminar flame. It is known, however, that the turbulent eddies are likely to substantially wrinkle the flame front, and that the stretch rate can significantly influence burning velocity. Thus, the freely propagating flame obtained from the one-dimensional detailed chemistry is only an approximation for the stretched and curved flame in a turbulent flow field. Although it has been suggested that this flamelet assumption may not be very restrictive [4.13], in order to address the above concerns, researchers have accounted for stretch rate effects within the laminar flamelet model [4.14] by defining the mean reaction rate as:

$$\bar{\dot{\omega}} = \int_{Y_{ca}}^{Y_{cb}} \int_{-\infty}^{\infty} \dot{\omega}(Y_c, \kappa) P(Y_c, \kappa) dY_c d\kappa \qquad (4.2)$$

where Y_c is the sample space variable for c, κ is the stretch rate, $P(Y_c, \kappa)$ is the joint PDF of Y_c and κ, and $\dot{\omega}(Y_c, \kappa)$ is the reaction rate in the strained laminar flame obtained from flamelet calculations.

More recently, following a similar approach, strained flamelets, characterized using the scalar dissipation rate of the progress variable, have been employed to describe the flamelet structure [4.6-4.7]. Specifically, based on counter-flow flamelets at various strain rates, the chemical flame structure is stored inside a look-up table in terms of coordinates that include the progress of reaction and the scalar dissipation rate. The mean flame structure is then presumed as:

$$\bar{\dot{\omega}} = \iint \dot{\omega}(Y_c, \chi) P(Y_c, \chi) dY_c d\chi \qquad (4.3)$$

where Y_c is the sample space variable for c, χ is the scalar dissipation rate, $P(Y_c,\chi)$ is the joint PDF of Y_c and χ, and $\dot{\omega}(Y_c,\chi)$ is the reaction rate in the strained laminar flame obtained from flamelet calculations.

The joint PDF is then written, using Bayes theorem, as a function of the conditional scalar dissipation rate, $\chi|Y_c$, resulting in the following formulation to obtain the mean reaction rate:

$$\bar{\dot{\omega}} = \int_{Y_{co}}^{Y_{cb}} P(Y_c)dY_c \left[\int_{(\chi|Y_c)_q}^{(\chi|Y_c)_o} \dot{\omega}(Y_c,\chi) P(\chi|Y_c) d\chi \right] \qquad (4.4)$$

where the subscripts o and q respectively denote the unstrained and the extinguished flames. The conditional-PDF, $P(\chi|Y_c)$, is assumed as a log-normal distribution [4.6-4.7,4.15] while the PDF of the progress variable is assumed as a beta (β) function [4.6-4.7]. RANS calculations of laboratory flames have indicated the effectiveness of the approach over the unstrained-flamelet formulation. Specifically, it has been suggested that the latter over-predicts the mean reaction rate leading to a faster consumption of fuel and concomitant heat release resulting in a smaller flame brush than observed experimentally. This is understandable, given that strain effects can result in reducing the effective reaction rate; ignoring or inadequately representing the effects of strain can therefore result in predictive inaccuracies. As previously mentioned, for flames trapped in the shear layer behind a backward-facing step, the strain effects near the step are important in reducing the effective reaction rate and preserving the Kelvin-Helmholtz instability. In other words, if laminar flame is assumed independent of strain rate, the heat release in the shear layer inhibits the growth of the instability, resulting in a near smooth flame [4.16]. Likewise, in case of confined swirling flames, significant strain effects can provoke extinction of the flame that stabilizes in the outer shear layer of the annular jet, particularly in lean conditions [4.17-4.18].

This work therefore follows the approach adopted in [4.6-4.7] and extends it to an LES framework in order to further improve the fidelity and predictive accuracy of the numerical analysis. Chemistry tabulation is performed using the flamelet generated manifold (FGM) technique [4.4], and strained premixed flamelets generated using Chemkin for an axisymmetric stagnation configuration (with the GRI 3.0 reaction mechanism) are utilized. In addition to including the effect of strain, heat losses are also explicitly accounted for, by computing the flamelets for different inlet temperatures, and employs the enthalpy as an additional coordinate. The effects of heat loss can be significant in case of confined swirling flames, as it has been reported that the presence of the flame in the outer

shear layer in lean conditions is critically dependent on the thermal conditions at/near the walls [4.17-4.18]. It has been suggested that when adiabatic computations are performed, or when the influence of strain is inadequately represented, the flame is predicted to stabilize in the outer shear layer (OSL) as well. These observations indicate that the flame holding features are sensitive to the thermal condition on the walls, and strain computations in the OSL.

To summarize, the chemical flame structure is reproduced by a collection of laminar pre-mixed flames calculated at different strain rates (to account for flame strain), and at various inlet temperatures (i.e enthalpy levels, to account for heat losses) using detailed chemistry. A lookup table is thus generated that stores the chemical information using the progress of reaction (Y_c), the scalar dissipation rate (χ) and the enthalpy (h), as the coordinates, and thereby incorporates detailed chemistry effects using only a few controlling variables, that describe the internal flame structure. All the required mixture properties thus tabulated can be accessed in terms of the coordinates Y_c, χ and h as $\varphi = \varphi(Y_c, \chi, h)$ and the mean value for a property can be determined after integration over the joint PDF of the variables as:

$$\bar{\varphi} = \int_{Y_{cu}}^{Y_{cb}} \int_{-\infty}^{\infty} \int_{h_{min}}^{h_{adb}} \varphi(Y_c, \chi, h) P(Y_c, \chi, h) dY_c d\chi dh \tag{4.5}$$

When density weighted PDF is used, the mean filtered value is obtained as:

$$\begin{aligned} \tilde{\varphi} &= \frac{1}{\bar{\rho}} \int_{Y_{cu}}^{Y_{cb}} \int_{-\infty}^{\infty} \int_{h_{min}}^{h_{adb}} \rho\varphi(Y_c, \chi, h) P(Y_c, \chi, h) dY_c d\chi dh \\ &= \int_{Y_{cu}}^{Y_{cb}} \int_{-\infty}^{\infty} \int_{h_{min}}^{h_{adb}} \varphi(Y_c, \chi, h) \tilde{P}(Y_c, \chi, h) dY_c d\chi dh = \tilde{\varphi}(Y_c, \chi, h) \end{aligned} \tag{4.6}$$

The coordinates of the FGM database can be normalized prior to integration in order to simplify the computations, as in [4.19]. The mean filtered value can then be estimated as:

$$\tilde{\varphi} = \int\int\int \varphi(\hat{Y}_c, \hat{\chi}, \hat{h}) \tilde{P}(\hat{Y}_c, \hat{\chi}, \hat{h}) d\hat{Y}_c d\hat{\chi} d\hat{h} = \tilde{\varphi}(\hat{Y}_c, \hat{\chi}, \hat{h}) \tag{4.7}$$

where ^ denotes the corresponding normalized variable.

The joint PDF can be re-written, using Bayes theorem and conditional PDFs, as in (4.4). In this work, however, the variables are assumed to be statistically independent, for simplicity, allowing the filtered values to be determined as:

$$\tilde{\varphi} = \iiint \varphi(\hat{Y}_c, \hat{\chi}, \hat{h}) \tilde{P}_{\hat{Y}_c}(\hat{Y}_c) \tilde{P}_{\hat{\chi}}(\hat{\chi}) \tilde{P}_{\hat{h}}(\hat{h}) d\hat{Y}_c d\hat{\chi} d\hat{h} \tag{4.8}$$

where the normalized values are computed based on the system configuration, as in [4.19].

The mean filtered values for any particular thermo-physical property can therefore be obtained by computing the corresponding integral using presumed-PDFs. An additional lookup table that tabulates the results of this integration can then be generated prior to performing the numerical simulations. Typically beta (β) distribution for the progress variable, log-normal distribution for the scalar dissipation rate, and delta (δ) function for enthalpy are considered. In this work, the presumed probabilities for Y_c and χ take the form of β distributions, while a δ function serves as the probability distribution for h, as shown:

$$P_\beta(x) = \frac{\Gamma(a+b)}{\Gamma(a)\Gamma(b)}(x)^{a-1}(1-x)^{b-1}, P_\delta(x) = \delta(x-\bar{x}) \tag{4.9}$$

The β distribution is chosen to presume the PDF because of its ability to reproduce a δ function when variance is zero, a Gaussian function when variance is low, and a bimodal function for large variance. This is possible since the free parameters of the distribution depend on the mean and variance:

$$\tilde{x} = \int_0^1 x\tilde{P}(x)dx = \frac{a}{a+b},\ \widetilde{x_v} = \int_0^1 (x-\tilde{x})^2\tilde{P}(x)dx = \frac{ab}{(a+b)^2(1+a+b)} \quad (4.10), (4.11)$$

Alternatively, the free parameters can also be computed, as in [4.20], using:

$$\tilde{x} = \int_0^1 x\tilde{P}(x)dx = \frac{a}{a+b},\ \widetilde{x^2} = \int_0^1 x^2\tilde{P}(x)dx = \frac{a(1+a)}{(a+b)(1+a+b)} \quad (4.12), (4.13)$$

Therefore, once the relevant statistics for the progress variable and the scalar dissipation are known, along with the mixture enthalpy, the mean filtered value for any thermo-physical property as well as the reaction source term can be obtained:

$$\begin{aligned}\tilde{\varphi} &= \iiint \varphi\left(\hat{Y}_c,\hat{\chi},\hat{h}\right)\tilde{P}_{\hat{Y}_c}\left(\widetilde{\hat{Y}_c},\widetilde{\hat{Y}_{cv}}\right)\tilde{P}_{\hat{\chi}}\left(\widetilde{\hat{\chi}},\widetilde{\hat{\chi}_v}\right)\tilde{P}_{\hat{h}}\left(\hat{h}\right)d\hat{Y}_c d\hat{\chi}d\hat{h} = \tilde{\varphi}\left(\widetilde{\hat{Y}_c},\widetilde{\hat{Y}_{cv}},\widetilde{\hat{\chi}},\widetilde{\hat{\chi}_v},\hat{h}\right), \text{ or} \\ \tilde{\varphi} &= \iiint \varphi\left(\hat{Y}_c,\hat{\chi},\hat{h}\right)\tilde{P}_{\hat{Y}_c}\left(\widetilde{\hat{Y}_c},\widetilde{\hat{Y}_c^2}\right)\tilde{P}_{\hat{\chi}}\left(\widetilde{\hat{\chi}},\widetilde{\hat{\chi}^2}\right)\tilde{P}_{\hat{h}}\left(\hat{h}\right)d\hat{Y}_c d\hat{\chi}d\hat{h} = \tilde{\varphi}\left(\widetilde{\hat{Y}_c},\widetilde{\hat{Y}_c^2},\widetilde{\hat{\chi}},\widetilde{\hat{\chi}^2},\hat{h}\right)\end{aligned} \quad (4.14), (4.15)$$

As can be inferred, in order to incorporate the above formulation within the context of LES, it is necessary to estimate the statistics corresponding to the progress variable and scalar dissipation with reasonable accuracy. This has been a subject of considerable research and is discussed in the next section.

4.2.2. Presumed-PDF LES Modeling and Governing Equations

The first moment of the progress of reaction can be obtained by solving for its transport equation, which can be written as:

$$\frac{\partial \rho Y_c}{\partial t} + \nabla.(\rho u Y_c) = \nabla.(\rho D \nabla Y_c) + \rho \dot{\omega}_{Y_c} \tag{4.16}$$

Post-filtering, the governing equation is obtained as:

$$\frac{\partial \overline{\rho} \widetilde{Y}_c}{\partial t} + \nabla.(\overline{\rho} \tilde{u} \widetilde{Y}_c) = -\nabla.\left(\overline{\rho u Y_c} - \overline{\rho} \tilde{u} \widetilde{Y}_c\right) + \nabla.(\overline{\rho} D \nabla \widetilde{Y}_c) + \overline{\rho \dot{\omega}_{Y_c}} \tag{4.17}$$

which can be re-written as:

$$\frac{\partial \overline{\rho} \widetilde{Y}_c}{\partial t} + \nabla.(\overline{\rho} \tilde{u} \widetilde{Y}_c) = \nabla.\left(\overline{\rho}\left[D + \frac{\mu_t}{Sc_t}\right] \nabla \widetilde{Y}_c\right) + \overline{\rho \dot{\omega}_{Y_c}} \tag{4.18}$$

While the computation of the first moment is relatively straight-forward, the variance calculation requires careful consideration [4.21]. One approach is to derive the filtered balance equation for the variance, as in [4.19]. The transport equation for $\widetilde{Y}_c^2$ is first written as:

$$\frac{\partial \overline{\rho} \widetilde{Y_c^2}}{\partial t} + \nabla.(\overline{\rho} \tilde{u} \widetilde{Y_c^2}) = -\nabla.\left(\overline{\rho u Y_c^2} - \overline{\rho} \tilde{u} \widetilde{Y_c^2}\right) + \nabla.(\overline{\rho} D \nabla \widetilde{Y_c^2}) - 2\overline{\rho} \widetilde{\chi_{Y_c}} + 2\overline{\rho} \widetilde{\dot{\omega}_{Y_c} Y_c} \tag{4.19}$$

where the scalar dissipation, which represents the rate at which cold unburned reactants and hot fully burned products are mixed and burned, is defined as:

$$\overline{\rho} \widetilde{\chi_{Y_c}} = \overline{\rho D \left|\nabla Y_c\right|^2} = \overline{\rho} D \left|\nabla \widetilde{Y}_c^2\right| + \widetilde{s_{X_{Y_c}}} \tag{4.20}$$

Here $\widetilde{s_{X_{Y_c}}}$ is the unresolved part requiring additional modeling. Subsequently, the equation for $\widetilde{Y}_c^2$ can be written as:

$$\begin{aligned} \frac{\partial \overline{\rho} \widetilde{Y}_c^2}{\partial t} + \nabla.(\overline{\rho} \tilde{u} \widetilde{Y}_c^2) = & -\nabla.\left(2\widetilde{Y}_c\left[\overline{\rho} \tilde{u} \widetilde{Y}_c - \overline{\rho} \tilde{u} \widetilde{Y}_c\right]\right) + \\ & \nabla.(\overline{\rho} D \nabla \widetilde{Y}_c^2) + 2\left(\overline{\rho} \tilde{u} \widetilde{Y}_c - \overline{\rho} \tilde{u} \widetilde{Y}_c\right).\nabla \widetilde{Y}_c - 2\overline{\rho} D \left|\nabla \widetilde{Y}_c\right|^2 + 2\overline{\rho} \widetilde{\dot{\omega}_{Y_c} Y_c} \end{aligned} \tag{4.21}$$

The equation for the variance, $\widetilde{Y}_{cv} = \widetilde{Y}_c^2 - \widetilde{Y}_c^2$, can therefore be represented as:

$$\begin{aligned} \frac{\partial \overline{\rho} \widetilde{Y}_{cv}}{\partial t} + \nabla.(\overline{\rho} \tilde{u} \widetilde{Y}_{cv}) = & -\nabla.\left[\left(\overline{\rho u Y_c^2} - \overline{\rho} \tilde{u} \widetilde{Y_c^2}\right) - \left(2\widetilde{Y}_c\left[\overline{\rho} \tilde{u} \widetilde{Y}_c - \overline{\rho} \tilde{u} \widetilde{Y}_c\right]\right)\right] + \\ & \nabla.(\overline{\rho} D \nabla \widetilde{Y}_{cv}) - 2\left(\overline{\rho} \tilde{u} \widetilde{Y}_c - \overline{\rho} \tilde{u} \widetilde{Y}_c\right).\nabla \widetilde{Y}_c - 2\widetilde{s_{X_{Y_c}}} + 2\overline{\rho}(\widetilde{\dot{\omega}_{Y_c} Y}_c - \widetilde{\dot{\omega}_{Y_c}} \widetilde{Y}_c) \end{aligned} \tag{4.22}$$

It has been suggested that the transport equation thus obtained involves modeling of the production source term, $-2\left(\overline{\rho} \tilde{u} \widetilde{Y}_c - \overline{\rho} \tilde{u} \widetilde{Y}_c\right).\nabla \widetilde{Y}_c$, which can be inaccurately depicted in numerical simulations in case of premixed combustion. As a consequence, the variance estimation can be

adversely affected; therefore, it has been suggested to solve for the deviation from the maximum variance, rather than computing the variance directly [4.21]. Alternatively, the transport equation for $\widetilde{Y_c^2}$ may also be utilized [4.2], [4.20] resulting in the following equation, which has been used in the current work:

$$\frac{\partial \overline{\rho}\widetilde{Y_c^2}}{\partial t}+\nabla.(\overline{\rho}\tilde{u}\widetilde{Y_c^2})=\nabla.\left(\overline{\rho}\left[D+\frac{\mu_t}{Sc_t}\right]\nabla\widetilde{Y_c^2}\right)-2\underbrace{\left(\overline{\rho}D\left|\nabla\widetilde{Y_c}^2\right|+\widetilde{s_{X_{Y_c}}}\right)}_{\widetilde{\chi_{Y_c}}}+2\overline{\rho}\widetilde{\dot{\omega}_{Y_c}Y_c} \quad (4.23)$$

Note that the source term in the equation above can also be pre-integrated and stored within the lookup table, in order to improve the computational efficiency. Further, in order to provide an accurate closure for the equation above, a model that appropriately accounts for the scalar dissipation rate must be provided. The scalar dissipation rate also serves as an additional coordinate for the lookup operation; therefore, its accurate estimation is critical to predictive accuracy.

Various approaches have previously been adopted to model the scalar dissipation rate [4.22-4.24]. The classical technique involves expressing the filtered scalar dissipation using the linear relaxation type closure that assumes equilibrium between production and dissipation in the balance equation for the scalar dissipation rate, giving:

$$\widetilde{\chi_{Y_c}}\approx\frac{\widetilde{Y_{cv}}}{\tau_t}=C_\chi\widetilde{Y}_{cv}\frac{\tilde{\varepsilon}}{\tilde{k}} \quad (4.24)$$

where k and ε are the turbulent kinetic energy and its dissipation rate respectively. The model however is typically applicable to combustion with small heat release and/or low Damköhler number. Also, the modeling constant C_χ should typically depend on the local flame structure since a premixed turbulent flame contains thin reaction zones that strongly impact small-scale gradients. The exact determination of its local value however is not straight-forward. Additionally, researchers have also provided another formulation for the scalar dissipation rate, coupling thin reaction zones with turbulent micro-mixing [4.19]. More recently, a model has been proposed that includes the effects of dilatation due to heat release [4.25], to express the scalar dissipation rate as:

$$\overline{\rho}\widetilde{\chi_{Y_c}}=\overline{\rho D\left|\nabla Y_c\right|^2}=\overline{\rho}D\left|\nabla\widetilde{Y}_c\right|^2+\overline{\rho}\left(1+\frac{2}{3}C_{sc}\frac{s_L^0}{\tilde{k}^{1/2}}\right)\left(C_{Dc}\frac{s_L^0}{\delta_L^0}+C_D\frac{\tilde{\varepsilon}}{\tilde{k}}\right)\widetilde{Y}_{cv} \quad (4.25)$$

where s_L^0 and δ_L^0 are the laminar burning velocity and flame thermal thickness respectively; C_{sc}, C_{Dc}, and C_D are model parameters. It has been suggested that the model performs better at large

Damkohler and Reynolds numbers, while the classical model over-predicts the value of the scalar dissipation rate resulting in an under-prediction of the variance thereby resulting in an under-estimation of the interior PDF values and the mean reaction rate. The current work, however, employs the following formulation for estimating the scalar dissipation rate [4.20]:

$$\begin{aligned}\overline{\rho}\widetilde{\chi_{Y_c}} &= \overline{\rho D\left|\nabla Y_c\right|^2} = \overline{\rho}D\left|\nabla\widetilde{Y}_c^2\right| + \widetilde{s_{X_{Y_c}}} \\ &= \overline{\rho}D\left|\nabla\widetilde{Y}_c\right|^2 + \frac{\overline{\rho}\widetilde{Y_{cv}}}{\tau_t} = \overline{\rho}D\left|\nabla\widetilde{Y}_c\right|^2 + \overline{\rho}C''\frac{\upsilon_t}{Sc_t}\frac{\widetilde{Y}_{cv}}{\Delta^2} \approx \overline{\rho}D\left|\nabla\widetilde{Y}_c\right|^2 + C_d\frac{\mu_t}{Sc_t}\frac{\widetilde{Y_c^2}-\widetilde{Y}_c\widetilde{Y}_c}{\Delta^2}\end{aligned} \tag{4.26}$$

where C_d is a model parameter.

The variance of the dissipation rate in this work is considered as a constant for simplicity. Also, note that including the scalar dissipation rate as an additional coordinate only marginally increases the look-up duration and does not significantly impact the computational cost. In addition, an enthalpy equation is also solved to account for heat losses, and may be represented as:

$$\frac{\partial\overline{\rho}\tilde{h}}{\partial t} + \nabla.(\overline{\rho}\tilde{u}\tilde{h}) = \nabla.\left(\overline{\rho}\left[\alpha+\alpha_t\right]\nabla\tilde{h}\right) \tag{4.27}$$

where α, h refer to the thermal diffusivity and enthalpy respectively.

Thus, once the relevant values for the variables serving as the coordinates are obtained, the mean, filtered values for the thermo-physical properties can be obtained from the lookup table. The computational efficiency and predictive accuracy both depend on the resolution of the pre-integrated tables employed within the presumed-PDF framework; utilization of finer resolution tables can result in more precise predictions using the numerical techniques, while using faster look-up procedures can maintain a balance with computational efficiency. Appropriate choice of the presumed PDFs for the reaction progress variable and the scalar dissipation rate, depending on the combustor configuration, can also lead to improved LES predictions in practical systems [4.26].

4.3 Validation Study: Axi-Symmetric Bluff-Body

An axi-symmetric bluff-body in a cylindrical chamber [4.27] provides a reasonably comprehensive framework for validation since it comprise of many aspects of practical combustors such as anchored flames, regions of recirculation and shear layers. A parallelized, unstructured, finite volume LES code for solving compressible 3D Navier Stokes equations with second order spatial and temporal accuracy is used, and the one-equation eddy viscosity model is employed to estimate the sub-grid scale (SGS) stress terms. The numerical predictions are compared against experimental data

for non-reacting and reacting cases, and the relative performance of the conventional (Y_c, h as coordinates) and the modified (Y_c, χ, h as coordinates) presumed-PDF approaches is investigated.

4.3.1 Experimental Configuration

The combustion chamber, depicted in figure 4.1, is comprised of a stainless steel conical bluff-body of base diameter (D) 44.45 mm, and an apex angle (λ) 45°, mounted coaxially at the center of the combustor, serving as a flame-holder. The burner enclosure (in experiments) consists of a square cross-section with round corners; the simulation model however assumes an axi-symmetric geometry (radius, R = 39 mm), as in [4.28]. A mixture of air and methane is introduced at an equivalence ratio (φ) of 0.59, at a bulk inlet velocity (U_{BR}) of 15 m/s and at 24% free stream turbulence (Reynolds number, Re_{BR} ~ 23,500, based on the inlet pipe radius $D/2$ and the bulk fluid velocity U_{BR}). The inlet temperature (T_B) is 300 K and the nominal pressure is 101 kPa.

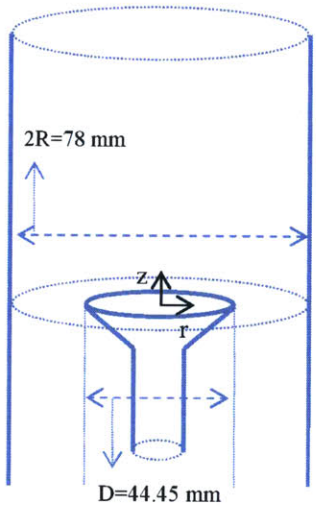

Figure 4.1: Axi-symmetric bluff-body configuration used for flame stabilization.

4.3.2 Simulation Setup

The choice of the numerical grid is governed by estimates of the physical length scales associated with the flow configuration. For example, the bluff-body boundary layer plays a critical role in the shear layer formation. Its thickness is inversely proportional to the square root of the macroscopic Reynolds number, Re_{BR} and is thus estimated to be 6.5 mm. In comparison to this, the Kolmogorov length scale ($Re_{BR}^{-3/4}L$) is noted to be 11.7 μm. In addition to the boundary layer thickness, it has been suggested that in order to directly capture the bulk of the energy containing structures and resolve at least 80% of the turbulent kinetic energy, a filter-width (Δ) to integral length scale (L_I)

ratio of approximately 0.083 should be maintained [4.29]. Using the bluff-body base radius ($D/2$) as the integral length scale, the filter-width can be estimated to be 1.8 mm. It should be noted, however, that the above theory does not focus on resolving near-wall structures and may not be applicable for reacting flow. Therefore, appropriate grid clustering may be required to resolve the structures near the walls and in the shear layer region for reacting flow. Based on these arguments, the non-uniform mesh utilized in the present work is comprised of approximately 0.6 million hexahedral cells, and gets coarser along the stream-wise direction. The numbers of cells in the axial, radial and tangential directions, downstream of the bluff-body, are 140, 42, and 96 respectively. The average Δx in the wake region is approximately 1.0 mm.

Temporal resolution is determined based on physical time scale estimates, in order to prevent excessive numerical dissipation and numerical instability, as well as on chemical time scales. The integral time scale can be obtained using the ratio of the length scale (L) and the measured turbulent velocity fluctuation in the shear layer (u') as 4.4 ms, while the Kolmogorov time scale (proportional to the product of the integral time scale and the inverse square root of the macroscopic Reynolds number), in comparison, is estimated at 28.7 μs. In addition, using the CFL criterion ($C_{max} = (U_{BR}+U_s)\Delta t/\Delta x$, $C_{max} = 1$, $U_s = 340$ m/s, $\Delta x = 1$ mm), the time step for the simulations is estimated to be approximately 2.8 μs. Based on these considerations, a conservative value of 1 μs is used in the reacting flow simulations, to take into account local refinement and acceleration of the fluid above the bulk inlet velocity, and to adequately resolve the chemical time scales.

At the inlet, Dirichlet conditions are used for all variables except the pressure, for which zero Neumann conditions are specified. The inlet velocity has a flat profile on which fluctuations of 24% turbulence intensity are imposed, corresponding with the experimental measurements [4.27]. At the exit, zero Neumann conditions are specified for all variables except the pressure, for which wave-transmissive conditions are used. No-slip conditions are applied for the flow at the walls, while zero Neumann conditions are specified for the other variables. Heat transfer is also considered at the walls to account for any thermal losses. In order to maintain reasonable computational efficiency, appropriate wall functions are utilized to resolve the flow features in the wall boundary layer. Numerical computations start from quiescent conditions and the unsteady flow characteristics evolve naturally. In order to initiate the flame, a high temperature pulse is applied at the inlet section which ignites the fuel; the reacting mixture convects downstream, and eventually stabilizes as a flame at the edge of the bluff-body. Averaging is performed over nearly 10 flow-through cycles once the

flow is established in the computational domain. Note that in order to better understand the effect of heat release on the flow, the range of the magnitudes for the contours of some of the flame-flow variables have been fixed corresponding to the non-reacting and reacting cases. The key quantities relevant to the configuration are summarized in table 4.1.

Table 4.1 Parameters for the axi-symmetric bluff-body configuration.

PARAMETER	SYMBOL/EXPRESSION	VALUE
Combustor Chamber Radius	R	39 mm
Bluff-Body Base Diameter (Characteristic Length)	D	44.45 mm
Integral Length Scale	$L_I\ (=D/2)$	22.225 mm
Equivalence Ratio	φ	0.59
Bulk Inlet Velocity (Characteristic Flow Velocity)	U_{BR}	15 m/s
Macroscopic Reynolds Number	Re_{BR}	23,500
Inlet Temperature	T_B	300 K
Nominal Pressure	P	101 kPa
Bluff-Body Boundary Layer	$Re_{BR}^{-1/2}$	6.5 mm
Kolmogorov Length Scale	$Re_{BR}^{-3/4}L$	11.7 μm
Cold Flow Filter Width (Pope's Criterion)	$\Delta=0.083L_I$	1.8 mm
Shear Layer Fluctuation (measured)	u'	~5 m/s
Integral Time Scale	$T_I=L/u'$	4.4 ms
Kolmogorov Time Scale	$Re_{BR}^{-1/2}T_I$	28.7 μs
CFL Criterion Time Scale	$C_{max}\,\Delta x/(U_{BR}+U_s)$	2.8 μs

4.3.3 Results and Discussions: Non-Reacting Flow

Cold flow is considered prior to simulating reacting flow, with the prominent flow features in the wake region of the bluff-body comprising of the annular jet, the shear layer and the shed vortices, the central recirculation zone (CRZ), and the rear stagnation region (figure 4.2).

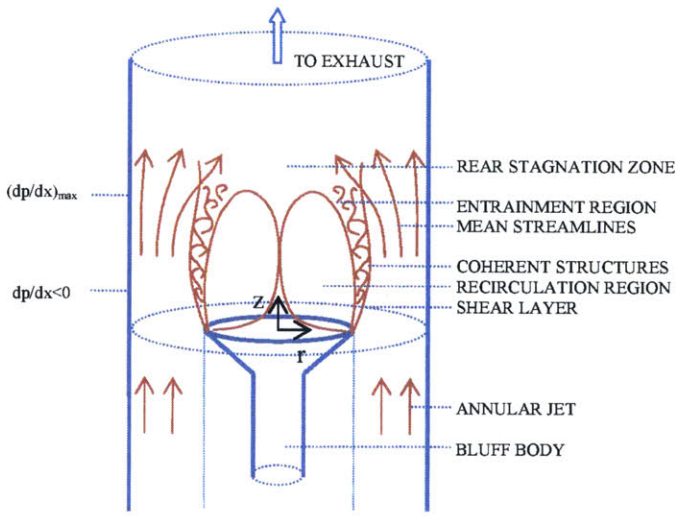

Figure 4.2: Fundamental flow features for confined isothermal flow around an axi-symmetric bluff-body configuration

The flow structures begin to form as the boundary layer along the bluff-body separates at its edge, developing into a thin shear layer. As the flow progresses downstream, unsteady behavior is observed, and the shear layer develops and grows in size as the turbulent eddies contained within begin to coalesce. These coherent vortices entrain irrotational fluid from the non-turbulent region outside the shear layer, which causes the formation of a three-dimensional low velocity recirculating vortex structure in the wake region downstream of the bluff-body. Due to the favorable pressure gradient created by the fluid entrained, the shear layer curves towards the centerline axis eventually resulting in a rear stagnation zone. In the proximity of this region, flow reversal takes place as seen in the instantaneous radial velocity contour in figure 4.3a. Note that the location of this region fluctuates due to the inherently unsteady motion of the shear layer.

In figure 4.3b, the LES contour of the instantaneous out-of-plane vorticity at a specific time-instant is shown, depicting the vortices that develop due to the roll-up of the vortex sheets formed at the bluff-body edges. The large-scale coherent structures break down into smaller eddies as they convect downstream, eventually dissipating due to vortex stretching and viscosity effects. This is also evident from the average vorticity magnitude contour shown in figure 4.3c, which indicates that high vorticity is confined to the narrow shear layer region surrounding the recirculation region, and that the intensity drops significantly in the section downstream of the rear stagnation zone.

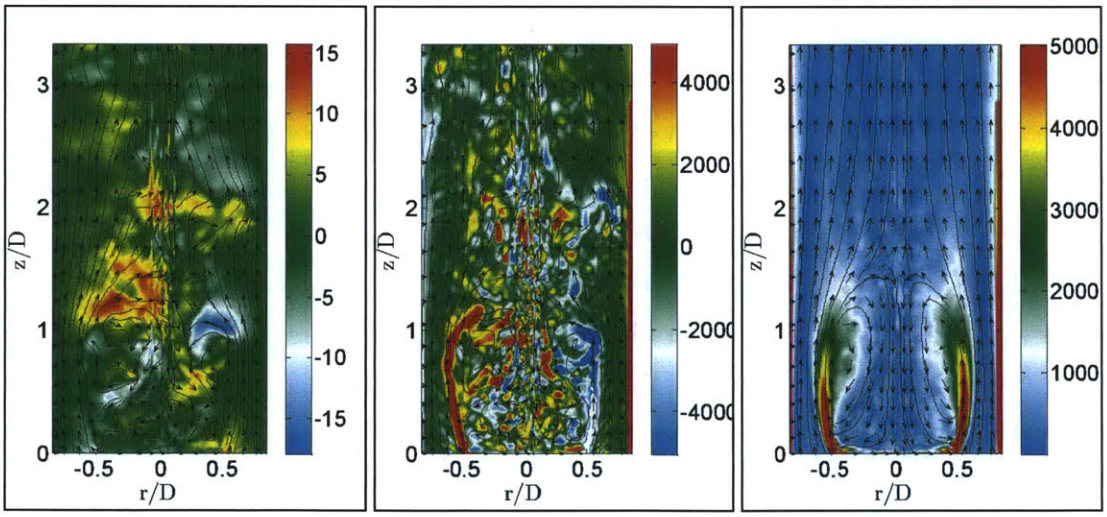

Figure 4.3: (a) Instantaneous radial velocity (m/s), (b) Instantaneous out-of-plane vorticity (1/s), (c) Average vorticity magnitude (1/s). The corresponding 2D velocity vectors and streamlines are also shown.

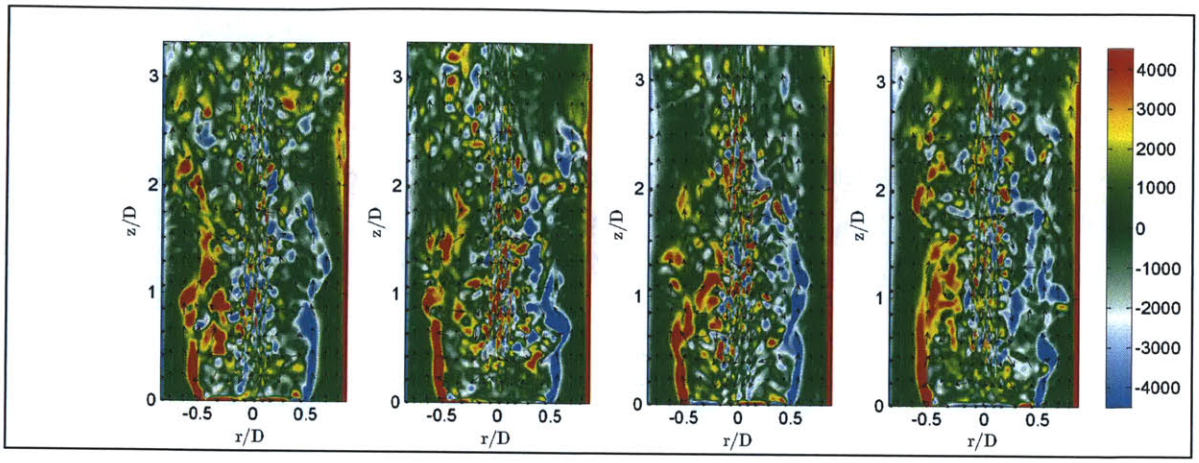

Figure 4.4: Instantaneous out-of-plane vorticity (1/s) with instantaneous 2D velocity vectors.

In figure 4.4, the instantaneous out-of-plane vorticity at different time instants is shown, depicting the prominent flow features in the wake region. The presence of the wall plays a critical role in altering the fundamental flow structures in this case, primarily affecting the streamline curvature and development of the shear layer. The chamber wall restricts the radially outward spread of the annular jet, and causes the streamlines to be smoother than in an unconfined scenario, resulting in a narrower and presumably longer recirculation zone [4.30-4.31]. Coupled with the presence of a thin annular jet, this affects the growth of the shed vortices, and influences the thickness of the mixing layer as well. Confinement also accelerates the incoming flow, thereby decreasing the wall static pressure (indicated by negative value of dP/dx). As estimated in experiments [4.30], deceleration typically sets in near the axial location corresponding to maximum recirculation zone width, while the maximum value of dP/dx is typically associated with the axial location of the rear stagnation region (figure 4.5).

In figure 4.6a, the contour of the average axial velocity is depicted, along with the mean streamlines. The cross-sections at which LES and experimental data are compared are also shown. The flow is dominated by the presence of strong recirculation zone with the zero velocity contours (shown in white) running through its core. As noted from the flow streamlines, on average, the CRZ extends to a length of approximately $1.4D$ downstream of the bluff-body.

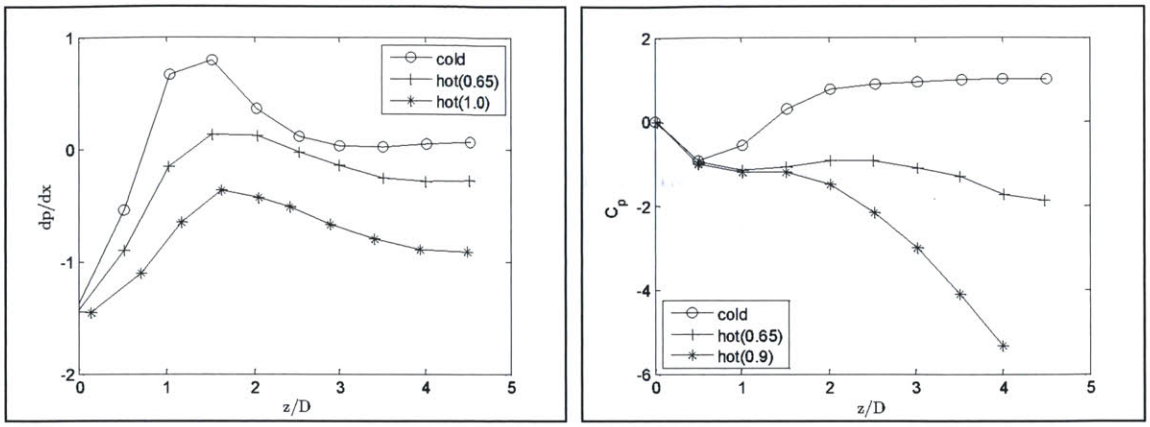

Figure 4.5: (a) Combustor wall pressure gradients in confined isothermal and reacting flows (U_z= 10m/s), (b) Axial pressure coefficient for different equivalence ratios (U_z= 15m/s). [4.30]

Note that the turbulent flow development in the wake of the bluff-body is sensitive to the inlet turbulence intensity. For a similar geometry [4.30], it has been shown that the recirculation zone length decreases from *1.5D* to *1.2D* when the level of turbulence intensity in the inlet stream is increased from 2% to 17% during experiments. This is due to the fact that the free stream turbulence intensity can alter the mixing layer growth rate by influencing the evolution of large-scale structures within the layer; the enhanced fluctuation levels within the separated shear layer cause an increase in the entrainment, thereby causing the shear layer to curve towards the centerline axis further upstream, as opposed to the flow with lower inlet turbulence intensity.

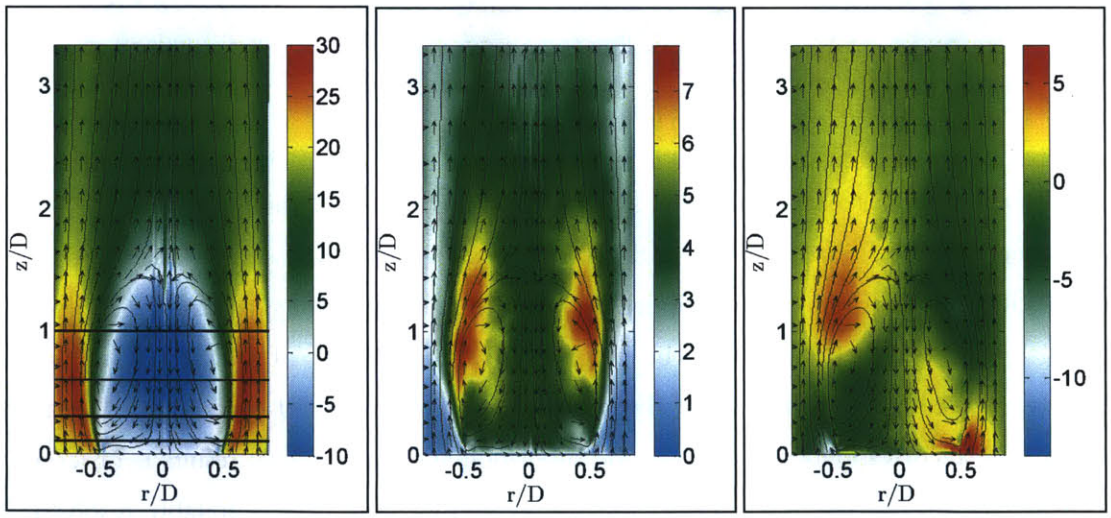

Figure 4.6: (a) Average axial velocity (m/s), (b) rms axial velocity (m/s), (c) Average radial velocity (m/s). The corresponding 2D velocity vectors and streamlines are also shown.

In figure 4.6b, the contour of the rms axial velocity is shown indicating high turbulence activity in the shear layers, primarily around the periphery of the recirculation zone, in the region corresponding to significant vortex shedding activity (figure 4.4). The coherent structures generated in the mixing layer, and shed downstream due to Kelvin–Helmholtz instability, contribute significantly to the generation of turbulent kinetic energy in the shear layer. The flow field fluctuations are also generally high near the rear stagnation zone where entrainment and flow reversal takes place, as evident from the mean radial velocity contour shown in figure 4.6c. The unsteady nature of the shear layer, as evident from the instantaneous axial velocity contours (at different time instants) shown in figure 4.7 also contributes to increasing the turbulent kinetic energy in the region. As the flow proceeds downstream, the large coherent structures break down into smaller eddies, which subsequently dissipate due to viscous effects. In the downstream section, near the exhaust, the relative influence of the large-scale vortical structures on turbulence reduces, and the turbulent flow field becomes significantly more isotropic.

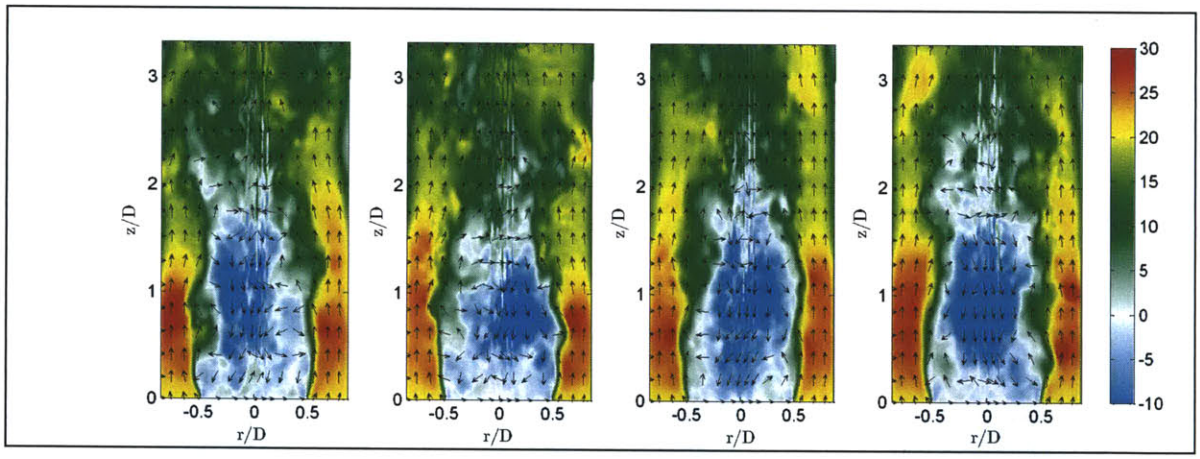

Figure 4.7: Instantaneous axial velocity (m/s) with instantaneous 2D velocity vectors.

In figure 4.8, LES predictions for the average axial velocity, rms axial velocity, and average radial velocity are compared with experimental data, obtained from [4.28], at cross-sections in the region downstream of the bluff-body. The experimental measurements of the radial profiles of the variables are available from the axis of the burner to approximately 10 mm into the shear layer (r/D=0.6). Close correspondence between the simulation and experimental results is observed for the velocity statistics in the wake region and the underlying flow field is suitably resolved. The location of the shear layer is predicted with reasonable accuracy, as is the extent of the central recirculation zone.

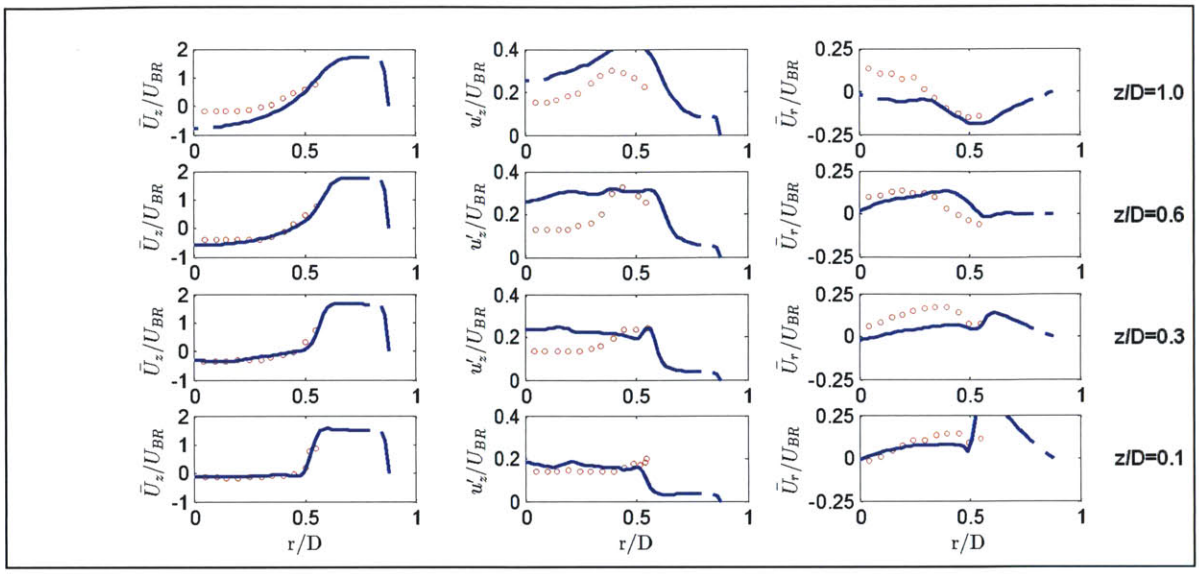

Figure 4.8: Normalized profiles for average axial velocity (left), rms axial velocity (middle), average radial velocity (right). ooo Experiment, – – – LES

Examining the rms profiles, it is observed that fluctuations peak in the shear layer and increase sharply in the stream-wise direction before gradually reducing in magnitude as the flow proceeds downstream. The turbulence eventually becomes nearly isotropic, as the large-scale turbulent structures induced by the bluff-body break down and dissipate (figure 4.5b). While this trend is reproduced using LES, and there is fair agreement between the experimental data and the simulation predictions close to the bluff-body, some discrepancies exist around the centerline near the stagnation region, as have been reported previously [4.28, 4.32-4.33]. It should be pointed out that the simulations model the chamber as an axi-symmetric geometry instead of a rectangular cross-section with rounded corners, as in [4.28]. Although this does not significantly impact the fundamental flow features observed, the quantitative differences in the profiles may be attributed to the modeling assumption.

4.3.4 Results and Discussions: Reacting Flow

Next, reacting flow for the configuration is considered, and simulations are performed using the conventional and modified approaches. The characteristic flame-flow features are outlined in the schematic in figure 4.9, comprising of a thin flame anchoring at the edge of the flame-holder, along with a thick reaction zone that 'necks' in the vicinity of the rear stagnation zone region. These features are also evident from the instantaneous LES contours for the temperature, normalized

reaction rate and normalized progress variable depicted in figure 4.10, along with the corresponding streamlines.

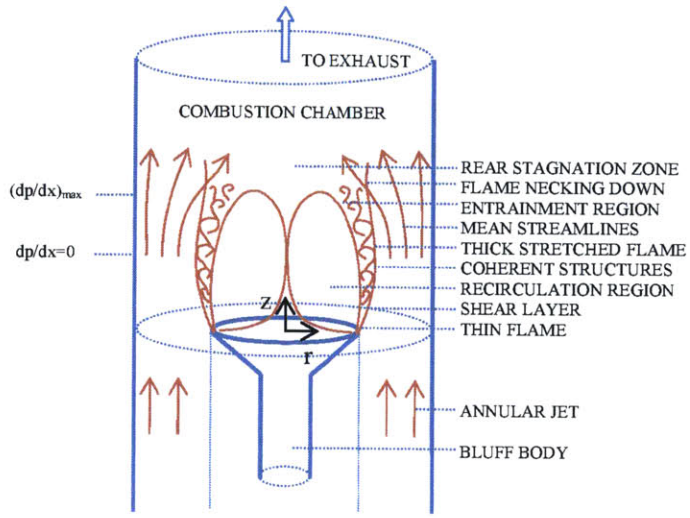

Figure 4.9: Fundamental flow features for confined reacting flow around an axi-symmetric bluff-body configuration.

The flame in this case stabilizes due to the recirculation of the combustion products in the wake region; in the upstream section, it is essentially confined to a surface originating in the shear layers downstream of the flame-holder edges. Large scale mixing between cold reactants and hot products takes place in these shear layer regions, forming a composition in which combustion can occur. Further downstream, the reaction zone thickens, particularly in the region of the large eddy structures surrounding the CRZ, and near the rear stagnation zone (figure 4.10), and the flame also appears to intermittently propagate into the central recirculation zone.

It is well established that turbulent combustion and stabilization of the flame in the reacting shear layer is a sequential phenomenon that involves preheating of the incoming reactant mixture near the flame-holder base, followed by its ignition due to the heat flux transported radially outward from the recirculation zone. These processes result in a relatively thin reaction zone near the bluff-body periphery and combustion in this ignition/thin-flame region is typically characterized by reaction kinetics for low equivalence ratios, given the low flame propagation speed and heat release rates. In such scenarios, the flame stabilizes in the presence of an elongated recirculation zone, often larger than that for the cold flow [4.30]. This is primarily due to the fluid dynamic effects of heat release (ie reduced vortex activity and lower adverse pressure gradients). However, for this particular scenario, the high inlet turbulence intensity does result in increased heat release rates and turbulent flame propagation speed while reducing the mixing time and enhancing entrainment. The

recirculation zone in this high Reynolds number combustion process, therefore, decreases to its value for the fully developed, cold turbulent flow wake (with similar approach turbulence intensity). The change in the recirculation vortex size could also be attributed to the enhanced flame propagation effects, which tend to significantly influence the flow field topology. Additionally, the higher shear layer growth rate due to the inlet turbulence also contributes to shortening of the recirculation length [4.30].

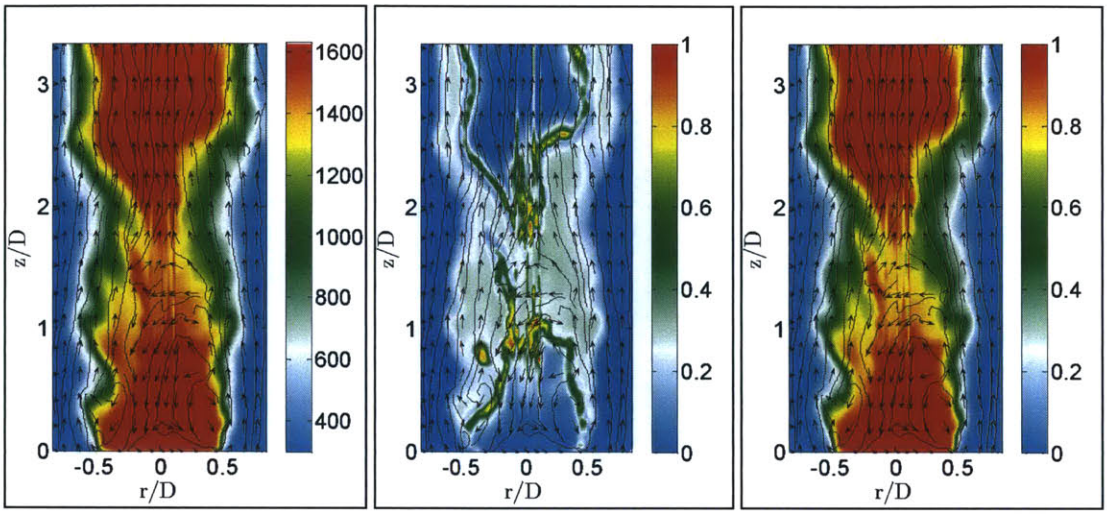

Figure 4.10: (a) Instantaneous temperature (K), (b) Instantaneous normalized reaction rate, (c) Instantaneous normalized reaction progress variable. The corresponding 2D velocity vectors and streamlines are also shown.

Now, as the flow progresses downstream of the bluff-body edge, the shear layer expands, and subsequently, due to Kelvin-Helmholtz instability, transforms into a series of roll up eddies. The small-scale shear-generated turbulence in the region augments entrainment and results in appreciable velocity and scalar (temperature, density) fluctuations in the mixing layer. This also contributes to anchoring the flame as well as increasing its intensity, since the penetration of the inner layers of the shear layer by small eddies can cause the reaction rate to be strongly affected by turbulence, while significantly enhancing heat diffusion from inner layers towards the preheat zone. As the eddy structures are carried downstream through the mixing layer, they begin to grow in size and spacing, developing into large-scale coherent structures as they convect downstream and coalesce. These form as folds around the flame edge, resulting in a slightly convoluted reaction zone that consists of partially burned-unburned gases. These vortex structures, therefore, result in a thickened average flame that is characterized by mixing and entrainment processes, and the flow field in the region is dominated by turbulent dilatation effects. Furthermore, the curving of the shear layer towards the

centerline results in a slight necking of the flame. The region in the vicinity of the stagnation point is comprised of isolated pockets of hot-product and cold-reactant gas, and significant flow and scalar oscillations are observed in the region, resulting from flow reversal and mixing events. The high turbulence in the region decreases mixing time and increases entrainment between the fresh mixture and the flame, ie the flame loading is increased and the reaction zone is thickened. These flame-flow interactions can also be inferred from the instantaeous normalized reaction rate contours shown in figure 4.11.

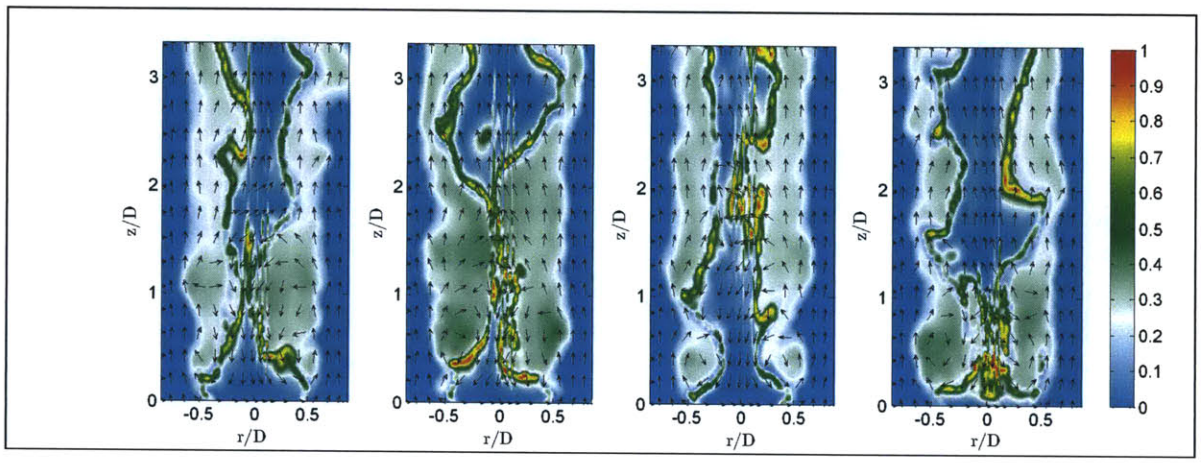

Figure 4.11: Instantaneous normalized reaction rate with instantaneous 2D velocity vectors.

In figure 4.12a, the average vorticity magnitude contour is shown along with the corresponding streamlines, and suggests a strong vorticity field in the mixing layer, as observed for the non-reacting flow. These transient eddies issued from the bluff-body edge are primarily responsible for the downstream convection of the hot products, stored inside the wake. The shed vortices also significantly enhance entrainment, and the mixing of the combustion products with the incoming fuel-air mixture, thereby playing a dominant role in stabilizing the flame. As the flow convects downstream, the vortices undergo pairing and during this process the flame is wrinkled and its surface area increases rapidly, enhancing both turbulent mixing and combustion. In the downstream section, heat release in the vortex cores results in breakdown of the eddies, and the fluid dynamic effects of heat release (increase in viscosity, dilation effect of combustion, and flow acceleration in the shear layer) appear to exert a significant influence on the flow, resulting in reduction of overall vorticity (despite the combustion induced baroclinic effects).

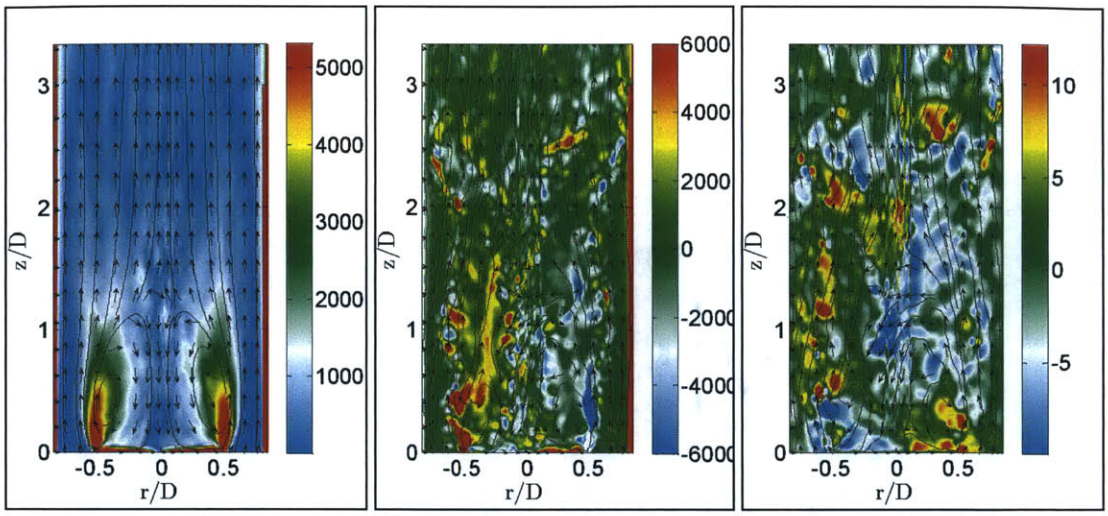

Figure 4.12: (a) Average vorticity magnitude (1/s), (b) Instantaneous out-of-plane vorticity (1/s), (c) Instantaneous radial velocity (m/s). The corresponding 2D velocity vectors and streamlines are also shown.

In figure 4.13, the instantaneous out-of-plane vorticity contours at different time instants are shown suggesting intense vortex activity in the mixing layer. The large vortices contain the reaction zone of the flame and the roll-up of each eddy corresponds to engulfment of hot products from the recirculation zone into the layer of fresh reactants in which the reaction front propagates. This process also results in a thicker flame as the flow proceeds downstream, as seen in figure 4.11.

Further examination of the contours suggests that vorticity is significant in the shear layer in the vicinity of the flame-holder edges. In general, exothermicity results in an increase in temperature dependent viscosity and consequently a reduction in the Reynolds number. While this factor alone may not appreciably affect the flame or flow structure, it can cause a marginal increase in the stability of the initial layer, a lengthening of the distance of the eddy formation position with respect to the step edge, thicker vortical structures, and a decrease in the small scale turbulence inside the large eddies. Thus, as compared to the isothermal case, the large-scale vortices in reacting shear layer flows are typically broken up soon after they have been formed, due to heat release and thermal expansion in the vortex cores, resulting in a diffuse vorticity field. The reduced shear layer growth rate as a consequence also results in elongation of the recirculatory flow field. Flow acceleration that overcomes the adverse pressure gradients along with the momentum dissipation effects may also impact the size of the CRZ. Despite these heat-release induced effects on the flow field, there is close resemblance in the development of eddies in the non-reacting and reacting shear layers, in terms of their formation position and rate of growth, for the axi-symmetric bluff-body

configuration. This can be attributed to the high inlet turbulence intensity coupled with the moderately high inlet equivalence ratio, which eventually result in a significant shortening of the axial span of the CRZ; the generation of large coherent structures downstream of the flame-holder, therefore, is largely unchanged.

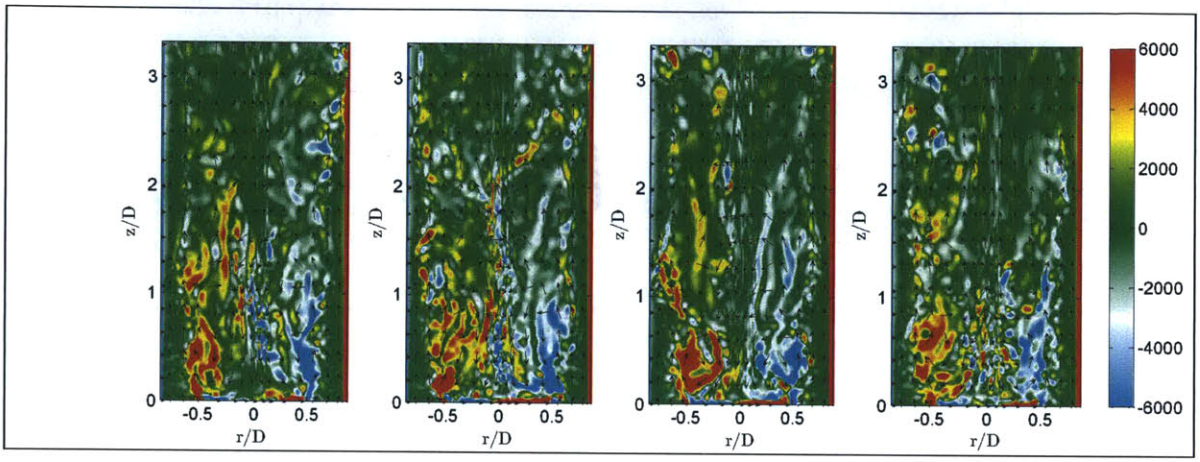

Figure 4.13: Instantaneous out-of-plane vorticity (1/s) with instantaneous 2D velocity vectors.

In figure 4.14a and 4.14b, the contours of the average and rms axial velocity are depicted along with the corresponding streamlines. The cross-sections at which LES and experimental data are compared are also shown. A strong recirculation zone in the immediate wake region downstream of flame-holder is observed that serves to stabilize the flame: hot products stored inside the wake convect downstream and periodically mix with the co-flowing fresh mixture due to the shed vortices, while chemical reaction takes place predominantly in the shear layer. Moreover, in contrast to the isothermal flow, the average reverse velocity is higher due to exothermicity, and peaks at the axial plane of maximum recirculation zone width.

Further investigation of the mean flow-field in the wake region suggests that the primary recirculation zone required to stabilize the flame extends to a length of about *1.25D* downstream of the bluff-body. As suggested earlier, it is worth noting that the approach turbulence intensity has a significant impact on the CRZ size aside from the heat release. Typically, for low equivalence ratios, and low inlet turbulence intensity, the CRZ is marginally more elongated than in the isothermal flow. An underlying physical explanation is that coupled with momentum dissipation effects, the acceleration of the flow due to turbulent dilatation together with prevention of mean streamline curvature by the confining walls causes the flow to better overcome the adverse pressure gradients; this increase is however lower than in a corresponding open flame, since the back pressure generated due to flow confinement restricts the elongation of the recirculation zone [4.30]. The

reduced shear layer growth rate (as a consequence of heat release and thermal expansion in the vortex cores), the reduction in the Reynolds number (due to the increase in viscosity with reaction), and the marginal suppression of entrainment in the mixing layer (due to the lower adverse pressure gradients), may also contribute to elongation of the recirculation zone.

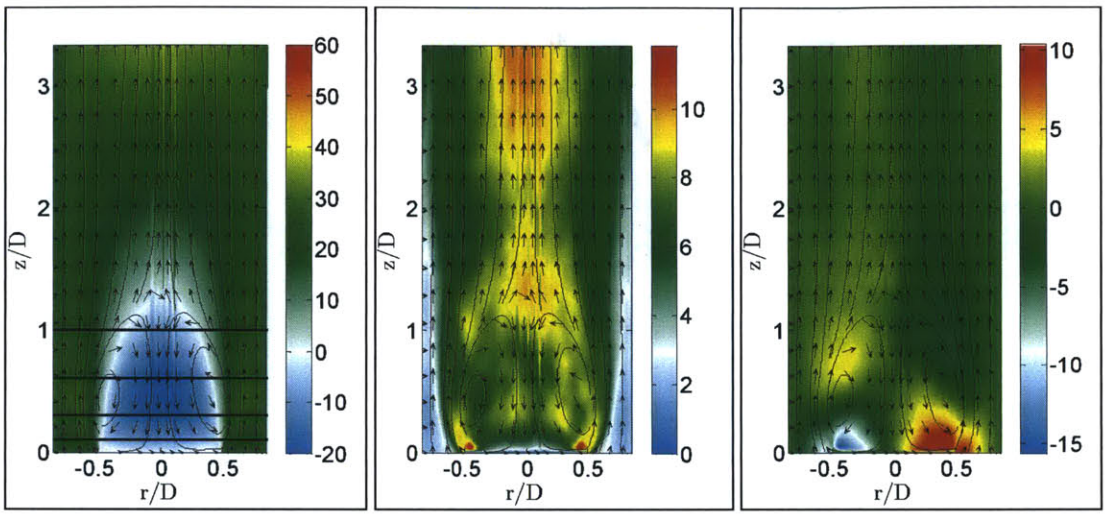

Figure 4.14: (a) Average axial velocity (m/s), (b) rms axial velocity (m/s), (c) Average radial velocity (m/s). The corresponding 2D velocity vectors and streamlines are also shown.

However, high inlet turbulence intensity, as in the present case, can cause an increase in shear layer growth rate, the turbulent burning velocity and also enhance flame propagation. These effects tend to have a relative strong influence, over the fluid dynamic effects of heat release, resulting in the eventual shortening of CRZ. It has been shown during experiments for a similar configuration [4.30] that the recirculation zone length reduces from *2.1D* to *1.2D* as the level of inlet fluctuations rise from 2% to 17% (figure 4.15a). This also suggests that an increase in the equivalence ratio would have a similar shortening effect on the CRZ. In fact, as the equivalence ratio further increases, it is observed that the length of wake region reduces to even lower than that in the cold flow (figure 4.15b), as a consequence of the enhanced flame propagation effects, and despite a significant drop in the adverse pressure gradients (figure 4.5a).

Additionally, the experimental study also showed that the recirculation strength, as indicated by the reverse mass flow rate, is similar in magnitude to that in the cold flow, principally because the effects of higher mean reverse flow velocity in the combusting flow (due to exothermicity) and reduction in the Reynolds number (due to increase in temperature dependent viscosity) are compensated by the appreciable reduction in gas density, thereby not significantly influencing the net recirculated mass flow. With an increase in equivalence ratio, the magnitude of the adverse

pressure gradient decreases further, which suppresses entrainment and reduces reverse mass flow in the CRZ.

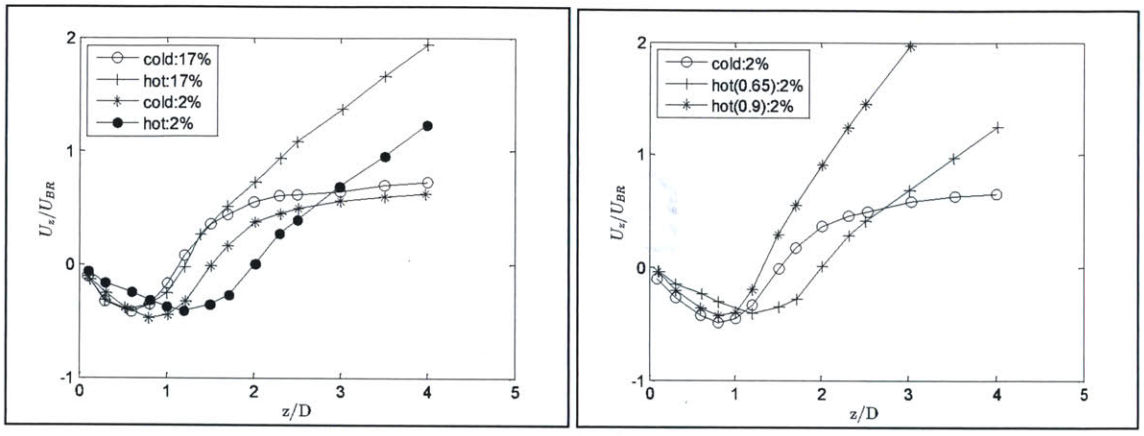

Figure 4.15: (a) Mean centerline velocities for cold and hot (φ=0.65) flows, (b) Mean centerline velocity for different equivalence ratios (2% fluctuation). [4.30]

Next, the contours of the velocity fluctuation are presented in figure 4.16, along with the streamlines. In case of confined combusting flows, it has been observed that the locations of zero stress lines do not coincide with those of zero mean velocity gradient [4.30]. This indicates that not only shear stresses (production term) but also normal stresses (dilatation term) play a significant role in modifying the turbulence flow field. In other words, while in the non-reacting case, vortex stretching and pairing dominate the vortical flow development, in the reacting case, these mechanisms are combined with volumetric expansion and baroclinic vorticity production. For the present scenario, the axial turbulence intensity within the reacting shear layer is somewhat similar to the non-reacting case despite the damping effects of turbulent dilatation and viscous dissipation, due to the effect of high inlet turbulence intensity. In general, the suppression of shear-generated turbulence due to dilatation results in generally lower level of fluctuations in the mixing layer; due to the significant inlet flow fluctuations, however, the eddy development in the shear layer resembles the isothermal scenario, and appreciable turbulence activity is noted near the flame stretch region due to vortex pairing activity (figure 4.13). High axial turbulence intensity is also observed near the stagnation zone because in the proximity of the region, flow direction quickly reverses: the fluid parcels are stretched and strong gradients of mean and turbulence quantities are present. Subsequently, due to combustion induced turbulence, mixing is enahnced, and axial flow fluctuation intensity is significant in this section of the combustion chamber.

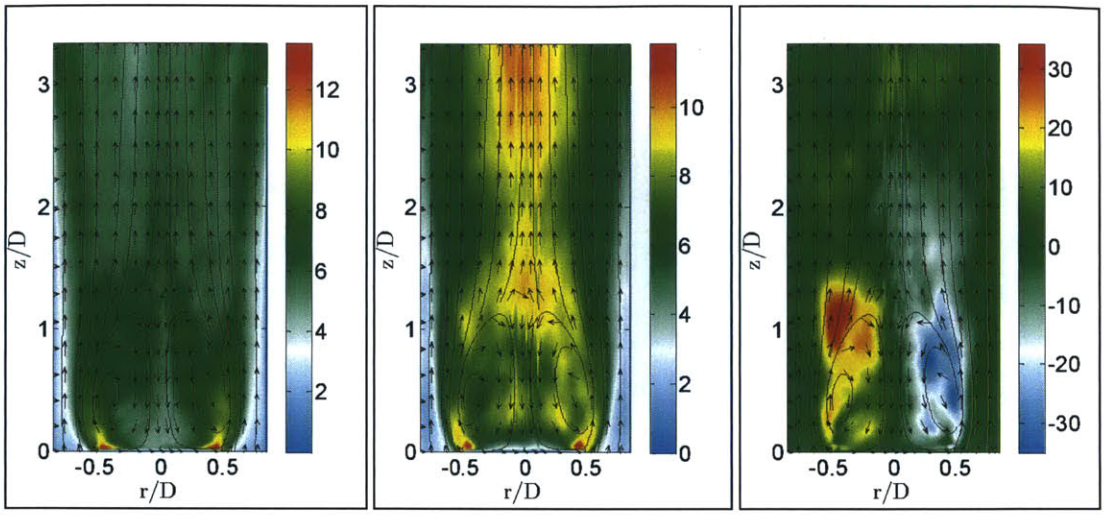

Figure 4.16: (a) rms radial velocity (u_r', m/s), (b) rms axial velocity (u_z', m/s), (c) Reynolds stress tensor term ($u_r'u_z'$, m^2/s^2). The corresponding 2D velocity vectors and streamlines are also shown.

Further, examination of the radial turbulence intensity contour suggests that the average fluctuation level is fairly constant within the recirculation region. The turbulence anisotropy, however, is high close to close to the stretched flame region that surrounds the recirculating cell. Near this location of maximum recirculation zone width, the reactive flow has a skewed turbulence structure presumably due to the presence of a large-scale eddy formed in the mixing layer (figure 4.11b), thereby enhancing the turbulent kinetic energy and resulting in high flow and temperature fluctuations (figure 4.16c). The axial and radial turbulence intensities are significant in this flame stretch region, and marked anisotropy of turbulence prevails, with the radial turbulence component dominant in the zone between the centerline and the flame necking. Note that in this region, high flow and temperature fluctuations exist, because the rapid curving of the outer flow streamlines in the vicinity bring cold reactants rushing towards the hot products in the center of the combustor. The unsteady nature of the shear layer, as evident from the instantaneous axial velocity contours (at different time instants) shown in figure 4.17 also contributes to increasing the turbulence intensity in the region.

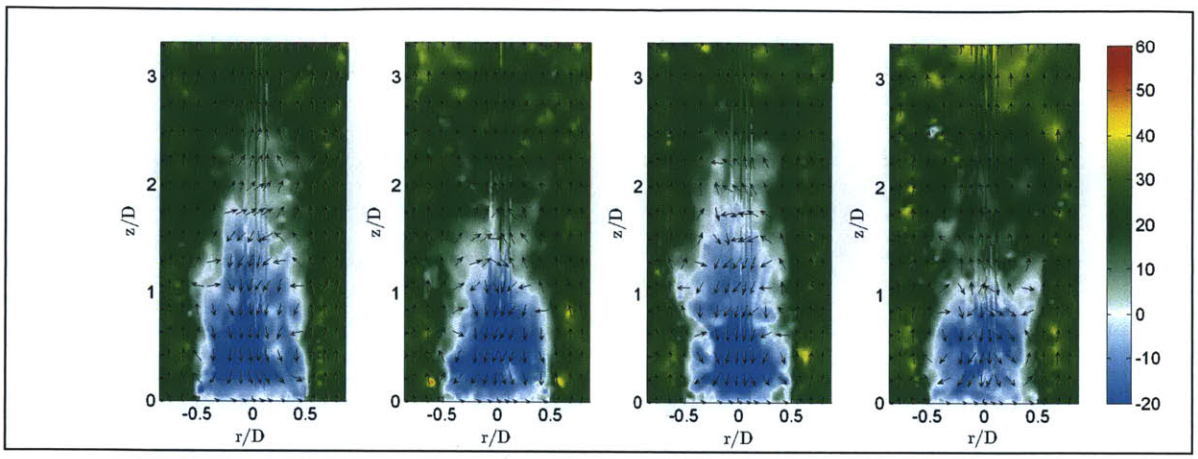

Figure 4.17: Instantaneous axial velocity (m/s) with instantaneous 2D velocity vectors.

The influence of wall confinement on the flow field topology also cannot be ignored, since it typically elongates the recirculation zone by accelerating the flow and narrows it by preventing any significant deflection of mean flow streamlines (by restricting the radially outward spread of the annular jet). As compared to an open flame, it also results in higher mean reverse flow velocity and an increase in recirculated mass flow, as experimentally observed [4.30]. Further, turbulence production is mainly due to Reynolds-stress/shear-strain interaction, and therefore restricted to the shear layer surrounding the maximum width of the recirculation zone. If confinement is removed, however, turbulent dilatation and mean pressure gradients (i.e. normal and not Reynolds stresses) combined with large streamline curvature would contribute to turbulence production. In other words, the suppression of mean streamline curvature by confinement results in reducing the relative influence of turbulent advection and shear-generated turbulence; in the absence of this strong turbulence production mechanism, turbulent dilatation and viscous dissipation processes dominate, resulting in somewhat lower Reynolds shear stresses, turbulence intensities and turbulent kinetic energy. In contrast, for an open flame, large streamline curvature may even compensate for any damping of turbulence by dilatation, and generate larger axial and radial turbulence intensities and turbulent kinetic energy as compared to confined flows [4.30]. Additionally, when the combustion process is confined, it also influences the wall static pressure (dP/dx), as indicated in figure 4.5b.

As regards the impact of inlet turbulence intensity and equivalence ratio on the turbulence production in reacting flows is concerned, an increase in either enhances the turbulent burning velocity and heat release which presumably augments the magnitude of both the shear generated turbulence and turbulent dilatation. In the presence of wall confinement and small streamline curvature, however, the net effect is typically a reduction in the turbulence intensity in the shear

layer, when compared to isothermal flow. Further, these effects generally result in shortening of the recirculation zone that shifts the regions with strong concentration of both shear stress and turbulent kinetic energy from the outer periphery of the CRZ to radially inward locations [4.30].

Further downstream, the large coherent structures break down into smaller eddies which subsequently dissipate due to viscous effects. Thus, the relative influence of the large-scale vortical structures on turbulence reduces, and the turbulent flow-field becomes somewhat isotropic. The axial turbulence intensity, however, remains high in the downstream section, due to the effects of turbulent dilatation and combustion induced turbulence, especially in case of confined flows. The viscous dissipation per unit volume, Θ, and dilatation, ψ, are shown in figure 4.18, and estimated in Cartesian coordinates [4.34, 4.35] as follows:

$$\Theta = 2\mu\left[\left(\frac{\partial u_x}{\partial x}\right)^2+\left(\frac{\partial u_y}{\partial y}\right)^2+\left(\frac{\partial u_z}{\partial z}\right)^2-\frac{1}{3}\left(\frac{\partial u_x}{\partial x}+\frac{\partial u_y}{\partial y}+\frac{\partial u_z}{\partial z}\right)^2\right] + \mu\left[\left(\frac{\partial u_x}{\partial y}+\frac{\partial u_y}{\partial x}\right)^2+\left(\frac{\partial u_y}{\partial z}+\frac{\partial u_z}{\partial y}\right)^2+\left(\frac{\partial u_z}{\partial x}+\frac{\partial u_x}{\partial z}\right)^2\right] \tag{4.28}$$

$$\psi = \nabla.\boldsymbol{u} = \frac{\partial u_x}{\partial x}+\frac{\partial u_y}{\partial y}+\frac{\partial u_z}{\partial z} \tag{4.29}$$

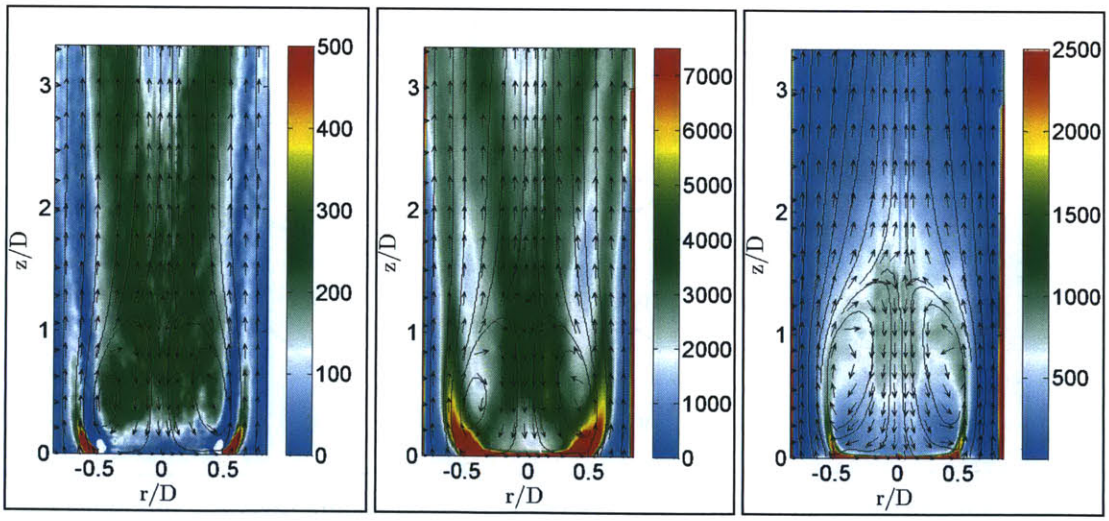

Figure 4.18: (a) Turbulent dilatation (1/s, reacting), (b) Viscous dissipation (kg/ms^3, reacting), (c) Viscous dissipation (kg/ms^3, isothermal). The corresponding 2D velocity vectors and streamlines are also shown.

Clearly, the viscous dissipation and turbulent dilatation have a significant influence on the flame-flow features, given their relative contribution as opposed to the isothermal flow. Specifically,

the size of the CRZ, the vortex activity in the shear layer along with the mixing layer growth rate, as well as the flow and scalar fluctuations in the downstream section are appreciably impacted due to the dissipation and dilatation effects, as aforementioned.

In figure 4.19, the normalized profiles for the average axial velocity, average temperature, and average radial velocity are compared with experimental observations, obtained from [4.30], in the wake region downstream of the flame-holder. The experimental measurements of the radial profiles of the variables are available from the axis of the burner to approximately 10 mm into the shear layer (r/D=0.6). The mean trends for the velocity and temperature are reproduced with reasonable accuracy in the simulations, indicating that the fundamental flow features in the recirculation zone are suitably resolved using LES. Results also indicate that the modified approach results in more accurate predictions in the recirculation zone. Closer examination of the plots reveals that in the immediate wake of the flame-holder, axial velocity peaks within the shear layer, as does the reverse centerline velocity within the CRZ. Subsequently, as the flow convects downstream of the rear stagnation zone, the centerline axial velocity accelerates, primarily due to the effects of heat release and turbulent dilatation.

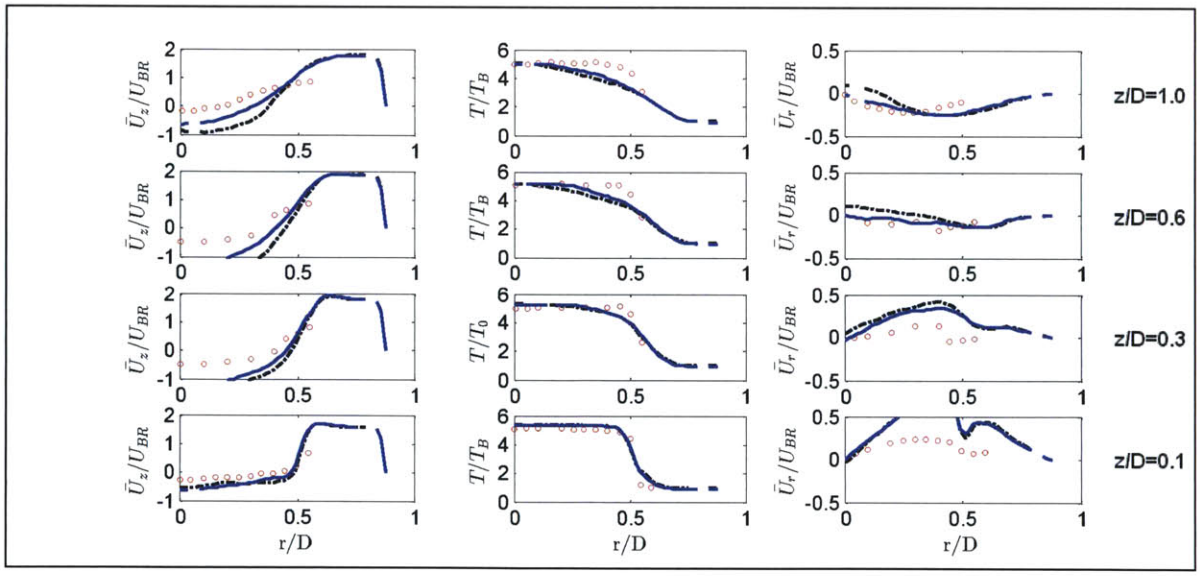

Figure 4.19: Normalized mean profiles: axial velocity (left), temperature (middle), and radial velocity (right). ooo Experiment, −·−· LES (Unstrained Flamelets), −−− LES (Strained Flamelets).

Despite the correct prediction of these trends, the magnitude of the negative centerline axial velocity is slightly over-predicted, and has been reported before [4.28, 4.32-4.33]. The location of the shear layer, indicated by the steep gradient in axial velocity at the edge of the flame-holder (r/D ≈

0.5) adjacent to the recirculation zone, is well reproduced numerically, along with its growth rate, although the predictions could be improved by using finer resolution pre-integrated tables and less diffuse numerical schemes. Note, however, that the burner is modelled with an axi-symmetric geometry instead of a rectangular cross-section with rounded corners. This may slightly affect the flame location and the structure of the turbulent flame zone, including the temperature in the flame shear layer, and therefore explain the quantitative discrepancies in the comparative profiles. However, the modeling assumption does not appreciably affect the prominent flame-flow features and the dominant flame stabilization mechanism in a qualitative sense.

Focusing on the temperature profiles, it can be seen that the temperature distribution is nearly uniform radially within in the recirculation zone, indicating that combustion in the region is almost complete (figure 4.20a). The temperature then drops steeply to the ambient temperature conditions radially outward from the shear layer, into the incoming reactant mixture. These locations of high temperature gradients, where cold and hot gases mix, are predicted accurately, especially in regions close to the flame-holder. However, the mean temperature gradient in the shear layer region near the edge of the recirculation zone ($x/D \approx 1.0$) is slightly under-predicted, suggesting either an under-prediction of heat release and/or over-prediction of fluid mixing processes. It is observed, however, that the modified combustion model predicts the temperature distribution in the region more accurately.

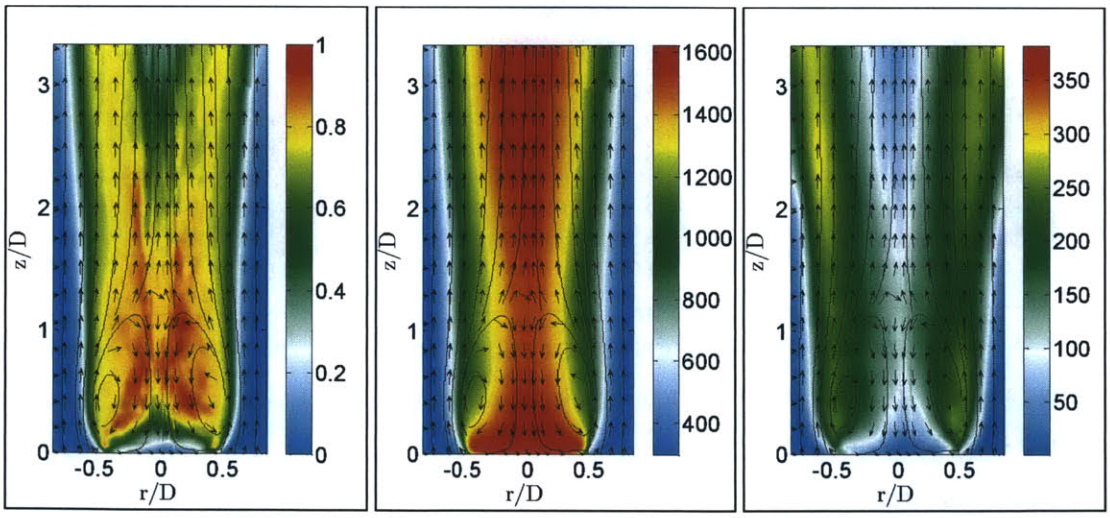

Figure 4.20: (a) Normalized average reaction rate, (b) Average temperature (K), (c) rms temperature (K). The corresponding 2D velocity vectors and streamlines are also shown.

Subsequently, the mean temperature gradually increases in the downstream section and spreads radially outwards as well, as seen in figure 4.20b. This may be primarily attributed to the

relative increase in the flame surface and effective reaction rate brought about by the combustion induced turbulence, and enhanced mixing. The increase in the average flame thickness, however, reduces the scalar fluctuations along the centerline, by inhibiting heat transport between the hot products and the cold reactants (figure 4.20c).

These trends can also be inferred from the normalized progress variable contours shown in figure 4.21, shown along with the normalized scalar dissipation rate contours. It can be observed that the reaction is almost complete in the CRZ adjacent to the flame-holder surface. A steep gradient in the temperature and progress variable profiles is observed near the shear layer emanating from the bluff-body edges; as the shear layer rolls-up in a sequence of large-scale structures, the mixing layer spreads due to the growth of the vortices downstream, corresponding to an increase in the flame thickness. Subsequently, near the exhaust section, the high temperature region spreads radially outwards from the centerline, where high combustion induced turbulence results in enhancing the flame wrinkling, and producing intermittent, fast local heat release. This also results in significant scalar fluctuations in the region (figure 4.20c).

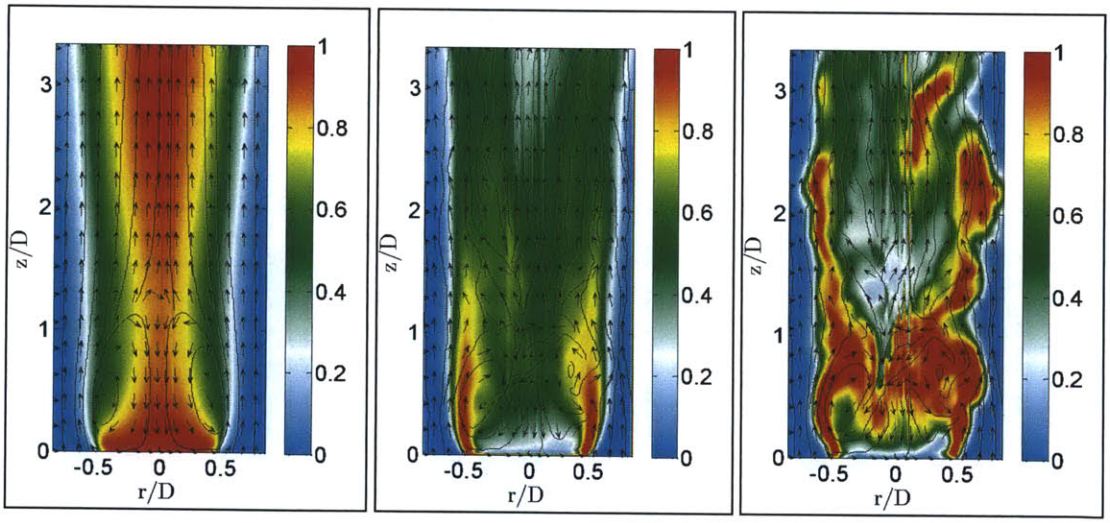

Figure 4.21: (a) normalized average reaction progress variable, (b) normalized average scalar dissipation rate, (c) normalized instantaneous scalar dissipation rate. The corresponding 2D velocity vectors and streamlines are also shown.

4.4 Conclusions

This chapter focuses on investigating the predictive capabilities of the presumed-PDF LES combustion model as applied to a well-studied, laboratory-scale axi-symmetric bluff-body-stabilized flame. The simulation results are compared with experimental measurements, and the turbulent

flame-flow features are reproduced fairly well; more accurate predictions are obtained using a modified formulation for the combustion model that accounts explicitly for the strain via the scalar dissipation rate. It should be noted that the computational efficiency and predictive accuracy both depend on the resolution of the pre-integrated tables employed within the presumed-PDF framework; utilization of finer resolution tables can result in more precise predictions using the numerical techniques, while using faster look-up procedures can maintain a balance with computational efficiency. Appropriate choice of the presumed PDFs for the reaction progress variable and the scalar dissipation rate, depending on the combustor configuration, can also lead to improved LES predictions in practical systems.

5 DYNAMIC MODE DECOMPOSITION TECHNIQUE

5.1 Overview

The description of coherent features of fluid flow is essential to the understanding of fluid-dynamical and transport processes. Different methods have been introduced that are able to extract dynamic information from flow fields that are either generated by numerical simulation or measured in a physical experiment. A common approach for identifying coherent structures is the proper orthogonal decomposition (POD) method, which determines the most energetic structures in the flow field. However, there are major drawbacks of the technique: (a) the energy may not in all circumstances be the correct measure to rank the flow structures, and (b) due to the choice of second-order statistics as a basis for the decomposition, valuable phase information is lost, which can be critical when classifying the dynamic processes contained in the flow field. In this regard, the dynamic mode decomposition (DMD) approach has been introduced [5.1] to assess the dynamic behavior of fluid flows represented by experimentally measured or numerically determined data sequences. The dynamic mode decomposition technique is an Arnoldi-like method, based on the Koopman operator to analyze non-linear dynamic system data and to estimate the eigenvalues and eigenvectors of an approximate linear model. The fundamental principle underlying the approach is to decompose the data into a series of complex Fourier harmonics to obtain the spatial basis functions (dynamic modes) and time-dependent complex coefficients. The frequencies and growth rate of each mode can be obtained by the magnitude and phase of its corresponding eigenvalue. In addition, the modes can be sorted by their energy content as well. Further details about the methodology and the theoretical principles behind DMD analysis can be found in [5.1-5.10]. A brief explanation of the approach, as implemented in this work, is presented below.

The matrix of N snapshots at M grid points obtained from experiments or simulations can be represented as:

$$V_1^N = [v_1\ v_2\ \ldots\ v_N]; v_i = \begin{bmatrix} v_i^1 \\ \cdot \\ \cdot \\ v_i^M \end{bmatrix}, i \in [1, N] \tag{5.1}$$

Then, it is hypothesized that a linear operator A exists, such that:

$$\begin{aligned} v_{k+1} &= Av_k, \forall k \in [1, N-1] \\ V_1^N &= \left(v_1, Av_1, \ldots, A^{N-1}v_1\right) : \textit{Krylov Matrix} \end{aligned} \tag{5.2}$$

The fundamental objective is to determine the eigenvectors and eigenvalues of A, without the knowledge of A. It is further assumed that the data represents the entire dynamics of the system and is not redundant. The hypotheses may be written as:

$$\begin{aligned} &\{v_1,\ldots,v_{N-1}\} \text{ are linearly independent} \\ &v_N \in span\{v_1,\ldots,v_{N-1}\} \Rightarrow v_N = c_1 v_1 + \ldots + c_{N-1} v_{N-1} + r \end{aligned} \tag{5.3}$$

This limits the choice of the time step between the snapshots, as well as the number of snapshots (such that the residual, $||r||$, is small). Combining the two hypotheses, the following equations are obtained:

$$\begin{aligned} AV_1^{N-1} &= V_2^N = V_1^{N-1}C + r\varepsilon_{N-1}^T \\ V_1^{N-1} &= [v_1\ v_2\ \ldots\ v_{N-1}], V_2^N = [v_2\ v_3\ \ldots\ v_N] \\ C &= \begin{bmatrix} 0 & 0 & \ldots & 0 & c_1 \\ 1 & 0 & \ldots & 0 & c_2 \\ . & . & \ldots & . & . \\ 0 & 0 & \ldots & 1 & c_{N-1} \end{bmatrix} \end{aligned} \tag{5.4}$$

where C is termed the companion matrix.

The consequence of equation (5.4) is that decreasing the residual increases the overall convergence and therefore the eigenvalues of C (empirical Ritz values) converge toward, and approximate, some eigenvalues of A. The convergence can be attained by evaluating and monitoring the residual during the process and plotting its L^2-norm. In such a scenario, the eigenvalues of C determine the temporal behavior of the dynamic modes.

Since some of the eigenvalues of C approximate some of the eigenvalues of A, and the corresponding eigenvectors are also in proportion to the modes of C, methods have been formulated to compute the unknown coefficients of the companion matrix such that the residual is minimized. One of the approaches is to utilize QR decomposition to estimate the unknown coefficients of the companion matrix:

$$\begin{aligned} \boldsymbol{c} &= [c_1\ \ldots\ c_{N-1}] \\ v_N &= V_1^{N-1}\boldsymbol{c} = QR\boldsymbol{c} \Rightarrow \boldsymbol{c} = R^{-1}Q^H v_N \end{aligned} \tag{5.5}$$

Therefore, the companion matrix can be computed as:

$$\begin{aligned} V_1^{N-1} &= QR \\ C &= R^{-1}Q^H V_2^N \end{aligned} \tag{5.6}$$

Alternatively, the SVD approach can be used to obtain the companion matrix, as follows:

$$V_1^{N-1} = U\Sigma W^T$$
$$C = W\Sigma^{-1}U^T V_2^N \tag{5.7}$$

Once the companion matrix has been determined, the dynamic modes can be obtained using the Vandermonde matrix, S, which is represented as:

$$S = \begin{bmatrix} 1 & \lambda_1 & \dots & \lambda_1^{N-2} \\ 1 & \lambda_2 & \dots & \lambda_2^{N-2} \\ . & . & \dots & . \\ 1 & \lambda_{N-1}^2 & \dots & \lambda_{N-1}^{N-2} \end{bmatrix} \tag{5.8}$$

where λ_k refers to the k^{th} eigenvalue of the companion matrix.

After constructing the Vandermonde matrix, the companion matrix can be diagonalized, following which the dynamic modes (Ritz vectors) are obtained, as shown below:

$$C = S\Lambda S^{-1}$$
$$\Phi = V_1^{N-1} S^{-1} \tag{5.9}$$

The Ritz vectors approximate the spatial eigenmodes, and the growth rate and the frequency of each mode can be estimated as:

$$\sigma_k = \Re e \frac{\log(|\lambda_k|)}{\Delta t}, \omega_k = \Im m \frac{\log(|\lambda_k|)}{\Delta t} \tag{5.10}$$

where σ_k and ω_k are related to λ_k, the Ritz values, which approximate the complex eigenvalues of the linearized system observed at N equally spaced instants of time. Using σ_k and $\omega_k (=2\pi\nu_k)$, the stability and the temporal characteristics of a given dynamic mode can be assessed. Those modes for which the magnitude of the Ritz values are near unity are the neutrally stable modes (zero growth-rate), while those lying well inside the unit circle are considered spurious due to their large decay-rate. The temporal frequency of modes increases as the Ritz values move from the right-half to the left-half of the unit circle.

The snapshots can now be reconstructed as sums of temporally orthogonal modes as:

$$v_k = \Re e\left[\sum_{k=1}^{N-1} \varphi_i e^{(\sigma_k + i\omega_k)t}\right] \tag{5.11}$$

Note that the complex dynamic modes (Ritz vectors) in general are complex valued and consist of a real part and an imaginary part. The reconstruction may then be written as:

$$\Re e\left(e^{\lambda t}\varphi\right) = e^{\sigma t}\left(\cos(\omega t)\Re(\varphi) - \sin(\omega t)\Im(\varphi)\right) \tag{5.12}$$

where $\mathfrak{Re}$ and $\mathfrak{Im}$ refer to the real and imaginary components respectively. Here we are able to see the interplay between the real and imaginary components of φ_k and λ_k. The two components of φ_k define a cyclic spatial structure with frequency of ω_k. Specifically, the real component of φ_k represents the same structure as the imaginary component of φ_k phase shifted by $\pi/2$.

As a technique for creating reduced-order representations of larger data sets, much work has been done on the order of the modes (comprised of a Ritz vector and its associated Ritz value) produced by the DMD algorithm in terms of their overall significance to the full dataset. Proper orthogonal decomposition (POD) is a related and much better established technique that ranks modes purely based on their L^2-norm, $||\varphi||^2$, corresponding to kinetic energy for incompressible flows. Although such a metric can be used for DMD as well (taking the L^2-norm of the Ritz vectors), the structure of the temporal coefficient provides more data for better sorting.

The real part of the Ritz value represents the temporal growth rate of the mode. For a stationary process (one with a time-invariant mean), we expect that all cyclic processes will tend towards a zero growth rate as the size of the data set tends toward infinity. For finite data sets, however, these same processes may have slightly positive or negative growth rates. Not all modes represent true cyclic processes within the data set however. The temporal coefficients of these modes decay rapidly, however the Ritz vectors themselves may have relatively large norms. To compensate for this, a modification is made to the energy function, taking into account the decay rate as well as the L^2-norm. This function takes the form [5.11]:

$$E_k = \frac{1}{T}\int_0^T \left|\varphi_k \lambda_k^{t/\Delta t}\right|^2 dt = \left|\varphi_k\right|^2 \frac{e^{2\sigma_k T}-1}{2\sigma_k T} \qquad (5.13)$$

where E_k is the energy of the k^{th} mode, and $T=N\Delta t$ is the sampling duration (total time-span of the data set).

This energy function can be used to create a ranking of each mode for the purposes of constructing a reduced order data set. Often, however, when DMD is used as a means of searching for cyclic structures in the flow field that may have physical relevance beyond reduced order reconstruction, the energy of the respective modes can be used as a means of eliminating spurious modes, followed by selection of the modes with specific frequencies (typically, frequencies that are known from Fourier analysis of experimental data).

Note that an alternative approach is to diagonalize the companion matrix using its eigenvectors. In such as scenario, the (unscaled) modes Ψ can be computed as:

$$C = Y\Lambda_1 Y^{-1}$$
$$\Psi = V_1^{N-1} Y \tag{5.14}$$

To reconstruct the snapshots, appropriate scaling needs to be performed, such that $\Phi=\Psi D_1$, where D_1 is the scaling matrix and recovered using:

$$V_1^{N-1} S^{-1} = V_1^{N-1} Y D_1 \Rightarrow D_1^{-1} = SY \tag{5.15}$$

The framework above works well when the snapshot matrix is full-rank. In case of rank deficiency or when the experimental data is contaminated by noise, the method can be ill-conditioned. A more robust approach is to use the framework adopted in [5.12], which employs the SVD approach, as follows:

$$V_1^{N-1} = U\Sigma W^T \Rightarrow V_1^N = AU\Sigma W^T \Rightarrow AU = UU^T V_1^N W\Sigma \tag{5.16}$$

Next, a matrix that is self-similar to C is defined and subsequently diagonalized:

$$\tilde{C} = \Sigma W^T C W \Sigma^{-1} = U^T V_2^N W \Sigma^{-1}$$
$$\tilde{C} = Z\Lambda_2 Z^{-1} \tag{5.17}$$

Therefore:

$$AU = UZ\Lambda_2 Z^{-1} \Rightarrow AUZ = UZ\Lambda_2 \tag{5.18}$$

The eigenvalues of the self-similar matrix $\tilde{C}$ and the companion matrix C are the same while their eigenvectors are related by:

$$Y = W\Sigma^{-1} Z \tag{5.19}$$

The dynamic (unscaled) modes can now be obtained as:

$$\Omega = UZ \ (= V_1^{N-1} W\Sigma^{-1} Z = V_1^{N-1} Y = \Psi) \tag{5.20}$$

It is important to note that the norm $||\ ||_P$ of the columns of Ω is unity. The modes can again be scaled, using the scaling matrix D_2, as follows:

$$\Phi = \Omega D_2$$
$$U\Sigma W^T = \Omega D_2 S = UZD_2 S \Rightarrow D_2^{-1} = SW\Sigma^{-1} Z \ (= SY) \tag{5.21}$$

The snapshots can now be reconstructed, as well as arranged by frequency, stability and/or energy content. As aforementioned, the results are typically sensitive to the time step, the number of snapshots and spatial coverage of the snapshots; it is therefore suggested that the residual be computed in order to obtain an accurate modal decomposition. Next, validation test cases are presented that illustrate the application of DMD as applied to complex flows, and also highlight the attractive features of DMD over conventional approaches such as POD.

5.2 DMD Illustration I

A fabricated pattern, as in [5.13], comprising of two superimposed waves is first considered:

$$u_1(x,y,t) = e^{-(y/b)^2}\cos(kx - \varpi t)$$
$$u_1(x,y,t) = 1.1\times e^{-(y/b)^2}\cos\left(\frac{k}{5}x - \frac{\varpi}{2}t\right) \tag{5.22}$$

Here field u_1 and u_2 differ in their amplitude and frequency content (figure 5.1). The parameter values utilized are displayed in table 5.1.

Table 5.1: Parameters corresponding to test pattern used for DMD illustration I.

b	ϖ	k	T	Domain	Cells
0.02	20π	π/b	$2\pi/\omega$	$10b$ x $2.5b$	100 x 100

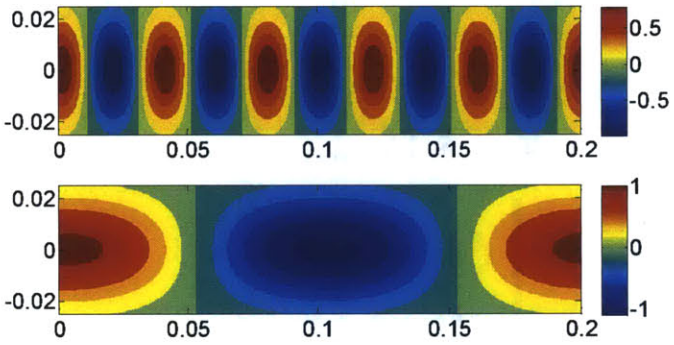

Figure 5.1: Test pattern components used for DMD validation and illustration, at $t=0$.

For the DMD analysis, 150 snapshots covering the domain $x \in [0, 0.2]$, $y \in [-0.025, 0.025]$ are utilized. The number of points in each dimension is 100, and the time interval between the snapshots is set at 0.1s. The aforementioned POD-DMD framework is utilized and the modes are sorted by their energy content. The extracted eigenvalues of the low-dimensional system matrix are shown in figure 5.2a, while in figure 5.2b, the frequency and growth rate of each mode, obtained using a logarithmic mapping of the respective eigenvalues, are depicted. Note that the sizes of the markers indicate the energy content of the respective mode. The eigenvalues are found to occur in complex conjugate pairs, with the DMD spectrum symmetric about the frequency axis.

In figure 5.3a, energy content of each mode as a function of frequency ($\nu = \omega/2\pi$) is shown. Results indicate the presence of four energetic structures that correspond to the two flow-field components of the fabricated pattern, thereby establishing that the dominant modes reproduced using DMD analysis (including the complex conjugate pairs) resemble the super-imposed waves. The frequency and growth rate of the four high-energy modes are plotted in figure

5.3b. Results show well-separated frequencies, and the harmonics are perfectly recovered, although results may deteriorate as noise is added to the system [5.13].

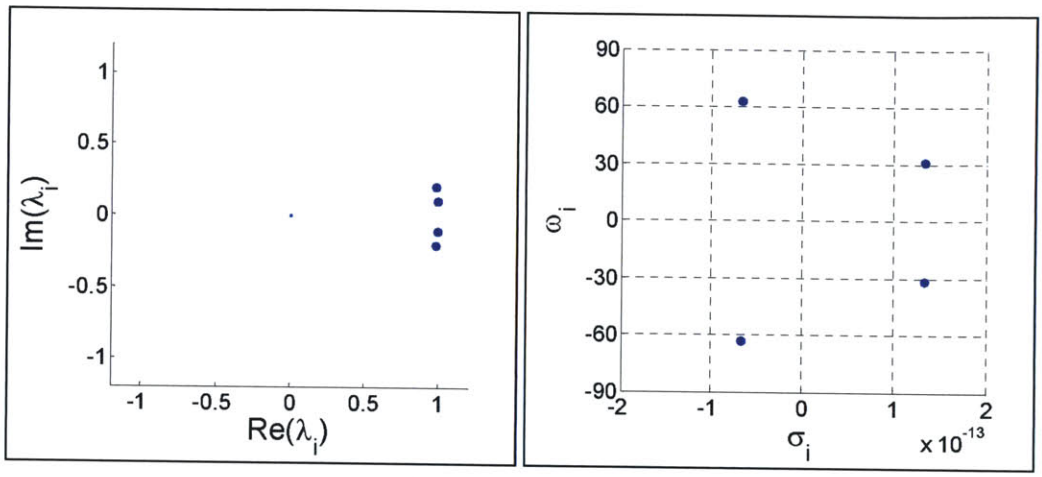

Figure 5.2: (a) Eigenvalues of system matrix, (b) Frequency, ω, and growth rate, σ, for each dynamic mode.

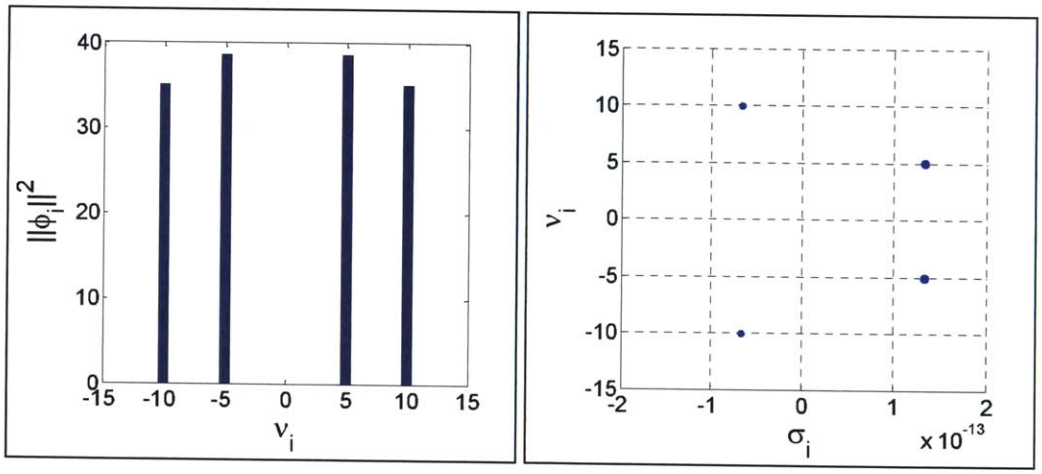

Figure 5.3: (a) Energy content and frequency, ν, for each mode, (b). Frequency, ν, and growth rate, σ, of high-energy modes.

The dynamic modes corresponding to the real and imaginary parts, respectively, obtained from the analysis are shown next in figures 5.4 and 5.5. Note that the imaginary parts appear in conjugate pairs. The evolution of the coefficients of each mode in time is shown in figure 5.6a, and the corresponding FFT is depicted in figure 5.6b that indicates the presence of a dominant frequency for each mode; the frequencies of the temporal amplitudes match perfectly with that of the sampling function (fabricated pattern, u).

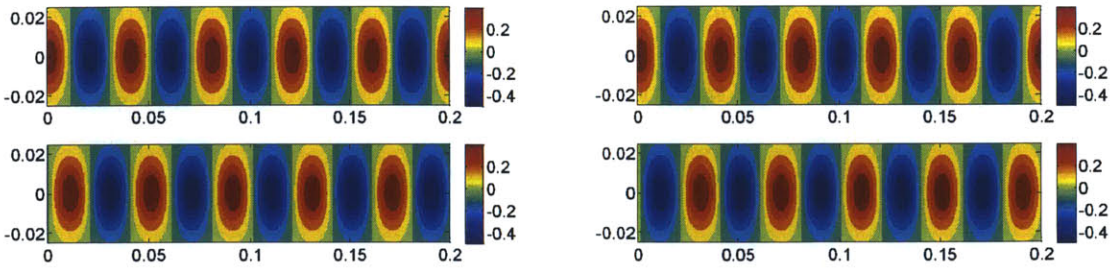

Figure 5.4: (a) Dynamic mode corresponding to u_1 with real component (top) and imaginary component (bottom), (b) The conjugate mode with negative imaginary part.

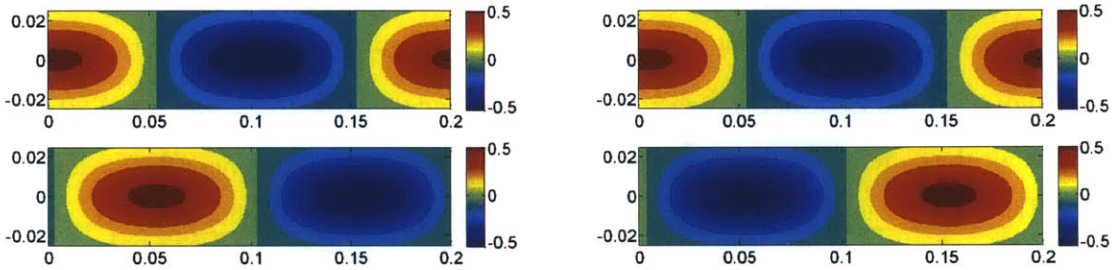

Figure 5.5: (a) Dynamic mode corresponding to u_2 with real component (top) and imaginary component (bottom), (b) The conjugate mode with negative imaginary part.

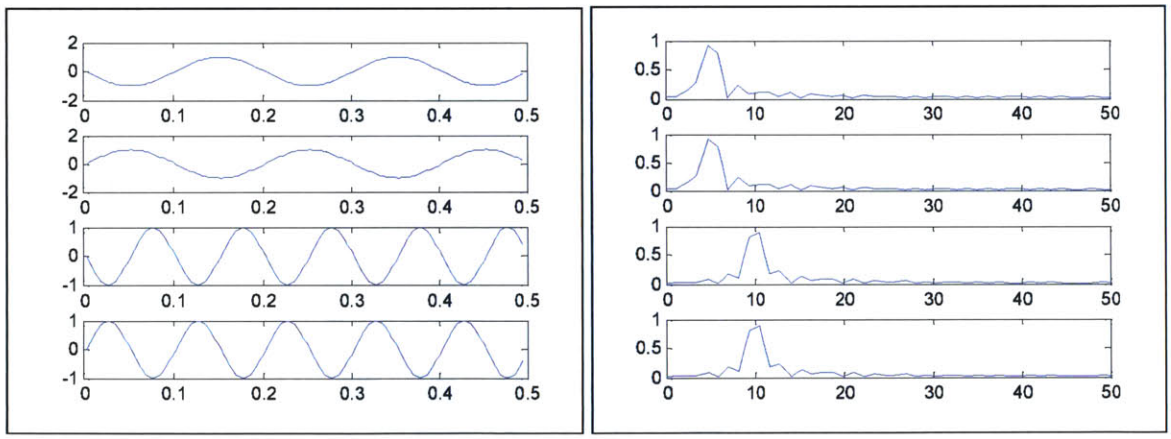

Figure 5.6: (a) Temporal evolution of modal coefficients, (b) FFT of temporal coefficients showing the dominant frequency corresponding to each mode.

5.3 DMD Illustration II

Next, a more complex fabricated pattern, as in [5.14], is considered to better elucidate the features of the DMD technique. The sampling function, u, is comprised of four super-imposed flow fields:

$$u = u_0 + u_1 + u_2 + u_3$$

$$u_0(x,y,t) = e^{-\left(\frac{y^2}{0.7}\right)} \tag{5.23}$$

$$u_n(x,y,t) = \alpha_n(t) \sum_{m=-\infty}^{m=\infty} (-1)^m e^{-\left[\frac{(x-\beta_n m-\gamma_n t)^2}{a_n x+b_n} + \frac{y^2}{a_n x+b_n}\right]}$$

Here u_0 is a stationary field, while the parameters for the other patterns are defined such that they have different initial sizes, travel with a fixed velocity, and while u_1 neither grows nor decays in time, u_2 decays in time and u_3 grows in time. Note that $a_n x + b_n$ is the diameter of the structure, where a_n and b_n are constants, β_n is the wavelength factor, γ_n refers to the pattern velocity, and α_n is the growth/decay factor. The corresponding parameter values are displayed in table 5.2, while the pattern at *t=0* is shown in figure 5.7, along with the component flow fields.

Table 5.2: Parameters corresponding to test pattern used for DMD illustration II.

n	a_n	b_n	β_n	γ_n	$\alpha_n(t)$
1	0.030	0.005	0.8	0.377	1
2	0.010	0.100	0.4	0.252	$e^{-t/80} - 0.1$
3	0.005	0.050	0.3	0.126	$\left(1 - e^{-t/15}\right) + 0.2$

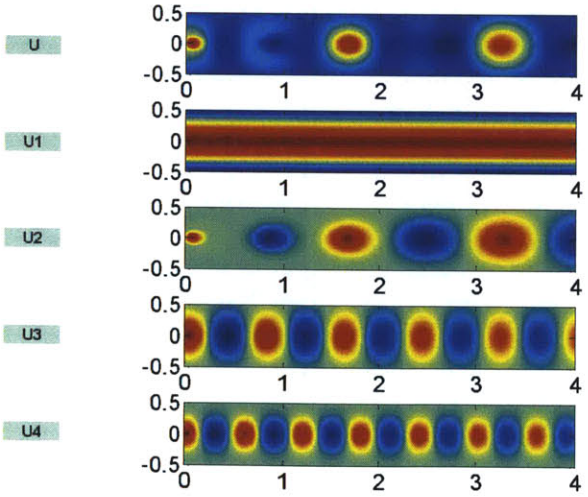

Figure 5.7: Test pattern used for DMD validation and illustration at *t=0*, (*U*), and the component flow fields (*Ui*, corresponding to u_i, *i=1-4*).

For the DMD analysis, 100 snapshots covering the domain $x \in [0, 4], y \in [-0.5, 0.5]$ are utilized. The number of points in each dimension is 200, and the time interval between the snapshots is set at 0.2s. The aforementioned POD-DMD framework is utilized and the modes are sorted by their norm. The extracted eigenvalues of the low-dimensional system matrix are shown in figure 5.8a, with the empirical Ritz values, sized by energy norm, lying on a unit circle. In figure 5.8b, the frequency and growth rate of each mode, obtained using a logarithmic mapping of the respective eigenvalues, are depicted. As can be inferred, the eigenvalues are found to occur in complex conjugate pairs, with the DMD spectrum symmetric about the frequency axis, and the unstable modes are noted to have a positive growth rate.

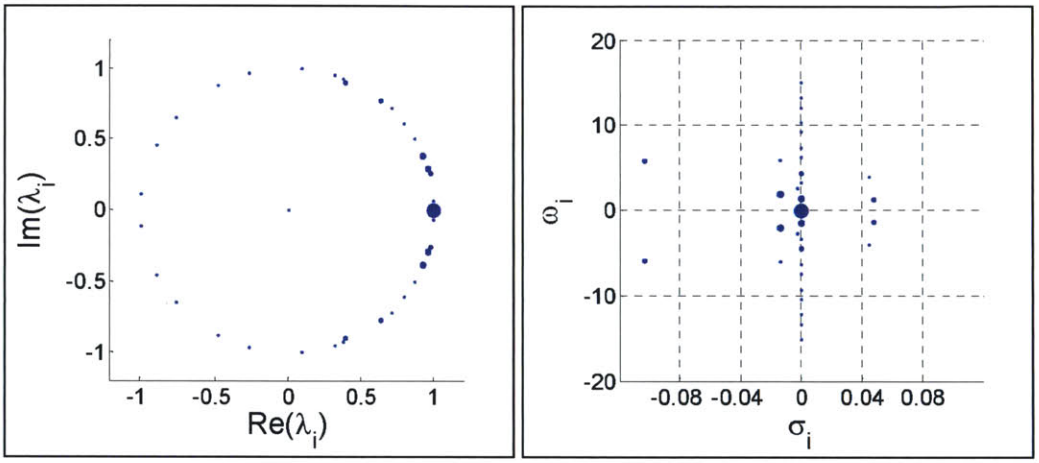

Figure 5.8: (a) Eigenvalues of system matrix, (b) Frequency, ω, and growth rate, σ, for each dynamic mode.

In figure 5.9a, the norm of each mode as a function of frequency ($\nu = \omega / 2\pi$) is shown. Results indicate the presence of four energetic structures (each with a corresponding complex conjugate) that correspond to the flow-field components of the fabricated pattern, thereby establishing that the dominant modes reproduced using DMD analysis resemble the super-imposed waves. Since the decomposed data is real, the DMD spectra are symmetric about the frequency. The negative frequency corresponds to the mode with the same real part, but negative imaginary part (complex conjugate mode). The frequency and growth rate of the four high-energy modes are plotted in figure 5.9b.

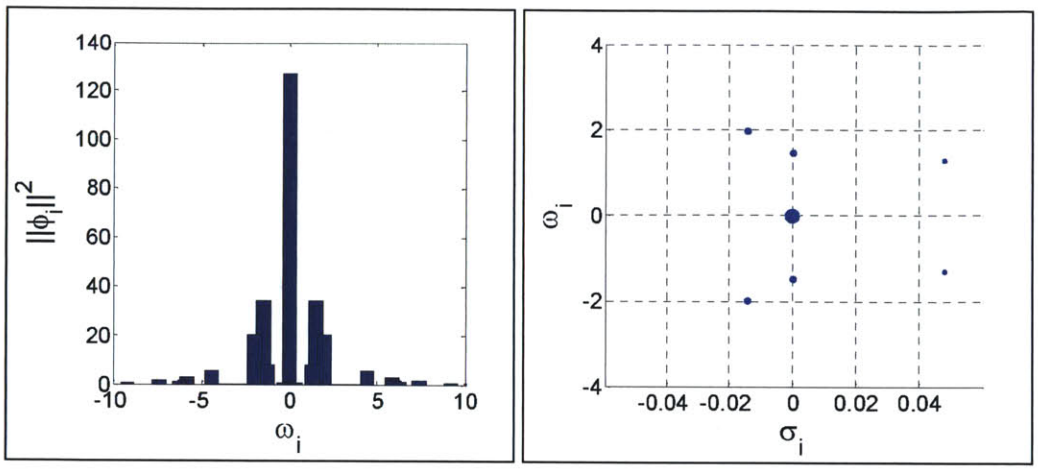

Figure 5.9: (a) Norm and frequency, ω, for each mode, (b). Frequency, ω, and growth rate, σ, of high-energy modes.

In figure 5.10 (A), the original and reconstructed snapshots (utilizing all the modes) at an initial instant are depicted, showing good agreement. The eigenvalue appearing at the origin in figure 5.9b accounts for the steady state contained in the pattern. The real and imaginary components of this mode are shown in figure 5.10 (M1), and represent the pattern u_0. The second DMD mode, lies on the σ axis, i.e., it neither grows nor decays over time. The real and imaginary components of this mode are shown in figure 5.10 (M2), and represent the pattern u_1 with $\alpha = 1$. The third mode lies in the stable region ($\sigma < 0$) and decays over time. The real and imaginary components extracted from the analysis are shown in figure 5.10 (M3), and represent the pattern u_2 with $\alpha < 1$. Finally, the fourth mode is observed in the unstable region ($\sigma > 0$), and grows in time. The modal components, shown in figure 5.10 (M4), represent the pattern u_3 with $\alpha > 1$. Note that for each mode, the corresponding conjugate pair with the negative imaginary component also exists.

Additionally, the time evolution of the respective coefficients of each mode is shown in figure 5.11a, and the growth/decay of the constituent patterns can be easily inferred from the temporal plots. The corresponding FFT of the temporal coefficients is also depicted, in figure 5.11b, which indicates the presence of a dominant frequency ($\nu = \omega / 2\pi$) for each dynamic mode.

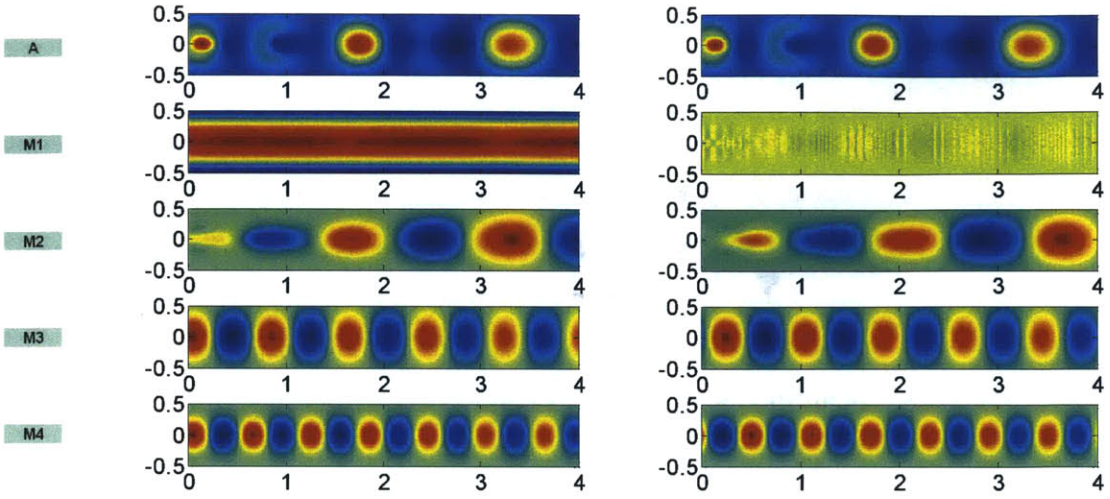

Figure 5.10: (A) Original (left) and reconstructed (right) snapshots at a specific time instant, (M1-M4) Dominant modes obtained using DMD: real component (left), imaginary component (right).

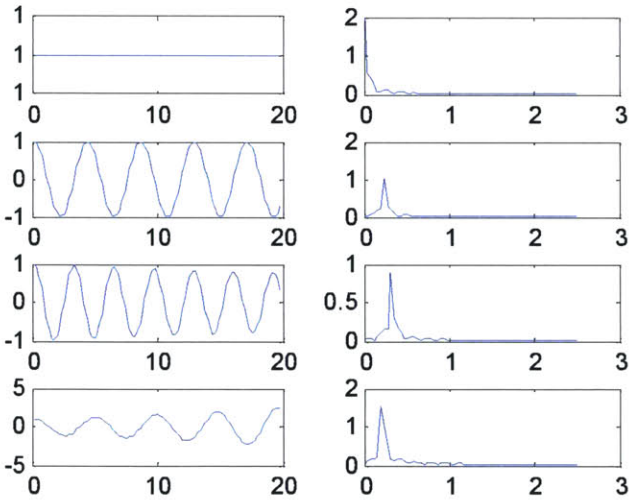

Figure 5.11: (a) Temporal evolution of modal coefficients, (b) FFT of temporal coefficients showing the dominant frequency corresponding to each mode.

5.4 Conclusions

This chapter introduces the dynamic mode decomposition (DMD) technique and illustrates how the method decomposes the patterns in the data on the basis of frequency content and reveals important dynamic information. The methodology therefore has some distinct advantages over the conventional proper orthogonal decomposition (POD) technique (that computes modal structures

solely on the basis of energy content with temporal coefficients comprising of signals of multiple frequencies). Therefore, the framework can serve as an effective tool for the analysis of dynamic systems, and can extract valuable dynamic information from flow fields that are either generated by numerical simulation or measured in a physical experiment. It can also be particularly useful to evaluate the dynamic characteristics of combustion systems from PIV/LES data, as well as to analyze the accuracy of the LES solvers in predicting the experimentally observed dynamics, by comparing the modes obtained from numerical and experimental data samples respectively. In other words, quantitative comparisons of the sizes and shapes of the unsteady modes obtained from simulations and from experiments respectively can lead to clearer assessment of the strengths and weaknesses of the numerical framework in order to reproduce the measured dynamics. Additionally, results from the application of DMD to the flow field data, as well as the heat release data, can provide a quantitative means for understanding the flame-flow interactions by analysis of the flow modes and the heat release modes.

6 PREMIXED COMBUSTION ANALYSIS IN A SWIRL CONFIGURATION

6.1 Overview

The vast majority of gas turbine systems employ swirl injectors that produce a central toroidal recirculation zone to serve as the dominant flame stabilization mechanism. As a result, over the past few years, extensive efforts have been made by the research community to understand the dynamics and stability of lean premixed swirl-stabilized combustion [6.1-6.3]. For example, turbulent swirling flows injected into a coaxial dump chamber at different swirl numbers has been studied using large-eddy simulations, to gain an insight into several salient features of swirling flows (including vortex breakdown, and shear-layer instability), and results have been validated against experimental data in terms of mean flow velocity and turbulence properties [6.4-6.5]. Numerical studies have also been performed to investigate the combustion dynamics of swirl-stabilized combustors, and the physical processes responsible for driving combustion instabilities (including the coupling between acoustic wave motions, vortex shedding, and flame oscillations) have been identified [6.6-6.7]. In another study, the unsteady flame dynamics and transition of flame structure from a stable to an unstable state, in a lean-premixed swirl-stabilized combustor, has been analyzed [6.8]. The inlet temperature and equivalence ratio were identified as important variables determining the stability characteristics of the combustor.

It is now well known that the change of equivalence ratio can significantly influence flame stability, and has been an active area of research. For example, recent experiments for an acoustically-coupled backward-step combustor configuration have shown distinct dynamic regimes based the operating range for the equivalence ratio [6.9]. At high but lean equivalence ratios, the flame is unstable and oscillates strongly as it is wrapped around the large unsteady wake vortex. At intermediate equivalence ratios, weakly oscillating quasi-stable flames are observed. Near the lean blowout limit, long stable flames extending from the corner of the step are formed. Similarly, distinct flame-flow regimes have been observed in case of a cylindrical sudden expansion swirl combustor [6.10]. At high but lean equivalence ratios, the flame is unstable and oscillates strongly while weakly oscillating quasi-stable flames are observed at intermediate equivalence ratios. Near the lean blowout limit, long stable flames are formed. In line with such observations, significant effort has gone into the study of equivalence ratio changes on flame-flow interactions, both experimentally and numerically. While progress has been made in this regard, further investigation is warranted,

beginning with the analysis of acoustically-uncoupled systems, with a focus on understanding the fundamental physics underlying the flame-flow interactions, as the heat loading is changed.

Previously, researchers have attempted to study the impact of modifying the equivalence ratio on the dynamic flow features for wake-stabilized flames. Experiments corresponding to an axi-symmetric bluff-body system [6.11] have shown that increasing equivalence ratio dramatically decreases the recirculation zone size, while the turbulent kinetic energy (TKE) is somewhat suppressed due to dilatation. Combustion near the lean extinction limit, on the other hand, tends to result in a rapid growth in temperature fluctuations. In case of a swirl combustor, changes in the flame stabilization location and vortex breakdown bubble topology [6.12] with increasing heat release rates have been identified. The present work attempts to build upon the previous studies by focusing on a laboratory-scale cylindrical sudden expansion swirl combustor configuration, and investigating the influence of equivalence ratio variation on the flow features using state-of-the-art experimental as well as numerical techniques.

Particle Image Velocimetry (PIV) has been widely used in experimental research to study the spatial flow features in turbulent non-reacting and reacting flows. The technique has distinct advantages over the conventional point-velocity measurement approaches such as Laser Doppler Velocimetry (LDV) or using a hot wire anemometer, since the entire flow field can be resolved to study the interaction between the flame surface and the flow. Further, recent developments in high-speed lasers and cameras have enabled high-repetition rate measurements which allow resolving of the flow structures over a wider range of time and length scales. On the other hand, Large Eddy Simulation (LES) is considered as one of the more promising numerical approaches, balancing computational complexity and predictive accuracy. In LES, rather than averaging the effect of turbulence, the equations are filtered, enabling the larger scales of turbulence to be explicitly resolved, while the effect of the smallest ones on the large scales is modeled. Resolving the large scales enables capturing part of the inherent unsteadiness in the flow, which is particularly important when dynamics at the large scales play an important role, while modeling the sub-grid scale effects ensures that the approach is computationally manageable. This study, therefore, employs experimental (PIV) and numerical (LES) approaches to investigate the impact of equivalence ratio variation on the dynamics of flame-flow interaction corresponding to the swirl combustor configuration. Note, however, that these numerical simulations and experimental measurements of combustion processes are often utilized to obtain time-averaged spatial flow fields and generate point-wise statistics, and fail to accurately capture the characteristic dynamic features of the flow. In

order to address this deficiency, the dynamic mode decomposition technique [6.13-6.15] is utilized to decompose the experimental and numerical instantaneous flow field data, and develop a deeper insight into the prominent dynamic spatial flow features that correspond to dominant frequencies observed in the flow-field.

The next section provides a description of the experimental PIV system, the combustor configuration and the simulation setup. The data obtained from the experimental measurements and numerical predictions (using the thickened flame model) is then presented corresponding to different flame configurations. It is observed that the variation in the equivalence ratio can appreciably influence the large-scale coherent flow features as well as the dynamics of the flow. The results are summarized along with discussions, and the modes computed from the DMD analysis are also shown. Preliminary results suggest that the LES framework is able to predict the transition of the flame macrostructure, as well as reproduce the fundamental dynamic flow features, corresponding to each heat loading scenario, as observed in the laboratory setup.

6.2 Cylindrical Sudden Expansion Swirl Combustor

A canonical swirl geometry [6.16-6.17] that is acoustically-uncoupled is employed for investigations into the effect of heat loading on flame-flow features. Equivalence ratios corresponding to different flame shape modes are considered for the reacting flow, apart from initially performing cold flow analysis. In this section, details are provided about the combustor configuration, and the corresponding numerical setup.

6.2.1 Experimental Configuration

The cylindrical combustor setup, shown in figure 6.1, is designed to stabilize combustion using a combination of swirl and sudden expansion, and is comprised of an inlet pipe of diameter (D) 38 mm, with a combustion chamber of radius (R=D) 38 mm downstream of the expansion plane. A mixture of air and methane is introduced at equivalence ratios corresponding to different flame shape configurations, at a bulk inlet velocity (U_{CD}) of 8.4 m/s (Reynolds number, Re_{CD} ~ 20,000, based on the inlet pipe radius $D/2$ and the bulk fluid velocity U_{CD}). The mixture inlet temperature (T_C) is 300 K and the nominal pressure is 101 kPa. The swirler, located 50 mm upstream of the expansion plane, has 8 blades each inclined at (θ) 45° to the cylinder cross-section, with an estimated swirl number of 0.7. The first 40 cm downstream where the flame is anchored consists of a quartz tube for optical access. The overall acoustic length of the combustor (from the choke plate to the end of exhaust tube) is 4.5 m. The flow is choked upstream to prevent equivalence ratio oscillations and provide a known acoustic boundary condition.

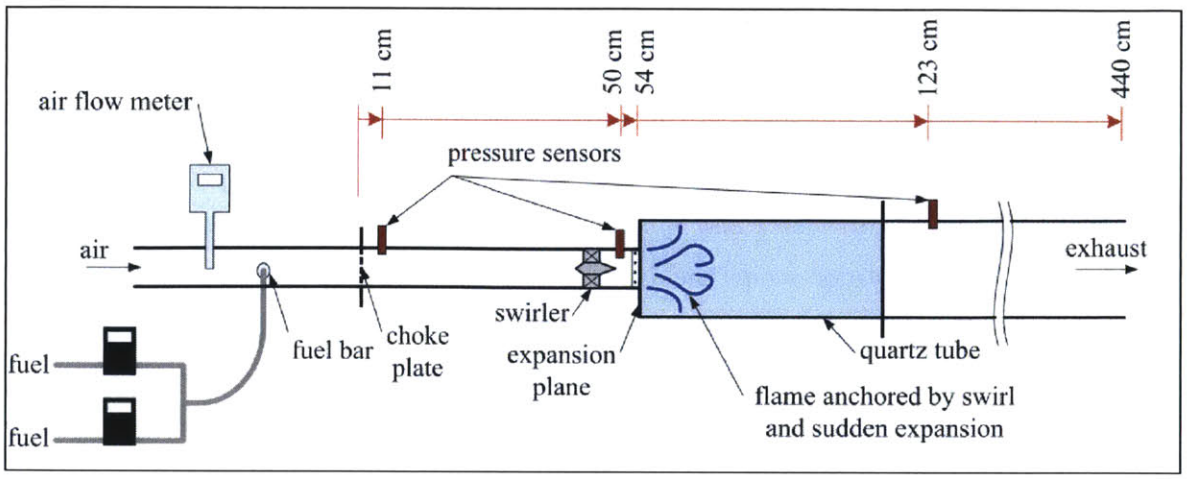

Figure 6.1: Experimental setup for premixed combustion in a swirl combustor.

6.2.2 PIV Setup

Planar velocity fields and flame surface topology are obtained using phase-locked particle image velocimetry (PIV). 2-D velocity maps were measured using a high-speed CMOS camera mounted above the combustor, recording images at 1 to 2 kHz. The schematic of the setup is shown in figure 6.2. The light source consists of a Nd:YLF laser of wavelength 527 nm capable of producing dual pulses at a rate up to 5 kHz with a peak power output of 25 mJ/pulse. A 1280 x 1024 pixel NAC GX-1 CMOS camera, with an Fmount Nikon 60 mm micro-lens with an aperture of f/8 was used for imaging. The interval between the laser pulses was set to 10–30 μs depending on the flow velocity. A light sheet less than 1 mm thick in the imaged region across the diameter of the main combustion chamber was generated using a spherical lens with a focal length of 1000 mm and a cylindrical lens with a focal length of 20 mm. The former was used to reduce the diameter of the beam and the latter was used to diverge the beam to generate a sheet. The inner surface of the combustion chamber, below the light sheet, was sandblasted in order to reduce specular reflections. Bypass air, taken from the inlet pipe upstream of the choke plate, is routed through a cyclone-type seeder. Seeding particles consisting of 1.5–3 μm diameter Al_2O_3 are injected into the main air immediately downstream of the choke plate.

The PIV measurements are processed using the LaVision DaVis 7.2 software. The distance between the imaging plane and the camera was set to 0.6 m based on the desired field of view. The corresponding viewing area for the PIV measurements is 120 mm x 120 mm, generating 800 x 800 pixel images of the seeding particles. These images are processed using a multi-pass approach, with the final pass using a 16 x 16 pixel window with 50% overlap. This produces velocity fields with a

spatial resolution of 1.14 mm. Further details about the setup and experiments can be found in [6.16-6.17].

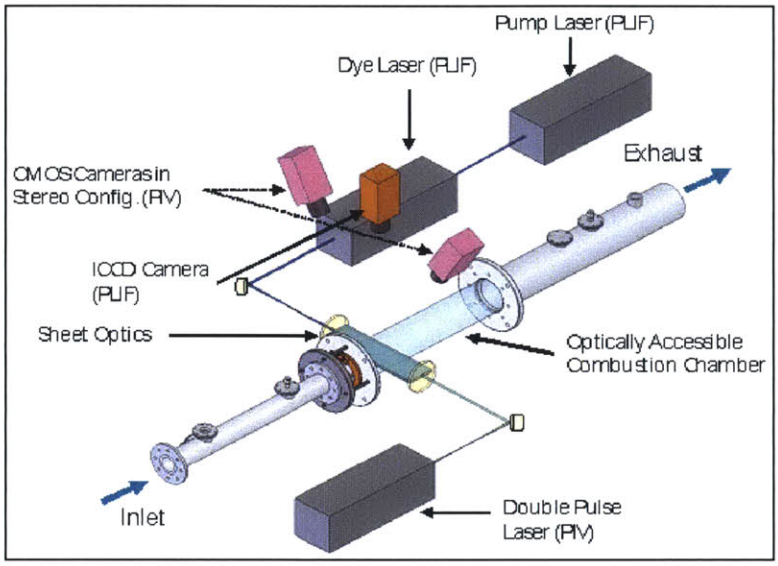

Figure 6.2: Experimental PIV/PLIF setup for measurements in a swirl combustor.

6.2.3 Simulation Setup

The geometry corresponding to the computational domain is depicted in figure 6.3. The choice of the numerical grid is governed by estimates of the physical length scales associated with the flow configuration. Based on Pope's criterion defined earlier, and using the inlet pipe radius ($D/2$) as the integral length scale, the filter-width can be estimated to be 1.6mm. Again, it should be noted that the above theory does not focus on resolving near-wall structures and may not be applicable for reacting flow. Therefore, appropriate grid clustering may be required to resolve the structures near the walls and in the shear layer region for reacting flow. The non-uniform mesh utilized in the current work is comprised of 0.55 million hexahedral cells, and gets coarser along the stream-wise direction. The numbers of cells in the axial, radial and tangential directions, in the combustion chamber, are 145, 35 and 96 respectively; therefore, the average Δx and Δr values in the wake region are approximately 1.35 mm and 1.00 mm respectively, while the minimum Δx and Δr values, in the shear layer region, are approximately 0.75 mm and 0.50 mm respectively.

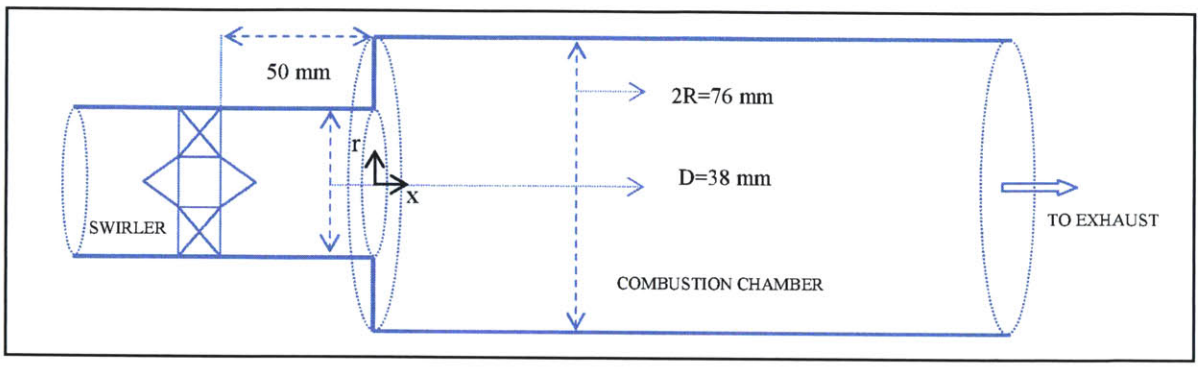

Figure 6.3: Cylindrical swirl configuration used for flame stabilization.

Temporal resolution is determined based on physical time scale estimates in order to prevent excessive numerical dissipation and numerical instability. Based on the CFL criterion ($C_{max} = (U_{CD}+U_s)\Delta t/\Delta x$; $C_{max} = 1$, $U_s = 340$m/s, $\Delta x = 1$ mm), the time step for the simulations is estimated at approximately 2.2μs. A conservative value of 1μs is used in the reacting flow simulations to account for local refinement and acceleration of the fluid above the bulk inlet velocity, and to adequately resolve the chemical time scales. The key quantities relevant to the configuration are summarized in table 6.1.

Table 6.1: Parameters for the cylindrical swirl combustor configuration.

PARAMETER	SYMBOL/EXPRESSION	VALUE
Inlet Pipe Diameter	D	38 mm
Combustion Chamber Radius (Characteristic Length)	$R\ (=D)$	38 mm
Integral Length Scale	$L_I\ (=D/2)$	19 mm
Equivalence Ratio	λ	0.51, 0.55, 0.60, 0.65
Swirl Number	S	0.7
Bulk Inlet Velocity (Characteristic Flow Velocity)	U_{CD}	8.4 m/s
Macroscopic Reynolds Number	Re_{CD}	20,000
Inlet Temperature	T_C	300 K
Nominal Pressure	P	101 kPa
Kolmogorov Length Scale	$Re_{CD}^{-3/4}L$	11.3 μm
Cold Flow Filter Width (Pope's Criterion)	$\Delta=0.083L_I$	1.6 mm
Precessing Vortex Frequency	f_{pvc}	120 Hz
Precessing Vortex Time Scale	$1/f_{pvc}$	8.3 ms
Shear Layer Fluctuation (measured)	u'	~5 m/s
Integral Time Scale	$T_I=L/u'$	4 ms
Kolmogorov Time Scale	$Re_{CD}^{-1/2}T_I$	28.3 μs
CFL Criterion Time Scale	$C_{max}\Delta x/(U_{CD}+U_s)$	2.2 μs

To provide a more conclusive comparison between numerical predictions and experimental measurements, a stand-alone configuration that involved fully meshing the swirler geometry (rather than specifying swirl velocity profiles) was considered, as depicted in figure 6.4. At the inlet, Dirichlet conditions are used for all variables except the pressure, for which zero Neumann conditions are specified. At the exit, zero Neumann conditions are specified for all variables except

the pressure, for which wave-transmissive conditions are used. No-slip conditions are applied for the flow at the walls, while zero Neumann conditions are specified for the other variables. Heat transfer is also considered at the walls to account for any thermal losses. In order to maintain reasonable computational efficiency, appropriate wall functions are utilized to resolve the flow features in the wall boundary layer. Numerical computations start from quiescent conditions and the unsteady flow characteristics evolve naturally. In order to initiate the flame, a high temperature pulse is applied at the inlet section which ignites the fuel; the reacting mixture convects downstream, and eventually stabilizes as a flame in the wake of the swirler. Averaging is performed over nearly 10 flow-through cycles once the flow is established in the computational domain.

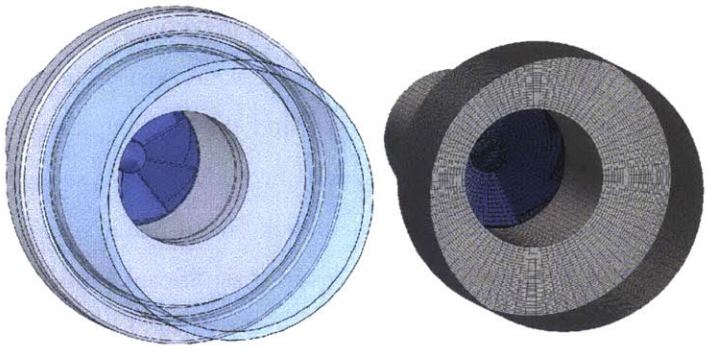

Figure 6.4: Swirler geometry and corresponding mesh for numerical computations.

Note that during the simulations, the inlet velocity (specified upstream of the swirler; see figure 6.3) is considered to have a flat profile on which fluctuations of 5% turbulence intensity are imposed, as experimental data is available only downstream of the expansion plane, which is optically accessible. This is a suitable approximation, considering that the presence of the swirler vanes in this scenario has a relatively dominating influence on the flow as it enters the combustion chamber, as opposed to the free stream turbulence intensity upstream.

Further, in order to allow better comparison between the numerical predictions and the experimental measurements, and to relate the flame-flow interactions across the different configurations, the range of the magnitudes for the contours of some of the flame-flow variables have been fixed. Additionally, for clarity, the radial direction is represented as the y-axis in the diametric cross-sectional plane for which the flame-flow variables' contours are depicted.

6.2.4 Results and Discussions: Non-Reacting Flow

Cold flow is considered prior to simulating reacting flow, with the prominent flow features comprising of the inner recirculation zone (IRZ), the precessing vortex layer surrounding the IRZ, shear layers at the boundaries of the annular jet, as well as the outer recirculation zone (ORZ) at the

corners (figure 6.5). These flow structures are also evident from the LES contours of the average vorticity magnitude, depicted in figure 6.6a, along with the streamlines.

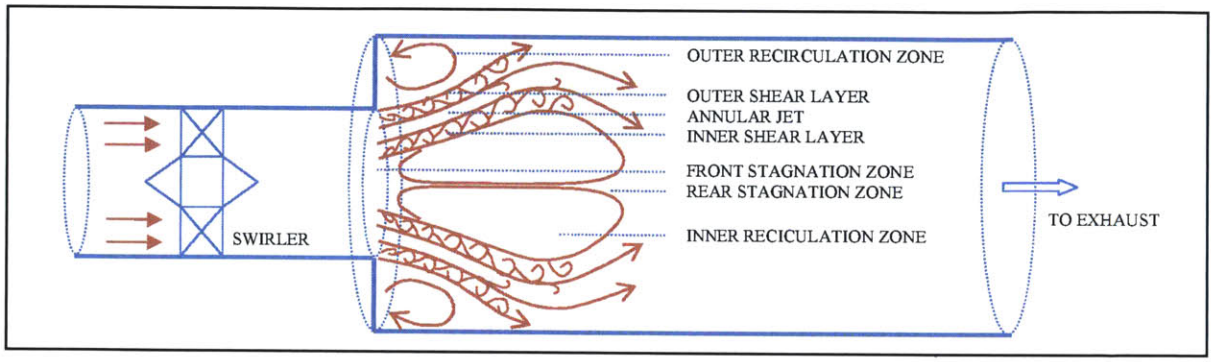

Figure 6.5: Fundamental flow features in a backward facing step configuration.

As the flow evolves downstream of the expansion plane, strong shear layers develop, due to the velocity difference between the annular jet flow and the ambient fluid. Large-scale coherent structures are generated in the shear layer regions, and shed downstream sequentially due to Kelvin–Helmholtz instability, as suggested by the instantaneous out-of-plane vorticity contour shown in figure 6.6b. Note that these vortex structures can exert a significant influence on the combustion process by modulating the mixing processes among the inlet fuel-air mixture, and the hot combustion products stored within the inner recirculation zone. Further downstream, beyond the axial location corresponding to the impingement of the annular jet and the walls of the chamber, these vortices break down into smaller eddies, eventually dissipating due to vortex stretching and viscosity effects, as the flow convects towards the exhaust (figure 6.7).

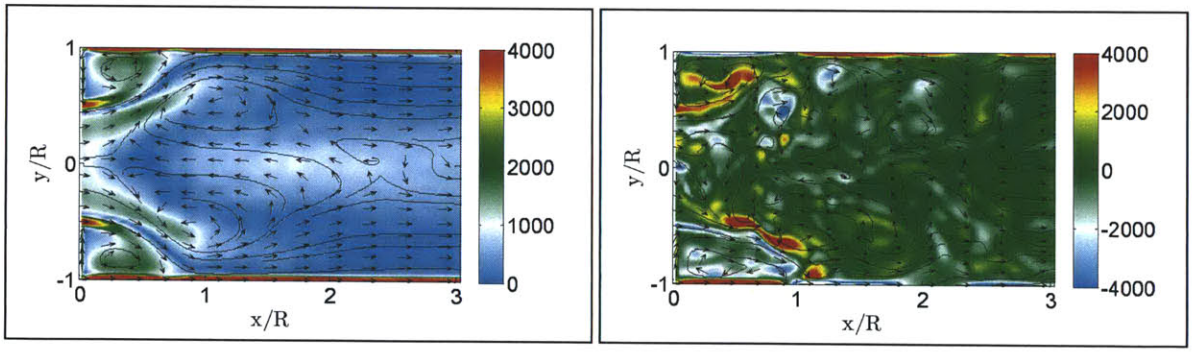

Figure 6.6: (a) Average vorticity magnitude (1/s), (b) Instantaneous out-of-plane vorticity (1/s). The corresponding 2D velocity vectors and streamlines are also shown (LES).

The presence of the wall also plays a critical role in altering the fundamental flow structures in this case, primarily affecting the width of the IRZ, as well as influencing the development of the shear layers. The chamber wall restricts the radially outward spread of the annular jet, resulting in a

narrower and presumably longer recirculation zone. Confinement also accelerates the incoming flow and affects the growth of the shed vortices as well, thereby influencing the thickness of the mixing layer.

One of the important flow characteristics in a swirl configuration is the vortex breakdown phenomenon, which manifests itself as an abrupt change in the core of a slender vortex, and usually develops downstream into an inner recirculating bubble, as indicated by the mean streamlines in figure 6.6a. Note that the axial span of this region varies due to the inherent unsteadiness of the flow. Owing to the rapid flow expansion resulting from the strong swirling motion and geometric confinement, an outer recirculation zone (ORZ) is also formed and is much shorter than the inner recirculation zone. Typically, the azimuthal (tangential) velocity component prevails in the corner recirculation zone, with the other two components being relatively weaker, owing to geometric constraints. This is due to the fact that the displacement of the vortex core squeezes the flow-field at one side against the chamber wall, and causes a considerable increase in the tangential velocity in that region due to the conservation of angular momentum [6.1, 6.18-6.19]. For the present configuration, high vorticity is observed in these outer recirculating vortex cells, as depicted in figure 6.6a.

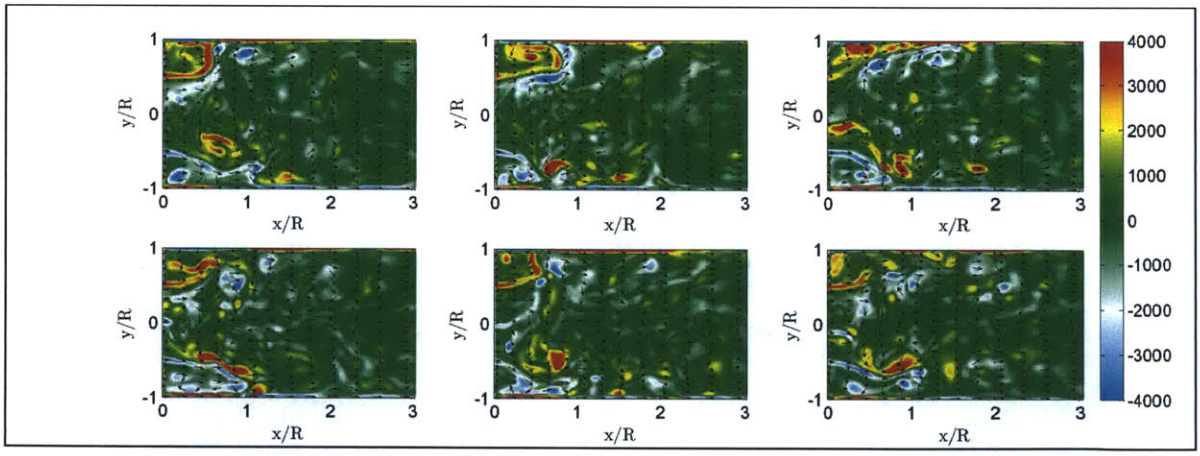

Figure 6.7: Instantaneous out-of-plane vorticity (1/s) at different time-instants, with the corresponding 2D velocity vectors (LES).

Another principal feature of swirling flows is the precessing vortex core (PVC) that develops when the central vortex core precesses around the symmetry-axis at a specific frequency (that depends on the swirl number, the chamber configuration, and the flow rate). The phenomenon is usually linked to vortex breakdown and the associated recirculation zone in high Reynolds number flows, with the PVC situated at the boundary of the reverse flow zone, near the zero velocity region.

For the present configuration, the PVC frequency in the isothermal case is observed to be 110 Hz (figure 6.8), by sampling the radial velocity component downstream of the sudden expansion (x = 0.013 m, r = -0.010 m, z = 0.000 m), and performing an FFT analysis on the signal.

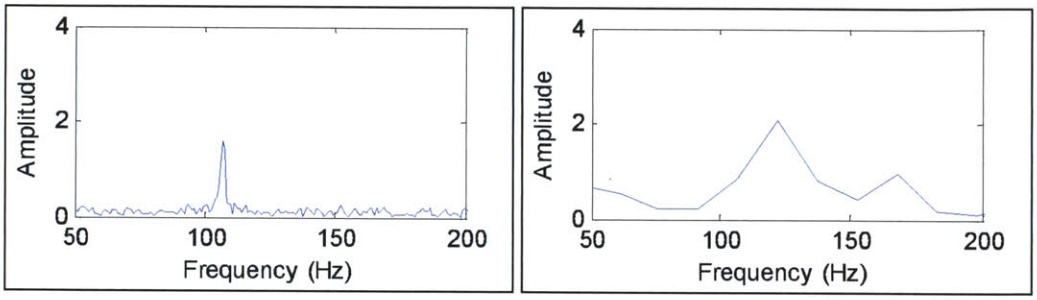

Figure 6.8: FFT analysis of radial velocity component signal (PIV: left, LES: right).

Next, the contours of the average axial velocity, along with the corresponding streamlines, obtained experimentally and numerically, are depicted in figure 6.9. The cross-sections at which LES and PIV data are compared are also shown. Results show the presence of the vortex breakdown bubble (VBB) consisting of a single, recirculating cell of fluid in the inner recirculation zone (IRZ). This structure serves as the dominant flame stabilization mechanism in reacting flows, and is characterized by the existence of internal stagnation points and reversed flow. Smaller vortices (actually vortex ring) at the corners of the chamber are also evident, forming the outer recirculation region. Overall, there is reasonable agreement between the experimental measurements and numerical predictions in estimating the growth and size of these vortex structures, and the radial spread of the annular jet, as also evident from the average radial velocity contours (figure 6.10).

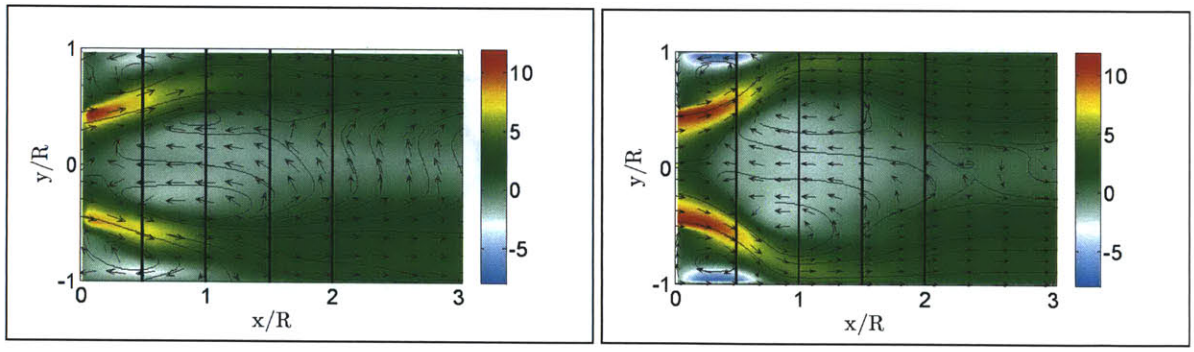

Figure 6.9: Average axial velocity along with the 2D velocity vectors and streamlines (PIV: left, LES: right). The cross-sections at which data are compared are also shown.

Further examination of the flow field contours suggests that the reverse centerline velocity peaks in the core of the recirculation zone and subsequently reduces in magnitude, though it remains marginally negative further downstream. Although flow recirculation continues downstream, strong

flow reversal is predominant up to a distance of approximately *3.0R* into the cylindrical chamber, with the upstream stagnation point located at a distance of *0.25R* downstream of the expansion plane. Additionally, the outer recirculation zones formed at the corners extend to a distance of about *1.1R* downstream of the expansion plane. These flow structures are suitably resolved in the simulations, comparing quite well with the experimental data.

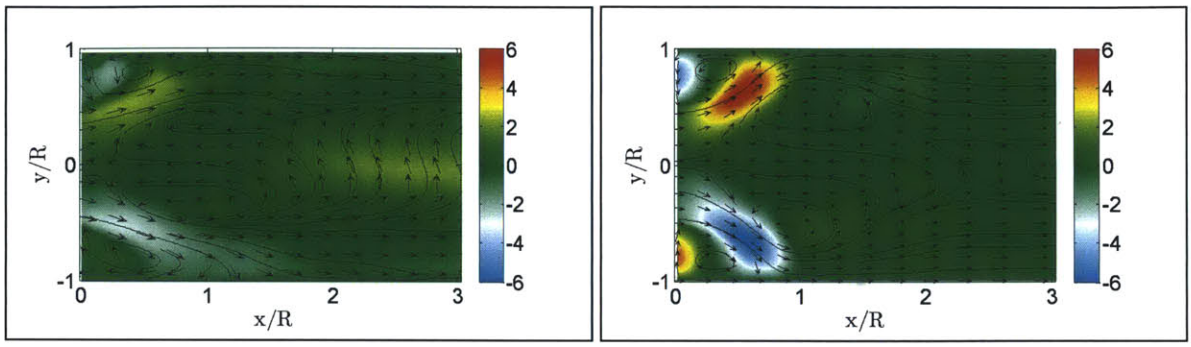

Figure 6.10: Average radial velocity along with the 2D velocity vectors and streamlines (PIV: left, LES: right).

In figure 6.11, the contours of the rms axial velocity field are shown which exhibit high-turbulence intensity in the shear layers around the periphery of the IRZ. This is associated with strong shear layer development, along with the existence of the PVC; the vortex structures generated in the mixing layer and shed downstream due to Kelvin-Helmholtz instability contribute significantly to the generation of turbulent kinetic energy in the shear layers. The flow fluctuations are also high near the walls at the axial location of maximum IRZ width, and can be attributed to the impingement of the annular jet on the chamber wall. In the downstream section, the large-scale eddies subsequently break down into smaller strcutures, which dissipate due to viscous effects, and the turbulent flow field becomes significantly more isotropic.

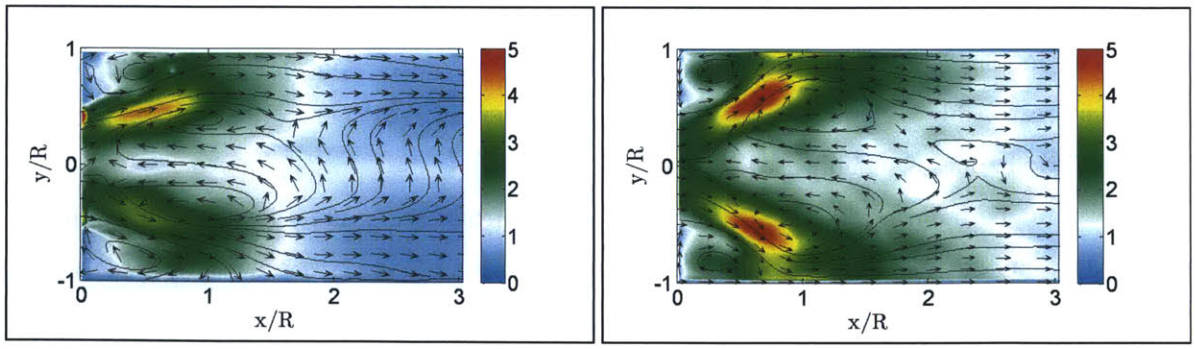

Figure 6.11: rms axial velocity along with the 2D velocity vectors and streamlines (PIV: left, LES: right).

In figure 6.12, the viscous dissipation per unit volume and the average azimuthal (tangential) velocity obtained from simulations are shown. High azimuthal (tangential) component of velocity is observed in the annular jet immediately downstream of the expansion plane, as expected, arising primarily due to the swirling nature of the flow. Viscous dissipation plays a significant role in influencing the flow field topology (especially the development of the shear layer vortices), and is appreciably high in the mixing layer region, surrounding the recirculation zone. The viscous dissipation per unit volume, Θ, can be as estimated in Cartesian coordinates [6.20] as:

$$\Theta = 2\mu\left[\left(\frac{\partial u_x}{\partial x}\right)^2+\left(\frac{\partial u_y}{\partial y}\right)^2+\left(\frac{\partial u_z}{\partial z}\right)^2-\frac{1}{3}\left(\frac{\partial u_x}{\partial x}+\frac{\partial u_y}{\partial y}+\frac{\partial u_z}{\partial z}\right)^2\right] + \mu\left[\left(\frac{\partial u_x}{\partial y}+\frac{\partial u_y}{\partial x}\right)^2+\left(\frac{\partial u_y}{\partial z}+\frac{\partial u_z}{\partial y}\right)^2+\left(\frac{\partial u_z}{\partial x}+\frac{\partial u_x}{\partial z}\right)^2\right] \quad (6.1)$$

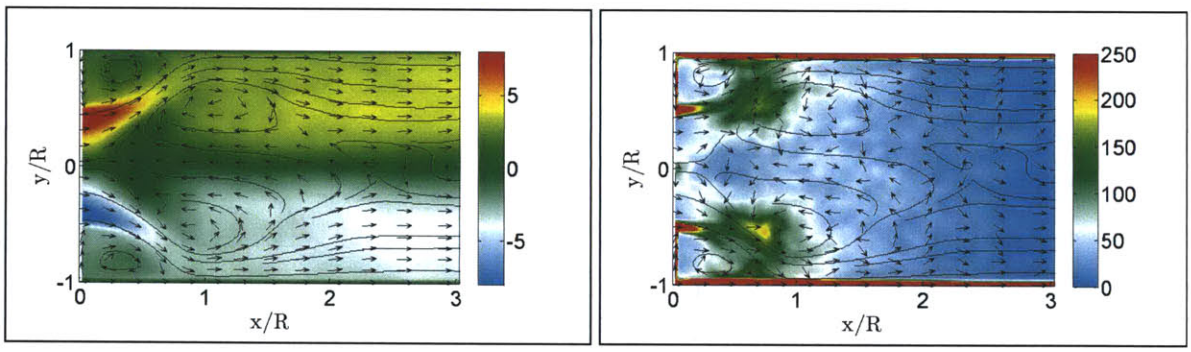

Figure 6.12: (a) Average azimuthal (tangential) velocity (m/s), (b) Viscous dissipation per unit volume (kg/ms^3). The corresponding 2D velocity vectors and streamlines are also shown (LES).

Figure 6.13 compares the normalized profiles for the average axial velocity and rms axial velocity obtained computationally and experimentally at cross sections downstream of the expansion plane of the cylindrical chamber. As explained earlier, the axial velocity peaks in the shear layer forming an annular jet that surrounds the IRZ. The width and the spreading rate of the jet are reproduced reasonably accurately using LES as is the maximum axial velocity. The development of the recirculation zones is suitably predicted as well.

Examining the rms plots, it is observed that the fluctuations peak in the shear layer initially, and tend to quickly become isotropic further downstream ($x/R>2$) as the influence of the precessing vortex core (PVC), and of the vortices generated in the shear layer, diminishes due to viscous dissipation. Flow field fluctuations are also high near the walls at the axial location corresponding to the maximum IRZ width ($x/R\approx1$), where the annular jet impinges on the chamber

wall. Thus, the aerodynamic blockage caused by the IRZ causes a radially outward deflection of the separation streamlines at the edge of the ISL which results in squeezing of the annular gaseous jet towards the chamber walls. Consequently, this shifts turbulence production radially outward and the turbulence intensity, which is now primarily due to the interaction of Reynolds stress and shear strain, appears to be concentrated in the shear layer around the periphery of the IRZ, and at the location where the jet impinges the wall.

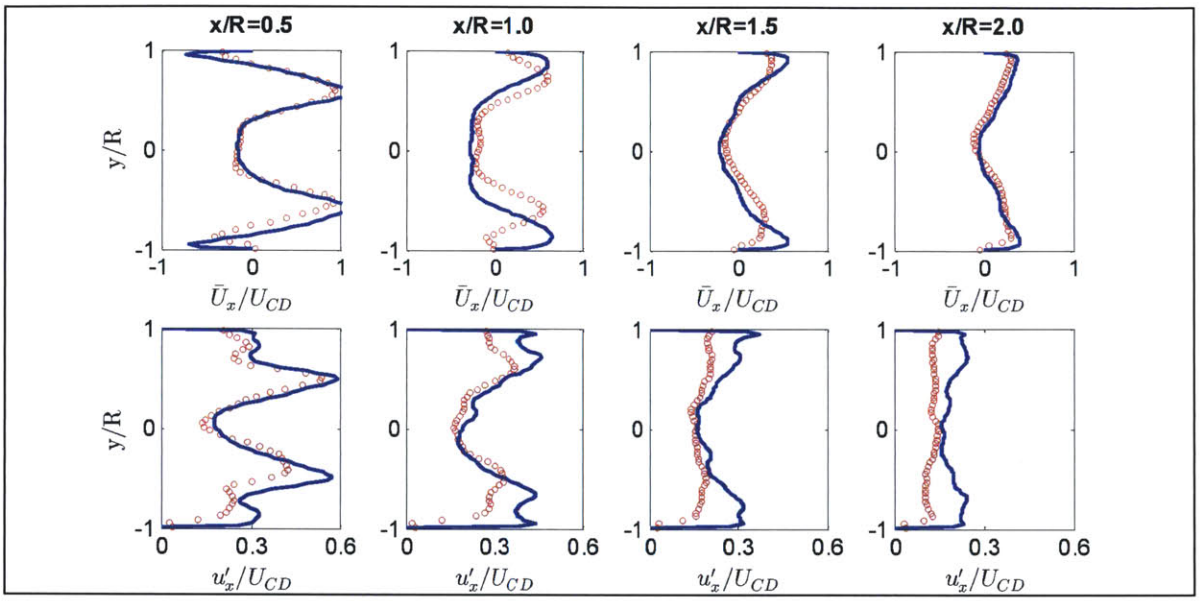

Figure 6.13: Normalized profiles for average axial velocity (top) and rms axial velocity (bottom). ooo PIV, — — — LES

The simulations predict marginally higher shear layer fluctuations than measured, and these discrepancies could be attributed to the sensitivity of resolved flow features to geometric features in the inlet pipe, upstream flow perturbations, and the grid resolution in the boundary layer of the inlet duct [6.21]. Likewise, the slight over-estimation of fluctuations in the region corresponding to jet impingement could be improved by appropriate mesh resolution near the walls and by the choice of suitable wall functions. Adjustments to the PIV setup for the measurement of higher resolution flow fluctuation data in downstream locations can also be performed.

6.2.5 Results: Reacting Flow

As depicted in figure 6.14, the turbulent premixed flame in a swirl combustor can exhibit different configurations, depending upon the equivalence ratio. This is based upon whether the flame is stabilized near the front stagnation region of the vortex breakdown bubble, within the primary recirculation zone, or the low velocity regimes of the inner and/or outer shear layers. Fundamental

flow field characteristics such as the vortex breakdown bubble structure, the annular jet thickness, and the outer recirculation zone topology corresponding to these flame macro-structures can differ substantially, and is investigated using LES.

The following flame configurations are considered: I. columnar wake flame (φ=0.51), II. bubble-type wake flame (φ=0.55), III. inner shear layer flame (φ=0.60), and IV. inner shear layer/outer shear layer/outer recirculation zone flame (φ=0.65). In the following sections, each case is presented, describing the topological features for the mean and fluctuating flow field in the combustion chamber, and elucidating the spatial reaction-zone macro-structure as well as the flame-flow interactions. The point-wise velocity statistics obtained from numerical simulations and experimental measurements respectively are also compared at axial locations downstream of the expansion plane. Additionally, the modal structures obtained from dynamic mode decomposition analysis, as applied to LES and PIV data respectively, are also presented.

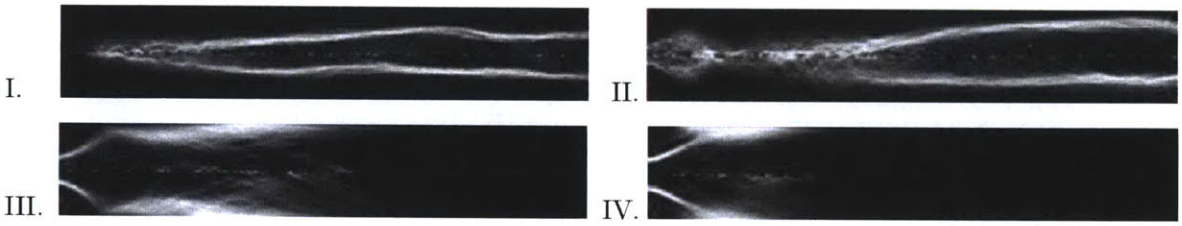

Figure 6.14: Flame macrostructures in the experimental swirl combustor (Abel-transformed flame images): I. columnar wake flame ($\varphi \approx 0.51$), II. bubble-type wake flame ($\varphi \approx 0.55$), III. inner shear layer flame ($\varphi \approx 0.60$), IV. inner shear layer/outer shear layer/outer recirculation zone flame ($\varphi \approx 0.65$).

6.2.5.1 Configuration I: LES Analysis

The CH chemiluminescence and Abel-transformed flame images for Configuration I, displayed in figure 6.15, suggest the presence of a thin, weakly burning flame that stabilizes downstream of the expansion plane (within the IRZ, around the centerline). The lifting of the flame may be associated with the low burning velocity and low extinction strain rate, which prevent the propagation of the reaction zone upstream in high strain shear layer regions. Further, the downstream extension of the tubular flame is significantly longer than the compact flame envelope noted for configuration IV (figure 6.14), with the reaction zone extending into the exhaust tube.

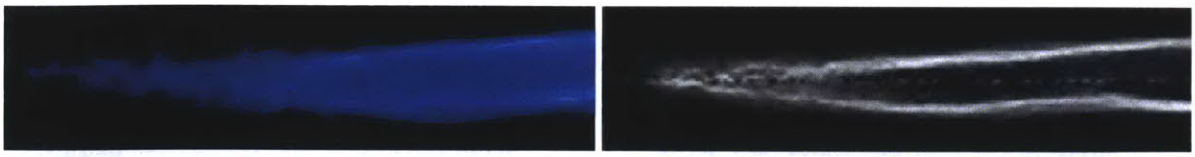

Figure 6.15: (a) Time resolved flame from CH chemiluminescence image, (b) Abel-transformed flame image.

The instantaneous LES contours for the normalized heat release and the temperature are shown in figure 6.16, indicating the presence of a convoluted reaction zone, with the flamelets stabilizing locally within the recirculation vortex, which is characterized by existence of internal stagnation points and low velocity regions.

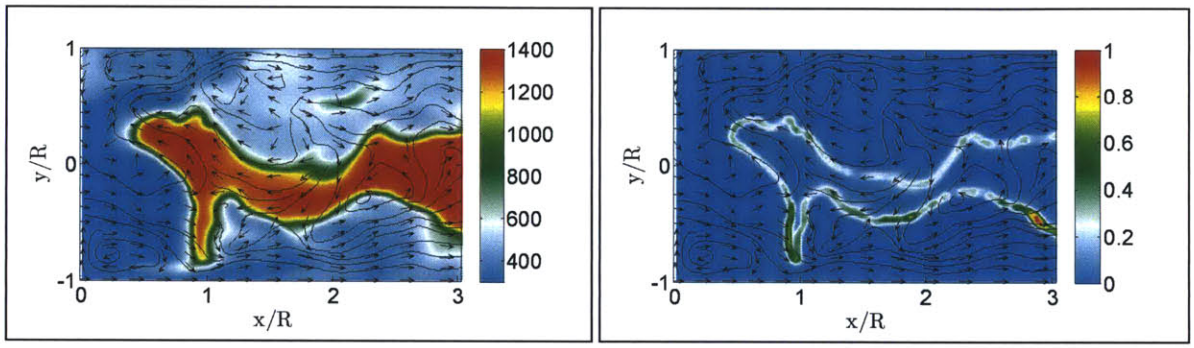

Figure 6.16: (a) Instantaneous temperature (K), (b) Instantaneous normalized heat release. The corresponding 2D velocity vectors and streamlines are also shown (LES).

The flamelets are characterized by low turbulent burning velocity and reduced heat release rates; along with the PVC generated turbulence, this results in a low intensity, wrinkled instantaneous flame structure in this upstream section that is predominantly characterized by reaction kinetics and has a localized presence, eventually forming a diffuse, moderately thick average reaction zone (figure 6.17). As shown in the instantaneous CH_4 and CO mass fraction contours in figure 6.18, the flame intensity increases in the vicinity of the rear stagnation zone where flow reversal intensifies mixing, allowing flamelets to stabilize; additionally, shear generated turbulence appreciably enhances heat diffusion from the region consisting of hot combustion products towards the preheat zone. The turbulence in the region also increases entrainment, substantially wrinkles the flame, thereby enhancing the reaction rates and the flame surface area, and thickens the reaction zone.

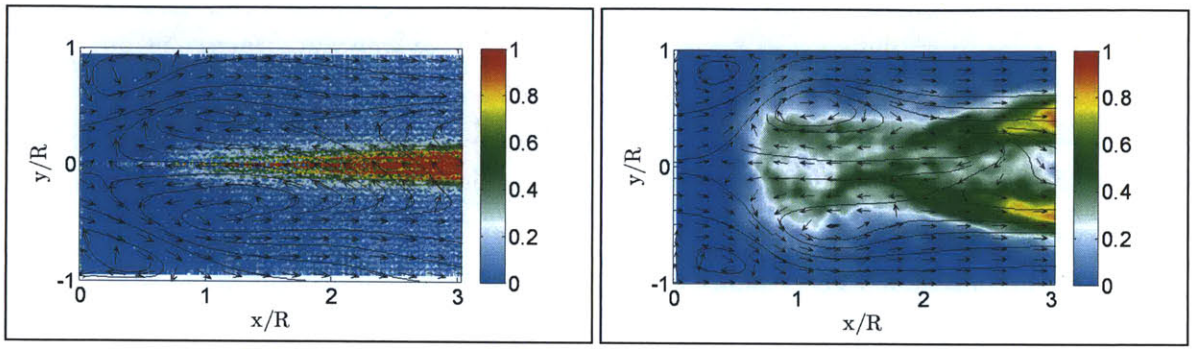

Figure 6.17: (a) Normalized deconvolved CH chemiluminescence intensity, (b) Average normalized heat release (LES). The corresponding 2D velocity vectors and streamlines are also shown.

As the flow convects downstream, the flame is predominantly shaped due to dilatation and transport effects, forming a smooth, tubular macrostructure around the centerline axis. In this section, mixing and transport contribute significantly to flame stabilization; the intense mixing activity arising out of combustion generated turbulence results in higher heat release and large temperatures in the region. Combustion continues as the flow proceeds into the exhaust duct, with the flame thickening in the downstream section and taking a columnar shape due to the effects of dilatation and wall confinement.

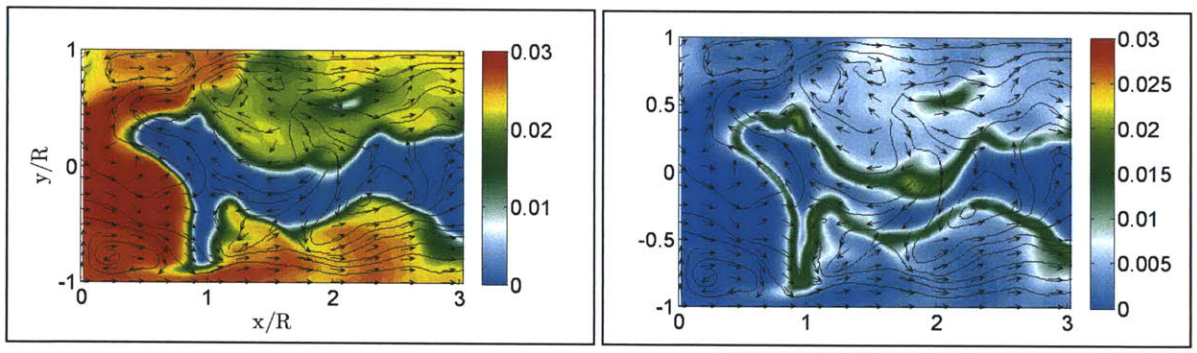

Figure 6.18: (a) Instantaneous CH_4 mass fraction, (b) Instantaneous CO mass fraction. The corresponding 2D velocity vectors and streamlines are also shown (LES).

In figure 6.19, the instantaneous contours for the CO mass fraction at different time-instants is shown along with the corresponding 2D velocity vectors. No persistent flame is observed along the shear layer or within the ORZ, as also evident from the average temperature contour in figure 6.20; the rms temperature contour suggests that the reaction zone only intermittently extends into the ISL. A further reduction in the equivalence ratio results in flame extinction in the IRZ region, eventually followed by blow-off (observed during the experiments, at an equivalence ratio of 0.47). In contrast, with an increase in equivalence ratio, the higher flame speed and extinction strain rate

result in propagation of the flamelets into the strained inner shear layer regions, forming a bubble-type flame corresponding to Configuration II. As the heat loading continues to increase, the flamelets begin to propagate radially outwards, towards the high velocity annular flow near the chamber walls, forming the conical flame macrostructures corresponding to Configurations III, IV.

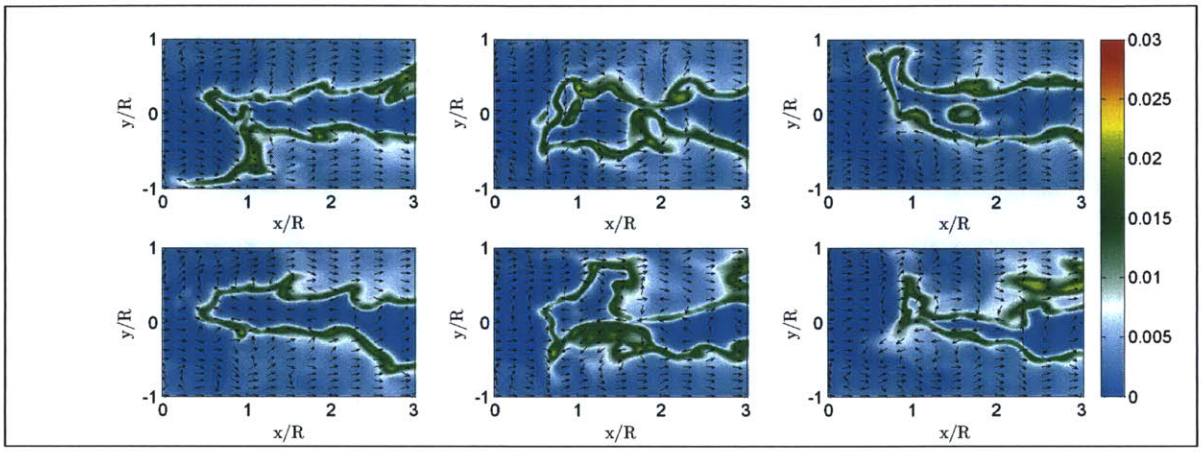

Figure 6.19: Instantaneous CO mass fraction at different time-instants, with the corresponding 2D velocity vectors (LES).

It is worth noting that the chamber walls significantly influence the flow field pattern as well as the flame structure in the wake region (figure 6.15). Confinement restricts the radially outward spread of the annular jet, thereby influencing the inner recirculation zone topology. It also enhances the dilatation effect of heat release, accelerating the flow as it convects downstream into the exhaust. Due to the low burning velocity, the reaction zone is unable to propagate into the high velocity annular flow in the vicinity of the chamber walls, and the flame maintains a smooth, columnar shape around the centerline axis.

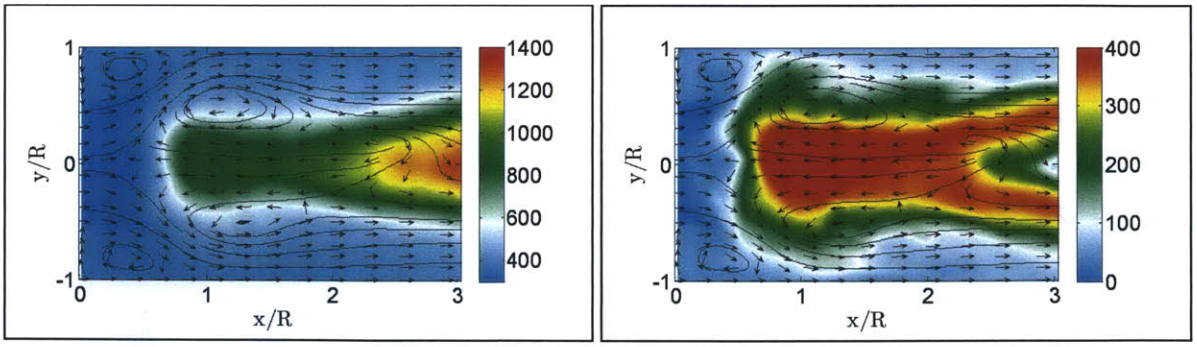

Figure 6.20: (a) Average temperature (K), (b) rms temperature (K). The corresponding 2D velocity vectors and streamlines are also shown (LES).

Next, in figure 6.21, LES contours of the average vorticity magnitude and instantaneous out-of-plane vorticity (at a specific time-instant) are depicted, suggesting significant vortex activity in the shear layers, and in the ORZs, due to the convective vortices and the swirling nature of flow, respectively. The vorticity field is similar to the isothermal case in the upstream section, which is understandable, given that the flame stabilizes further downstream of the expansion plane.

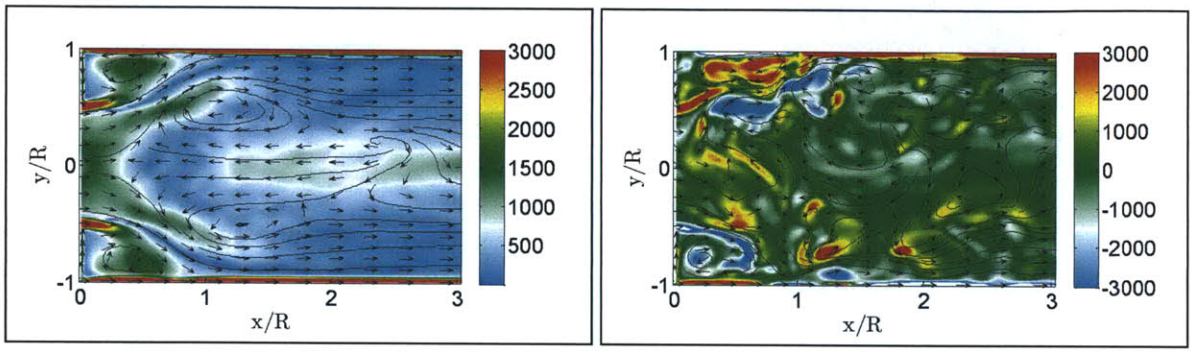

Figure 6.21: (a) Average vorticity magnitude (1/s), (b) Instantaneous out-of-plane vorticity (1/s). The corresponding 2D velocity vectors and streamlines are also shown (LES).

A strong precessing vortex is observed in this case as well, and the relative contribution of the PVC to the observed vorticity field in the upstream section is substantial. The PVC frequency is observed to be 110 Hz (figure 6.22), by sampling the radial velocity component downstream of the sudden expansion (x = 0.013 m, r = -0.010 m, θ = 0.000 m), and performing an FFT analysis on the signal. Additionally, the average vorticity magnitude contour indicates appreciable vortex activity along the centerline, in the section downstream of the rear stagnation region, where the flame stabilizes. The increase in vorticity in the region could be due to combustion induced baroclinic effects combined with strong azimuthal flow around the centerline. In contrast, the vorticity strength is negligible near the chamber walls where dilatation effects result in significant axial flow acceleration in the presence of wall confinement.

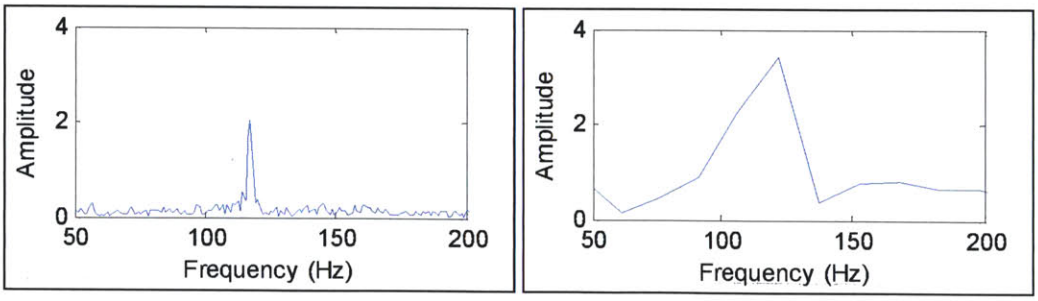

Figure 6.22: FFT analysis of radial velocity component signal (PIV: left, LES: right).

In figure 6.23, the instantaneous out-of-plane vorticity contours are shown at different time-instants, indicating significant vorticity in the shear layers, due to the convective vortices. Further downstream, however, the breakdown of the vortices into smaller eddies due to heat release and thermal expansion in the vortex cores result in a diffuse out-of-plane vorticity field. These eddies subsequently dissipate due to vortex stretching and viscosity effects, as the flow convects towards the exhaust; coupled with the effects of dilatation, this results in a low intensity out-of-plane vorticity field in the downstream section.

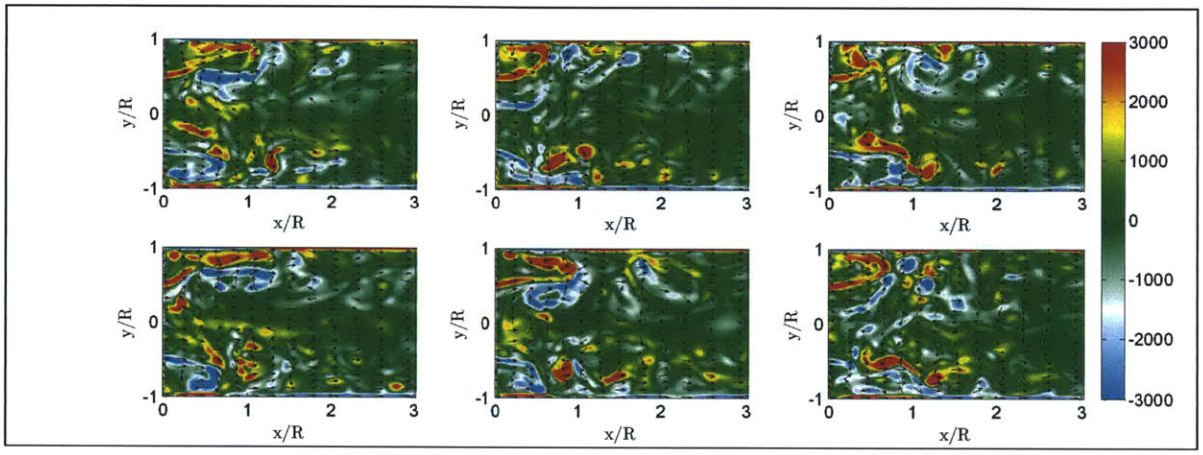

Figure 6.23: Instantaneous out-of-plane vorticity (1/s) at different time-instants, with the corresponding 2D velocity vectors (LES).

Next, the contours of the average axial velocity, obtained experimentally and numerically, are displayed in figure 6.24. The cross-sections at which numerical and experimental data are compared are also shown. The prominent topological flow features comprise of the annular jet, the shear layers at the boundaries of the jet, and the inner and outer recirculation zones.

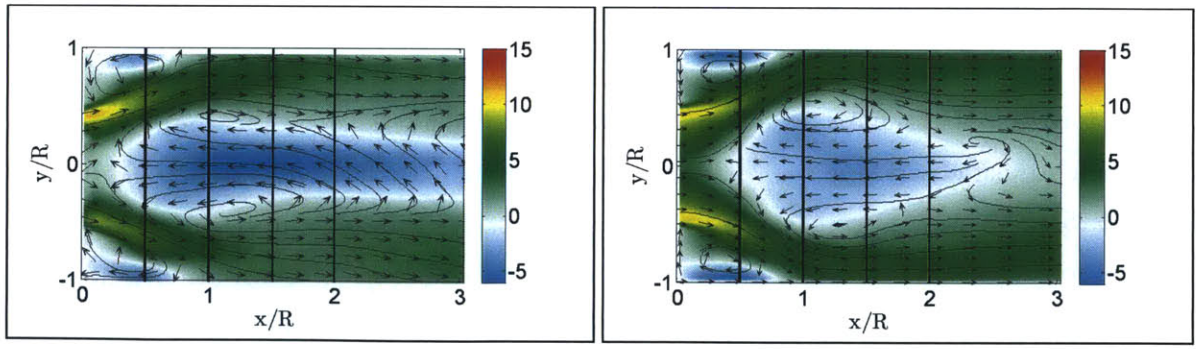

Figure 6.24: Average axial velocity along with the 2D velocity vectors and streamlines (PIV: left, LES: right). The cross-sections at which data are compared are also shown.

Similar to the isothermal case, the vortex breakdown bubble has a single-cell type recirculating structure with the front stagnation point located downstream of the expansion plane. In contrast, a split-cell type recirculating vortex has a centerline jet with positive axial velocity, as in [6.12]. Although some flow recirculation does occur in the downstream section ($x/R>3$) surrounding the centerline axis (figure 6.25), the IRZ principally extends to a distance of approximately *2.5R* into the combustion chamber, and closely resembles the vortex structure observed in the cold flow scenario. However, considerably higher reverse flow velocity is observed within the IRZ, owing to exothermicity. The recirculation intensity, as indicated by the reverse mass flow rate, is also strong, similar to the non-reacting flow, despite the reduction in density. This may be attributed to the augmentation of the mean reverse flow velocity as well as lowering of the Reynolds number (due to increase in viscosity arising from temperature increase from combustion), which promotes recirculation. Additionally, while the peak annular jet velocity around the IRZ is similar in magnitude to the isothermal case, there is a marginal increase its value beyond the rear stagnation zone; the dilatation of the flow arising from heat release and thermal expansion, coupled with wall confinement causes the flow to accelerate in the downstream section near the walls.

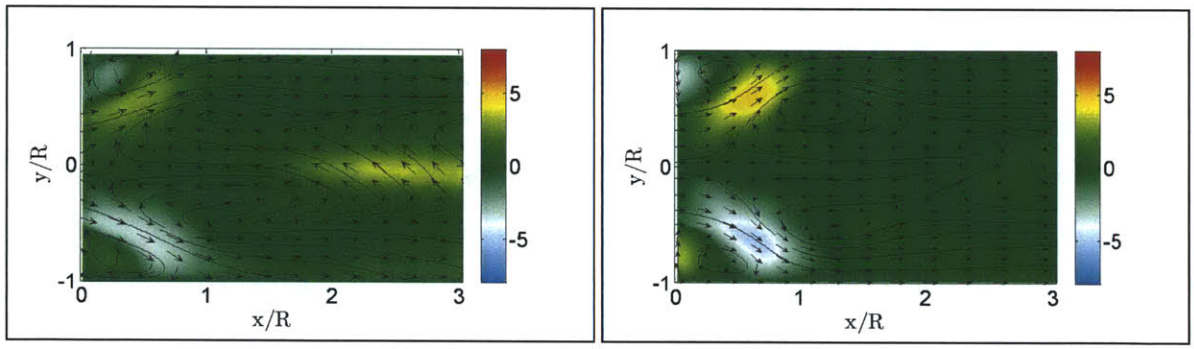

Figure 6.25: Average radial velocity along with the 2D velocity vectors and streamlines (PIV: left, LES: right).

Moreover, the annular jet thickness and the spreading angle of the shear layers are comparable to that observed in the cold flow, resulting in topologically similar recirculation zones (figure 6.25). This is due to the flame stabilizing further downstream, which enables the flow upstream to evolve in a manner similar to that in the isothermal scenario. Consequently, the flow-field fluctuations also show similar level of intensity as in the non-reacting case.

In figure 6.26, the contours for the rms axial velocity fluctuations are shown indicating high turbulence activity in the shear layers, especially in the locations corresponding to the existence of the PVC, and at the axial location corresponding to the maximum IRZ width, where the jet

impinges the wall. The fluctuations in the flow are also high within the IRZ, around the centerline, where the presence of the flame base (consisting of localized flamelets) contributes to turbulence anisotropy.

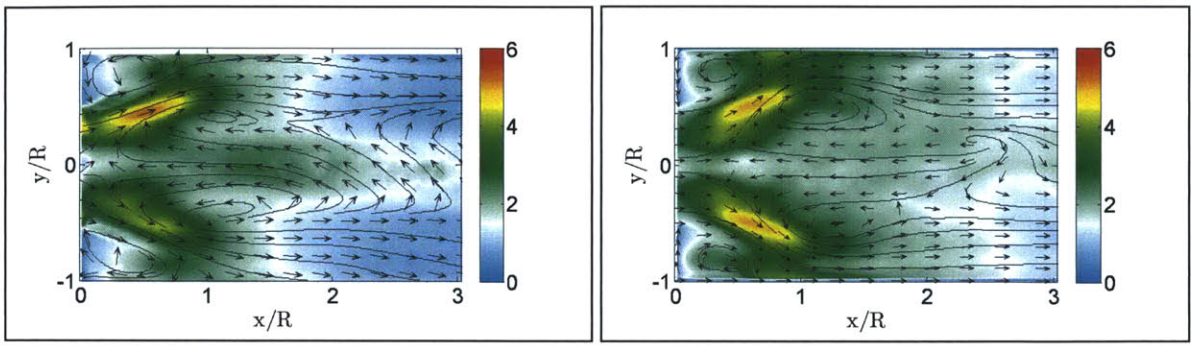

Figure 6.26: rms axial velocity along with the 2D velocity vectors and streamlines (PIV: left, LES: right).

Further downstream, however, turbulence anisotropy is significantly suppressed due to effects of dissipation, and dilatation, which dominates in the presence of wall confinement. Fluctuation intensity is, however, slightly higher in magnitude, relative to the non-reacting scenario, as a result of combustion induced turbulence. The viscous dissipation per unit volume, and dilatation, which influence the flame structure and the flow field significantly, are shown in figure 6.27, where dilatation, Ψ, can be as estimated in Cartesian coordinates [6.22] as:

$$\psi = \nabla . \boldsymbol{u} = \frac{\partial u_x}{\partial x} + \frac{\partial u_y}{\partial y} + \frac{\partial u_z}{\partial z} \qquad (6.2)$$

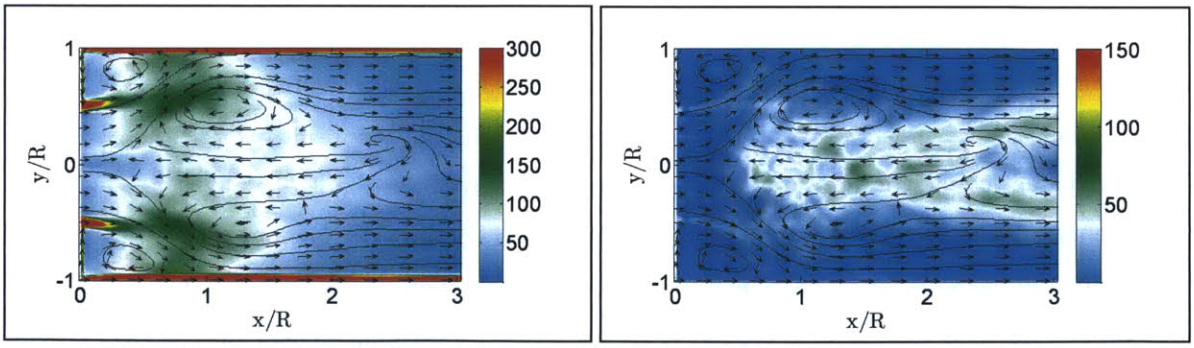

Figure 6.27: (a) Viscous dissipation per unit volume (kg/ms^3), (b) Turbulent dilatation (1/s). The corresponding 2D velocity vectors and streamlines are also shown (LES).

In figure 6.28, the contours for the rms radial velocity and the Reynolds stress tensor term are depicted, suggesting high turbulence fluctuations in the section immediately downstream of the expansion plane. The aerodynamic blockage caused by the IRZ causes a radially outward deflection

of the separation streamlines at the edge of the ISL which results in squeezing of the annular gaseous jet towards the chamber walls. Consequently, this shifts the initial shear turbulence production radially outward and the turbulent kinetic energy in the region, which is primarily due to the interaction of Reynolds stress and shear strain, appears to be concentrated in the shear layer around the periphery of the IRZ, and especially near the location where the jet impinges the wall (figure 6.28a). The precessing vortex and the swirling turbulent flow also contribute to turbulence intensity in this upstream section. Additionally, there is enhanced flow fluctuation within the IRZ, brought about by the local flame perturbations, and near the rear stagnation zone as well, where flow reversal and mixing takes place; the incoming reactants mix intensely with the hot products, typically generating substantial flow field fluctuation, as well as scalar field (temperature, density) oscillation (figure 6.20).

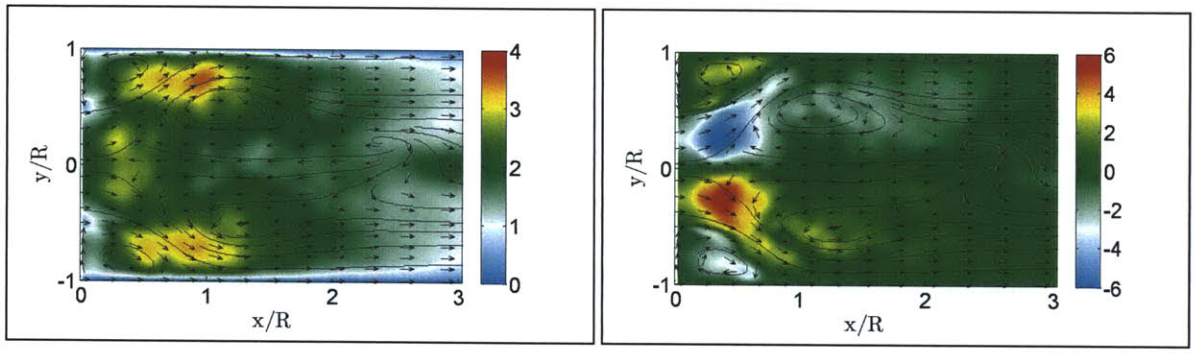

Figure 6.28: (a) rms radial velocity (u_r', m/s), (b) Reynolds stress tensor term ($u_r'u_x'$, m^2/s^2). The corresponding 2D velocity vectors and streamlines are also shown (LES).

In figure 6.29, the normalized profiles for the average axial velocity and rms axial velocity, comparing the numerical predictions with the experimental data at different cross sections in the wake region, are shown. The peak annular jet velocity and the radial spread of the shear layers are predicted quite accurately in the simulations, and the thickness of the annular jet closely matches the experimental measurements as well. The flow is squeezed towards the chamber walls due to the presence of the recirculation zone, which eventually results in high axial velocity in the region. The magnitude of the peak reverse axial velocity is also observed to be slightly higher than the isothermal case, due to exothermicity. As regards the turbulence generation, it peaks in the shear layers, as a result of the vortex shedding activity and due to the presence of a strong precessing vortex; immediately downstream of the expansion plane, the turbulence intensity is similar to that for the cold flow and is suitably resolved numerically. Slightly further downstream, flow field fluctuations peak near the walls, where the accelerated annular jet impinges the wall. Turbulence is also high

around the centerline axis near the rear stagnation zone ($x/R \approx 2$). As mentioned before, this can be associated with flow reversal that takes place in the region, coupled with the acceleration of the flow as the streamlines curve towards axial location and intense mixing of the cold reactants with the hot gaseous mixture take place. The presence of the flame, which locally stabilizes in the proximity of the region, thus appears to contribute to the anisotropy of turbulence.

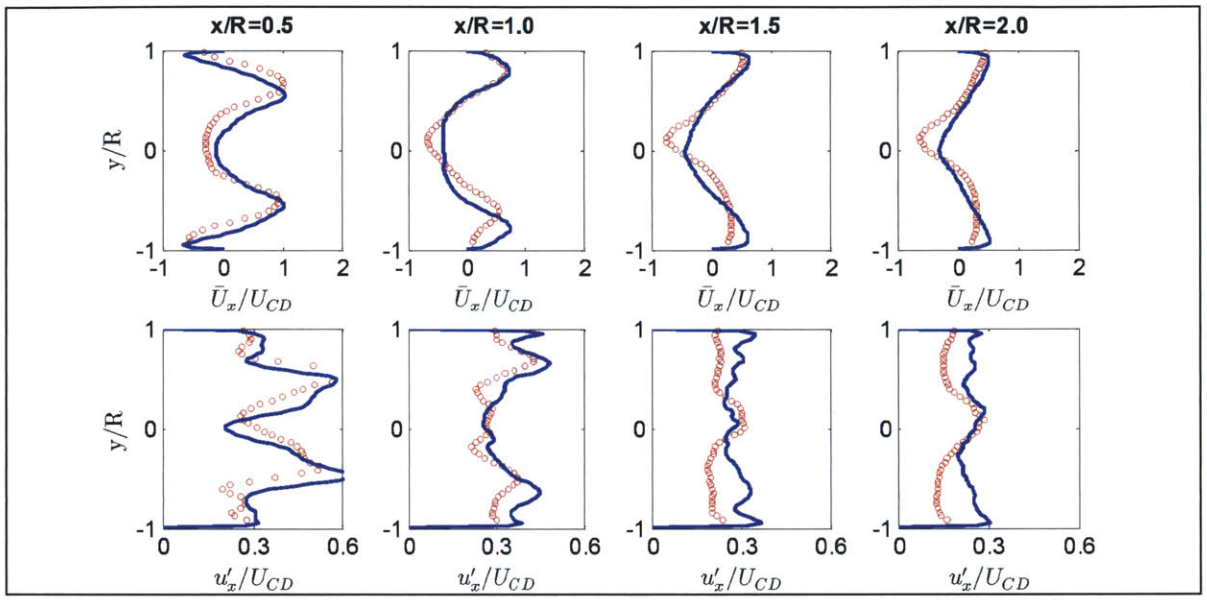

Figure 6.29: Normalized profiles for average axial velocity (top) and rms axial velocity (bottom). ooo PIV, — — — LES

Further downstream (not shown in figure 6.29), where a strong tubular flame exists, the relative effect of turbulent dilatation on the flow field increases, especially in the presence of confinement, resulting in acceleration of the fluid. The combustion induced turbulence also results in enhancing the flow fluctuation intensity, especially around the columnar reaction zone region, in contrast to the isothermal flow. These flow-field features are suitably resolved numerically, although the predictions could be further improved by appropriate mesh resolution near the walls. Adjustments to the PIV setup for the collection of higher resolution flow fluctuation data in downstream locations may also be performed.

6.2.5.2 Configuration I: PIV DMD Analysis

As mentioned in Chapter 5, the DMD framework serves as an effective tool for the analysis of dynamic flow features, and can extract valuable dynamic information from flow fields that are either measured in a physical experiment, or generated by numerical simulations. The method decomposes

the patterns in the data on the basis of frequency content and therefore has some distinct advantages over the conventional POD approach.

In figure 6.30, the results of the DMD analysis of the experimental flow field measurements are presented. The PIV data is sampled at a frequency of 1000Hz, and the analyzed flow field is comprised of the axial and radial velocity components of the velocity vector (i.e $\boldsymbol{V} = [u_x; u_r]$) corresponding to 400 snapshots taken at equal time intervals. The selection of modes is based on the frequencies of interest as determined in the experiments. The real and imaginary parts of the Ritz values, sized by the energy of the mode, are depicted in figure 6.30a, along with the modal frequency (ω) and growth rate (σ) in figure 6.30b. The Ritz values for all of the most energetic modes lie near the unit circle, indicating neutral stability.

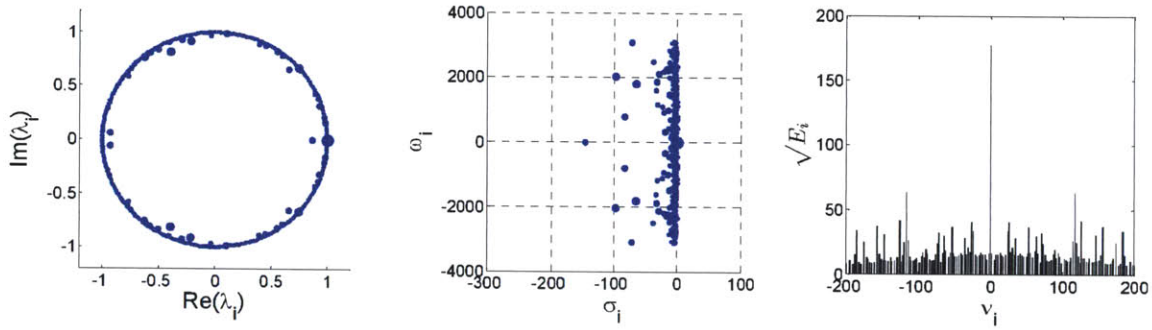

Figure 6.30: (a) Ritz vectors on the complex plane, (b) Frequency, ω, and growth rate, σ, of dynamic modes, (c) Energy content of dynamic modes.

As noted previously (figure 6.22), the Fourier transform of the velocity signal at a point located within the vortex breakdown bubble suggests that the flow regime is dominated by strong fluid dynamic instabilities leading to large flow oscillations. In conjunction with these observations, the energy spectrum shows that apart from the mean mode, the most intense DMD mode corresponds to a frequency ($\upsilon = \omega/2\pi$) of 120 Hz (figure 6.30c), associated with the precessing of the vortex core. A lower energy mode in 30Hz range is also observed that presumably relates to the frequency of swirling flow's advection around the centerline.

In figure 6.31, the vorticity contours for the real and imaginary parts of the mode that corresponds to the mean flow pattern are shown, along with the FFT analysis of the temporal coefficients corresponding to the real component of the dynamic mode. As expected, the primary and secondary recirculation vortices, along with the inner and outer shear layers, are suitably highlighted, and dominate the average flow field.

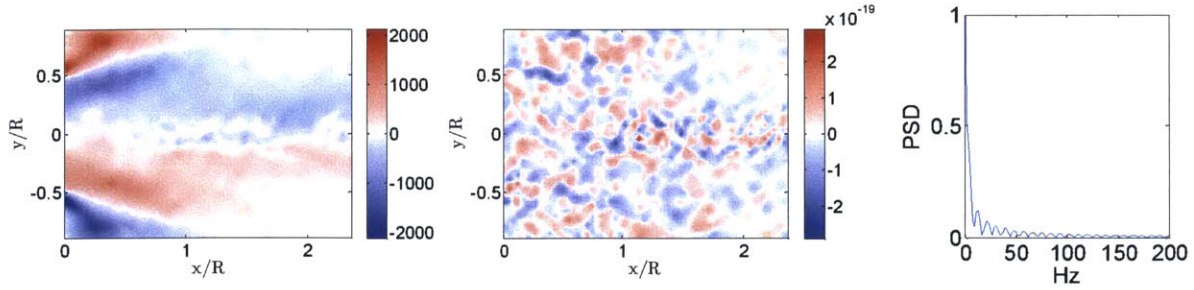

Figure 6.31: 0Hz dynamic mode (Real component: left, Imaginary component: middle, Frequency spectrum of temporal coefficient of real component of dynamic mode: right).

Likewise, vorticity contours for the real and imaginary components of the 120 Hz mode are depicted in figure 6.32, indicating the presence of a vortex field influenced by the PVC. The mode corresponds to changes in the radial velocity near the front stagnation zone and in the outer and inner mixing layers, with the flow dynamics associated with limit cycle oscillations due to flow global instability (corresponding to the PVC).

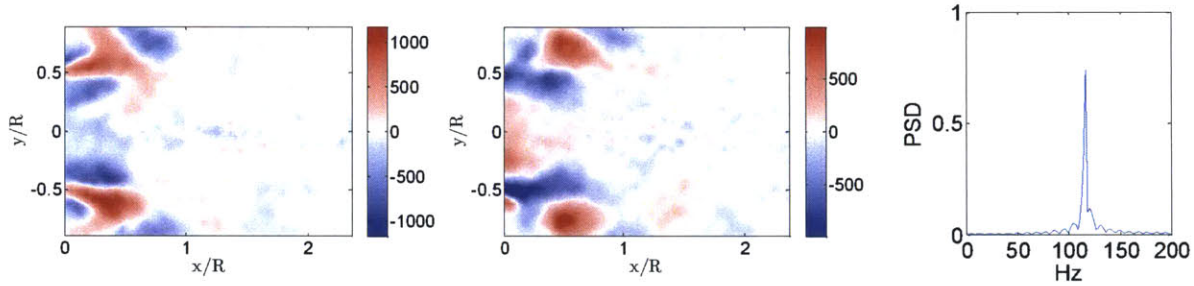

Figure 6.32: 120Hz dynamic mode (Real component: left, Imaginary component: middle, Frequency spectrum of temporal coefficient of real component of dynamic mode: right).

In figure 6.33, the phase-shifted realizations of the dynamic mode are shown, and are composed of the real and imaginary parts of the Ritz vectors, as outlined in equation (5.12). The vorticity field can be attributed to the development of the flow corresponding to precession of the vortex core; the flow structures are observed to have the same rotation, giving rise to a symmetric vorticity field about the central axis of the combustor, as also noted in [6.23].

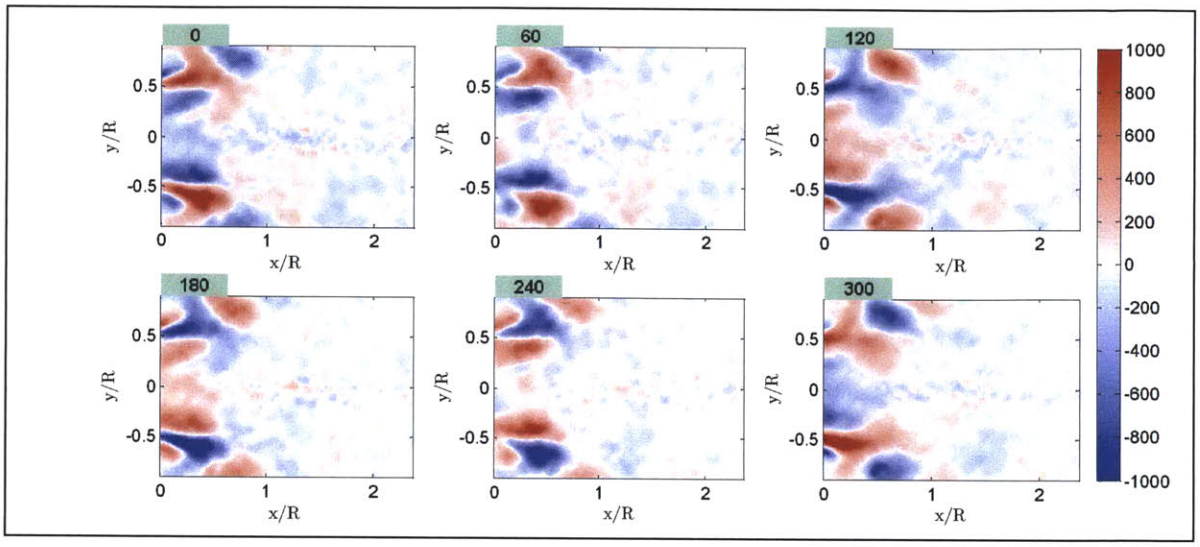

Figure 6.33: Phase shifted realizations of 120 Hz dynamic mode composed of the real and imaginary components along with their temporal coefficients.

6.2.5.3 Configuration I: LES DMD Analysis

The DMD framework can also be particularly useful to evaluate the accuracy of the LES solvers in predicting the dynamic characteristics of combustion systems as experimentally observed, by comparing the modes obtained from numerical and experimental data samples respectively. In other words, quantitative comparisons of the sizes and shapes of the unsteady modes obtained from simulations and from experiments respectively can lead to clearer assessment of the strengths and weaknesses of the numerical framework in order to reproduce the measured dynamics.

Next, the DMD modes from analysis of the LES flow field data (200 snapshots) are presented, and are noted to closely correspond with the modal structures obtained using the experimental PIV measurements.

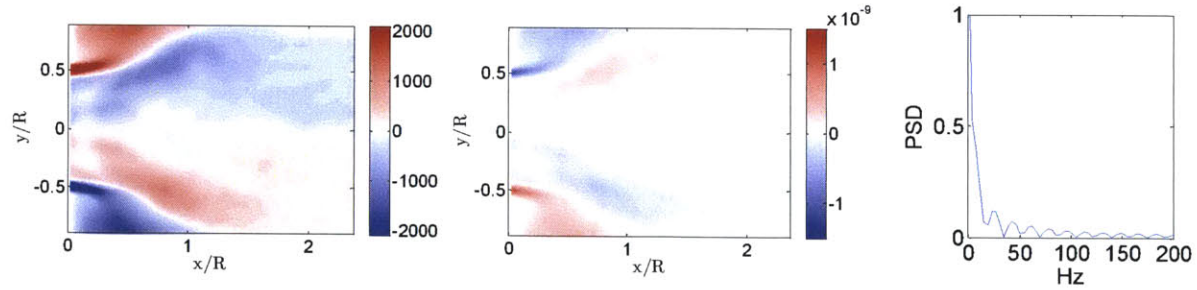

Figure 6.34: 0Hz dynamic mode (Real component: left, Imaginary component: middle, Frequency spectrum of temporal coefficient of real component of dynamic mode: right).

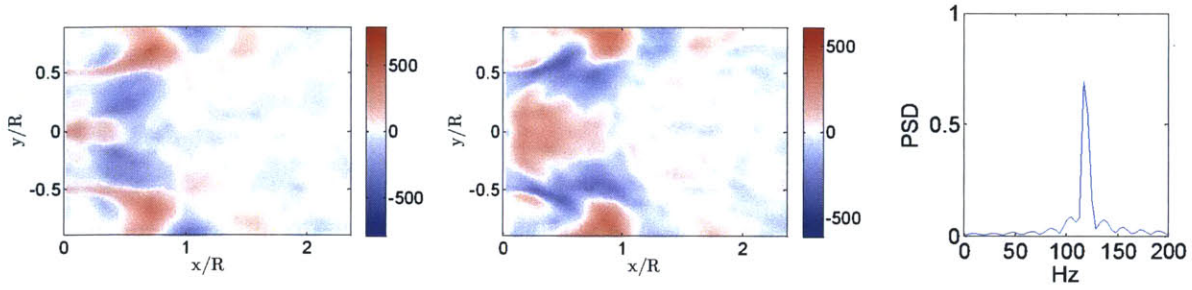

Figure 6.35: 120Hz dynamic mode (Real component: left, Imaginary component: middle, Frequency spectrum of temporal coefficient of real component of dynamic mode: right).

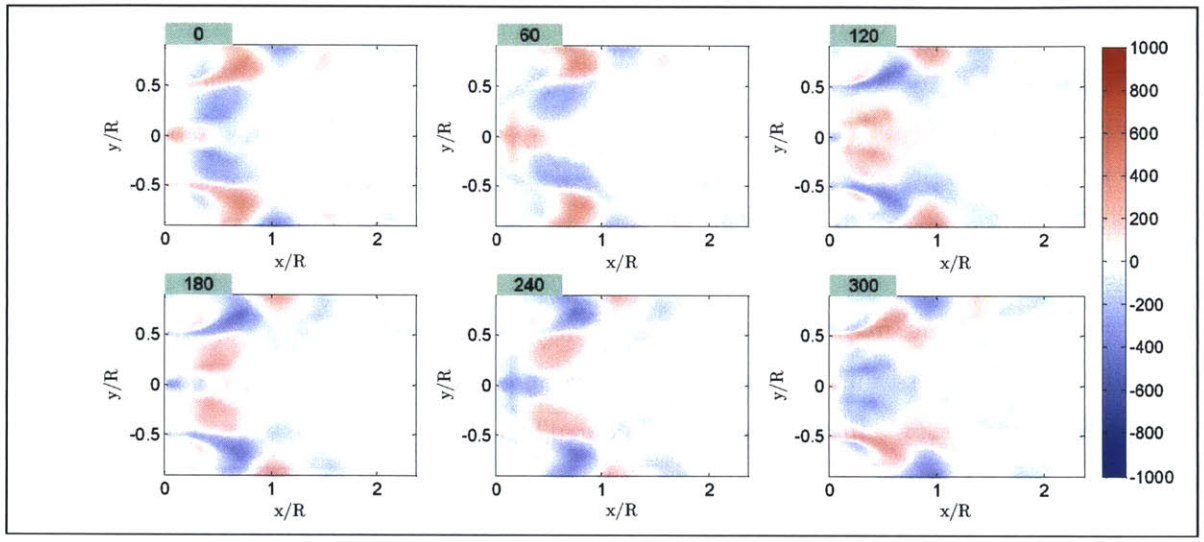

Figure 6.36: Phase shifted realizations of 120 Hz dynamic mode composed of the real and imaginary components along with their temporal coefficients.

6.2.5.4 Configuration II: LES Analysis

The CH chemiluminescence and Abel-transformed flame images for flame configuration II, displayed in figure 6.37, indicate the presence of a diffuse bubble-type flame front in the wake region, which is primarily confined to the interior of the IRZ. With an increase in equivalence ratio, and the corresponding rise in burning velocity and extinction strain rate, the flame brush begins to propagate into the ISL, with the experiment suggesting that the weakly burning average reaction zone moves upstream of the expansion plane, into the inlet pipe. The combustion process continues around the IRZ periphery, forming a conical flame front, which subsequently 'necks' near the rear stagnation zone, thereby taking the shape of a bubble-type macrostructure. The reaction zone continues into the exhaust tube, forming a tubular structure in this downstream section, as observed in Configuration I, which is significantly longer than the compact flame envelope noted for

configurations III and IV (figure 6.14).

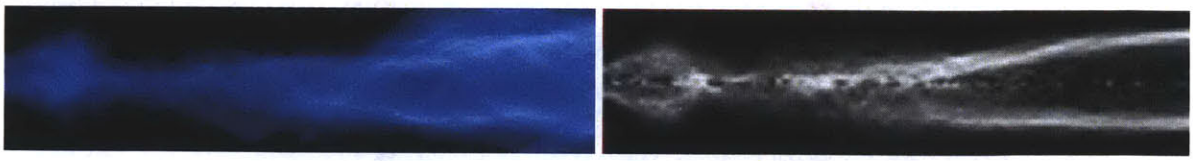

Figure 6.37: (a) Time resolved flame from CH chemiluminescence image, (b) Abel-transformed flame image.

The instantaneous LES contours for the normalized heat release and temperature are depicted in figure 6.38, indicating a wrinkled flame surface that stabilizes slightly downstream of the expansion plane, in the central wake structure that exhibits internal stagnation points and low velocity regions. The reaction, on average, does not appear to propagate into the inlet pipe, although the 'radially outward spread' of the flamelets does increase, in contrast to Configuration I, and the flamelets also show a presence in the inner shear layer. This suggests that the simulations correspond to a flame macrostructure that is still in transition between the two experimentally observed Configurations (I and II). Due to practical considerations, the exact value of the equivalence ratio at which flame macrostructure transitions completely may differ slightly between the experiments and simulations. Nevertheless, the results from LES corresponding to the equivalence ratio considered in the laboratory setup for Configuration II are presented here.

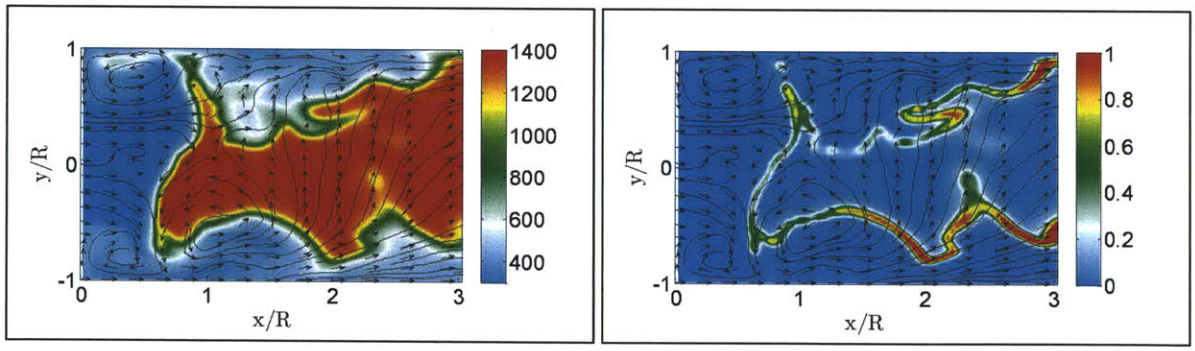

Figure 6.38: (a) Instantaneous temperature (K), (b) Instantaneous normalized heat release. The corresponding 2D velocity vectors and streamlines are also shown (LES).

As noted in experiments, the flame is now able to overcome the high strain environment in the upstream region, as a consequence of the increased extinction strain rate limit and turbulent burning velocity, and persists in the ISL, although the reaction zone is absent in the ORZ or in the high strain OSL region. The swirl induced turbulence as well as the transient eddies in the shear layers also promote mixing between the reactant mixture and combustion products (within the IRZ) and play a prominent role in stabilizing the flame; the penetration of the inner layers of the reaction

zone by small eddies causes the reaction rate to be strongly affected by turbulence while heat diffusion from the inner layers towards the preheat zone is significantly enhanced, stabilizing the flame in this upstream region.

Thus, the instantaneous flame surface is thin and wrinkled, with regions of local extinction, as the flamelets begin to intermittently propagate into the ISL. Near the front stagnation zone, reaction kinetics play a signifcant role in characterizing the flame front and appreciable scalar oscillations are observed in the region surrounding the IRZ, where the flame brush locally stabilizes. Eventually, a thick, average reaction zone is formed, with a broader radial span than observed in Configuration I. Additionally, the average reaction front propagates further upstream into the ISL, with both experimental measurements and numerical predictions (to a lesses extent) also suggesting appreciable heat release within the IRZ around the centerline (figure 6.39).

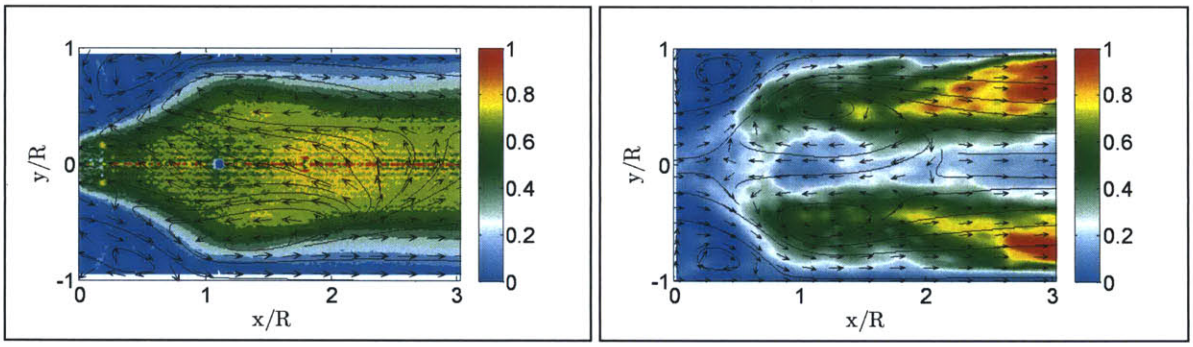

Figure 6.39: (a) Normalized deconvolved CH chemiluminescence intensity, (b) Average normalized heat release (LES). The corresponding 2D velocity vectors and streamlines are also shown.

As the eddy structures are carried downstream through the mixing layer, they begin to grow in size, forming as folds around the flame edge, resulting in a convoluted reaction zone in the region, as suggested by the instantaneous CO mass fraction contour in figure 6.40. Near this location, the impingement of the annular jet with the chamber wall also generates turbulence and the augmented mixing promotes combustion, thereby increasing the flame intensity.

In the vicinity of the rear stagnation point, the flow field, comprising of isolated pockets of hot-product and cold-reactant gas, is characterized by flow reversal and mixing events that contribute significantly to flame stabilization. The high turbulence in the region decreases mixing time and increases entrainment between the fresh mixture and the flame, ie the flame loading is increased and the reaction zone is thickened as well. However, the flow accelerates significantly in the annular region around the periphery and a strong flame is unable to persist in the combustor section; owing to the high flow velocities in the region (due to wall confinement along with flow

acceleration) and moderate strained flame propagation speed, the flamelets are concentrated towards the low velocity rear stagnation zone, forming a bubble-type flame macrostructure.

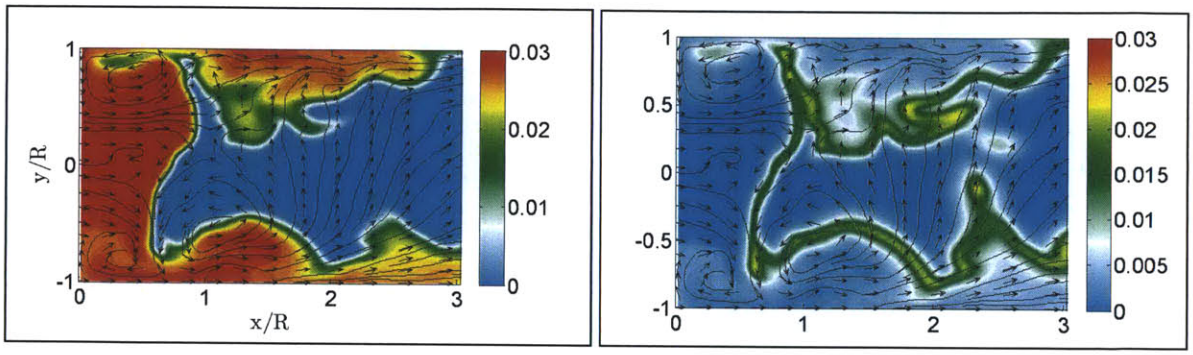

Figure 6.40: (a) Instantaneous CH_4 mass fraction, (b) Instantaneous CO mass fraction. The corresponding 2D velocity vectors and streamlines are also shown (LES).

This flame behavior is somewhat evident from the instantaneous contours for the CO mass fraction at different time instants, shown in figure 6.41. Additionally, no flame is observed within the OSL, as well as the ORZ, as also evident from the temperature contours in figure 6.42. For the present scenario, the flame does (partially) propagate upstream into the ISL, as suggested by the rms temperature contours; however, a persistent strong flame in the region is not observed in the simulations. Subsequently, as the flow convects further downstream, toward the exhaust duct, the combustion process continues, resulting in a tubular reaction zone that is predominantly shaped due to dilatation and transport effects. The thickened flame in the region is dominated by the mixing and entrainment process, and resembles the columnar flame front noted in Configuration I; however, a more intense reaction zone and a larger radial spread is observed, due to the increased heat loading.

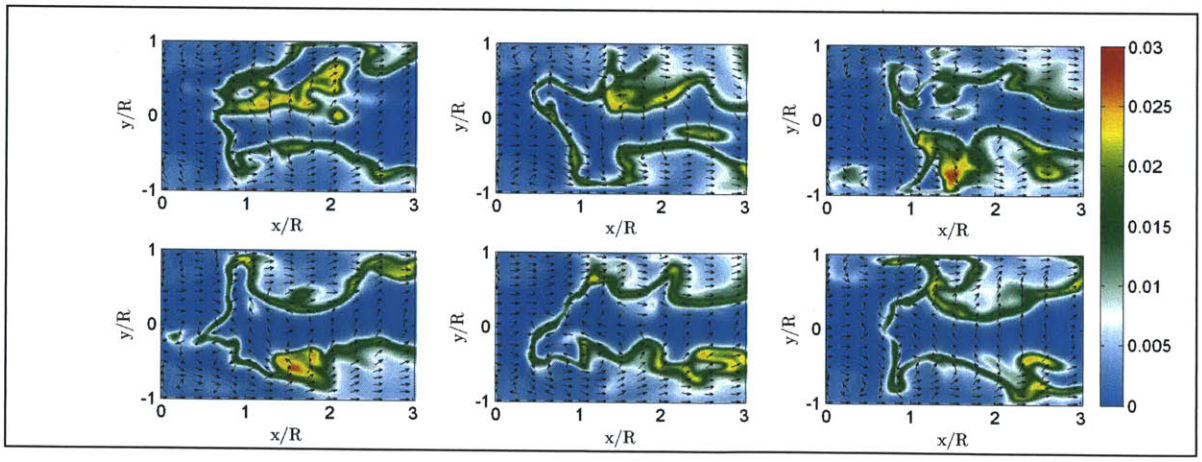

Figure 6.41: Instantaneous CO mass fraction at different time-instants, with the corresponding 2D velocity vectors (LES).

The equivalence ratio, therefore, significantly influences the flame shape: with a further increase in its value, the higher flame speed results in propagation of the reaction zone along the inner shear layer into the inlet pipe, with the flame anchoring on the swirler body. In the downstream section, the reaction front cuts across the annular jet as well, thereby resulting in a high intensity, conical flame macrostructure corresponding to Configuration III. Conversely, a reduction in equivalence ratio results in the formation of a 'lifted' flame. It is well known that shear introduces aerodynamic straining on the flame, which alters the local temperature and burning rate. If the shear rate and consequent flame strain rate is large, the flame locally extinguishes and either stabilizes at another location, by transitioning across configurations, or blows out of the combustor completely. While for φ=0.51, the above phenomena results in a 'suspended' flame stabilizing near the low velocity region in the recirculation zone, flame blow-off is noticed for leaner mixtures (φ<0.47). The blow-off phenomenon typically also occurs because a decrease in equivalence ratio causes an increase in the magnitude of adverse pressure gradient and the Reynolds number. Therefore, the entrainment of cold reactants in the reaction zone downstream is enhanced, causing flamelet extinction, and a further increase in adverse pressure gradient and subsequent entrainment. Eventually, the flame in the preheat-ignition region gets quenched and blows off.

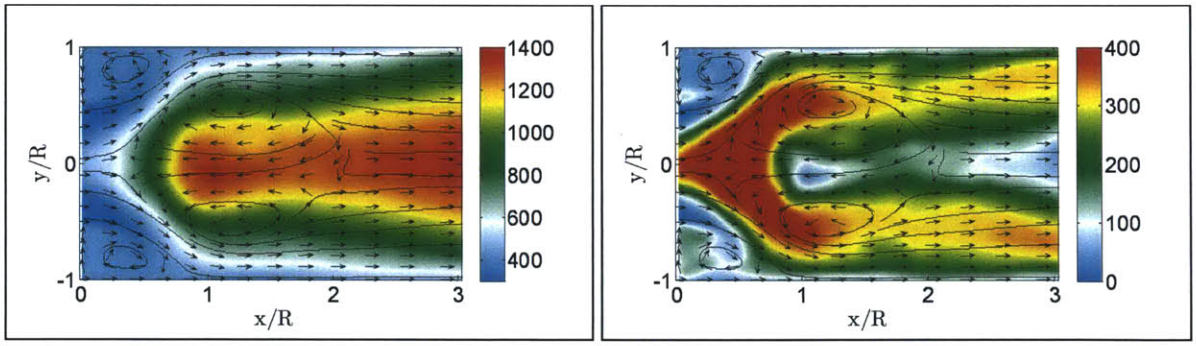

Figure 6.42: (a) Average temperature (K), (b) rms temperature (K). The corresponding 2D velocity vectors and streamlines are also shown (LES).

Next, in figure 6.43, LES contours of the average vorticity magnitude and instantaneous out-of-plane vorticity are depicted, along with the respective streamlines. Significant vortex activity is observed in the ORZs, due to the swirling nature of the flow, and in the ISL as it surrounds the IRZ, due to the shed vortices. Furthermore, the average vorticity contours suggest appreciable vortex activity along the centerline, in the downstream section near the rear stagnation region, as also noted in case of Configuration I. The vorticity is however reduced near the walls in this

downstream region, where dilatation effects appear to dominate significantly, especially in the presence of wall confinement.

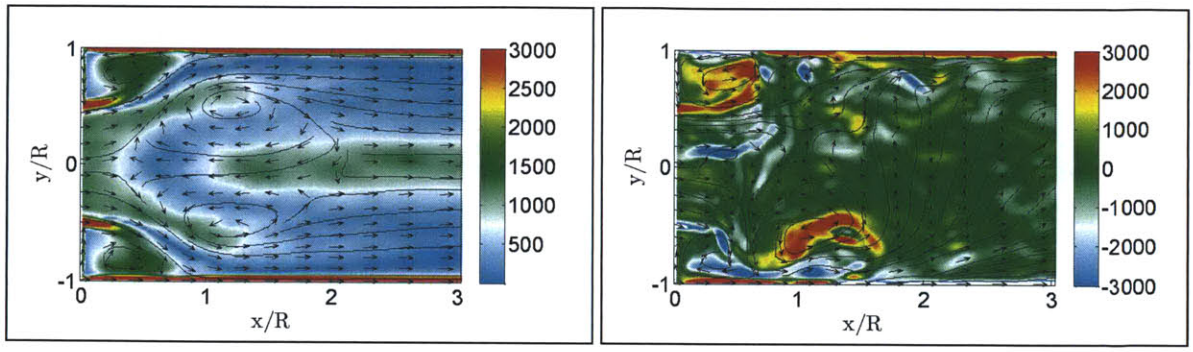

Figure 6.43: (a) Average vorticity magnitude (1/s), (b) Instantaneous out-of-plane vorticity (1/s). The corresponding 2D velocity vectors and streamlines are also shown (LES).

Additionally, a significantly weaker PVC is observed (figure 6.44), as indicated by the FFT analysis of the signal of the radial velocity component downstream of the sudden expansion (x = 0.013 m, r = -0.010 m, z = 0.000 m). Thus, the relative contribution of the PVC to the observed vorticity field in the region is marginal, in contrast to Configuration I. This suppression of the PVC strength might be associated with the propagation of the flame brush into the ISL and subsequent heat release and thermal expansion; the phenomenon is more pronounced as the equivalence ratio further increases (Configurations III, IV).

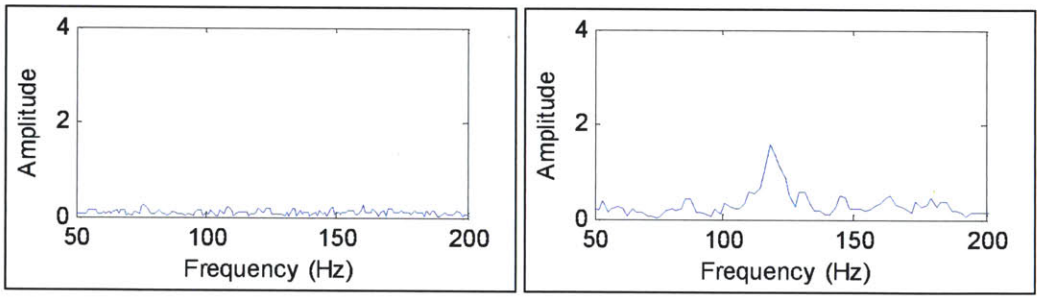

Figure 6.44: FFT analysis of radial velocity component signal (PIV: left, LES: right).

In figure 6.45, the instantaneous out-of-plane vorticity contours are shown at different time-instants, indicating significant vorticity in the shear layers, due to the convective vortices. However, the reduction in adverse pressure gradients and the Reynolds number due to appreciable heat release in this upstream section might be responsible in reducing the eddy development in the shear layer. Further downstream, the breakdown of the coherent structures, due to heat release and thermal expansion in the vortex cores, results in a diffuse out-of-plane vorticity field. The small-scale eddies subsequently dissipate due to vortex stretching and viscosity effects, as the flow convects towards

the exhaust; coupled with the effects of dilatation, this results in reducing the out-of-plane vorticity in the downstream section.

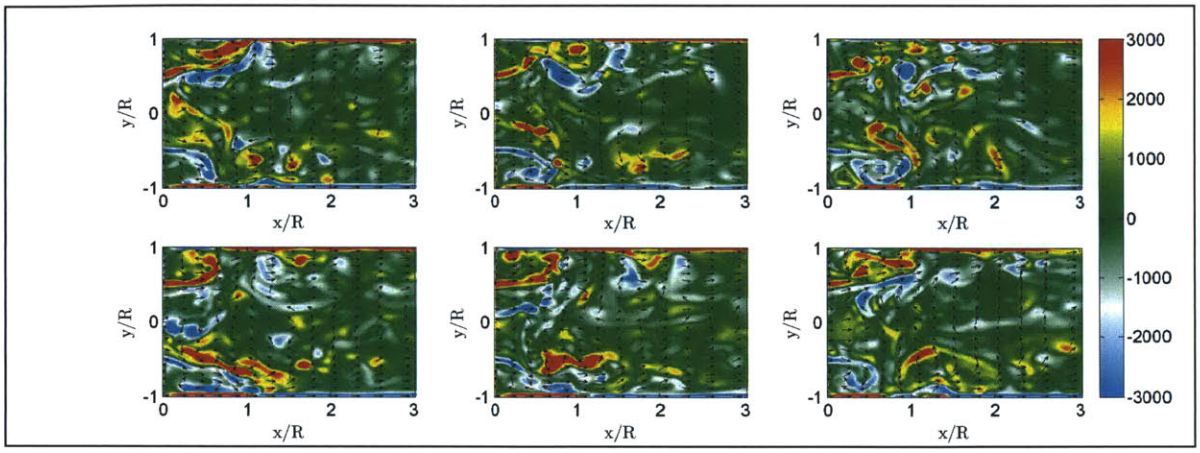

Figure 6.45: Instantaneous out-of-plane vorticity (1/s) at different time-instants, with the corresponding 2D velocity vectors (LES).

In figure 6.46, the contours of the average axial velocity, obtained experimentally and numerically, are depicted along with the corresponding streamlines. The cross-sections at which numerical and experimental data are compared are also shown. Topologically, the flow field, measured in experiments, differs from that observed in Configuration I, in terms of the size of the IRZ, and the thickness of the annular jet; the ORZ consists of a small vortex ring, as observed in the previous scenario.

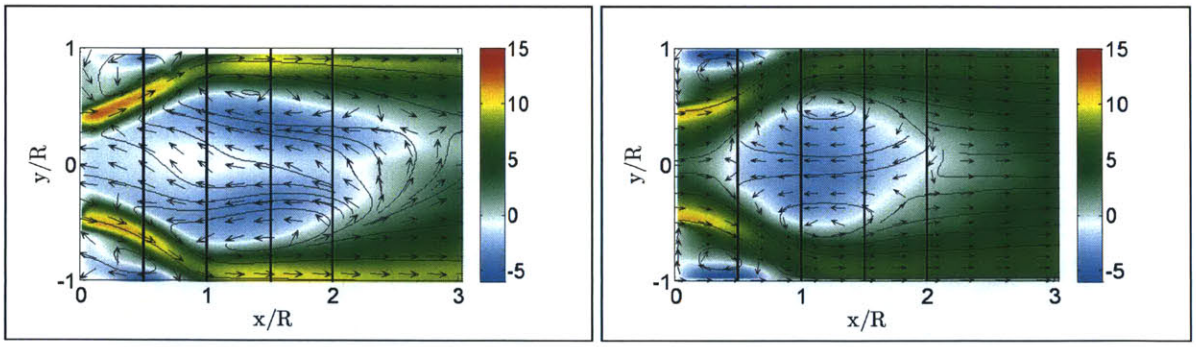

Figure 6.46: Average axial velocity along with the 2D velocity vectors and streamlines (PIV: left, LES: right). The cross-sections at which data are compared are also shown.

In contrast to Configuration I, experimentally, the vortex breakdown bubble appears to have a somewhat toroidal, yet single-cell type IRZ, which extends upstream of the expansion plane. Further, a closed recirculating vortex structure is formed, and the thin reverse velocity region which extended further downstream in case of the columnar-wake flame, is no longer present. The IRZ

now extends to a length of approximately *3.0R*, and is also broader. This may be attributed to the acceleration of the flow through the combustor, together with restriction of significant mean streamline curvature by the confining walls, which causes the flow to better overcome the adverse pressure gradients [6.11, 6.24]. Coupled with a gradual dissipation of momentum in the wake region, an elongated IRZ is formed, which also widens radially, presumably due to the presence of the reaction zone within the IRZ.

Furthermore, the reverse centerline velocity briefly reduces in magnitude in the core of the IRZ ($x/R \approx 1$), nearly approaching a positive value, which would result in the formation of a split-cell type recirculation zone. While this could perhaps be due to the presence of the flame in the vicinity of the region, further examination of the flow-field is required to elucidate the underlying physics behind the development of this flow structure. Note that the numerical simulations do not predict the presence of this flow feature, and under-predict the expansion in size of the IRZ. While LES is able to capture the difference in the topological flow features with the transition in the flame structure (to an extent), some quantitative differences from experimental measurements exist, as mentioned earlier, due to practical considerations.

Observing the mean streamlines in figure 6.47, it is noted that the annular jet thickness and the spreading angle of the shear layers are also different for Configuration II; on average, the spreading angle of the streamlines is enhanced, corresponding with the broadening of the IRZ. Also, due to the interaction of the flame brush with the incoming flow, the axial jet velocity increases, as a result of exothermicity and gaseous expansion. The jet thickness is also noted to be lower, while a similar sized ORZ, as observed in Configuration I, is formed. The growth of the shear layer eddies appears to be suppressed, due to heat release, as well as reduction in the adverse pressure gradients and the Reynolds number (which lowers entrainment and development of the mixing layer).

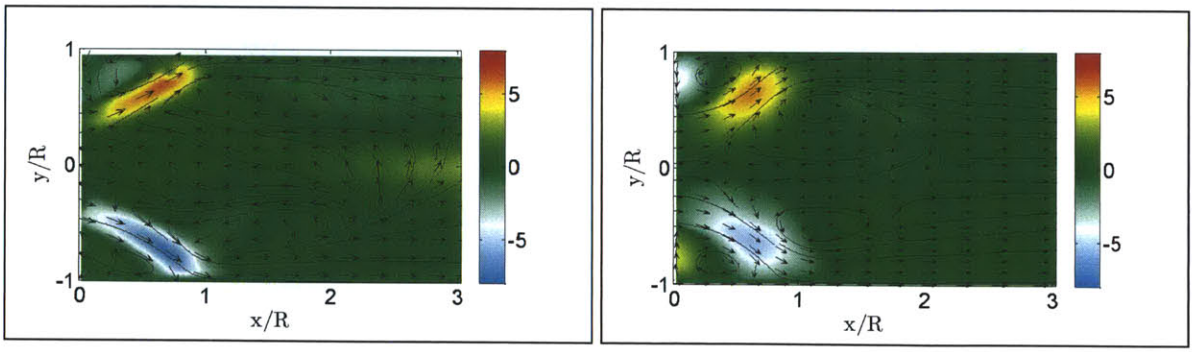

Figure 6.47: Average radial velocity along with the 2D velocity vectors and streamlines (PIV: left, LES: right).

In figure 6.48, the contours for the rms axial velocity fluctuations are shown, indicating a marginal reduction in small-scale turbulence within the mixing layer, near the expansion plane. The absence of a strongly precessing vortex structure, along with heat release and reduction in the Reynolds number, results in a slight lowering of the turbulence intensity in the shear layers. Additionally, the influence of dilatation and viscous dissipation (figure 6.49) on the flow field fluctuation is relatively stronger than the effect of combustion induced turbulence, resulting in a moderate level of flow perturbations in the region.

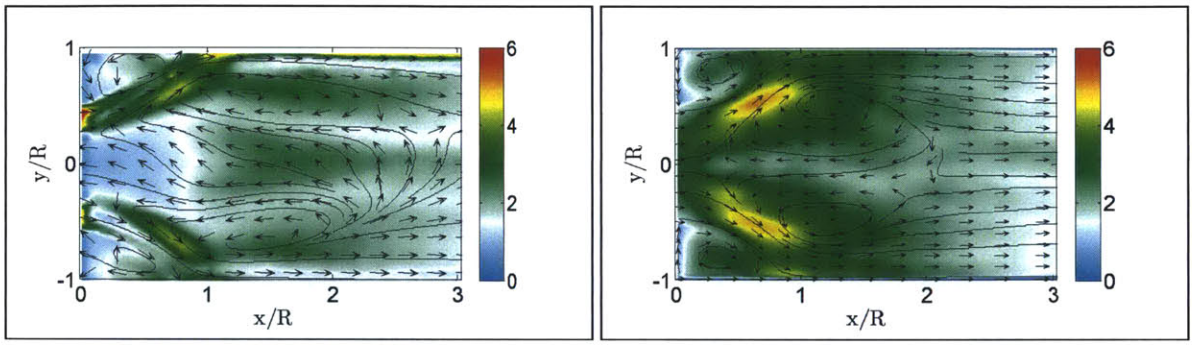

Figure 6.48: rms axial velocity along with the 2D velocity vectors and streamlines (PIV: left, LES: right).

Turbulence intensity in the axial flow is fairly high within the IRZ, where the presence of local flamelets can cause flow distortions. Besides, axial velocity fluctuations are also significant near the axial plane of maximum IRZ width (due to the annular jet impinging the wall), and near the location corresponding to the 'necking' of the flame (due to flow reversal and acceleration). Further downstream, the flow field fluctuations reduce in magnitude, due to the effects of dilatation, in the presence of wall confinement. However, combustion induced turbulence does result in a moderate level of fluctuation intensity in the region.

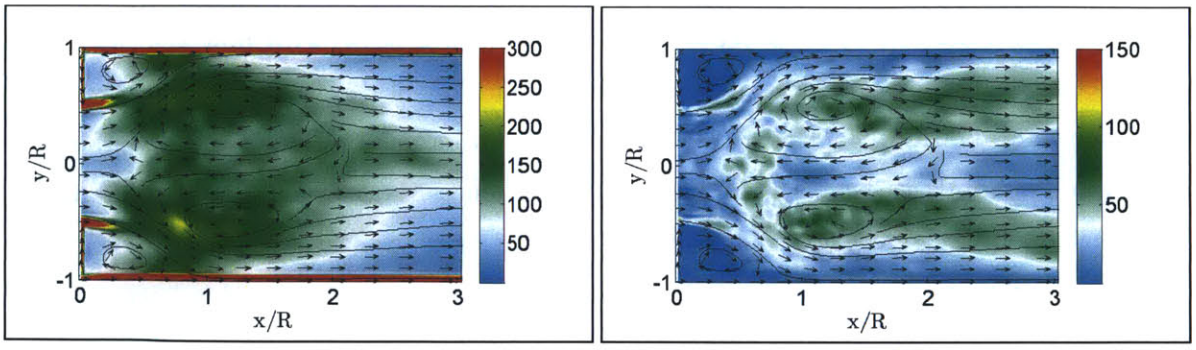

Figure 6.49: (a) Viscous dissipation per unit volume (kg/ms^3), (b) Turbulent dilatation (1/s). The corresponding 2D velocity vectors and streamlines are also shown (LES).

In figure 6.50, the LES contours for the rms radial velocity and the Reynolds stress tensor term are presented, depicting a slight reduction in the radial turbulence component within the shear layers, as compared to Configuration I. Heat release in the region, coupled with reduction in adverse pressure gradients and the Reynolds number influence the eddy development in the shear layer and somewhat suppress the entrainment process, contributing to the lower radial flow field fluctuations. However, significantly higher flow fluctuations are seen near the rear stagnation zone where flow reversal and mixing takes place; the incoming reactants from the annular jet that curves towards the centerline axis mix intensely with the hot products, generating substantial flow oscillations. Near this region, flow direction quickly reverses, the fluid parcels are stretched and strong gradients of mean and turbulence quantities are present.

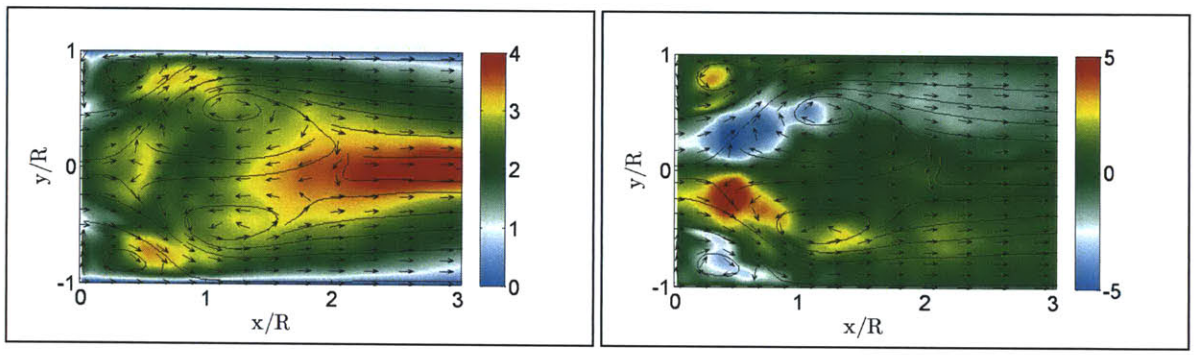

Figure 6.50: (a) rms radial velocity (u_r', m/s), (b) Reynolds stress tensor term ($u_r'u_x'$, m^2/s^2). The corresponding 2D velocity vectors and streamlines are also shown (LES).

In figure 6.51, the normalized profiles for the average axial velocity and rms axial velocity experimentally measured at different cross sections are compared with LES predictions. While the thickness and the spreading angle of the annular jet are resolved reasonably accurately, some discrepancies in predicting the radial expanse of the IRZ, and the centerline velocity inside the recirculation zone are observed. As opposed to Configuration I, higher axial flow velocity of the annular jet is noted as a consequence of the squeezing of the flow-field against the chamber wall due to broadening of the IRZ, coupled with the effects of thermal expansion. However, the turbulence intensity in the shear layer that envelops the IRZ slightly reduces, due to the damping of turbulence brought about by heat release, along with the absence of a strongly precessing vortex core. Consequently, the point-wise experimental statistics for the axial velocity indicate a lower level of fluctuation in the annular jet immediately downstream of the expansion plane, as compared to Configuration I. In the downstream section, the intensity of flow turbulence reduces due to the

influence of dilatation, though a moderate level of flow fluctuations is observed as a consequence of combustion induced turbulence.

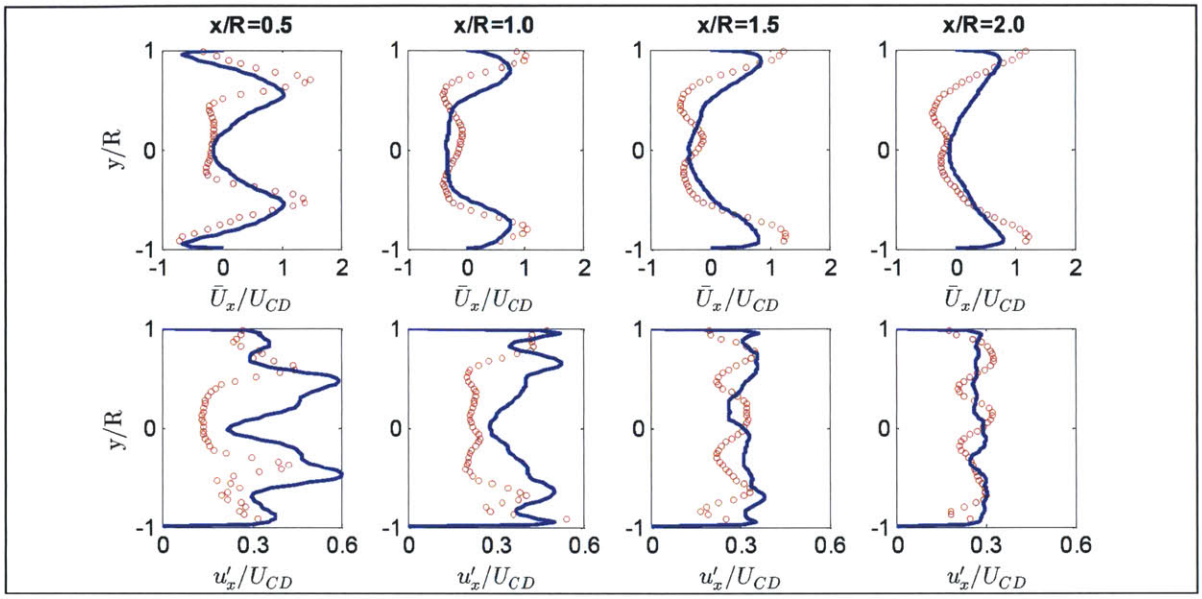

Figure 6.51: Normalized profiles for average axial velocity (top) and rms axial velocity (bottom). ooo PIV, – – – LES

It is also noted that the simulations generally predict a wider annular jet and higher shear layer fluctuations near the expansion plane ($x/R \approx 0.5$) than measured in the laboratory setup. This could be associated with the numerics not reproducing the complete flame transition behavior at the given equivalence ratio, due to practical considerations. The discrepancies could be attributed to the sensitivity of resolved flow features to geometric features in the inlet pipe, upstream flow perturbations, and the grid resolution in the boundary layer of the inlet duct [6.9]. Further improvement in the LES predictions could therefore be achieved by accurately accounting for these factors. Adjustments to the PIV setup for collection of higher resolution flow field data near the walls may also be performed.

6.2.5.5 Configuration II: PIV DMD Analysis

Next, the DMD modes from analysis of the PIV flow field are presented. Experiments indicate that the large scale motions corresponding with the precessing vortex are absent for this flow regime (figure 6.44). Consequently, the DMD analysis of the PIV data indicates the presence of the mean flow field structure as the dominant energy mode (figure 6.52c).

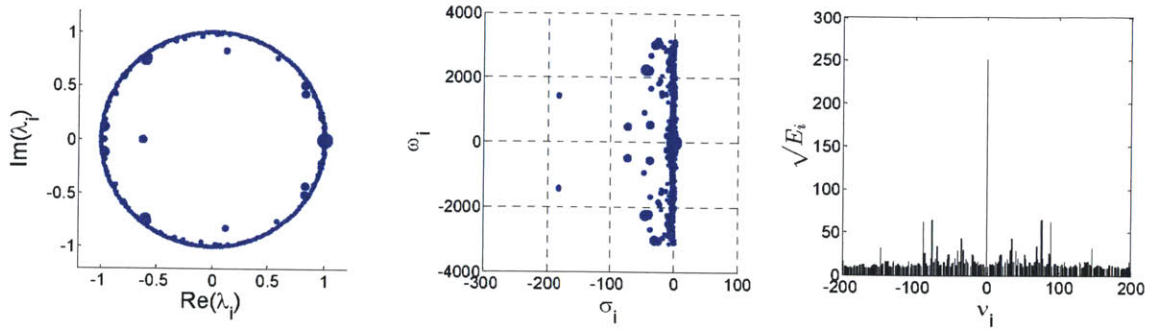

Figure 6.52: (a) Ritz vectors on the complex plane, (b) Frequency, ω, and growth rate, σ, of dynamic modes, (c) Energy content of dynamic modes.

In figure 6.53, the vorticity contours for the real and imaginary parts of the mode that corresponds to the mean flow pattern are shown, along with the FFT analysis of the temporal coefficients corresponding to the real component of the dynamic mode. As expected, the inner and outer recirculation vortices are suitably highlighted, along with the shear layers, and dominate the average flow field. The secondary, low-intensity circulation region around the centerline axis, within the core of the IRZ, is also observed.

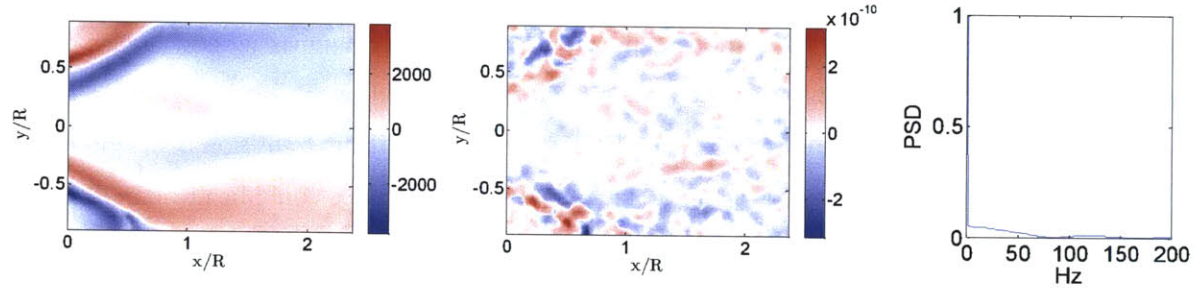

Figure 6.53: 0Hz dynamic mode (Real component: left, Imaginary component: middle, Frequency spectrum of temporal coefficient of real component of dynamic mode: right).

Aside from the mean mode, a relatively strong 30Hz mode is also observed, associated with the advection of the swirling flow, around the centerline. The vorticity contours for the mode, shown in figure 6.54, indicate that the mode is comprised of small-scale eddy structures that appear to be strongly influenced by the swirling jet, and by the flame as it is advected around the centerline. This is also evident from the phase-shifted realizations of the dynamic mode (comprising of the real and imaginary parts of the Ritz vectors) depicted in figure 6.55.

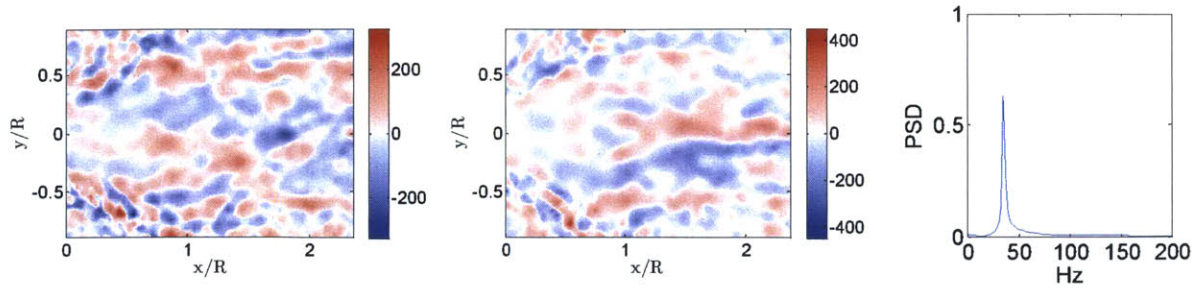

Figure 6.54: 30Hz dynamic mode (Real component: left, Imaginary component: middle, Frequency spectrum of temporal coefficient of real component of dynamic mode: right).

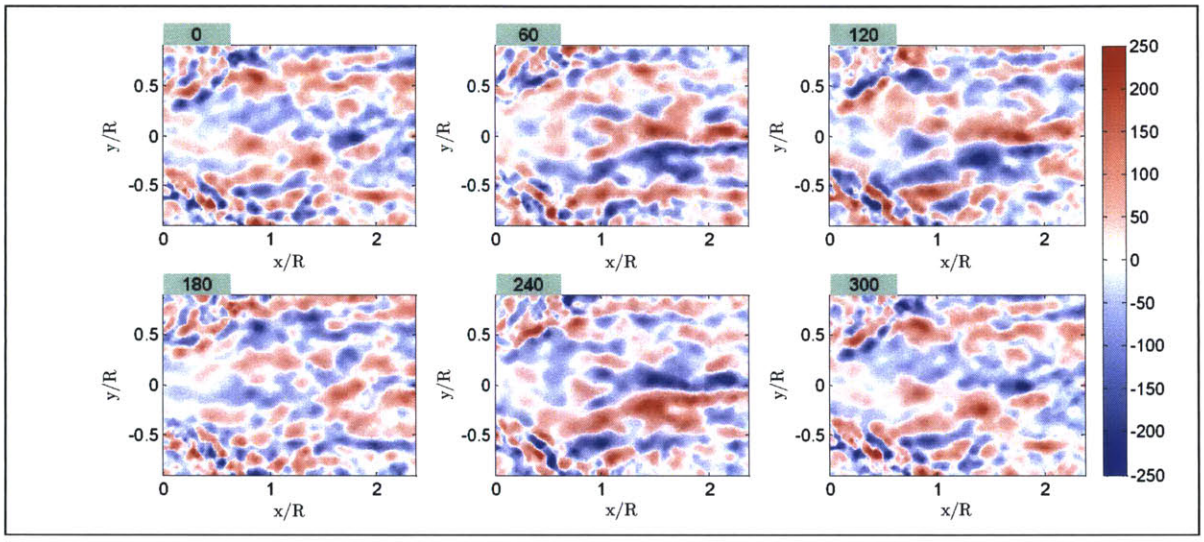

Figure 6.55: Phase shifted realizations of 30 Hz dynamic mode composed of the real and imaginary components along with their temporal coefficients.

6.2.5.6 Configuration II: LES DMD Analysis

Next, the DMD modes from analysis of the LES flow field data (200 snapshots) are presented, and correspond reasonably well with the modal structures obtained using the PIV measurements.

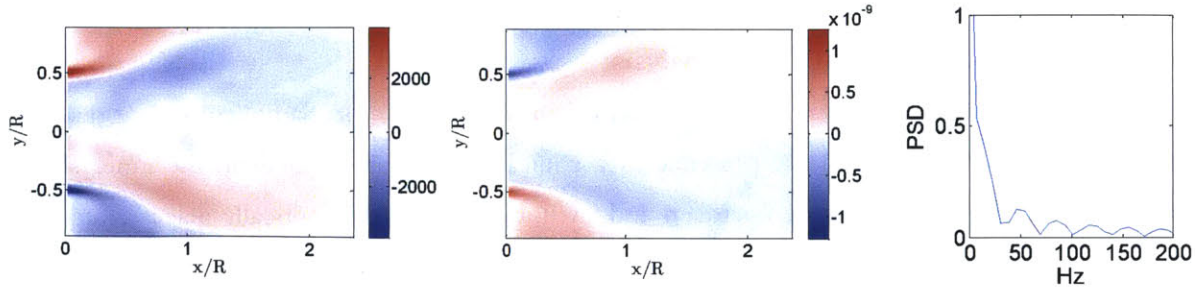

Figure 6.56: 0Hz dynamic mode (Real component: left, Imaginary component: middle, Frequency spectrum of temporal coefficient of real component of dynamic mode: right).

While the numerical simulations are able to resolve the dynamic characteristics of the flow, as observed experimentally, some quantitative discrepancies exist, since the simulations correspond to a flame macrostructure that is still in transition between the two experimentally observed Configurations (I and II), which alters the flow field predictions as well.

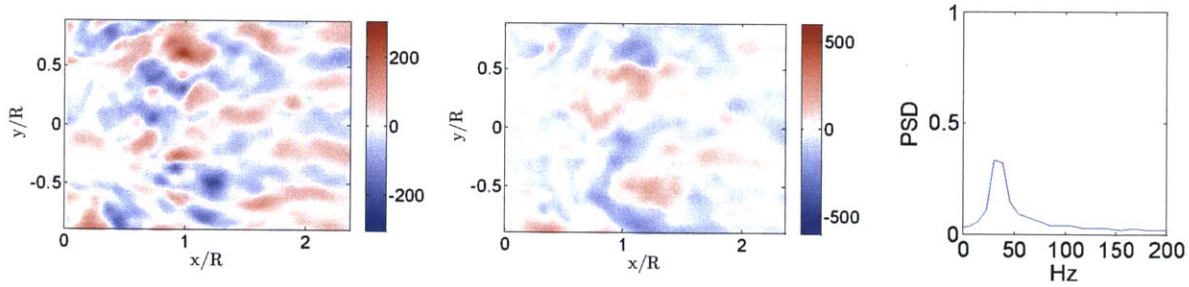

Figure 6.57: 30Hz dynamic mode (Real component: left, Imaginary component: middle, Frequency spectrum of temporal coefficient of real component of dynamic mode: right).

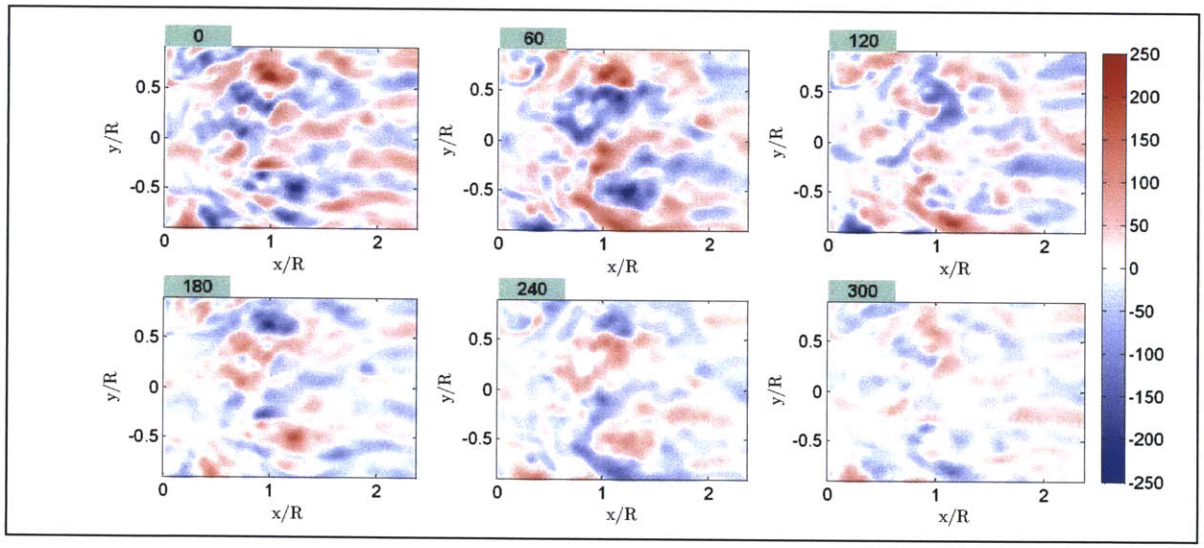

Figure 6.58: Phase shifted realizations of 30 Hz dynamic mode composed of the real and imaginary components along with their temporal coefficients.

6.2.5.7 Configuration III: LES Analysis

The CH chemiluminescence and Abel-transformed flame images for flame configuration III, displayed in figure 6.59, suggest the presence of a conical flame that stabilizes in the inner shear layer, and is observed to propagate upstream and anchor on the swirler (optically inaccessible and not shown). This transition of the flame macrostructure can be accounted for by noting that the inner shear layer is a high-strain environment relative to the interior of the IRZ. While the absolute strain rates in the ISL change only marginally between Configurations II and III, the extinction

strain rates increase with equivalence ratio and the flame becomes less likely to be extinguished in the ISL. Thus, the reaction zone is no longer bounded by the moderate strain rates of the ISL, nor is confined to the interior of the IRZ. The increase in the burning velocity also contributes to the transition to flame macrostructure III, allowing the flame brush to stabilize and persist in the ISL, with the reaction zone propagating upstream into the inlet pipe and anchoring on the swirler body.

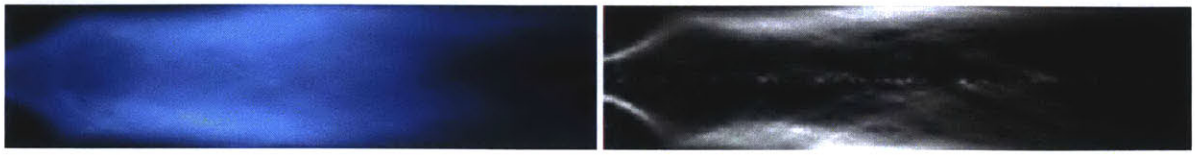

Figure 6.59: (a) Time resolved flame from CH chemiluminescence image, (b) Abel-transformed flame image.

Further, while no reaction zone is observed in the interior of the IRZ, the ORZ, or in the high strain OSL region, the flame front crosses the annular jet, continues along the wall shear layer and extends further downstream. Near the rear stagnation zone, a slight 'necking' of the flame is also observed and in this region, the reaction zone is observed to be thick with high CH intensity. Additionally, the downstream extension of the strongly burning flame is significantly longer than the compact flame envelope noted for configuration IV (figure 6.14); in comparison with Configurations I and II, however, the axial span of the flame region is shorter and does not extend into the exhaust tube, indicating that combustion is complete before the flow exits the chamber.

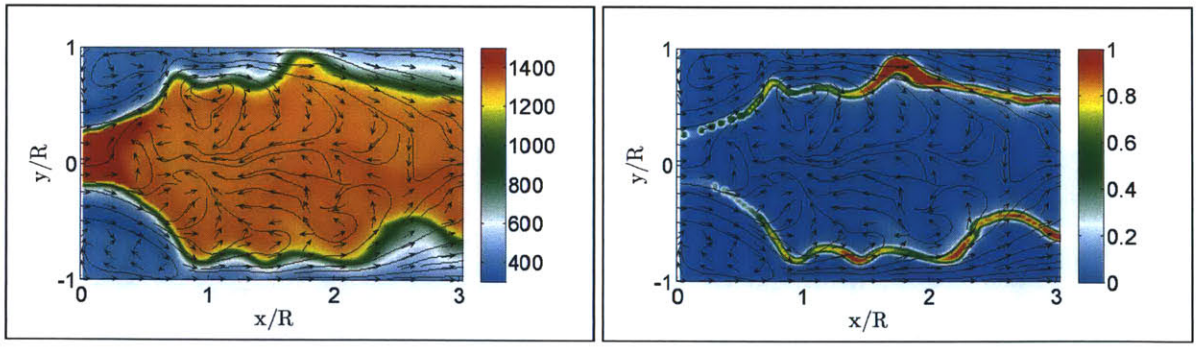

Figure 6.60: (a) Instantaneous temperature (K), (b) Instantaneous normalized heat release. The corresponding 2D velocity vectors and streamlines are also shown (LES).

The instantaneous LES contours for the normalized heat release and the temperature, depicted in figure 6.60, indicate a similar flame structure. It is worth noting that the flame holding features are sensitive to the thermal condition on the walls, and strain computations in the OSL [6.25-6.26]. It has been suggested, for a similar geometry, that when adiabatic computations are performed, or when the influence of strain is inadequately represented, the flame is predicted to

stabilize in the outer shear layer (OSL) as well, even though the experimental measurements indicate an ISL flame only. Correspondingly, the numerical framework in this work utilizes high fidelity LES solvers that explicitly incorporate the influence of strain and account for heat loss from the walls as well, thereby accurately predicting the flame macrostructure conforming to Configuration III.

As aforementioned, a thin reaction zone characterized by moderate burning velocity and heat release rates is observed in the ISL that continues upstream into the inlet pipe (figure 6.61). Consequently, the flow field in the section is characterized by vortex stretching and pairing, as well as volumetric expansion and baroclinic vorticity production. In general, the flow field can have a significant influence on the flame front: the small-scale shear-generated turbulence in the ISL augments entrainment and contributes to stabilizing the flame in this region; the penetration of the inner layers of the shear layer by transient eddies can cause the reaction rate to be affected by turbulence, while significantly enhancing heat diffusion from inner layers towards the preheat zone. Additionally, the reaction zone can also appreciably alter the flow field: the augmented heat release rates enhance the relative influence of turbulent dilatation as well as baroclinic vorticity production. The thermal expansion in the vortex cores, as well as reduction in the adverse pressure gradients and the Reynolds number can significantly alter the shear layer development. Likewise, the propagation of the flame upstream and the ensuing combustion generated turbulence (especially for high equivalence ratios) also modify the flow pattern appreciably. These factors, therefore, combine to define the flame-flow interactions, resulting in the formation of distinct flame patterns and the corresponding flow behavior.

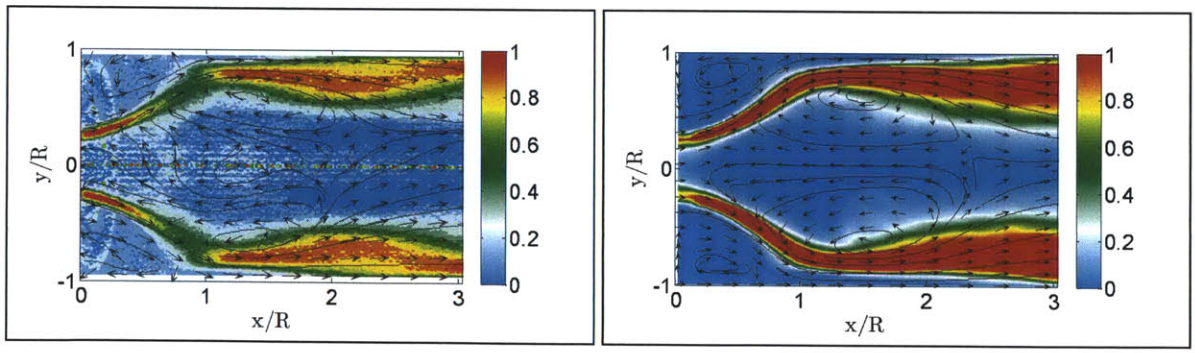

Figure 6.61: (a) Normalized deconvolved CH chemiluminescence intensity, (b) Average normalized heat release (LES). The corresponding 2D velocity vectors and streamlines are also shown.

Now, for this Configuration, as the flow convects downstream, the relatively smooth flame front, stretched along the ISL, subsequently curves near the axial location of maximum IRZ width, where the annular jet impinges the chamber wall. The flame brush continues along the wall shear

layer being supported by entrainment phenomena brought about by the coherent eddy structures that are convected downstream, as well as mixing processes augmented due to the turbulence generated in the region where jet impingement occurs. The increase in the burning velocity also allows the flamelets to persist in the region, in contrast to Configuration II. This behavior is also evident from the instantaneous CH_4 and CO mass fraction contours shown in figure 6.62, which suggest substantial wrinkling of the flame in this downstream section.

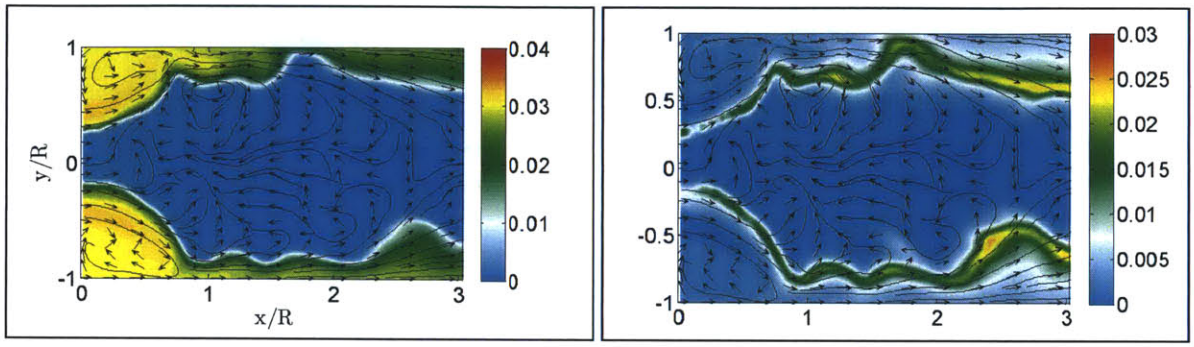

Figure 6.62: (a) Instantaneous CH_4 mass fraction, (b) Instantaneous CO mass fraction. The corresponding 2D velocity vectors and streamlines are also shown (LES).

Subsequently, owing to the high flow velocities in the region (due to wall confinement along with flow acceleration) and moderate strained flame propagation speed, the flamelets also begin to propagate towards the low velocity rear stagnation zone, resulting in a slight 'necking' of the flame surface in the region (figure 6.63). In this section, which is characterized by high turbulence and flow reversal, mixing and transport contribute significantly to flame stabilization. The high turbulence in the region decreases mixing time and increases entrainment between the fresh mixture and the flame, ie the flame loading is increased and the reaction zone is thickened (figure 6.61). In this flame, scalar thermodynamic variables of temperature, density, and composition fluctuate moderately, and combustion appears to be characterized by mixing and entrainment phenomena. The reaction process continues in the downstream section, and the fuel is consumed well before the flow proceeds into the exhaust duct.

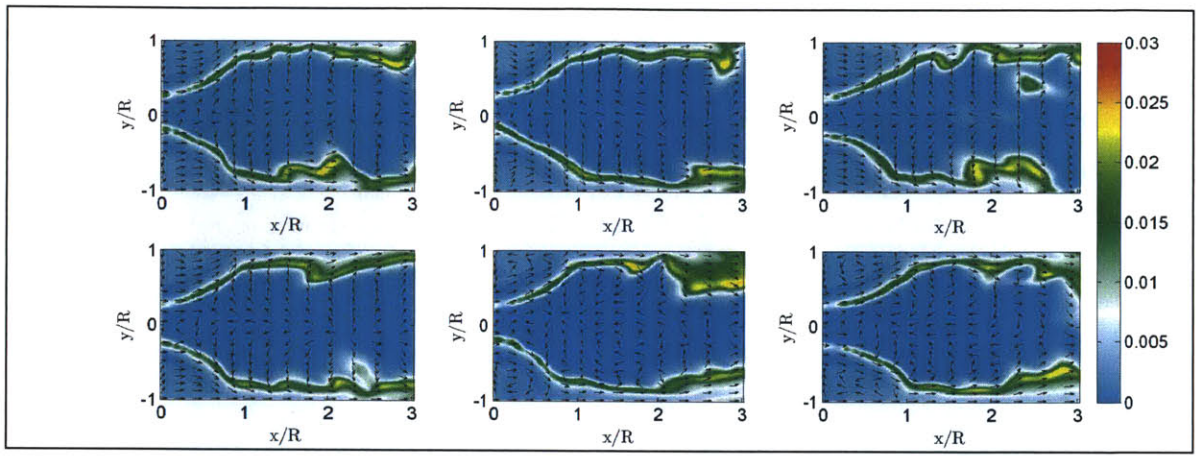

Figure 6.63: Instantaneous CO mass fraction at different time-instants, with the corresponding 2D velocity vectors (LES).

Additionally, no flame is observed inside the ORZ/OSL, as evident from the temperature contours in figure 6.64. This can be associated with the high strain in the region, as well as heat loss from the walls [6.25], which can cause extinction of the flamelets in the region. Thus, the chamber walls have a significant influence on the flow field pattern as well as the flame structure in the wake region. Wall confinement results in reduction of the streamline curvature, generation of turbulence in the region of annular jet impingement with the wall, as well as acceleration of the flow in the downstream section. Consequently, the average and fluctuating flow field as well as reaction zone thickness and intensity are critically impacted due to wall confinement.

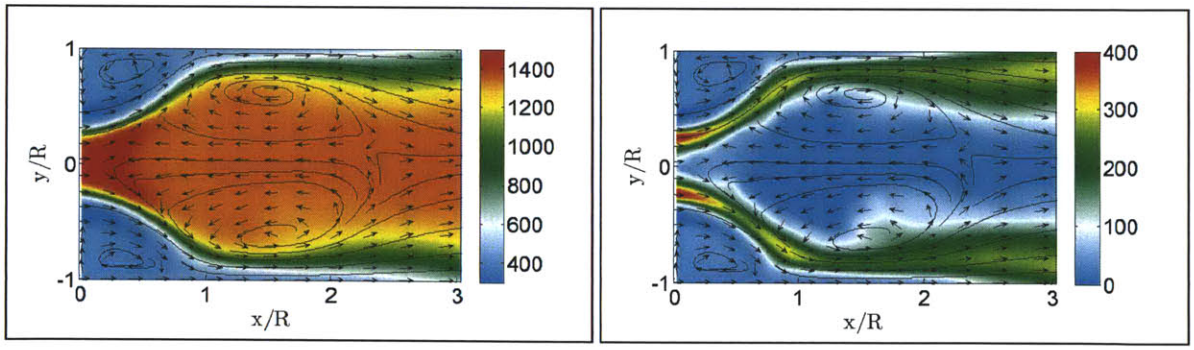

Figure 6.64: (a) Average temperature (K), (b) rms temperature (K). The corresponding 2D velocity vectors and streamlines are also shown (LES).

Next, in figure 6.65, LES contours of the average vorticity magnitude and instantaneous out-of-plane vorticity are depicted, suggesting significant vortex activity in the ISL region. Combustion, in general, results in shear-generated turbulence as well as flow dilatation. For low equivalence ratios, the propagation of the flame along the ISL and the resultant flow acceleration tend to reduce eddy

development in the mixing layer; heat release and thermal expansion in the vortex cores, along with reduction in adverse pressure gradients and Reynolds number that suppress entrainment, contribute to reducing the strength of the vorticity field. Combustion induced turbulence and baroclinic vorticity production, on the other hand, result in enhancing the vorticity intensity, especially in case of high inlet equivalence ratios.

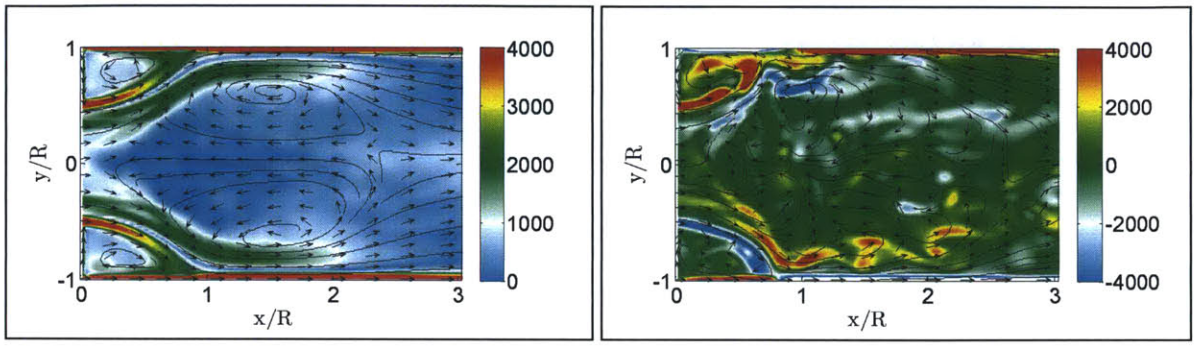

Figure 6.65: (a) Average vorticity magnitude (1/s), (b) Instantaneous out-of-plane vorticity (1/s). The corresponding 2D velocity vectors and streamlines are also shown (LES).

For Configuration III, the flow in the wake region is characterized by the absence of a strong precessing vortex core (figure 6.66), as indicated by the FFT analysis of the radial velocity component downstream of the sudden expansion (x = 0.013 m, r = -0.010 m, z = 0.000 m). This trend in the flow behavior is suitably reproduced in the numerical simulations as well, and can be attributed to flow acceleration brought about by thermal expansion in the inlet section.

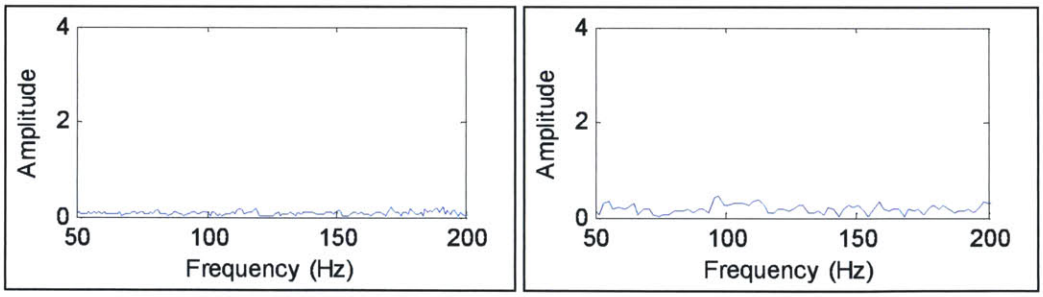

Figure 6.66: FFT analysis of radial velocity component signal (PIV: left, LES: right).

However, despite the fluid dynamic effects of heat release, the instantaneous out-of-plane vorticity contours (figure 6.67) depict appreciable vortex activity in the inner and outer shear layers, due to combustion induced baroclinic effects, in the presence of significant streamline curvature (due to broadening of the IRZ). Further downstream, beyond the rear stagnation zone, dilatation effects appear to dominate significantly, and coupled with dissipation effects, contribute to reducing the out-of-plane vorticity.

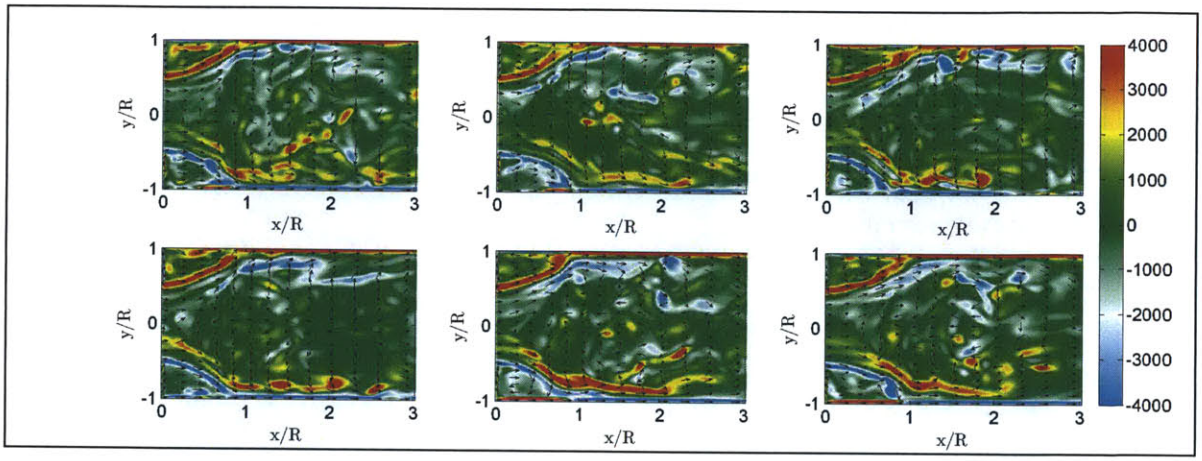

Figure 6.67: Instantaneous out-of-plane vorticity (1/s) at different time-instants, with the corresponding 2D velocity vectors (LES).

In figure 6.68, the contours of the average axial velocity, obtained experimentally and numerically, are displayed. The cross-sections at which numerical and experimental data are compared are also shown. The prominent flow features comprising of the annular jet, the shear layers at the boundaries of the jet, and the inner and outer recirculation zones are suitably resolved in the simulations and closely match with the experimental measurements; the primary topological flow difference from Configuration II is principally in the structure of the IRZ. Examining the shape of the experimental IRZ shows the presence of a toroidal, split-cell type vortex breakdown bubble. Thus, a secondary recirculating cell exists within the central core of the toroidal primary vortex structure and the axial velocity along the centerline reaches a positive value as well, forming an interior region of flow that propagates downstream. While the presence of the flame within the inlet section could explain the existence of this flow feature, further examination of the flow-field is required to elucidate the underlying physics behind the development of this structure. Additionally, the numerical simulations do not predict this flow feature, and results indicate the presence of a single-cell type IRZ with high peak reverse velocity along the centerline, although the size and shape of the primary vortex is well reproduced, as is the transition of the flame shape.

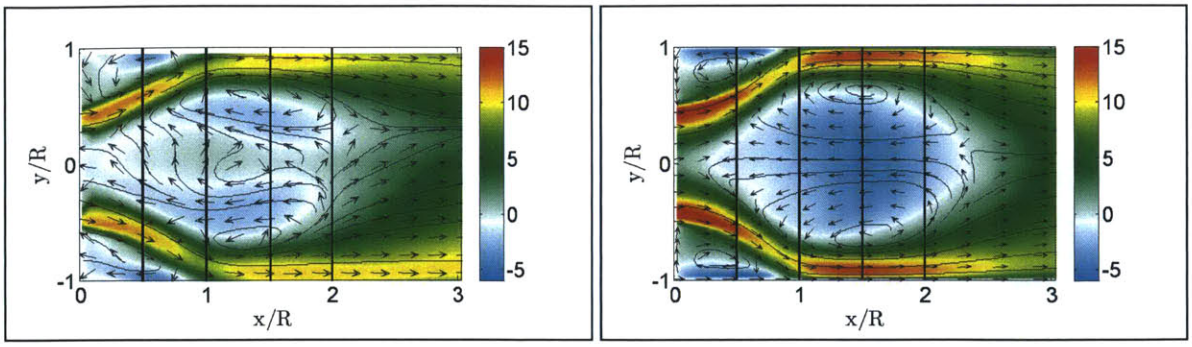

Figure 6.68: Average axial velocity along with the 2D velocity vectors and streamlines (PIV: left, LES: right). The cross-sections at which data are compared are also shown.

Further inspection of the average flow streamlines (figure 6.69) suggests that in contrast to Configuration II, the IRZ is marginally shorter, extending to a length of approximately *2.5R* downstream of the expansion plane, despite the augmented heat release. This change in the structure of the vortex breakdown bubble could be attributed primarily to the relatively stronger influence of flame propagation on the flow in this scenario. In case of reacting flows, the acceleration of the flow (due to dilatation effects of combustion), together with restriction of significant mean streamline curvature by the confining walls, cause the flow to better overcome the adverse pressure gradients. Therefore, for low to moderate equivalence ratios, the fluid dynamic effects of heat release, in general, result in elongation of the IRZ, as compared to isothermal flow (as seen in Configuration II). However, with an increase in heat loading, the enhanced turbulent burning velocity causes the flamelets to propagate upstream, which tends to strongly impact the recirculation region topology [6.11, 6.24], eventually reducing the axial span of the IRZ (as observed in Configuration III). This phenomenon is more pronounced with a further increase in equivalence ratio, as noted in flame macrostructure IV.

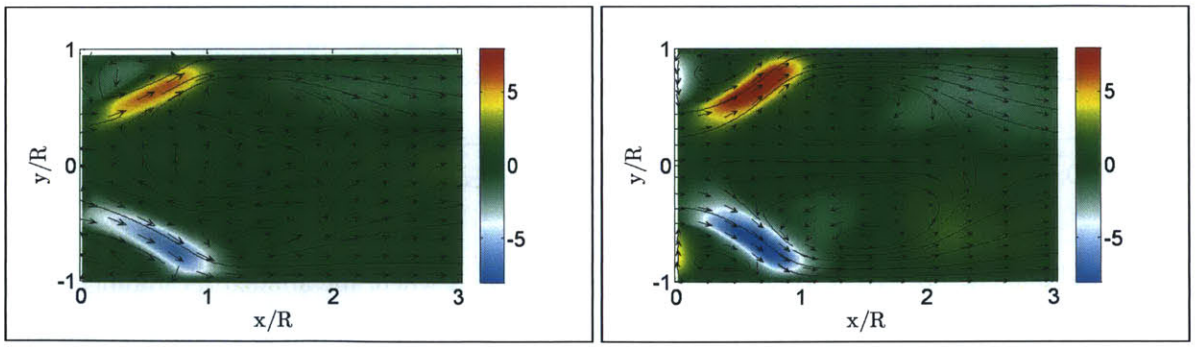

Figure 6.69: Average radial velocity along with the 2D velocity vectors and streamlines (PIV: left, LES: right).

Correspondingly, the heat release within the inlet pipe would typically result in flow acceleration of the incoming reactant mixture, thereby substantially altering the annular flow field in the combustion chamber. Specifically, it would result in reduced radial spread of the annular jet, narrowing of the IRZ, and suppression of eddy development in the shear layer. However, despite these effects, the influence of flame propagation on the flow field results in similar IRZ width, and spreading angle of the annular jet, as observed in experiments corresponding to Configuration II. Additionally, the jet thickness is also noted to be similar, although the magnitude of the velocity increases as a consequence of exothermicity and thermal expansion of the jet fluid.

In figure 6.70, the contours for the rms axial velocity fluctuations are shown indicating moderately high turbulence activity in the shear layers, especially in the locations corresponding to maximum IRZ width, where the annular jet impacts the chamber walls. Typically, for reacting flows involving high turbulent burning velocity and heat loading, the enhanced heat release augments the magnitude of the shear generated turbulence as well as turbulent dilatation. For Configuration III, it is observed that immediately downstream of the expansion plane, the effects of dilatation and dissipation tend to slightly suppress the shear turbulence (which generates small eddies that convect downstream). This generally results in a marginal lowering of the Reynolds shear stresses, and turbulent kinetic energy in the mixing layer. The absence of the PVC also contributes to reducing the flow fluctuations. However, the turbulence intensity in the shear layer remains moderately high, as in Configuration II, due to the generation of combustion induced turbulent kinetic energy.

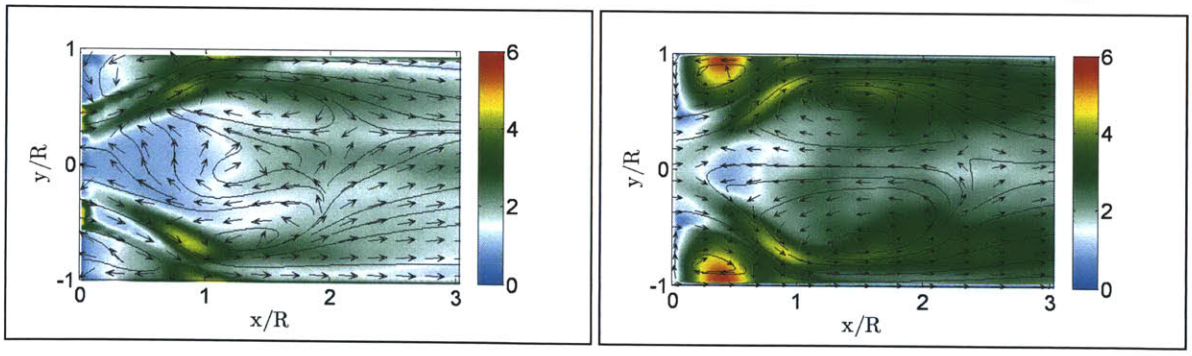

Figure 6.70: rms axial velocity along with the 2D velocity vectors and streamlines (PIV: left, LES: right).

Additionally, turbulence is also enhanced in the region where the annular jet impinges the wall, extending further downstream along the wall shear layer, where combustion generated turbulence augments the flow fluctuations. Turbulence intensity is also high near the rear stagnation zone where flow reversal and mixing takes place; in the proximity of the region, flow direction

quickly reverses, the fluid parcels are stretched and strong gradients of mean and turbulence quantities are present. Some turbulent activity is also observed in the ORZ which corresponds with the intermittent appearance of the reaction zone in the ORZ, and the corresponding flow perturbations due to heat release in the region. Subsequently, as the flow proceeds downstream towards the exhaust tube, the fluctuations in the flow field are suppressed and become more isotropic, as a consequence of dissipation and dilatation effects (figure 6.71), although appreciable level of combustion induced turbulence does prevail in the region.

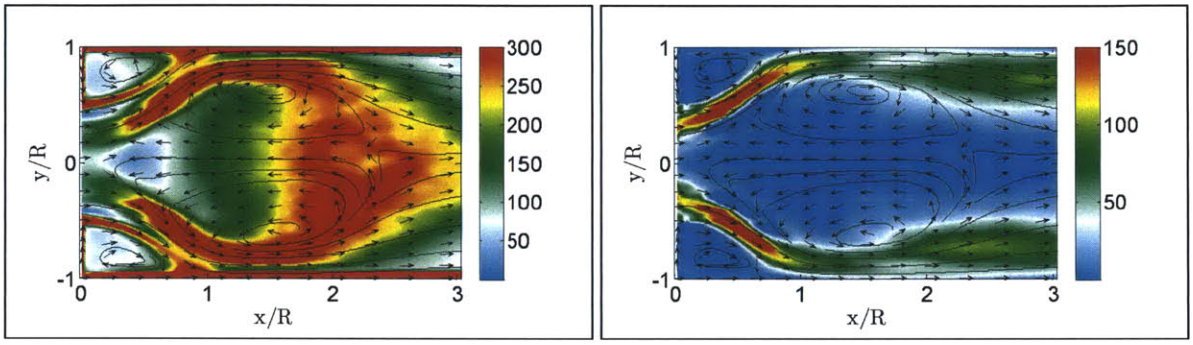

Figure 6.71: (a) Viscous dissipation per unit volume (kg/ms^3), (b) Turbulent dilatation (1/s). The corresponding 2D velocity vectors and streamlines are also shown (LES).

In figure 6.72, the contours for the rms radial velocity and Reynolds stress tensor term are shown, suggesting significant flow fluctuations in the region where a secondary shear layer is formed between hot products and the reactant mixture (near the wall). The transient eddies formed in the mixing layer that convect downstream and wrinkle the flame cause flow distortions along with the turbulence generated by the jet-wall impingement; the rapid necking of the outer flow streamlines in the vicinity brings the reactants rushing towards the hot products flowing through the center of the combustor leading to intense flow perturbations and a skewed turbulence structure, as shown.

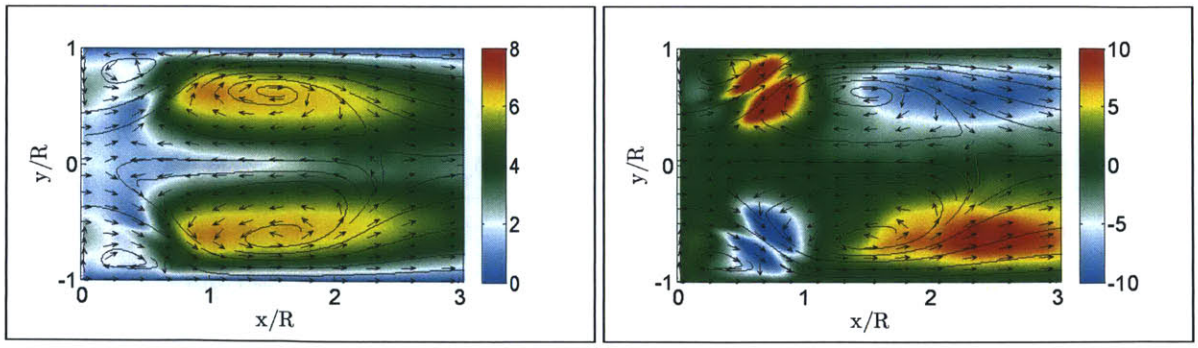

Figure 6.72: (a) rms radial velocity (u_r', m/s), (b) Reynolds stress tensor term ($u_r'u_x'$, m^2/s^2). The corresponding 2D velocity vectors and streamlines are also shown (LES).

In figure 6.73, the normalized profiles for the average axial velocity and rms axial velocity, comparing numerical predictions with experimental measurements at different cross sections are shown. There is excellent agreement between LES and PIV data, and the annular jet velocity along with the radially outward spread of the shear layers is resolved quite accurately. The flow accelerates near the wall due to heat release and squeezing of the annular jet towards the wall (due to aerodynamic blockage by the IRZ), and the peaking of the axial velocity is suitably reproduced in the simulations. However, while experiments suggest a secondary vortex in the core of the IRZ, as described before, LES results predict high peak reverse velocity along the centerline as a result of exothermicity.

As regards the turbulence generation, it peaks in the shear layers, although immediately downstream of the expansion plane, turbulence intensity is slightly lower than for Configuration II. This may be attributed to the absence of a strong precessing vortex, and the presence of the reaction zone in the ISL (which, along with reduced adverse pressure gradients and Reynolds number, reduces eddy development in the layer). Further downstream, flow fluctuations tend to peak near the chamber walls, where the impact of the annular jet with the wall generates small-scale turbulence. Turbulent kinetic energy is also high near the wall shear layer in the downstream section, where the high intensity flame exists, and combustion induced turbulence results in flow oscillations.

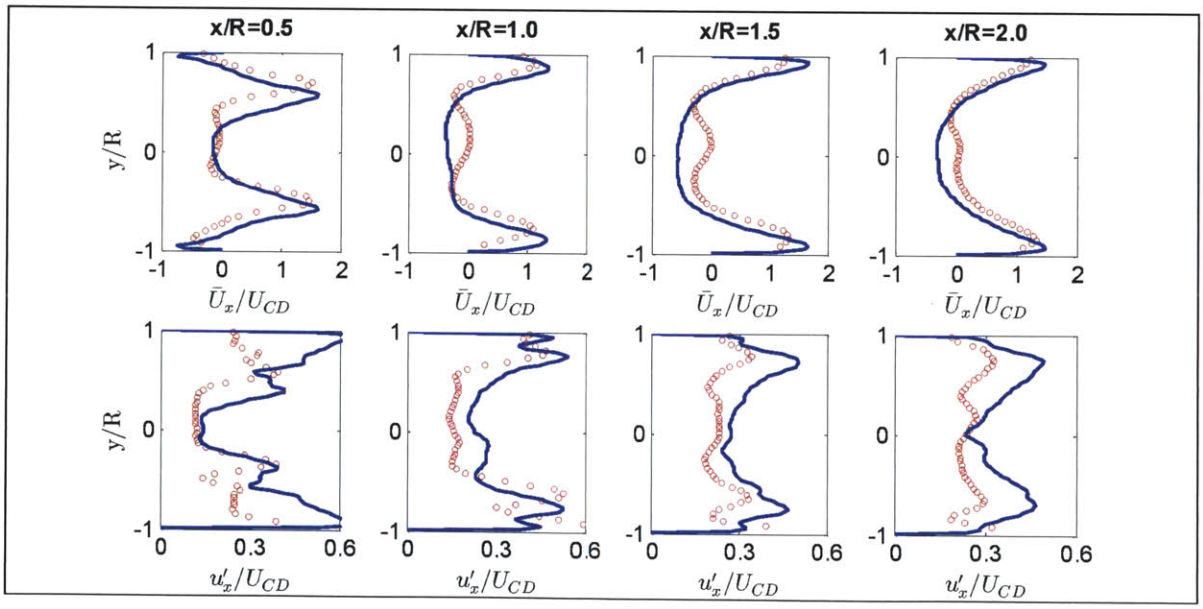

Figure 6.73: Normalized profiles for average axial velocity (top) and rms axial velocity (bottom). ooo PIV, — — — LES

Additionally, small-scale oscillations also begin to manifest in the ORZ, enhancing the turbulence anisotropy, and seem to correspond with heat release perturbations in the region, as noted in experiments. These flow-field changes are suitably resolved numerically, although the predictions could be further improved by appropriate mesh resolution near the walls. Adjustments to the PIV setup for the collection of higher resolution flow fluctuation data in downstream locations may also be performed.

6.2.5.8 Configuration III: PIV DMD Analysis

Next, the DMD modes from analysis of the PIV flow field are presented. For Configuration III, intermittency in the outer shear layer as measured by the CH chemiluminescence signal is observed, and corresponds to the intermittent propagation of the reaction zone into the ORZ, resulting in weak flame and flow oscillations in the region. In figure 6.74, a sample of the time series of the integral CH signal, and the power spectral density of the integral CH series, at a location near the ORZ, are depicted. The power spectral density plots show two regions of interest. A sharply peaked, high frequency oscillation observed at approximately 30 Hz as the dominant low-frequency mode, which corresponds to the frequency at which the flame is advected around the centerline with the swirling flow. A weak low-frequency activity around 10 Hz is also observed, and is attributed to the phenomena of the 'flickering flame' in the ORZ [6.27].

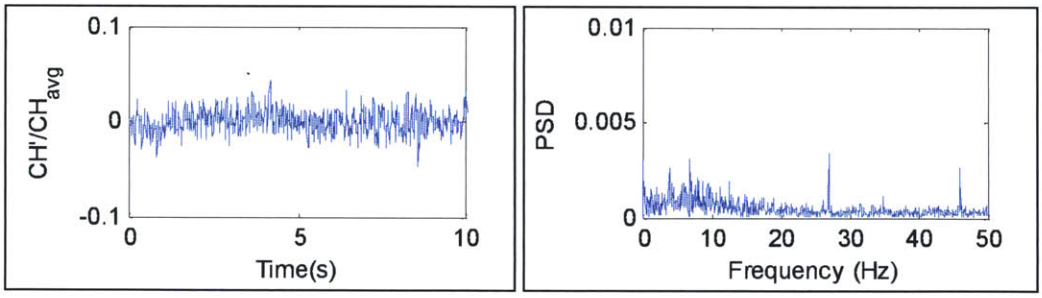

Figure 6.74: (a) Time series of the integral CH signal, (b) Frequency content of CH signal

As noted in figure 6.75c, aside from the prominent mean flow field, the dynamic mode decomposition of the experimental data reveals dominant energy modes in the 10-30 Hz range, which corresponds to the experimentally observed frequencies of interest. The suppression of the PVC is also evident, as suggested by the absence of a strong 120Hz mode (as observed in Configuration I).

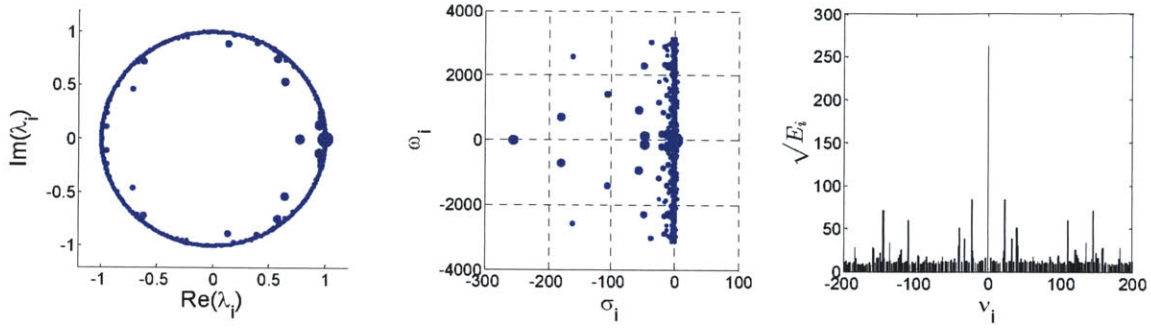

Figure 6.75: (a) Ritz vectors on the complex plane, (b) Frequency, ω, and growth rate, σ, of dynamic modes, (c) Energy content of dynamic modes.

In figure 6.76, the vorticity contours for the real and imaginary parts of the mode that corresponds to the mean flow pattern are shown, along with the FFT analysis of the temporal coefficients corresponding to the real component of the dynamic mode. As expected, the inner and outer recirculation vortices are suitably highlighted, along with the shear layers, and dominate the average flow field. The secondary, low-intensity circulation region around the centerline axis, within the core of the IRZ, is also observed.

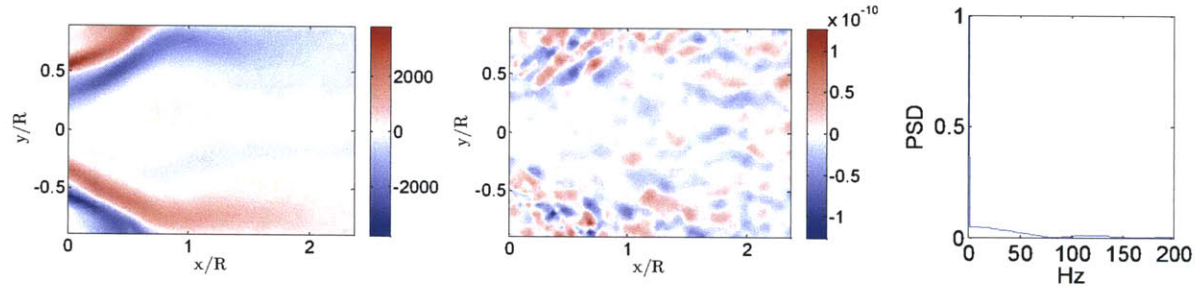

Figure 6.76: 0Hz dynamic mode (Real component: left, Imaginary component: middle, Frequency spectrum of temporal coefficient of real component of dynamic mode: right).

In figure 6.77, the 10 Hz mode obtained from the DMD analysis is presented, which is predominantly comprised of small-scale eddy vortices in the shear layer along with appreciable vortex shedding activity in the OSL/ORZ region.

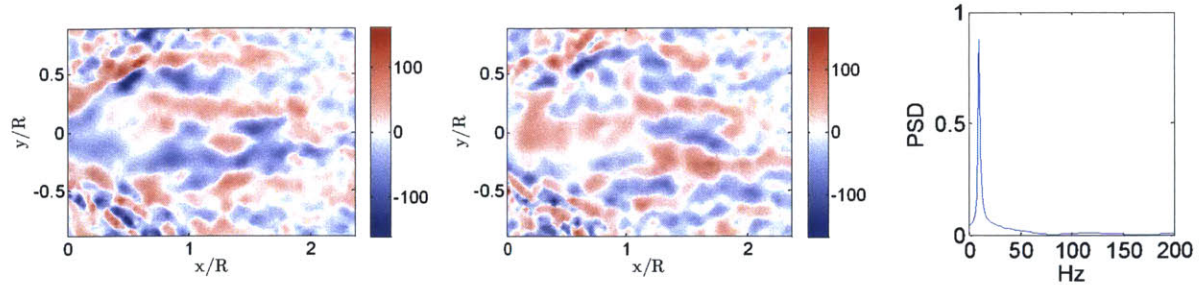

Figure 6.77: 10Hz dynamic mode (Real component: left, Imaginary component: middle, Frequency spectrum of temporal coefficient of real component of dynamic mode: right).

Figure 6.78 shows phase-shifted realizations of the 10 Hz dynamic mode, and is composed of the real and imaginary parts of the Ritz vectors. The mode presumably consists of the convective vortices, related to the instabilities in the shear layer. However, it is worth mentioning that as the flame transitions to Configuration IV, significantly stronger, and persistent 'flickering' is observed at the intermediate equivalence ratios ($0.61<\varphi<0.64$). The corresponding DMD analysis for the experimental data reveals a dominant low frequency mode in the 10Hz range [6.27] that is associated with a stationary vortex in the annular jet, unrelated to any instability in the shear layer, and it has been suggested that the vortex is linked to vorticity generated by the intermittent expansion of the outer recirculation zone as the flame jumps in and out of the outer shear layer while transitioning between macrostructures III and IV.

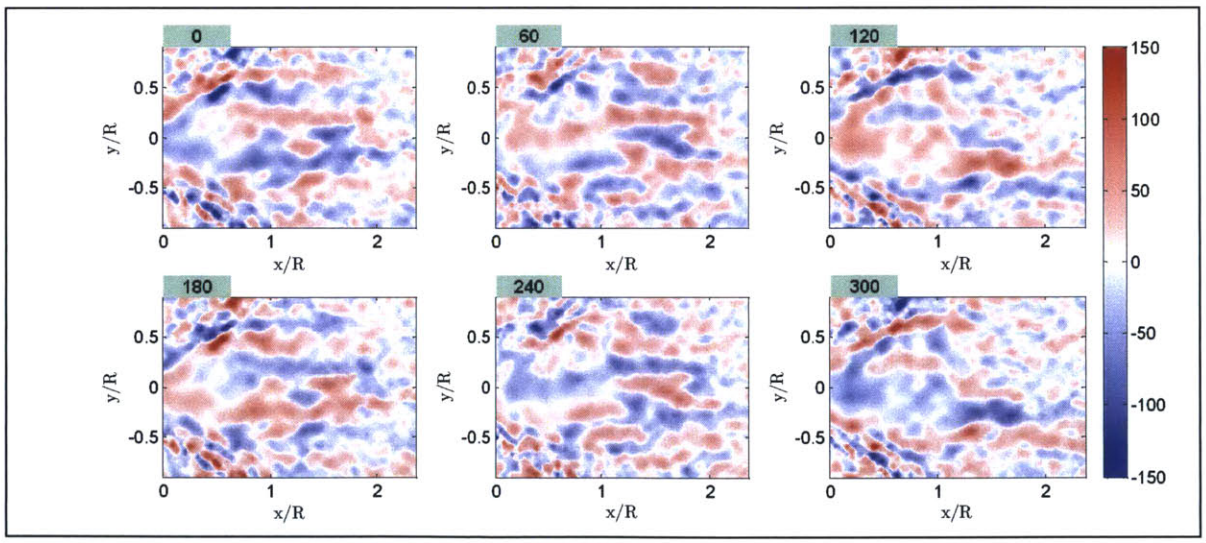

Figure 6.78: Phase shifted realizations of 10 Hz dynamic mode composed of the real and imaginary components along with their temporal coefficients.

Figure 6.79 shows the 30 Hz mode as obtained from the DMD analysis of the PIV data, while the phase-shifted realizations of the dynamic mode, composed of the real and imaginary parts of the Ritz vectors, are depicted in figure 6.80. The mode is predominantly comprised of small-scale vortices in the shear layers at the boundary of the annular jet, and near the walls; these eddies are significantly influenced by the flame as it is advected around the centerline due to the swirling flow, and resembles the 30 Hz mode observed for Configuration II.

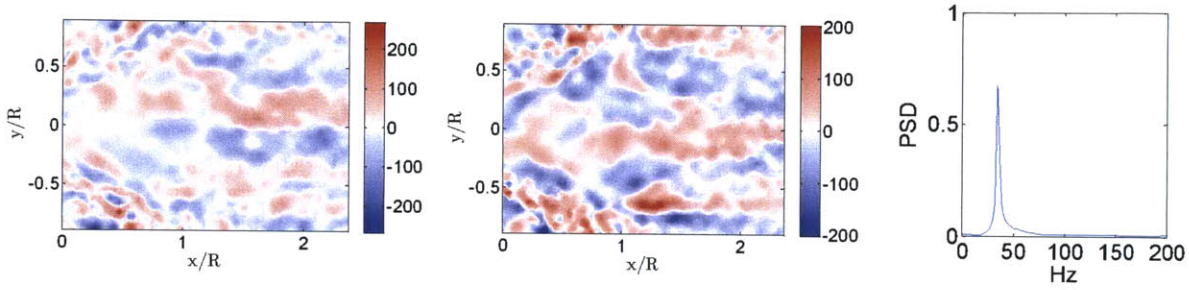

Figure 6.79: 30Hz dynamic mode (Real component: left, Imaginary component: middle, Frequency spectrum of temporal coefficient of real component of dynamic mode: right).

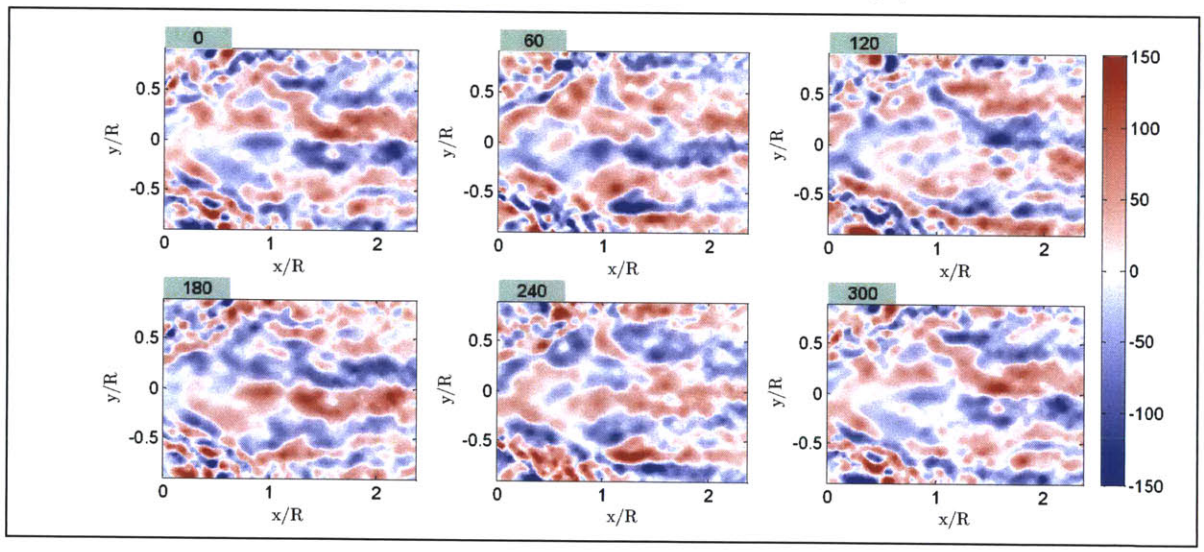

Figure 6.80: Phase shifted realizations of 30 Hz dynamic mode composed of the real and imaginary components along with their temporal coefficients.

6.2.5.9 Configuration III: LES DMD Analysis

Next, the DMD modes from analysis of the LES flow field data (200 snapshots) are presented, and correspond reasonably well with the modal structures obtained using the PIV measurements.

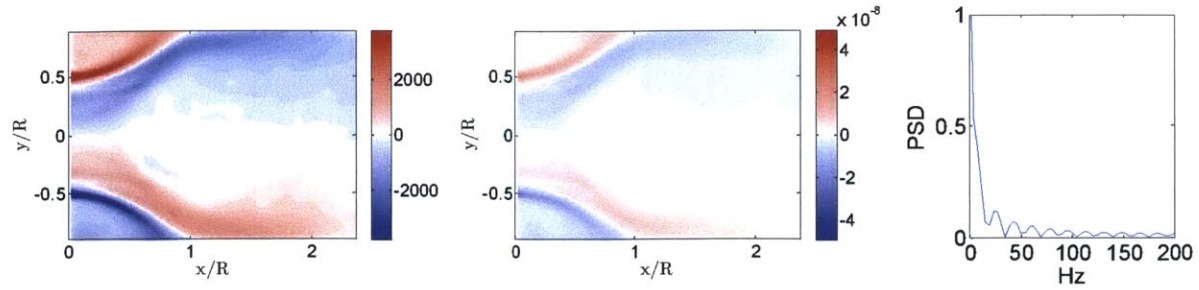

Figure 6.81: 0Hz dynamic mode (Real component: left, Imaginary component: middle, Frequency spectrum of temporal coefficient of real component of dynamic mode: right).

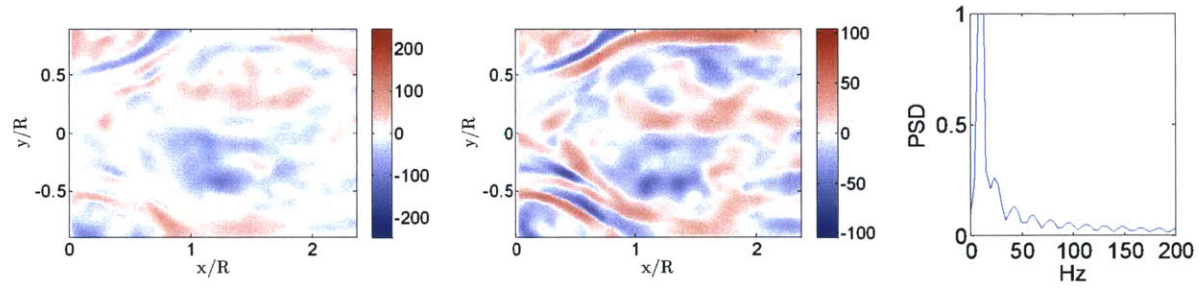

Figure 6.82: 10Hz dynamic mode (Real component: left, Imaginary component: middle, Frequency spectrum of temporal coefficient of real component of dynamic mode: right).

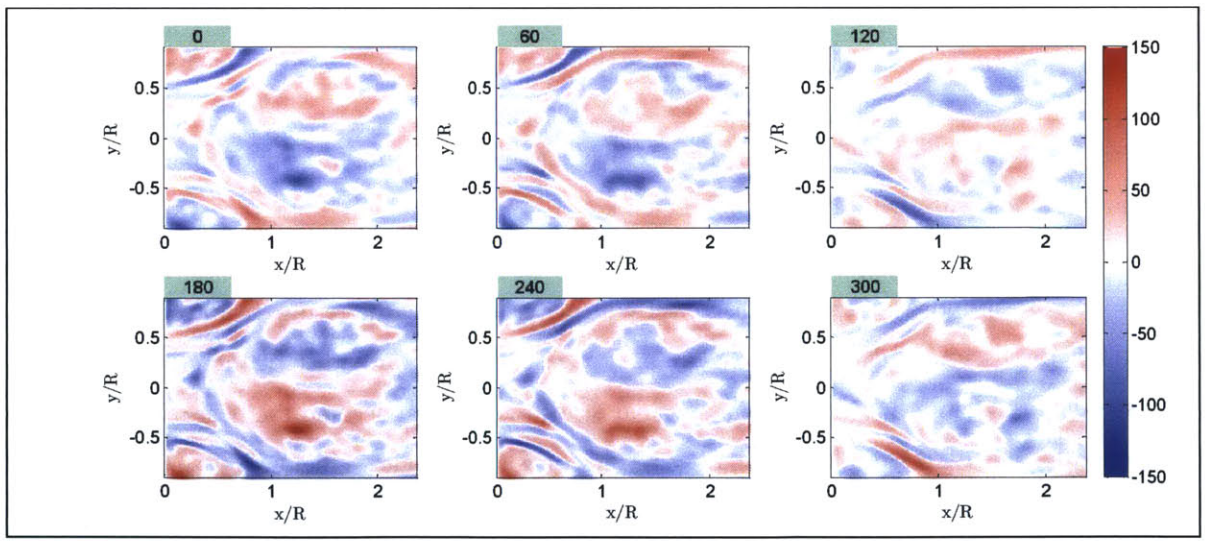

Figure 6.83: Phase shifted realizations of 10 Hz dynamic mode composed of the real and imaginary components along with their temporal coefficients.

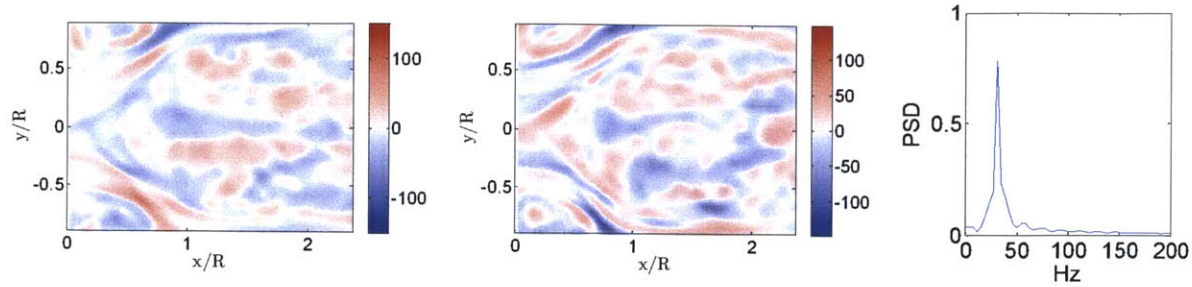

Figure 6.84: 30Hz dynamic mode (Real component: left, Imaginary component: middle, Frequency spectrum of temporal coefficient of real component of dynamic mode: right).

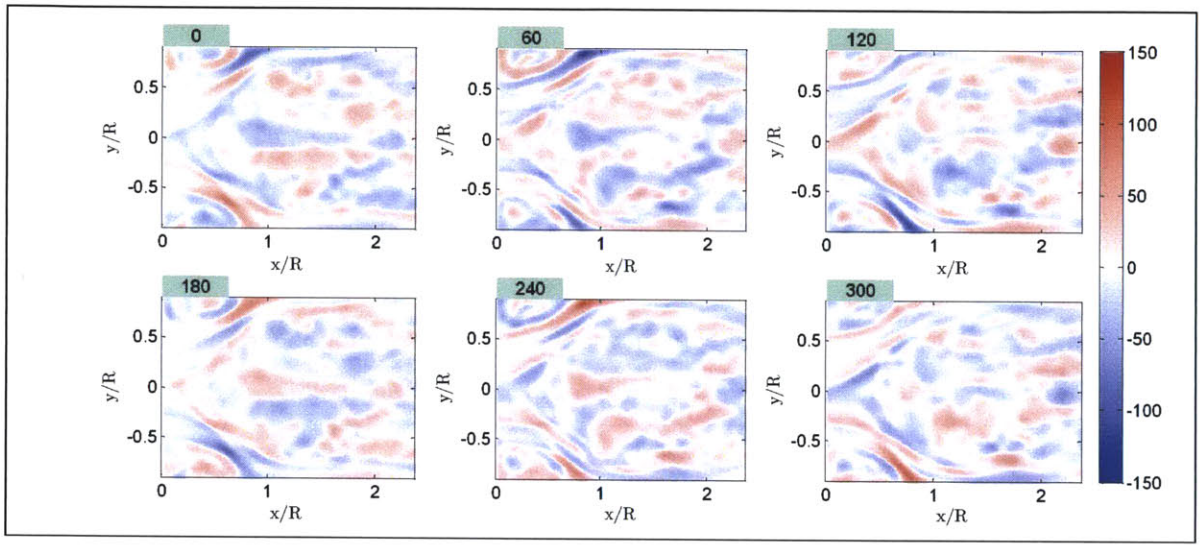

Figure 6.85: Phase shifted realizations of 30 Hz dynamic mode composed of the real and imaginary components along with their temporal coefficients.

As explained in Chapter 5, the DMD analysis generates a global frequency spectrum and each mode corresponds to a specific discrete frequency. Therefore, the results from the application of DMD to the flow field data, as well as the heat release data, can provide a quantitative means for understanding the flame-flow interactions by analysis of the flow modes and the heat release modes. Consequently, the DMD modes from LES results of the heat release field (200 snapshots) that correspond to the frequency of the flow field modes indicated above, are also obtained, as in [6.28]. The modes suggest intense activity in the shear layer region close to the location where the jet impinges the wall, as well as in the wall shear layer, where appreciable flame front perturbations are observed. Further investigations may also be performed to explain the flame flickering behavior, and to elucidate the mechanism of flame transition to Configuration IV, as the equivalence ratio is further increased.

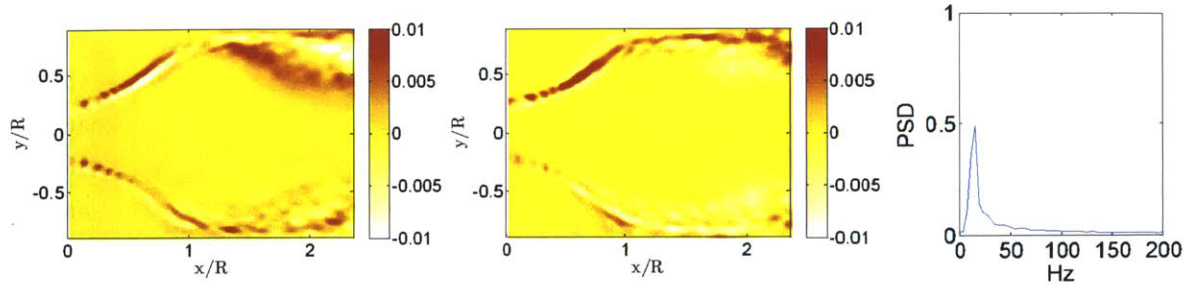

Figure 6.86: 10Hz dynamic mode (Real component: left, Imaginary component: middle, Frequency spectrum of temporal coefficient of real component of dynamic mode: right).

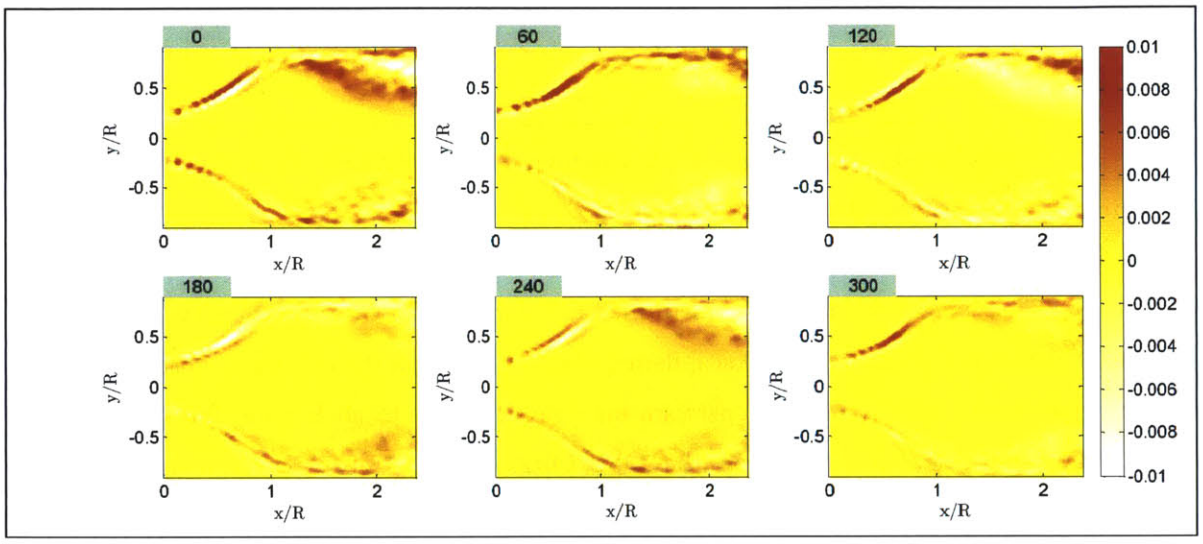

Figure 6.87: Phase shifted realizations of 10 Hz dynamic mode composed of the real and imaginary components along with their temporal coefficients.

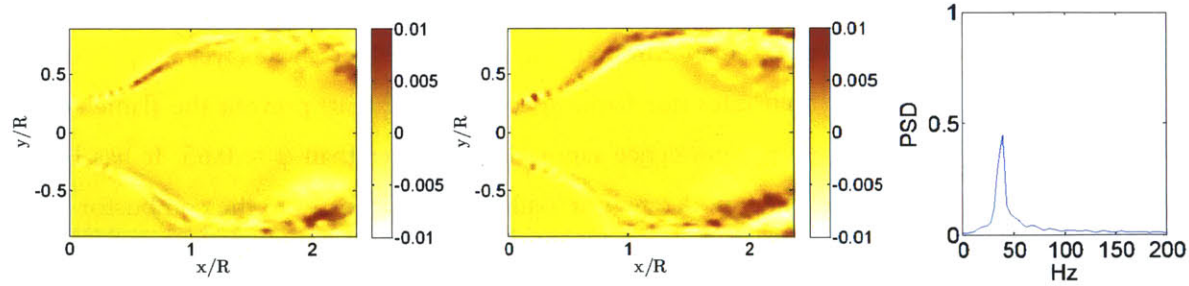

Figure 6.88: 30Hz dynamic mode (Real component: left, Imaginary component: middle, Frequency spectrum of temporal coefficient of real component of dynamic mode: right).

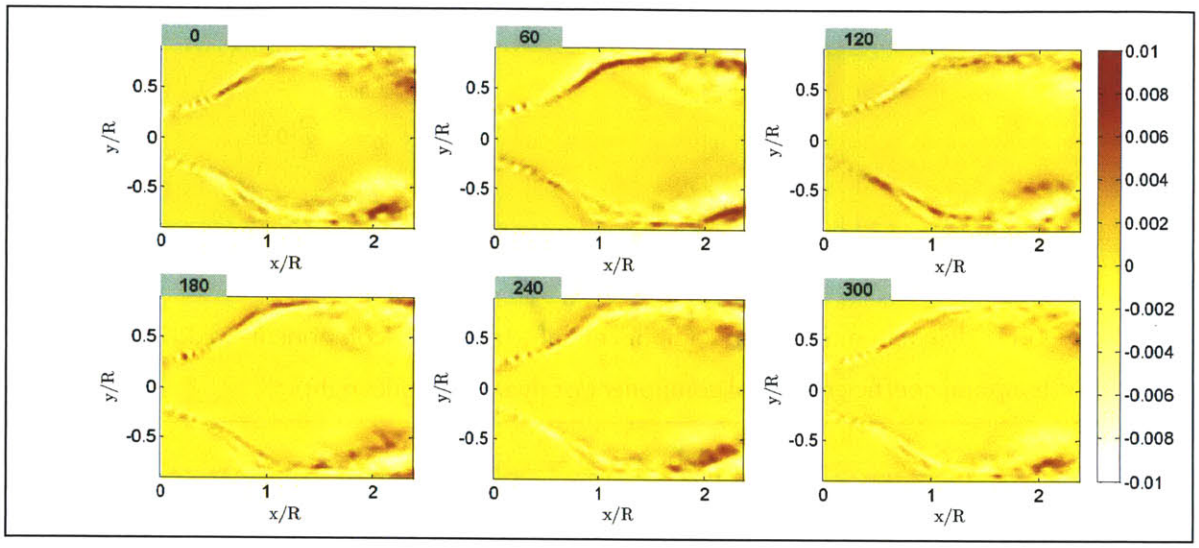

Figure 6.89: Phase shifted realizations of 30 Hz dynamic mode composed of the real and imaginary components along with their temporal coefficients.

6.2.5.10 Configuration IV: LES Analysis

The CH chemiluminescence and Abel-transformed flame images for Configuration IV, displayed in figure 6.90, depict the presence of a conical flame, which stabilizes in the ISL and wall shear layer, as in Configuration III, and propagates upstream into the inlet pipe to anchor ion the swirler body. Additionally, a diffuse flame brush in the OSL/ORZ region is also evident. Thus, for this configuration, given the augmented burning velocity and high extinction strain rate, the flame overcomes the high strain environment in the OSL, propagating upstream and anchoring on the periphery of the inlet tube.

Now, the strain rates in this outer region are similar in magnitude to those observed in the inner shear layer; the observation of an intermittent flame in the outer shear layer at φ = 0.60, therefore, suggests that neither strain rates nor flame speed (to an extent) prevent the flame from stabilizing in the outer shear layer at equivalence ratios slightly lower than φ = 0.65. It has been suggested that for these cases involving moderate heat loading, the heat losses to the combustor wall rapidly quench the flame; once the specific heat release rate crosses a critical threshold, a persistent flame can stabilize in the outer recirculation zone [6.12]. Thus, the flame holding features are sensitive to the thermal condition on the walls, and an OSL flame manifests only for significantly high heat loading (φ>=0.65), resulting in flame macrostructure IV.

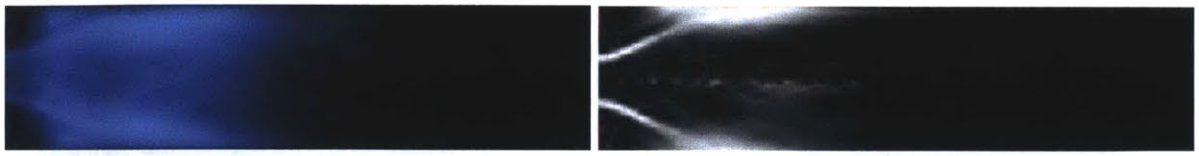

Figure 6.90: (a) Time resolved flame from CH chemiluminescence image, (b) Abel-transformed flame image.

The instantaneous LES contours for the normalized heat release and the temperature, depicted in figure 6.91, indicate a similar flame structure. Moreover, it is observed that the strongly burning flame exhibits a compact envelope that extends to a distance of approximately 3.0R downstream of the expansion plane, which is significantly shorter than the flame extension for configurations I-III (figure 6.14). The reaction zone intensity is appreciably high in the wall shear layer region, and combustion is complete as the flow convects downstream of this thick flame region.

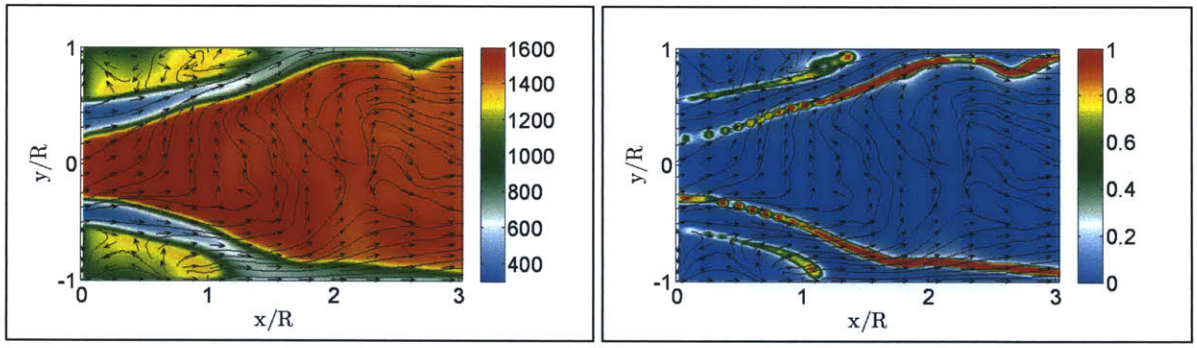

Figure 6.91: (a) Instantaneous temperature (K), (b) Instantaneous normalized heat release. The corresponding 2D velocity vectors and streamlines are also shown (LES).

It is well known that turbulent combustion and stabilization of the flame in the shear layer region is a sequential phenomenon that involves preheating of the incoming reactant mixture, followed by its ignition due to the heat flux transported radially outward from the recirculation zone. These processes result in a relatively thin reaction zone around the IRZ periphery and combustion in this region is typically characterized by increased heat release rates and high flame propagation speed (figure 6.92). As in the previous scenario, the flame-flow field in the upstream section is impacted both by the shear stresses (production term) and also the normal stresses (dilatation term). However, the relative influence of combustion induced turbulence increases with a further increase in heat loading, and turbulence is slightly enhanced in the mixing layer in this case. This contributes to increasing the reaction rate and flame intensity in the ISL, as seen in figure 6.92.

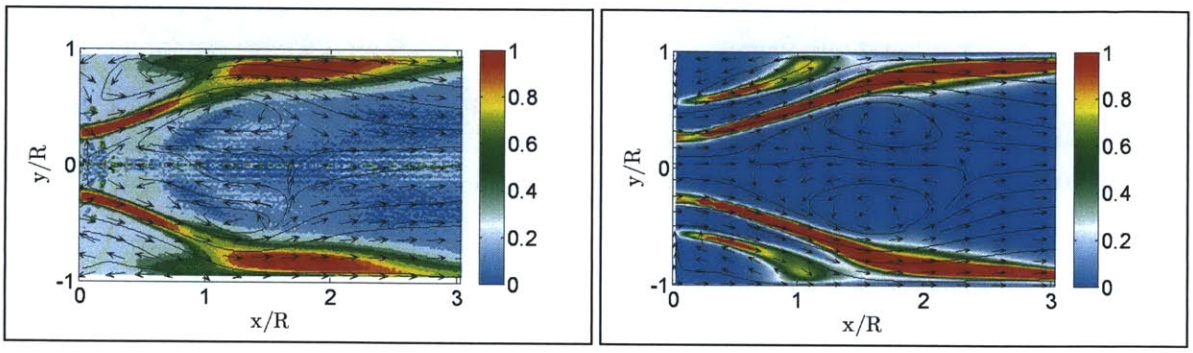

Figure 6.92: (a) Normalized deconvolved CH chemiluminescence intensity, (b) Average normalized heat release (LES). The corresponding 2D velocity vectors and streamlines are also shown.

Downstream of this thin flame region, the temperature remains fairly constant, and primarily entrainment of reactants and products occurs. In this region, coherent structures develop within the reacting inner shear layer and form as folds around the flame edge, growing in size downstream to produce a slightly wrinkled reaction zone. These coherent bodies of gas eventually result in thickening of the flame (figure 6.93), which is characterized by the entrainment process.

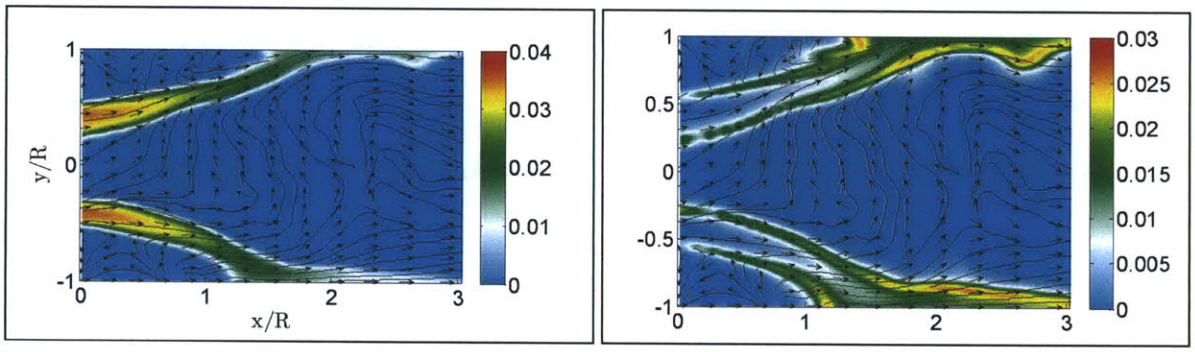

Figure 6.93: (a) Instantaneous CH_4 mass fraction, (b) Instantaneous CO mass fraction. The corresponding 2D velocity vectors and streamlines are also shown (LES).

The reaction zone also thickens near the periphery of the IRZ, where the annular jet impinges the wall, and the high rate of mixing in the region augments heat release, as well as the temperature perturbations. As shown in the instantaneous CO mass fraction contours in figure 6.94, a weakly-burning flame also propagates along the OSL, resulting in moderately high scalar fluctuations in the region (figure 6.95).

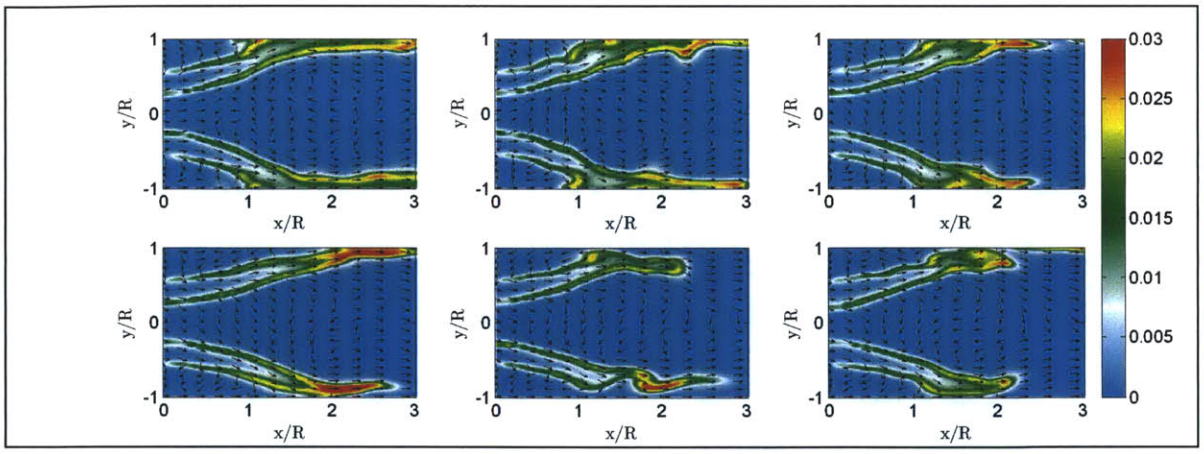

Figure 6.94: Instantaneous CO mass fraction at different time-instants, with the corresponding 2D velocity vectors (LES).

Besides the propagation of the flame along the OSL, the increase in the equivalence ratio also influences the flame-flow behavior in the ISL as well as in the downstream sections. Due to the intense burning in the region, associated with the enhanced burning velocity, combustion is almost complete along the wall shear layer as the flow proceeds downstream of the axial location corresponding to the rear stagnation zone ($x/R \approx 3$). In contrast, a significantly thicker reaction zone is observed in Configuration III, associated with intermittent appearance of the weakly propagating flame brush in the low velocity rear stagnation zone, which also extends further downstream into the combustion chamber. Correspondingly, relatively lower magnitude of scalar fluctuations are observed in the region, for Configuration IV (figure 6.95).

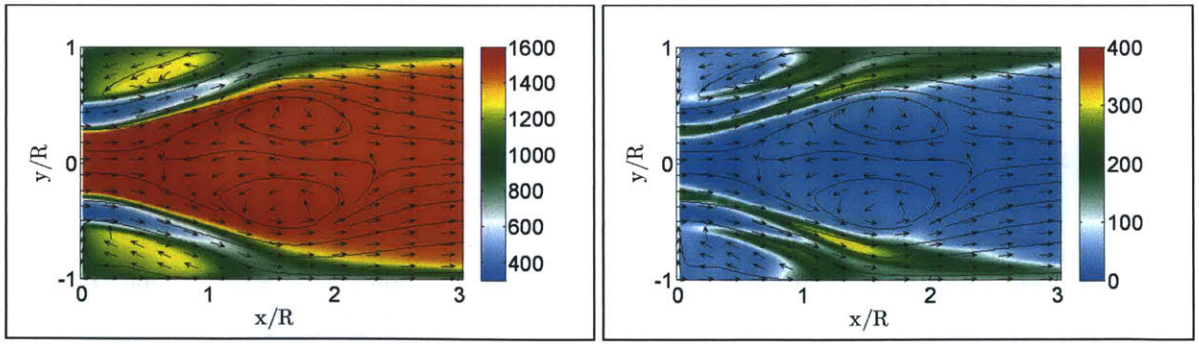

Figure 6.95: (a) Average temperature (K), (b) rms temperature (K). The corresponding 2D velocity vectors and streamlines are also shown (LES).

Next, in figure 6.96, LES contours of the average vorticity magnitude and instantaneous out-of-plane vorticity are depicted, indicating appreciable vortex activity in the mixing layer region. While heat release and thermal expansion in the inner shear layer, along with reduction in the

Reynolds number, suppresses the growth and development of the eddy structures to some extent, combustion induced baroclinic vorticity production does enhance the vorticity magnitude in the region. Correspondingly, the out-of-plane vorticity in the outer shear layer remains high, although the vorticity strength reduces within the ORZ as a result of heat release in the region.

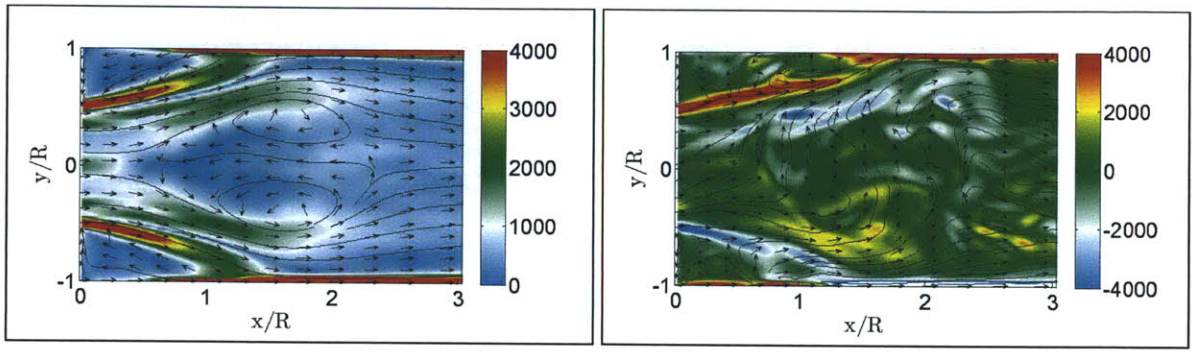

Figure 6.96: (a) Average vorticity magnitude (1/s), (b) Instantaneous out-of-plane vorticity (1/s). The corresponding 2D velocity vectors and streamlines are also shown (LES).

Observing the FFT analysis results of the radial velocity component in the wake region (x = 0.013 m, r = -0.010 m, z = 0.000 m), it is observed that the flow is characterized by the absence of a strongly precessing vortex, as noted in Configuration III. However, experimental measurements indicate that small-scale fluctuations (at a characteristic frequency of 110 Hz) exist in the region (figure 6.97), and can be associated with transient eddies that are generated as a result of combustion induced turbulence; the simulations also predict this flow behavior for Configuration IV, which was not observed for the moderate equivalence ratio scenarios: the high heat loading in this case may, therefore, be responsible for the generation of these small-scale eddies.

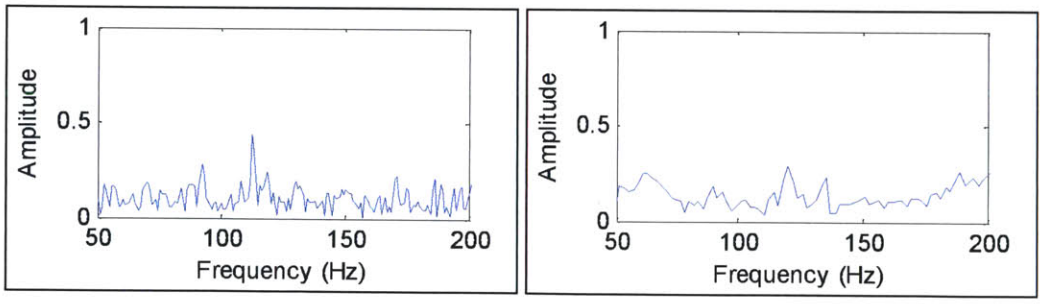

Figure 6.97: FFT analysis of radial velocity component signal (PIV: left, LES: right).

Consequently, as a result of the significant combustion induced vorticity production, intense vortex activity is observed in the shear layers, as observed in the instantaneous out-of-plane vorticity contours shown in figure 6.98. Further downstream, however, due to the effects of dissipation, and due to turbulent dilatation, reduced strength of the vorticity field is noted, as in Configuration III.

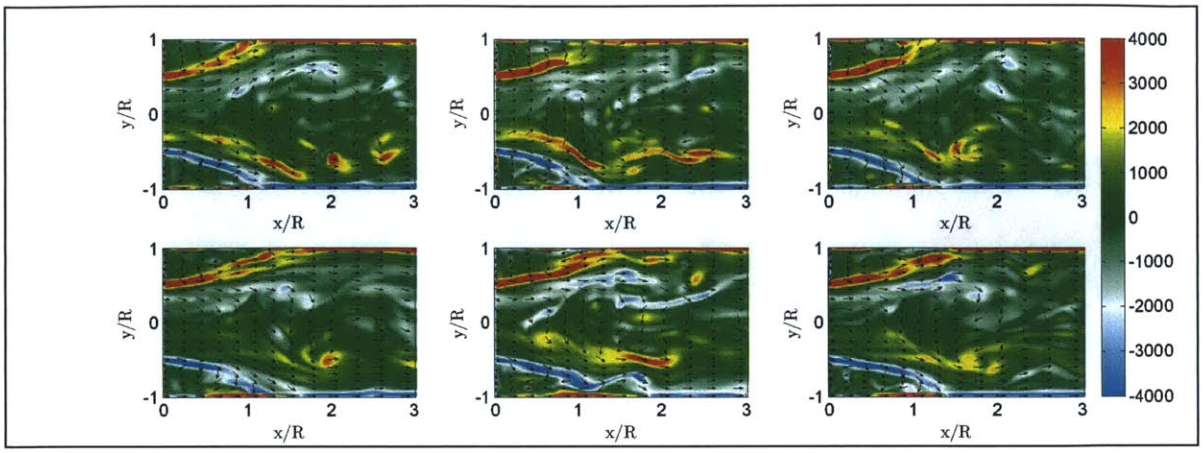

Figure 6.98: Instantaneous out-of-plane vorticity (1/s) at different time-instants, with the corresponding 2D velocity vectors (LES).

In figure 6.99, the contours of the average axial velocity, obtained experimentally and numerically, are depicted. The cross-sections at which numerical and experimental data are compared are also shown. Drastic changes in the mean flow field from the previous configuration are evident, principally in the size and strength of the primary and secondary recirculation zones. A substantial decrease in the axial and radial span of the IRZ is observed, along with the narrowing and elongation of the ORZ. There is significant drop in the streamline curvature (spreading angle of the annular jet), corresponding with the reduction in width of the IRZ. Additionally, the thickness of the annular jet increases, as does the velocity of the jet fluid. The vortex structure within the core of the IRZ, observed with Configuration III, also disappears in this scenario, with the primary vortex structure resembling that observed in Configuration I.

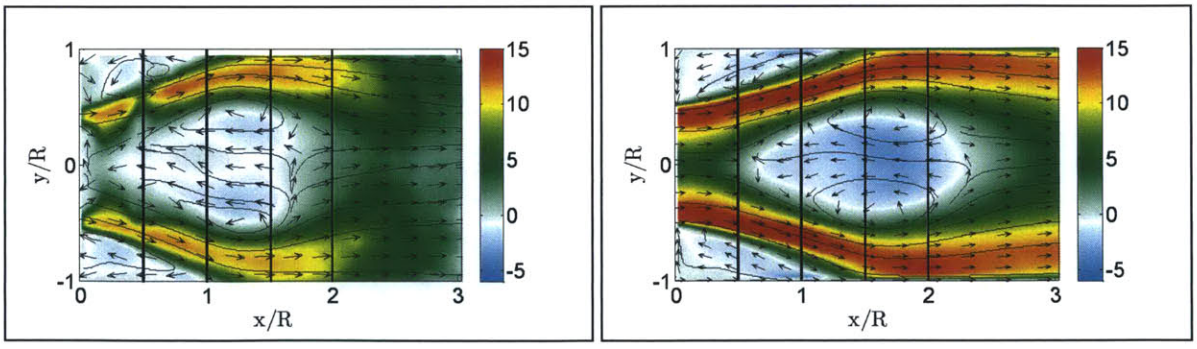

Figure 6.99: Average axial velocity along with the 2D velocity vectors and streamlines (PIV: left, LES: right). The cross-sections at which data are compared are also shown.

Further examination of the axial velocity contours suggests the presence of a single-cell type, closed vortex breakdown bubble, with the front stagnation point located downstream of the

expansion plane. As noted from the mean streamlines in figure 6.100, the IRZ is spatially more compact, spanning a length of approximately *2.0R* downstream of the sudden expansion.

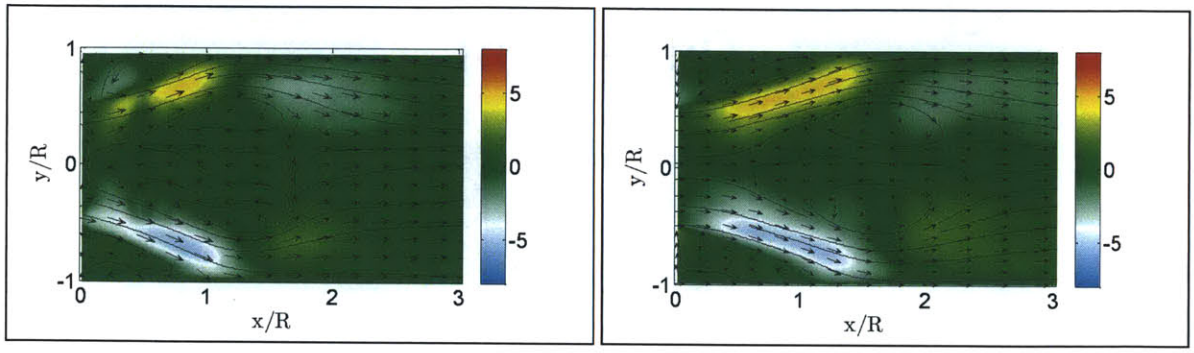

Figure 6.100: Average radial velocity along with the 2D velocity vectors and streamlines (PIV: left, LES: right).

The shortening of the IRZ could be attributed primarily to the influence of flame propagation on the mean flow field. IN general, for low equivalence ratios, the fluid dynamic effects of heat release (turbulent dilatation, increase in viscosity, and a gradual dissipation of momentum) result in elongation of the IRZ, as compared to the non-reacting flow, as noted in Configuration III. The acceleration of the flow (due to dilatation effects of combustion) causes the flow to better overcome the adverse pressure gradients. However, as the heat loading increases, the relative influence of the effect of flame propagation on the flow field topology increases. Eventually, this results in shortening of the recirculation zone, close to its value for the isothermal flow (figure 6.101). This behavior of the recirculation zone size with the change in the equivalence ratio has been observed previously for an axi-symmetric bluff-body stabilized flame [6.11, 6.24] as well.

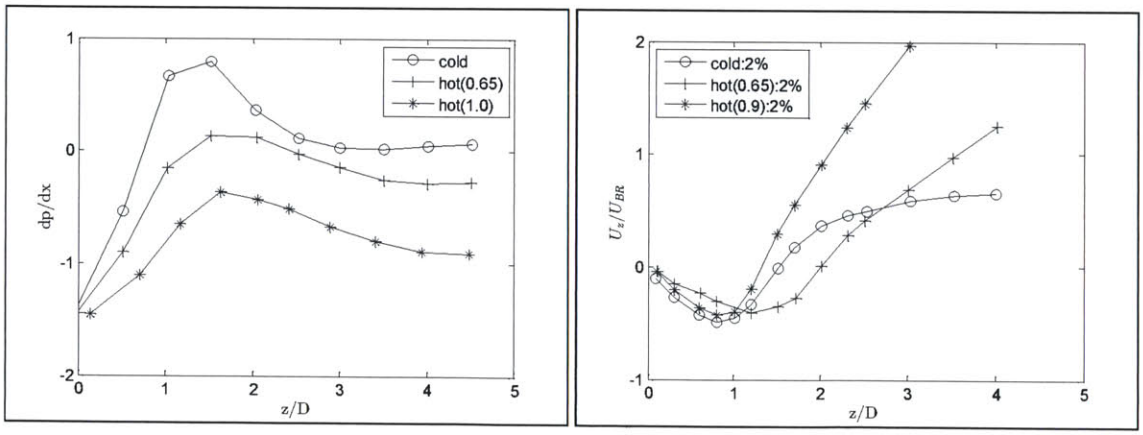

Figure 6.101: (a) Combustor wall pressure gradients in confined isothermal and reacting flows (U_z = 10m/s), (b) Mean centerline velocity for different equivalence ratios (2% fluctuation).

Additionally, the significant narrowing of the IRZ could be attributed to the presence of the reaction zone in the inlet pipe, which accelerates the fluid entering the combustion chamber, thereby reducing the streamline curvature, especially in the presence of wall confinement. Moreover, the propagation of the flame along the OSL and into the ORZ appreciably impacts the mean and fluctuating flow field in the periphery of the IRZ, by suppressing the strong azimuthal flow in the corner region. The elongation of the ORZ also takes place as a result of heat release and gaseous expansion. Coupled with the reduced adverse pressure gradients, it also contributes to the reduced spreading angle of the annular jet. Due to exoethermicity in the shear layer, the flow velocity in the annular jet is also enhanced. Further, in conjunction with narrowing of the inner and outer recirculation zones, the thermal expansion of the jet fluid and the augmented entrainment activity due to combustion generated turbulence, result in increasing the thickness of the annular jet.

In figure 6.102, the contours for the rms axial velocity fluctuations are shown indicating high turbulence activity in the inner and outer shear layers around the periphery of the IRZ. Typically, for reacting flow involving high turbulent burning velocity and heat loading, the enhanced heat release presumably augments the magnitude of both the shear generated turbulence and turbulent dilatation. While the effects of dilatation decrease the turbulent kinetic energy in the mixing layers, fluctuations are reasonably high due to combustion induced turbulence that promotes small-scale eddy development in the shear layer.

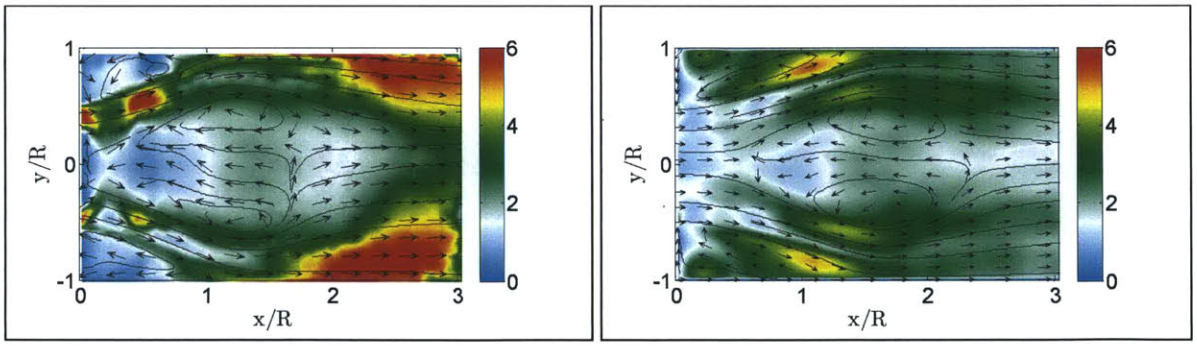

Figure 6.102: rms axial velocity along with the 2D velocity vectors and streamlines (PIV: left, LES: right).

Flow perturbations are also high in the proximity of the wall due to jet impingement, and along the wall shear layer, as a result of combustion induced turbulence. As the flow convects downstream, the effects of dissipation and dilatation (figure 6.103) result in significant suppression of turbulence intensity, and the fluctuating flow field is significantly more isotropic as the fluid convects into the exhaust tube.

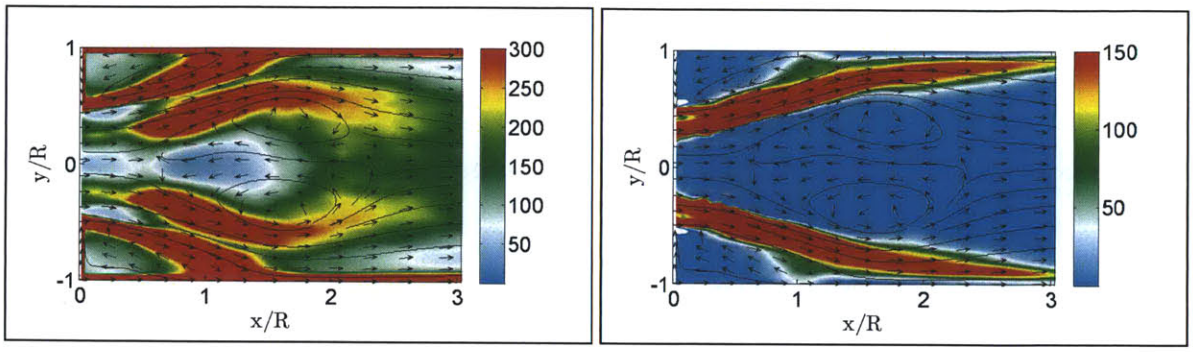

Figure 6.103: (a) Viscous dissipation per unit volume (kg/ms^3), (b) Turbulent dilatation (1/s). The corresponding 2D velocity vectors and streamlines are also shown (LES).

In figure 6.104, the contours of the rms radial velocity and Reynolds stress tensor term are shown, suggesting a slight increase in the radial velocity fluctuations in the shear layers, in contrast to Configuration III, as a consequence of combustion generated shear turbulence. Additionally, the narrowing of the recirculation zone results in enhancing the shear stress and the turbulent kinetic energy in the inward locations of the recirculation zone. Further downstream, however, the flow perturbations near the wall shear layer show a significant reduction, relative to Configuration III, due to the presence of a compact, high intensity flame in the region, and due to the effects of dilatation. Consequently, turbulence anisotropy in the region is also somewhat suppressed, relative to the flow in Configuration III.

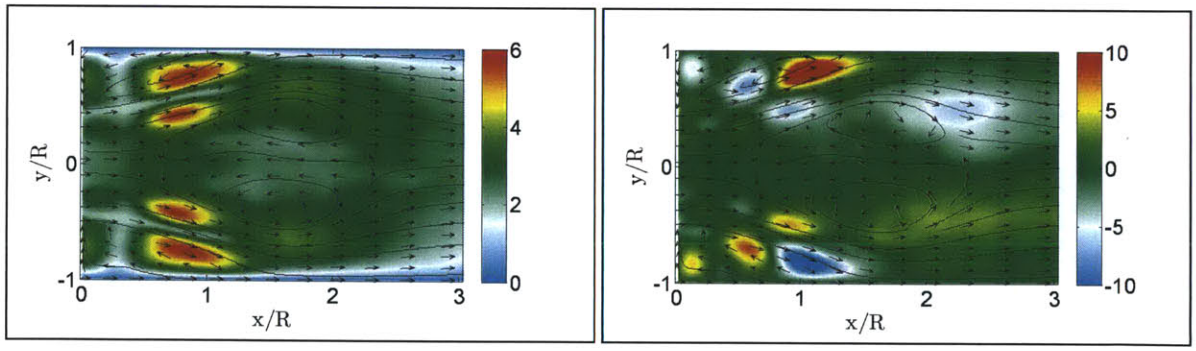

Figure 6.104: (a) rms radial velocity (u_r', m/s), (b) Reynolds stress tensor term ($u_r'u_x'$, m^2/s^2). The corresponding 2D velocity vectors and streamlines are also shown (LES).

In figure 6.105, the normalized profiles for the average axial velocity and rms axial velocity, obtained experimentally and numerically, are compared at different cross sections in the wake region. The LES predictions for the spreading angle and the width of the annular jet as well as the magnitude of the peak axial velocity show good agreement with the PIV measurements. The flow accelerates near the wall due to heat release and thermal expansion, and the magnitude of the peak

jet velocity is observed to be higher than the previous configurations. A gradual spreading angle is also observed, corresponding to the narrowing of the IRZ, and the annular jet is noted to be thicker in this case. Thus, a substantial shift in the mean annular jet structure is seen between Configurations III and IV, and is suitably resolved in the simulations.

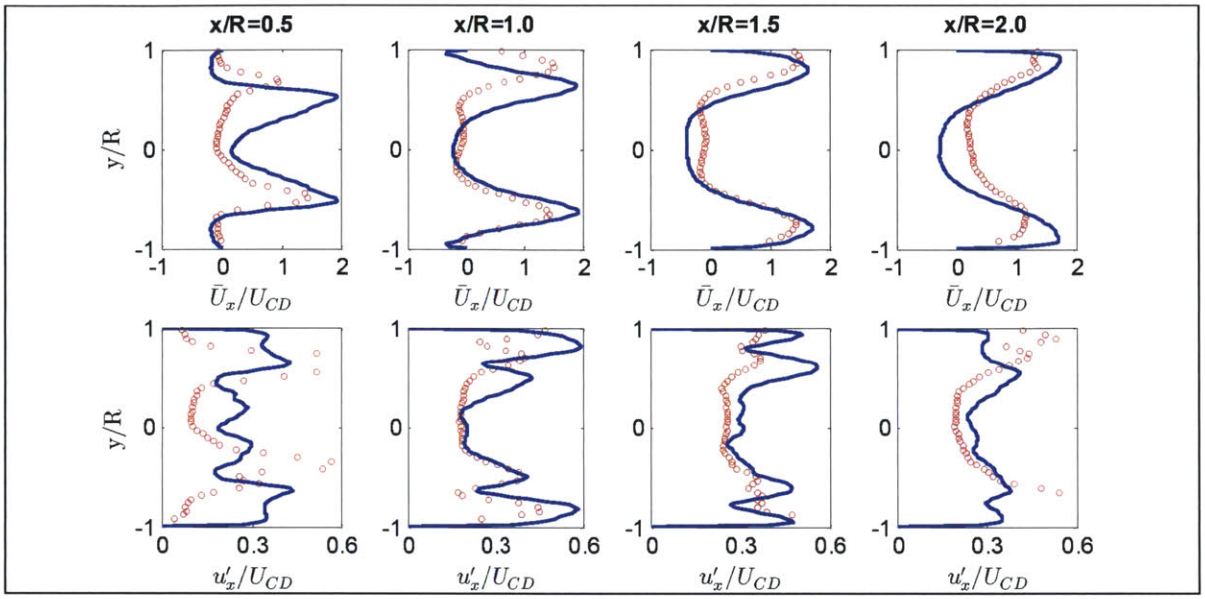

Figure 6.105: Normalized profiles for average axial velocity (top) and rms axial velocity (bottom). ooo PIV, — — — LES

Further, high axial flow oscillations are observed in the inner and outer shear layers, due to combustion generated turbulence, and near the region where the annular jet impinges the wall ($x/R \approx 1$). The turbulence intensity is suitably resolved numerically, although the predictions could be further improved by appropriate mesh resolution near the walls. Adjustments to the PIV setup for the collection of higher resolution flow fluctuation data in downstream locations and near the chamber walls may also be performed. Some discrepancies in the flow-field predictions also exist in the section near the expansion plane ($x/R \approx 0.5$), due to a slight delay in the development of the vortex breakdown bubble, immediately downstream of the sudden expansion, in the simulations. This could be attributed to the sensitivity of resolved flow features to geometric features in the inlet pipe, upstream flow perturbations, and the grid resolution in the boundary layer of the inlet duct [6.9]. Further improvement in the LES predictions could therefore be achieved by accurately accounting for these factors.

6.2.5.11 Configuration IV: PIV DMD Analysis

Next, the DMD modes from analysis of the PIV flow field are presented. As shown in figure 6.97, strong oscillations (~110 Hz) are observed in the shear layer region when the equivalence ratio is increased to 0.65; subsequent analysis of instantaneous velocity field in the shear layer section suggests that the mixing layer is comprised of combustion generated turbulent eddies that are convected as the flow progresses downstream. Additionally, intermittency in the outer shear layer, as measured by the CH chemiluminescence signal for $\varphi = 0.65$, is observed. In figure 6.106, a sample of the time series of the integral CH signal, and the power spectral density of the integral CH series, at a location near the ORZ, are depicted. The power spectral density plots show multiple peaks, including the 10 Hz and 30 Hz frequencies, as observed in Configuration III.

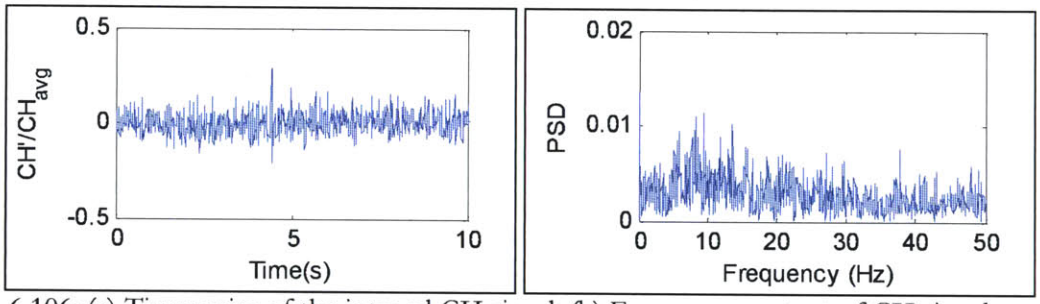

Figure 6.106: (a) Time series of the integral CH signal, (b) Frequency content of CH signal.

Correspondingly, the DMD mode spectrum in figure 6.107c shows an energetic mode corresponding to 110 Hz, as well as flow modes which exhibit oscillations at frequencies in the 10-30 Hz range.

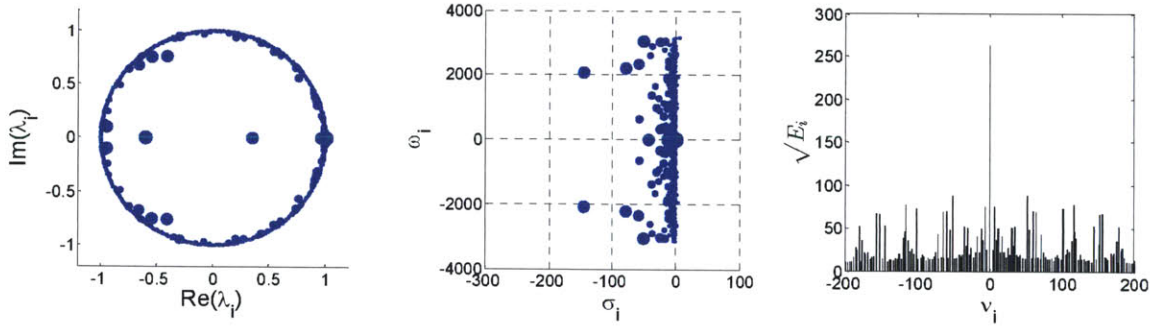

Figure 6.107: (a) Ritz vectors on the complex plane, (b) Frequency, ω, and growth rate, σ, of dynamic modes, (c) Energy content of dynamic modes.

In figure 6.108, the mean mode obtained from the DMD analysis is presented. The averaged flow structure exhibits a central recirculation zone that appears due to breakdown of the vortex core, and the flow is characterized by intense turbulent pulsations in the inner and outer mixing

layers, as expected. The shortening of the IRZ and significant vortex activity in the OSL, as opposed to Configurations II and III, can also be inferred.

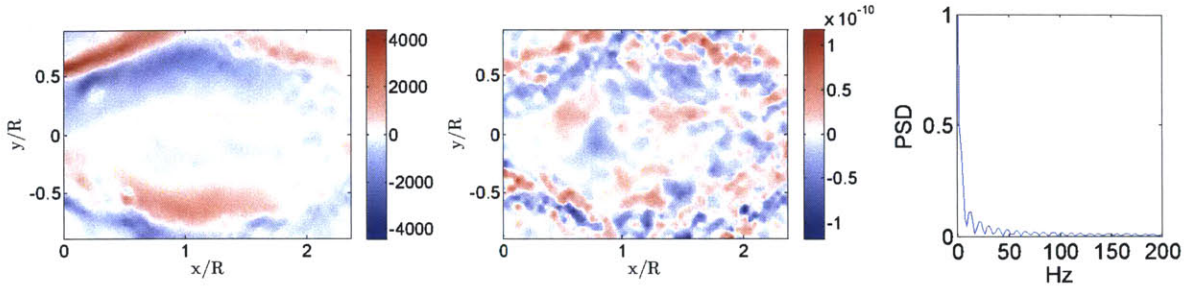

Figure 6.108: 0Hz dynamic mode (Real component: left, Imaginary component: middle, Frequency spectrum of temporal coefficient of real component of dynamic mode: right).

In figure 6.109, the 10 Hz mode is shown, and flow oscillations in the outer mixing layer, near the base of the flame, are observed. The vortex field thus generated is related to the pulsations of heat release observed in the region.

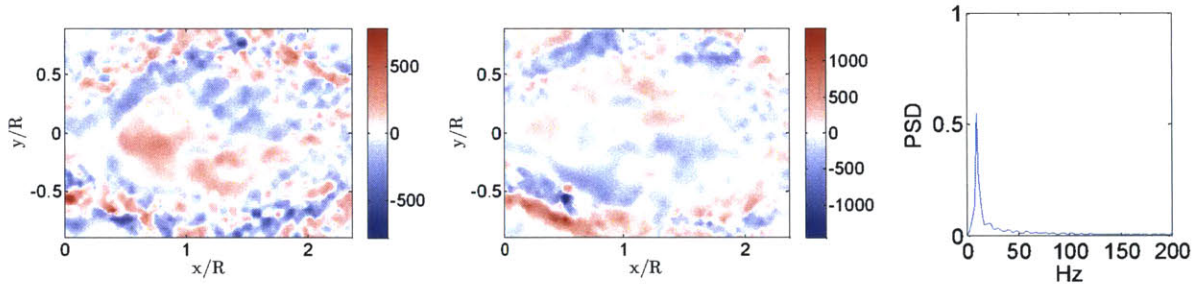

Figure 6.109: 10Hz dynamic mode (Real component: left, Imaginary component: middle, Frequency spectrum of temporal coefficient of real component of dynamic mode: right).

Figure 6.110 shows phase-shifted realizations of the dynamic mode, and is composed of the real and imaginary parts of the Ritz vectors. The eddy vortices correspond to a local instability mode associated with variations of the flow intensity in the OSL/ORZ region, and are influenced by the unsteady heat release in the region.

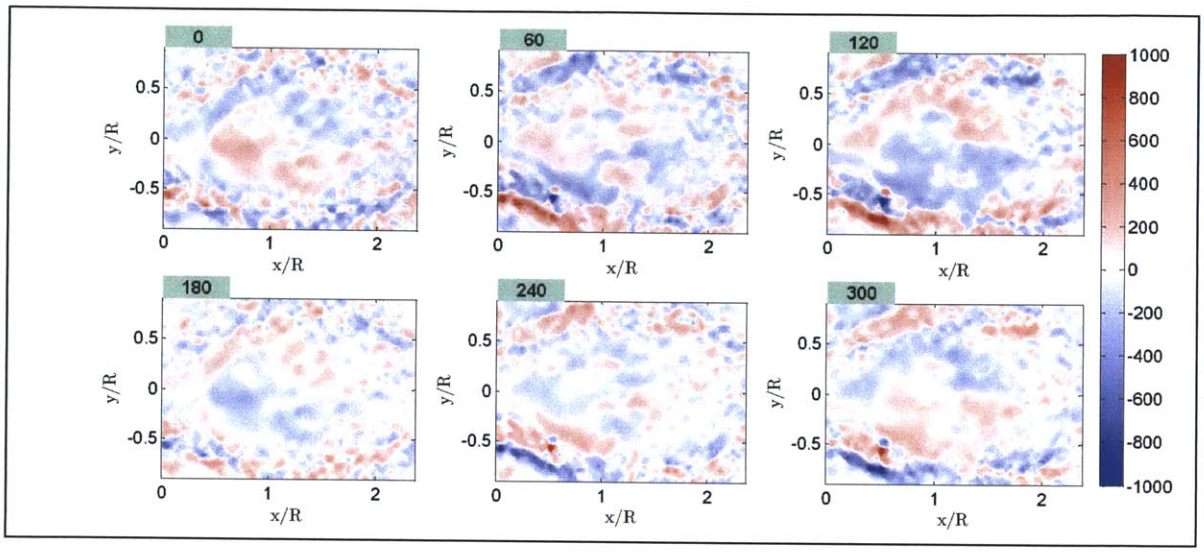

Figure 6.110: Phase shifted realizations of 10 Hz dynamic mode composed of the real and imaginary components along with their temporal coefficients.

Figure 6.111 shows the 30 Hz mode as obtained from the DMD analysis of the PIV data, while the phase-shifted realizations of the dynamic mode, composed of the real and imaginary parts of the Ritz vectors, are depicted in figure 6.112. The mode is comprised of the vortices influenced by the flame advected due to the swirling flow, and resembles the 30 Hz modes observed for Configurations II and III.

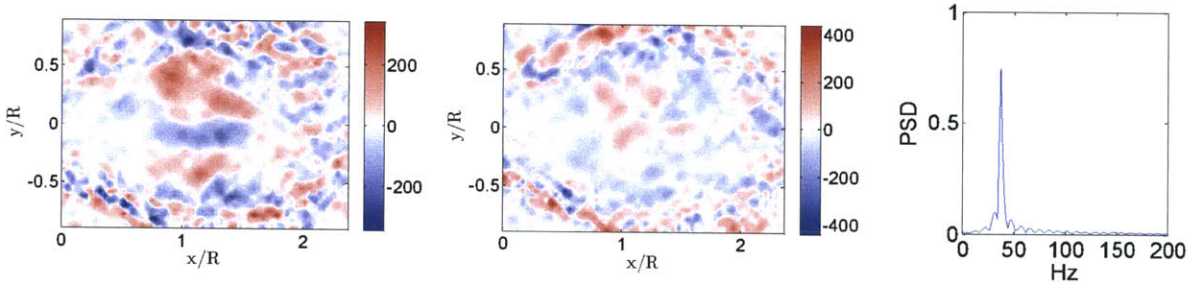

Figure 6.111: 30Hz dynamic mode (Real component: left, Imaginary component: middle, Frequency spectrum of temporal coefficient of real component of dynamic mode: right).

Additionally, by analyzing PIV velocity field data for Configuration IV, using dynamic mode decomposition, it may also be stated that the 30 Hz periodicity of the flame correlates with the convective vortices in the shear layer, and near the region where the jet impinges on the combustor walls. The significance of this observation is evident in the context of an acoustically-coupled combustor configuration, wherein the establishment of a flame in the ORZ at φ=0.65 also corresponds to the first dynamic mode of instability at nearly 35-40 Hz. Thus high-amplitude

acoustic oscillations are observed, in conjunction with the intermittency of the flame in the ORZ, suggesting a resonance between inherent flow/flame instability and the first acoustic mode. However, further investigations are required to elucidate the mechanism of transition from the stable to the unstable flame in an acoustically coupled combustor configuration, and the DMD technique can be an effective tool in understanding the phenomenon.

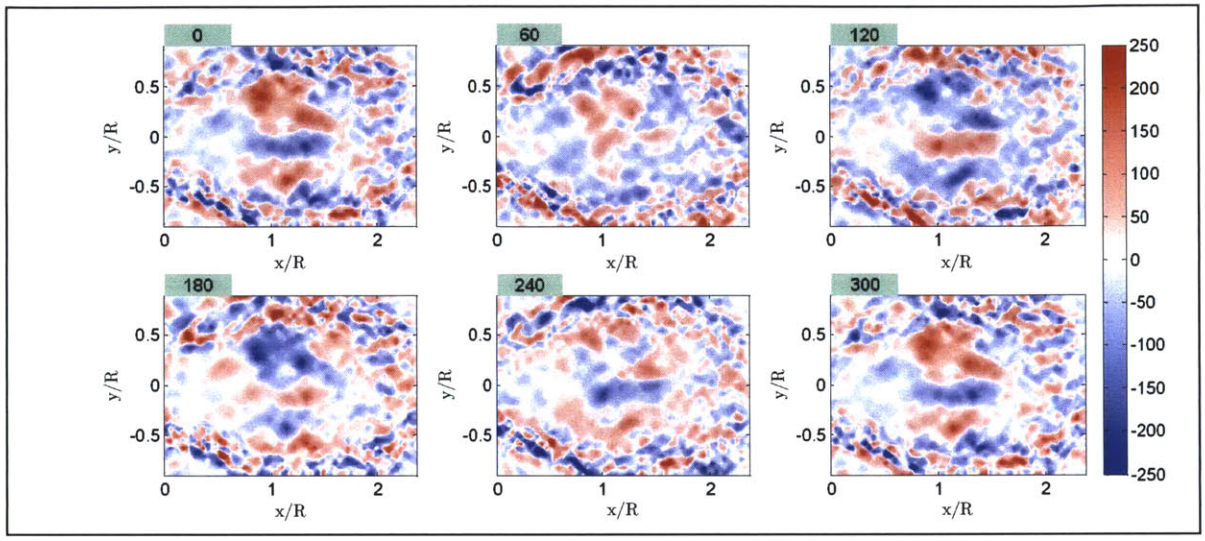

Figure 6.112: Phase shifted realizations of 30 Hz dynamic mode composed of the real and imaginary components along with their temporal coefficients.

In figure 6.113, the 110Hz mode is shown, followed by the phase-shifted realizations of the dynamic mode, composed of the real and imaginary parts of the Ritz vectors, in figure 6.114. The mode is predominantly comprised of eddy vortices in the shear layers, generated due to combustion induced turbulence, in case of Configuration IV, as a result of the augmented heat loading.

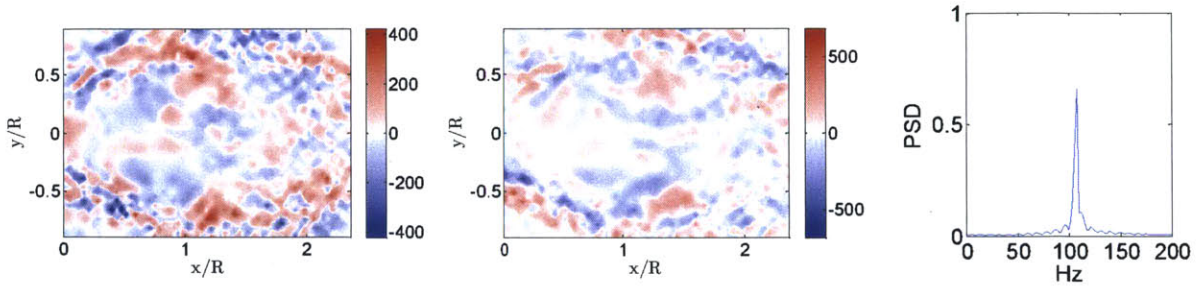

Figure 6.113: 110Hz dynamic mode (Real component: left, Imaginary component: middle, Frequency spectrum of temporal coefficient of real component of dynamic mode: right).

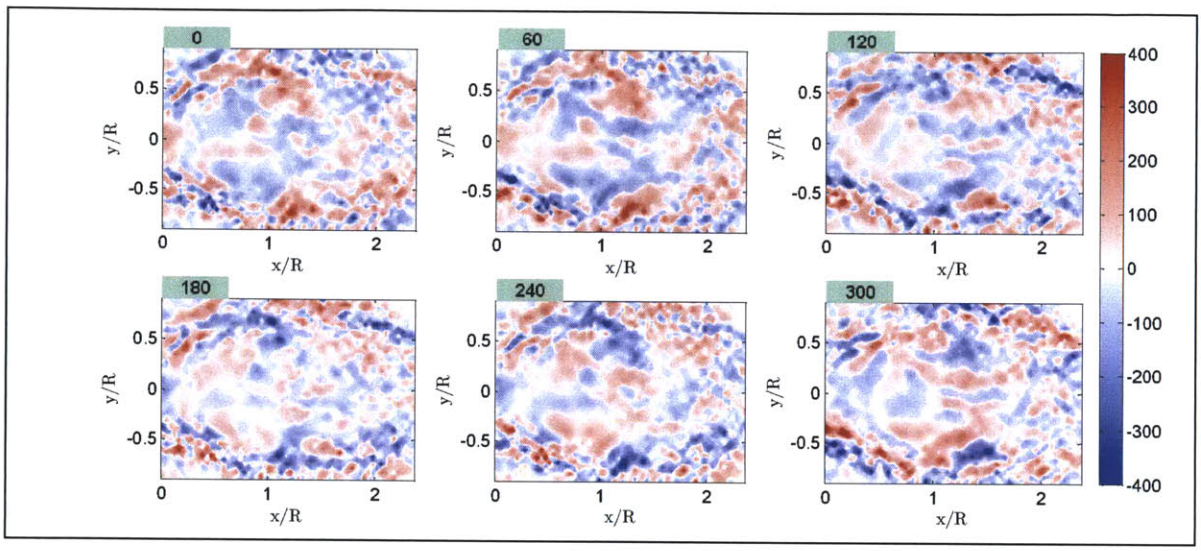

Figure 6.114: Phase shifted realizations of 110 Hz dynamic mode composed of the real and imaginary components along with their temporal coefficients.

6.2.5.12 Configuration IV: LES DMD Analysis

Next, the DMD modes from analysis of the LES flow field data (200 snapshots) are presented, and correspond reasonably well with the modal structures obtained using the PIV measurements.

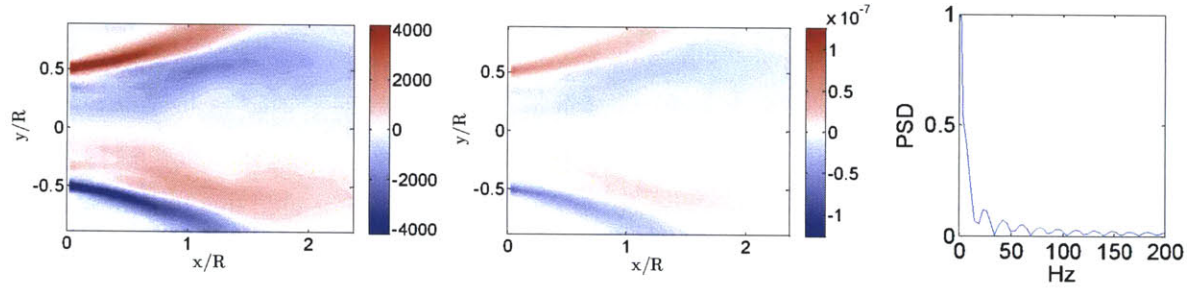

Figure 6.115: 0Hz dynamic mode (Real component: left, Imaginary component: middle, Frequency spectrum of temporal coefficient of real component of dynamic mode: right).

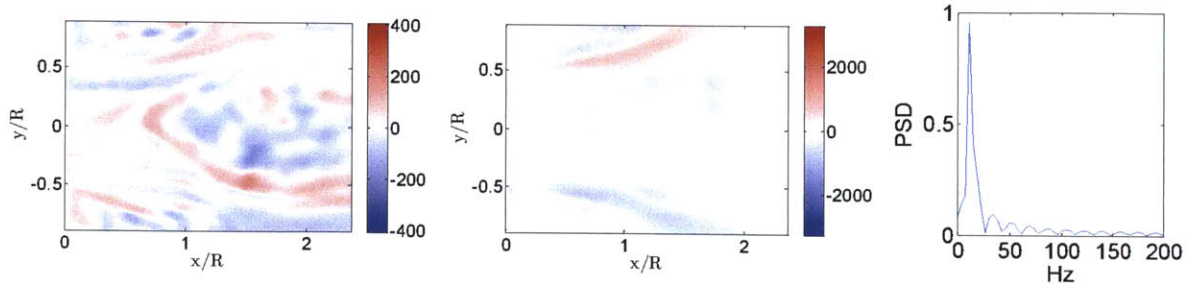

Figure 6.116: 10Hz dynamic mode (Real component: left, Imaginary component: middle, Frequency spectrum of temporal coefficient of real component of dynamic mode: right).

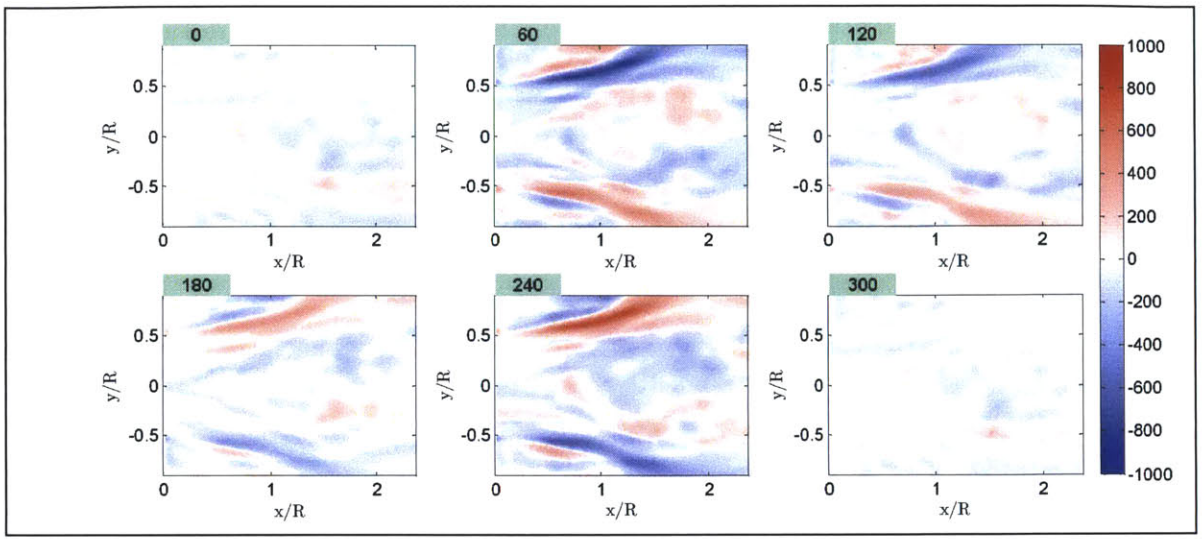

Figure 6.117: Phase shifted realizations of 10 Hz dynamic mode composed of the real and imaginary components along with their temporal coefficients.

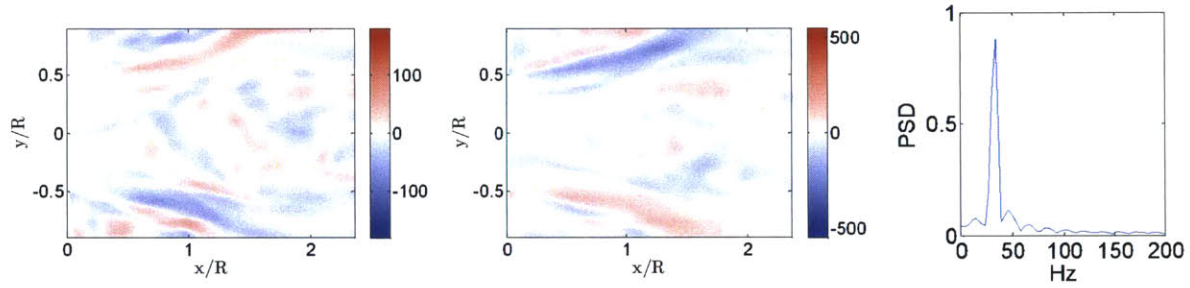

Figure 6.118: 30Hz dynamic mode (Real component: left, Imaginary component: middle, Frequency spectrum of temporal coefficient of real component of dynamic mode: right).

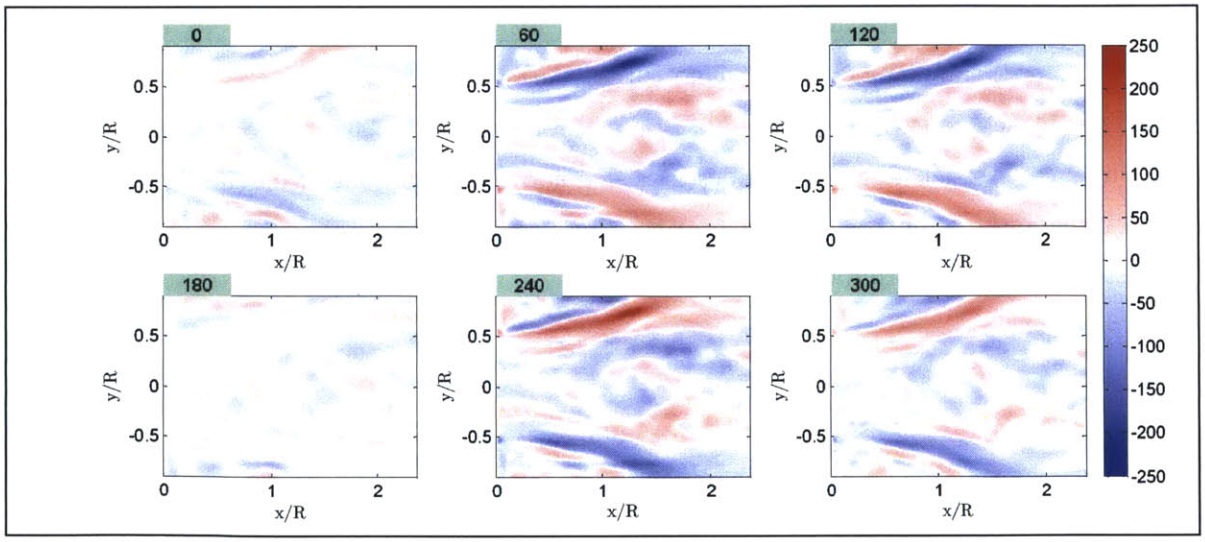

Figure 6.119: Phase shifted realizations of 30 Hz dynamic mode composed of the real and imaginary components along with their temporal coefficients.

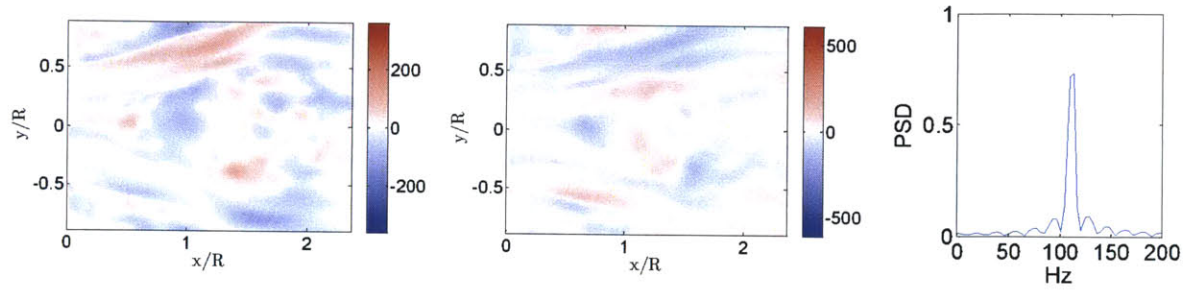

Figure 6.120: 110Hz dynamic mode (Real component: left, Imaginary component: middle, Frequency spectrum of temporal coefficient of real component of dynamic mode: right).

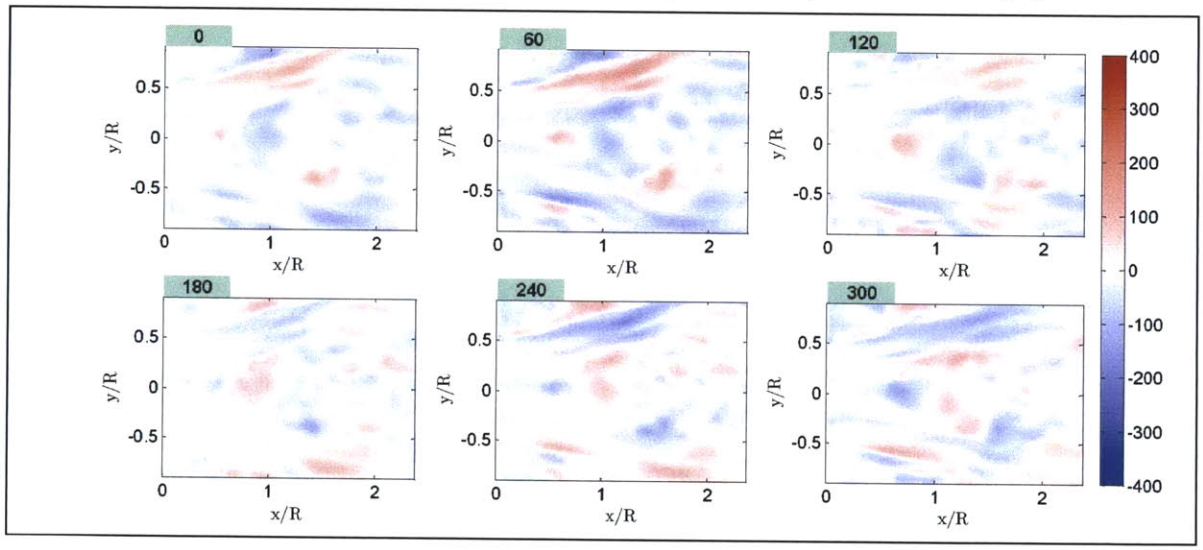

Figure 6.121: Phase shifted realizations of 110 Hz dynamic mode composed of the real and imaginary components along with their temporal coefficients.

The DMD modes from LES results of the heat release field (200 snapshots) that correspond to the frequency of the flow field modes indicated above, are also obtained. The modes suggest intense activity in the inner and outer shear layer regions, as well as in the wall shear layer, where appreciable flame front perturbations are observed.

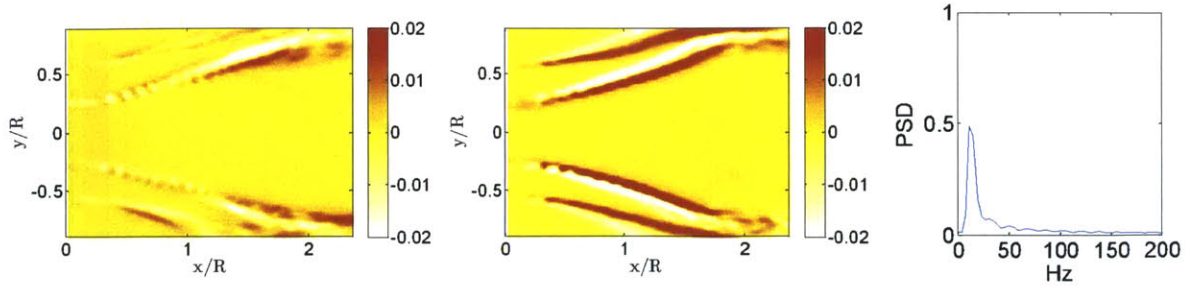

Figure 6.122: 10Hz dynamic mode (Real component: left, Imaginary component: middle, Frequency spectrum of temporal coefficient of real component of dynamic mode: right).

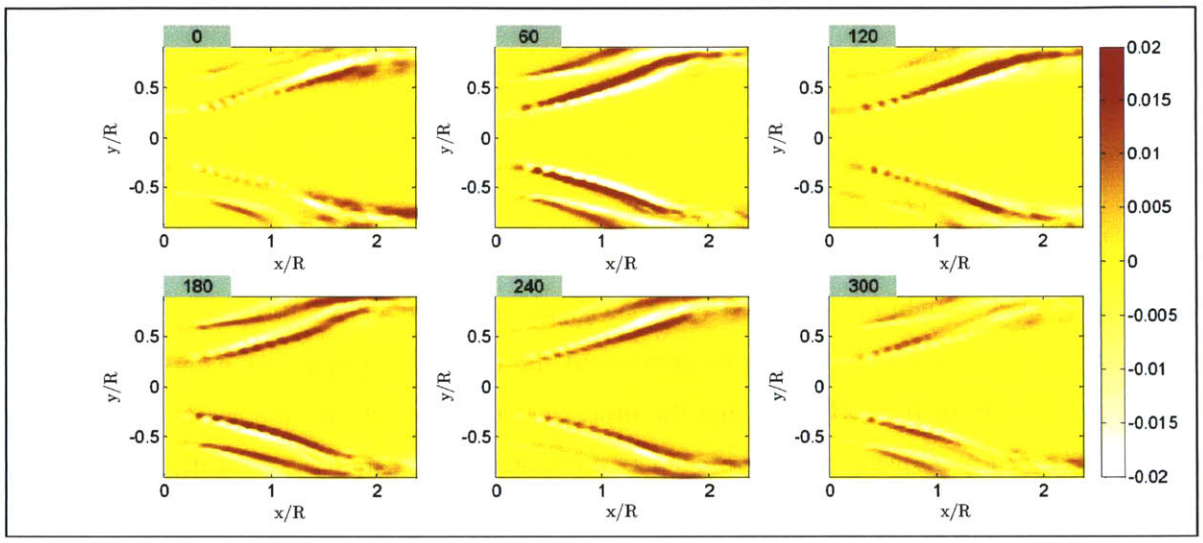

Figure 6.123: Phase shifted realizations of 10 Hz dynamic mode composed of the real and imaginary components along with their temporal coefficients.

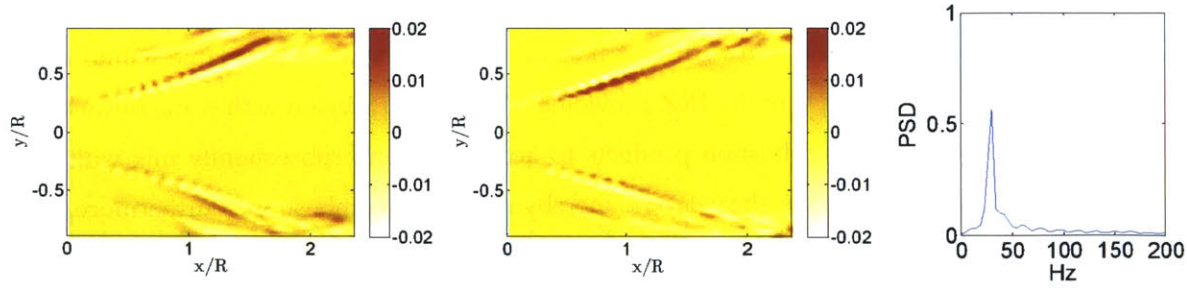

Figure 6.124: 30Hz dynamic mode (Real component: left, Imaginary component: middle, Frequency spectrum of temporal coefficient of real component of dynamic mode: right).

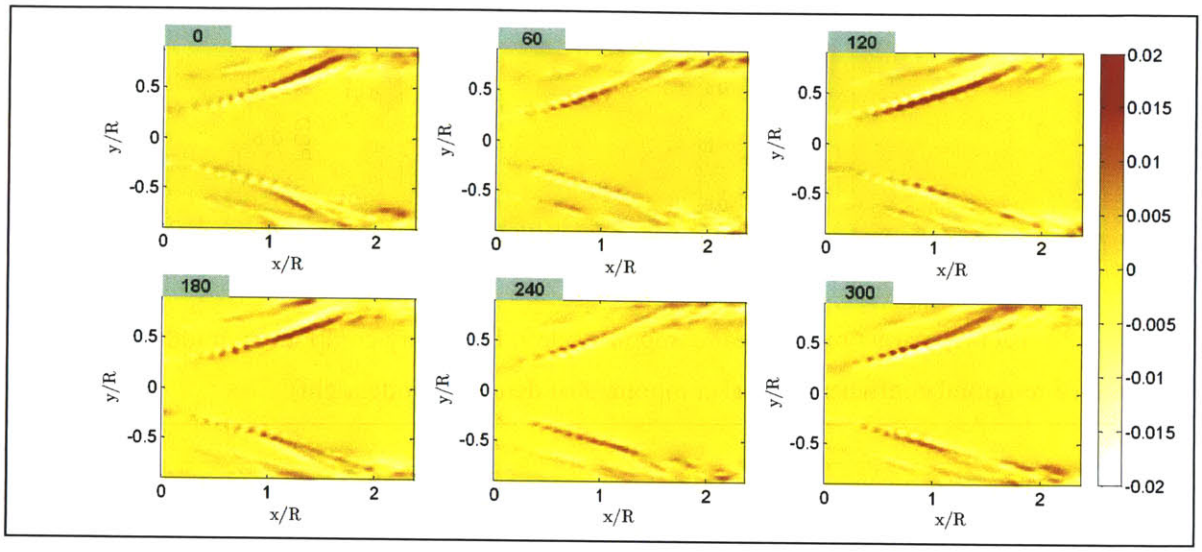

Figure 6.125: Phase shifted realizations of 30 Hz dynamic mode composed of the real and imaginary components along with their temporal coefficients.

6.2.6 Discussion: Reacting Flow

In order to gain an insight into the impact of equivalence ratio on the flame-flow interactions in case of a swirl combustor, it is important to understand the underlying physics of flame stabilization mechanisms involved. It is observed that the time-averaged flow field for the swirler geometry is comprised of the following primary regions: the outer recirculation zone (ORZ, a toroidal recirculating regime), the inner recirculation zone (IRZ, the vortex breakdown bubble), the high velocity, annular fluid jet that divides these regions and expands outwards from the periphery of the inlet pipe, and the shear layers at the edge of the annular jet, denoted here as the outer shear layer (OSL) and inner shear layer (ISL), respectively.

The flow region associated with vortex breakdown serves as the dominant flame stabilization mechanism, with the reversed flow in the IRZ providing a low velocity region with some turbulence intensity. This allows the hot combustion products to accumulate and subsequently mix with the incoming reactant mixture near the shear layers, thereby stabilizing combustion. Furthermore, the blockage induced by the recirculation zone reduces the effective flow passage area, and consequently accelerates the flow velocity in the outer region, also resulting in strong shear stress and turbulence intensity near the wall, which can aid in the mixing process. Depending upon the equivalence ratio, however, the flame can exhibit different configurations (figure 6.126), based upon whether it is stabilized near the stagnation region of the primary recirculation zone (IRZ), or the low velocity regimes of the inner and/or outer shear layers. Aside from the flame macrostructure, fundamental

flow field characteristics such as vortex breakdown bubble structure, annular jet spreading angle, and secondary recirculation zone (ORZ) topology vary substantially between these configurations, as does the turbulence intensity flow field.

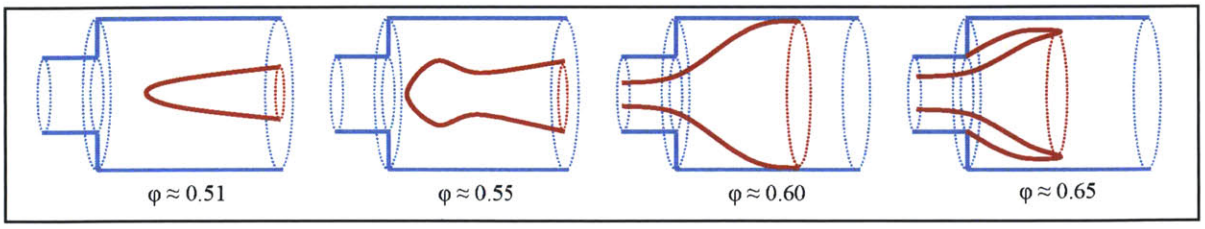

Figure 6.126: Basic flame-shape configurations in a cylindrical swirl combustor: columnar flame, bubble-type wake flame, ISL flame, ISL/OSL/ORZ flame.

Briefly, as the heat release rates increase, the recirculation bubble initially expands, corresponding with the radial spread of the flame, and subsequently contracts, corresponding with the shortening of the flame; thus, the flow field topology, as well as the flame shape, are affected due to heat loading. In order to better elucidate the influence of flame propagation and heat release on the flame macrostructure and flow dynamics, three regions of interest are identified (figure 6.127): ***A.*** region from the dump plane to the location of maximum recirculation zone width, ***B.*** region from the where the jet impinges on the wall to the rear stagnation point, and ***C.*** region downstream of the rear stagnation point. Additionally, the impact of the wall confinement on turbulent flame-flow interaction is also considered, as in [6.11].

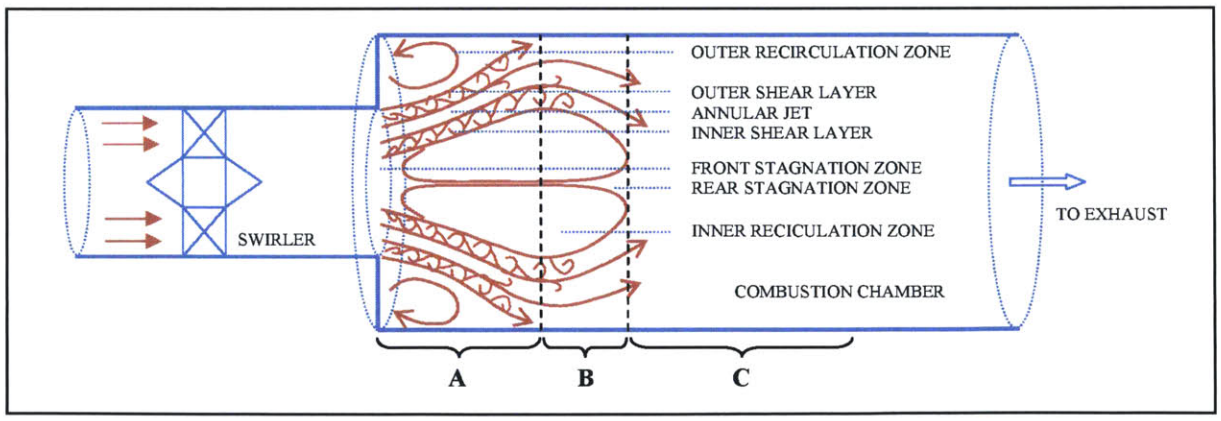

Figure 6.127: Fundamental flow features in a cylindrical swirl configuration.

6.2.6.1 Flame Structure

- **Columnar Wake Flame**

For the lean combustion case, the flame predominantly stabilizes within the IRZ in proximity to the low velocity rear stagnation region (region B). Moderate heat release in this case results in a 'lifted',

weakly burning flame that is characterized by reaction kinetics. The low flame propagation speed inhibits the flame front from penetrating the high strain regions upstream and it mostly exists enveloping the centerline axis in regions B and C forming a tubular structure that extends downstream into the exhaust.

- **Bubble-Type Wake Flame**

For the moderate equivalence ratio, owing to enhancement of the turbulent burning velocity and extinction strain rate, the flame begins to propagate into the ISL, and is predominantly confined to the region within the IRZ. The reaction zone is initiated near the front stagnation zone close to the expansion plane with the flowing reactants preheated and ignited by the heat flux transported outward from the IRZ. In this region, combustion is characterized by the reaction kinetics, resulting in significant scalar fluctuations. While the flame exists in regions A, B, and C, it does show a waist-like feature near region C. The flow accelerates in the annular wall shear layer near region B, and the low propagation speed inhibits the flame surface from stabilizing in this region. It thus 'necks' down towards the low velocity stagnation location, forming a bubble-type macrostructure. The flame brush extends downstream, as the flow convects into the exhaust, as in the previous case, but has a higher intensity brought about by augmented heat release rates.

- **ISL Flame**

With a further rise in the equivalence ratio, a high intensity flame develops that propagates strongly into the ISL, extends into the inlet pipe boundary layer, and anchors on the swirler due to increased flame speed and high extinction strain rate. The ignition of incoming reactants takes place inside the inlet pipe, and a thin, intense flame is observed in this region, due to enhanced heat release rates. The flame front extends into the inner shear layer downstream of the expansion plane (region A), subsequently giving rise to a conical reacting shear layer. The strongly burning flame envelops the IRZ (region B), is characterized by mixing and transport mechanisms, and subsequently thickens due to the entrainment process in the region. As a result of the increased burning velocity, the significant 'necking-down' of the flame in region C also reduces. Additionally, while a weak intermittent flame may appear in the ORZ, high shear strain combined with lean conditions and velocity fluctuations would typically provoke extinctions. Likewise, no persistent flame is observed in the OSL as well, and can be associated with heat losses coupled with moderate heat release.

- **ISL/OSL/ORZ Flame**

A conical flame macrostructure is observed for this case, which however has a persistent reaction zone that extends into the ORZ and the OSL, and can be associated with the augmented burning

velocity, enhanced heat release and higher extinction strain rate. The compact flame primarily exists in regions A and B and is characterized by mixing and entrainment processes. The increase in the heat release and the extinction strain rate allows the flame to propagate and persist in the OSL, and has been observed in similar swirl geometries [6.11]. The reaction zone also has higher intensity in region B, along the wall shear layer, as compared to the flame in Configuration III.

To summarize, different factors contribute to altering the flame macrostructure, as the heat loading increases. For example, the mean and fluctuating flow field (eg precessing of the flow, and the strain in the shear layers), can influence flame stabilization and its intensity. On the other hand, the heat release also substantially impacts the flow (eg vorticity production, increase in viscosity, and flow acceleration). Depending on these flame-flow interactions, the flame exhibits different configurations as the equivalence ratio is varied, based upon whether it is stabilized near the stagnation region of the primary recirculation zone (IRZ), or the low velocity regimes of the inner and/or outer shear layers. The contours for the magnitude of the strain rate tensor are shown in figure 6.128, indicating the high strain regions, which can influence the flame stabilization location.

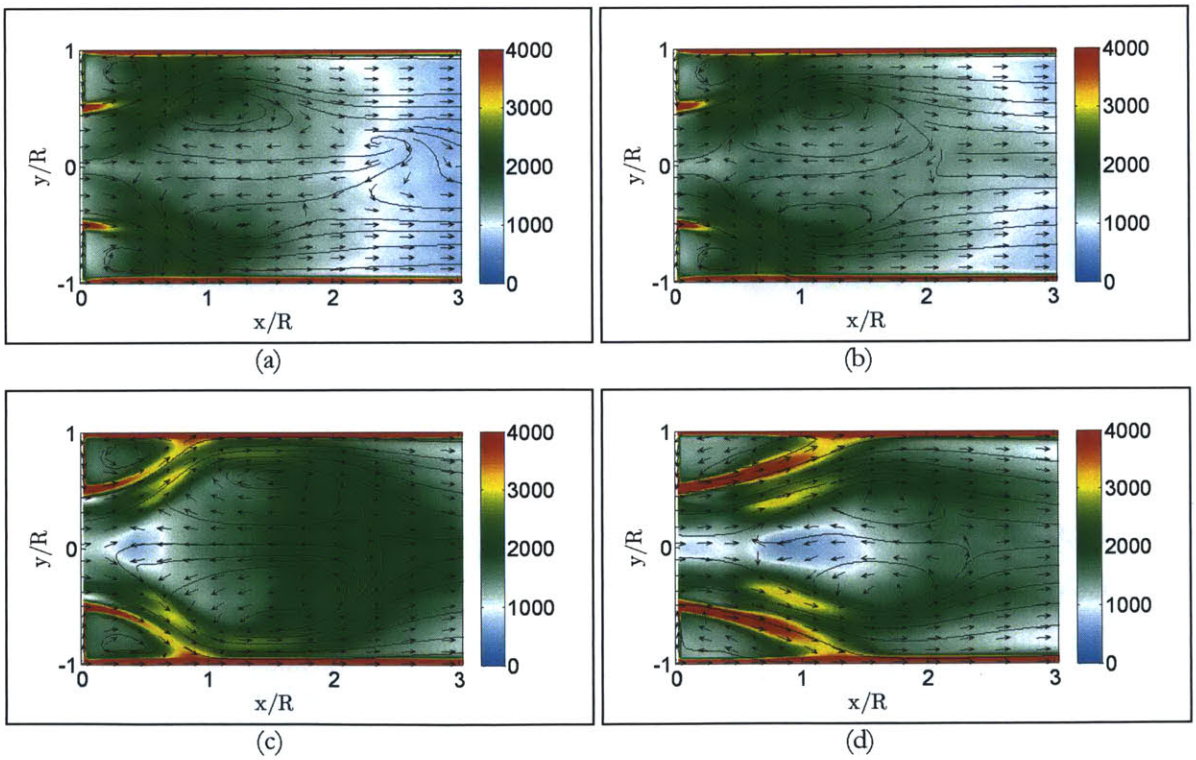

Figure 6.128: Contours of magnitude of strain rate tensor: (a) Columnar wake flame, (b) Bubble-wake flame, (c) ISL flame, (d) ISL/OSL/ORZ flame.

Besides influencing the flow field topology, as a result of heat release, the change in the heat loading also influences the flame speed, specific heat release, extinction strain rate, as well as the wall heat flux. This can significantly impact the flame stabilization location, as well as locations of intense heat release within the combustor chamber. The volumetric heat release rate contours, obtained using a common normalizing factor for all the equivalence ratios, are shown in figure 6.129, and highlight the influence of equivalence ratio on the net heat release rate as well as the location of the average reaction zone.

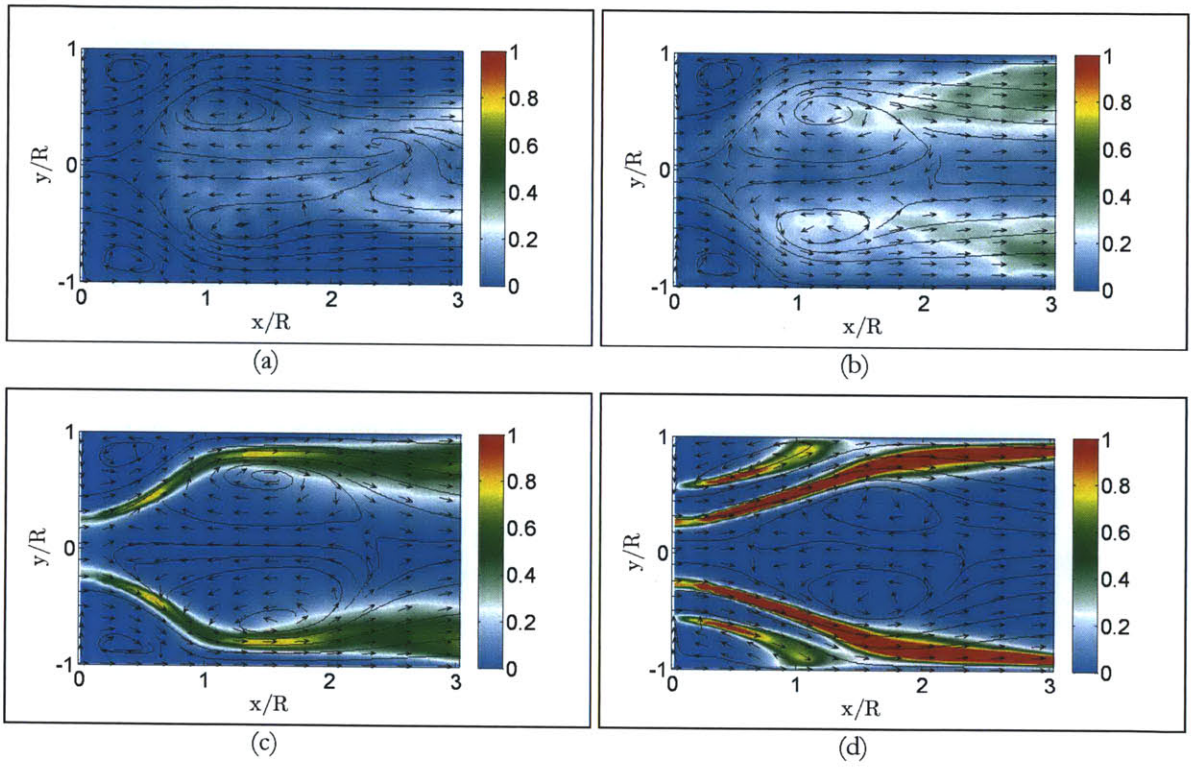

Figure 6.129: Contours of normalized heat release rate: (a) Columnar wake flame, (b) Bubble-wake flame, (c) ISL flame, (d) ISL/OSL/ORZ flame.

6.2.6.2 Average Flow Field

- **Columnar Wake Flame**

For the low equivalence ratio case, the fundamental flow structures are somewhat similar to those in the isothermal case, primarily due to the downstream location of flame stabilization. A single-cell recirculation region is observed, with reverse mass flow occurring even in downstream locations (region C). The presence of flame however does result in a slight enhancement of the reverse flow velocity in the IRZ due to exothermicity.

- **Bubble-Type Wake Flame**

For the bubble-type flame, the annular jet flow takes the shape of a cone, and the radial spreading angle of the jet is also greater. The increased deflection of the mean separation streamlines result from a larger recirculation zone width in region A, and the incoming fresh mixture behaves more as a thin annular jet than as a thick jet spreading into the combustor. Thus, streamlines around the IRZ periphery are crowded and mean velocity gradient increased, particularly in the narrow shear layer region. The IRZ is broader in region B, and forms a closed recirculation bubble, while the flow significantly accelerates downstream of the rear stagnation region. However, the LES flow field predictions differ slightly from the experimental measurements, since the complete transition of the flame macro-structure is not reproduced in the simulations.

- **ISL Flame**

With a further increase in equivalence ratio, the axial location of maximum recirculation zone width shifts upstream in region A, the IRZ marginally contracts in region B, and there is greater acceleration of the flow in region C due to an increase in dilatation from higher heat release rates. The mean reverse flow velocity along the centerline also reduces, due to the formation of a secondary vortex region within the IRZ, which results in the formation of a toroidal vortex breakdown bubble (VBB). The strongly burning flame propagates into the ISL, and significantly influences the flow as it enters the combustion chamber. Heat release and thermal expansion of the mixture in the inlet pipe result in suppression of the precessing vortex activity, as well as appreciable flow acceleration of the fluid in the annular jet. The radial spreading angle of the jet however remains high, due to the presence of a broad vortex breakdown bubble, which squeezes the annular jet towards the wall.

- **ISL/OSL/ORZ Flame**

In this case, a drastic decrease in the streamline curvature, as well as the width of the recirculation zone is observed; the axial span of the IRZ also reduces significantly. This flow behaviour may be attributed to the augmented propagation effects of the flame, which result in the formation of a compact flame front and significantly influences the flow field topology. The flame propagates into the inlet pipe, which accelerates the incoming reactant jet mixture, and also contributes to the narrowing of the spreading angle of the annular jet, as it enters the combustion chamber.

To summarize, different factors contribute to altering the radial and axial extent of the IRZ, as the heat loading increases. Typically, flow acceleration due to turbulent dilatation together with prevention of mean streamline curvature by confinement causes the flow to better overcome the

adverse pressure gradients. Coupled with the gradual dissipation of momentum, the fluid dynamic effects of heat release tend to elongate the IRZ (as seen in Configuration II). In contrast, enhanced flame propagation effects tend to shorten the core vortex structure, with the streamlines curving towards the centerline further upstream (as seen in Configuration IV). Depending on which phenomena dominate, the axial extent of the IRZ expands or shrinks. As regards, the radial extent of the recirculation strength, the location of the flame appears to dictate the IRZ width; for the bubble-type wake flame, the presence of the flame within the VBB leads to flow expansion and widening of the IRZ. As the heat loading increases and the reaction zone enters the boundary layer, this results in a slight narrowing down of the IRZ. For the high heat release scenario where the flame persists in the ORZ, and results in elongation of this outer vortex cell, a significant reduction in the radial spread of the annular jet, and narrowing of the IRZ, is observed.

6.2.6.3 Flow Perturbations

- **Columnar Wake Flame**

For the low equivalence ratio case, the flow fluctuations in region A are somewhat similar to those in the isothermal case, primarily due to the downstream location of flame stabilization, and peak in the shear layers due to the presence of the PVC. Further downstream, in region C, there is a slight increase in turbulence intensity, as compared to isothermal flow, as a result of combustion induced turbulence.

- **Bubble-Type Wake Flame**

For this configuration, the aerodynamic blockage caused by the IRZ causes a radially outward deflection of the separation streamlines at the edge of the ISL which results in squeezing of the annular gaseous jet towards the chamber walls at the axial location of maximum IRZ width. Consequently, this shifts turbulence production radially outward and the turbulence intensity is concentrated in the shear layer around the periphery of the IRZ in region A. The flow field fluctuations are also generally high near the rear stagnation zone in region B where flow reversal takes place; the incoming reactants from the annular jet that curves towards the centerline axis mix intensely with the hot products stored inside the IRZ, generating substantial flow oscillations.

- **ISL Flame**

With an increase in the equivalence ratio, the higher heat release rates result in increasing the turbulent dilatation as well as combustion induced turbulence. For the moderate equivalence ratio case, the velocity fluctuations in the shear layer region are now of slightly reduced intensity. However, flow fluctuations are significantly high in the region where the annular jet impinges the

wall, and in the wall shear layer region, where a strongly burning flame exists (that also partially 'necks' towards the rear stagnation zone).

- **ISL/OSL/ORZ Flame**

For the high heat release scenario, while small-scale eddy growth is enhanced in the shear layer in region A, dilatation effects significantly influence the turbulent flow field in region C. Additionally, the existence of flame upstream in the boundary layer accelerates the annular jet as it enters the combustion chamber, and reduces the spreading angle of the jet. This generally results in narrowing the recirculation zone, which shifts the regions with strong concentration of both shear stress and turbulent kinetic energy to radially inward locations of the IRZ. Also, combustion is almost complete around the wall shear layer in region C, and reduced axial turbulence intensity is observed in the region of the rear stagnation zone (as compared to Configuration III).

6.2.6.4 Impact of Wall Confinement

Wall confinement, in general, prevents any significant deflection of mean flow streamlines by restricting the radially outward spread of the annular jet, thereby narrowing the IRZ in contrast to an open flame, and also produces flow acceleration to elongate the IRZ. As compared to an open flame, it also results in higher mean reverse flow velocity and an increase in recirculated mass flow [6.11]. Further, turbulence production is mainly due to Reynolds-stress/shear-strain interaction, and therefore restricted to the shear layer surrounding the maximum width of the recirculation zone. If confinement is removed, however, turbulent dilatation and mean pressure gradients (i.e. normal and not Reynolds stresses) would contribute to generation of turbulent kinetic energy. In other words, suppression of mean streamline curvature by confinement results in reducing the relative influence of turbulent advection and shear-generated turbulence; turbulent dilatation and viscous dissipation processes dominate, especially for high heat loading scenarios, resulting in somewhat lower Reynolds shear stresses, turbulence intensities and turbulent kinetic energy. In contrast, for an open flame, large streamline curvature may even compensate for any damping of turbulence by dilatation and generates larger axial and radial turbulence intensities and turbulent kinetic energy as compared to confined flows [6.11].

Additionally, as shown in figure 6.130, the combustor wall also results in heat losses and can appreciably influence the stabilization of the flame in the OSL, particularly for moderate equivalence ratios [6.12, 6.25]. This can also be inferred from the wall heat flux contours, as depicted in figure 6.131, where the heat flux over the wall circumference is projected normally onto a diametrical cross-section. Results indicate appreciable heat flux for moderate to high equivalence ratio scenarios,

which can significantly impact the temperature field in the ORZ/OSL region, provoke extinction, and influence the stabilization of the flame.

Figure 6.130: Contours of reaction source term: a. Original TFC model, b. Extended TFC model: 'flame speed without heat loss effects', c. Extended TFC model: 'flame speed with strain and heat loss effects'.

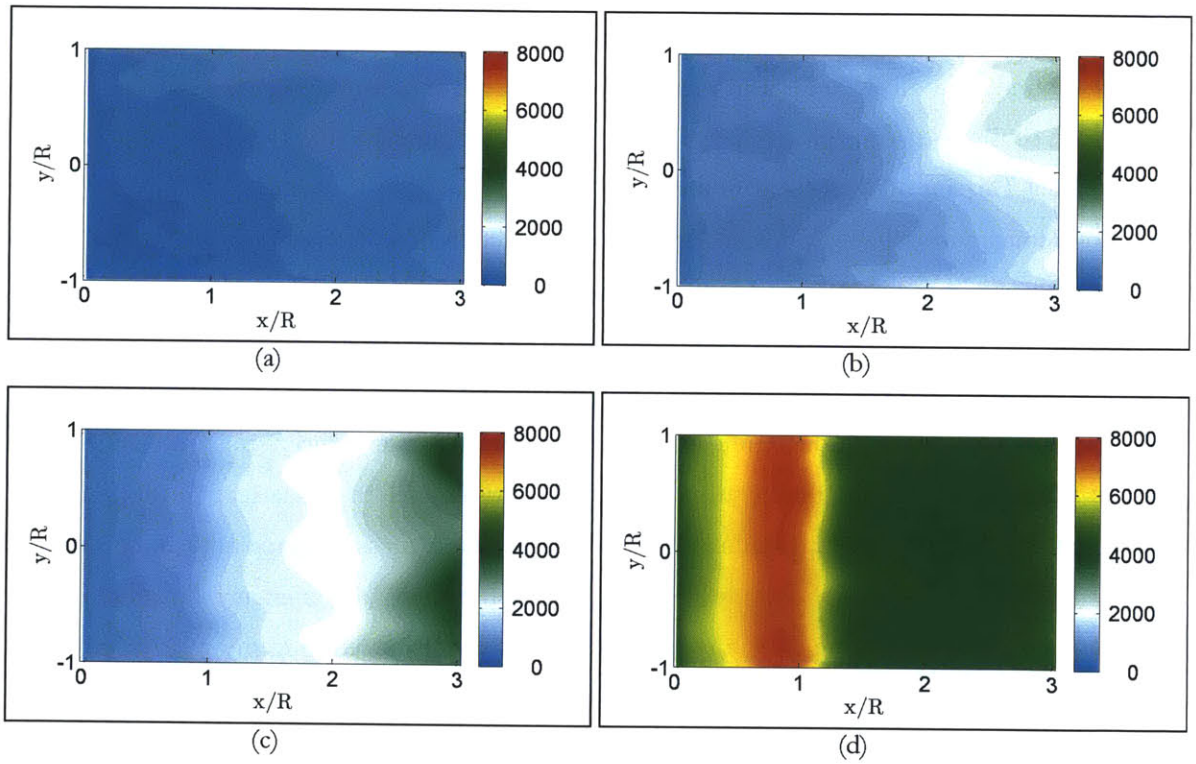

Figure 6.131: Contours of wall heat flux: (a) Columnar wake flame, (b) Bubble-wake flame, (c) ISL flame, (d) ISL/OSL/ORZ flame.

6.3 Conclusions

In this chapter, a preliminary analysis is conducted to assess the effect of equivalence ratio variation on flame-flow dynamics using PIV and LES techniques. The spatial distribution of the flame in the combustion chamber is governed by its stabilization location and can significantly influence the heat loadings to combustor hardware, thereby having important implications on combustor operability, durability, and emissions. For example, the heat transfer to the recirculation zones, the degree of flame spreading to combustor walls, or the location of the flame can be fundamentally different

between flame configurations. In an acoustically uncoupled configuration, flames take on stationary configurations, anchoring within the shear layers of the flow, dependent upon geometry, Reynolds number and equivalence ratio. These aspects can consequently have implications on combustion stability as well. This work, therefore, attempts to numerically predict the variation in flame macro-structure with equivalence ratio, as observed experimentally for an acoustically uncoupled, laboratory-scale swirl combustor. The results indicate that the numerical simulations can suitably reproduce the flame transition phenomena, and the predictions for the flame-flow field correspond well with the experimental measurements. Further, the dynamic mode decomposition analysis of the PIV and LES data suggests that the simulation framework can adequately capture the dynamic characteristics of the flow field, as observed in the laboratory setup.

7 PREMIXED COMBUSTION ANALYSIS IN A BACKWARD-FACING STEP CONFIGURATION

7.1 Overview

To analyze the phenomenon of flame dynamics and to understand turbulence-chemistry interactions in the context of lean premixed combustion, the backward-facing step configuration, in which the flame is stabilized in a two-dimensional turbulent mixing layer formed at the edge of the step, is often studied. The setup preserves the essential features of premixed combustion with stabilization achieved by recirculation of hot products and is also a simpler configuration to observe and model. Over the past few years, numerous studies have been performed [7.1-7.3] to assess the effect of combustion on the mean flow field properties such as mixing layer growth, entrainment rate, and reattachment length.

The significant impact of modifying the equivalence ratio and/or fuel composition on the dynamic flow features has also been analyzed for wake-stabilized flames. For example, the dependence of the recirculation zone size and structure on the fuel composition for C3H8/H2/air lean premixed flames, stabilized in a backward-facing step combustor, has recently been studied using high-speed particle image velocimetry (PIV) and chemiluminescence measurements [7.4]. Results have shown an intricate coupling between the flame anchoring and the recirculation zone structure and length, as well as shear layer growth rate. In another experimental study, the influence of the flow parameters and the equivalence ratio on the recirculation zone structure and the turbulence properties within and surrounding this zone have been studied for an axi-symmetric bluff body [7.5]. It also has been shown that the recirculation zone size, in contrast to the isothermal case, initially increases when reaction takes place, and subsequently, with an increase in equivalence ratio, reduces back to the cold flow value [7.6-7.7]. A similar phenomenon is observed in case of a swirl combustor, where increasing the equivalence ratio dramatically influences the recirculation zone size, as well as the flame dynamics [7.8].

It is now well known that the change of equivalence ratio can also significantly influence flame stability, and the phenomenon has been an active area of research in the past few years. For example, recent experiments for an acoustically-coupled backward-step combustor configuration have shown distinct dynamic regimes based the operating range for the equivalence ratio [7.9]. At high but lean equivalence ratios, the flame is unstable and oscillates strongly as it is wrapped around the large unsteady wake vortex. At intermediate equivalence ratios, weakly oscillating quasi-stable

flames are observed. Near the lean blowout limit, long stable flames extending from the corner of the step are formed. Similarly, distinct flame-flow regimes have been observed in case of a cylindrical sudden expansion swirl combustor [7.10]. At high but lean equivalence ratios, the flame is unstable and oscillates strongly while weakly oscillating quasi-stable flames are observed at intermediate equivalence ratios. Near the lean blowout limit, long stable flames are formed.

Therefore, significant effort has gone into the study of equivalence ratio changes on flame-flow interactions, both experimentally and numerically [7.11-7.18]. While progress has been made in this regard, further investigation is warranted, beginning with analysis of acoustically-uncoupled systems. The present work attempts to build upon the previous research by focusing on a backward-facing step, and investigating the influence of equivalence ratio variation on the flow features using state-of-the-art experimental and numerical techniques.

The next section provides a description of the experimental configuration and simulation setup utilized in the current work. The data obtained from the experimental PIV system and numerical LES code is then presented corresponding to the acoustically-uncoupled geometry. It is observed that the variation in the equivalence ratio can appreciably influence the large-scale coherent flow features as well as the dynamics of the flow, which can significantly impact combustion instability in acoustically-coupled systems. Finally, forced response of the flame to imposed velocity fluctuations at the inlet is studied numerically using LES and DMD approaches, and conclusions are presented.

7.2 Backward Facing Step Combustor

An acoustically-uncoupled canonical backward facing step configuration [7.11] is employed for analysis of stable reacting flow, apart from initially performing cold flow analysis. In this section, details are provided about the combustor configuration, the corresponding PIV system, as well as the numerical setup.

7.2.1 Experimental Configuration

The backward facing step configuration, shown in figure 7.1, consists of a step of height (H) 20 mm and a rectangular cross section of 40 mm x 160 mm downstream of the step. A mixture of air and propane is introduced at equivalence ratios of 0.63 and 0.85, at a bulk inlet velocity (U_{SH}) of 5.3 m/s (Reynolds number, Re_{SH} = 6500, based on the step height H and the bulk fluid velocity U_{SH}). The inlet temperature (T_S) is 293 K and the nominal pressure is 101 kPa. The first 40 cm downstream where the flame is anchored consists of a quartz tube for optical access. The overall acoustic length of the combustor (from the choke plate to the end of exhaust tube) is 4.5 m. The flow is choked

upstream to prevent equivalence ratio oscillations and to provide a known acoustic boundary condition.

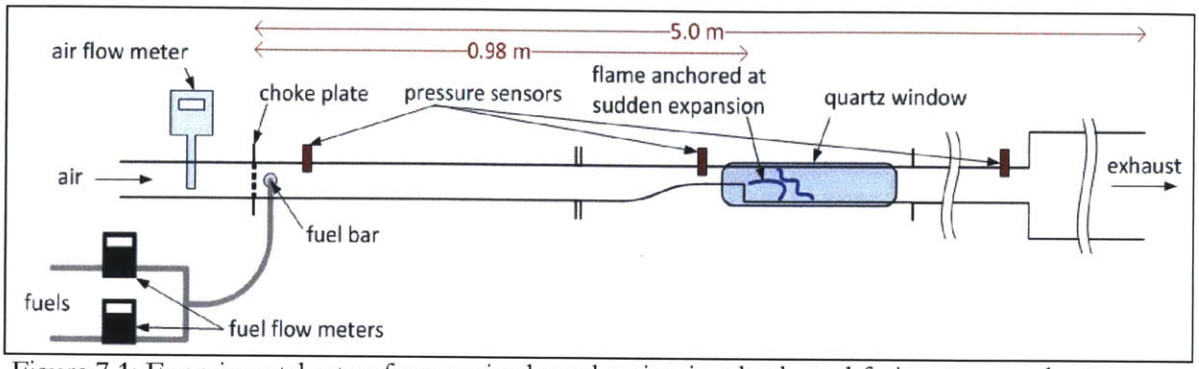

Figure 7.1: Experimental setup for premixed combustion in a backward facing step combustor.

7.2.2 PIV System

Planar velocity fields and flame surface topology are obtained using phase-locked particle image velocimetry (PIV). The schematic of the setup is shown in figure 7.2. The light source consists of a Nd:YLF laser of wavelength 527 nm capable of producing dual pulses at a rate up to 5 kHz with a peak power output of 25 mJ/pulse. A 1280 x 1024 pixel NAC GX-1 CMOS camera, with an Fmount Nikon 60 mm micro-lens with an aperture of f/8 was used for imaging. The interval between the laser pulses was set to 10–30 μs depending on the flow velocity. A light sheet less than 1 mm thick in the imaged region was generated using a spherical lens with a focal length of 1000 mm and a cylindrical lens with a focal length of 20 mm. The former was used to reduce the diameter of the beam and the latter was used to diverge the beam to generate a sheet. Bypass air, taken from the inlet pipe upstream of the choke plate, is routed through a cyclone-type seeder. Seeding particles consisting of 1.5–3 μm diameter Al_2O_3 are injected into the main air immediately downstream of the choke plate.

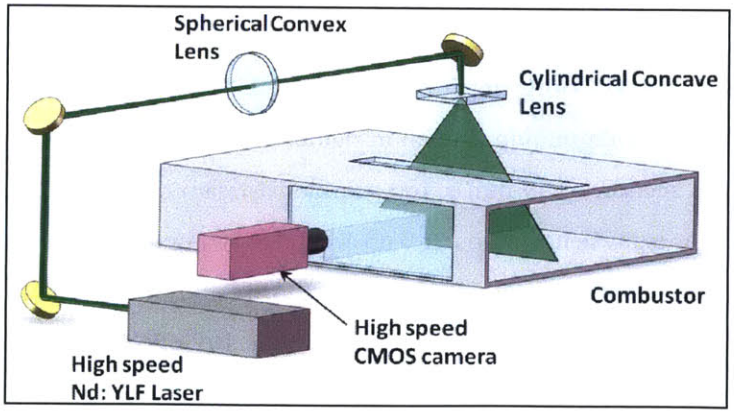

Figure 7.2: Experimental PIV setup for measurements in a backward facing step combustor.

The PIV measurements are processed using the LaVision DaVis 7.2 software. The distance between the imaging plane and the camera was set to 0.6 m based on the desired field of view. The corresponding viewing area for the PIV measurements is 120 mm x 120 mm, generating 800 x 800 pixel images of the seeding particles. These images are processed using a multi-pass approach, with the final pass using a 16 x 16 pixel window with 50% overlap. This produces velocity fields with a spatial resolution of 1.14 mm. Further details about the setup and experiments can be found in [7.12]. The velocity statistics were compared using the high resolution data, while the contours were plotted using the coarse resolution data.

Table 7.1: Parameters for the backward facing step PIV configuration.

PARAMETER	VALUE (HIGH RESOLUTION)	VALUE (LOW RESOLUTION)
Grid Size	0.052 mm/pixel	0.098 mm/pixel
Vector Spacing	0.83 mm	1.56 mm
Field of View (FOV)	66 mm	125 mm
Downstream FOV	56 mm	117 mm

7.2.3 Simulation Setup

The geometry corresponding to the computational domain is depicted in figure 7.3. The choice of the numerical grid is governed by estimates of the physical length scales associated with the flow configuration. It has been suggested that in order to directly capture the bulk of the energy containing structures and resolve at least 80% of the turbulent kinetic energy, a filter-width (Δ) to integral length scale (L_I) ratio of approximately 0.083 should be maintained [7.19]. Using the step height (H) as the integral length scale, the filter-width can be estimated to be 1.66 mm. It should be noted that the above theory does not focus on resolving near-wall structures and may not be applicable for reacting flow. Therefore, appropriate grid clustering may be required to resolve the structures near the walls and in the shear layer region for reacting flow. Based on the above, the non-uniform mesh utilized in the current work is comprised of approximately 16,600 hexahedral cells in the x-y plane, and gets coarser along the stream-wise direction. Downstream of the step, the number of cells in the x and y directions are 270 and 59 respectively, while the average Δx and Δy in the shear layer region downstream of the step are approximately 1.0 mm and 0.5 mm respectively.

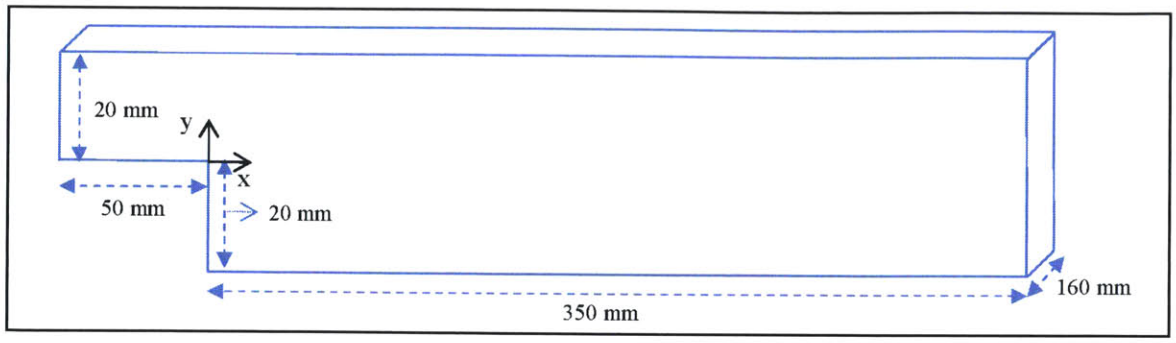

Figure 7.3: Backward facing step configuration used for flame stabilization.

Temporal resolution is determined based on physical time scale estimates, in order to prevent excessive numerical dissipation and numerical instability, as well as on chemical time scales. Based on the CFL criterion ($C_{max} = (U_{SH}+U_s)\Delta t/\Delta x$; $C_{max} = 1$, $U_s = 340$m/s, $\Delta x = 1.0$ mm), the time step for the simulations is estimated at approximately 2.8 μs. A conservative value of 1 μs is used in the reacting flow simulations, to take into account local refinement and acceleration of the fluid above the bulk inlet velocity, and to adequately resolve the chemical time scales.

Simulations are performed with periodic boundary conditions in the span-wise direction over the entire width of the channel. At the inlet, Dirichlet conditions are used for all variables except the pressure, for which zero Neumann conditions are specified. At the exit, zero Neumann conditions are specified for all variables except the pressure, for which wave-transmissive conditions are used. No-slip conditions are applied for the flow at the top and bottom walls of the duct, while zero Neumann conditions are specified for the other variables. Heat transfer is also considered at the walls to account for any thermal losses. In order to maintain reasonable computational efficiency, appropriate wall functions are utilized to resolve the flow features in the wall boundary layer. Numerical computations start from quiescent conditions and the unsteady flow characteristics evolve naturally. In order to initiate the flame, a high temperature pulse is applied at the inlet section which ignites the fuel; the reacting mixture convects downstream, and eventually stabilizes as a flame in the wake of the step. Averaging is performed over nearly 10 flow-through cycles once the flow is established in the computational domain. Note that in order to better understand the effect of heat release on the flow, the range of the magnitudes for the contours of some of the flame-flow variables have been fixed corresponding to the non-reacting and reacting cases. The key quantities relevant to the configuration are summarized in table 7.2.

Table 7.2: Parameters for the backward facing step combustor configuration.

PARAMETER	SYMBOL/EXPRESSION	VALUE
Step Height (Characteristic Length)	H	20 mm
Integral Length Scale	L_I (=L)	20 mm
Equivalence Ratio	γ	0.63, 0.85
Bulk Inlet Velocity (Characteristic Flow Velocity)	U_{SH}	5.3 m/s
Macroscopic Reynolds Number	Re_{SH}	6,500
Inlet Temperature	T_S	300 K
Nominal Pressure	P	101 kPa
Kolmogorov Length Scale	$Re_{SH}^{-3/4}L$	27.6 μm
Cold Flow Filter Width (Pope's Criterion)	$\Delta=0.083L_I$	1.66 mm
Shear Layer Fluctuation (measured)	u'	~1 m/s
Integral Time Scale	$T_I=L/u'$	20 ms
Kolmogorov Time Scale	$Re_{SH}^{-1/2}T_I$	0.25 ms
CFL Criterion Time Scale	$C_{max}\,\Delta x/(U_{SH}+U_s)$	2.8 μs

7.2.4 Results: Non-Reacting Flow

Non-reacting flow is simulated prior to considering reacting flows. The inlet velocity for the numerical computations is conditioned based on the measured experimental velocity statistics at x/H=-0.25. A parabolic velocity profile is specified at the inlet, and turbulent fluctuations are imposed in a manner that results in the corresponding profiles (at x/H=-0.25) as shown in figure 7.4. While the spatial profiles match adequately, a further improvement in matching the fluctuations in the boundary layer close to the wall (viscous sub-layer) is possible.

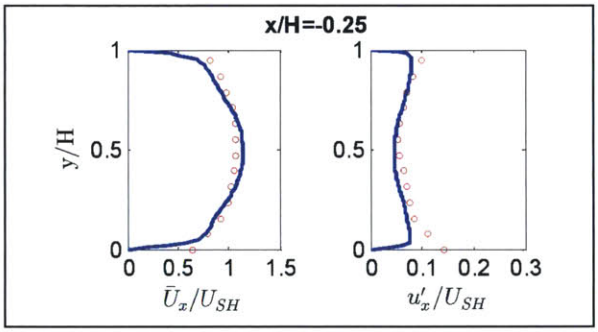

Figure 7.4: Normalized axial velocity statistics upstream: ooo PIV, —— LES

The free stream turbulence intensity and the boundary layer fluctuations upstream of the step can considerably affect the growth of the free shear layer, by influencing the evolution of large-scale structures in the mixing layer [7.6], and therefore have a significant effect on the reattachment of the shear layer behind the step. It has been suggested that an increase in free stream turbulence intensity causes reduction in the reattachment length, attributed to the enhancement of turbulence intensity levels within the separated shear layer immediately downstream of the step [7.1] and a corresponding augmentation of the mixing layer growth rate. The impact of the separation boundary layer upstream, however, is difficult to isolate due to its dependency on Reynolds number and

boundary layer thickness at separation. The combined effect of boundary layer state and thickness on the reattachment length has been defined in terms of the momentum thickness Reynolds number, Re_θ, and found to be highly non-linear [7.20, 7.21]. As depicted in figure 7.5a, the reattachment length increases sharply to a peak value with the change in boundary layer state from laminar to transitional (small-scale disturbances) and then decreases gradually to a steady value as the boundary layer thickens and becomes turbulent. Likewise, a reduction in reattachment length with increase in the turbulent boundary layer thickness at separation has been observed (figure 7.5b) and can be attributed to the increase in the spreading rate of the separated shear layer downstream of the step. These observations clearly highlight the significance of appropriately matching the magnitude of perturbations at the inlet boundary to predictive accuracy. Additionally, the fluctuating behavior of the inlet flow in time should also be accounted for, in the simulations, by analyzing the temporal spectrum of the inlet velocity data from the experimental measurements.

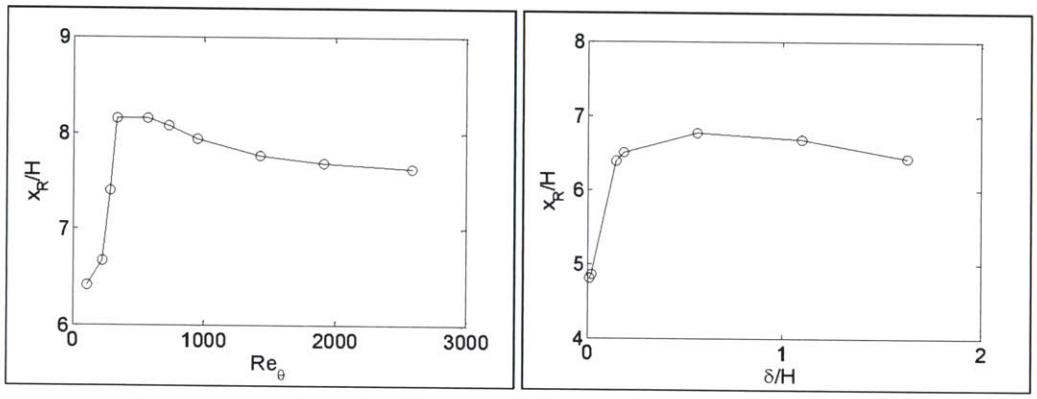

Figure 7.5: (a) Reattachment length as a function of boundary layer state, (b) Reattachment length as a function of boundary layer thickness.

The fundamental flow features for the isothermal flow comprise of the mixing layer and the shed vortices, the primary and corner recirculation zones, and the reattachment zone. As indicated by the contour of the instantaneous z-vorticity depicted in figure 7.6 along with the instantaneous streamlines, vortices begin to develop slightly downstream of the step, as a consequence of Kelvin Helmholtz instability, and the shear layer grows in size as the turbulent eddies contained within begin to coalesce. Unsteady flow features in the shear layer, such as shedding, convection and pairing of the small vortices are thus suitably resolved using LES, and the roll-up of the mixing layer into a sequence of large-scale structures that convect downstream along with the turbulence generated eddies can be observed in figure 7.7.

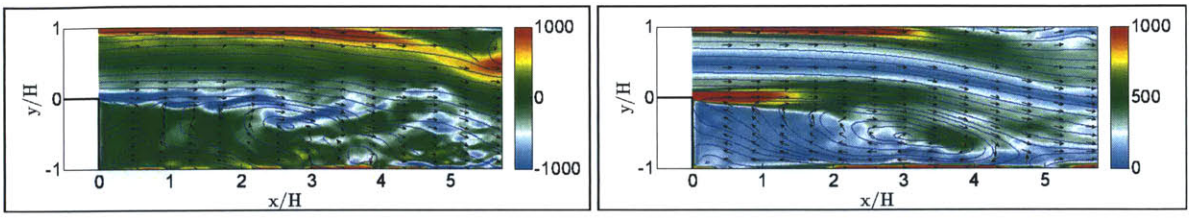

Figure 7.6: (a) Instantaneous z-vorticity (1/s), (b) Average vorticity magnitude (1/s). The corresponding 2D velocity vectors and streamlines are also shown (LES).

The average flow field, as indicated by the mean streamlines in figure 7.6, is comprised of two vortices within the recirculation region: a primary eddy between the shear layer and the bottom wall, and a secondary eddy adjacent to the vertical step wall (rotating in the opposite direction to the primary vortex). Additionally, the strongest vorticity is observed near the edge of the step, while the intensity tends to decrease subsequently, as the vortices dissipate in the downstream section.

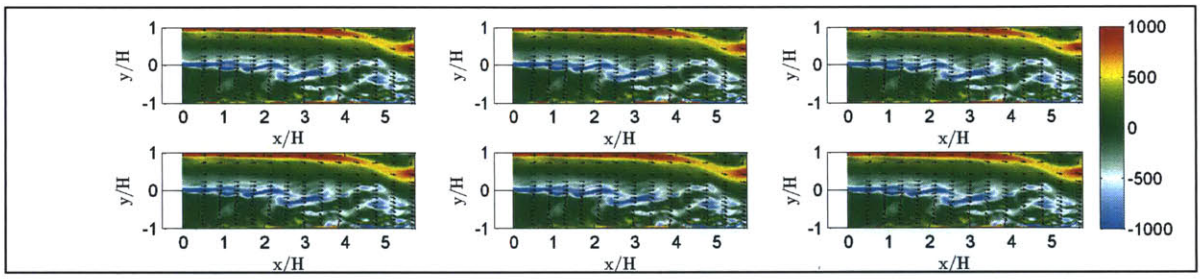

Figure 7.7: Instantaneous z-vorticity (1/s) at different time-instants, with the corresponding 2D velocity vectors (LES).

In figure 7.8, the contours of the average axial velocity, obtained experimentally and numerically, are depicted. The cross-sections at which numerical and experimental data are compared are also shown. A strong primary recirculation zone downstream of the step is observed, with the zero axial velocity region (shown in white) running through the core of the mean vortex structure. The size of the separation bubble is reproduced reasonably accurately in the simulations, along with the shear layer growth rate, although flow separation from the upper wall is predicted to occur slightly upstream in the simulations as compared to the experiments. The reattachment length, on average, is numerically found to be *5.2H*, while the secondary recirculation zone at the corner of the step, which nearly spans the step height and extends to a length of approximately *0.6H* downstream, is suitably resolved in the simulations. Note that the reattachment length is not directly determined in the experiments within the PIV field of view, although the 'center' of the recirculation zone is observed to be located at a distance of approximately *3.5H* from the expansion plane (numerically, the value is estimated to be *3.0H*). The marginal shortening of the primary eddy could

be attributed to the use of periodic boundary conditions in the span-wise direction, along with the inadequate resolution of the inlet boundary layer turbulence, in the simulations.

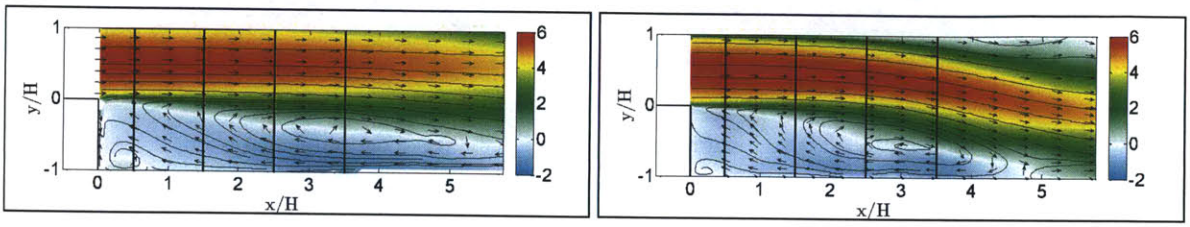

Figure 7.8: Average axial velocity with the 2D velocity vectors and streamlines (PIV: left, LES: right). The cross-sections at which data are compared are also shown.

The rms axial velocity and rms transverse velocity contours obtained experimentally and numerically are depicted in figures 7.9 and 7.10 respectively. Examination of the flow field fluctuations suggests strong turbulence intensity in the shear layer region slightly downstream of the step, corresponding to the gradual rolling up of the mixing layer into a sequence of large-scale structures. These coherent vortices grow and convect downstream, along with the turbulence generated eddies, resulting in generation of turbulent kinetic energy in the layer.

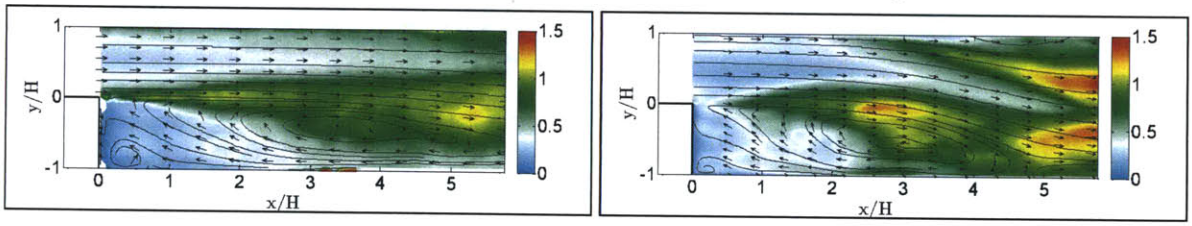

Figure 7.9: rms axial velocity with the 2D velocity vectors and streamlines (PIV: left, LES: right).

A high fluctuation region is also seen close to the upper wall, which arises near the inlet section primarily due to the significant flow disturbances in the inlet stream, and in the downstream section due to flow separation. Turbulence intensity is also high near the reattachment zone, associated with the flapping of the shear layer, along with flow reversal in the region (figure 7.10). In contrast, the corner recirculation zone is comprised of a nearly stationary vortex with very low level of turbulent fluctuations, primarily due to geometric constraints.

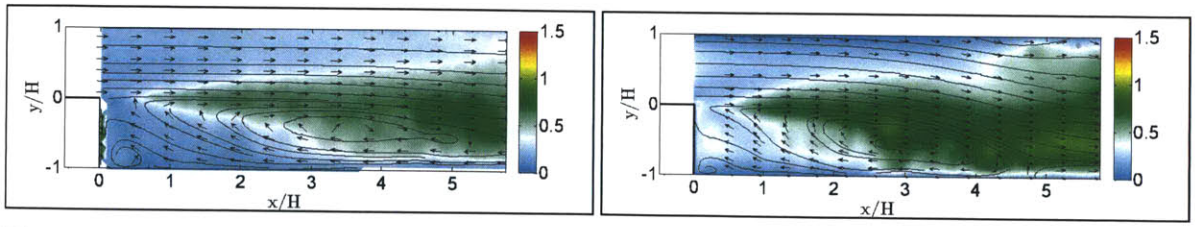

Figure 7.10: rms transverse velocity with the 2D velocity vectors and streamlines (PIV: left, LES: right).

The normalized profiles for the average axial velocity and rms axial velocity, at cross-sections downstream of the step, are shown in figure 7.11. Predicted results show reasonable agreement with experimental measurements and the underlying flow field in the recirculation zone and shear layer region is suitably resolved, as indicated by the mean velocity statistics. The shear layer growth rate as well as the extent of the primary recirculation zone is predicted with reasonable accuracy. The upper wall flow separation is however predicted to occur slightly upstream, as opposed to the experiments, resulting in a slight discrepancy in the velocity statistics downstream. Appropriately matching the inlet fluctuations, improving the grid resolution in the boundary layer, and performing fully three-dimensional simulations (to incorporate any thickening of the boundary layer due to front and rear walls, and accounting for vortex stretching effects) are expected to result in more accurate resolution of the flow field.

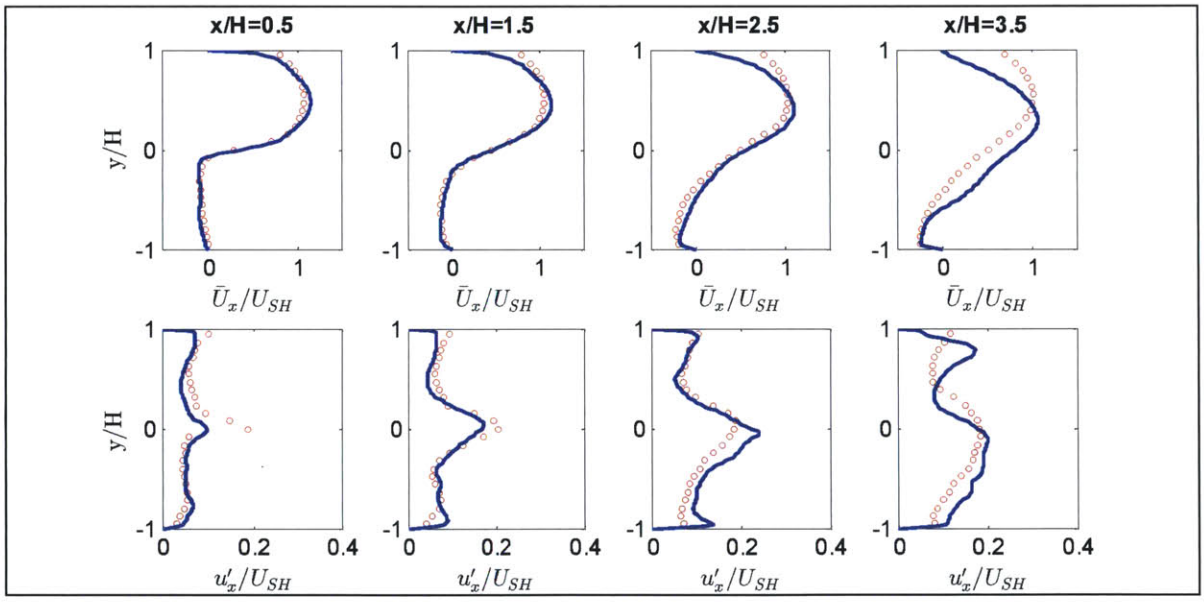

Figure 7.11: Normalized profiles for average axial velocity (top) and rms axial velocity (bottom). ooo PIV, — — — LES

High fluctuations are observed in the region close to the upper wall, where moderately high turbulence intensity arises primarily due to significant perturbations in the inlet velocity boundary layer near the wall. Turbulence intensity also peaks in the in the vicinity of the step, within the free shear layer, which grows in size downstream of the step due to the formation and interaction of the large coherent structures. Note that the turbulent intensity in the mixing layer is also influenced by the upstream boundary layer disturbances near the lower wall, which tend to enhance its spreading rate and inherent fluctuations. Further downstream, however, the turbulence tends to become

somewhat isotropic, as the relative influence of the shear-generated turbulent eddies begins to diminish, and large-scale structures dominate the flow. Subsequently, the large coherent vortices dissipate into smaller eddies as the flow convects downstream into the exhaust section, due to vortex stretching and dissipation effects. While the shapes of the simulated rms velocity profiles show a reasonable match with the experimental observations, the marginal over-prediction of the fluctuations near the walls could be corrected by appropriate grid resolution in the corresponding simulated domain.

7.2.5 Discussions: Non-Reacting Flow

The important flow features in the wake region of a backward facing step [7.20-7.23] can be distinguished into the shear layer region, the separation bubble or recirculation zone and the reattachment zone, as highlighted in figure 7.12. The flow structures begin to form as the upstream boundary layer separates at the edge of the step, subsequently developing into a thin shear layer. If the boundary layer is laminar, transition begins soon after separation, unless the Reynolds number is very low. The separated shear layer appears to be much like a plane-mixing layer through the initial region of the separated flow region. The dividing streamline is only marginally curved and the shear layer is thin enough to not be affected by the presence of the wall. As the flow progresses downstream, the shear layer grows in size with the coalescence of the turbulent structures contained within.

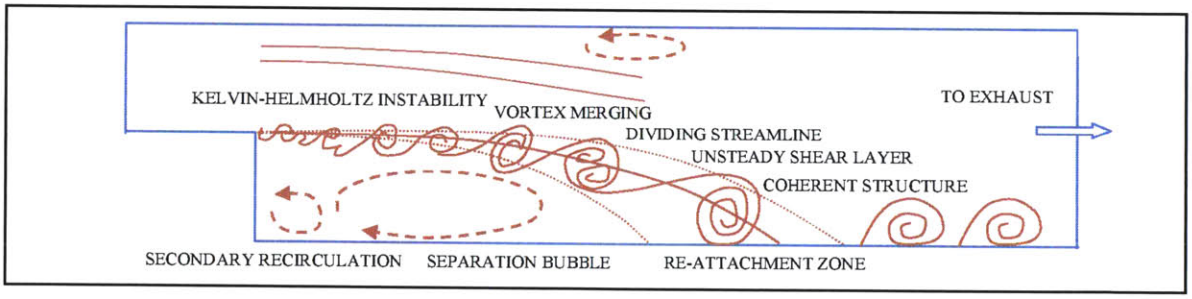

Figure 7.12: Fundamental flow features in a backward facing step configuration.

The turbulent eddy structures in the shear layer entrain irrotational fluid from the non-turbulent region outside the layer, which causes the formation of a low velocity recirculation in the wake region. The recirculation zone is mainly comprised of a primary vortex (located between the shear layer and the bottom wall) and a secondary vortex formed primarily due to geometric constraints (and rotates in the opposite direction to the primary eddy). Due to the favorable pressure gradient created by the fluid entrained, the shear layer eventually curves down and impinges the wall, resulting in the formation of the reattachment zone; however, the reattachment location is observed

to fluctuate significantly, due to the inherent unsteady motion of the shear layer. The mixing layer differs substantially from the plane-mixing layer, and is subjected to the effects of stabilizing curvature, adverse pressure gradients, and strong interaction with the wall in the reattachment zone [7.6]. A part of the fluid in the reattaching shear layer is deflected upstream into the recirculatory flow by strong adverse pressure gradients, and the flow on the low-speed side of the layer is highly turbulent, as opposed to the low turbulence level stream in a typical plane-mixing layer.

It should also be noted that for low-level turbulence intensity in the boundary layer, the initial layer has an enhanced growth rate, eddies are further separated and there is higher small-scale turbulence inside the large vortices, as compared to the undisturbed initial layer. These large coherent structures that form, play a prominent role in the development of the free shear layer, and dominate the reacting and non-reacting flows. On the other hand, a highly turbulent boundary layer upstream of the edge of the step inhibits the formation and interaction of the large coherent structures in the shear layer. Although large-scale structures are not completely absent from the flow, regular and distinctly identifiable structures are no longer visible [7.1]. The introduction of turbulent fluctuations delays the formation of vortices in the free shear layer as it thickens the initial vorticity layer, making it less susceptible to flow disturbances. This obstructs the large-scale interaction in the initial stages of the formation of the mixing layer, though eventually the role of the large-scale structures is re-established.

7.2.6 Results: Reacting Flow

Next, reacting flow for the configuration is considered and simulations are performed using the thickened flame model. Similar to the cold flow case, the inlet velocity for the numerical computations is conditioned based on the measured experimental velocity statistics upstream of the step (x/H=-0.25). A parabolic velocity profile is specified at the inlet, and turbulent fluctuations are imposed in a manner that results in the corresponding profiles (at x/H=-0.25) as shown in figure 7.13. While the profiles match adequately, a further improvement in matching the fluctuations in the boundary layer close to the wall (viscous sub-layer) is possible.

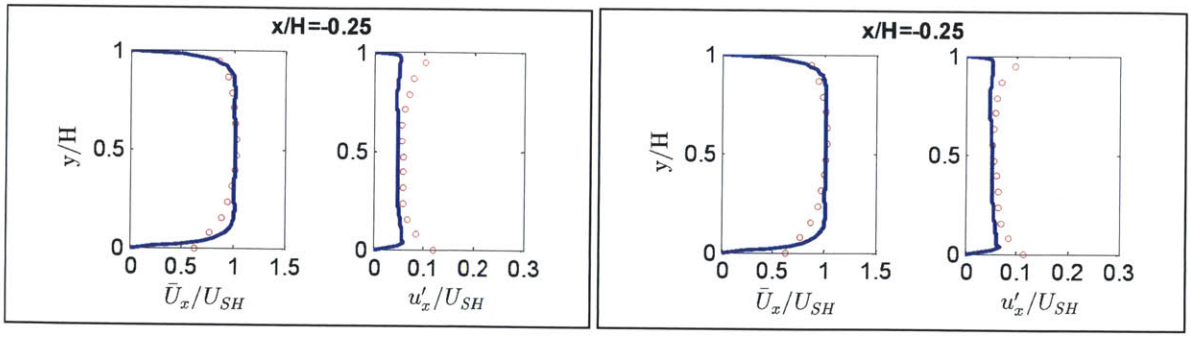

Figure 7.13: Normalized axial velocity statistics upstream (φ=0.63: left, φ=0.85: right): ooo PIV, —— LES

As mentioned earlier, the formation and interaction of the large coherent structures and the resulting shear layer growth is influenced by the level of upstream disturbances. Further, in case of reacting flows, the high free stream fluctuations can augment the turbulent burning velocity, and the relative increase in the effects of flame propagation reduces the size of the recirculation zone. Moreover, higher small-scale turbulence lowers mixing time, and increases entrainment, thereby influencing the flame front as well as the scalar fluctuations. Appropriately matching the magnitude of perturbations at the inlet boundary can, therefore, be quite critical to predictive accuracy. Additionally, the fluctuating behavior of the inlet flow in time should also be accounted for, in the simulations, by analyzing the temporal spectrum of the inlet velocity data from the experimental measurements

In figure 7.14, the CH chemiluminescence image obtained from the reacting flow experiments is depicted, indicating that the flame stabilizes in proximity to the step for the high equivalence ratio scenario (φ=0.85). The augmented turbulent burning velocity and high extinction strain rate allows the flamelets to propagate upstream and stabilize near the edge of the step. In the vicinity of the region, the average reaction zone is thin, and shear generated turbulence acts as one of the dominant processes in sustaining the flame front in this region. The penetration of the inner layers of the reacting shear layer by the convecting eddies causes the kinetics to be affected by turbulence, while enhancing the heat diffusion from the inner layers towards the preheat zone, thereby, allowing the flame brush to persist in this upstream section.

Figure 7.14: Time resolved flame from CH chemiluminescence image. φ=0.85

As the flow proceeds downstream, the instantaneous reaction zone, characterized by intense heat release, takes the form of a slightly wrinkled sheet-like interface. Subsequently, the average reaction zone thickens in the downstream section, with entrainment as the dominant mechanism, and combustion is characterized by transport and mixing processes. The high turbulence in the region, due to eddy breakdown and induced by combustion, enhances mixing and entrainment, resulting in increased heat release and a strongly burning flame, as highlighted by the augmented chemiluminescence intensity in the region. Further downstream, the reacting flow field is characterized by dilatation and dissipation effects, with the flame front stabilizing towards the upper wall, and combustion is almost complete as the flow convects into the exhaust duct.

In contrast, for the low equivalence ratio case (φ=0.63), the flame stabilizes significantly further downstream of the step, owing to the reduced flame propagation speed and low extinction strain rates. The moderate heat release rates lower the reaction zone intensity, and the angle between the upper and lower edges of the average flame zone also reduces, since the weakly propagating flamelets are unable to penetrate the high velocity flow convecting in the upper half of the channel. Additionally, flame wrinkling at the macro-scale in the upstream section is somewhat reduced, since the large-scale shear layer vortices do not appear to interact strongly with the reaction interface, and the flame sheet is not significantly impacted by the shear layer eddies. Observing the CH chemiluminescence image in figure 7.15, it is also noted that the weakly burning flame front is predominant in the high turbulence region downstream of the reattachment location, where mixing events, coupled with combustion induced turbulence, enhance the heat release, allowing the flame brush to stabilize. Additionally, the combustion process continues in the lower half of the channel as the flow convects downstream into the exhaust duct.

Figure 7.15: Time resolved flame from CH chemiluminescence image. φ=0.63

In figure 7.16, the contours for the average and instantaneous temperature obtained from the numerical simulations are shown (φ=0.85). A steep gradient in the mean temperature profile is observed immediately downstream of the step, and associated with the presence of the reacting shear layer in the region. The temperature is appreciably high within the primary eddy, which recirculates the hot combustion products in the region. Subsequently, a broadening of the high

temperature region is observed, which corresponds with the propagation of the flame front towards the upper wall of the channel (figure 7.17).

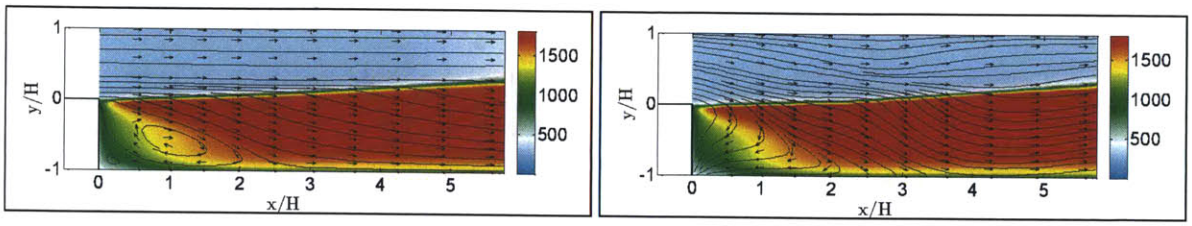

Figure 7.16: (a) Average temperature (K), (b) Instantaneous temperature (K). The corresponding 2D velocity vectors and streamlines are also shown (LES). φ=0.85

The temperature in the downstream section remains substantially high, as a result of exothermicity, and due to the flame surface inhibiting heat transport between the hot products and the cold reactants flowing through the upper section of the duct. A low temperature zone in the corner, at the location of the secondary eddy, is also observed and could be attributed to the weak circulation of hot products in the region, as well as heat transfer from the wall region adjacent to the step. However, it should be noted that the simulations predict a thin, relatively smooth average reaction zone in the wake region, while the experimental measurements suggest a thicker mean flame. This could be improved by appropriately resolving the inlet flow conditions (as measured in the laboratory setup, in terms of the spatial as well as temporal profiles), and by suitable resolution of the numerical grid in the shear layer region.

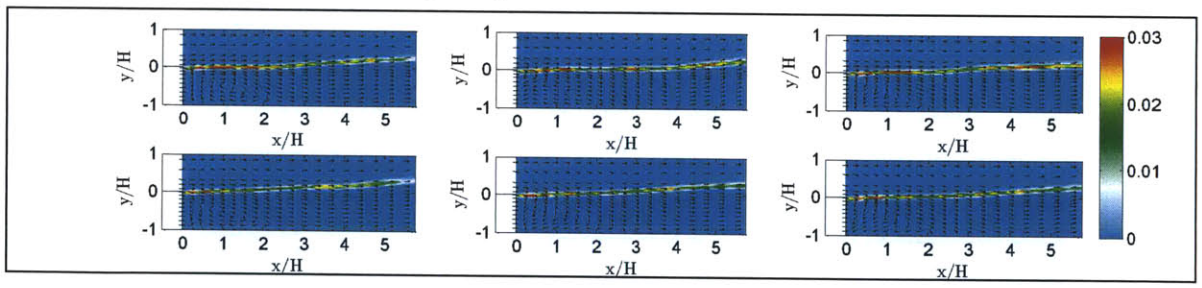

Figure 7.17: Instantaneous CO mass fraction at different time-instants, with the corresponding 2D velocity vectors (LES). φ=0.85

In figure 7.18, the LES contours for average vorticity magnitude and instantaneous z-vorticity are depicted. Downstream of the step, eddies begin to form within the shear layer as a result of Kelvin-Helmholtz instability, eventually increasing in size and spacing, and forming large-scale coherent structures as they convect downstream and coalesce. For the reacting flow configuration, it is observed that vorticity is significant in the shear layer region, immediately downstream of the step, owing to the transient eddies. Note, however, that exothermicity results in

an increase in temperature dependent viscosity and consequently a reduction in the Reynolds number. While this factor alone may not appreciably affect the flame or flow structure, it can cause a marginal increase in the stability of the initial layer (detrimental to flame stability), a lengthening of the distance of the eddy formation position with respect to the step edge, thicker vortical structures, and a decrease in the small scale turbulence inside the large eddies.

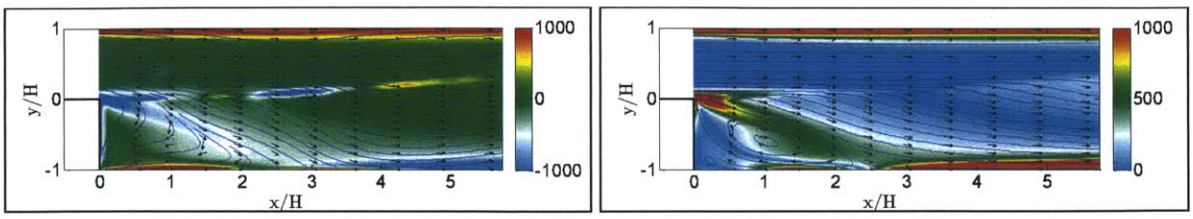

Figure 7.18: (a) Instantaneous z-vorticity (1/s), (b) Average vorticity magnitude (1/s). The corresponding 2D velocity vectors and streamlines are also shown (LES). φ=0.85

In the downstream section, heat release in vortex cores result in breakdown of eddies, and the fluid dynamic effects of heat release (increase in viscosity, dilation effect of combustion, and flow acceleration in the shear layer), coupled with the dissipation effects, results in reduction of overall vorticity in the lower half of the channel. Additionally, the instantaneous z-vorticity contours (figure 7.19) also suggest weak vortex activity at the location of the average flame surface, which can be associated with combustion induced baroclinic vorticity generation in the region.

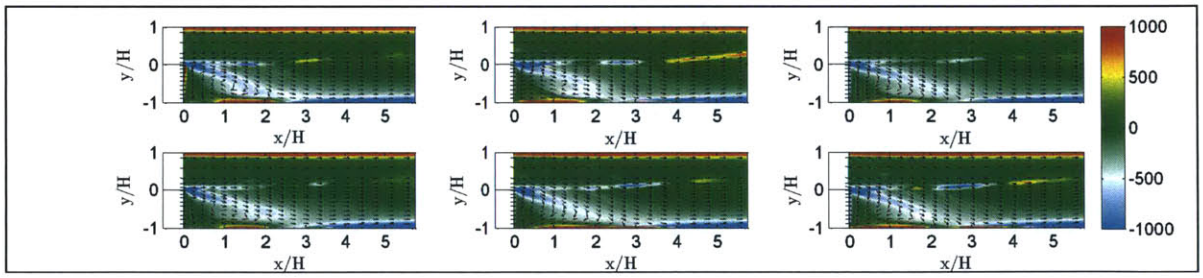

Figure 7.19: Instantaneous z-vorticity (1/s) at different time-instants, with the corresponding 2D velocity vectors (LES). φ=0.85

In figure 7.20, the average axial velocity contours, obtained experimentally and numerically, are shown (φ=0.85). Investigation of the average flow field suggests some marked changes in the recirculation region topology, as compared to the isothermal case, since the primary wake vortex is significantly shorter, and the secondary recirculation zone is almost absent, for the reacting scenario. Due to the appreciable reduction in the size of the primary wake region and the higher streamline curvature, the secondary eddy is squeezed towards the step wall.

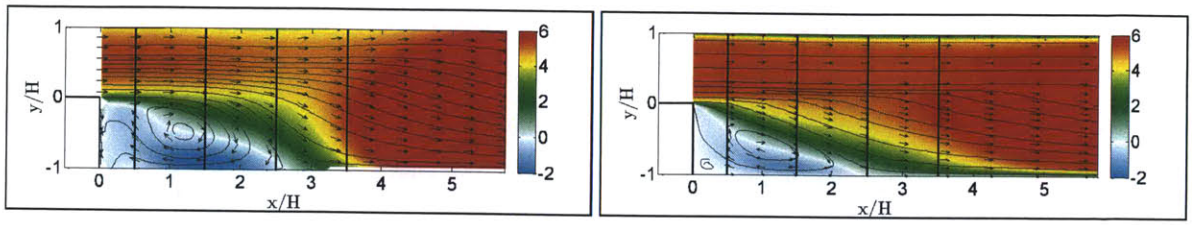

Figure 7.20: Average axial velocity with the 2D velocity vectors and streamlines (PIV: left, LES: right). The cross-sections at which data are compared are also shown. φ=0.85

For the high equivalence ratio case, a much shorter primary recirculation zone is observed, on average, with a drastic decrease in the reattachment length to 2.5*H*, i.e., significantly less than that for the cold flow (7.0*H*). Due to heat release and gaseous expansion, the mean axial velocity is also significantly accelerated downstream of the reattachment point, while flow separation from the upper wall is also delayed. An underlying physical explanation for the reduction in recirculation zone size as compared to isothermal flow is the relatively strong influence of flame propagation and resultant temperature gradients, on the flow field.

In general, for configurations involving turbulent combustion in reacting shear layers, at low equivalence ratios, the fluid dynamic effects of heat release tend to result in elongation of the recirculation zone size. This is associated with acceleration of the fluid due to thermal expansion, which causes the flow to better overcome the adverse pressure gradients; coupled with momentum dissipation effects, turbulent dilatation typically results in an elongation of the recirculating vortex. With an increase in equivalence ratio, however, due to the augmentation of flame propagation speed and heat release rates, a reduction in the recirculation zone size is observed [7.6].

This reduction in primary recirculation zone is also evident for the case with φ=0.63, although to a lower extent (figure 7.21). Additionally, the secondary vortex appears to be larger in size, due to the moderate shear layer curvature.

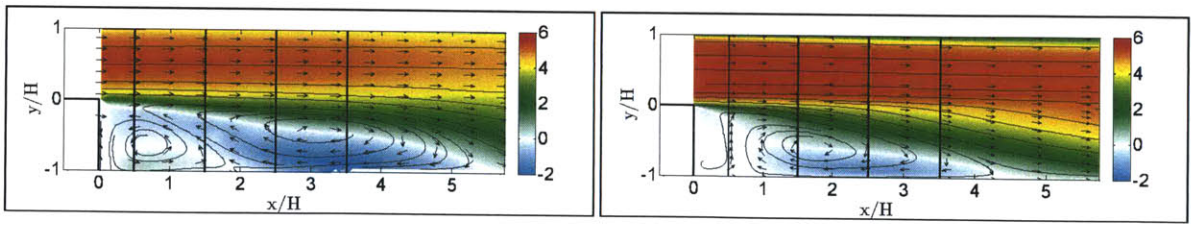

Figure 7.21: Average axial velocity with the 2D velocity vectors and streamlines (PIV: left, LES: right). The cross-sections at which data are compared are also shown. φ=0.63

In figure 7.22, the rms axial velocity contours, obtained experimentally and numerically, are shown (φ=0.85). High fluctuations are seen within the shear layer caused due to the growth of a

local instability mode along the layer and the roll-up of coherent vortex structures, although there is a marginal reduction in small scale turbulence in the mixing layer, immediately downstream of the step, due to heat release in the shear layer (which typically result in somewhat lower Reynolds stresses, turbulence intensities and turbulent kinetic energy within the layer). Subsequently, however, combustion induced shear turbulence results in high flow fluctuations within the shear layer. The high streamline curvature also shifts the high turbulence region to within the recirculation zone, while the turbulence intensity is also high near the reattachment location, where flow reversal and flapping of the shear layer takes place. Further downstream, due to combustion induced turbulence, the flow oscillations increase. However, turbulence anisotropy reduces in the region, as a consequence of dilatation and dissipation effects that primarily govern the flow, and the relative influence of the large-scale coherent vortex structures on the flow-field oscillations reduces.

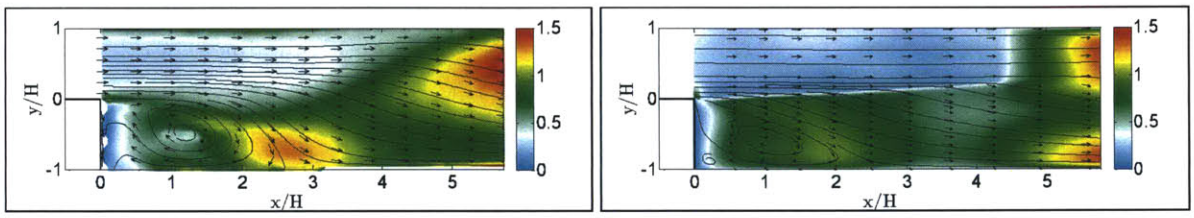

Figure 7.22: rms axial velocity with the 2D velocity vectors and streamlines (PIV: left, LES: right). φ=0.85

It should be mentioned that in reacting flows, turbulent dilatation and viscous dissipation processes suppress flame turbulence, whereas turbulent advection and shear-generated turbulence augment flame turbulence. At high equivalence ratios, the shear turbulence is significant, owing to the high streamline curvature and combustion induced turbulent kinetic energy; turbulence intensity in the shear layer is therefore almost similar to that observed in the cold flow scenario despite the effects of heat release in the shear layer. For moderate equivalence ratios, however, given the relatively low mean streamline curvature, the production of turbulence is primarily due to shear-stress/mean-strain interaction and is a fraction of the damping due to dilatation and dissipation, resulting in an overall suppression of turbulence intensity in the shear layer (figure 7.23). Additionally, the region of high turbulence shifts to the lower half of the channel: turbulence intensity is observed to be high within the primary recirculation zone underneath the flame, and could also be associated with (long-wave) oscillations of the longitudinal and transverse flow velocities, coupled with flapping of the shear layer. Near the reattachment region, flow direction is

quickly reversed, fluid parcels are stretched and strong gradients of mean and turbulence quantities are present, with the axial turbulence intensity showing a peak value in this region.

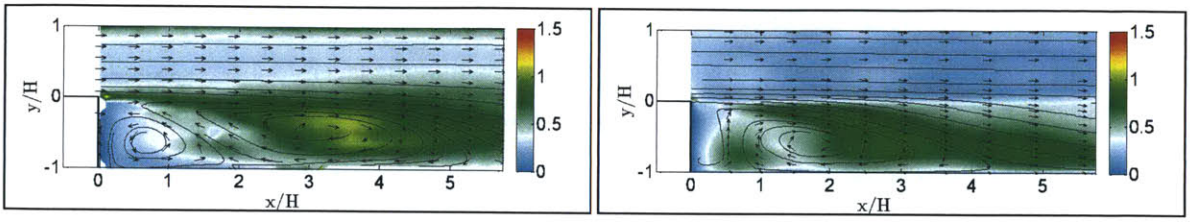

Figure 7.23: rms axial velocity with the 2D velocity vectors and streamlines (PIV: left, LES: right). φ=0.63

In figure 7.24, the normalized profiles for the average axial velocity and rms axial velocity, at different cross-sections downstream of the step, are shown (φ=0.85). The results indicate reasonable agreement with experimental data; the peak reverse velocity is observed to be significantly higher in this case, as compared to the non-reacting flow, resulting from exothermicity and gaseous expansion. The reduction in the mean streamline curvature is also quite evident and suitably resolved in the simulations.

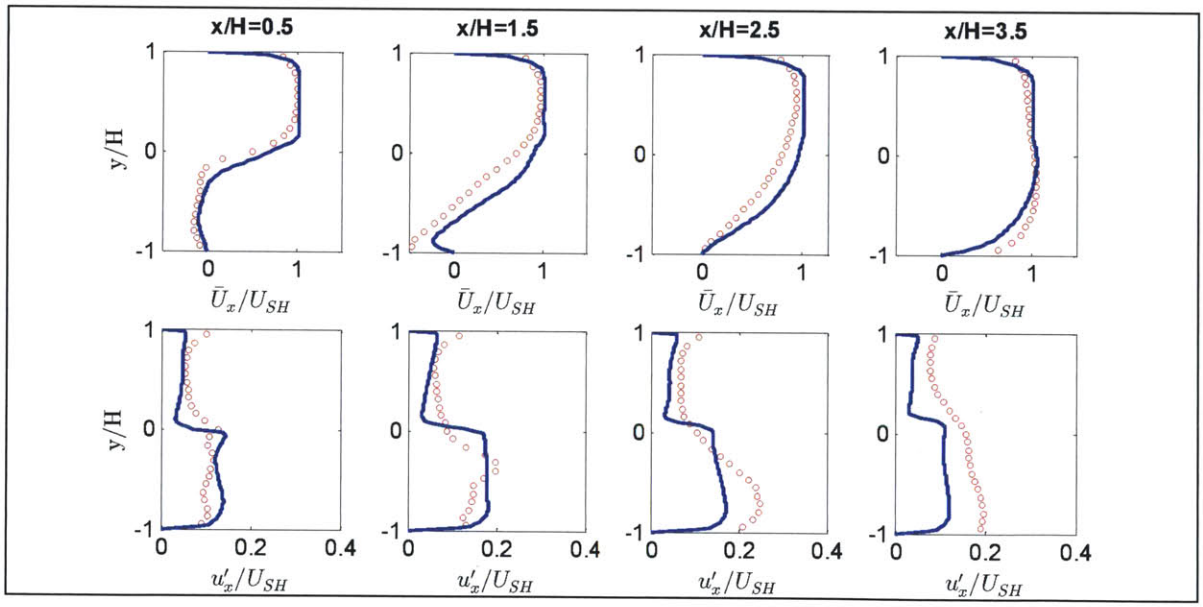

Figure 7.24: Normalized profiles for average axial velocity (top) and rms axial velocity (bottom). ooo PIV, – – – LES. φ=0.85

High turbulence intensity is also observed in the region surrounding the shear layer where entrainment and mixing occurs. The drastic shortening of the recirculation zone also shifts regions with strong concentration of both shear stress and turbulent kinetic energy from the outer periphery of the recirculation zone to inward locations; the turbulence intensity appears to be concentrated in

the region around the maximum streamline curvature near the reattachment zone, where the rapid necking-down of the outer flow streamlines in the vicinity of the reattachment point results in significant flow perturbations; the unsteady nature of the shear layer as well as its impact with the lower wall also contributes to high turbulence in the region. However, a he marginal under-prediction of the velocity fluctuations in the lower half of the duct is observed, which could be improved by appropriately matching the turbulent fluctuations at the inlet, performing fully three-dimensional simulations, and enhancing the grid resolution near the wall.

Finally, the normalized profiles for the average and rms axial velocity for φ=0.63, obtained experimentally and numerically, are shown in figure 7.25. The appreciable change in the shear layer curvature is suitable predicted in the simulations. Further, it is observed that the region of high turbulence is bounded by the shear layer in the upstream section, and tends to widen with downstream distance from the step, owing to combustion induced turbulence.

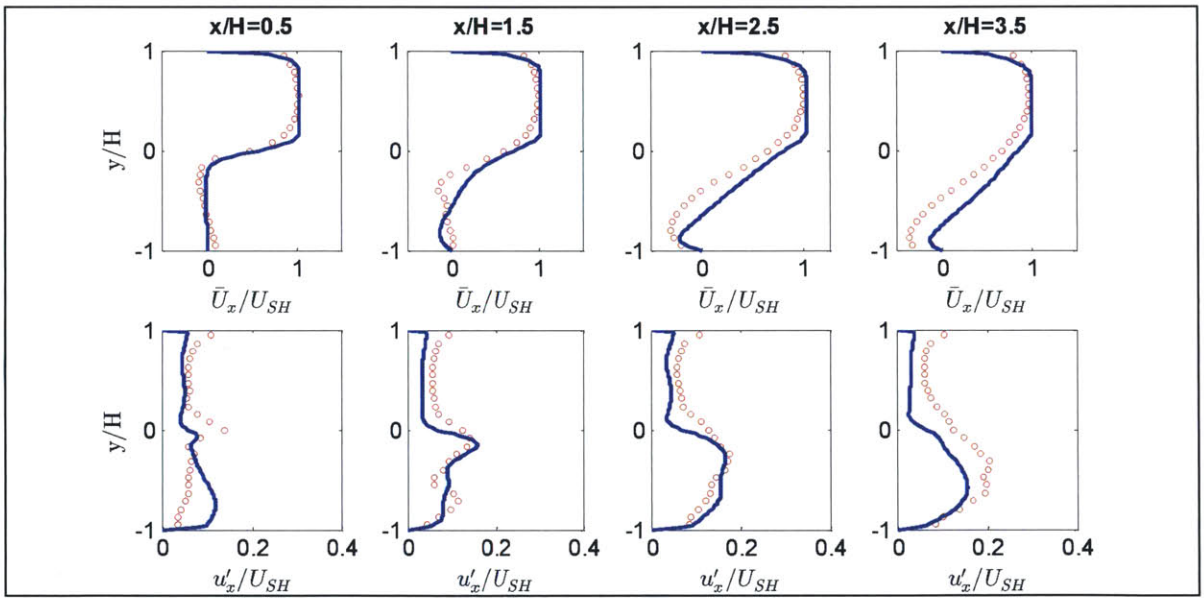

Figure 7.25: Normalized profiles for average axial velocity (top) and rms axial velocity (bottom). ooo PIV, ——— LES. φ=0.63

7.2.6 Discussions: Reacting Flow

The flow field in case of a backward step configuration is comprised of a laminar shear layer leaving the step, which expands a short distance away and subsequently, due to Kelvin-Helmholtz instability, is transformed into a series of eddies. As the flow convects downstream, the shear layer region expands, as the vortices increase in size and spacing due to combustion and coalescence with adjacent eddies (figure 7.26). The propagation of the flame is intricately connected and influenced by

the growth of these eddies, since these coherent structures 'contain' the reaction zone of the flame, and the roll up of each eddy corresponds to engulfment of hot products from the recirculation zone into the layer of fresh reactants in which the reaction front propagates.

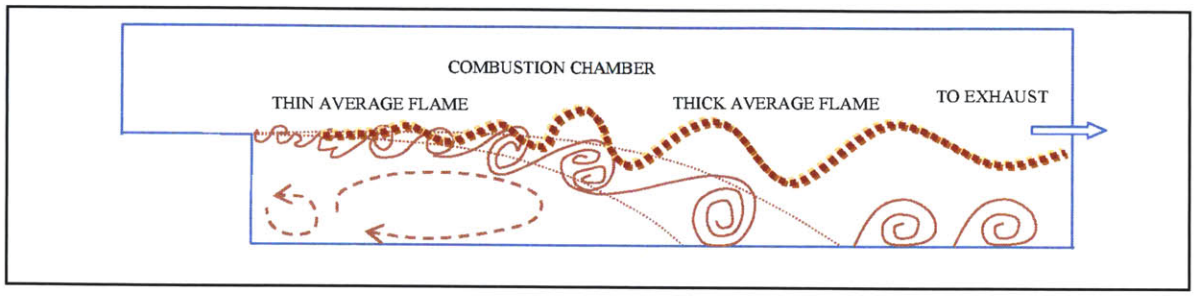

Figure 7.26: Fundamental flame-flow features in a backward facing step configuration.

Although the mixing layer is dominated by transient vortices in both reacting and non-reacting flows, the presence of the flame causes a significant modification of the turbulent flow field, due to the effects of flame propagation as well as turbulent dilatation. Therefore, while vortex stretching and pairing dominate the vortical flow development in the non-reacting case, these mechanisms are combined with volumetric expansion and baroclinic vorticity production in the case of reacting flows.

Further, experimental results suggest a strong coupling between the average flow field topology and the location as well as intensity of the flame [7.4]. For a fixed fuel composition, at relatively low equivalence ratios, the time-averaged recirculation zone is comprised of two counter rotating eddies: a primary eddy between the shear layer and the bottom wall, and a secondary eddy adjacent to the vertical step wall. The flame stabilizes downstream of the saddle point of the dividing streamline between the two vortices (the location where separating streamlines between the two eddies intersect with the zero stream-wise velocity line). As the equivalence ratio is raised, the flame moves upstream, pushing the saddle point with it and reducing the size of the recirculation zones. The influence of heat loading on the flame macro-structure, as well as its interaction with the flow field, is discussed next in further detail.

7.2.6.1 Flame Structure

In case of a backward facing step combustor, the turbulent flame structure surrounding the recirculation zone is comprised of a thin-flame region in the vicinity of the step, a reacting shear-layer region of large-scale coherent structures, and a thick-flame region beyond the reattachment point (figure 7.26). A significant distortion of flow structure is also evident in these regions, due to shear generated turbulence and flow reversal respectively, resulting in high turbulence anisotropy.

For different equivalence ratios, experiments suggest a similar relative position of the flame with respect to the recirculation zone: the flame tip is located downstream of the saddle point, indicating that the flame is stabilized in the low-velocity region formed by recirculating flows in the shear layer. For the low equivalence ratio case, the low turbulent burning velocity and extinction strain rates prevents the flame from penetrating the high strain shear layer regions upstream. Due to the low heat release rates, the flame is weak and characterized by the reaction kinetics. The average reaction zone is sustained due to shear-turbulence that augments entrainment, local mixing, and heat release, and primarily located in the section downstream of the reattachment location, in the lower half of the channel. As the equivalence ratio increases, the flame propagation speed is enhanced and the flame front moves closer to the edge of the step, forming a thin, strongly burning reaction zone. The saddle point also gradually approaches the step, with the flame tip located slightly downstream of the point. The reaction zone spreads in the downstream section, where the flame is thick and entrainment is the dominant process, and the angle between the upper and lower edges of the average reaction zone becomes larger. The strong intensity flame is controlled by mixing and eddy transport mechanisms, interacts more strongly with the shear layer coherent structures, and is significantly more wrinkled than lower heat loading configurations.

7.2.6.2 Mean Flow Field

The development of the shear layer is found to be slightly different corresponding to the reacting and non-reacting flows, suggesting that growth of the vortices, equivalence ratio dependent heat release, and propagation of the flame are intimately linked. Release of heat energy, which results in expansion and increase in kinematic viscosity of the gas mixture in the mixing layer, can considerably affect the vortex shedding behavior behind the step. The dilation effect of combustion, and flow acceleration in the shear layer (which typically allows the flow to overcome the adverse pressure gradients) can result in lowering the spreading rate of the shear layer, thereby elongating the recirculation vortex. In contrast, the propagation effect of the flame can result in shortening of the recirculation zone.

For moderate to high equivalence ratios, as observed in the backward step combustor experiments, the augmented flame propagation effects contract the vortex structure in the wake region, with the shear layer curving towards the wall further upstream (figure 7.27). Thus, the flame location moves upstream, along with the primary recirculation zone. The primary eddy becomes more compact as the heat loading increases, while the secondary eddy reduces in size, almost collapsing at $\varphi = 0.88$. Further, the reverse velocity in the recirculation zone also increases with

equivalence ratio, due to enhanced exothermicity, as does the positive flow velocity in the section downstream of the reattachment location.

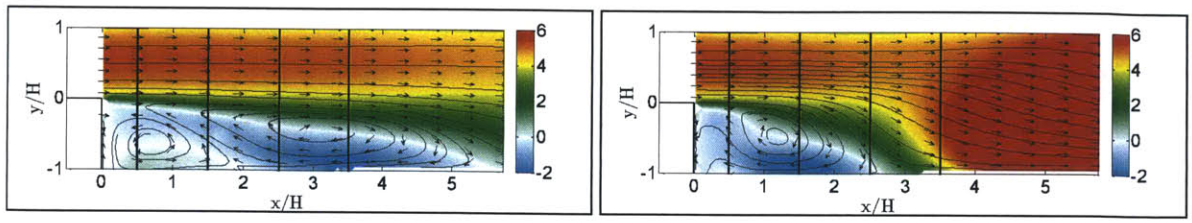

Figure 7.27: Average axial velocity with the 2D velocity vectors and streamlines (φ=0.63: left, 0.85: right) (PIV).

The experimental observations showing reacting flows with shorter but more intense recirculation zones (due to the gas expansion associated with heat release) agree with previous studies comparing reacting and isothermal flow fields. As the equivalence ratio is raised, the temperature (density) gradient across the flame becomes significant, raising the velocity and reducing the shear. These observations suggest that the change in the recirculation zone structure and size is a function of the temperature ratio across the flame. However, the changes in the flow-field are not solely determined by the temperature difference across the flame [7.4].

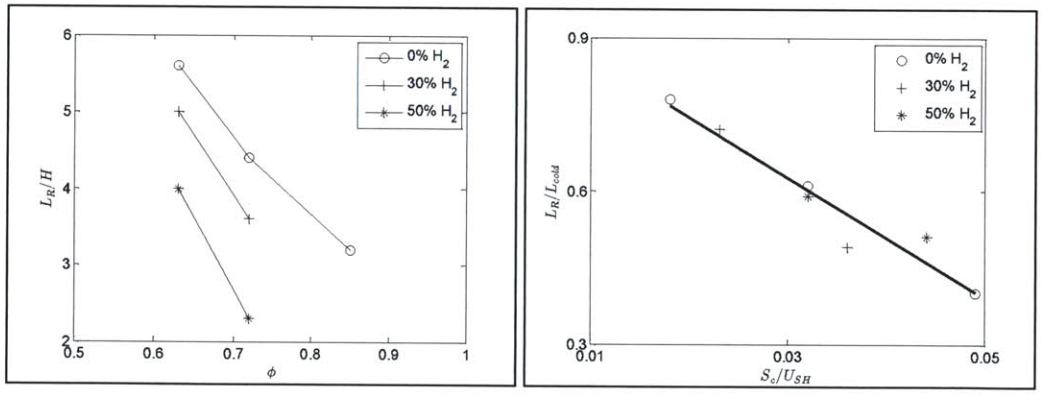

Figure 7.28: (a) Normalized reattachment length as a function of φ for different X_{H2}, (b) Normalized reattachment length as a function of normalized consumption speed.

In another set of experiments, it is observed that the flow field is significantly impacted by adding H_2 to the fuel mixture at a given equivalence ratio, despite maintaining similar equilibrium burnt gas temperatures. Specifically, as the composition of hydrogen in the fuel mixture (X_{H2}) increases, the primary eddy moves closer to the step while the secondary eddy becomes smaller, similar to those observed at a higher equivalence ratio for propane/air mixtures (figure 7.28). The reattachment length (L_R) gradually reduces as X_{H2} increases (at a fixed φ), or as φ increases (at a given X_{H2}). In fact, it is observed that L_R decreases almost linearly with increasing φ while also becoming

shorter for higher X_{H2}, suggesting a correlation between the reattachment length and the consumption speed (S_l). As shown in figure 7.27, the plot of L_R as a function of S_t (normalized by the approach flow velocity, U_{SH}) indicate that the dependence of the reattachment length on the fuel mixture composition collapses onto a single characteristic line, demonstrating that the size and structure of recirculation zones formed over a backward-facing step are a function of the consumption speed, rather than a temperature jump across the flame.

7.2.6.3 Flow Perturbations

Besides altering the mean flow field, the combustion process also impacts the turbulent flow-field fluctuations, especially in confined configurations. It is well established that turbulent dilatation and viscous dissipation processes suppress flame turbulence, whereas turbulent advection and shear-generated turbulence (due to shear-stress/mean-strain interaction) augment flame turbulence. Depending upon which process dominates (as heat release rates increase), either additional turbulence is generated, or the existing turbulence is damped. For the reacting flow experiments, the turbulent kinetic energy is generally concentrated in the shear layer around the recirculation zone periphery, and is primarily shear generated. Flow field fluctuations are also high near the reattachment zone where the unsteady shear layer impacts the wall and where flow reversal takes place. As the equivalence ratio increases, turbulent shear production increases (with the shear layer curvature) as does the turbulent dilatation (with the heat release). While the turbulence intensity in the shear layer appears to be similar to that observed in the isothermal configuration for the high equivalence ratio case, turbulence does reduce in the mixing layer for the moderate heat loading scenario, since dilatation effects dominate and combustion induced turbulence is limited. Additionally, due to the shortening of the recirculation zone, the turbulence shifts inwards and is relatively strong inside the recirculating vortex. Further downstream, flow fluctuations remain high, as a result of combustion generated turbulence, especially in the presence of wall confinement.

7.2.6.4 Impact of Wall Confinement

The presence of the wall, in general, can influence the curvature of the shear layer, particularly in case of high equivalence ratio scenarios, as well as influence the fluid acceleration in the downstream section. Confinement can prevent the shortening of the primary recirculation zone, in contrast to an open flame, and also produce flow acceleration to elongate the primary eddy. This can influence the vortex field in the wake region, thereby impacting the flame stabilization location, as well as result in high flow oscillations further downstream (due to dilatation and combustion induced turbulence).

The presence of the wall can also impact flame stability in the vicinity of the step, due to the heat losses that may occur from the wall region (figure 7.29).

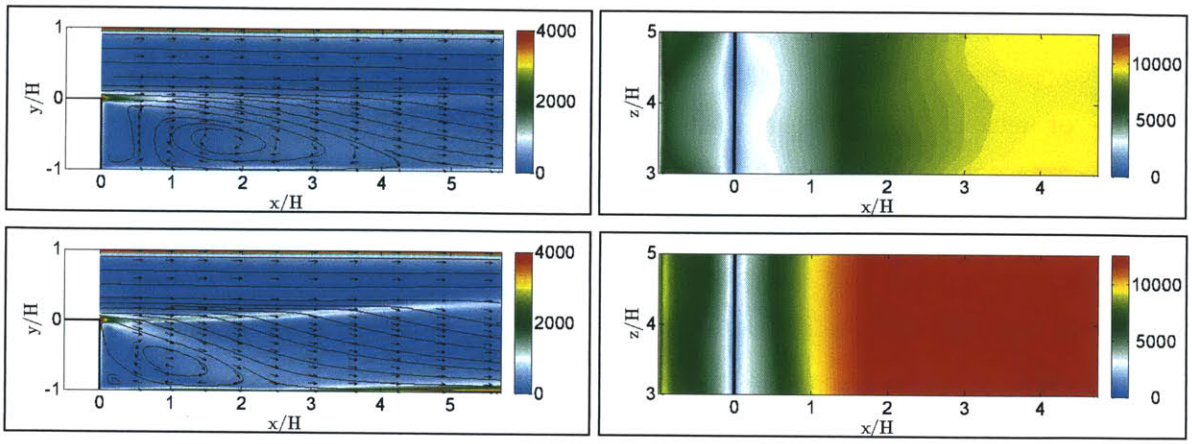

Figure 7.29: Magnitude of strain rate tensor (left) and the heat flux at the vertical step wall and bottom wall (right), for φ=0.63 (top), and φ=0.85 (bottom).

Clearly, the impact of equivalence ratio on the flame-flow dynamics is significant, and warrants further investigation in order to understand the fundamental physics, that would enable in elucidating the transition to combustion instability in case of acoustically coupled configurations. Further, the unsteady release of sensible heat and flow dilation in combustion processes create pressure fluctuations which, particularly in premixed flames, can couple with the acoustics of the combustion system, resulting in thermo-acoustic instabilities that can damage the combustor, reduce combustion efficiency, and increase pollutant formation.

Numerical simulations of these processes are often validated against experimental measurements using time-averages and point-wise statistics, as performed above. However, the approach fails to capture how the fluctuations are spatially and/or temporally distributed. In order to better understand combustion dynamics, forced response simulations are performed, followed by the application of dynamic mode decomposition technique on the heat release data as well as the flow field predictions. This allows for a deeper insight into the sizes and shapes of the unsteady flame/flow modes and can subsequently lead to a better understanding of the flame-flow interactions in unsteady combustion systems.

7.3 Self-Sustained Combustion Instability

Combustion instability is a process which is characterized by large-amplitude oscillations of one or more natural acoustic modes of the combustor, and is a resonant phenomenon that results from positive feedback interactions among the combustion process, acoustic modes, and unsteady flow

dynamics (figure 7.30). In other words, when the unsteady heat release from combustion couples with the natural acoustic modes of the combustor, it results in self-excited oscillations that can even lead to structural vibrations and damage. However, it should be noted that even in the absence of an acoustic feedback mechanism, self-sustained oscillations (at a frequency which may be different than the acoustic frequency) can be generated, and are usually driven by fluid dynamics in the unsteady shear layer.

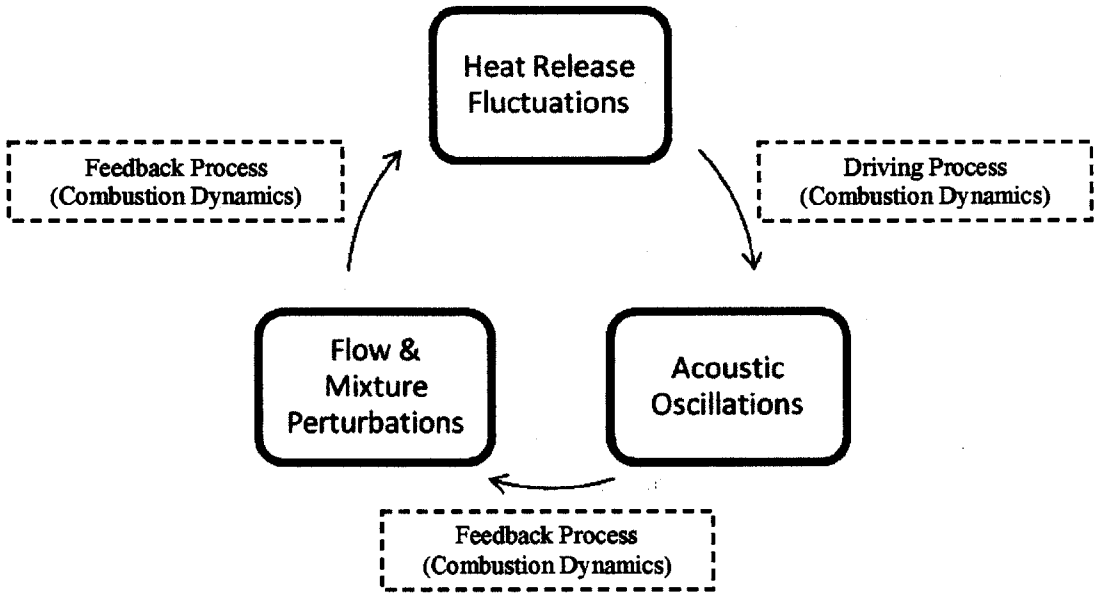

Figure 7.30: Illustration of generic combustion instability mechanism.

The factors generally responsible for driving combustion instabilities, therefore, either affect the heat release fluctuation, the pressure oscillations, or both. Heat release is largely controlled by the local air-to-fuel mixture ratio and mass flow rate, along with the instantaneous local pressure and temperature. In general, heat release fluctuations arise due to the modification of the burning rate at the flame or the modification of the flame's surface area as a result of the above processes. The physical phenomena capable of inducing pressure or heat release rate fluctuations are summarized in table 7.3.

Table 7.3: Basic elementary processes as a source of pressure or heat release rate fluctuations.

PRESSURE FLUCTUATIONS	HEAT RELEASE FLUCTUATIONS
Chamber acoustic properties	Flame-acoustic wave interactions
Hydrodynamic instabilities	Flame-vortex interactions
Injection system fluctuations	Flame-wall interactions
Chamber noise	Equivalence ratio fluctuations
Local heat release	Unsteady stretch rate effects
	Chemical kinetics effects

Although combustion dynamics has been actively studied by a number of researchers in the past, much remains uncertain due to the complex nature of the phenomena involving multi-scale interactions between the unsteady flow dynamics and combustion process. As aforementioned, a variety of complex physical processes may be involved in the development of instabilities, depending on the system characteristics, operating conditions, etc. Clearly, the study of flame-flow characteristics and thermo-acoustic interactions is critical to analyzing combustion instability.

The mechanism of flame-vortex interactions is one of the more significant instability mechanisms in large-scale gas turbine combustors, and has received considerable attention in the recent past [7.17-7.18]. Parametric studies carried out experimentally by varying the equivalence ratio, inlet temperature and fuel composition to examine the flame-vortex interaction driven combustion dynamics in the atmospheric backward step combustor have demonstrated the presence of different regimes in which the flame is impacted by different flow structures depending on the operating parameters. The response curves of the combustor -- the pressure amplitude as a function of the equivalence ratio -- for a range of inlet temperatures and fuel compositions have been obtained, where the measured pressure fluctuations have been reported in terms of the overall sound pressure level (OASPL) using a pressure sensor located close to the flame. The OASPL in dB is defined as:

$$OASPL = 10\log_{10}\left[\overline{\frac{p(t)-\overline{p(t)}}{p_o}}\right]^2 \qquad (7.1)$$

where over-bars indicate average values, $p(t)$ is the pressure measured in an interval $t_1<t<t_2$, p_o = $2x10^5$ Pa

As seen in figure 7.31a, when the inlet temperature is 300 K, three distinct operating modes at sound pressure levels of 158-160 dB, 145-150 dB and 130-135 dB are observed, corresponding respectively to the unstable, quasi-stable, and stable combustor operating modes. As a result of the unsteady interaction between the flame and the vortices formed in the wake region, the heat release rate oscillates significantly. When the periodic heat release supported by the flame-vortex interaction couples positively with the acoustic field, self-sustained oscillations are formed, resulting in significant sound pressure level. Additionally, while the impact of the Reynolds number on the stability map is found to be negligible, hydrogen enrichment as well as increase of the inlet temperature to 500 K (figure 7.31b) result in lowering the lean blowout limit and in shifting the transitions between the operating modes to lower equivalence ratios.

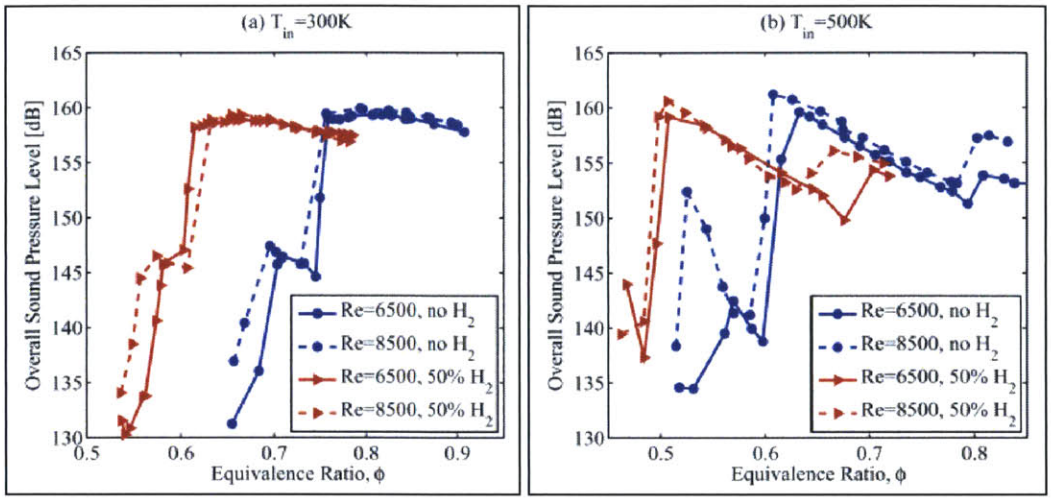

Figure 7.31: OASPL as a function of equivalence ratio for propane-hydrogen fuel mixtures at different Reynolds numbers at (a) T = 300 K (b) T = 500K.

The combustor frequency response map for Reynolds number of 6500 and inlet temperature of 300 K, without hydrogen enrichment (figure 7.32a) shows that as the equivalence ratio is varied from 0.90 to 0.75, the acoustic mode around 40 Hz is excited and the combustor operates in the unstable mode. As the equivalence ratio is reduced to 0.70, there is a slight increase in the resonant frequency, and a transition to the quasi-stable operating mode is observed. The resonant frequency subsequently drops, as the equivalence ratio is decreased further until the lean blowout limit.

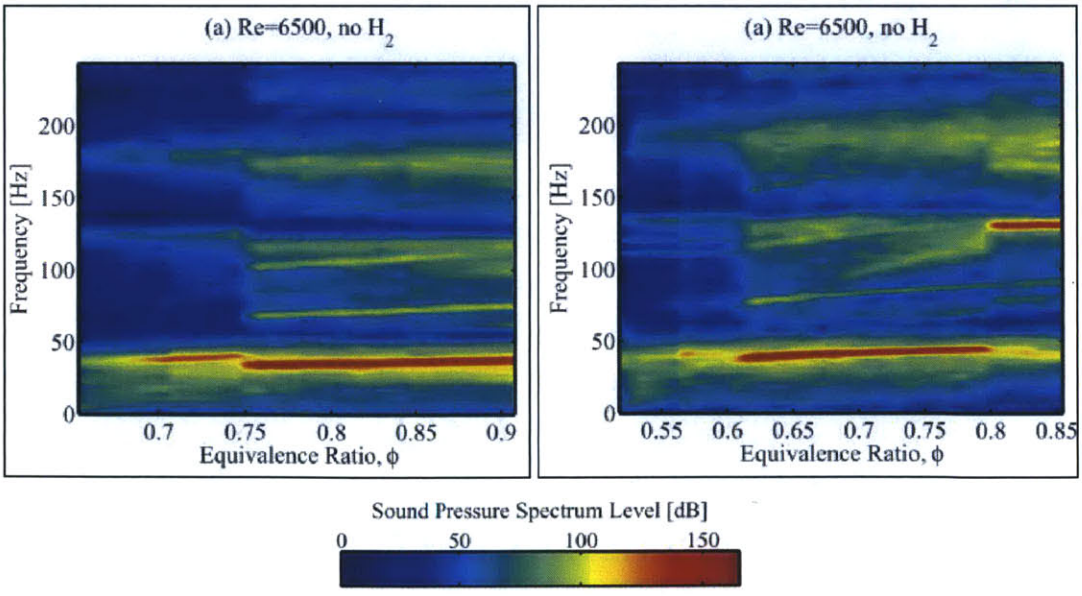

Figure 7.32: Sound pressure spectrum level maps as a function of equivalence ratio for propane fuel for Reynolds number of 6500 at (a) T = 300 K (b) T = 500K.

When the inlet temperature is raised to 500 K (figure 7.32b), there are significant changes in the acoustic response of the combustor. As the equivalence ratio is varied from 0.85 to 0.80, the combustor resonates around 130 Hz. As the equivalence ratio is reduced further, the 40 Hz mode is excited as the combustor continues to operate in the unstable regime. However, at equivalence ratio near 0.60, the OASPL drops significantly (corresponding to the transition from an unstable to a quasi-stable mode), then increases until the equivalence ratio reaches 0.57, and subsequently decreases until blowout occurs.

In figure 7.33, the CH chemiluminescence images obtained from experiments are shown, corresponding to the distinct operating modes associated with the OASPLs of 158-160 dB, 145-150 dB and 130-135 dB when the equivalence ratio is varied (T_{in}=300K, Re=6500). It is also observed that the variation in the inlet temperature yields the same set of operating modes; however, the equivalence ratios at which transition between the modes takes place are shifted.

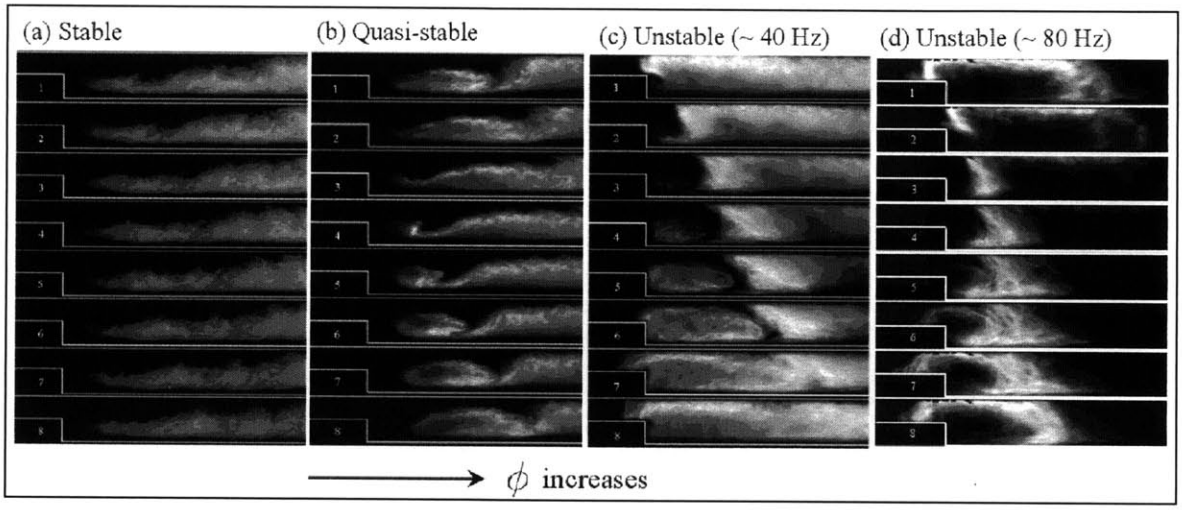

Figure 7.33: CH chemiluminescence images for the acoustically-coupled backward facing step combustor at different equivalence ratios (fuel=propane).

In figure 7.34, the simultaneous heat release rate and velocity measurements corresponding to the unstable mode shown in figure 7.33c are depicted, along with the FFT analysis of the respective signals. It is observed that the maximum of the heat release almost coincides with zero velocity, indicating a phase difference of $\pi/2$, approximately). In this work, acoustically forced simulations for the backward facing step geometry have been performed, corresponding to the self-excited instability scenario shown in figure 7.34, in order to evaluate the applicability of the numerical framework to predict the dynamic mode transitions in acoustically-coupled systems, and to better understand the mechanism of flame-flow interactions in unsteady combustion phenomena.

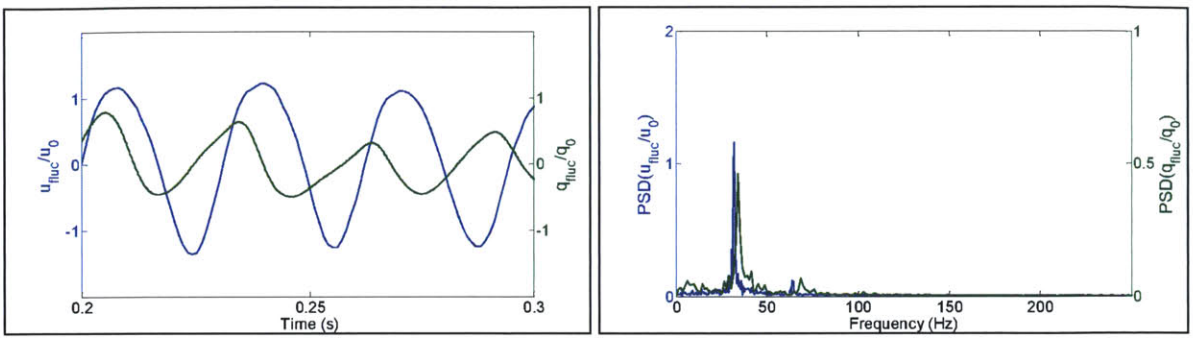

Figure 7.34: (a) Experimentally measured velocity and heat release signals corresponding to self-excited instability, (b) frequency content of the signals (φ= 0.85, Re=6500, T_{in}=300K, fuel=propane, f=36 Hz).

7.4 Forced Reacting Flow

Thermo-acoustic characterization of gas turbine combustion systems is crucial for successful development of gas turbine engines to meet emission and efficiency targets. In this context, it becomes necessary to predict the limit cycle amplitudes of thermo-acoustic induced combustion instabilities to ascertain if they can be tolerated or if they are above the critical design limit and can, therefore, cause damage to the engine. For the prediction of limit cycle amplitudes, the non-linear flame response of the combustion system is needed, which is often represented by the Flame Describing Function (FDF). The identification of the FDF and the response of the flame to acoustic perturbations therefore have been attempted for different combustor geometries [7.24-7.28]. Understanding the amplitude dependence of the flame response and the effect of the presence of harmonics is, therefore, critical to predict the limit cycle behavior accurately, and to understand the non-linear processes controlling the limit cycle. In this regard, significant efforts have gone into studying the dynamic response mechanism of the flame to imposed acoustic forcing [7.28-7.35].

In this section, large eddy simulations are utilized to study the forced response of the flame to inlet velocity perturbations. The results from the spectral analysis of the heat release and velocity signals recorded during the calculations are compared with those obtained from experimental measurements. Subsequently, the flame and flow field contours reproduced numerically are analyzed, in order to gain an insight into the dynamics of the process, as well as to understand the flame-flow interactions. The dynamic mode decomposition of the numerical data is also performed to gain an insight into the dynamic modes characterizing the system.

7.4.1 Dynamic Response

In order to gain an insight into the flame-flow dynamics, the forced response of the flame is studied numerically by imposing velocity fluctuations at the inlet, such that:

$$u = u_o + u' = u_o\left[1 + A\sin\left(2\pi f\ t\right)\right] \qquad (7.2)$$

where u_o is the mean velocity, f is the frequency and A is the amplitude of forcing over time t. Three cases are considered for analysis:

I. φ = 0.85, A = 1.00, f = 35 Hz

II. φ = 0.85, A = 0.25, f = 35 Hz

III. φ = 0.63, A = 1.00, f = 35 Hz

Case I corresponds to the reacting flow experiment for the acoustically-coupled backward step combustor (figure 7.34), for which a self-excited unstable flame is observed for the propane-air mixture (φ=0.85, T_{in}=300K, Re=6500), at a resonant frequency of approximately 35Hz, and a velocity fluctuation, u', with a peak value equal in magnitude to the mean bulk flow velocity, U_{SH}.

The simulation results are recorded once the initial transients disappear and a stable limit cycle is attained. In figures 7.35-7.36, the sinusoidal inlet-fluctuating-velocity forcing-signal and the corresponding volumetric heat release is shown for cases I and III, along with the respective frequency spectra. For case I, as noticed in the experiments, the heat release response from the simulations coincides with the zero forcing inlet velocity (indicating a phase difference of $\pi/2$, approximately). The heat release response is cyclic; however, at the higher forcing amplitude scenario shown here, the response steepens on the decreasing slope of the cycle, as has been observed before in case of a bluff-body combustor [7.32]. Thus, the flame response is no longer a pure sine wave.

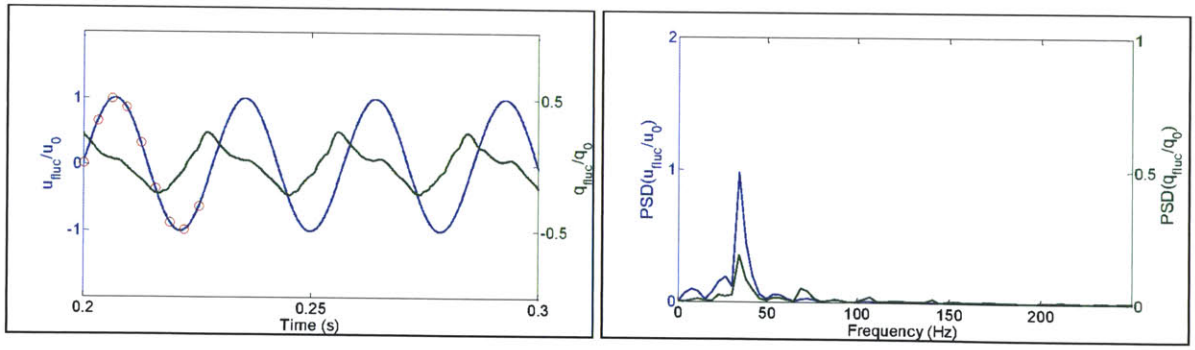

Figure 7.35: (a) Inlet velocity forcing signal and volumetric heat release response, (b) frequency content of the signals (φ = 0.85, A = 1.00, f = 35 Hz).

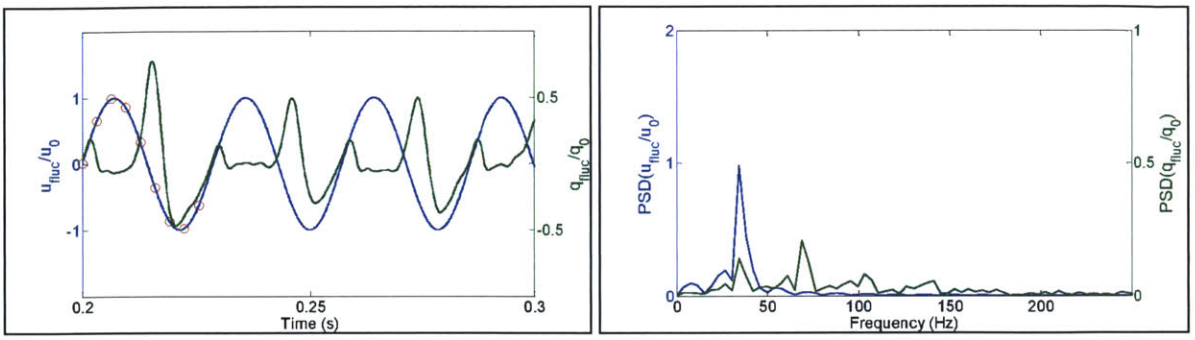

Figure 7.36: (a) Inlet velocity forcing signal and volumetric heat release response, (b) frequency content of the signals (φ = 0.63, A = 1.00, f = 35 Hz).

Observing the PSD plot in figure 7.35b, the peaks in the spectra corresponding to the forcing frequency are evident in both the input and the response. Additionally, harmonics are visible in the heat release response at multiples of the forcing frequency, due to the non-linearity of the process. Moreover, non-harmonic peaks of lower magnitude are also observed, which suggests that the combustion dynamics also encompasses supplementary physics that can be characterized as a result of the turbulent reacting flow-field and its interaction with the flame. Similar results have also been observed by other researchers [7.36].

In figures 7.37-7.38, the vorticity contours along with the corresponding streamlines and the heat release contours are shown through a cycle of forcing for case I. In frame 1, fresh reactants enter the combustor at the moment of maximum inlet acceleration and the wake vortex begins to form at the step edge. As the velocity at the combustor inlet rises, the wake eddy grows in size and strength, while the vortex that formed in the shear layer in the previous cycle convects downstream. Meanwhile the secondary vortex at the corner has low intensity. The primary vortex that is formed at the tip of the flame surface, distorts the flame front near the step. As it convects downstream, it draws the reaction zone with it and the flame begins to roll-up around the growing vortex structure. Further downstream, the flame has a smooth profile, and the heat release begins to decrease in magnitude from its peak value, following the end of intense burning from the previous cycle.

In frames 2 and 3, at phases 40° and 80°, near the moment of maximum velocity, the heat release is approaching towards its minimum value. As the inlet velocity increases, the wake vortex from the previous cycle has convected further downstream and 'collapses', while the strength of the upstream vortex core is increasing and the recirculation is re-establishing. With the increase in velocity, the flame also bends down towards the lower wall. Thus, by the time the forcing velocity fluctuation has increased to its peak value, the integrated heat release fluctuation has fallen to close

to zero. The secondary corner recirculation also begins to take shape and move up along the step wall towards the shear layer.

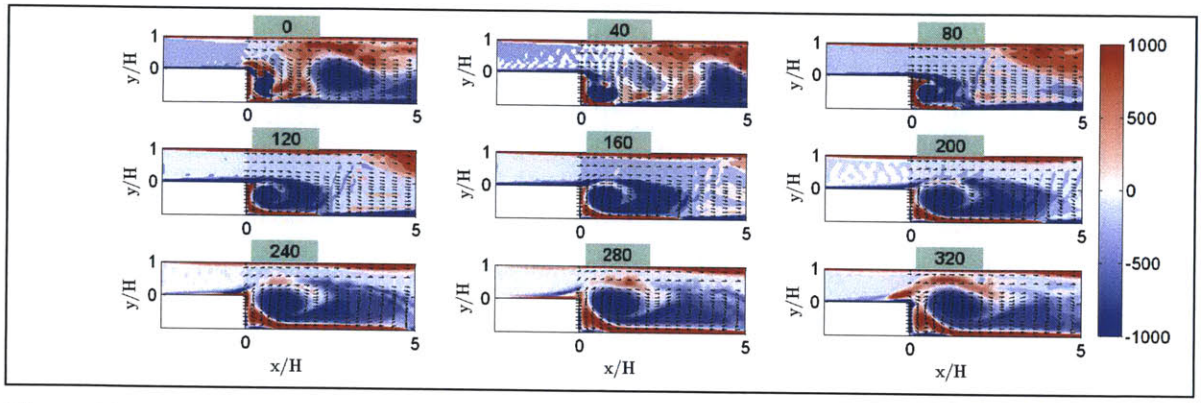

Figure 7.37: Instantaneous z-vorticity through a cycle of forcing (φ = 0.85, A = 1.00, f = 35 Hz).

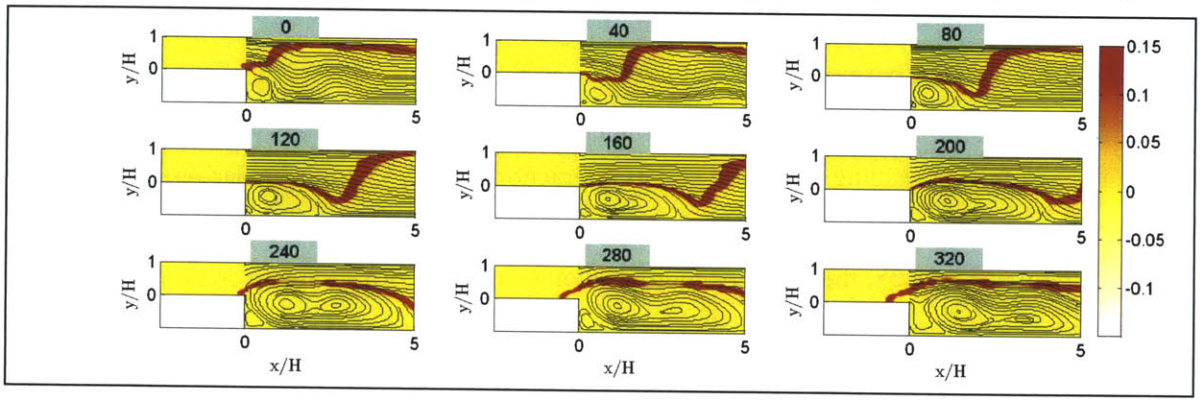

Figure 7.38: Instantaneous heat release through a cycle of forcing (φ = 0.85, A = 1.00, f = 35 Hz).

In frames 4 and 5, as the velocity drops from its maximum value, the primary coherent eddy continues to grow; the shear layer at the inlet rolls up and moves along the flame, drawing the flame sheet towards the wall of the enclosure, and distorting the flame front. The large primary vortex has moved further downstream, and begins to elongate and break up, thereby lengthening the flame front formed during the new cycle. Further downstream a region of unburned reactants is consumed by the flame front formed in the previous cycle. Subsequently, the inlet velocity drops below its average, slowing the downstream motion of the vortex, which begins to grow more in the transverse direction, moving the flame front towards the upper wall.

In frames 6 and 7, when the inlet velocity is close to its minimum, the vortex is close to reaching its maximum size, and the breakup of the vortex followed by the formation of small-scale eddy structures begins to take place, which enhances the heat release. The corner recirculation zone also grows in size and subsequently moves up along the wall and interacts with the flame front as it

flashes back into the inlet duct. In frames 8 and 9, given the low velocity magnitude, the flame begins to move upstream, causing flashback, and the heat release increases rapidly. The flame front is significantly elongated, and the breakdown of the primary vortex also distorts the flame brush in the downstream section. Subsequently, the flow begins to accelerate and the cycle repeats as fresh reactants enter the combustor and a new wake vortex begins to form.

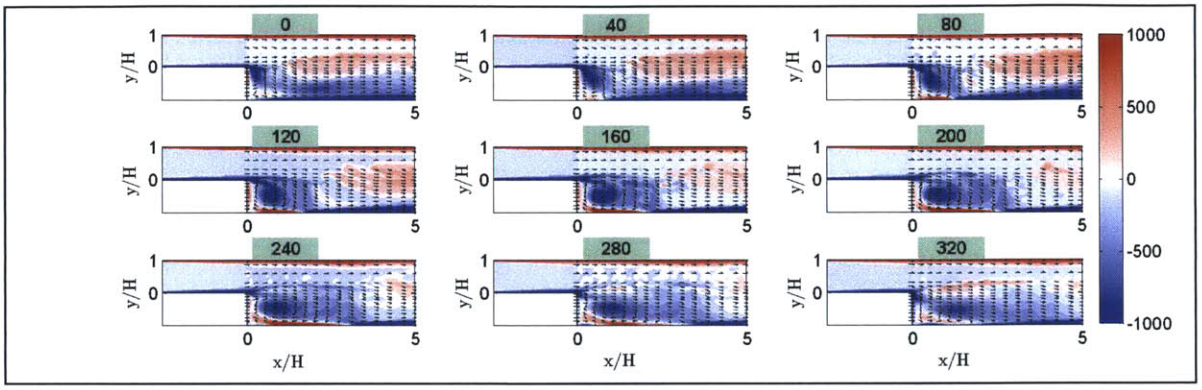

Figure 7.39: Instantaneous z-vorticity through a cycle of forcing (φ = 0.85, A = 0.25, f = 35 Hz).

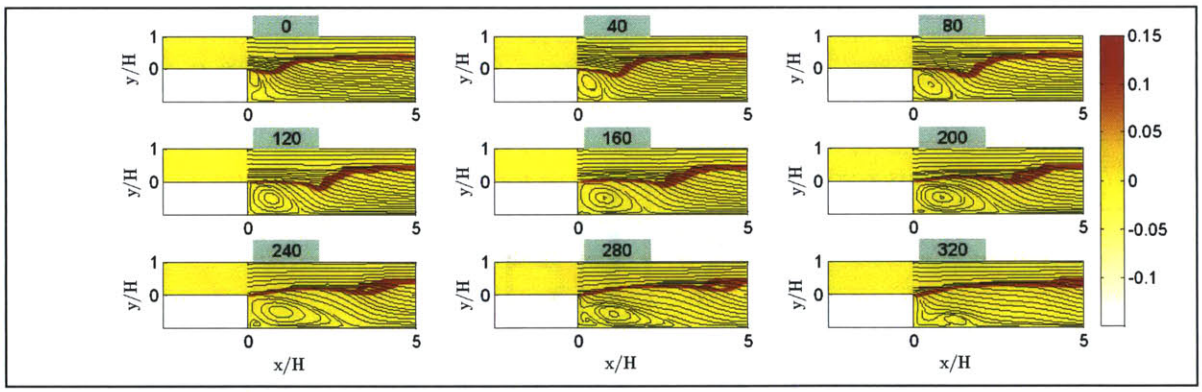

Figure 7.40: Instantaneous heat release through a cycle of forcing (φ = 0.85, A = 0.25, f = 35 Hz).

In figures 7.39-7.40, the vorticity and heat release contours corresponding to case II are depicted. At relatively low forcing amplitudes, the primary recirculation does not move or affect the reaction zone significantly, and the secondary vortex is also absent. In fact, as the inlet velocity changes, the shape of the flame remains largely unchanged, with only a slight distortion rippling down the flame sheet, forcing it slightly towards the lower wall of the enclosure as the 'center' of the primary recirculation vortex moves downstream. The flame sheet is anchored on the step edge, extends almost parallel to the walls of the duct, until it reaches the downstream exhaust section.

Comparing the results from cases I and II, it is evident that the flame at higher forcing amplitude is distorted much more dramatically. The flame sheet forms a convoluted contour around

the vortices which roll-up the reaction front, with the primary vortex structure drawing the flame front with it, as it grows and convects downstream. Subsequently, vortex breakup stretches and distorts the flame surface, and the flame sheet also begins to propagate upstream. Eventually, the primary and secondary vortices merge and the cycle repeats again. These dynamic flame-flow interactions are characteristic of case I and are significantly suppressed in case II.

In figure 7.41-7.42, the vorticity and heat release contours for case III are shown, which indicate significant flame-flow oscillations. This is not unreasonable, given that at low forcing frequencies, the gain of the flame transfer function (FTF), given by $[q'/\bar{Q}]/[u'/U_{SH}]$, is typically higher for low equivalence ratios (at fixed perturbation amplitude), as previously shown in [7.25].

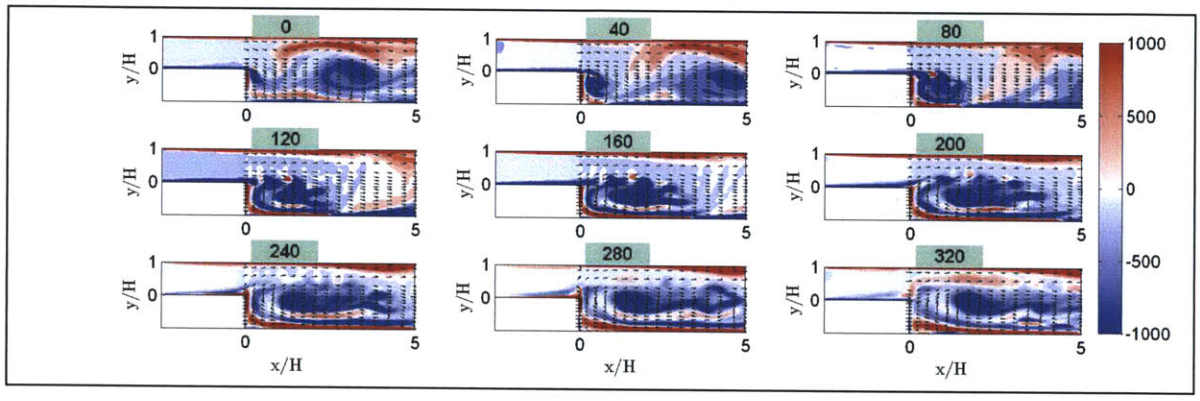

Figure 7.41: Instantaneous z-vorticity through a cycle of forcing (φ = 0.63, A = 1.00, f = 35 Hz).

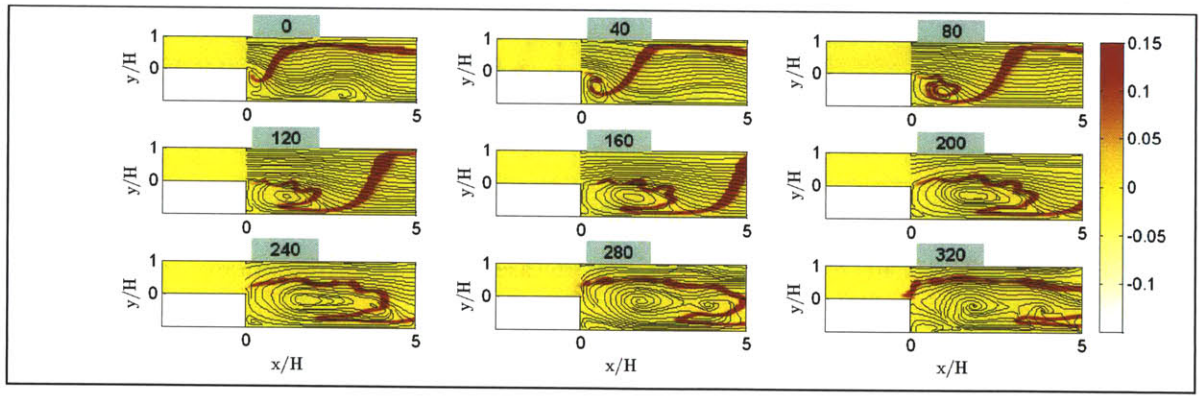

Figure 7.42: Instantaneous heat release through a cycle of forcing (φ = 0.63, A = 1.00, f = 35 Hz).

7.4.2 Dynamic Mode Decomposition Analysis

As mentioned in Chapter 5, the DMD framework serves as an effective tool for the analysis of dynamic flow features, and can extract valuable dynamic information from flow fields that are either measured in a physical experiment, or generated by numerical simulations. The method decomposes the patterns in the data on the basis of frequency content and therefore has some distinct advantages

over the conventional POD approach. In other words, the DMD analysis generates a global frequency spectrum and each mode corresponds to a specific discrete frequency. Therefore, the results from the application of DMD to the flow field data, as well as the heat release data, can provide a quantitative means for understanding the flame-flow interactions by analysis of the flow modes and the heat release modes. In this section, therefore, the DMD modes obtained from a preliminary analysis of the LES data corresponding to the forced response simulations (case I) are presented. The snapshots are sampled at a frequency of 1000Hz, and a truncated region of the combustor section ($0<x/H<5$) is considered. The analysis is performed on the flow-field that is comprised of the axial and radial velocity components (i.e $\boldsymbol{V} = [u_x; u_y]$), as well as the heat release contour. Note that the results from DMD analysis are typically sensitive to the region, the sampling duration, and the time step (or number of snapshots).

7.4.2.1 Flow Field

The real and imaginary parts of the Ritz values, sized by the energy of the mode, are depicted in figure 7.43a, along with the modal frequency (ω) and growth rate (σ) in figure 7.43b. The Ritz values lie near the unit circle, indicating neutral stability. In conjunction with the observations in figures 7.35, the energy spectrum shows that apart from the mean mode, the DMD modes with high energy intensity correspond to the forcing frequency ($\upsilon=\omega/2\pi$) of 35 Hz and its harmonics (figure 7.43c).

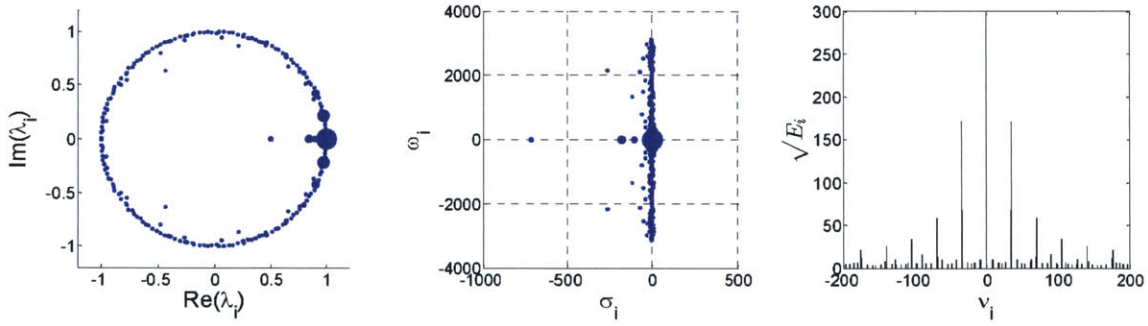

Figure 7.43: (a) Ritz vectors on the complex plane, (b) Frequency, ω, and growth rate, σ, of dynamic modes, (c) Energy content of dynamic modes.

In figure 7.44, the vorticity contours for the real and imaginary parts of the mode that corresponds to the mean flow pattern are shown, along with the FFT analysis of the temporal coefficients corresponding to the real component of the dynamic mode. As expected, the primary and secondary recirculation vortices are suitably highlighted, that dominate the average flow field.

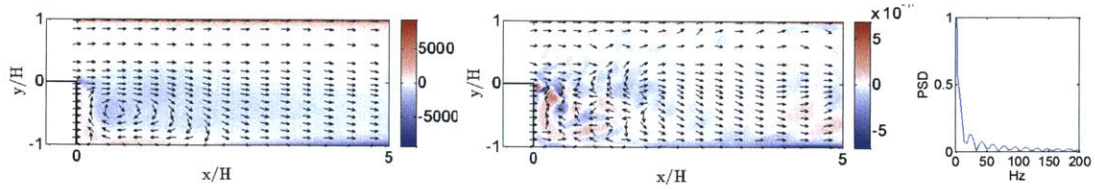

Figure 7.44: 0Hz dynamic mode (Real component: left, Imaginary component: middle, Frequency spectrum of temporal coefficient of real component of dynamic mode: right).

The vorticity contours for the real and imaginary components of the 35 Hz mode are depicted in figure 7.45, indicating the presence of a coherent vortex structure along the shear layer, near the flame tip, and is associated with the global flow instability mode along the mixing layer.

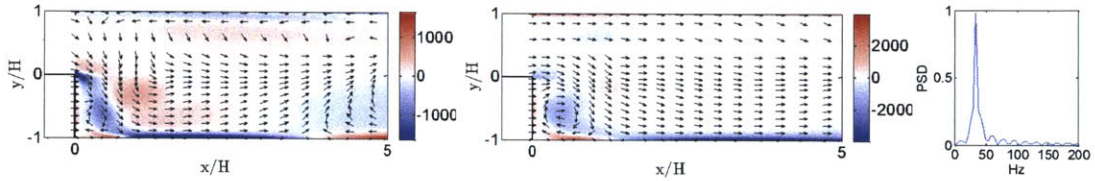

Figure 7.45: 35Hz dynamic mode (Real component: left, Imaginary component: middle, Frequency spectrum of temporal coefficient of real component of dynamic mode: right).

In figure 7.46, the phase-shifted realizations of the dynamic mode are shown, and are composed of the real and imaginary parts of the Ritz vectors, as outlined in equation (5.12). The flow features can be attributed to the breakdown of the shear layer vortices, resulting in the formation of the recirculation eddy. The influence of the secondary recirculation zone on the shear layer development and growth of the coherent vortex that convects downstream is also evident.

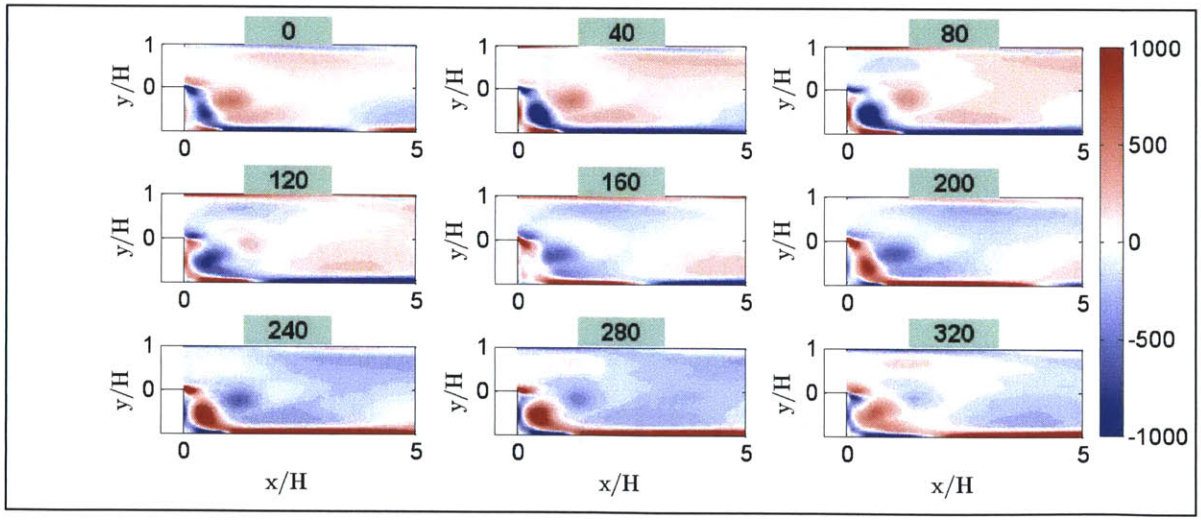

Figure 7.46: Phase shifted realizations of 35 Hz dynamic mode composed of the real and imaginary components along with their temporal coefficients.

In figures 7.47-7.50, the 70 Hz and 105 Hz dynamic modes and their corresponding phase-shifted realizations are shown. These oscillatory modes appear to correspond to the flapping of the mixing layer, and the vortex breakdown activity in the shear layer, due to local flow instability.

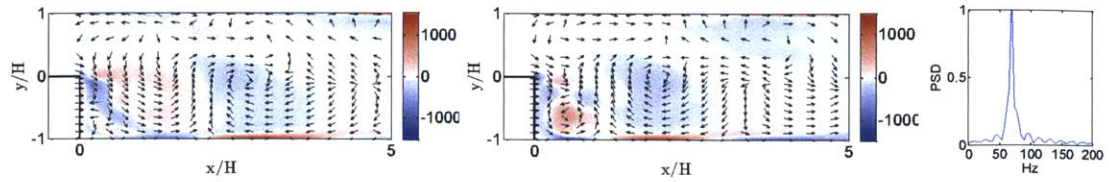

Figure 7.47: 70Hz dynamic mode (Real component: left, Imaginary component: middle, Frequency spectrum of temporal coefficient of real component of dynamic mode: right).

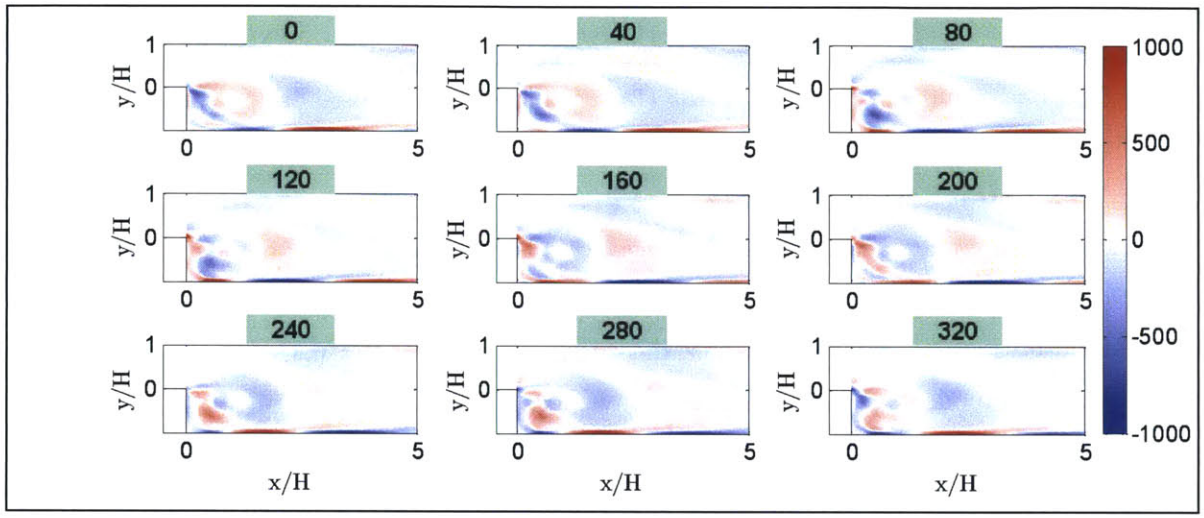

Figure 7.48: Phase shifted realizations of 70 Hz dynamic mode composed of the real and imaginary components along with their temporal coefficients.

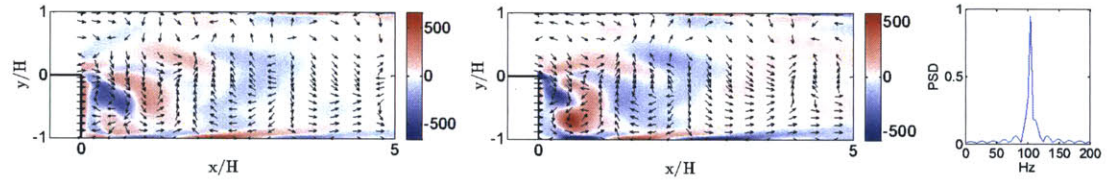

Figure 7.49: 105Hz dynamic mode (Real component: left, Imaginary component: middle, Frequency spectrum of temporal coefficient of real component of dynamic mode: right).

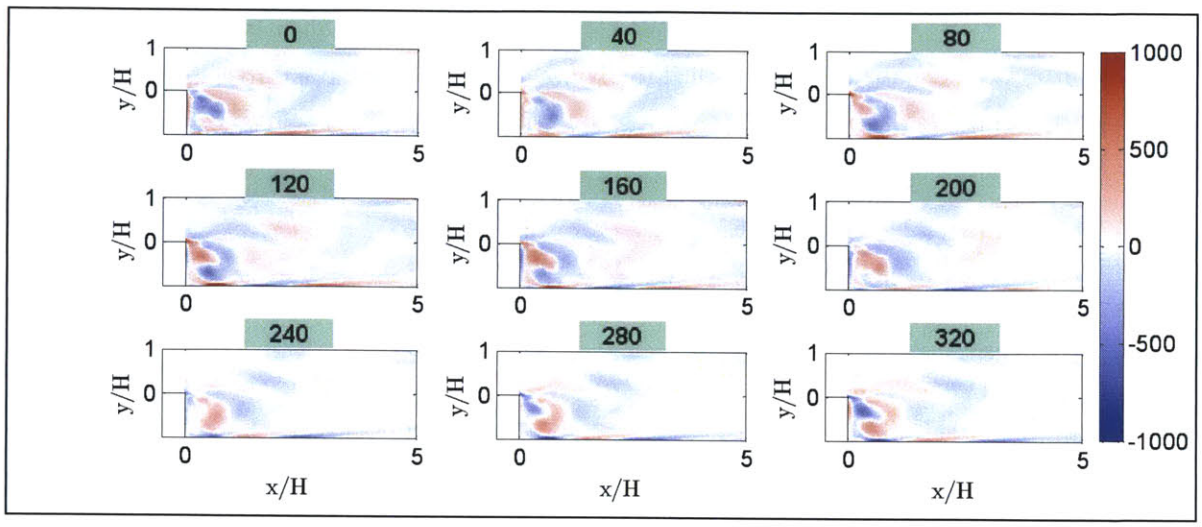

Figure 7.50: Phase shifted realizations of 105 Hz dynamic mode composed of the real and imaginary components along with their temporal coefficients.

7.4.2.2 Heat Release

The real and imaginary parts of the Ritz values, sized by the energy of the mode, are depicted in figure 7.51a, along with the modal frequency (ω) and growth rate (σ) in figure 7.51b. In conjunction with the observations in figures 7.32-7.33, the energy spectrum shows that apart from the mean mode, the DMD modes with high energy intensity correspond to the forcing frequency ($\upsilon=\omega/2\pi$) of 35 Hz and its harmonics (figure 7.51c). However, other than the expected forcing frequency and its harmonics, there are also additional peaks of lower magnitude, suggesting that in addition to the velocity mode response (corresponding to forcing frequency and its harmonics), combustion dynamics also contains additional physics that can be associated with the turbulent reacting flow, as also noted in [7.37].

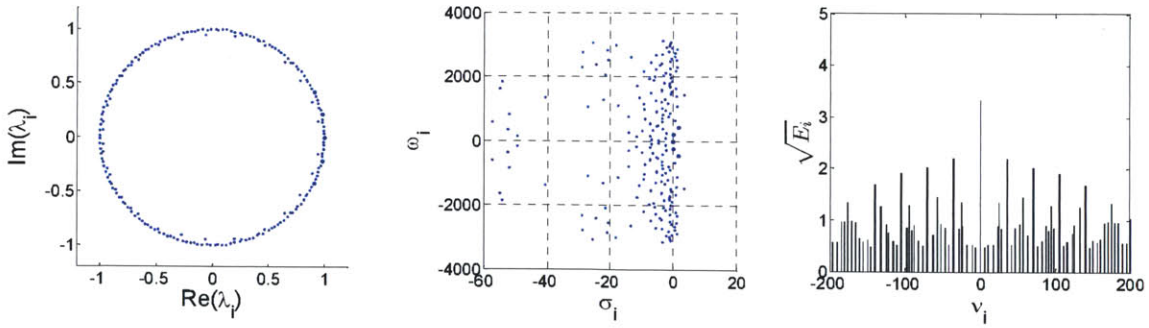

Figure 7.51: (a) Ritz vectors on the complex plane, (b) Frequency, ω, and growth rate, σ, of dynamic modes, (c) Energy content of dynamic modes.

In figure 7.52, the heat release contours for the real and imaginary parts of the mode that corresponds to the mean reaction zone are shown, along with the FFT analysis of the temporal coefficients corresponding to the real component of the dynamic mode. The mean flame-front is comprised of a reaction zone that is extends upstream of the step-edge (associated with flame flashback noted earlier). Further downstream, the mean heat release zone spreads significantly, associated with the convolution of the flame-front as it interacts with the convecting vortices.

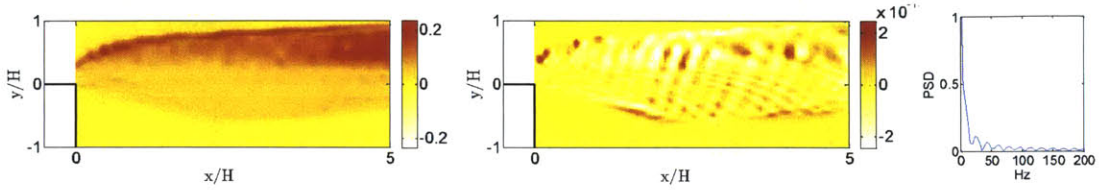

Figure 7.52: 0Hz dynamic mode (Real component: left, Imaginary component: middle, Frequency spectrum of temporal coefficient of real component of dynamic mode: right).

Likewise, heat release contours for the real and imaginary components of the 35 Hz mode are depicted in figure 7.53, along with the phase-shifted realizations of the dynamic mode (composed of the real and imaginary parts of the Ritz vectors) in figure 7.54. These indicate the pulsating behavior of the flame, driven by the forcing frequency. There appears to be a significant variation in the location of the high intensity thermal release regions over each cycle of oscillation at the forcing frequency.

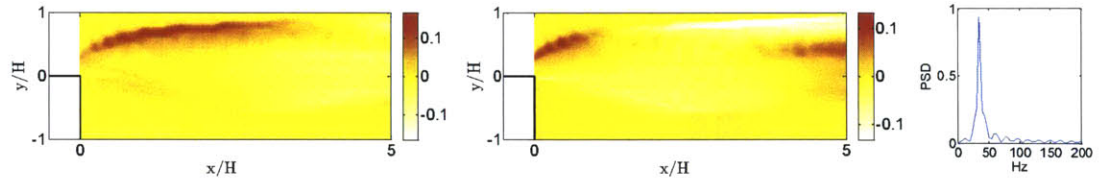

Figure 7.53: 35Hz dynamic mode (Real component: left, Imaginary component: middle, Frequency spectrum of temporal coefficient of real component of dynamic mode: right).

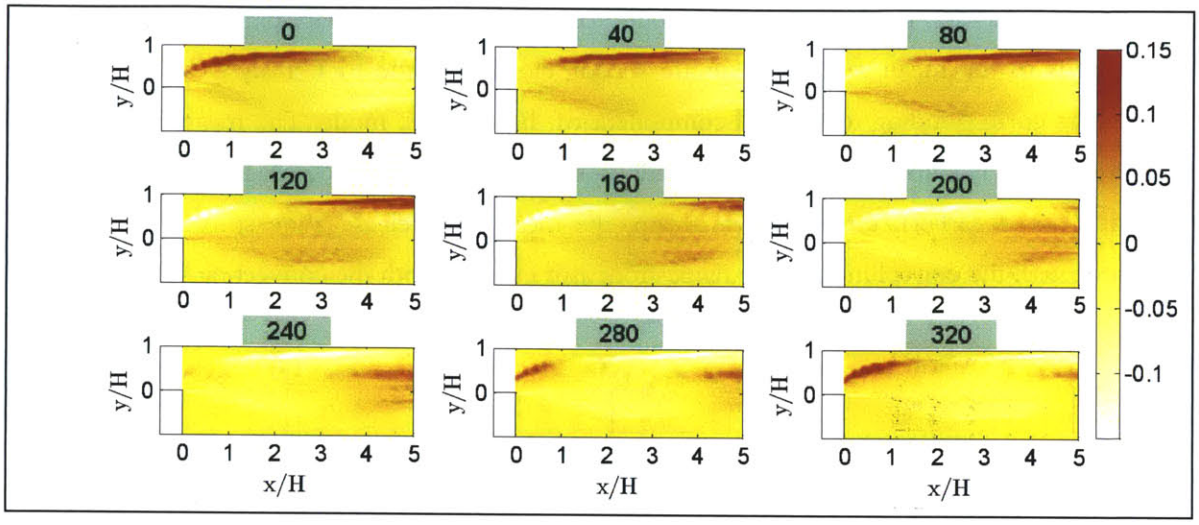

Figure 7.54: Phase shifted realizations of 35 Hz dynamic mode composed of the real and imaginary components along with their temporal coefficients.

In figures 7.55-7.58, the 70 Hz and 105 Hz dynamic modes and their corresponding phase-shifted realizations are shown. These oscillatory modes show similar spatial configurations, and demonstrate that combustion begins to occur in locations alternate to the primary response region of the 35 Hz mode. Given the moderately high energy intensity of these modes, relative to the primary oscillatory mode, the results further suggest that the flow modes at harmonic frequencies contribute significantly to the alterations of the combustion process in the chamber (in regions of the duct that differ from the heat release locations corresponding to the forcing frequency mode).

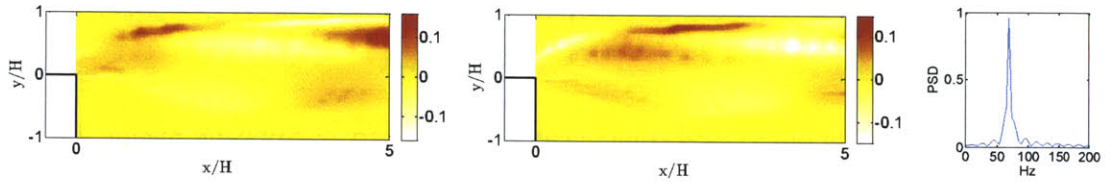

Figure 7.55: 70Hz dynamic mode (Real component: left, Imaginary component: middle, Frequency spectrum of temporal coefficient of real component of dynamic mode: right).

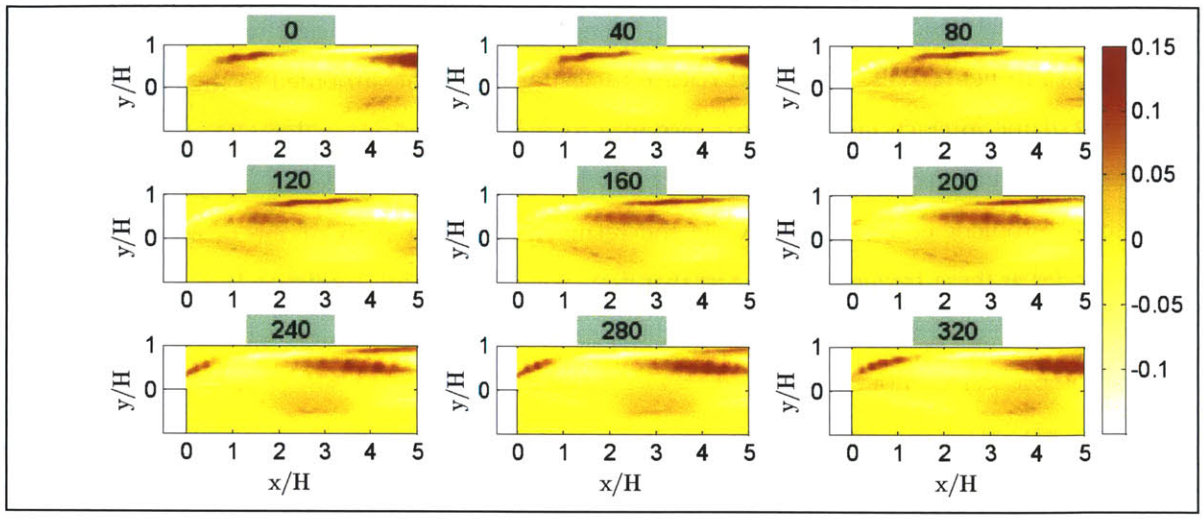

Figure 7.56: Phase shifted realizations of 70 Hz dynamic mode composed of the real and imaginary components along with their temporal coefficients.

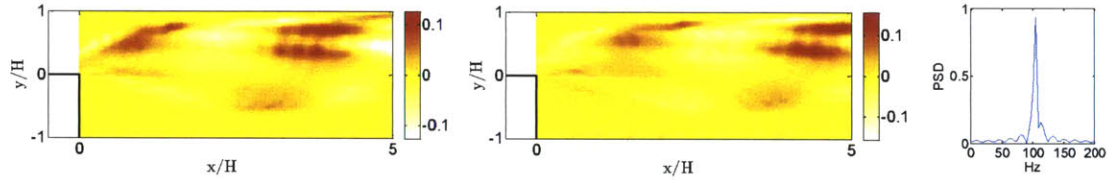

Figure 7.57: 105Hz dynamic mode (Real component: left, Imaginary component: middle, Frequency spectrum of temporal coefficient of real component of dynamic mode: right).

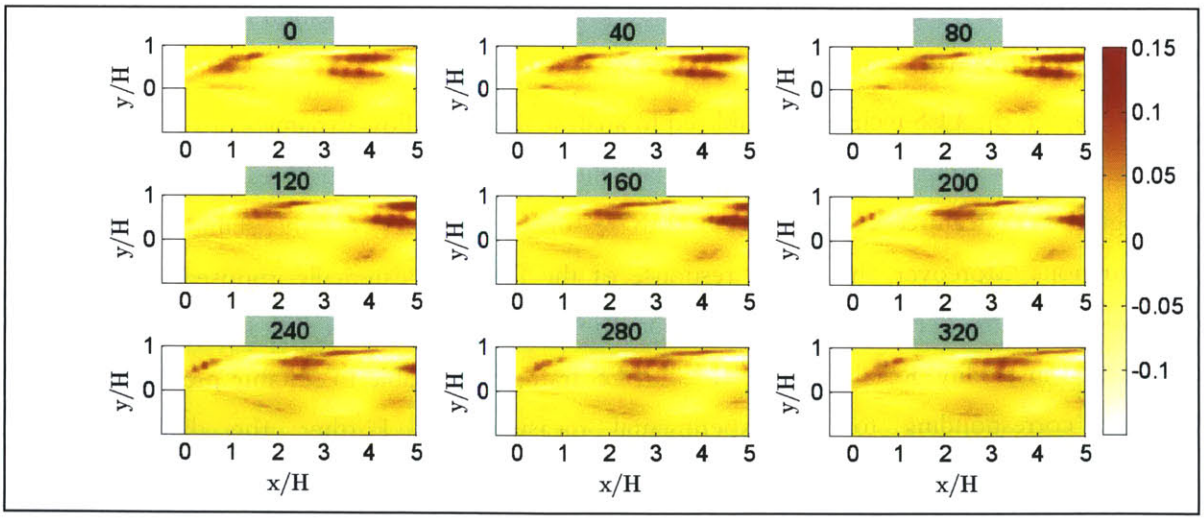

Figure 7.58: Phase shifted realizations of 105 Hz dynamic mode composed of the real and imaginary components along with their temporal coefficients.

Additional modes are also observed, at non-harmonic frequencies, with a representative mode shown in figure 7.59. These heat release oscillations could be attributed to the phenomena of turbulence-flame interactions; the flame response to these frequencies is dominated by small-scale combustion, which may correspond to the breakdown of the large-scale shear layer vortices into small-scale turbulent eddies [7.37]. While the relatively lower strength of the peaks for the heat release modes at these frequencies suggest that they may play a slightly weaker role in influencing the combustion phenomena (as opposed to the primary, harmonic modes), their impact on the combustion process cannot be neglected.

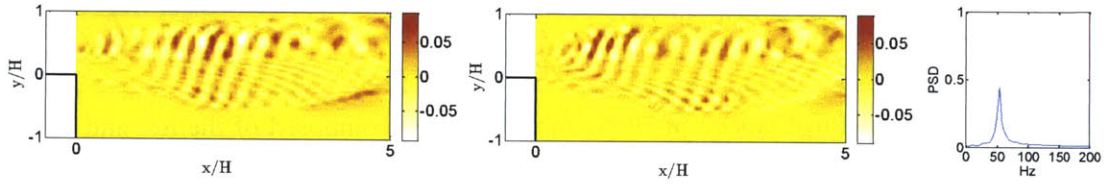

Figure 7.59: A non-harmonic dynamic mode (Real component: left, Imaginary component: middle, Frequency spectrum of temporal coefficient of real component of dynamic mode: right).

These results demonstrate the capability of DMD analysis to highlight the physical phenomena that are otherwise not typically evident or revealed using standard decomposition techniques such as proper orthogonal decomposition (POD). The framework can be utilized to evaluate the dynamic characteristics of combustion systems from LES data, as well as to gain a deeper insight into the turbulence-chemistry interactions governing combustion instability.

7.5 Conclusions

In this chapter, the LES technique is utilized to analyze the flame-flow dynamics in a backward-step combustor. The simulation results show that the numerical framework resolves the different topological flow features effectively and with reasonable accuracy, for the stable reacting flow configurations. Moreover, the forced response of the flame, to externally imposed inlet velocity fluctuations, is also performed to evaluate the applicability of the numerical approach to analyze combustion instability. Results show that the LES framework is able to suitably predict the flame behavior corresponding to the experimental measurements. Further, the dynamic mode decomposition analysis of the flow and heat release data, obtained from the simulations, provides an insight into the dynamic characteristics of the combustion process, as well as the turbulence-chemistry interactions, in case of the backward facing step configuration.

8 CONCLUSIONS

8.1 Combustion Modeling & Validation

High efficiency, low emissions and stable operation over a wide range of conditions are some of the key requirements of modern-day combustors. To achieve these objectives, lean premixed flames are generally preferred as they achieve efficient and clean combustion. A drawback of lean premixed combustion, however, is that the flames are more prone to dynamics. The unsteady release of sensible heat and flow dilatation in combustion processes create pressure fluctuations which, particularly in premixed flames, can couple with the acoustics of the combustion system. This acoustic coupling creates a feedback loop with the heat release that can lead to severe thermo-acoustic instabilities that can damage the combustor. Understanding these dynamics, predicting their onset and proposing passive and active control strategies are critical to large-scale implementation. For the numerical study of such systems, large eddy simulation (LES) techniques are highly appropriate, as they balance computational complexity and predictive accuracy. This work, therefore, has explored the applicability of these methods to the study of premixed wake stabilized flames.

An important component of LES is the turbulent combustion sub-grid model, which is necessary to incorporate the effect of turbulence-chemistry interactions at the unresolved scales on the reaction rate. Various approaches have been developed, that can be broadly categorized into finite reaction zone approaches (eddy break-up type models, eddy dissipation concept etc), flame front topology methods (flame surface density and flame wrinkling descriptions, the level-set flame front tracking technique, or G-equation approach etc), statistical framework based approaches (presumed or transported PDF method), and finite-rate chemistry models (artificially thickened flame technique, partially stirred reactor concept etc). Evaluating the performance of these sub-models in simulating turbulence-chemistry interactions is crucial to developing higher fidelity CFD methods for predicting flame-flow dynamics and conducting combustion instability studies. In this work, specifically, finite-rate chemistry and statistics-based LES models that can effectively capture the interaction between different turbulent scales and the combustion fronts have been implemented, and applied for the analysis of premixed turbulent flame dynamics in laboratory-scale combustor configurations.

Firstly, the artificial flame thickening approach, along with an appropriate reduced chemistry mechanism, is utilized for modeling turbulence-combustion interactions at small scales. The thickened flame model has distinct advantages over some of the other approaches, in that it allows

the use of suitably detailed reaction chemistry and can be applied to different combustion regimes, in general. A critical aspect of the modeling technique is the determination of the efficiency function that accounts for the reduced wrinkling of the thickened flame front due to turbulence. Current models define the efficiency function using an algebraic formulation for the flame wrinkling, which is estimated based on the assumption of local-equilibrium between production and destruction of SGS flame surface density. It has been suggested that in case of highly unsteady systems or in configurations prone to thermo-acoustic instabilities, deviation from local-equilibrium and the lack of 'time-history effects' in the simpler algebraic models can result in prediction inaccuracies. Therefore, further development of the model is warranted so that the approach can be applied to the analysis of strongly unsteady systems.

This work has addressed some of these concerns, by incorporating a dynamic formulation for the efficiency function that explicitly incorporates the influence of strain and 'time-history effects' on flame wrinkling by solving a transport equation for the flame surface area evolution, rather than using local-equilibrium-based algebraic models. Multiple-step reaction chemistry that can be appropriately used with the thickened flame approach has also been included. A preliminary analysis has been conducted to assess the performance of the proposed model on LES predictions for different combustor configurations. The simulation results are compared with experimental measurements, and the turbulent flow features are reproduced fairly well, while more accurate predictions are obtained using a dynamic formulation for the efficiency function. Specifically, it is observed that the fluctuations in the shear layer are resolved more accurately using the modified approach, both for the triangular bluff-body and the backward step combustor. This suggests that the proposed approach is an improvement over the existing models, since deviation from local equilibrium, and the absence of time history and strain effects in the equilibrium models can result in inaccurate predictions, especially in case of lean premixed flames under highly unsteady conditions. In addition, the model employs the strained laminar flame speed in its calculations to account for the effects of strain and curvature on the laminar flame speed, which can further enhance the accuracy of the numerical predictions.

Secondly, the presumed-PDF approach, coupled with the flamelet generated manifold (FGM) technique, has been implemented for modeling turbulence-combustion interactions. In the context of premixed combustion, the presumed-PDF model have mostly focused upon using the reaction progress variable and the enthalpy as coordinates to presume the probability density function (PDF) to obtain the filtered thermo-chemical properties and reaction rates. However, it is

well known that in case of highly unsteady systems or in configurations prone to thermo-acoustic instabilities, strain can play a significant role in altering the flame speed and thus the turbulence-chemistry interactions. Therefore, it is imperative to explicitly account for the strain, while simulating turbulent premixed combustion. More recently, this has been attempted in a RANS context by incorporating strain via the scalar dissipation rate as an additional coordinate to presume the PDF, while utilizing strained laminar flamelets to obtain the chemical database.

In this work, the modified formulation has been implemented within an LES context. Additionally, the flamelet generated manifold (FGM) technique, which generates mathematically reduced databases in order to estimate the chemical flame structure efficiently and effectively, has been employed to account for the detailed chemistry effects. The predictive capabilities of the presumed-PDF LES combustion model as applied to a well-studied, laboratory-scale axi-symmetric bluff-body-stabilized flame have been investigated. The simulation results are compared with experimental measurements and the turbulent flame-flow features are reproduced fairly well; more accurate predictions are obtained using the proposed formulation that accounts explicitly for the strain via the scalar dissipation rate.

8.2 Premixed Flame Dynamics Analysis

The vast majority of gas turbine systems employ swirl injectors that produce a central toroidal recirculation zone to serve as the dominant flame stabilization mechanism. As a result, over the past few years, extensive efforts have been made by the research community to understand the dynamics and stability of lean premixed swirl-stabilized combustion. The spatial distribution of the flame in the combustion chamber is governed by its stabilization location and can significantly influence the heat loadings to combustor hardware, thereby having important implications on combustor operability, durability, and emissions. For example, the heat transfer to the recirculation zones, the degree of flame spreading to combustor walls, or the location of the flame can be fundamentally different between flame configurations. In an acoustically uncoupled configuration, flames take on stationary configurations, anchoring within the shear layers of the flow, dependent upon geometry, Reynolds number and equivalence ratio. These aspects can consequently have implications on combustion stability as well.

The present work has investigated the influence of equivalence ratio variation on the flame-flow dynamics, for a laboratory-scale cylindrical sudden expansion swirl combustor, using the numerical LES code. Increasing the equivalence ratio can appreciably influence the dominant flow features in the wake region, including the size and shape of the recirculation zone(s), as well as the

flame dynamics. Specifically, varying the heat loading results in altering the dominant flame stabilization mechanism, thereby causing transitions across distinct flame configurations, while also modifying the inner recirculation zone topology significantly. It is observed that the numerical simulations can suitably predict the flame transition phenomena, and the results correspond well with the experimental measurements. Subsequently, the dynamic mode decomposition (DMD) technique has also been utilized to extract dynamic information from experimental and simulated data and to identify coherent flame-flow features. The approach allows for quantitative comparisons of the sizes and shapes of the unsteady modes, by comparing the modes obtained from numerical and experimental data samples respectively, and leads to clearer assessments of the strengths and weaknesses of the ability of the simulations to reproduce the measured dynamics. The DMD analysis of the PIV and LES data in this work suggests that the simulation framework can adequately capture the dynamic characteristics of the flow field, as observed in the experiments.

In addition to the swirl combustor geometry, backward-facing step configuration, in which the flame is stabilized in a two-dimensional turbulent mixing layer formed at the edge of the step, is also often employed to analyze the phenomenon of flame dynamics and understand turbulence-chemistry interactions in the context of lean premixed combustion. The setup preserves the essential features of premixed combustion with stabilization achieved by recirculation of hot products and is also a simpler configuration to observe and model. Over the past few years, numerous studies have been performed to assess the effect of combustion on the mean flow field properties such as mixing layer growth, entrainment rate, and reattachment length. The significant impact of modifying the equivalence ratio and/or fuel composition on the dynamic flow features has also been analyzed for wake-stabilized flames. Results have shown an intricate coupling between the flame anchoring and the recirculation zone structure and length, as well as shear layer growth rate, and it is now well known that the change of equivalence ratio can also significantly influence flame stability, and the phenomenon has been an active area of research in the past few years.

The present work has attempted to build upon the previous research by focusing on a laboratory-scale backward-facing step combustor, and investigating the influence of equivalence ratio variation on the flow features using state-of-the-art numerical techniques. Preliminary results show that the numerical framework reproduces the different topological flow features effectively and with reasonable accuracy, for the stable flame configurations. Additionally, the flame-flow interactions in acoustically forced scenarios are also analyzed using LES and dynamic mode decomposition (DMD). Specifically, acoustically forced numerical simulations are performed

corresponding to a self-excited combustion instability configuration as observed in the experiments, and it is observed that LES is able to suitably resolve the flame dynamics, and predicts the flame behavior corresponding to the experimental measurements. The DMD framework is also utilized to evaluate the dynamic characteristics of the combustion system from LES data, and reveals important information, not typically observed using conventional decomposition techniques such as POD. The fidelity of the solvers in predicting the system response to variation in heat loading and to acoustic forcing suggests that the LES framework can be suitably applied for the analysis of flame dynamics as well as to understand the fundamental mechanisms responsible for combustion instability.

THIS PAGE INTENTIONALLY LEFT BLANK

REFERENCES

Chapter 1

[1.1] Huang, Y., and Yang, V., "Dynamics and stability of lean-premixed swirl-stabilized combustion", Progress in Energy and Combustion Science, Vol. 35, 2009, pp. 293–364.
[1.2] Stone. C., and Menon, S., "Swirl control of combustion instabilities in a gas turbine combustor", Proceedings of the Combustion Institute, Vol. 29, Issue 1, 2002, pp 155-160.
[1.3] Schluter, J., "Static control of combustion oscillations by coaxial flows: a large eddy simulation investigation", Journal of Propulsion and Power, Vol. 20, Issue 3, pp 460-467.
[1.4] Franzelli, B., Riber, E., Gicquel, L., and Poinsot, T., "Large eddy simulation of combustion instabilities in a lean partially premixed swirl flame", Combust. Flame, Vol. 159, 2012, pp 621-637.
[1.5] Roux, S., Lartique, G., Poinsot, T., Meier, U., and Berat, C., "Studies of mean and unsteady flow in a swirled combustor using experiments, acoustic analysis, and large eddy simulations", Combustion and Flame, Vol. 141, Issues 1-2, 2005, pp 40-54.
[1.6] Huang, Y., Sung, H-G., Hsieh, S-H., and Yang V., "Large eddy simulation of combustion dynamics of lean premixed swirl stabilized combustor", Journal of Propulsion and Power, Vol. 19, Issue 5, 2003, pp 782-794.
[1.7] Angelberger, C., Veynante, D., Egolfopoulos, F., and Poinsot, T., "Large eddy simulations of combustion instabilities in premixed flames", Proc. of the Summer Program, Center for Turbulence Research, 1998.
[1.8] Fureby, C., "A Comparative Study of Flamelet and Finite Rate Chemistry LES for a Swirl Stabilized Flame", J. Eng. Gas Turbines Power, Vol. 134, Issue 4, 2012,
[1.9] Khanna, V.K., "A Study of the Dynamics of Laminar and Turbulent Fully and Partially Premixed Flames", PhD Thesis, Virginia Polytechnic Institute and State University, 2001.

Chapter 2

[2.1] Baudoin, E. "Large Eddy Simulation of Turbulent Premixed and Partially Premixed Combustion". Ph.D. Thesis, Lund Institute of Technology, 2010
[2.2] Durand, L., "Development, implementation and validation of LES models for inhomogeneously premixed turbulent combustion", Ph.D. Thesis, Technical University of Munich, 2007
[2.3] Wang, P. "Large Eddy Simulation of Turbulent Swirling Flows and Turbulent Premixed Combustion". Ph.D. Thesis, Lund Institute of Technology, 2005
[2.4] Lin, W., "Large-Eddy Simulation of Premixed Turbulent Combustion Using Flame Surface Density Approach", Ph.D. Thesis, University of Toronto, 2010.
[2.5] Garnier, E., Adams, N., and Sagaut, P., "Large eddy simulation for compressible flows", Springer, 2009.
[2.6] Perez, F.E.H., "Sub-filter scale modeling for large eddy simulation of lean hydrogen-enriched turbulent premixed combustion", Ph.D. Thesis, University of Toronto, 2011.
[2.7] Bilger, R.W., Pope, S.B., Bray, K.N.C., and Driscoll, J.F., "Paradigms in Turbulent Combustion Research", Proceedings of Combustion Institute 30, pp. 21-42, 2005.
[2.8] Manickam, B., Muppala, S.P.R., Franke, J., Dinkelacker, J.F., "Evaluation of algebraic flame surface wrinkling model for bluff body stabilized flames and large-eddy simulation quality assessment for non-reacting and combusting flows", Proceedings of European Combustoin Meeting, 2009.
[2.9] Lipatnikov, A.N., "Testing premixed turbulent combustion models by studying flame dynamics", International Journal of Spray and Combustion Dynamics", Vol. 1, Issue 1, pp. 39-66, 2009.
[2.10] Duclos, J.M., Veynante, D., and Poinsot, T., "A Comparison of Flamelet Models for Premixed Turbulent Combustion", Combustion and Flame, Vol. 95, pp. 101-117, 1993.
[2.11] Weller, H.G., Tabor, G., Gosman, A.D., and Fureby C., "Application of a Flame Wrinkling LES Combustion Model to a Turbulent Mixing Layer", 27th Symposium on Combustion, The Combustion Institute, pp. 899-907, 1998.
[2.12] Pitsch, H., and Lageneste, L.D., "Large-Eddy Simulation of Premixed Turbulent Combustion using a Level-Set Approach", Proceedings of Combustion Institute, Vol. 29, pp. 2001-2008, 2002.
[2.13] Bougrine, S., Richard, S., Colin, O., and Veynante, D., "Fuel Composition Effects on Flame Stretch in TurbulentPremixed Combustion: Numerical Analysis of Flame-Vortex Interaction and Formulation of a New Efficiency Function", Flow Turbulence and Combustion, Vol. 93 (2), pp. 259-281, 2014.
[2.14] Candel, S., and Poinsot, T., "Flame Stretch and the Balance Equation for the Flame Area", Combustion Science and Technology, Vol. 3, pp. 1-15, 1990.
[2.15] Colin, O., Ducros, F., Veynante, D., and Poinsot, T., "A Thickened Flame Model for Large Eddy Simulation of Turbulent Premixed Combustion," Phys. Fluids, Vol. 12, No. 7, pp. 1843–1863, 2000

[2.16] Charlette, F., Meneveau, C., and Veynante, D., "A Power-Law Flame Wrinkling Model for LES of Premixed Turbulent Combustion Part I: Non-Dynamic Formulation and Initial Tests," Combust. Flame, Vol. 131, pp. 159–180, 2002.
[2.17] Charlette, F., Meneveau, C., and Veynante, D., "A Power-Law Flame Wrinkling Model for LES of Premixed Turbulent Combustion Part II: Dynamic Formulation," Combustion and Flame, Vol. 131, pp. 181–197, 2002
[2.18] Karlsson, A., and Chomiak, J., "Flame Liftoff in Diesel Sprays", 26th Symposium on Combustion, pp. 2557-2564, 1996
[2.19] Norsin, P.A.N., "Complex Chemistry Modeling of Diesel Spray Combustion, Ph.D. Thesis, Imperial College of Science, Technology and Medicine, 2000
[2.20] Jones, W.P., and Lindstedt, R.P., "Global reaction schemes for hydrocarbon combustion," Combustion and Flame, Vol. 73, Issue 3, pp. 233-249, 1988
[2.21] Borghi, R., "Turbulent Combustion Modeling", Prog. Energy Combst. Sci., Vol. 14, pp.245-292, 1988.
[2.22] Veynante, D., and Vervisch, L., "Turbulent Combustion Modeling", Prog. Energy Combst. Sci., Vol. 28, pp.193-266, 2002.
[2.23] Vaos, E.M., and Lindstedt, R.P., "Transported PDF modeling of high-Reynolds-number premixed turbulent flames", Combustion and Flame, Vol. 145, pp. 495-511, 2006
[2.24] Haworth, D.C., "Progress in probability density function methods for turbulent reacting flows", Prog. Energy Combst. Sci., Vol. 36, pp.168-259, 2010.
[2.25] Bray, K.N.C., Champion, M., Libby, P.A., and Swaminathan, N., "Finite rate chemistry and presumed PDF models for premixed turbulent combustion", Combustion and Flame, Vol. 146, pp. 665-673, 2006.
[2.26] Echekki, T., and Mastorakos, E., "Turbulent Combustion Modeling: Advances, New Trends and Perspectives", Springer, 2011
[2.27] Westbrook, C.K., and Dryer, F.L., "Simplified Reaction Mechanisms for the Oxidation of Hydrocarbon Fuels in Flames", Combustion Science and Technology, Vol. 27, Issue 1-2, pp. 31-43, 1981.
[2.28] Andersen, J., Rasmussen, C.L., Giselsson, T., and Glarborg, P., "Global Combustion Mechanisms for Use in CFD Modeling under Oxy-Fuel Conditions", Energy and Fuels, Vol. 23, pp. 1379-1389, 2009.
[2.29] Westbrook, C.K., and Dryer, F.L., "Chemical Kinetic Modeling of Hydrocarbon Combustion", Prog. Energy Combst. Sci., Vol. 10, pp.1-57, 1984.
[2.30] Paczko, G., Lefdal, P.M., and Peters, N., "Reduced Reaction Schemes for Methane, Methanol, and Propane Flames", 21st Symposium on Combustion, pp. 739-748, 1986.
[2.31] Maas, U., and Pope, S.B., "Simplifying Chemical Kinetics: Intrinsic Low-Dimensional Manifolds in Composition Space", Combustion and Flame, Vol. 88, pp. 239-264, 1992.
[2.32] Kroeger, H., "Large-Eddy Simulation of Combustion Induced Vortex Breakdown in an Unconfined Turbulent Vortex using a Presumed-PDF Combustion Model", PhD Thesis, Rostock University, 2010.
[2.33] Oijen, J.A. van, "Flamelet-Generated Manifolds: Development and Application to Premixed Laminar Flames", PhD. Thesis, Technical University of Eindhoven, 2002.
[2.34] Nguyen, P-D, Vervisch, L., Subramanian, V., and Domingo, P., "Multidimensional flamelet-generated manifolds for partially premixed combustion", Combustion and Flame, Vol. 157, pp. 43-61, 2010.
[2.35] Strik, J., "Flamelet Generated Manifolds to Model Auto-ignition, Combustion and Pollutants in HDDI Diesel Engines", M.S. Thesis, Eindhoven University of Technology, 2010.

Chapter 3

[3.1] Echekki, T., "Turbulent combustion modeling: Advances, new trends and perspectives," Springer-Verlag, 2011.
[3.2] Roux, S., Lartigue, G., Poinsot, T., Meier, U., and Bérat, C., "Studies of mean and unsteady flow in a swirled combustor using experiments, acoustic analysis, and large eddy simulations", Combustion and Flame, Vol. 141, pp 40-54, 2005.
[3.3] Colin, O., Ducros, F., Veynante, D., and Poinsot, T., "A Thickened Flame Model for Large Eddy Simulation of Turbulent Premixed Combustion," Phys. Fluids, Vol. 12, No. 7, pp. 1843–1863, 2000.
[3.4] Strakey, P.A., and Eggenspieler, G., "Development and Validation of a Thickened Flame Modeling Approach for Large Eddy Simulation of Premixed Combustion", Journal of Engineering for Gas Turbines and Power, Vol. 132, 2010.
[3.5] Charlette, F., Meneveau, C., and Veynante, D., "A Power-Law Flame Wrinkling Model for LES of Premixed Turbulent Combustion Part I: Non-Dynamic Formulation and Initial Tests," Combust. Flame, Vol. 131, pp. 159–180, 2002.
[3.6] Charlette, F., Meneveau, C., and Veynante, D., "A Power-Law Flame Wrinkling Model for LES of Premixed Turbulent Combustion Part II: Dynamic Formulation," Combustion and Flame, Vol. 131, pp. 181–197, 2002.
[3.7] Weller, H.G., Tabor, G., Gosman, A.D., and Fureby C., "Application of a Flame Wrinkling LES Combustion

Model to a Turbulent Mixing Layer", 27th Symposium on Combustion, The Combustion Institute, pp. 899-907, 1998.
[3.8] Steinberg, A.M., Driscoll, J.F., "Straining and wrinkling processes during turbulence–premixed flame interaction measured using temporally-resolved diagnostics", Combustion and Flame, Vol. 156, Issue 12, pp. 2285-2306, 2009.
[3.9] Driscoll, J.F., "Turbulent premixed combustion: Flamelet structure and its effect on turbulent burning velocities", Prog. Energy Combst. Sci., Vol. 34, pp.91-134, 2008.
[3.10] Mueller, C.J., Driscoll, J.F., Sutkus, D.J., Roberts, W.L., Drake, M.C., and Smooke, M.D., "Effect of unsteady stretch rate on OH chemistry during a flame-vortex interaction: To assess flamelet models", Combustion and Flame, Vol. 100 (1-2), pp. 323-331, 1995.
[3.11] Selle, L., lartigue, G., Poinsot, T., Kaufmann, P., Krebs, W., and veynante, D., "Large Eddy Simulation of Turbulent Combustion for Gas Turbines with Reduced Chemistry", Proc. of Summer Program 2002, Center for Turbulence Research.
[3.12] Durand, L., and Polifke, W., "Implementation of the Thickened Flame Model for Large Eddy Simulation of Turbulent Premixed Combustion in a Commercial Solver," ASME Paper No. GT2007-28188, 2007.
[3.13] Polifke, W., Hirsch, C., Zellhuber, M., Komarek, T., and Chong, L., "Influence of strain and heat loss on flame stabilization in a non-adiabatic combustor", Proceedings of the European Combustion Meeting, 2009.
[3.14] Tabor, G, and Weller, H.G., "Large Eddy Simulation of Premixed Turbulent Combustion Using Ξ Flame Surface Wrinkling Model", Flow, Turbulence and Combustion, Vol. 72, pp. 1-28, 2004.
[3.15] Fichot, F., Lacas, F., Veynante, D., and Candel, S., "One-Dimensional Propagation of a Premixed Turbulent Flame With a Balance Equation for the Flame Surface Density", Combustion Science and Technology, Vol. 90, Issue 1, pp. 35-60, 1993.
[3.16] Hawkes, E.R., and Cant, R.S., "Implications of a Flame Surface Density Approach to Large Eddy Simulation of Premixed Turbulent Combustion", Combustion and Flame, Vol. 126, pp. 1617-1629, 2001.
[3.17] Trouve, A., and Poinsot, T., "The evolution equation for the flame surface density in turbulent premixed combustion", J. Fluid Mech., Vol. 278, pp. 1-31, 1994.
[3.18] Stahl, G, and Warnatz, J., "Numerical Investigation of Time-Dependent Properties and Extinction of Strained Methane- and Propane-Air Flamelets", Combustion and Flame, Vol. 85, pp. 285-299, 1991.
[3.19] Jones, W.P., and Lindstedt, R.P., "Global reaction schemes for hydrocarbon combustion," Combustion and Flame, Vol. 73, Issue 3, pp. 233-249, 1988.
[3.20] Hilbert, R., Tap, F., El-Rabii, H., and Thevenin, D., "Impact of detailed chemistry and transport models on turbulent combustion simulations", Progress in Energy and Combustion Science 30, pp. 61-117, 2004.
[3.21] Altay, H.M., Speth, R.L., Hudgins, D.E., and Ghoniem, A.F., "Flame–vortex interaction driven combustion dynamics in a backward-facing step combustor", Combustion and Flame, Vol. 156, pp. 1111-1125, 2009.
[3.22] Hong, S., Shanbhogue, S.J. and Ghoniem, A.F., "Impact of fuel composition on the recirculation zone structure and its role in lean premixed flame anchoring", Proceedings of the Combustion Institute, 35th International Symposium on Combustion, 2014.
[3.23] Giacomazzi, E., Battaglia, V., and Bruno, C., "The Coupling of Turbulence and Chemistry in a Premixed Bluff-Body Flame as Studied by LES". Combustion and Flame, Vol. 138, pp. 320-335, 2004.
[3.24] Cocks, P., Sankaran, V., and Soteriou, M., "Is LES of reacting flows predictive? Part1: Impact of numerics". AIAA Paper No. 2013-0170, 51st AIAA Aerospace Sciences Meeting, 2013.
[3.25] Porumbel, I., and Menon, S., "Large Eddy Simulation of Bluff-Body Stabilized Premixed Flame", 44th AIAA Aerospace Sciences Meeting and Exhibit, AIAA 2006-152, 2006.
[3.26] Fureby, C., "A Comparison of Flamelet LES Models for Premixed Turbulent Combustion", 44th AIAA Aerospace Sciences Meeting and Exhibit, AIAA 2006-155, 2006.
[3.27] Pope, S.B., "Turbulent Flows", Cambridge University Press, 2000
[3.28] Winter, H., "Viscous Dissipation Term in Energy Equations", AICHE Modular Instruction, Series C: Transport, Volume 7: Calculation and Measurement Techniques for Momentum, Energy and Mass Transfer, Module C 7.4, 1987.
[3.29] Pan J.C., Vangsness M.D., Ballal D.R., "Aerodynamics of Bluff-Body Stabilized Confined Turbulent Premixed Flames", J. Eng. Gas Turbines Power, Vol. 114, Issue 4, pp 783-789, 1992.
[3.30] Shabarian, N., Tullis, S., "Dilatation, Flame Strain and Curvature in Turbulent Premixed Flames using Direct Numerical Simulations", Proceedings of Combustion Institute – Canadian Section Spring Technical MeetingUniversity of Toronto, OntarioMay 12-14, 2008.
[3.31] Pitz, R.W., and Daily, J.W., "Combustion in a Turbulent Mixing Layer Formed at a Rearward Facing Step", AIAA Journal, Vol. 21, Issue 11, pp. 1565-1570, 1983.
[3.32] Fureby, C., "Comparison of Flamelet and Finite Rate Chemistry LESfor Premixed Turbulent Combustion". AIAA Paper No. 2007-1413, 45th AIAA Aerospace Sciences Meeting, 2007.

Chapter 4

[4.1] Haworth, D.C., "Progress in probability density function methods for turbulent reacting flows", Progress in Energy and Combustion Science, 36 (2010) 168–259.
[4.2] Kröger, H., Hassel, E., Kornev, N., Wendig, D., "LES of Premixed Flame Propagation in a Free Straight Vortex", Flow, Turbulence and Combustion, Vol 84, Issue 3, pp 513-541, 2010.
[4.3] Sadasivuni, S.K., "LES modelling of non-premixed and partially premixed turbulent flames", PhD Thesis, Loughborough University, 2009.
[4.4] Olbricht, C., Hahn, F., Ketelheun, A., and Janicka, J., "Strategies for presumed PDF modeling for LES with premixed flamelet-generated manifolds", Journal of Turbulence, Vol 11, No 38, pp 1-18, 2010.
[4.5] Pope, S.B., "PDF Methods for Turbulent Reactive Flows", Prog. Energy Combust. Sci., Vol. 11, pp. 119-192, 1985.
[4.6] Kolla, H., and Swaminathan, N., "Strained flamelets for turbulent premixed flames, I: Formulation and planar flame results", Combustion and Flame, 157 (2010) 943–954.
[4.7] Kolla, H., and Swaminathan, N., "Modelling of Turbulent Premixed Flames using Strained-Flamelets", Proceeding of the European Combustion Meeting, 2009.
[4.8] Najafi-Yazdi, A., Cuenot, B., and Mongeau, L., "Systematic definition of progress variables and Intrinsically Low-Dimensional, Flamelet Generated Manifolds for chemistry tabulation", Combustion and Flame, Vol. 159, pp. 1197-1204, 2012.
[4.9] Maas, U., and Pope, S.B., "Simplifying Chemical Kinetics: Intrinsic Low-Dimensional Manifolds in Composition Space", Combustion and Flame, Vol. 88, pp. 239-264, 1992.
[4.10] Oijen, J.A. van, and De Goey, L.P.H, "Modelling of Premixed Laminar Flames using Flamelet Generated Manifolds", Combustion Science and Technology, Vol. 161, Issue 1, pp. 113-137, 2000.
[4.11] F.E. Hernández-Pérez, F.T.C. Yuen, C.P.T. Groth, Ö.L. Gülder, "LES of a laboratory-scale turbulent premixed Bunsen flame using FSD, PCM-FPI and thickened flame models", Proceedings of the Combustion Institute, Volume 33, Issue 1, 2011, Pages 1365-1371
[4.12] B Fiorina, R Baron, O Gicquel, D Thevenin, S Carpentier & N Darabiha (2003): Modelling non-adiabatic partially premixed flames using flame-prolongation of ILDM, Combustion Theory and Modelling, 7:3, 449-470
[4.13] T. Poinsot, D. Veynante and S. Candel (1991). Quenching processes and premixed turbulent combustion diagrams. Journal of Fluid Mechanics, 228, pp 561-606
[4.14] D. Bradley, P.H. Gaskell, X.J. Gu, A. Sedaghat, Premixed flamelet modelling: Factors influencing the turbulent heat release rate source term and the turbulent burning velocity, Combustion and Flame, Volume 143, Issue 3, November 2005, Pages 227-245
[4.15] Yung-Cheng Chen, Robert W. Bilger, Experimental investigation of three-dimensional flame-front structure in premixed turbulent combustion—I: hydrocarbon/air bunsen flames, Combustion and Flame, Volume 131, Issue 4, December 2002, Pages 400-435
[4.16] Weller, H.G., Tabor, G., Gosman, A.D., and Fureby C., "Application of a Flame Wrinkling LES Combustion Model to a Turbulent Mixing Layer", 27th Symposium on Combustion, The Combustion Institute, pp. 899-907, 1998.
[4.17] Polifke, W., Hirsch, C., Zellhuber, M., Komarek, T., and Chong, L., "Influence of strain and heat loss on flame stabilization in a non-adiabatic combustor", Proceedings of the European Combustion Meeting, 2009
[4.18] Chterev, I., Foti, D., Seitzman, J., Menon, S. and Lieuwen, T., "Flow Field Characterization in a Premixed, Swirling Annular Flow," AIAA-2012-0450, 50th AIAA Aerospace Sciences Conference, Nashville, January 2012
[4.19] B. Fiorina, O. Gicquel, L. Vervisch, S. Carpentier, N. Darabiha, Premixed turbulent combustion modeling using tabulated detailed chemistry and PDF, Proceedings of the Combustion Institute, Volume 30, Issue 1, January 2005, Pages 867-874
[4.20] Kroeger, H., "Large-Eddy Simulation of Combustion Induced Vortex Breakdown in an Unconfined Turbulent Vortex using a Presumed-PDF Combustion Model", PhD Thesis, Rostock University, 2010.
[4.21] Pascale Domingo, Luc Vervisch, Sandra Payet, Raphaël Hauguel, DNS of a premixed turbulent V flame and LES of a ducted flame using a FSD-PDF subgrid scale closure with FPI-tabulated chemistry, Combustion and Flame, Volume 143, Issue 4, December 2005, Pages 566-586
[4.22] Ken Bray, Michel Champion, Paul A. Libby, N. Swaminathan, Scalar dissipation and mean reaction rates in premixed turbulent combustion, Combustion and Flame, Volume 158, Issue 10, October 2011, Pages 2017-2022
[4.23] Kolla, H., "Scalar Dissipation Rate based Flamelet Modelling of Turbulent Premixed Flames", PhD Thesis, University of Cambridge, 2009.
[4.24] Chakraborty, N., Rogerson, J.W., and Swaminathan, N., "A priori assessment of closures for scalar dissipation rate transport in turbulent premixed flames using direct numerical simulation", Physics of Fluids, Vol. 20, 2008.
[4.25] Swaminathan, N., and Bray. K.N.C., "Effect of dilatation on scalar dissipation in turbulent premixed flames", Combustion and Flame, Vol. 143, pp. 549-565, 2005.

[4.26] Bray, K.N.C., Champion, M., Libby, P.A., and Swaminathan, N., "Finite rate chemistry and presumed PDF models for premixed turbulent combustion", Combustion and Flame, Vol. 146, pp. 665-673, 2006.
[4.27] Nandula, S. P., Pitz, R. W., Barlow, R. S., and Fiechtner, G. J. (1996). AIAA 96-0937, .
[4.28] Nanduri, Assessment of RANS-Based Turbulent Combustion Models for Prediction of Emissions from Lean Premixed Combustion of Methane (2010).
[4.29] Pope, S.B., "Turbulent Flows", Cambridge University Press, 2000
[4.30] D. R. Ballal, S. P. Heneghan, W. J. Schmoll, F. Takahashi, and M. D. Vangsness , "Combustion and Heat Transfer studies utilizing Advanced Diagnostics", University of Dayton, Report WL-TR-92-2110, November 1992.
[4.31] Pan. J.C., and Ballal, D.R., "Chemistry and Turbulence Effects in Bluff-Body Stabilized Flames", 30th AIAA Aerospace Sciences Meeting and Exhibit, AIAA 92-0771, 1992.
[4.32] Cannon, S.M., Brewster, B.S., and Smoot, L.D. 1999. PDF modeling of lean premixed combustion using in situ tabulated chemistry. Combustion and Flame, 119, 233–252.
[4.33] Vicente, W., Salinas, M., Barrios, E., and Dopazo, C. 2004. PDF modeling of CO and NO formation in lean premixed methane flames. Combustion Science and Technology, 176, 585–601.
[4.34] Shabazian, N., Tullis, S., "Dilatation, Flame Strain and Curvature in Turbulent Premixed Flames using Direct Numerical Simulations", Proceedings of Combustion Institute – Canadian SectionSpring Technical MeetingUniversity of Toronto, OntarioMay 12-14, 2008.
[4.35] Winter, H., "Viscous Dissipation Term in Energy Equations", AICHE Modular Instruction, Series C: Transport, Volume 7: Calculation and Measurement Techniques for Momentum, Energy and Mass Transfer, Module C 7.4, 1987.

Chapter 5

[5.1] Schmid, P., "Dynamic mode decomposition of numerical and experimental data", J. Fluid Mech., Vol. 656, pp. 5-28, 2010
[5.2] Schmid, P.J., "Application of the dynamic mode decomposition to experimental data", Exp Fluids, Vol. 50, pp. 1123-1130, 2011.
[5.3] Schmid, P.J., "Dynamic mode decomposition of numerical and experimental data", J. Fluid Mech., Vol. 656, pp. 5-28, 2010.
[5.4] Schmid, P.J., "Dynamic Mode Decomposition of experimental data", 8th International Symposium on Particle Image Velocitmetry, 2009.
[5.5] Schmid, P.J., Meyer, K.E., and Pust, O., "Dynamic Mode Decomposition and Proper Orthogonal Decomposition of flow in a lid-driven cylindrical cavity", 8th International Symposium on Particle Image Velocitmetry, 2009.
[5.6] Schmid, P.J., Li, L., Juniper, M.P., and Pust, O., "Applications of the dynamic mode decomposition", Theoretical and Computational Fluid Dyanmics.
[5.7] Iucidiani, P., "Swirl stabilized premixed flame analysis using LES and POD", PhD. Thesis, Lund University, 2012.
[5.8] Abdurakipov, S.S., Dulin, V.M., Kozorezov, Y.S., Markovich, D.M., "Dynamics of Large-Scale Vortices in Periodically Forced Strongly Swirling Jets and Lifted Flames Investigated by Stereo PIV and DMD", 16th Int. Symp. on Applications of Laser Techniques to Fluid Mechanics, 2012.
[5.9] Gilka, G., Luchtenburg, D.M., Thiele, F., Morzynski, M., "Dynamic Characterization of an Actuated Bluff-Body Wake", V European Conference on Computational Fluid Dynamics, ECCOMAS CFD 2010.
[5.10] Sarmast, S., "Numerical study on instability and interaction of wind turbine wakes", Thesis, Royal Institute of Technology, 2013.
[5.11] Tissot, G., Noack, B.R., "Dynamic Mode Decomposition of PIV Measurements for Cylinder Wake Flow in Turbulent Regime", 2012
[5.12] Nour, Z.M., "Simulation and modal analysis of instability and transition in a steady eccentric stenotic flow", MS Thesis, KTH Stockholm, 2013
[5.13] Luchtenburg, D.M., and Frederich, O., "Modal Analysis of Complex Turbulent Flow", 7th International Symposium on Turbulence and Shear Flow Phenomena (TSFP-7), Ottawa, Canada, July 28-31, 2011
[5.14] Seena, A., and Sung, H.J., "Dynamic mode decomposition of turbulent cavity flows for self-sustained oscillations", Int. J. Heat and Fluid Flow, Vol. 32, pp. 1098-1110, 2011

Chapter 6

[6.1] Huang, Y., and Yang, V., "Dynamics and stability of lean-premixed swirl-stabilized combustion", Progress in Energy and Combustion Science, Vol. 35, 2009, pp. 293–364
[6.2] Gicquel, L.Y.M., Staffelbach, G., and Poinsot, T., "Large Eddy Simulations of gaseous flames in gas turbine combustion chambers", Prog. Energy and Combust. Sci., Vol. 38, pp. 782-817, 2012.

[6.3] Yoon, C., Geiji, R., Anderson, W.E., Sankaran, V., "Computational Investigation of Combustion Dynamics in a Lean Direct Injection Gas Turbine Combustor", 51st AIAA Aerospace Sciences Meeting including the New Horizons Forum and Aerospace Exposition, AIAA 2013-0166, 2013.
[6.4] Lu X., Wang, S, Sung, H-G, Hsieh, S-Y, and Yang, V., "Large-eddy simulations of turbulent swirling flows injected into a dump chamber", J. Fluid Mech., Vol. 527, pp. 171-195, 2005.
[6.5] Huang, Y., and Yang, V., "Effect of swirl on combustion dynamics in a lean-premixed swirl-stabilized combustor", Proceedings of Combustion Institute, Vol. 30, pp. 1775-1782, 2005.
[6.6] Huang, Y., Sung, H-G, Hsieh, S-Y, and Yang, V., "Large-Eddy Simulation of Combustion Dynamics of Lean-Premixed Swirl-Stabilized Combustor", Journal of Propulsion and Power, Vol. 19, Issue 5, 2003.
[6.7] Wang, S, Hsieh, S-Y, and Yang, V., "Unsteady flow evolution in swirl injector with radial entry. I. Stationary conditions", Physics of Fluids, Vol. 17, 2005.
[6.8] Huang, Y., and Yang, V., "Bifurcation of flame structure in a lean-premixed swirl-stabilized combustor: transition from stable to unstable flame", Combustion and Flame, Vol. 136, pp. 383-389, 2004.
[6.9] Altay, H.M., Speth, R. L., Hudgins, D. E. and Ghoniem, A.F., "The impact of equivalence ratio oscillations on combustion dynamics in a backward facing step combustor " Combustion and Flame , Vol. 156, 2009, pp.2106-2116
[6.10] Speth, R., Altay, H., Hudgins, D., Annaswamy, A., and Ghoniem, A. "Vortex-Driven Combustion Instabilities in Step and Swirl-Stabilized Combustors", in the 46th AIAA Aerospace Sciences Meeting, Reno, NV, January 2008
[6.11] D. R. Ballal, S. P. Heneghan, W. J. Schmoll, F. Takahashi, and M. D. Vangsness , "Combustion and Heat Transfer studies utilizing Advanced Diagnostics", University of Dayton, Report WL-TR-92-2110, November 1992
[6.12] Chterev, I., Foti, D., Seitzman, J., Menon, S. and Lieuwen, T., "Flow Field Characterization in a Premixed, Swirling Annular Flow," AIAA-2012-0450, 50th AIAA Aerospace Sciences Conference, Nashville, January 2012
[6.13] Markovich, D.M., Abdurakipov, S.S., Chikishev, L.M., and Dulin, V.M., "PIV study of vortex breakdown in low- and high-swirl flames in a model combustor", 10th International Symposium on Particle Image Velocimetry, 2013.
[6.14] Abdurakipov, S.S., Dulin, V.M., Kozorezov, Y.S., Markovich, D.M., "Dynamics of Large-Scale Vortices in Periodically Forced Strongly Swirling Jets and Lifted Flames Investigated by Stereo PIV and DMD", 16th Int. Symp. on Applications of Laser Techniques to Fluid Mechanics, 2012
[6.15] Abdurakipov, S.S., Alekseenko, S.V., Dulin, V.M., and Markovich, D.M., "Application of DMD to PIV Velocity Fields Measured in Forced Jets and Lifted Flames", 15th International Symposium on Flow Visualization, 2012.
[6.16] Taamallah, S., LaBry, Z.A., Shanbhogue, S.J. and Ghoniem, A.F., "Correspondence between uncoupled flame macrostructures and thermoacoustic instability in premixed swirl-stabilized combustion", Proceedings of ASME Turbo Expo 2014, 16-20 June 2014 (accepted/to be presented), Dusseldorf, Germany, Paper # GT2014-27316
[6.17] LaBry, Z., Shanbhogue, S., Speth, R., and Ghoniem, A., "Flow structures in a lean-premixed swirl-stabilized combustor with microjet air injection", Proceedings of the Combustion Institute, Vol. 33, pp 1575-1581, 2011
[6.18] Wang, P.W., Bai, X.S., Wessman, M., and Klingmann, J., "Large eddy simulation and experimental studies of a confined turbulent swirling flow", Physics of Fluid, Vol. 16, Issue 9, 2004.
[6.19] Paik, J., and Sotiropoulos, F., "Numerical simulation of strongly swirling turbulent flows through an abrupt expansion", International Journal of Heat and Fluid Flow, Vol. 31, pp. 390-400, 2010.
[6.20] Winter, H., "Viscous Dissipation Term in Energy Equations", AICHE Modular Instruction, Series C: Transport, Volume 7: Calculation and Measurement Techniques for Momentum, Energy and Mass Transfer, Module C 7.4, 1987.
[6.21] Taamallah, S., Vogiatzaki, K, Kewlani, G, GHoniem A, "Influence of Boundary Layer Trip on Non–Swirling and Swirling Reacting Jets Using Large Eddy Simulation", SIAM Numerical Combustion Conference, Texas, 2013
[6.22] Shabazian, N., Tullis, S., "Dilatation, Flame Strain and Curvature in Turbulent Premixed Flames using Direct Numerical Simulations", Proceedings of Combustion Institute – Canadian SectionSpring Technical MeetingUniversity of Toronto, OntarioMay 12-14, 2008.
[6.23] "Determining Instability Modes in a Gas Flame", S. S. AbdurakipovV. M. Dulin, D. M. Markovich*, and K. Hanjalic
[6.24] Pan J.C., Vangsness M.D., Ballal D.R., "Aerodynamics of Bluff-Body Stabilized Confined Turbulent Premixed Flames", J. Eng. Gas Turbines Power, Vol. 114, Issue 4, pp 783-789, 1992
[6.25] Polifke, W., Hirsch, C., Zellhuber, M., Komarek, T., and Chong, L., "Influence of strain and heat loss on flame stabilization in a non-adiabatic combustor", Proceedings of the European Combustion Meeting, 2009
[6.26] Tay-Wo-Chong, L., and Polifke, W., "Large Eddy Simulation-Based Study of the Influence of Thermal Boundary Condition and Combustor Confinement on Premix Flame Transfer Functions", Journal of Engineering for Gas Turbines and Power, Vol. 135, 2013.
[6.27] LaBry, Z.A., Taamallah,S., Kewlani, G., Shanbhogue, S.J. and Ghoniem, A.F., "Mode transition and intermittency in an acoustically uncoupled lean premixed swirl-stabilized combustor", Proceedings of ASME Turbo Expo 2014, 16-20 June 2014 (accepted/to be presented), Dusseldorf, Germany, Paper # GT2014-27266

[6.28] Cheng, H., Harvazinski, M., Anderson, W., and Sankaran, V., "Analysis of Self-Excited Combustion Instability using Decomposition Techniques", 51st AIAA Aerospace Sciences Meeting including the New Horizons Forum and Aerospace Exposition, AIAA 2013-1007, 2013

Chapter 7

[7.1] Sawyer, R., Ganji, A, "An experimental study of the flow field of a 2D premixed turbulent flame", AIAA, 1980
[7.2] Pitz, R.W., and Daily, J.W., "Combustion in a Turbulent Mixing Layer Formed at a Rearward-Facing Step", AIAA Journal, Vol. 21, Issue 11, 1983.
[7.3] Thurston, D.W., "An experimental investigation of flame spreading from bluff body flameholders", Engineer Thesis, California Institute of Technology, 1958
[7.4] Hong, S., Shanbhogue, S.J. and Ghoniem, A.F., "Impact of fuel composition on the recirculation zone structure and its role in lean premixed flame anchoring"", Proceedings of the Combustion Institute, in press, 2014, accepted for oral presentation in the 35th International Symposium on Combustion, 2014
[7.5] Pan J.C., Vangsness M.D., Ballal D.R., "Aerodynamics of Bluff-Body Stabilized Confined Turbulent Premixed Flames", J. Eng. Gas Turbines Power, Vol. 114, Issue 4, pp 783-789, 1992
[7.6] D. R. Ballal, S. P. Heneghan, W. J. Schmoll, F. Takahashi, and M. D. Vangsness , "Combustion and Heat Transfer studies utilizing Advanced Diagnostics", University of Dayton, Report WL-TR-92-2110, November 1992
[7.7] Pan, J.C., Schmoll, W.J., and Ballal, D.R., "Turbulent Combustion Properties Behind a Confined Conical Stabilizer", Journal of Engineering for Gas Turbines and Power, Vol. 114, 1992
[7.8] LaBry, Z.A., Taamallah,S., Kewlani, G., Shanbhogue, S.J. and Ghoniem, A.F., "Mode transition and intermittency in an acoustically uncoupled lean premixed swirl-stabilized combustor", Proceedings of ASME Turbo Expo 2014, 16-20 June 2014 (accepted/to be presented), Dusseldorf, Germany, Paper # GT2014-27266
[7.9] Speth, R., Altay, H., Hudgins, D., Annaswamy, A., and Ghoniem, A. "Vortex-Driven Combustion Instabilities in Step and Swirl-Stabilized Combustors", in the 46th AIAA Aerospace Sciences Meeting, Reno, NV, January 2008
[7.10] LaBry, Z., Shanbhogue, S., Speth, R., and Ghoniem, A., "Flow structures in a lean-premixed swirl-stabilized combustor with microjet air injection", Proceedings of the Combustion Institute, Vol. 33, pp 1575-1581, 2011
[7.11] Hong, S., Speth, R. L., Shanbhogue, S. J., Ghoniem, A. F., "Examining flow-flame interaction and the characteristic stretch rate in vortex-driven combustion dynamics using PIV and numerical simulation ", Combustion and Flame, Vol.160(8), pp.1381-1397, 2013
[7.12] Speth, R.L., Hong, S., Shanbhogue, S.J. and Ghoniem A.F., "Mode Selection in Flame-Vortex Driven Combustion Instabilities", 49th AIAA Aerospace Sciences Meeting, 4-7 January 2011, Orlando, Florida, Paper # AIAA2011-236
[7.13] Altay, H.M., Speth, R. L., Hudgins, D. E. and Ghoniem, A.F., "The impact of equivalence ratio oscillations on combustion dynamics in a backward facing step combustor " Combustion and Flame , Vol. 156, 2009, pp.2106-2116
[7.14] Khanna, V.K., "A Study of the Dynamics of Laminar and Turbulent Fully and Partially Premixed Flames", PhD Thesis, Virginia Polytechnic Institute and State University, 2001
[7.15] Wake, B.E., Choi, D., and Hendricks, G.J., "Numerical investigation of pre-mixed step-combustor instabilities", 34th AIAA Aerospace Sciences Meeting and Exhibit, AIAA 96-0816, 1996.
[7.16] Ghoniem, A.F., Park, S.P., Wachsman, A., Annaswamy, A., Wee, D., and Altay, H.M., "Mechanism of combustion dynamics in a backward-facing step stabilized premixed flame", Proceedings of Combustion Institute 30, pp.1783-1790, 2005.
[7.17] Altay, H.M., Speth, R.L., Hudgins, D.E., and Ghoniem, A.F., "Flame–vortex interaction driven combustion dynamics in a backward-facing step combustor", Combustion and Flame, Vol. 156, pp. 1111-1125, 2009.
[7.18] Najm, H.N., and Ghoniem, A.F., "Modeling Pulsating Combustion Due To Flow-Flame Interactions In Vortex-Stabilized Pre-mixed Flames", Combustion Science and Technology, Vol. 94, Issue1-6, pp. 259-278, 1993.
[7.19] Pope, S.B., "Turbulent Flows", Cambridge University Press, 2000
[7.20] Rajasekaran, J., "On the flow characteristics behind a backward-facing step and the design of a new axisymmetric model for their study", MS Thesis, University of Toronto, 2011
[7.21] Johnston, J., and Eaton, J., "A Review of Research on Subsonic Turbulent Flow Reattachment", AIAA Journal, Vol. 19, No. 9, 1981
[7.22] Rani, H.P., Sheu, T.W.H., and Tsai, E.S.F., "Eddy structures in a transitional backward-facing step flow", J. Fluid Mech., Vol. 588, pp. 43-58, 2007.
[7.23] Neto, A.S., Grand, D., Metais, O., and Lesieur, M., "A numerical investigation of the coherent vortices in turbulence behind a backward-facing step", J. Fluid Mech., Vol. 256, pp. 1-25, 1993.
[7.24] Chapparo, A., Landry, E., and Cetegen, B.M., "Transfer function characteristics of bluff-body stabilized, conical V-shaped premixed turbulent propane–air flames", Combustion and Flame, Vol. 145, pp. 290-299, 2006.

[7.25] Shreekrishna, "Response mechanisms of attached premixed flames subjected to harmonic forcing", PhD Thesis, Georgia Institute of Technology, 2011
[7.26] Krediet, H.J., Beck, C.H., Krebs, W., Schimek, S., and Paschereit, C.O., "Identification of the Flame Describing Function of a Premixed Swirl Flame from LES", MCS7, 2011.
[7.27] Chong, L.T.W., Komarek, T., Kaess, R., Foller, S., and Polifke, W., "Identification of Flame Transfer Functions from LES of a Premixed Swirl Burner", Proceedings of ASME Turbo-Expo 2010: Power for Land, Sea and Air, GT2010-22769, 2010.
[7.28] Pallies, P., Durox, D., Schuller, T., and Candel, S., "The combined dynamics of swirler and turbulent premixed swirling flames", Combustion and Flame, Vol. 157, pp. 1698-1717, 2010.
[7.29] Wang, S., and Yang, V., "Unsteady flow evolution in swirl injectors with radial entry. II. External excitations", Physics of Fluids, Vol. 17, 2005.
[7.30] Li, H-G, Sung, H-G, and Yang, V., "Large Eddy Simulation of Combustion Dynamics of Bluff Body Stabilized Flame", 49th AIAA Aerospace Sciences Meeting including the New Horizons Forum and Aerospace Exposition, AIAA 2011-783, 2011.
[7.31] Thibaut, D., and Candel, S., "Numerical Study of Unsteady Turbulent Premixed Combustion: Application to Flashback Simulation", Combustion and Flame, Vol. 113, pp. 53-65, 1998.
[7.32] Balachandran, R., Dowling, A.P., and Mastorakos, E., "Non-linear Response of Turbulent Premixed Flames to Imposed Inlet Velocity Oscillations of Two Frequencies", Flow Turbulence Combust, Vol. 80, pp. 455-487, 2008.
[7.33] Angelberger, C., Veynante, D., Egolfopoulos, F., and Poinsot, T., "Large eddy simulations of combustion instabilities in premixed flames", Proceedings of Summer Program, Center for Turbulence Research, 1998.
[7.34] Angelberger, C., Veynante, D., and Egolfopoulos, F., "LES of Chemical and Acoustic Forcing of a Premixed Dump Combustor", Flow, Turbulence and Combustion, Vol. 65, pp. 205-222, 2000.
[7.35] Sankaran, V., Erickson, R.R., and Soteriou, M.C., "Effects of Acoustic Excitation on Bluff-body Stabilized Premixed Reacting Flows", 48th AIAA Aerospace Sciences Meeting including the New Horizons Forum and Aerospace Exposition, AIAA 2010-1333, 2010.
[7.36] Armitage, C.A., Balachandran, R., Mastorakos, E., and Cant, R.S., "Investigation of the nonlinear response of turbulent premixed flames to imposed inlet velocity oscillations", Combustion and Flame, Vol. 146, pp. 419-436, 2006.
[7.37] Cheng, H., Harvazinski, M., Anderson, W., and Sankaran, V., "Analysis of Self-Excited Combustion Instability using Decomposition Techniques", 51st AIAA Aerospace Sciences Meeting including the New Horizons Forum and Aerospace Exposition, AIAA 2013-1007, 2013